ULTRASONIC TRANSDUCER CALIBRATION

by

R.G. White, B.A.

A Doctoral Thesis

Submitted in partial fulfilment of the requirements

for the award of

Doctor of Philosophy

of Loughborough University of Technology

September 1984

Supervisor: Dr. D.C. Emmony

ACKNOWLEDGEMENTS

The author would like to thank his supervisor Dr. D.C. Emmony for his help and guidance throughout the course of study. Thanks are also due to Mr. M.W. Godfrey, who developed a large portion of the computing facility used to process many of the results in this work, to Mr. R. Smith for his technical assistance, and to Miss P. Hurst for her patience in typing the manuscript.

The author would also like to thank the two sponsors of the work, the Admiralty Marine Technology Establishment at Holten Heath and Risley Nuclear Laboratories of the United Kingdom Atomic Energy Authority.

SUMMARY

When a material is placed under stress, small changes within the specimen release ultrasonic energy in the form of stress waves. The change may, for example, be a dislocation movement or the advancement of a crack tip. These ultrasonic pulses are termed Acoustic Emission and may be detected at the material surface by ultrasonic transducers. The detected pulse shape is related to the generating source, to the material geometry through which the pulse propagates and to the response of the ultrasonic transducer used to detect the waves. Work has been carried out to measure both the effect of wave propagation and to calibrate the response of ultrasonic transducers.

Three types of ultrasonic wave may exist in a material with a non-zero shear modulus; these are longitudinal waves, shear waves and surface or Rayleigh waves. In a large number of specimen geometries, the surface wave has the largest amplitude. The response of a transducer to this wave is therefore very important. Most transducers respond to the out of plane motion of a material surface carrying ultrasonic waves. Therefore, to successfully calibrate a transducer, some absolute measurement of the out of plane motion due to surface waves must be made. An interferometer has been designed and constructed for this purpose.

The calibration of ultrasonic transducers has enabled some development work to be carried out on high-fidelity piezoelectric transducers and on piezomagnetic transducers.

It is not always possible to measure an ultrasonic pulse

directly with a calibrated interferometric detector and therefore to enable a wider range of propagation problems to be investigated, various methods of ultrasonic pulse generation have been studied. These artificial sources of acoustic emission have included brittle fracture, laser impact and stimulation by piezoelectric transducers. This work has enabled theoretical calculations on pulse propagation to be verified.

CONTENTS PAGE

I. INTRODUCTION

The measurement of ultrasonic waves occurs in a number of different applications. Probably the best known of these is of course ultrasonic flaw detection used for non-destructive evaluation. For many years this method of flaw detection was merely concerned with being able to find defects or cracks within a material by monitoring reflections from these defects[1]. This technique requires that the emitting transducer produces a pulse which is large and has a short time duration, whilst the detecting transducer should have a large signal to noise ratio, again coupled with a fast time response[2]. No absolute calibrations of the transducers are specifically required.

Recent calculations[3] show that a great deal more information may be obtained from the reflected pulse than merely measuring the ultrasonic intensity reflected from the crack. In order to extract this information work has been performed to determine the feasibility of using non-contacting optical methods for both the generation and detection of the ultrasonic pulse[4,5]. These novel techniques have the great advantage of producing quantitative absolutely calibrated results whilst retaining the high temporal resolution associated with a short duration ultrasonic pulse.

Unfortunately, optical detection and generation suffer from an inherent lack of sensitivity on the detecting side and a shortcoming in terms of acoustic energy produced on the transmitting side. The use of these

optical methods in practical situations is effectively ruled out on these grounds of sensitivity. However, because of their great attribute of being able to produce a calibrated signal, use may be made of them in laboratory experiments to either verify ultrasonic propagation models or to calibrate the much higher sensitivity piezoelectric transducers. The method by which the calibration may be carried out was suggested by Hsu and Breckenridge[6]. This involves comparing the response of the uncalibrated transducer and that of some absolute measuring device, for example an optical detector or in their case a capacitive transducer. The two detectors are excited by some arbitrary high frequency bandwidth ultrasonic source in a symmetrical arrangement. Michaels et al[7] have shown that deconvolution of the output of a piezoelectric transducer can faithfully reproduce the surface displacement exciting the detector, demonstrating how effective calibration can be.

This interest in higher fidelity calibrated transducers is not unique to ultrasonic pulse-echo techniques for non-destructive testing. A great deal of the work concerning deconvolution of transducer signals and the calibration and development of broad frequency response devices has been carried out in the field of Acoustic Emission[7,8,9].

When a material is placed under stress, rapid stress relaxations within the specimen, typically of duration 0.1μs[10,11], generate ultrasonic pulses. The generating

source may, for example, be a dislocation movement or the advancement of a crack tip. These ultrasonic pulses are termed Acoustic Emission.

If the source is considered as a horizontal dislocation loop in a semi-infinite half space, then the surface movement at the epicentral position is that as indicated by Wadley et al[10]. This is shown in Figure 1. Changes in the source function, the relative positions of the source and detector or the specimen geometry all produce changes in the detected signal. The only change that is of interest in a materials testing sense is that associated with the source.

Various workers[8] have expressed the view that the force-time history of any given source should provide information about the particular mechanism associated with that source, intergranular cracking, dislocation movement etc. Consequently, all other factors modifying the signal must be compensated for. In order for this to be possible, then several conditions must be satisfied. Firstly, the detecting transducer must respond over a very wide frequency range, so that the events of duration 0.1μs as reported by Wadley et al[10] and Rouby et al[11] may be detected. This implies a frequency range up to 10MHz with a response which is not dominated by resonances and antiresonances. Secondly, the transducer must be calibrated. Finally, the transfer function from source to detector in the given specimen geometry must be determined.

In 1885, Lord Rayleigh[12] predicted the existence of surface waves in solids. These waves are found to decay

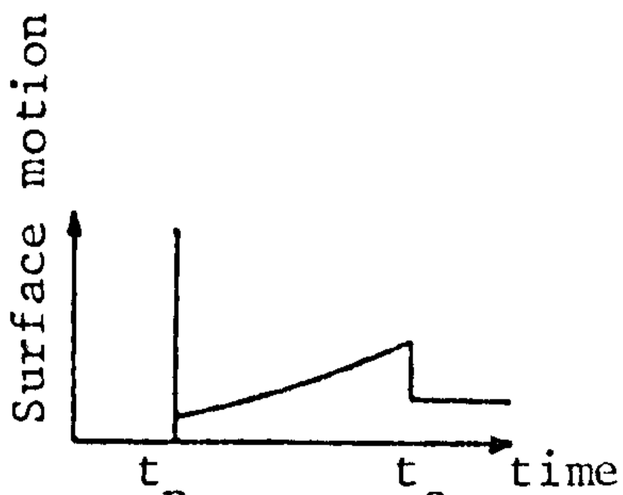

Figure 1: Vertical surface motion at the epicentre of a buried force dipole in a semi-infinite half space. (After Wadley et al[10]). t_p and t_s are the arrival times for longitudinal and shear waves respectively.

Figure 2: The vertical surface motion of the surface of a plate of thickness h at a distance of 4h from the epicentre of a buried force monopole in the centre of the plate. The large displacements are due to a combination of the Rayleigh wave and of multiple reflections. (After Pao et al[13]).

with distance according to an inverse square root law and to have in certain situations very large amplitudes compared to either longitudinal or shear waves. Many structures of engineering interest, for example pressure vessels, are essentially a large plate albeit a curving one. Pao et al[13] have shown that in such plate structures the Rayleigh wave amplitude is indeed large when the acoustic emission source is near the surface, see Figure 2. If an Acoustic Emission detector is therefore to have a large frequency bandwidth then its contact area with a structure must be small in order that the time of flight of the Rayleigh wave across its face is small. Simple geometric considerations further indicate that in any situation, other than the case when the detector is epicentral to the source, time of flight requirements are such that the detector must have a small contact area (see Figure 3).

Any method to calibrate ultrasonic transducers used in Acoustic Emission must clearly also have high spatial resolution on the specimen surface.

In a three-dimensional solid at least four variables are required to define the motion of any one point within the solid; these are the displacements in three orthogonal directions and time. It is very difficult to measure the in-plane vibrations on the surface of a solid in an absolutely calibrated manner. Shear wave transducers do respond to such movements, but these are not absolutely calibrated. It may be possible to use laser interferometry for such measurements by monitoring radiation scattered

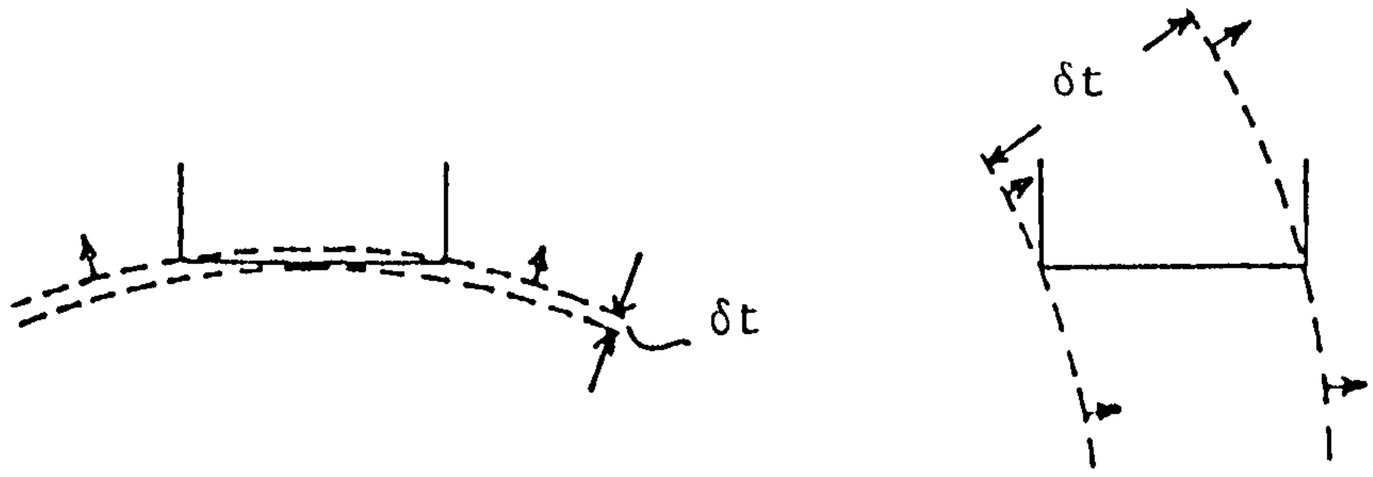

(a) (b)

Figure 3: An illustration of the variation in the time of flight, (δt), of an ultrasonic wavefront across a transducer face. Clearly in the epicentral case, (a), δt is very short compared to the off-epicentre case, (b).

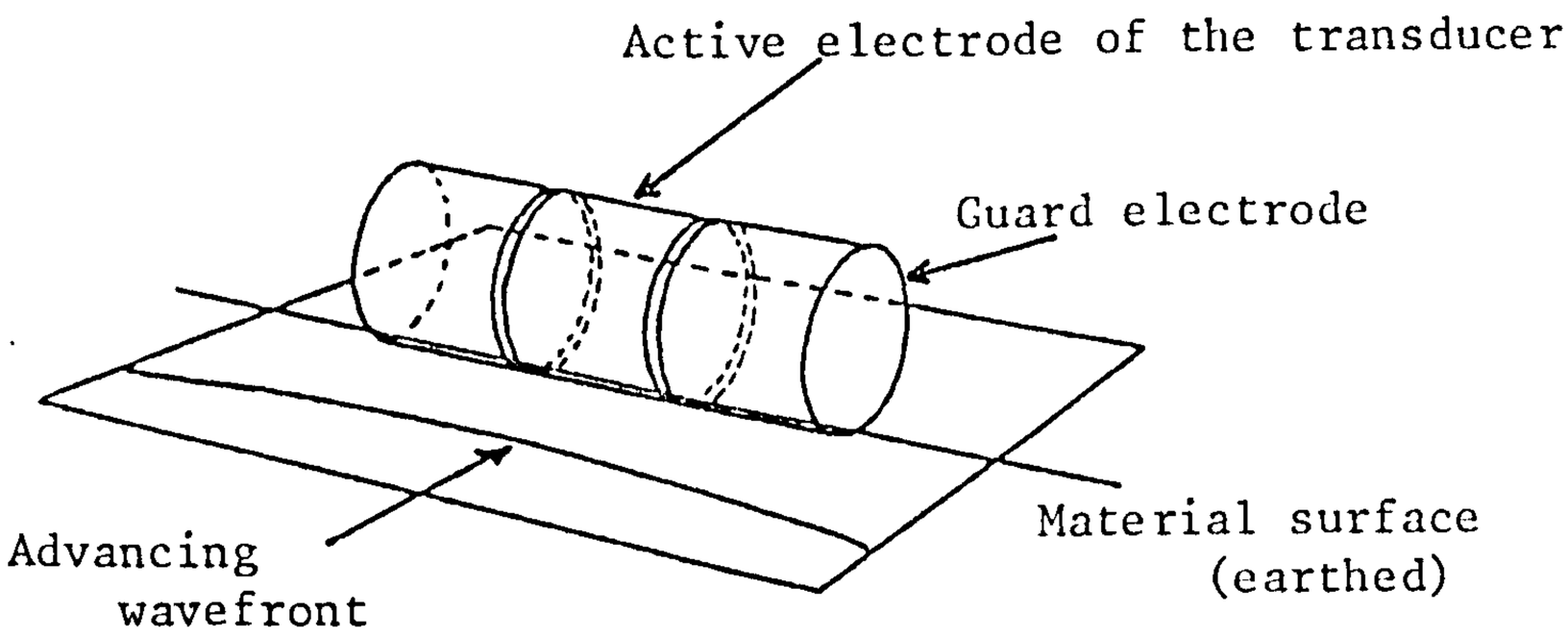

Figure 4: A schematic diagram of the capacitor used by Breckenridge et al[16] to measure surface ultrasonic waves.

parallel to the surface. Signal to noise requirements indicate a large laser power is required, of the order of 1W, and to the author's knowledge no such work has been performed. It therefore appears it may not be possible to obtain absolute information concerning the in-plane motion, however this may not be a serious drawback.

Most commercial transducers are coupled to the workpiece by some suitable couplant, oil or grease being common. Such materials do not efficiently transmit shear waves[14], implying that the transducers do not readily respond to the in-plane motion of a solid surface. It therefore appears that in order to calibrate a transducer, knowledge of the absolute out-of-plane motion will be sufficient in most cases. Furthermore, if this partial calibration can be performed then by comparing the transducer response to a variety of ultrasonic pulses containing different proportions of in-plane and out-of-plane motion, it will be possible to determine whether the partial calibration can be considered sufficient or not.

The out-of-plane motion of an ultrasonic pulse has been measured using capacitative detectors by a number of workers[8,10,15,16]. Most capacitors consist of flat plates. However these have dimensions which are large compared to the wavelengths of Rayleigh waves in the frequency range of interest (up to 10MHz). They are, therefore, of no use in calibration measurements. Breckenridge et al[16] overcame this problem by producing a capacitor as shown in Figure 4. This improves the spatial resolution, but because of the finite diameter of the cylindrical rod used as the upper

capacitor plate (the surface of the material being the other), the frequency response of the device for Rayleigh surface waves extended only up to 2.3MHz (3dB point). A method with a better spatial resolution would therefore be preferred.

Such a method is provided by optical interferometry[17]. The spatial resolution of such devices is of the order of ten microns and as such is adequate for the calibration requirements.

Optical interferometry suffers from two main disadvantages. These are its lack of sensitivity and its susceptibility to environmental disturbances. The sensitivity problem is a fundamental one[18] and may only be overcome by the use of higher power light sources. The effects of environmental disturbances, however, may be overcome to a large extent and do not rule out the use of an interferometer for ultrasonic measurements.

Transducer calibration removes only one problem associated with either trying to determine acoustic emission source characteristics or the shape of a scattered ultrasonic pulse. The other problem of ultrasonic pulse propagation within the specimen should also be investigated.

Theoretical calculations on the propagation of ultrasonic pulses in two simple geometries have been performed [13,19,20]. These are for the semi-infinite half space and the infinite plate. The calculations have not been directly tested by measuring both the source function and the detected waveform. Such a verification is of interest.

Clearly, specimen geometries are in general different

to the two shapes considered above. It is therefore of great practical interest to be able to measure the transfer or propagation function for other shapes both in the laboratory, for the case of commonly occurring but incalculable geometries, or in situ for any actual given structure.

As an interferometer can probe inside transparent materials it offers a unique tool for use in monitoring the propagation of ultrasonic pulses. A variety of transfer functions may therefore be measured experimentally. This allows both verification of the work of Pekeris[19] and Pao et al[13] in addition to determining the transfer functions of other geometries, for instance the finite solid cylinder. The effect of surface loading by ultrasonic transducers can also be determined. This problem of transducer loading has been mentioned by many workers[11,21] to be an area of uncertainty. However, no work has been carried out to determine the effects of such loading.

Measuring transfer functions in situ requires that a known source of ultrasound be available. Convenient sources include brittle fracture, laser impact and direct stimulation by piezoelectric transducers. To determine the actual source function one of two methods may be adopted. In the first, the calculations of Pekeris[19] and Pao et al[13] may be assumed correct and the source function determined by deconvolution of the signal at a distance. The second method uses the ability of the optical interferometer to probe inside transparent materials thus allowing the source

to be measured directly.

In summary, the problem of calibration of an ultrasonic transduction process requires both a knowledge of the transducer response, to the movement of the surface on which it is placed, in addition to knowledge about the transfer or propagation function within the material. Both these problems may be investigated by using a device which measures the absolute out-of-plane surface movement. An instrument which provides this facility is an optical interferometer.

II. REVIEW OF PREVIOUS WORK

The problems concerning the propagation and detection of ultrasonic signals have been associated, as mentioned previously, mainly in the field of Acoustic Emission. This is a result of the nature of the effect. Clearly, ultrasonic waves can be generated not only by stress relaxations in the test piece, but also by external influences such as machinery noise and vibration. Acoustic Emission, if it is to be used as a valid non-destructive testing technique, must at least be able to differentiate between the true sources which may lead to the failure of a specimen and the undesired external noise sources. This review therefore outlines the development of acoustic emission which has led to a study of ultrasonic propagation and detection. Recent interest in ultrasonic transducer calibration will then be covered in more detail.

II.1 Early experimental acoustic emission work

Acoustic Emission is not restricted to the generation of ultrasound for possible use in non-destructive evaluation, but may be found in many everyday situations. Examples of the effect being the audible sounds emitted by ice or by wood prior to fracture.

Some of the earliest scientific work was concerned with predicting rock bursts in mines[22]. This involved measuring the low amplitude sounds emitted by the rock. These sounds occurred at stress values below the crushing strength[22] of the rock thus allowing predictions of

imminent failure.

The early work on metallic samples was carried out in 1948 and 1950 by Mason[22]. This work was concerned with the ultrasound emitted from tin specimens during mechanical twinning. It has since been found that the generation of twins in tin produces very energetic and therefore high amplitude acoustic pulses. This is the well known "tin-squeal" commonly encountered by tin workers. Mason's early work produced no evidence of acoustic emission in aluminium which was later found to generate much lower amplitude emissions.

The first serious work on acoustic emission was carried out by Kaiser in 1950[22]. Emissions were found in polycrystalline samples of zinc, steel, aluminium, copper and lead. Kaiser discovered an irreversible effect which has since become known as the "Kaiser effect". If a material has already been stressed, then on re-applying the stress emission does not reoccur until the previous maximum stress is reached. The "Kaiser effect" occurs in most metals, being more distinct in some than others.

Further work[22] was later carried out by Schofield (1961) and Tatro (1959). Initially acoustic emission was thought by both workers to be a surface effect. Later, work by Schofield (1963 and 1964) discounted this hypothesis. Schofield's work was important in that the samples he used were single crystal. Emissions were still detected indicating the effect was an intrinsic material property and not due to grain boundary motion as suggested by Kaiser.

II.2 Theoretical work on ultrasonic pulse propagation

Soon after Kaiser's work on acoustic emission, various workers began to produce theoretical results for ultrasonic pulse propagation. Due to the complexity of the problem simple geometries were at first considered together with simple pulse generating functions.

The first geometry considered was a semi-infinite half space subjected to a point loading by a force having a Heaviside step time dependence. Such calculations formed a solution to a problem initially considered by Lamb in 1904[23]. Solutions were obtained for both a buried force[20] and a surface force[19] which are shown in Figure 5.

Semi-infinite half spaces do not of course exist in reality. However, for the case of surface pulses they may be approximated in practice. To do this a block of material is required which is of sufficient size that all the direct waves from the source reach the detection point before the first arrival of a pulse reflected from the material boundaries. The problem for a buried pulse is much more difficult in that no simple force may be applied to a point within a solid specimen.

To overcome this problem Knopoff[24] produced the result for the epicentral response of a thick infinite plate subjected to the same loading. It was found that the resulting displacement was similar to the semi-infinite half space displacement for a buried pulse at epicentre before multiple reflections occurred in the plate as indicated in Figure 6.

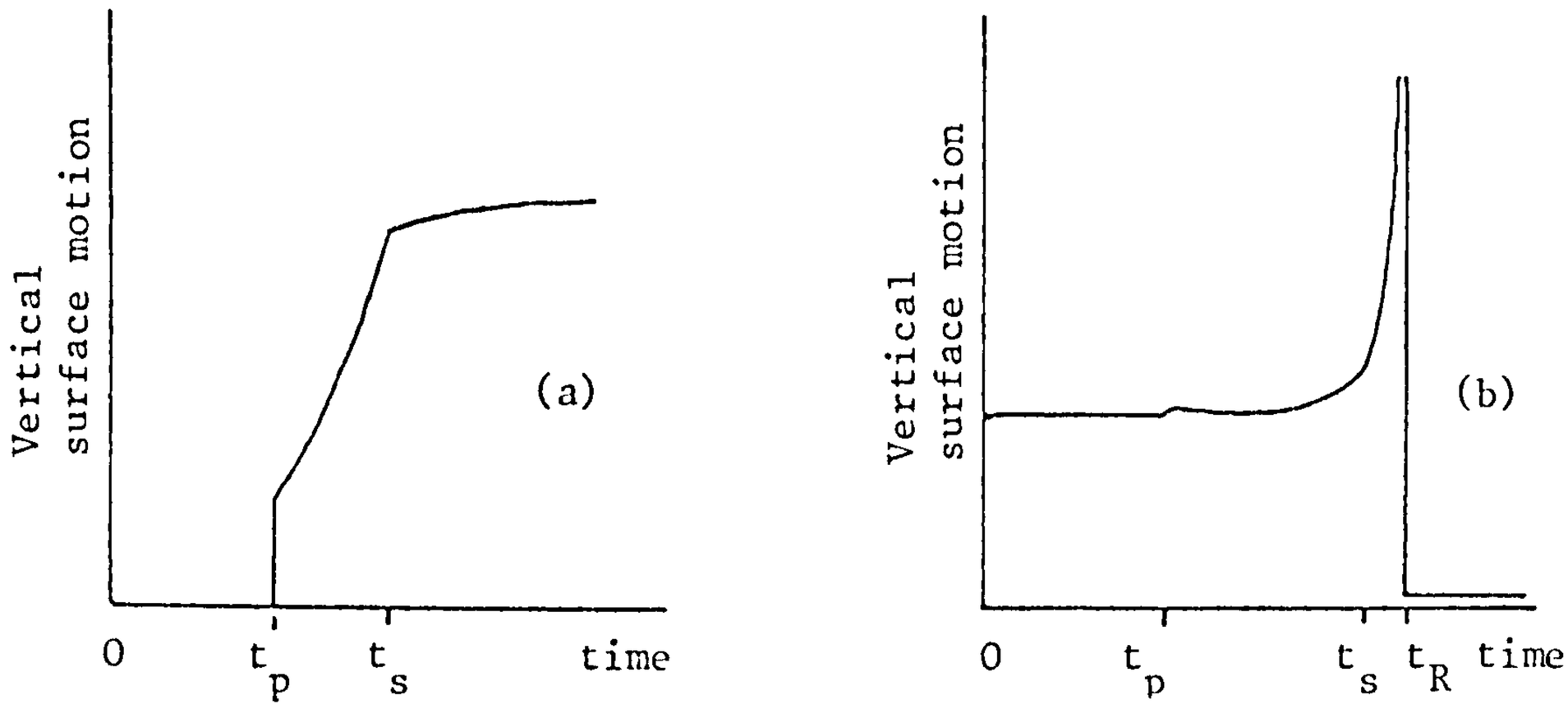

Figure 5: The vertical surface motion of a semi-infinite half space due to a force monopole excitation. (a) is for a buried pulse measured at the epicentre, whilst (b) is for a surface pulse. t_p, t_s and t_R are the arrival times for longitudinal, shear and Rayleigh waves respectively.

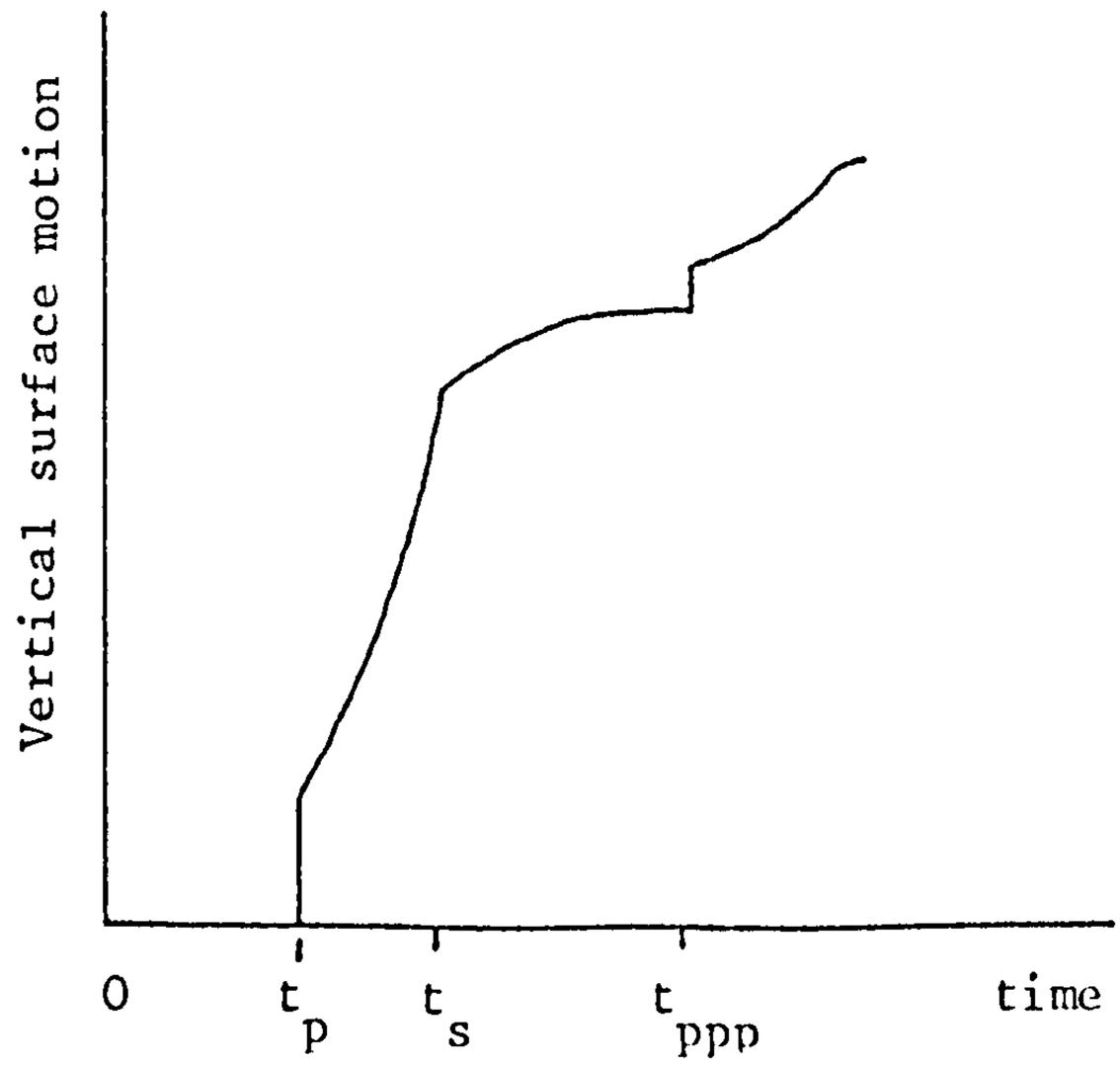

Figure 6: The vertical surface displacement at the epicentre of a force monopole stress input on a thick plate (after Knopoff[24]). t_p and t_s are the arrival times for direct longitudinal and shear waves, whilst t_{ppp} is the arrival time for a doubly reflected longitudinal wave.

These initial calculations have been extended by the use of computer numerical methods to cover the surface pulse on semi-infinite half spaces for a variety of values of the material's Poisson's ratio[25] and the motion of an infinite plate for off-epicentre detection positions[13].

Calculations for more complicated geometries are possible, but would require a great deal of numerical evaluation. The results for other geometries would however be of great practical use. A specific example being the finite solid cylinder which is often used as an acoustic waveguide. It should be possible to produce these results experimentally, but this has not yet been done[26].

II.3 Further experimental work on Acoustic Emission

Following the early work of Kaiser there was an increase in interest in acoustic emission. Its possible use for non-destructive evaluation and failure prediction was readily seen. The 1960's and early 1970's then saw a great deal of work being carried out in the field. This work was concerned both with laboratory tests on tensile and fracture specimens and on monitoring the structural integrity of large structures such as pressure vessels.

The early work had been concerned with audible or low ultrasonic frequencies[22] and as such was plagued by ambient noise. Dunegan in 1964 was the first to work at higher frequencies, typically in the hundreds of kilohertz range. This frequency was a compromise. Too low a frequency range resulted in excessive external influence,

as mentioned above, whilst too high a frequency (of the order of 1MHz or above) resulted in a great deal of ultrasonic attenuation, especially in common engineering steels. The centre frequency of detection is usually set by the fundamental thickness mode resonance frequency of the detectors employed in a test.

A typical detector output would be similar to that shown in Figure 7. This figure is taken from a calibration carried out by Procter[27]. Clearly, the type of trace bears little resemblance to theoretical results indicated in Figures 5 and 6. The differences arise because of the design of the transducer. The design is such that either transducer resonances are not efficiently suppressed or indeed in some cases where extra sensitivity is required resonances may be enhanced.

Certain parameters may be obtained from a trace such as that shown in Figure 7. These are indicated on the figure itself and are rise time, amplitude and ring-down count. Ring-down count is the number of times the output exceeds some threshold value. These parameters, whilst useful, are often more a result of the transducer response than of the surface displacement beneath the transducer. Such parameters can only really be captured and stored with the help of microcomputers and were therefore not used before the 1970's. Prior to this the parameters most extensively used were either total emission count or count rate.

Even though it was impossible to obtain absolute surface movement information from tests, some very good results

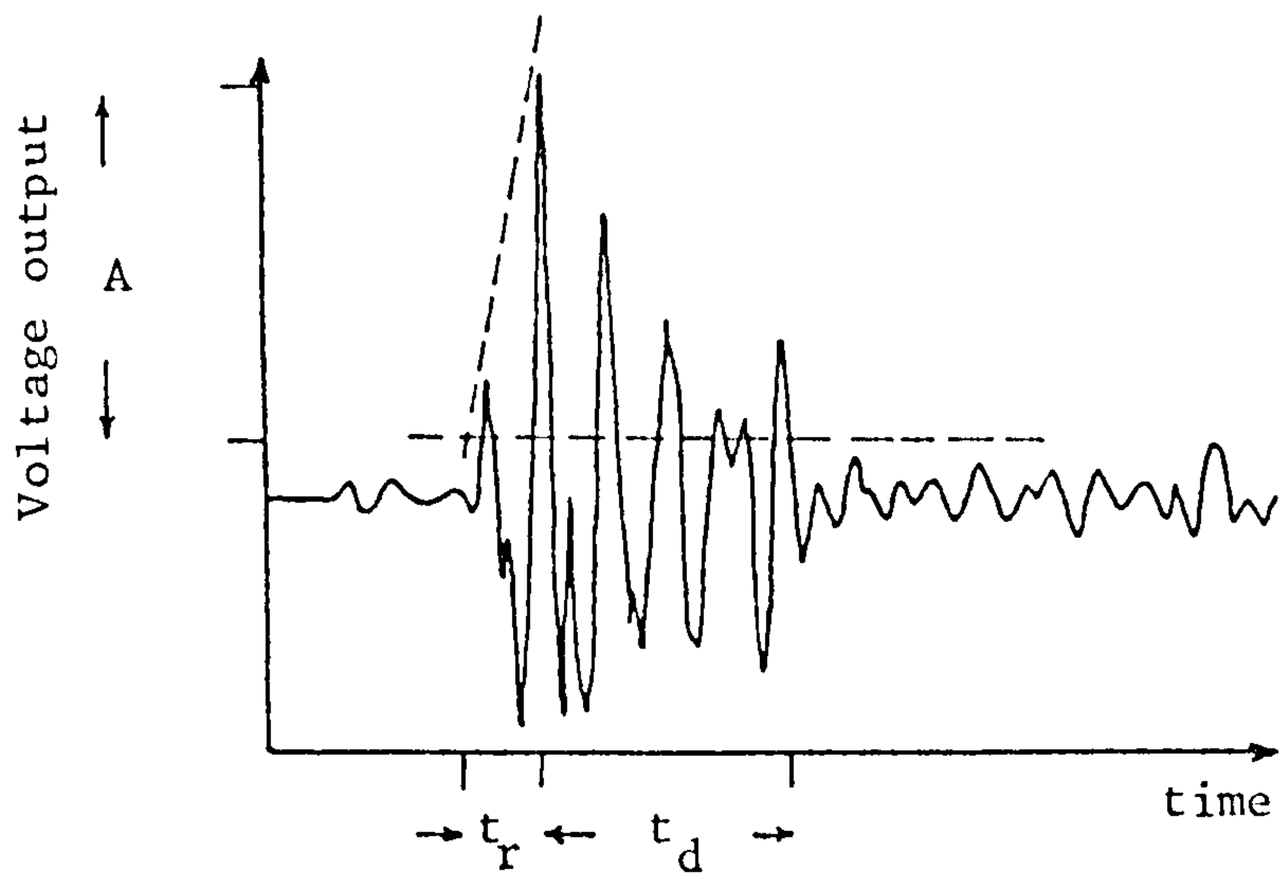

Figure 7: The voltage output of a conventional transducer generated by a surface displacement similar to that shown in Figure 5b. The oscillations are due to the transducer design. Parameters often used in acoustic emission work are A, the amplitude, t_r, the rise time, and finally ringdown count. The ringdown count is the number of peaks above a given threshold value in the time interval t_d and is here equal to 5.

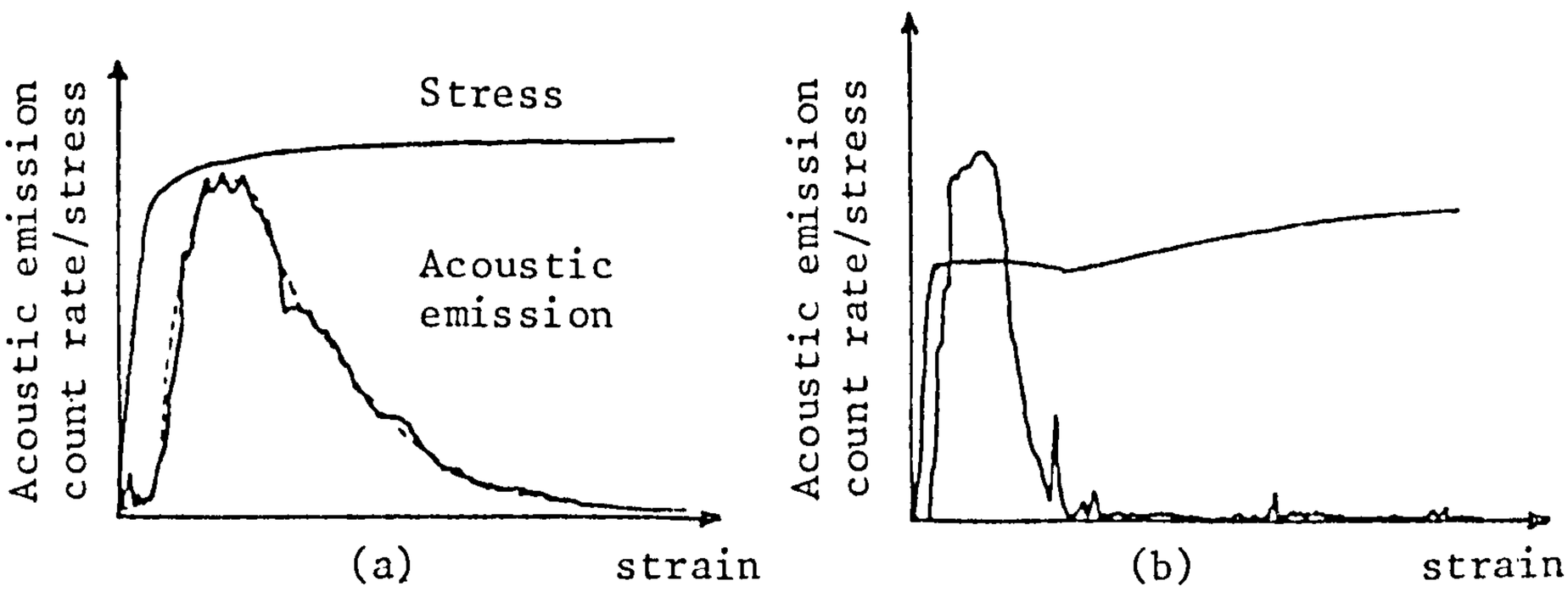

Figure 8: The results of acoustic emission work carried out by Dunegan and Harry[28] on tensile test specimens. Figure (a) shows the result for a 7075-76 aluminium specimen to which a fit of Gilman's mobile dislocation model[22] is given. Figure (b) was for a Iron-3% silicon specimen and here no such fit is possible.

have been produced. One such experiment was that carried out by Dunegan and Harris in 1969[28] in which acoustic emission was monitored as a function of strain in a 7075-TS aluminium tensile specimen. The result in terms of acoustic emission rate versus strain is shown in Figure 8a. The theoretical curve also shown in the figure is a fit of Gilman's mobile dislocation model[22]. This model predicts the mobile dislocation density as a function of plastic strain. The fit is clearly very good. Unfortunately, when other materials were tested it was not always possible to obtain a fit at all to Gilman's model. An example of such a case is indicated in Figure 8b. This figure shows the results of a test carried out by Dunegan and Harris[28] on an iron-3% silicon tensile specimen.

Resolving such discrepancies as these is indeed a difficult problem. The initial step towards solving the problem would be to determine the dynamic properties of the source function. To do this requires that both the propagation in the material and the transducer response be known. In effect, the entire ultrasonic system should be calibrated.

Tensile tests on metallic specimens were not the only laboratory tests carried out in the late 1960's and early 1970's. Many other sources of emission were identified and processes monitored. Such work has been reviewed extensively by Lord[22] and includes work on composites, welding, martensitic transformations and the acoustic Barkhausen effect.

Some initial structural integrity work was carried out on pressure vessels where acoustic emission is monitored during preservice hydrotesting or periodic proof testing. The technique is concerned with the detection of harmful defects within the pressure vessel. A change in acoustic emission activity is hoped for when a defect is present.

Harris and Dunegan[29] report such an experiment carried out on two pressure vessels, one with and one without a flaw. The unflawed vessel was proof tested during which time the acoustic emission was monitored. Figure 9a shows the result of the proof test. The vessel was then cycled five times to 46MN m^{-2}. No emission occurred during this cycling, suggesting the vessel was sound. Next the flawed vessel was proof tested and the emission monitored, Figure 9b. Clearly more acoustic emission was detected during the proof cycle of this vessel. On cycling the pressure to 46MN m^{-2} emission was detected on this flawed vessel indicating the flaw was extending, Figure 9b. This example indicates that acoustic emission can be used as a viable non-destructive testing technique.

Acoustic emission has also been used for in-flight monitoring of critical parts of an air-frame[26], for pipeline integrity[26], leak detection[30], flow monitoring in reactor channels (onset of turbulence etc.)[26], monitoring cranes and lift equipment[26,30] and in monitoring manufacturing processes[30].

Although acoustic emission has been shown to work in some instances and in some materials, there are other materials where emissions do not occur[26,31]. A greater understanding

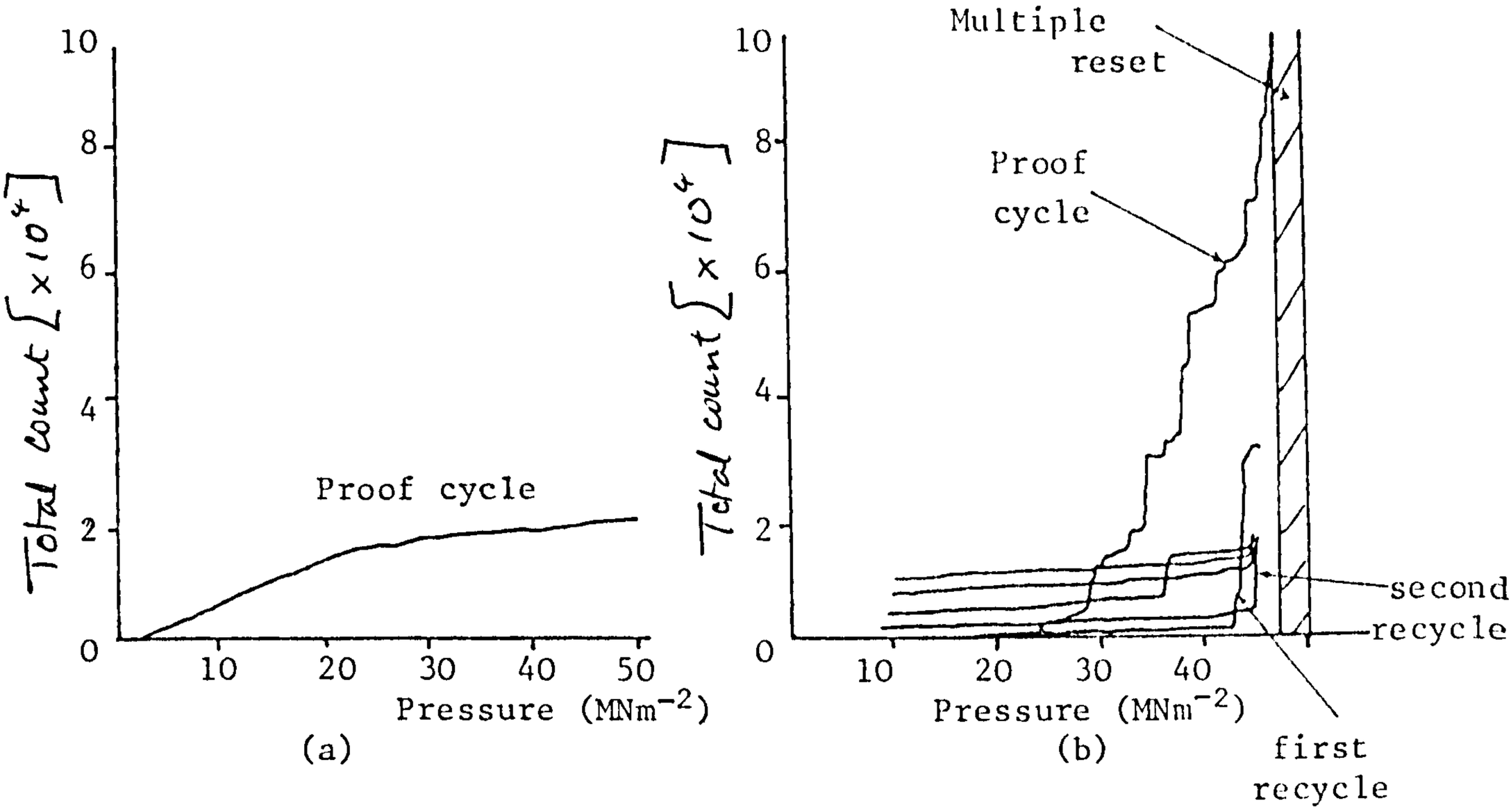

Figure 9: Acoustic emission monitored during pressurization of (a) an unflawed and (b) a flawed pressure vessel. (After Harris and Dunegan[29]).

Figure 10 (below): Schematic representation of the capacitor used by Scruby and Wadley[32] to measure acoustic waves at the epicentre of ultrasonic sources. The induced charge, δq, is proportional to A, V and $\delta\xi$ and inversely proportional to ξ.

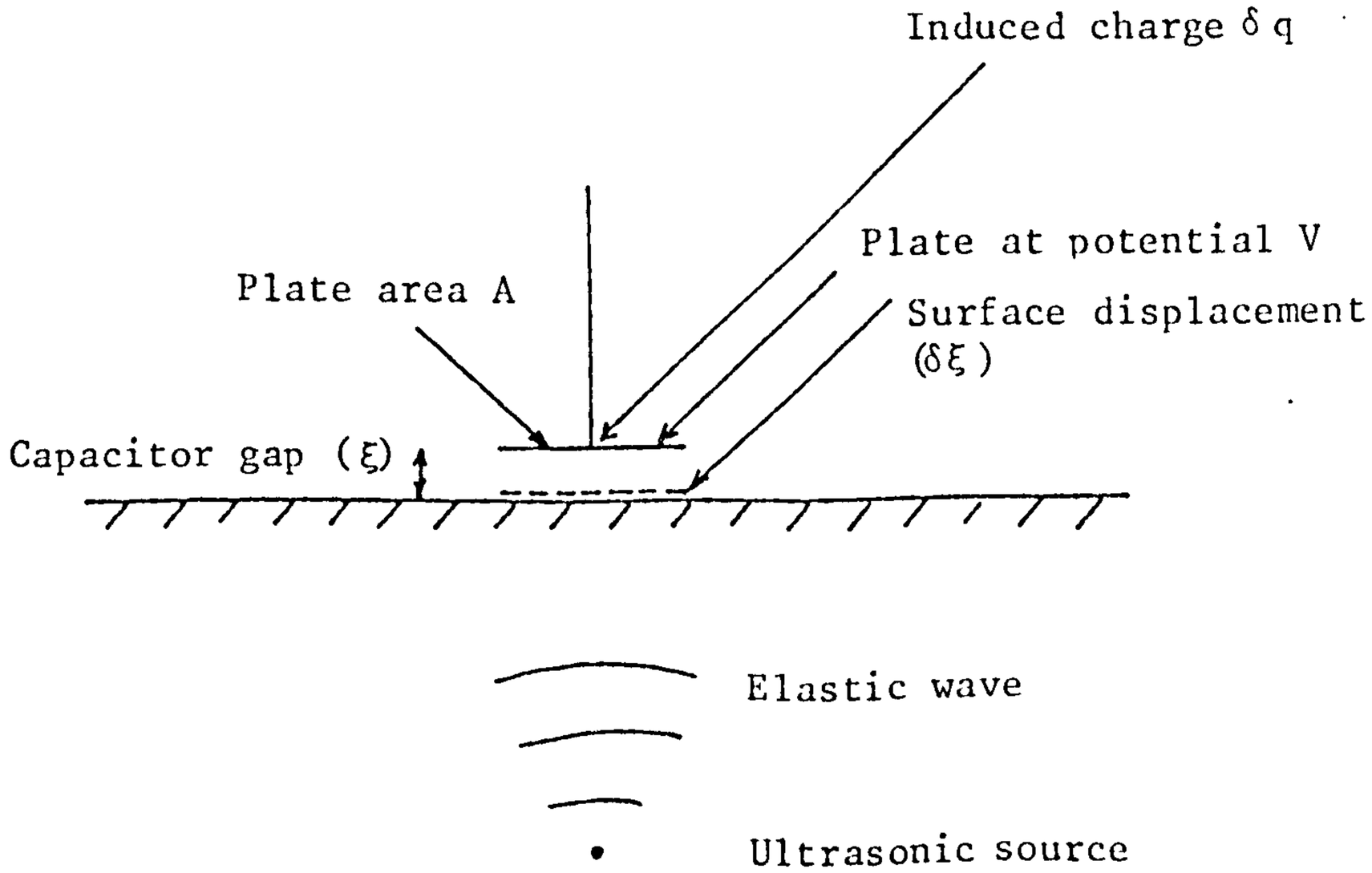

of the processes causing the emission must therefore be gained if the technique is ever to be widely accepted for non-destructive testing. The remainder of this review will now be concerned with the development of techniques designed to produce a better understanding of the generation of acoustic emission. This work deals mainly with the calibration of the ultrasonic system and as such is directly applicable to hi-fidelity ultrasonic pulse-echo techniques.

II.4 Absolutely calibrated transducers for ultrasonic detection

In an ultrasonic system the mechanisms of specific interest are those generating ultrasonic pulses. In acoustic emission these mechanisms are, as mentioned previously, stress relaxations in the material due to defect growth, whilst for ultrasonic pulse-echo techniques the sources are the particular reflections from existing defects. These reflections should be dependent on the defect size, shape and orientation[3]. Two factors hamper the absolute measurement of source parameters. Firstly, the propagation of the pulse through the material and, secondly, the detection of the pulse at the material surface. As a first move towards solving these problems, some method to absolutely detect the surface movement should be sought. Two transducers are available to perform this task. These are either capacitance devices or interferometric devices[6]. The use of these two devices will now be looked at in more detail.

II.4.1 Capacitance devices for the measurement of ultrasonic surface displacements.

One of two basic designs of capacitance transducer may be used for ultrasonic measurements. The particular design chosen depends primarily on the position, with respect to the ultrasonic source, in which it is to be used. For work concerned with measuring epicentral responses the capacitor in general consists of a flat circular plate held very close to the specimen surface. Such a device has been described by Scruby and Wadley[32] and is shown schematically in Figure 10. A similar device is described by Hsu and Hardy[33]. This device was composed of a narrow solid cylinder held upright above the specimen surface so that the flat end of the cylinder formed one capacitor plate and the specimen surface the other. These devices when used in this epicentral position provide a very wideband frequency response. Scruby and Wadley[32] calculate a rise time of 37ns giving an upper frequency limit of about 10MHz.

As discussed in the introduction if an ultrasonic transducer is to have a broad frequency response in positions off epicentre and specifically in response to surface waves then the effective area of the transducer must be small.

Hsu and Hardy[33] overcame this problem by making the capacitor plate in the form of a narrow strip. They do not provide any information as to the dimensions of the strip and therefore its upper frequency response is unknown. However, calculations given by Breckenridge and Greenspan[16] suggest it may not have been too large, possibly of the order of 1 or 2MHz.

Aindow et al[34] have measured the surface waves generated

by the impact of a Nd-YAG laser. These measurements were carried out using a capacitance probe. Unfortunately no details of the probe are given. A bandwidth up to 10MHz is assumed. However, their results suggest a system rise time of ∿ 0.15μs. Assuming this to be limited by the transducer rise time and not the diameter of the Nd YAG impact (i.e. the spot size is assumed less than ∿ 0.2mm in diameter) then an upper frequency limit of approximately 2MHz is obtained. This figure is then in agreement with that given by Breckenridge and Greenspan[16]. Of course, the rise time may be dominated not by transducer response, but by either material properties or source properties.

Surface waves on a specimen were first measured in 1975 (Breckenridge et al[35]). The capacitor used for these measurements consisted of a cylinder placed with its axis parallel to the specimen surface (see Figure 4). In 1981 Breckenridge and Greenspan[16] calculated the frequency response of the device. This response was found to be mainly dominated by the distributed capacitance of the transducer, its upper frequency limit being 2.3MHz. In terms of acoustic emission measurements this may be too small. Indeed, it has already been mentioned how a possible low system bandwidth for the measuring device used by Aindow et al[34] has led to uncertainty in the interpretation of results.

II.4.2 Interferometric and optical devices for the measurement of ultrasonic surface displacements.

Optical detection methods offer a great advantage over capacitance devices for the detection of surface waves. This

advantage is their small probe size. A coherent light beam may easily be focussed to a spot with a diameter of about 10μm. This corresponds to an upper frequency limit of 100MHz for surface waves on aluminium. It is generally found that the amplifier electronics are in fact the limit on frequency response and not the finite spot size.

Interferometry is by far the commonest technique employed in the optical detection of ultrasound. However in addition to this method both Schlieren (knife edge) techniques and diffraction techniques may be used. These techniques are both discussed by Palmer and Green[36]. Essentially in the knife edge technique a laser beam is focussed onto the material surface. Travelling surface waves produce tilting of the surface beneath the laser beam which is deflected as a consequence. The deflection of the reflected beam across a knife edge produces intensity changes at the photodetector. One of the shortcomings of the system is that it is not sensitive to waves from the epicentre.

In the diffraction technique a parallel laser beam is incident upon the material surface. Waves travelling along the surface with a fixed frequency create a phase grating and diffraction of the incident light results. Clearly this is not appropriate to ultrasonic pulse measurements in that a constant fixed frequency is required.

Interferometry is therefore the technique which must be investigated.

The interferometer used for high resolution spectroscopy work is the Fabry-Perot interferometer[37]. However, as pointed out by Hecht and Zajac[37] when the finesse of the

device is high, implying high resolution, the peak reflectance or transmission falls due to absorption in the reflecting coatings. The signal to noise ratio will then fall. Noise considerations in optical devices will be discussed in more detail later. Despite this the Fabry-Perot device has been used to detect standing surface acoustic waves (SAW). The waves were introduced onto one of the Fabry-Perot plates[38] thus causing a change in the static interferometer output. However the signal to noise problem was overcome by averaging which was possible as the surface acoustic waves were stationary.

All other interferometers used to measure the movement of a reflecting surface operate on a common principle. The interferometers are all based on the Michelson interferometer shown schematically in Figure 11. Differences in optical path length between the two arms of the device result in interference when the beams are overlayed. This leads to intensity variations which are picked up by the photodetector. The variation of intensity with path length difference is shown in Figure 12. Several conditions are necessary to derive this result. These conditions will be discussed in more detail in the following chapter.

The mode in which a Michelson interferometer is operated depends on the magnitude of the vibrations the device is being used to measure. For low frequency ($\lesssim$ 1kHz) vibration work the amplitudes of vibration are of the order of several microns. Measuring such vibrations effectively involves merely counting the number of fringes the photodetector passes through. For ultrasonic work however the vibration amplitudes are typically less than 10nm. The sensitivity of the

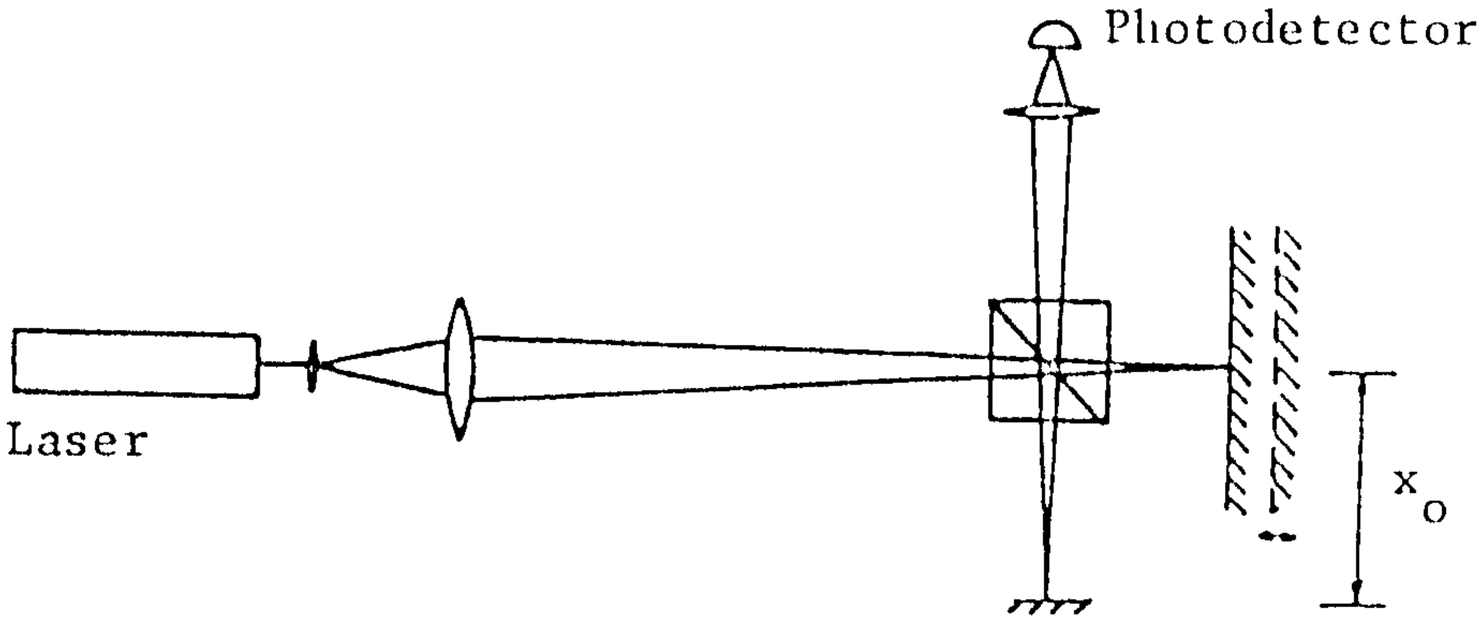

Figure 11: The laser Michelson interferometer

Figure 12: The intensity output of a well-adjusted Michelson interferometer.

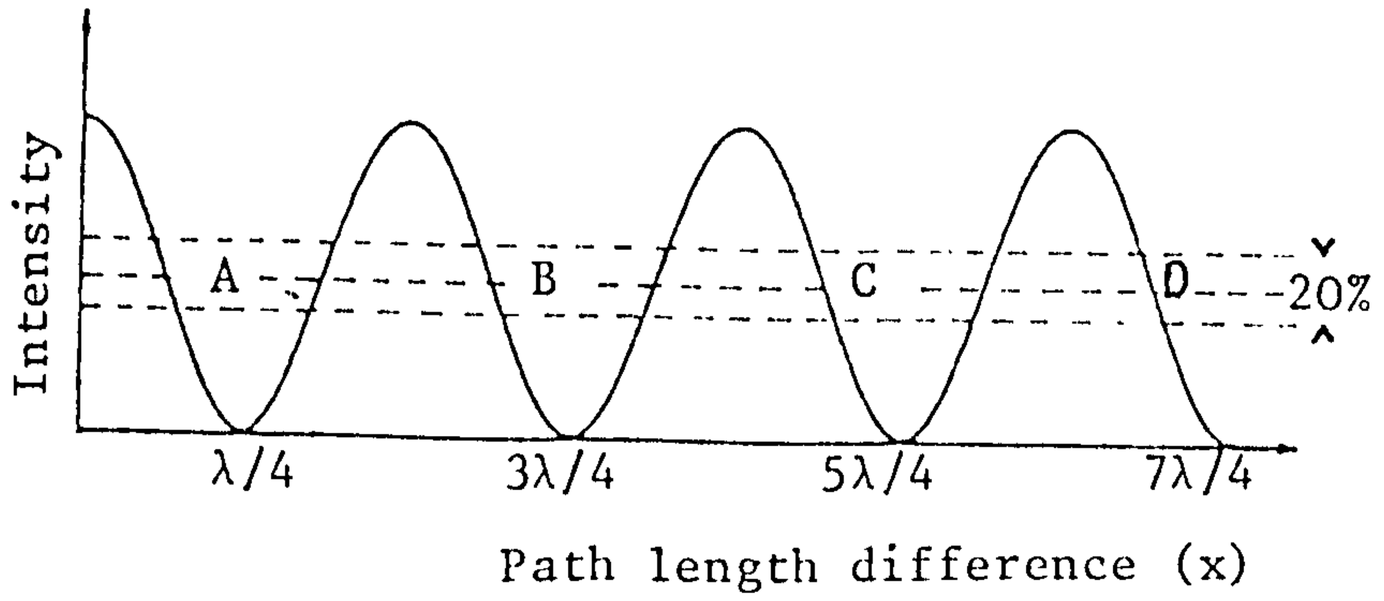

interferometer to small movements may be found by differentiating the function depicted in Figure 12 which is the cosine squared function given in equation (1):

$$I = \alpha I_o \cos^2 \left(2 \frac{\pi X}{\lambda} \right) \qquad (1)$$

where I is the intensity, I_o the laser output intensity, α a factor related to power losses within the interferometer, x the path length difference shown in Figure 11 and λ is the wavelength of the light used in the interferometer. The differential is then:

$$\delta I = \left(\frac{\delta I}{\delta x}\right)_{I_o,\lambda} \delta x + \left(\frac{\delta I}{\delta I_o}\right)_{x,\lambda} \delta I_o + \left(\frac{\delta I}{\delta \lambda}\right)_{I_o,x} \delta \lambda \qquad (2)$$

Therefore

$$\delta I = -(2\alpha I_o \pi/\lambda)(\sin(4\pi x/\lambda))\delta x + (\alpha/2)(1 + \cos(4\pi x/\lambda))\delta I_o + (2\alpha I_o \pi x/\lambda^2)(\sin(4\pi x/\lambda)\delta\lambda \qquad (3)$$

The light source commonly used for this type of interferometry is the Helium-Neon laser operating on the 632.8nm line. These lasers in general oscillate on a number of longitudinal modes (Corney[39]), the number of these modes being determined by the Doppler broadening of the lasing spectral line. The line half width for a Neon atom emitting at this frequency is 1700MHz. It can therefore be determined whether the third term in equation (3) is significant. Assuming $x \approx 100\lambda$, then this term becomes:

$$(2\alpha I_o \pi/\lambda)(x\delta\lambda/\lambda)(\sin(4\pi x/\lambda)) = (2\alpha I_o \pi/\lambda)(2 \times 10^{-10})(\sin(4\pi x/\lambda)) \qquad \ldots \qquad (4)$$

and is therefore negligible.

The second term cannot unfortunately be discarded in the same manner. Equating the coefficients of the first and second term in equation (3) yields:

$$\frac{\delta I_o}{I_o} = 2.10^{-3} . \delta x \qquad (\delta x \text{ in } \mathring{A}) \qquad (5)$$

The amplitude noise for Helium-Neon lasers is quoted as 1%[40]. This leads therefore to a minimum detectable displacement of $5\mathring{A}$ which is quite unacceptable. In designing any measuring device based on a Helium-Neon laser this problem should therefore always be considered.

Assuming the second term (equation (3)) may be removed in some way, for instance by use of a stable laser, then the sensitivity will be determined only by the first term. Consider now the form of this term. The sensitivity is seen to vary sinusoidally. To obtain maximum sensitivity, x must be selected such that:

$$(n + \tfrac{1}{2})\,\pi = \frac{4\pi x}{\lambda} \qquad (6)$$

In any normal laboratory environment low frequency vibrations exist which cause changes in x. These vibrations are sufficiently large to ensure that the sensitivity of the interferometer fluctuates between zero and maximum in an entirely random fashion. In order that measurements may be made in a variety of circumstances some method of stabilising x against low frequency vibrations must be employed. A variety of techniques have been developed to overcome this problem of stabilisation. These will now be discussed.

II.4.2i) Stabilisation of optical interferometers.

The simplest way of stabilising an interferometer is to

use the interferometer in a differential mode as described by Palmer and Green[36] and Garg and Claus[41]. In this device two laser beams are focussed onto the specimen surface (Figure 13) and the device output is then proportional to the difference in displacement between these two points. This output clearly depends on the wavelength of the ultrasound being monitored and is therefore not of use for measuring arbitrary pulses of ultrasound.

Optical heterodyning is a technique often applied to measurements of particle velocities[42,43]. The method may also be applied to vibration measurement[44]. .In a heterodyne interferometer the frequency of the light in the reference arm is shifted. This shifting may be done by using a Bragg cell[36] or Kerr cells[45]. In the absence of any mirror movement the interferometer output is then merely a sinusoidal function at the beat frequency given by the frequency shift between the two interferometer arms. When movements of the mirrors occur extra frequency shifts result as a consequence of the Doppler effect. If the Doppler frequencies introduced by unwanted vibrations are different to those produced by the vibrations of interest then simple filtering may be used to produce a calibrated constant sensitivity signal. Unfortunately, the low frequency disturbances produce Doppler shifts which are similar to those introduced by ultrasonic vibrations of the mirror surfaces and so the technique is not of use.

A fairly recent development in interferometry has been the introduction of fibre-optic interferometers. In these devices some or all of the optical paths in the interferometer

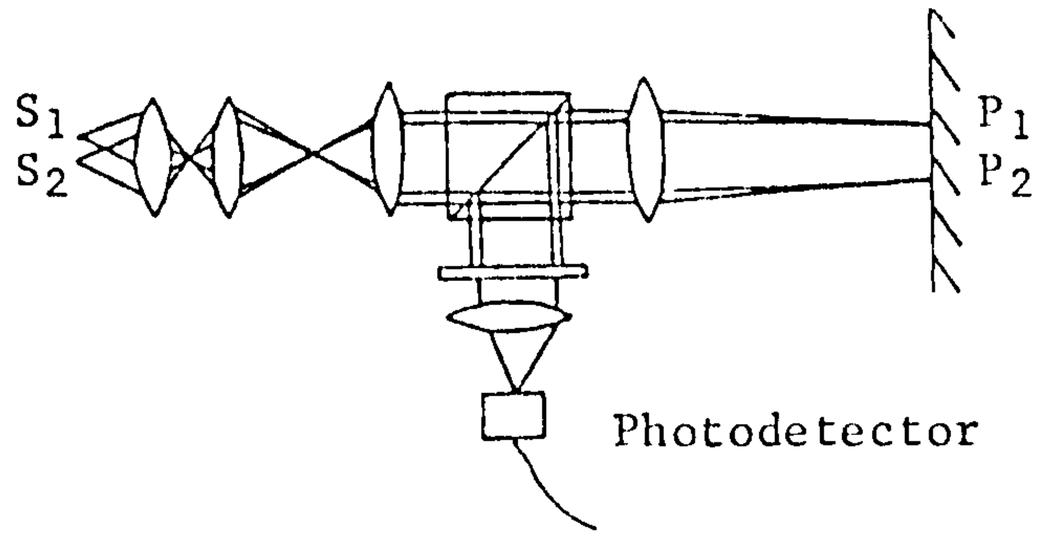

Figure 13: Schematic arrangement of a differential interferometer The two coherent sources, S_1, S_2 , are focussed to two positions on the specimen surface at P_1, P_2 giving a photodetector output intensity dependent on the relative movement of P_1 and P_2.

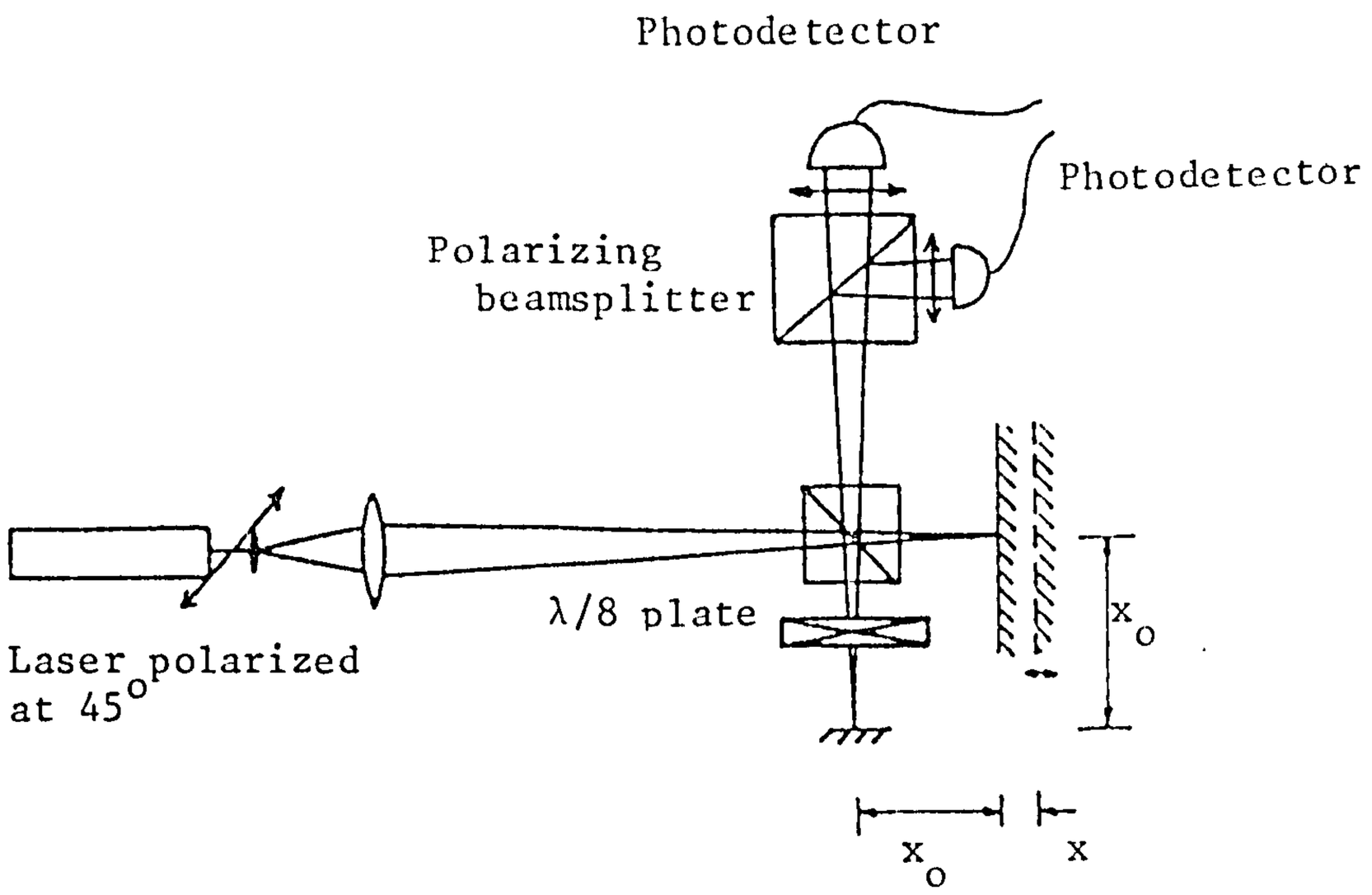

Figure 14: The quadrature dual beam interferometer.

are along optical fibres. This leads in general to an increase in the device's mechanical stability and also leads to a novel method of stabilising. The optical path length along a fibre depends not only on its physical length but also its state of stress. The latter arises because the refractive index is stress-dependent. By wrapping an optical fibre around a hollow piezoelectric cylinder which has been radially polarised large path length changes may be induced in the fibre[46,47] by applying a voltage to the piezoelectric cylinder and thus stretching the fibre. The device may therefore be stabilised.

Fibre interferometers have been used to measure ultrasound in fluid materials in both a Mach-Zehnder[37] configuration[46] and a Michelson configuration[48]. The ultrasound field passes over the fibre causing path length variations which are readily detected as variations in intensity at the detector.

A fibre Michelson interferometer has been used to measure surface acoustic waves on a $LiNbO_3$ SAW device[49]. In this work the problem of stabilisation was overcome by the use of phase sensitive detection. The high coupling efficiency (34%) back into the fibre and the small spot size (4μm) indicate that a broad frequency response ultrasonic detector could be produced. Stabilisation would be possible with the coiled fibre and piezoelectric stretcher technique.

An interferometer which has a useable sensitivity for any path length difference was suggested in 1953 by Peck and Obetz[50]. This device is termed a quadrature interferometer and one of the variations of such a device is depicted in

Figure 14. The interferometer is in effect two interferometers in one. These two interferometers are identified by the two orthogonal polarisations of the laser light. Both light polarisations cover exactly the same paths except through the $\lambda/8$ plate. In this plate one polarisation is phase retarded by 45^{o} on each traversal. Therefore the two outputs, corresponding to the two polarisations, are 90^{o} out of phase as shown in Figure 15. Clearly when one output has a low sensitivity to small path length variations, the other has a high sensitivity and vice versa. The sensitivity is therefore always at least 70% ($1/\sqrt{2}$) that of the possible maximum.

This device has been used to measure pulsed ultrasound[51] but has not been used to measure the non-repetitive signals associated with acoustic emission. Recently[52] a computer has been employed to extract information from the intensity outputs obtained from a continuous ultrasonic signal over a very large dynamic range indicating the great versatility of the device.

A quadrature interferometer is therefore a very useful tool for vibration measurements. It is not restricted to measuring large displacements (fringe counting) or very small displacements. This device was therefore chosen for some of the experimental measurements reported later.

In addition to the methods outlined above, three other methods of stabilising interferometers have been reported.

Two of these methods involve altering the frequency of the laser light in either one or both arms of the interferometer. Work by Speake[53] at Harwell has made use of Kerr cell

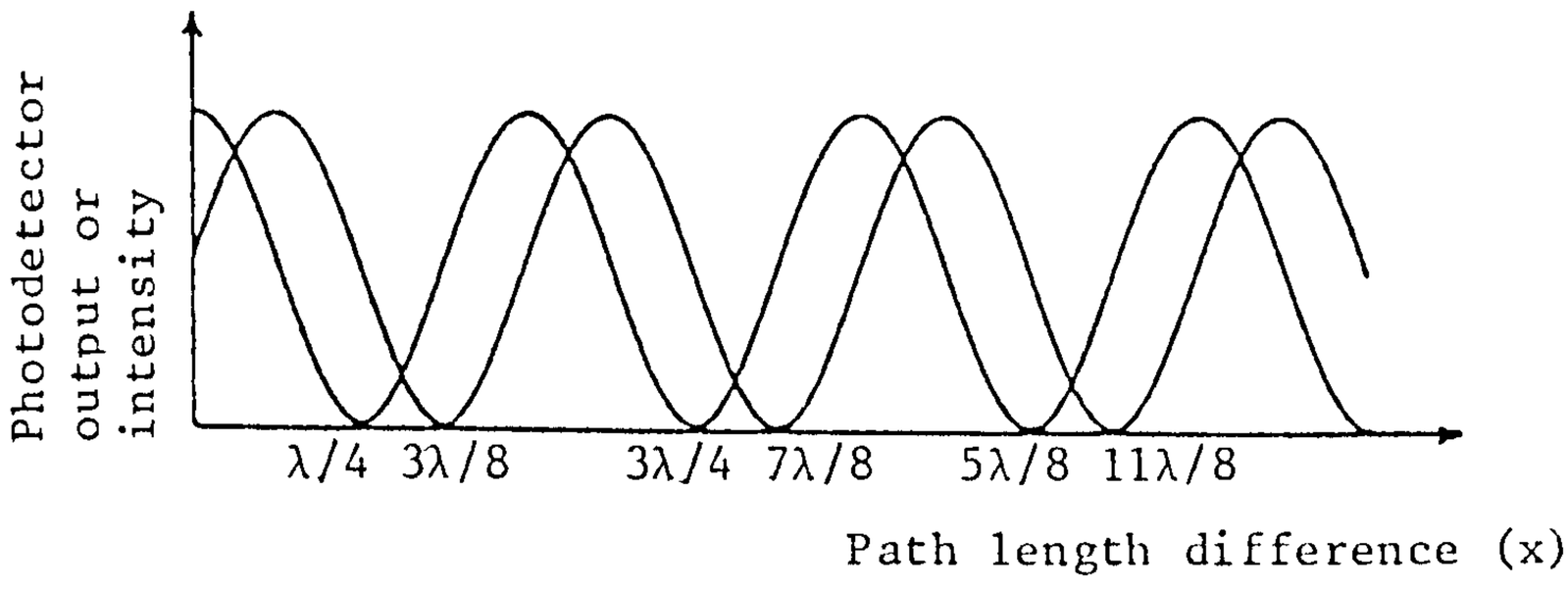

Figure 15: The intensity outputs of the two photodetectors in a well adjusted quadrature interferometer as shown in Figure 14.

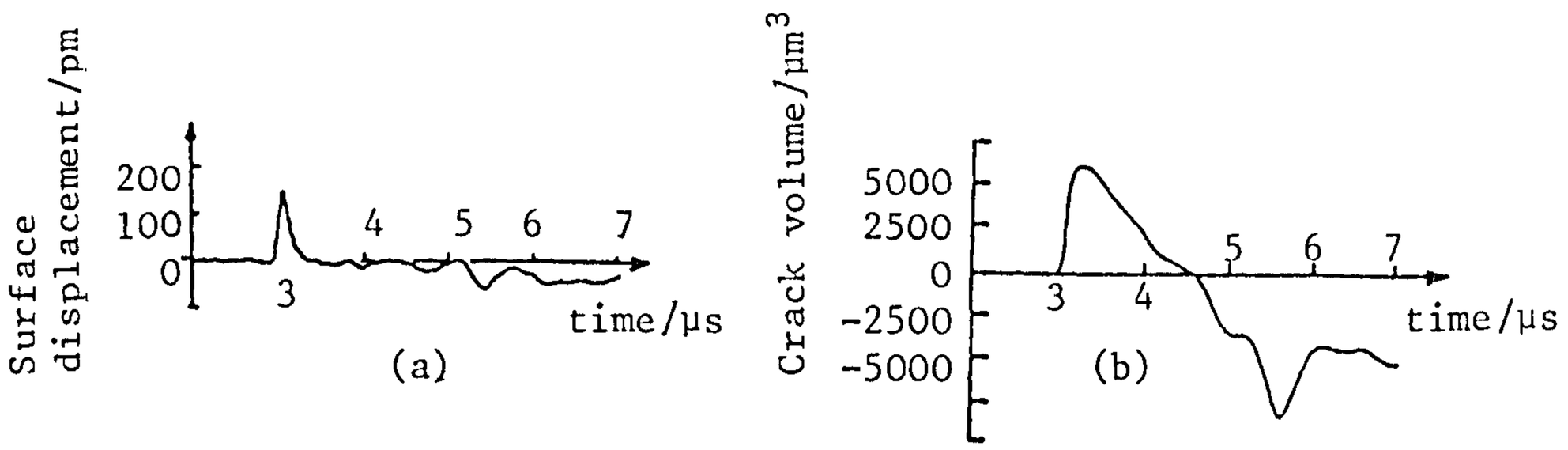

Figure 16(a): The surface displacement measured at the epicentre of a typical acoustic emission source during low temperature cleavage in mild steel (Wadley et al[10]).

Figure 16(b): The deconvoluted crack volume time history for this source.

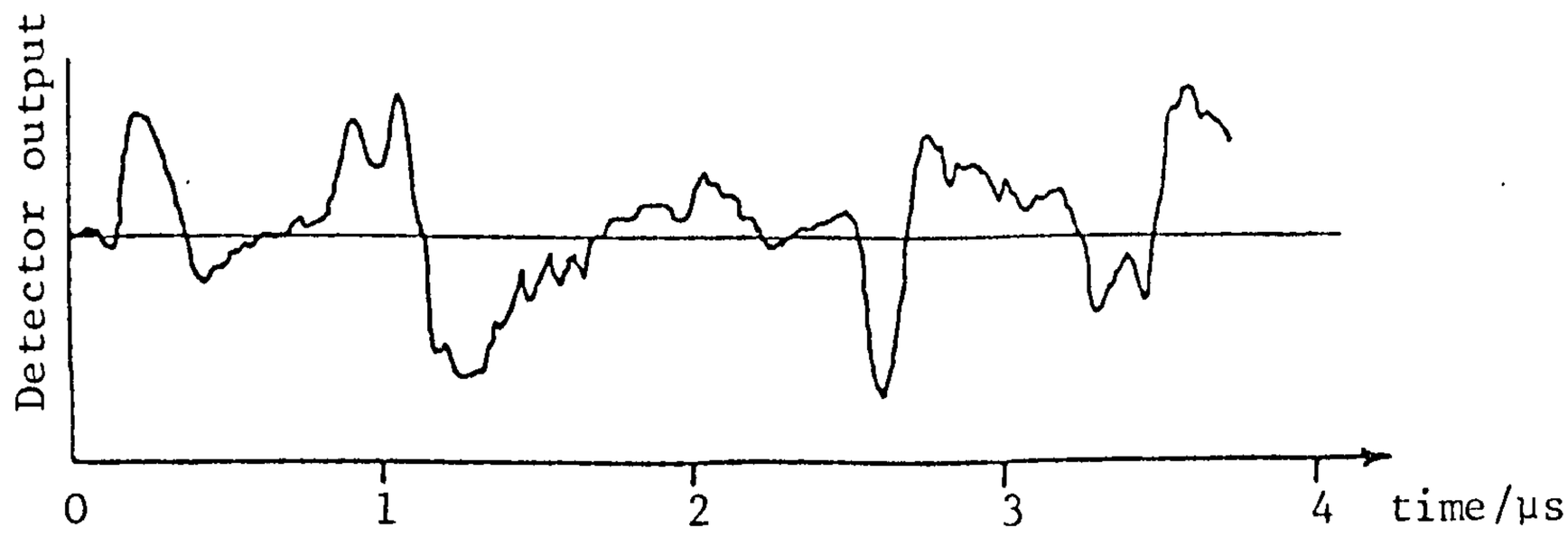

Figure 17: A typical acoustic emission captured during the tensile testing of a 2024 T351 aluminium alloy using a thick piezoelectric crystal. (After Rouby et al[11]).

frequency shifters[45]. The frequency of the laser light in the reference arm is continuously varied by a feedback loop in such a way that the unwanted phase variations at low frequencies are compensated for. This technique works because the frequency is merely the differential of phase. The mathematical basis of the method is outlined in Appendix 1. Even though this is an elegant stabilisation technique the complicated nature of the active stabilising element (Kerr cell) is a drawback.

The second type of stabilisation to employ frequency shifting was described by Olssen et al[54]. Referring to equation (1), the phase ($2\pi x/\lambda$) clearly depends on both λ and x. Olssen et al produced their stabilised interferometer by using a dye laser as the light source. The wavelength of this source was controlled by a negative feedback loop in such a way as to maintain maximum device sensitivity to ultrasonic vibrations. Again the complicated nature of the stabilisation makesthis method unattractive.

The final and by far the commonest stabilisation technique involves physically changing the path length in the reference arm. In order to do this the reference arm mirror is mounted on some position translator, the position of which is controlled in a negative feedback loop. The translator is usually simply a piezoelectric expansion mode crystal[17,55] and as such suffers unfortunately from a limited range of movement. Typical expansion coefficients being 0.5μm/kV[56]. In general the movement available is insufficient to achieve efficient stabilisation. Some other method for rapid mirror movement must therefore be found.

One such method is to mount the reference mirror on a piezoelectric multimorph crystal[57]. This method has not been previously used and is the method adopted to stabilise the Michelson interferometer used in the experiments described later.

An alternative way of producing displacements large enough to achieve efficient stabilisation might be to stack several piezoelectric crystals together. This method could have two drawbacks. The first is the increase in the capacitance of the translator which in turn leads to a need for a high voltage, high power drive amplifier. The second drawback might be the time response of the translator. Work by Yamashita[58] indicates a time response of 100μs. Problems may therefore arise with resonances of the translator causing instabilities in a controlling feedback loop.

II.4.2ii) Noise considerations in optical devices.

The sources of noise in an interferometric device can be broken down to three types.

Firstly, there is the practical difficulty associated with detecting low light levels. If the light power is low then the signal may not be large enough to overcome noise in any device used to amplify the signal. With the advent of lasers this is in general not a problem.

The second source of noise is the variation in laser intensity mentioned previously (Section II.4.2) Consider equation (3). When the third term is negligible and the device sensitivity is a maximum ($\sin(4\pi x/\lambda) = 1$), then;

$$\delta I = -(2\alpha I_o \pi/\lambda)\delta x + (\alpha/2)\delta I_o \qquad (7)$$

By monitoring the laser intensity (via a 50% beam splitter) δI_o can be determined. Correct amplification followed by analogue subtraction (in a difference amplifier) of this term from δI, then leaves just the signal information governed by δx. In a stabilised device laser noise is therefore not a fundamental problem. Calculations outlined in Appendix 2 show that a similar correction may be made in the case of a quadrature interferometer.

The final source of noise in an interferometer is a fundamental one. As laser power is continuously falling on the photodetector then a continuous DC current flows through this device. Statistical variations in this current give rise to shot noise. This is given as[18];

$$< i_S > = \sqrt{2ei_{DC}\Delta f} \qquad (8)$$

where $<i_S>$ is the average noise current, e the modulus of the electronic charge, i_{DC} the steady current and Δf the bandwidth. Fortunately, because the signal information depends on the laser power whilst the shot noise above depends on the square root of the laser power the minimum detectable displacement may be improved by using a higher power laser. Assuming a 10MHz bandwidth, a photodetector response of $0.6Aw^{-1}$, a laser power of 2mW and a 10% efficiency in the interferometer the shot noise limit is around 20pm. Palmer and Green[17] achieved a noise figure of 50pm for a 1MHz bandwidth. The equivalent figure for a 10MHz bandwidth would therefore be 150pm. Bondarenko[55] achieved a figure of 1000pm for a 150MHz bandwidth (250pm equivalent for 10MHz bandwidth). These figures clearly should be improved. The

experimental work reported later shows that improvements can be made in this area. It should be remembered that even the improved noise figure is still too high to allow in general direct observation of acoustic emission. The use of optical detectors should therefore be restricted to calibration and propagation studies.

II.5 Fundamental acoustic emission work using well or partially characterised transducers

The development of the capacitor detector has enabled fundamental work to be carried out in the laboratory. Wadley et al have monitored the emission in mild steel and electrolytic iron at 77K[10,59] by using a capacitor detector directly. A typical waveform is shown in Figure 16. together with the crack-volume time history deconvoluted from the displacement waveform using the theoretical Green's function for a semi-infinite half space. This work is of great interest because it provides information about the dynamics of real cracks. Unfortunately, these capacitor detectors which have a minimum detectable displacement of the order of 1 or 2pm can only capture very energetic events. This is why they are, like optical techniques, best suited to problems of calibration and propagation.

Rouby et al[11] have overcome this sensitivity problem by using thick piezoelectric crystals in which the time taken for an ultrasonic pulse to travel through the crystal exceeds the time scales of interest. The response of these crystals to plane waves arriving from the epicentre has been studied by Dewhurst et al[21]. They produce a good response and are sensitive.

A typical signal detected by Rouby et al is shown in Figure 17. Again, useful information can be deduced about the source.

Figure 18 shows a series of histograms relating the various crack parameters measured by Wadley et al[10]. Clearly different source functions (cracks) are characterised by different values of the parameters of lifetime and size. This therefore confirms the long-held view that a well characterised acoustic emission system can identify (at least partially) different crack mechanisms.

With this information it is clearly now worth pursuing the problems of transducer calibration and pulse propagation. It should be noted that the thick piezoelectric crystal is not a practical transducer due to its large aperture.

II.6 The problem of ultrasonic pulse propagation, deconvolutions of the source function and calibration of ultrasonic transducers

II.6.1 General theory.

The sequence of events leading to the detection of an ultrasonic pulse by a transducer is shown schematically in Figure 19[60]. A given acoustic emission event is characterised in terms of the dynamic force field change it causes. This stress relaxation creates an elastic wave which travels throughout the material causing a disturbance at the detector site. This disturbance is then transformed into an electrical signal by the transducer which is subsequently monitored. The corresponding problem in terms

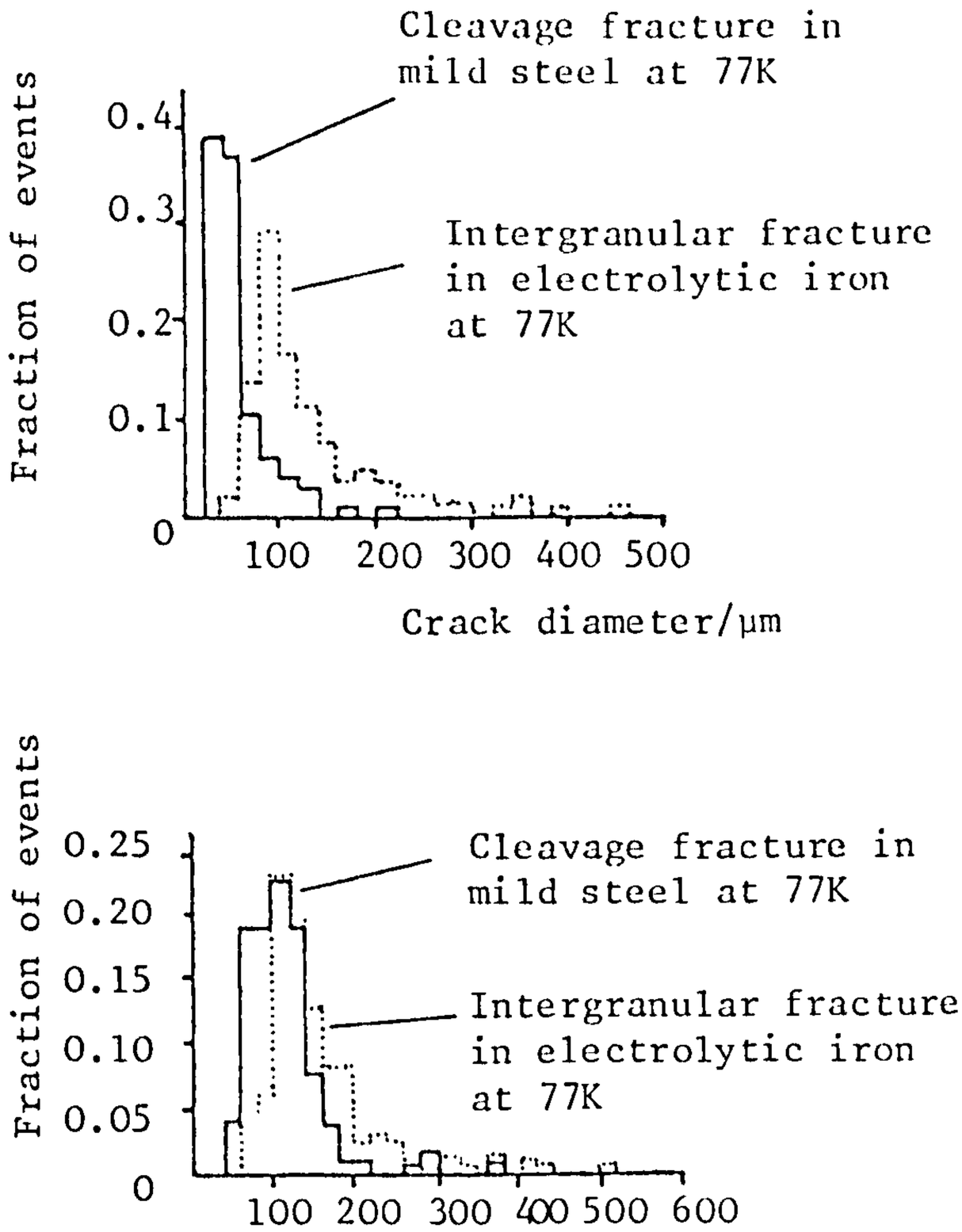

Figure 18: Histograms of crack diameter, lifetime and growth rate for the two different fracture processes of cleavage and intergranular fracture described by Wadley et al[10].

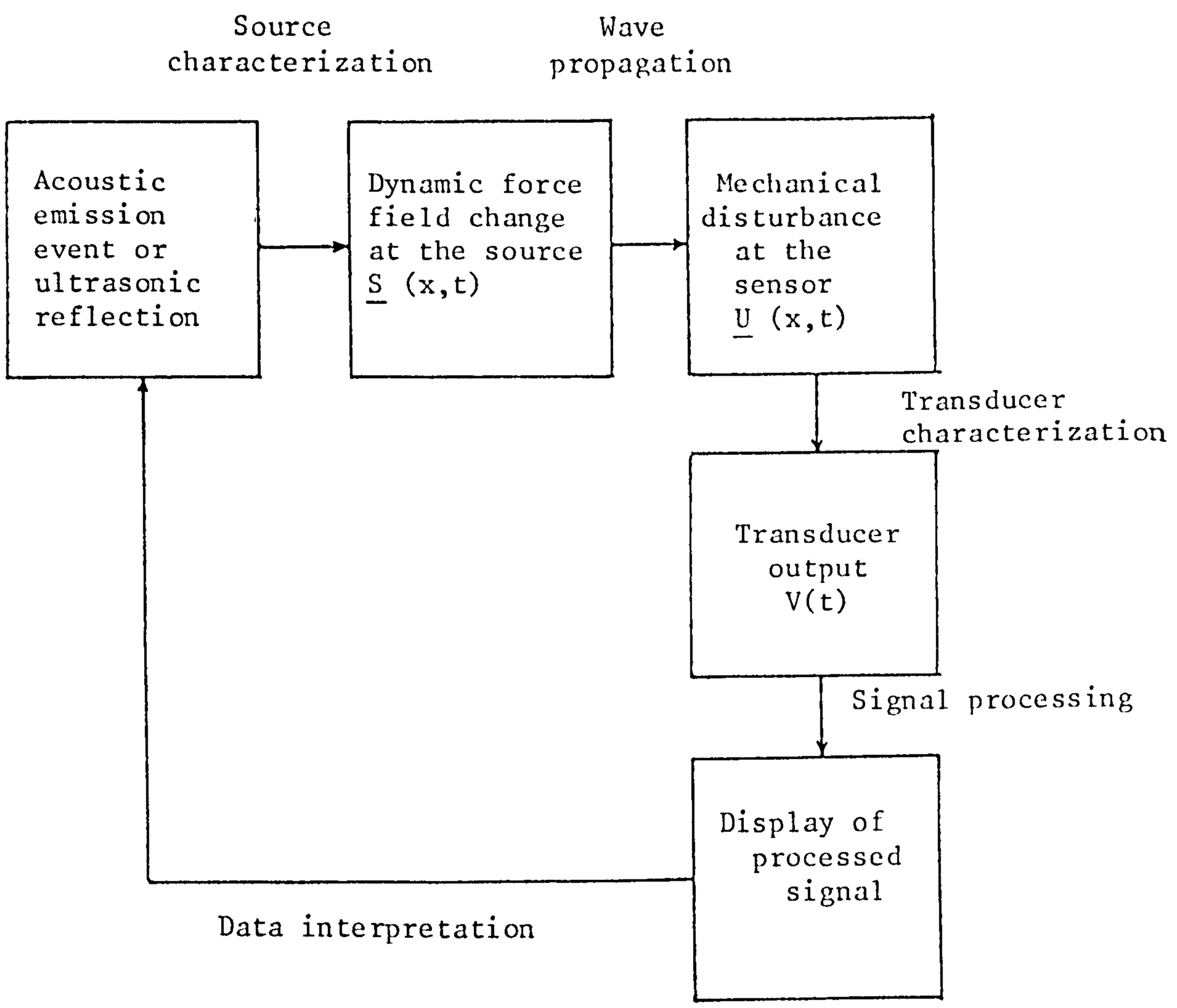

Figure 19: The causal chain of acoustic emission signal analysis. (After Hsu et al[60]).

of ultrasonic flaw location is identical apart from the source. The source in this case being the dynamic stress field about the flaw arising due to an incident elastic pulse.

To allow a practical solution to the problem outlined above requires that a series of simplifying assumptions be made[6,61]. Referring to Figure 20 the quantities to be detected are the force $\underline{F_o}(\underline{x},t)$ over a region $\partial_B(\underline{x})$ and the displacement $\underline{U_o}(\underline{x},t)$. Introducing a detector in general alters these variables so that over the region $\partial_B(\underline{x})$ the force and displacement are now $\underline{F}(\underline{x},t)$ and $\underline{U}(\underline{x},t)$ respectively. Hence the current and voltage out of the transducer are related to these changed quantities:

$$\left.\begin{matrix} I(t) \\ V(t) \end{matrix}\right\} \text{ related to } \left\{\begin{matrix} \underline{F}(\underline{x},t) \\ \underline{U}(\underline{x},t) \end{matrix}\right.$$

The quantities $\underline{F}$, $\underline{U}$ are of course vector quantities. An ultrasonic transducer will respond differently to shear motions of the surface on which it is placed than it will to vertical or longitudinal motions of the surface. The output of the transducer is of course scalar (voltage and current). Therefore in just monitoring these scalar quantities no information can be deduced as to whether the generating motion was shear or longitudinal. If the transducer is to be calibrated, it must be assumed that the transducer detects a single known disturbance mode. In other words the transducer uncouples the various modes and responds to each mode separately in such a way that the mode to which it responds can be analysed independent of the other modes. If

Local quantities to be measured

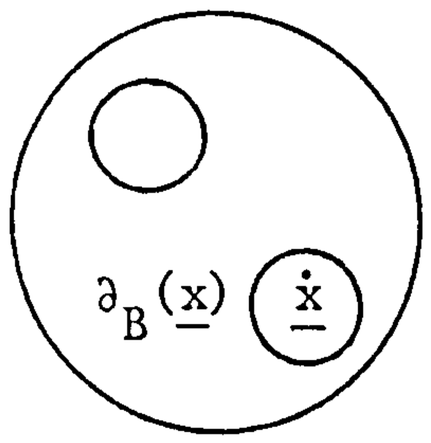

$\underline{F}_o(\underline{x},t)$: Force

$\underline{U}_o(\underline{x},t)$: Displacement

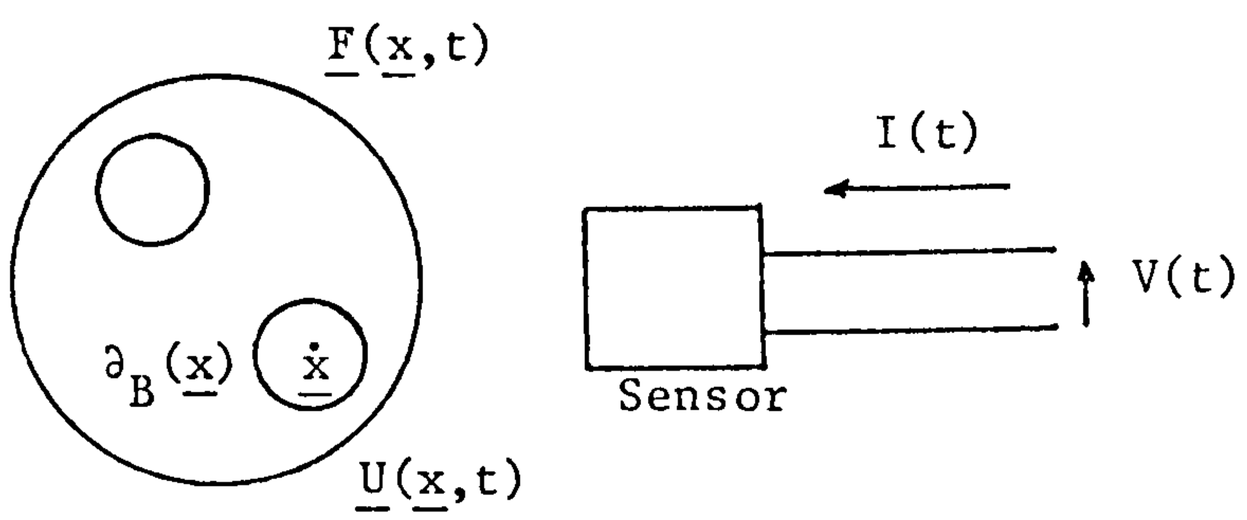

In general

$$\left.\begin{matrix} I(t) \\ V(t) \end{matrix}\right\} \text{ is related to } \left\{\begin{matrix} \underline{F}(\underline{x},t) \\ \underline{U}(\underline{x},t) \end{matrix}\right.$$

SIMPLIFYING ASSUMPTIONS

1. Mode uncoupling

$$\left.\begin{matrix} I(t) \\ V(t) \end{matrix}\right\} \text{ is related to } \left\{\begin{matrix} F(\underline{x},t) \\ U(\underline{x},t) \end{matrix}\right. \text{, a particular mode}$$

2. Field variable independency (either localized or uniform)

$$\left.\begin{matrix} I(t) \\ V(t) \end{matrix}\right\} \text{is related to } \left\{\begin{matrix} F(t) \\ U(t) \end{matrix}\right.$$

3. Linear system response

$$\begin{vmatrix} V \\ I \end{vmatrix} = \begin{vmatrix} A & B \\ C & D \end{vmatrix} \begin{vmatrix} F \\ U \end{vmatrix} \text{ for every frequency } \omega$$

4. Fixed coupling medium and electronics

$$V = \underline{T}F \qquad T = \text{transfer function}$$

Figure 20: Simplifying assumptions of the sensor transduction process to facilitate calibration. (After Hsu and Breckenridge[6]).

this is true then the vector representation of the field quantities $\underline{F}$ and $\underline{U}$ is no longer necessary and they can now be written as scalar quantities. Hence

$$\left.\begin{matrix} I(t) \\ V(t) \end{matrix}\right\} \text{ related to } \left\{\begin{matrix} F(\underline{x},t) \\ U(\underline{x},t) \end{matrix}\right. \text{ for one particular mode.}$$

This assumption of mode uncoupling is never obeyed perfectly in any piezoelectric transducer. However the coupling to the shear mode is in general weak and can sometimes be ignored. The degree of mode coupling (i.e. response to both shear and longitudinal disturbances together) can be determined by making surface wave calibrations and through-pulse or epicentral calibrations[6]. The epicentral response of an infinite plate to a step force unloading contains only vertical surface motion whereas the surface response contains roughly equal amounts of both the vertical and tangential motion.

The second assumption required to enable calibration is that of "field variable independency"[6]. This means the area $\partial_B(\underline{x})$ is sufficiently small that the field quantities F and U are uniform over all of $\partial_B(\underline{x})$. Consider a surface pulse as shown in Figure 5. As this pulse propagates it maintains its overall shape but spreads out along its direction of propagation. A large area transducer close to the source would therefore average over the entire waveform whilst one at some distance away would average over a smaller portion of the pulse. Clearly neither case represents the perfect response to a surface pulse. If, however, the area of the transducer is small enough to resolve the arrival of

the shear wave and Rayleigh wave then at any moment in time it will only be responding to one wave. (It must also of course only be responding to one mode of this wave - mode uncoupling). In this situation the spatial averaging becomes a frequency averaging effect. The size of the allowed aperture can be determined as follows:

Let the distance from the source to the detector be D and the velocities of the shear and Rayleigh waves V_S and V_R respectively. The arrival times of these waves t_S and t_R are then:

$$\left.\begin{aligned} t_S &= D/V_S \\ t_R &= D/V_R \end{aligned}\right\} \qquad (9)$$

The time resolution Δt for the transducer is related to its diameter d_T approximately by:

$$\Delta t \simeq 0.7(d_T/V_R) \qquad (10)$$

It is (somewhat arbitrarily) assumed that the two wave types are sufficiently resolved when around 30% of the energy of one wave is averaging in with the other wave. Therefore

$$\Delta t \simeq \frac{t_S - t_R}{3} \quad \text{(for resolution)} \qquad (11)$$

leading to $$D = 2.1 d_T V_S/(V_S - V_R) \qquad (12)$$

If d_T = 1mm and the velocities are those in aluminium (V_S = 3.111mm μs^{-1} and V_R = 2.906mm μs^{-1}) then:

$$D = 30\text{mm} \qquad (13)$$

Such calculations should always be considered when making surface pulse calibrations.

The third assumption required for successful calibration is that of a linear system response. This is in general true as measurements by Reibold and Molkenstruck[62] show. When this is the case Fourier's theorem[63] may be used to yield a transducer response as

$$\begin{bmatrix} V \\ I \end{bmatrix} = \begin{bmatrix} A & B \\ C & D \end{bmatrix} \begin{bmatrix} F \\ U \end{bmatrix} \quad \text{for all frequencies } \omega \qquad (14)$$

The transduction matrix is now measurable. However, one more simplification is usually made. If the sensor is reproducibly coupled to a fixed test medium and the input impedance of the preamplifier is fixed then F is related to U and V to I. This means that a transducer calibrated on aluminium will have a different response to the same transducer calibrated on steel as the relationships between F and U will vary for the two metals. Using the assumption above leads to:

$$V(\omega) = T(\omega).U(\omega) \qquad (15)$$

Using Fourier's theorem[63] the time domain response may be recovered as

$$V(t) = \int_o^t T(t - \tau).U(\tau)d\tau \qquad (16)$$

Using all the assumptions a calibration can be made if U can be measured either directly or indirectly.

The process of pulse propagation may also be reduced down to a convolution integral[8,60]. For a linear system (which is true in metals for the strains associated with ultrasonic pulses) then the Green's function, $\underline{G}$, for the material is

defined in terms of the displacement at a point in the material or on its surface $\underline{U}$ resulting from a force change at some other point $\underline{S}$ by[60]:

$$\underline{U}(\underline{x},t) = \int_o^t \underline{G}(\underline{x},\underline{x}_o,t-\tau)\underline{S}(\underline{x}_o,\tau)d\tau \qquad (17)$$

This assumes that $\underline{S}$ acts at a point which clearly is impossible. However, in terms of acoustic emission crack growth and detection this is a reasonable assumption. If $\underline{S} = 0$ for $\tau < 0$ then equation (17) may be rewritten as:

$$\underline{U}(\underline{x},t) = \int_{-\infty}^{+\infty} \underline{G}(\underline{x},\underline{x}_o,t-\tau)\underline{S}(\underline{x}_o,\tau)d\tau \qquad (18)$$

Using Fourier's theorem[63] the frequency response may then be written as

$$\underline{U}(\underline{x},\omega) = \underline{G}(\underline{x},\underline{x}_o,\omega).\underline{S}(\underline{x}_o,\omega) \qquad (19)$$

thus allowing $\underline{S}$ to be determined if $\underline{G}$ can be calculated and $\underline{U}$ measured:

$$\underline{S}(\underline{x}_o,\omega) = \underline{U}(\underline{x},\omega)/\underline{G}(\underline{x},\underline{x}_o,\omega) \qquad (20)$$

or defining an inverse function G^{-1} then

$$\underline{S}(\underline{x}_o,t) = \int_o^t \underline{G}^{-1}(\underline{x},\underline{x}_o,t-\tau).\underline{U}(\underline{x},\tau)d\tau \qquad (21)$$

Source functions may therefore be derived either by frequency domain deconvolution or by direct time-domain deconvolution by computing $\underline{G}^{-1}$.

The function $\underline{G}$ has been calculated for several geometries[6,8,13,19,20,24,25], whilst the inverse function $\underline{G}^{-1}$

has been calculated by various workers[6,8,64]. For digitised data numerical deconvolution is possible and has been discussed by Hsu and Hardy[8]. This is outlined in Appendix 3.

II.6.2 Experimental work carried out on propagation and deconvolution.

Nearly all the experimental work carried out in the area of propagation and deconvolution has been concerned with either determining the force-time dependencies of various artificial acoustic emission sources or verifying theoretical Green's functions in thick plates. The exception to this has been work by Wadley et al[10]. This latter work was concerned with determining the source functions for real acoustic emission sources and has been discussed in Section II.5.

The first experimental work[35] in 1975 was concerned merely with measuring the surface displacement on a thick plate at some distance from an artificial source. The source was a breaking glass capilliary. This capilliary is pseudo-statically loaded until fracture occurs. The resulting rapid stress release on the material surface sets up an elastic wave. This wave was detected by the capacitor depicted in Figure 4. This work was followed up in 1981[16] by a consideration of the frequency limits of the measuring device. The detected waveform (Figure 21) is very similar to the theoretical pulse expected assuming that the capilliary fracture is a step force release.

Deconvolution of an artificial source was first reported

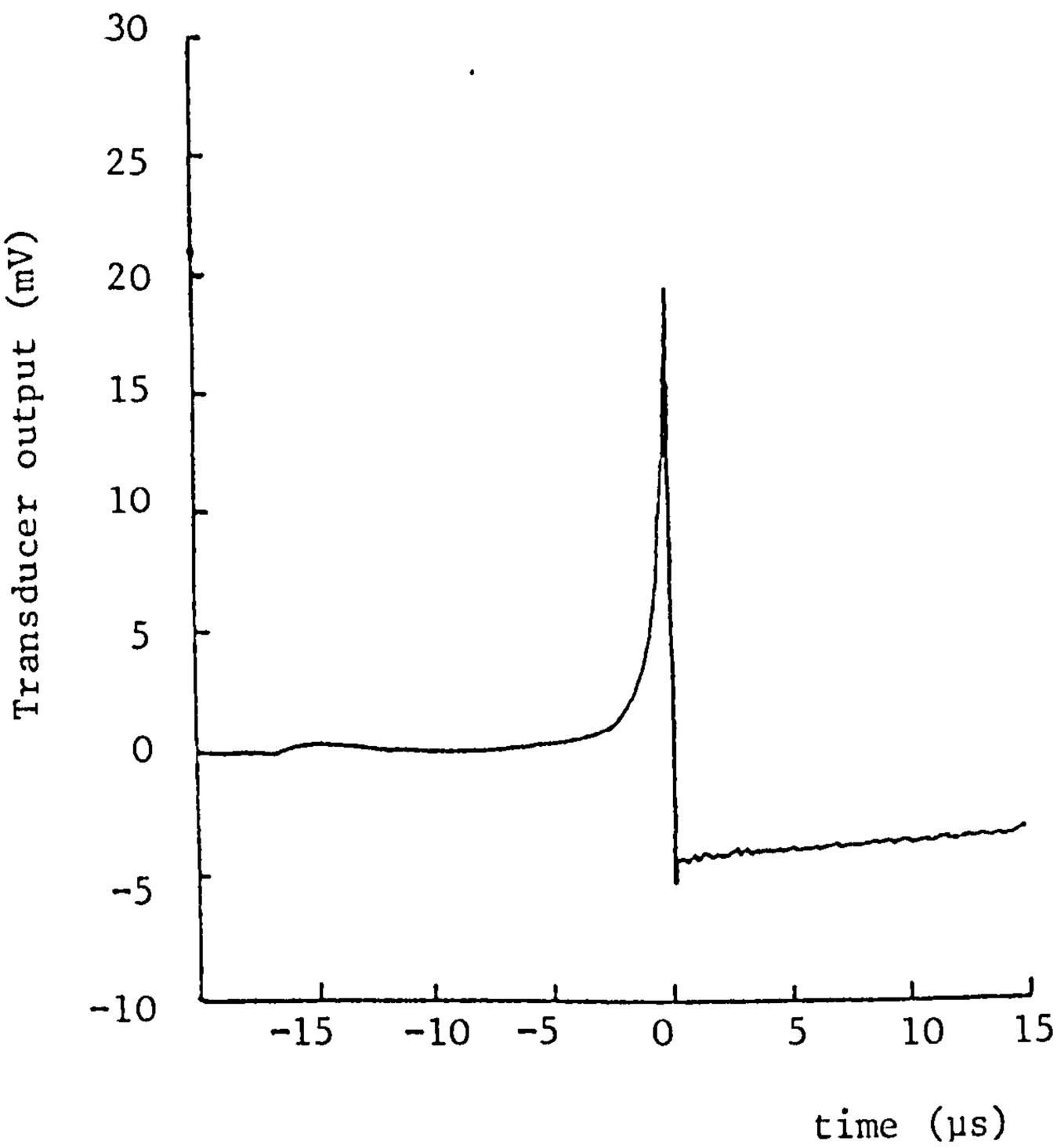

Figure 21: Experimental surface pulse waveform obtained by averaging 10 events generated by a glass capilliary fracture, as detected by the capacitor detector shown in Figure 4. (After Breckenridge and Greenspan[16]).

in 1977 by Hsu et al[60]. A thick aluminium plate was used as a transfer medium. Waveforms were detected epicentrally by a capacitance transducer. Theoretical Green's functions were used to deconvolute the driving force function for a wideband piezoelectric transducer which was used as the artificial source. The results of the work are summarised in Figure 22.

Further work was then reported in 1978 by Hsu and Hardy[8]. Using the same experimental arrangement and the same deconvolution techniques source force-time functions were reported for three artificial sources (Figure 23). These sources were the breaking glass capilliary, the impact of a 1.5mm steel ball dropped from 5cm and the fracture of a 0.5mm polymer pencil lead. To create this last function a section of lead is extended out of a conventional propelling pencil. As the tip of the exposed lead is pushed onto the material surface stress is built up in the lead and in the surface. Eventually this stress is rapidly released as the lead fractures.

Sachse and Ceranoglu[65,66] continued this type of work obtaining similar results to those above in what was essentially an identical experiment. Micheals et al[7] produced further results on the breaking pencil lead, capilliary fracture and ball impact sources. The detector used in this work was not an absolute measurement device, but was a broadband piezoelectric transducer which therefore required calibration. The experiments were performed as follows. Firstly, the transducer response to a glass capilliary broken epicentrally on a large plate was measured.

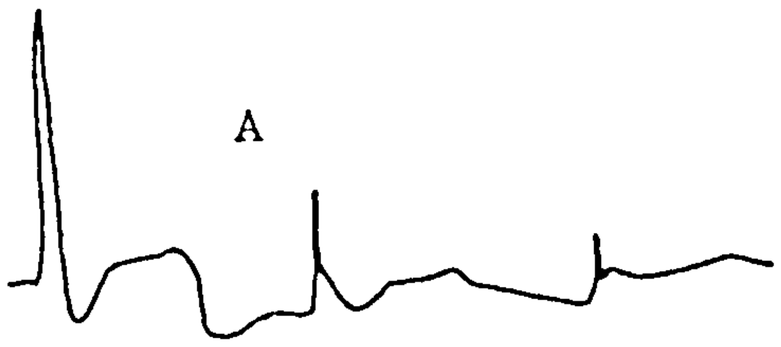

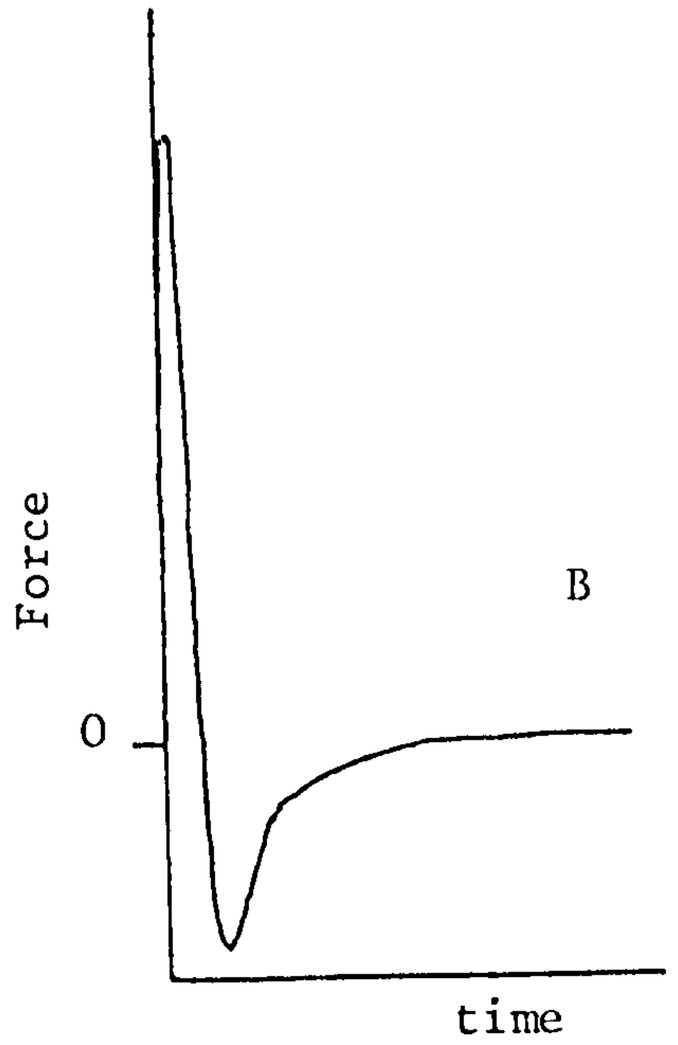

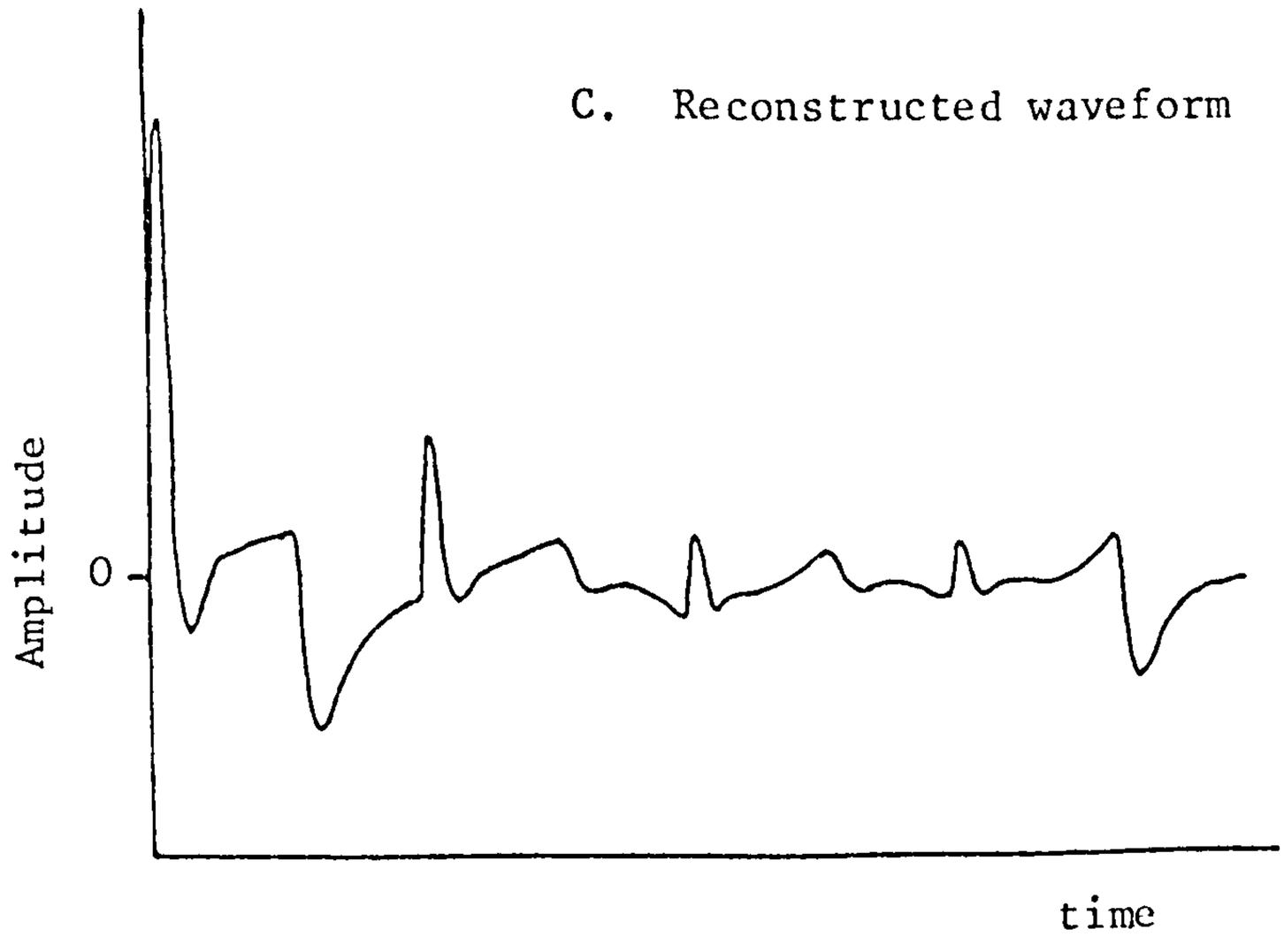

Figure 22: Source characterization through deconvolution. A is a trace of the detected epicentre displacement due to a stress pulse of unknown shape produced by a wideband ultrasonic transducer. B is the numerically computed input force function through deconvolution of A with the theoretical Green's function. C is the reconstructed waveform of B convoluted with Green's function. (After Hsu et al[60]).
It should be realised that this does not verify the Green's function but only demonstrates that the correct inverse was calculated.

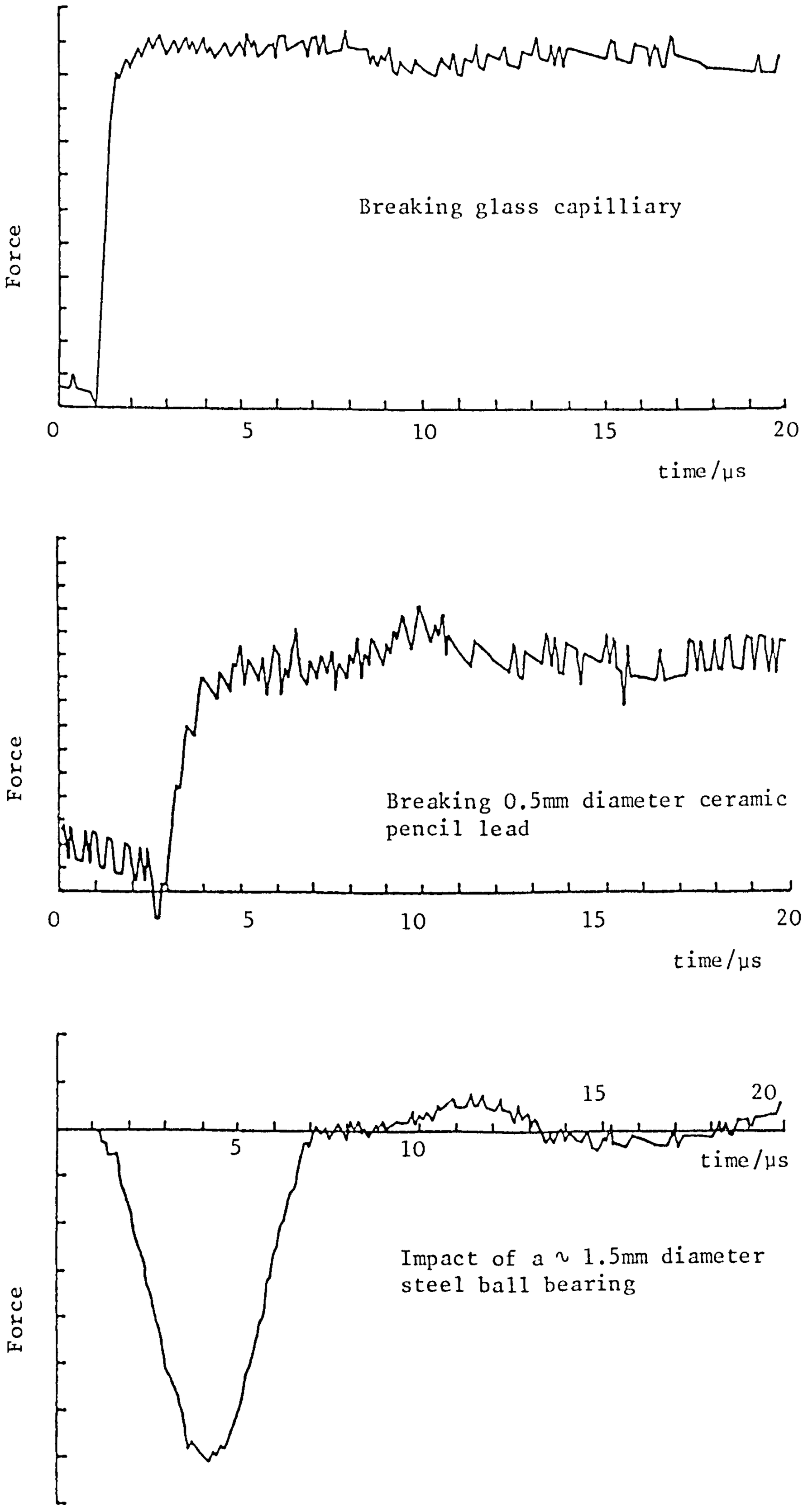

Figure 23: Source force-time functions for three artificial sources of acoustic emission (After Hsu and Hardy[8]) obtained by time domain deconvolution (see text).

Using the theoretical Green's function for the plate and assuming the glass capilliary to produce a force release with a Heaviside function time dependence then the transducer transfer function was determined. Such evaluation uses the equation outlined in section II.6.1.

The capilliary was now moved off epicentre and the Green's functions measured for the new geometries. The agreement between these deconvoluted traces and the theoretical transfer functions for the off-epicentral arrangements are shown in Figure 24. This arrangement is good but not perfect indicating some uncertainty may exist in the deconvolution process.

Now that the transducer and plate transfer function had been measured further sources could be substituted in place of the glass capilliary, thus allowing their force-time functions to be determined. Such a source function for a pencil lead fracture is shown in Figure 25. The final aspect of this work was to substitute a small plate for the large (effectively infinite) plate. Its transfer function was then determined.

This work should be considered important in that it shows how deconvolution techniques can be applied to piezoelectric transducers not specially designed to be broadband. However, the assumption that the glass capilliary fractures with a Heaviside time dependency may not be valid. Hsu and Hardy[8] report a rise time of 0.54μs for such an event. Michaels' results for the pencil fracture which indicate a rise time of ∿0.7μs might therefore contain some errors.

Work on the pencil fracture source has also been carried

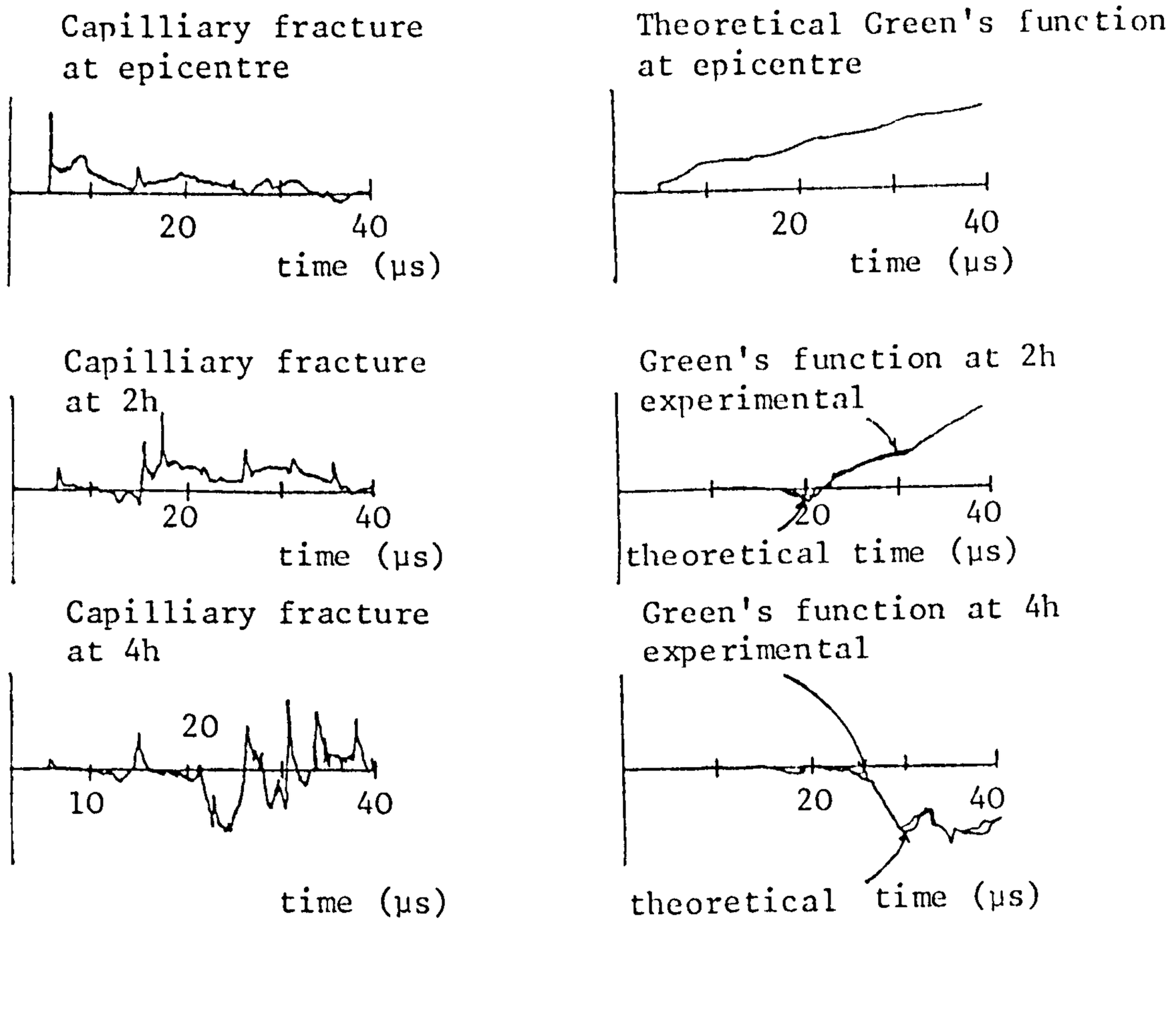

Figure 24: The time domain transducer outputs of a piezoelectric detector due to a capilliary fracture at the positions indicated (left) and (right) the theoretical and experimentally deconvoluted Green's function for these set-ups. (After Micheals et al[7]).

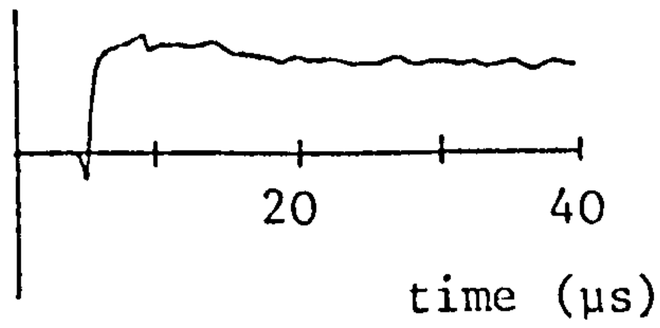

Figure 25: The source force-time function for a pencil lead fracture reported by Micheals et al[7].

out by Ohisa and Kishi[67]. Their work was similar to that of Hsu and Hardy[8] and Hsu et al[60] in that a capacitance transducer was used to detect epicentral responses on an infinite plate. The detailed form of their deconvoluted source function for the pencil shown in Figure 26 is not the same as that reported by Micheals et al[7] in that no negative dip is indicated prior to the main step. The reason for this discrepancy is not given.

Procter et al[68] have extended the results on propagation in an infinite plate by using a high-fidelity piezoelectric transducer. This will be described later. Using capilliary fracture to generate a point step force fair agreement between and experiment and the theoretical Green's functions for the infinite plate was obtained.

The discussion so far has centred on the propagation of ultrasonic pulses generated by brittle fracture, ball impact and piezoelectric transducer stimulation. In 1963 White[69] demonstrated that laser impact also produces fast ultrasonic pulses. A pulsed ruby laser was used in this initial work. Felix[70] continued with the study of elastic pulses produced by rapid laser heating. A thin liquid layer was used to absorb the laser radiation and therefore generate the ultrasonic waves. Many other workers have used lasers to generate such waves. This work is discussed by Sachse and Hsu[71] in a review on transducer calibration.

Recently lasers have been used in studies of ultrasonic pulse propagation and ultrasonic transducer calibration [15,21,72,73,74,75,76]. This work has been concerned with both the physical mechanisms behind the generation process

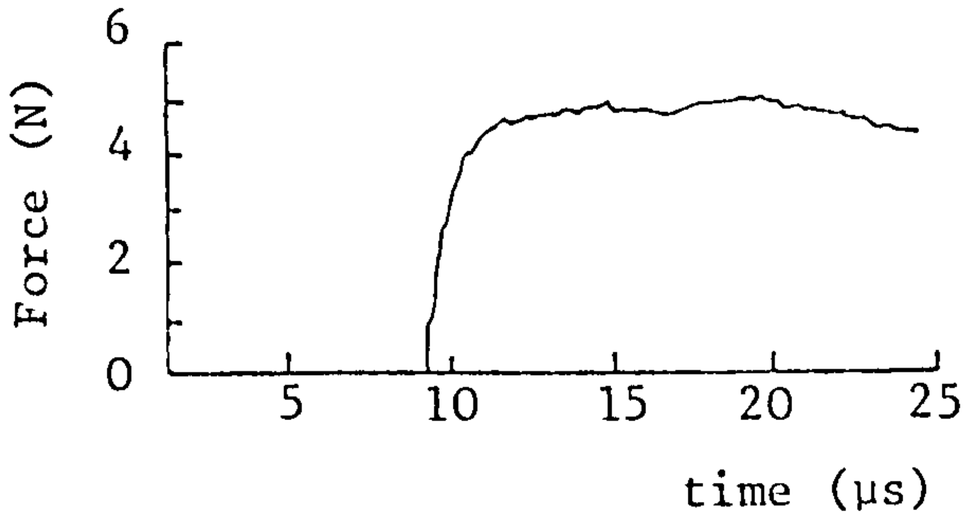

Figure 26: The source force-time function for a breaking ceramic pencil lead as reported by Ohisa and Kishi[67].

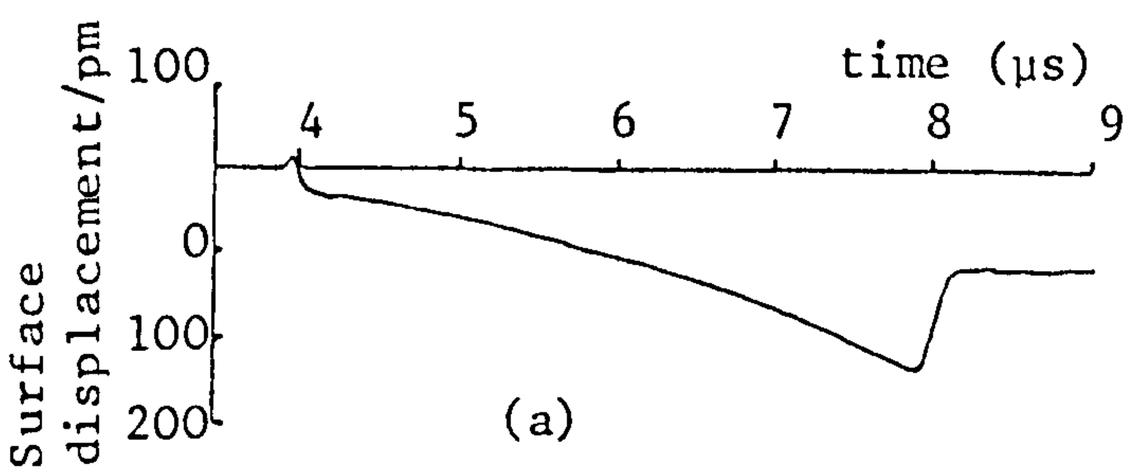

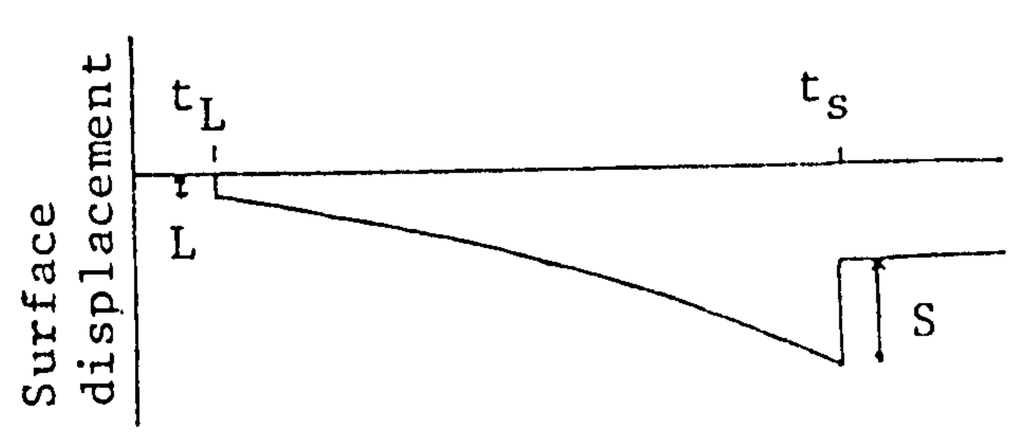

Figure 27(a): The experimentally measured vertical surface displacement at the epicentre of an artificial acoustic emission source. The source is the thermo-elastic heating of a material surface caused by the impact of a Nd-YAG laser.

Figure 27(b): The theoretical waveform for such an event assuming the source to be in the material surface only. t_L and t_s are the arrival times of the longitudinal and shear waves respectively. (S/L) is predicted to be 4.0. (After Scruby et al[72]).

and on the propagation of the resultant pulses. The generation process will be discussed later. Scruby et al[72] reported the measurement of epicentral elastic pulses in an aluminium alloy block. The ultrasonic transducer used was a capacitor transducer as discussed in section II.4.1. The source was assumed to be three orthogonal force dipoles in the material surface and the expected epicentral displacement was compared to the measured waveform. Close agreement was found (Figure 27). As the source was assumed to be at the material surface the Green's function for the force dipole acting perpendicular to this surface gave no displacement at the epicentre. The small positive pulse before the main longitudinal step is therefore not predicted by the preliminary theory considered in this work.

Subsequent work by Dewhurst et al[76] presented further results on the experimental arrangement described above, together with a more thorough theory which did predict all aspects of the detected pulses successfully using theoretical Green's functions and a more realistic model for the source. Even though improved agreement between theory and experiment is found, the result cannot be considered as an absolute test of the propagation calculations. As only one measurement is made (the vertical epicentral displacement) then the source cannot be fully defined and a degree of freedom in the source description arises.

The directivity of the ultrasound generated by laser impact has been studied experimentally by Hutchins et al[74]. Good agreement was found between the predicted directionality and that actually measured.

In addition to the epicentral pulses discussed above Aindow et al[15] have measured the surface pulses created by laser impact with a capacitative detector. Good qualitative agreement is found between the measured pulses and those predicted by the convolution of theoretical Green's functions with assumed source functions. This agreement is shown in Figure 28.

Similar work with laser impact has been carried out by Wadley et al[77] in which theoretical waveforms are compared to those measured with a broadband piezoelectric transducer.

In all the above work various assumptions have been made. The main assumption is that the theoretical Green's functions used are correct. Due to the good agreement between calculated and measured responses this assumption appears valid. However, no direct verification has been made by measuring both the source directly and the surface movement at some distance from the source. Such measurements would be of interest and may be possible with the use of optical transducers which can probe inside transparent materials.

Other assumptions are also made concerning the source etc. The specific areas of uncertainty to be investigated are:

i) Do the artificial sources have the form assumed (i.e. does the brittle fracture of a pencil lead produce just a vertical force with no component parallel to the material surface)?

ii) Is the instability of the deconvolution as mentioned by Scruby et al[72] and Hsu and Eitzen[64] important and are the slight errors due to noise found in all the deconvolutions

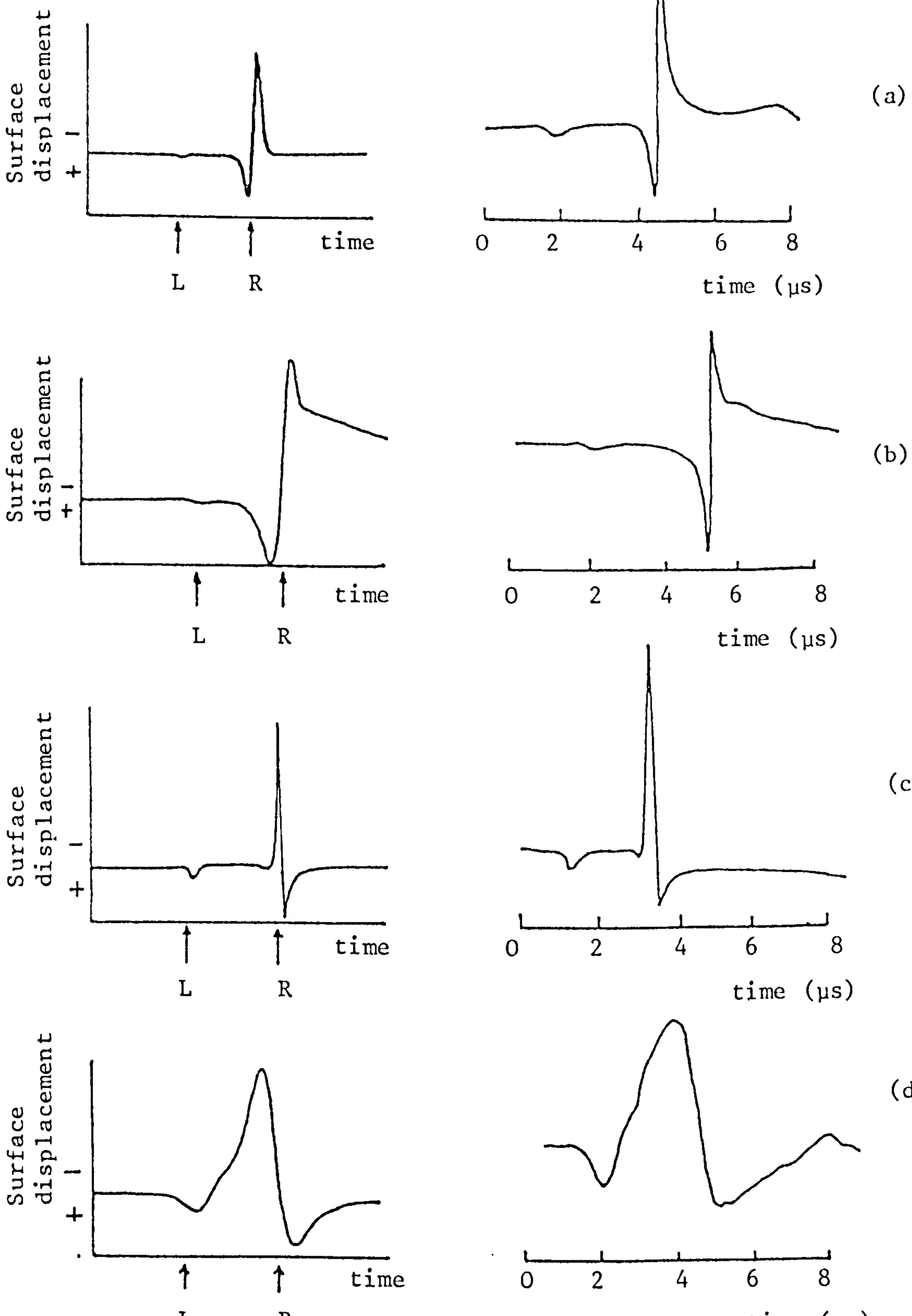

Figure 28: Theoretical (left) and experimental (right) vertical surface displacements caused by the impact of a Nd-YAG laser. Measurements and generation on the same surface of a thick plate.
(a) low temperature plasma. 20mm between source and detector
(b) high temperature plasma. 20mm between source and detector
(c) thermoelastic point source. 12mm between source and detector
(d) thermoelastic 3mm diameter source. 12mm between source and detector.

important? Noise in a signal can cause severe errors in a deconvolution process as the zeros of the noise do not coincide with the zeros of the signal. In inverting a signal unwanted singularities can therefore arise[78].

iii) Is attenuation in the materials significant, especially at high frequencies? Attenuation measurements have been made by various workers. The results of this work are summarised in Appendix 3.

The final point to be noted about these propagation studies is that only plates have been used for the material geometry. It would be of interest to measure the transfer functions of other geometries such as the solid cylinder[79].

II.6.3 Experimental work on ultrasonic transducer calibration.

Ultrasonic transducer calibration is most readily carried out in a laboratory where the situation can be easily controlled. Such work is useful for the development of transducers. In addition to laboratory calibrations, in situ calibration is also necessary to enable the effects of variations in transducer coupling efficiency and variations in specimen geometry to be measured.

II.6.3i) Laboratory calibration of ultrasonic transducers.

Two methods have been used[6] to perform laboratory calibration of transducers. These are the reciprocity method and the comparison method. A third method used by Dmitrevski et al[80] involves measuring the impedance of transducers. However this method appears only to give absolute values for the calibration when the wavelength of the ultrasound is much greater than the dimensions of the

receiver.

II.6.3i)a) The comparison method for transducer calibration.

A calibration facility has been set-up at the National Bureau of Standards (NBS) in the United States[6]. This facility is based on comparing the response of the transducer under test with the response of the standard capacitance transducer described by Breckenridge and Greenspan[16]. Both transducers are excited simultaneously in a symmetrical arrangement with a high frequency noise source. Usually this is a glass capilliary fracture.

The experimental arrangement taken from Procter[9] is shown in Figure 29. Using this arrangement conventional ultrasonic transducers and hi-fidelity piezoelectric transducers have been calibrated. The calibration results for such transducers are shown in Figure 30. The calibration is performed by calculating the Fourier transforms from the time responses for the capacitance transducer and the test transducer and then applying equation (15). Equation (15) for the capacitor is

$$V_C(\omega) = \alpha . U(\omega) \qquad (22)$$

and for the test transducer

$$V_T(\omega) = T_T(\omega) . U(\omega) \qquad (23)$$

thus allowing $T_T(\omega)$ to be determined as α is a known constant.

A similar technique has been used to calibrate ultrasonic fluid transducers by Badoux et al[81]. The standard transducer used in this work is the thick piezoelectric slab described

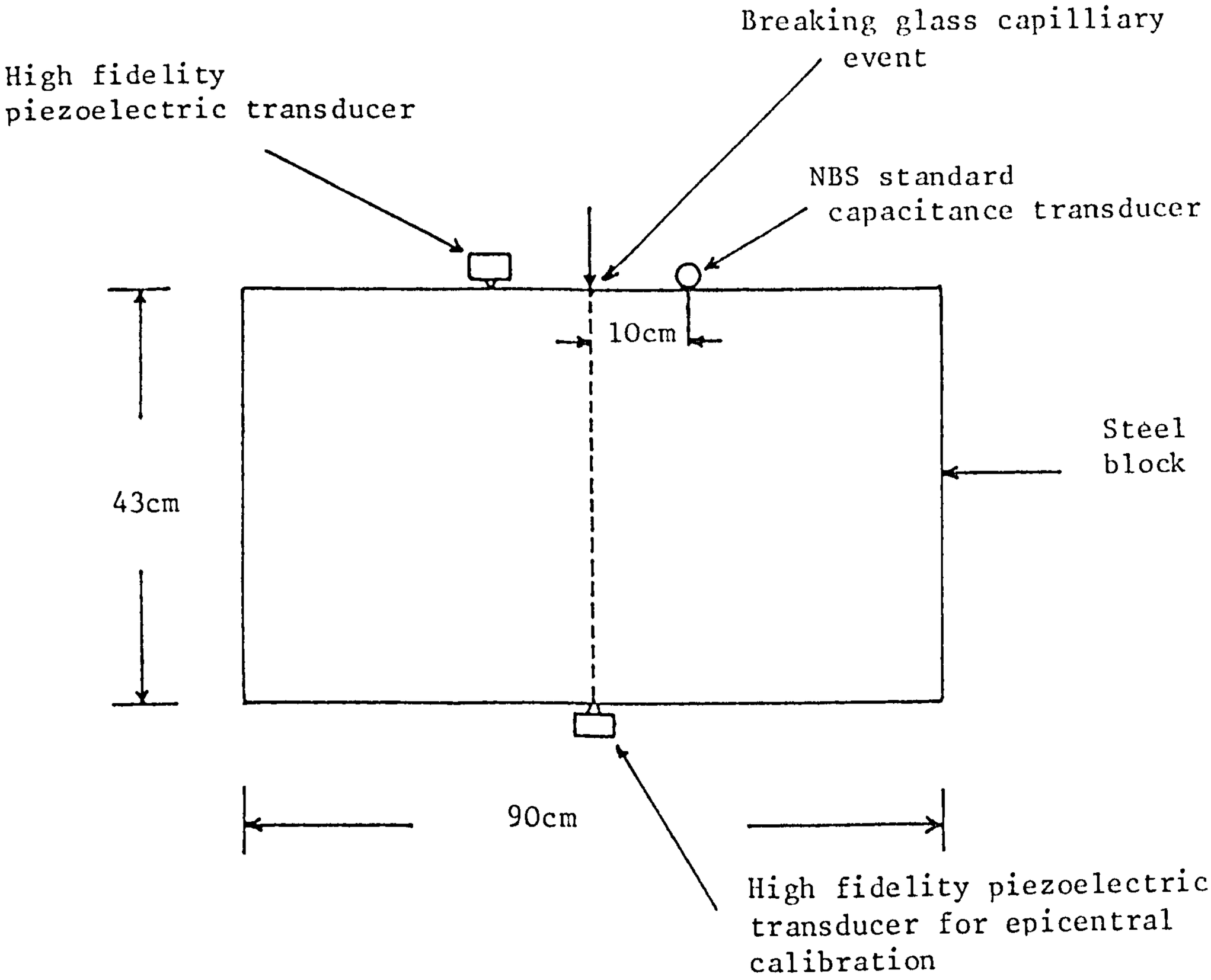

Figure 29: Schematic of the surface pulse and epicentral pulse calibration arrangements used by Procter[9].

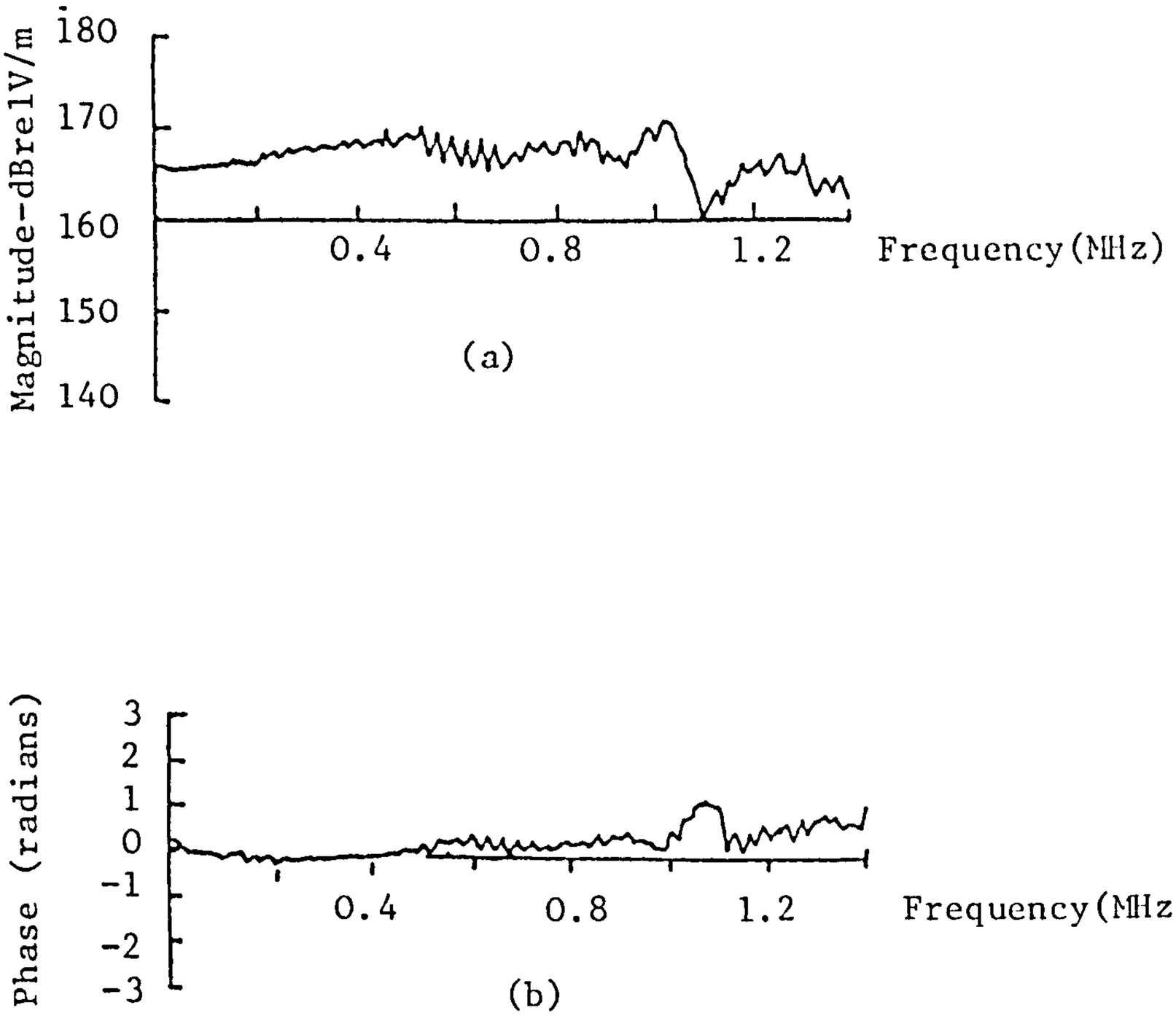

Figure 30: The frequency response of the high fidelity transducer shown in Figure 34 determined by the methods outlined in Figure 29. (a) and (b) are the magnitude and phase of the transducer response to a surface pulse whilst (c) is the magnitude of the response to the epicentral pulse.

by Dewhurst et al[21]. There is, however, uncertainty about the loading effect of this transducer on the pressure field in the fluid transfer medium.

It should be noted that because of the variability of the glass capilliary fracture then in the through pulse calibration of Figure 29 the response of the test transducer must be compared to that for a theoretical step release. This is unsatisfactory and some repeatable source would be preferred, for example a pulsed piezoelectric transducer.

II.6.3i)b) The reciprocity method for transducer calibration.

An alternative calibration method has been used by Hatano and Mori[82]. This is the reciprocity method outlined by Hsu and Breckenridge[6]. In such a calibration three transducers are attached to some suitable transfer medium, a large plate being used by Hatano and Mori. The transducers must be reciprocal and are then tested in pairs. For each independent pair one transducer is used to transmit ultrasound and the other to receive it. Measurements are made of the output voltage of each receiver and the input voltage to each transmitter, together with the free impedance of all the transducers. Once a reciprocity parameter has been calculated absolute calibration is possible.

The method has been extended by Higo et al[83] so that once the transducer sensitivities have been derived on a standard transfer geometry, then the transfer function of an arbitrary geometry may be measured.

The reciprocity method has several disadvantages. First of all a general reciprocity theorem for transducers coupled

to a solid has not been proven[84]. Secondly, the reciprocity parameter must be independently measured. Thirdly, the transducers used must be reciprocal and the mechanical wave fields must be precisely vertical displacements resulting from vertical force inputs. The final disadvantage is that phase information is lost. This calibration method will therefore not be used in the experimental studies.

II.6.3ii) In situ calibration of ultrasonic transducers.

Two approaches to this problem have been made. The first uses a reciprocity technique[83]. However, this method requires that the ultrasonic transducers used be reciprocal. It can not therefore be applied in all situations. The second in situ calibration method uses some artificial known source of ultrasound. This is the method used by most acoustic emission workers. The artificial source is applied to various points over the structure under test and the response of the transducer measured. Knowing the source function allows the material transfer function combined with the transducer transfer function to be determined. Work based on this method has been reported by Kishi and Ohira[85] in which the fracture of a pencil lead was used to find the combined specimen and transducer transfer function. The results from these calibrations were then used to obtain the source function for real cracks by deconvolution. Other work by Takashima, Higo and Nunomura[86,87,88] did not involve full deconvolution. In their work the modulus of the frequency response of the combined system was determined by use of the pencil fracture. This then allowed the modulus

of the frequency spectrum for the real sources to be calculated, via equations (19) and (20).

Such work as that discussed above clearly requires independent measurements of the artificial sources to be made. These will now be discussed in more detail.

II.7 Artificial sources

A number of sources are available to produce discrete high frequency ultrasonic pulses. These are listed by Hsu and Breckenridge[6]. For a source to be useful it must be well characterised, localised, reproducible, contain high frequencies and be discrete. Such considerations lead to three possibilities: brittle fracture, laser impact and electrical spark. The electrical spark[89] is reproducible, but always causes surface damage and can be hazardous in certain environments. It will therefore not be considered further.

The brittle fracture reported so far may be subdivided into glass capilliary fracture, pencil lead fracture and the fracture of small SiC particles. The various sources are now discussed separately.

II.7.1 Glass capilliary fracture.

The fracture of a glass capilliary has been assumed to create a rapid point step release of stress built up in the material surface by the loading process. All the information derived about the source has therefore been obtained by measuring the surface displacement at some remote point on a specimen and deconvoluting this with the Green's

function for a vertical surface force. The monitoring transducers have usually been capacitors whilst the specimen geometries have been plates[7,8,16,35,65,66]. The actual force released varies somewhat but may be monitored in the loading mechanism[8,16].

The deconvoluted source function has been shown to be a step[8,65,66] (see Figure 23). However the rise time of the step is subject to uncertainty, ranging from ⩽ 0.1μs reported by Breckenridge et al[35] to 0.54μs reported by Hsu et al[60].

No direct measurement of the source has been made. This would be of interest to both test the calculations and resolve such uncertainties as the rise time.

II.7.2 Pencil lead fracture.

This is again assumed to be a vertical surface force and the form of the force has been determined by deconvolution [7,8,67]. Typical results are shown in Figures 23,25 and 26. Clearly these traces are not identical, differing mainly in the negative dip shown in Figure 25. The cause of this dip may be the state of stress experienced by the lead prior to fracture or may be due to tangential forces exerted by the lead in the material surface.

Again a variety of rise times are quoted ranging from 360ns and 540ns for a pencil of diameter 0.3mm reported by Shibata[90] (using results derived by Scruby and Wadley[32]) to the 0.9μs given by Ohisa and Kushi[67] for a 0.5mm lead.

Even though the pencil is widely used as an artificial source not much work has been reported on it. No work has been reported on the effect of changing the angle of contact

between the protruding lead and the surface, although some work has been reported on the effect of changing the length and thickness of the lead[8]. The latter work is however sketchy. Finally, most of the work that has been performed was concerned with measurements on the reverse side of a plate whilst little has been done on the surface pulse. All of these areas require further experimental investigation together with direct observation of the source if possible.

The reproducibility in terms of the amplitude of the pencil artificial source has been studied using conventional piezoelectric transducers[91,92]. This work is very thorough but unfortunately information about the reproducibility in the frequency domain is limited, because of the nature of conventional transducers. Further work is therefore required on such reproducibility.

II.7.3 Other brittle fracture.

Graham and Alers[93] and Pardee and Graham[94] have studied the elastic ultrasonic pulses resulting from the fracture of SiC particles. Two experiments were performed. The first involved detecting the elastic waves with conventional piezoelectric transducers on a thick plate. These results were somewhat qualitative. The second experiment involved measuring the waves with a capacitor transducer. The results indicate that high frequencies can be generated although no attempt was made to determine the source function, results being given in the frequency domain for epicentral waveforms on a large plate.

A possible further brittle fracture source may be the fracture of small glass spheres. Such spheres are easily

obtained, one of their uses being in laser fusion studies. However, to the author's knowledge no work has been carried out on their use as an artificial acoustic emission source.

II.7.4 Laser impact.

The use of laser impact for propagation studies has been discussed previously (Section II.6.2). The discussion here will be concerned with the source mechanism and its dependence on energy, energy density and spot size.

The elastic wave generating mechanism for laser impact can be either thermoelastic in which a small area of material is transiently heated, or it can be ablation in which the energy density is large enough to cause a vaporisation of some of the surface material. The thermo-elastic generation can be altered by introducing various surface modifications for example oil or water covering[70,76]. However, in terms of an artificial acoustic emission source this is undesirable. The discussion will therefore be limited to laser impact on an unmodified solid surface.

Most of the experimental studies regarding such generation have been made using capacitor transducers detecting the epicentral waves from laser impact. The study of surface wave generation has been previously discussed (Section II.6.2). However, it should be mentioned that in order to generate a surface pulse of sufficient high frequency to be useful as an artificial source, then the laser has to be focussed down to a small spot. The use of laser impact as a buried artificial source does not suffer from this drawback which is why epicentral studies are useful for determining generating functions.

At low power densities the laser heats a small section of material[76]. This section then attempts to expand. However, because of the surrounding cold material this is not possible. The heating therefore results in a rapid stress build up. The theoretical treatment of such a process is given by Dewhurst et al[76]. If thermal diffusion is assumed to occur during the heating, then agreement is found between the predicted pulse (Figure 31) and the detected pulse shown in Figure 27. In this thermoelastic region the resultant elastic pulse is proportional to the incident laser energy[15], but independent of the energy density[76].

As the energy density is increased a point is reached where some of the surface material is evaporated and a plasma occurs. The generation mechanism here is essentially a recoil process or momentum transfer[76]. Just above the threshold for plasma formation the plasma burns only while the laser pulse exists[76]. The resulting epicentral waveform from such a source consists of a longitudinal wave pulse together with thermoelastic effects still remaining[76]. At very large power densities the plasma burns for several microseconds[76] and so the generating source is a vertical step loading of the surface. The shape of the waveform is therefore dependent on laser power density. For a constant power density the size of the waveform is proportional to the laser energy whilst the shape of the waveform is constant. Theoretical and experimental waveforms in the plasma region are shown in Figure 32.

The directionality of the source of course also changes as the source mechanism changes and this has been studied by

Figure 31: The theoretical epicentral pulse from a thermoelastic laser impact when thermal diffusion is assumed during the heating process. (After Dewhurst et al[76]).

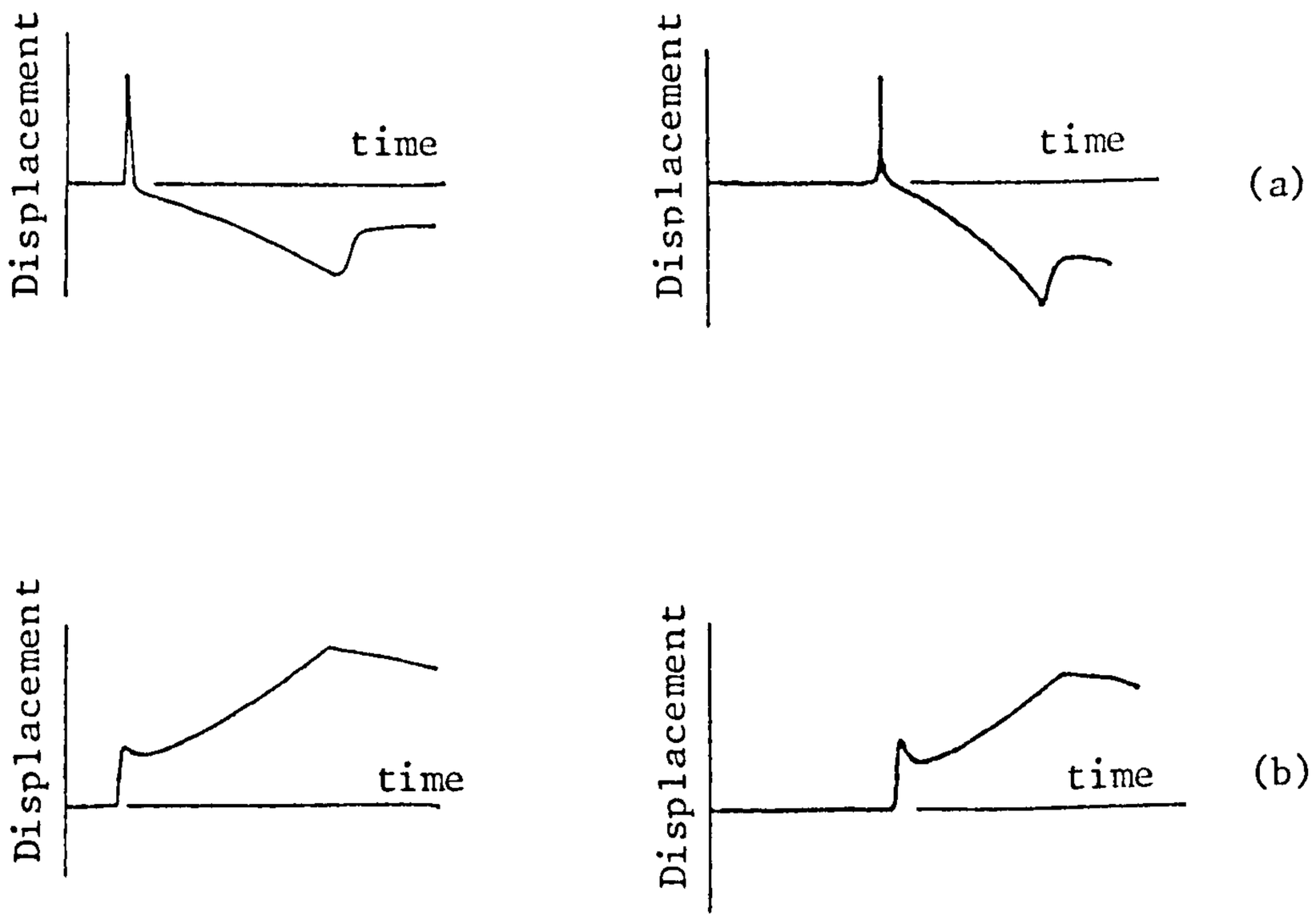

Figure 32: Theoretical (left) and experimental (right) waveforms measured at the epicentre of a laser impact. Both types of trace result from a combination of an ablation process and a thermoelastic process. (a) is for a low energy plasma giving only a small ablation component whilst (b) results from a plasma which burns for some time hence giving a large ablation component.

Hutchings et al[74] as discussed previously.

II.8 Hi-fidelity piezoelectric transducers

Conventional piezoelectric transducers, similar to that shown in Figure 33, have many problems associated with them[9]. The device is subject to multiple resonances. Ultrasonic wave interference associated with certain features such as the wear plate also has a large effect on the transducer response. Aperture effects (see Figure 3) are also a major problem for acoustic emission measurements.

Procter[9] has suggested an alternative form of transducer shown in Figure 34 in which the area in contact with the surface is small so as to minimise the aperture effect. The ultrasonic pulses passing through the transducer enter the brass backing where the energy is eventually dissipated. Resonances of the cone are therefore minimised. The shape of the cone itself also appears to reduce resonance effects. Further work[95] suggested the size of the brass backing could be reduced. Development of this transducer is not complete and questions concerning the effect of changing the cone angle, the cone depth, the backing size and the problem of coupling to a workpiece need all to be answered. The calibration should also be carried further than the 1.4MHz limit quoted by Procter[9].

Another type of high fidelity transducer has been described by Niewisch and Krämmer[96] (Figure 35). A small contact area is also a feature of this device and transducer resonances are reduced by the damping body shown. This transducer exhibits a good time response. The time responses

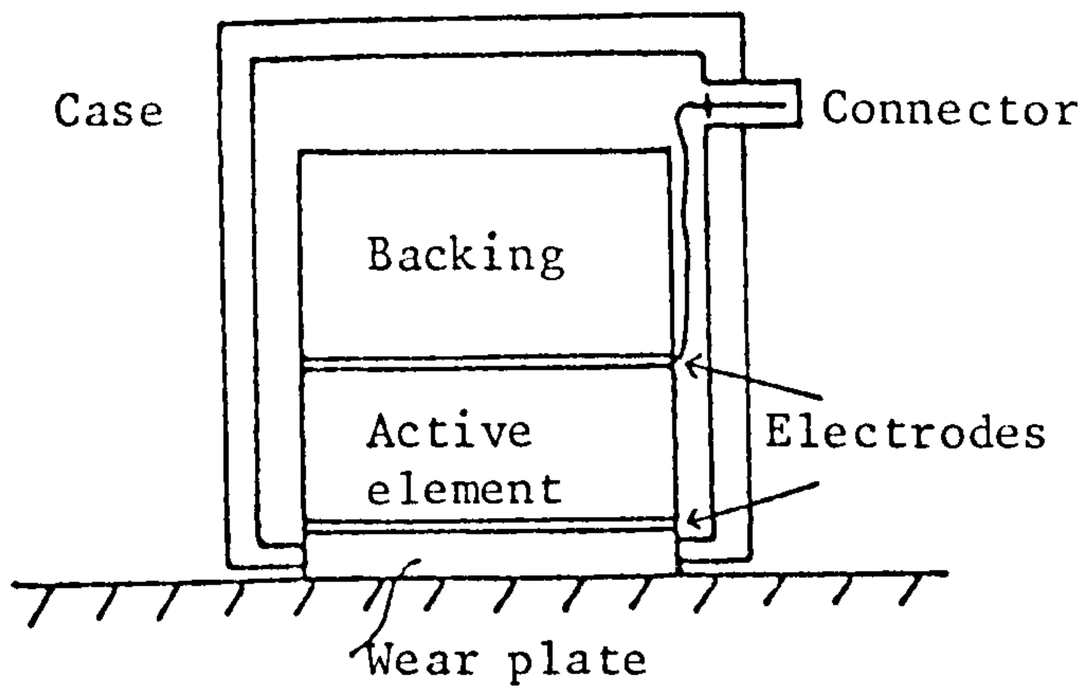

Figure 33: Schematic arrangement of a conventional piezoelectric transducer. (After Procter[9]).

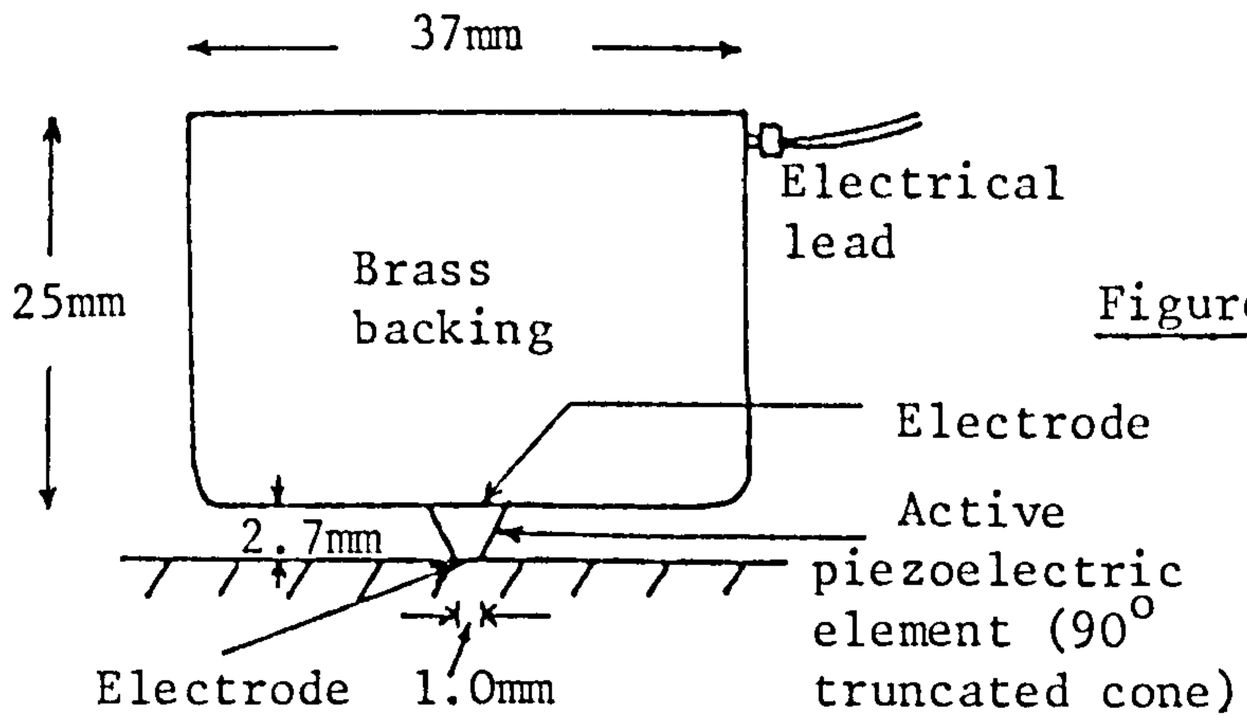

Figure 34: Schematic diagram of the NBS conical hi-fidelity transducer (After Procter[9]).

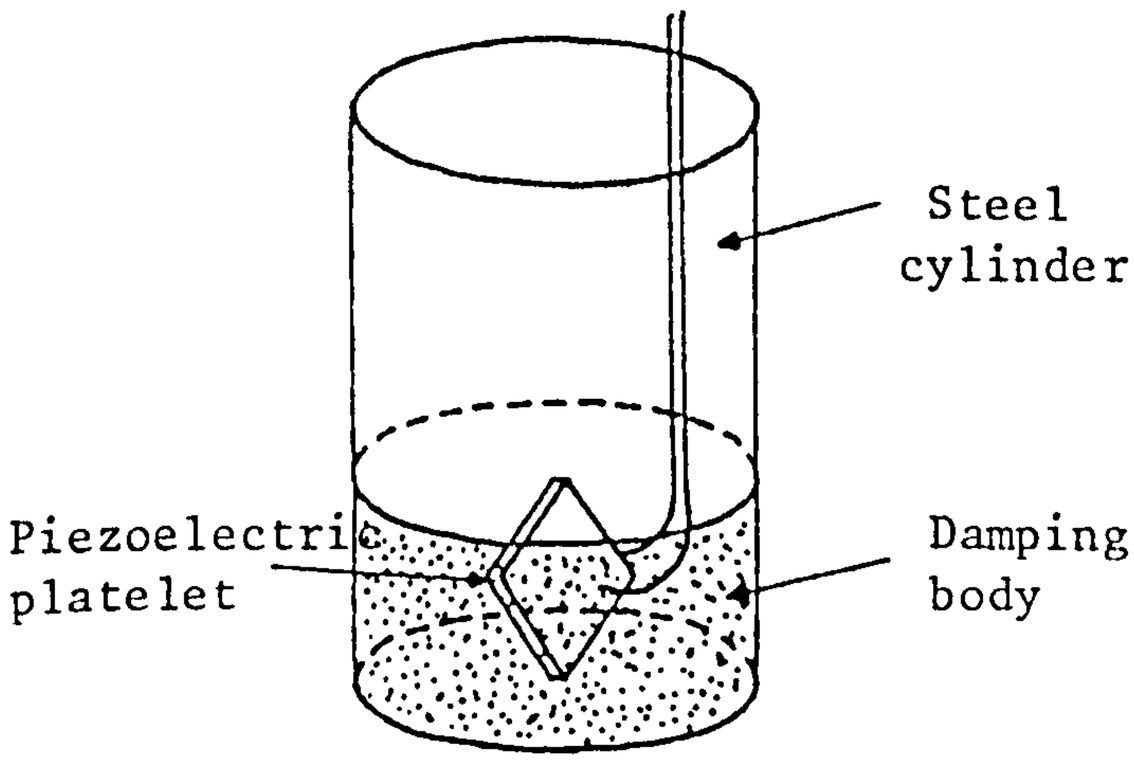

Figure 35: Schematic arrangement of the hi-fidelity transducer described by Niewisch and Krämmer[96].

of both these high fidelity transducers to surface pulses are shown in Figure 36, together with a capacitance measured waveform.

II.9 Magnetostrictive transducers

In a piezoelectric material the application of a stress to the specimen results in the generation of internal electric fields. Ultrasonic energy may therefore be transformed to electrical energy. For a magnetostrictive device the application of a stress field results in a change in magnetisation of the specimen[97].

Magnetostrictive or inverse magnetostrictive transducers have been used for some time[98]. However this early work was concerned with low frequency (< 100kHz) echo depth recorders. Their use in ultrasonic measurements has been limited. This is a result of their lower sensitivity than piezoelectric devices and their somewhat limited frequency response due to eddy current effects[97].

In certain situations waveguides are used to couple piezoelectric transducers to inhospitable surfaces, for example to hot surfaces. Magnetostrictive transducers offer the possibility of direct coupling including welded coupling if the magnetostrictive material is of the correct metallic form. Such an application therefore precludes the use of ferrite disc magnetostrictive devices described by Vetrano and Jolly[99]. A second possible advantage of using a magnetostrictive device made from some easily workable material (e.g. nickel) is that transducer resonances and reflections may be more easily controlled by careful design.

Magnetostrictive transducers have been used to measure

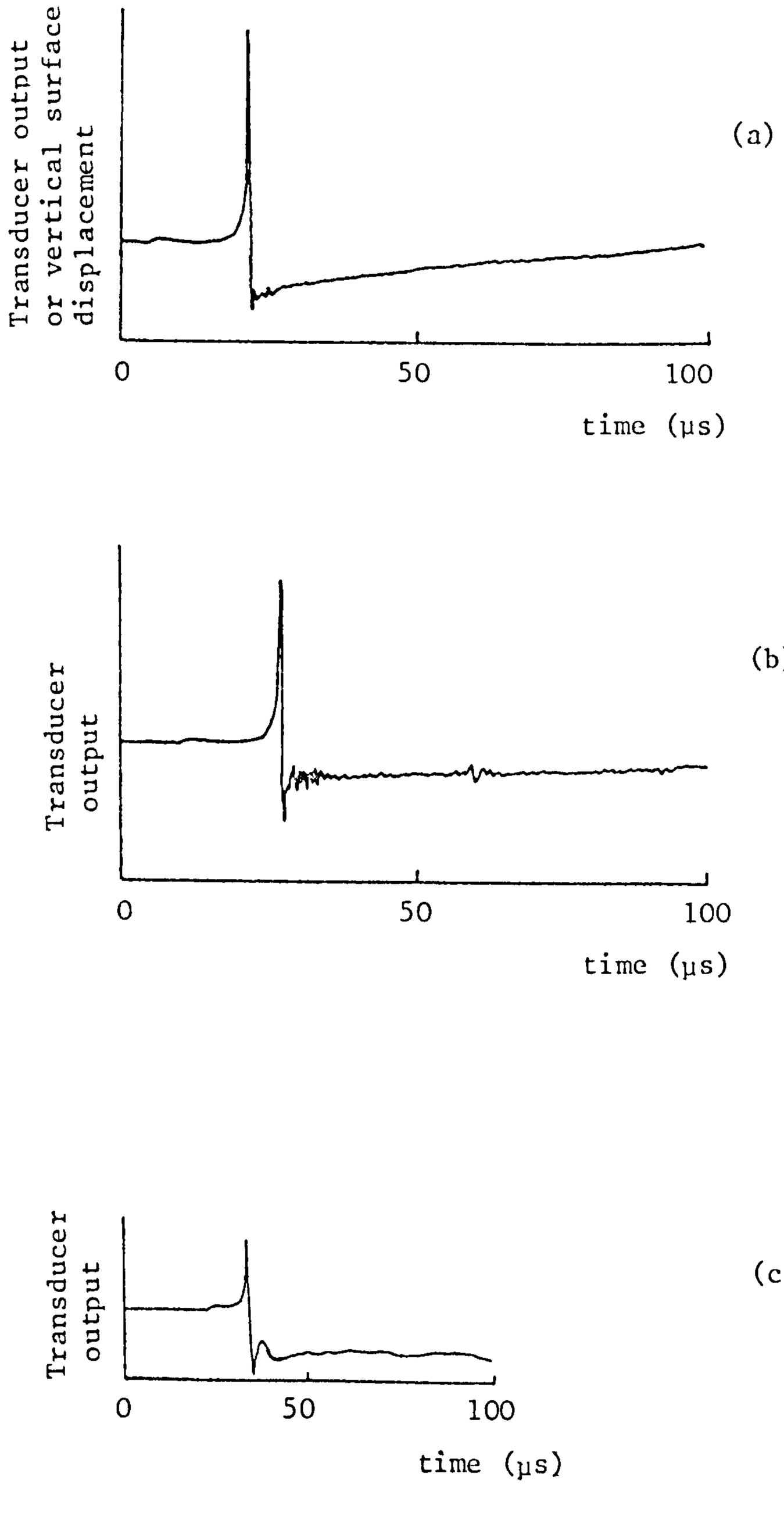

Figure 36: The response of hi-fidelity transducers to the surface pulse created by a breaking glass capilliary. (a) is the output from a capacitative transducer, which is assumed to give an absolute measure of the vertical surface displacement. (b) shows the output from the transducer shown in Figure 34 whilst (c) gives the output from the device given in Figure 35.

attenuation in rods by Lynnworth et al[100] and to measure vibration by Lynnworth and Bradshaw[101]. In this latter work the transducers were in the shape of long thin rods approximately 1 to 3mm in diameter which thus avoided dispersion. Such shapes enabled vibrations to be measured in rotating shafts. To do this the rods were fixed to the ends of the shafts and the changes in magnetisation detected by coils wrapped around the transducers. Frequency ranges up to ~ 1MHz were reported.

The various advantages of direct coupling to hot surfaces, easy shaping of devices to reduce resonance and the ability to be attached to rotating machinery therefore suggest that magnetostrictive transducers are worth investigating further.

III. THE DEVELOPMENT OF OPTICAL ULTRASOUND TRANSDUCERS

The discussions of chapter II indicate that the best choice for an optical ultrasound detector would be a modified Michelson interferometer - the modifications required being those necessary to maintain a constant detection sensitivity. Two such methods have been investigated experimentally and shall now be discussed. These are the quadrature interferometer and an actively stabilised interferometer, the stabilisation being effected by mounting the reference mirror on the movable end of a cantilever mounted piezoelectric multimorph element.

III.1 The Michelson interferometer used with a point light source

The Michelson interferometer in its original form employed light from an extended spatially incoherent source[37] (Figure 37), which when the mirrors are parallel gives an interference pattern localised at infinity. When the mirrors are not parallel then the device is equivalent to a thin air wedge and as such the fringes are no longer localised at infinity. Such an effect means that the intensity at a fixed image plane is highly dependent on mirror parallelism or tilt. This dependence is undesirable as the stablising element (piezoelectric multimorph) necessarily introduces mirror tilt as well as mirror displacement. A point, spatially coherent, source is therefore preferred for a practical interferometer.

To operate an interferometer efficiently the light source should be as powerful as possible. The light sources used

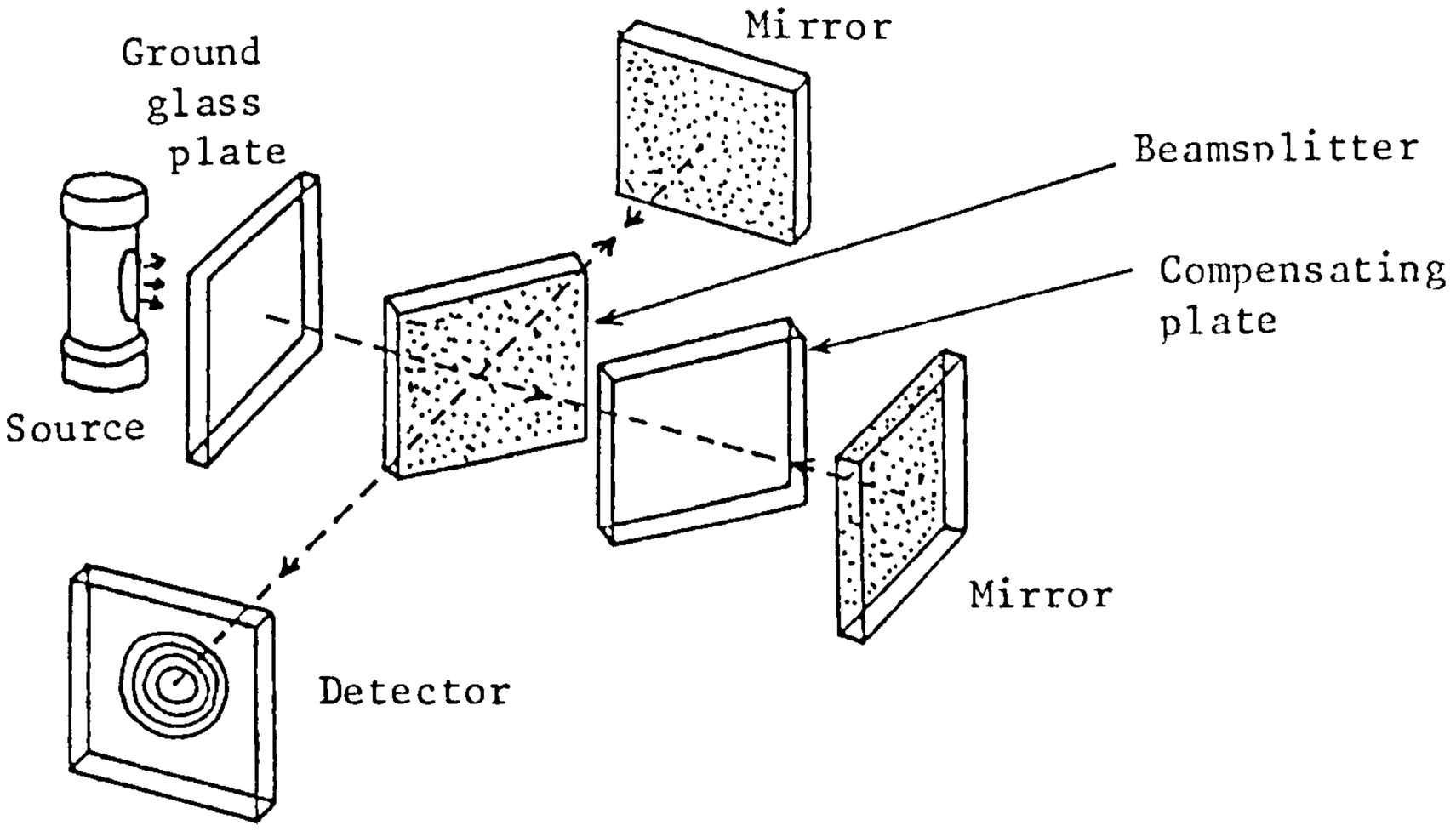

Figure 37: The Michelson interferometer employing a broad spatially incoherent source.

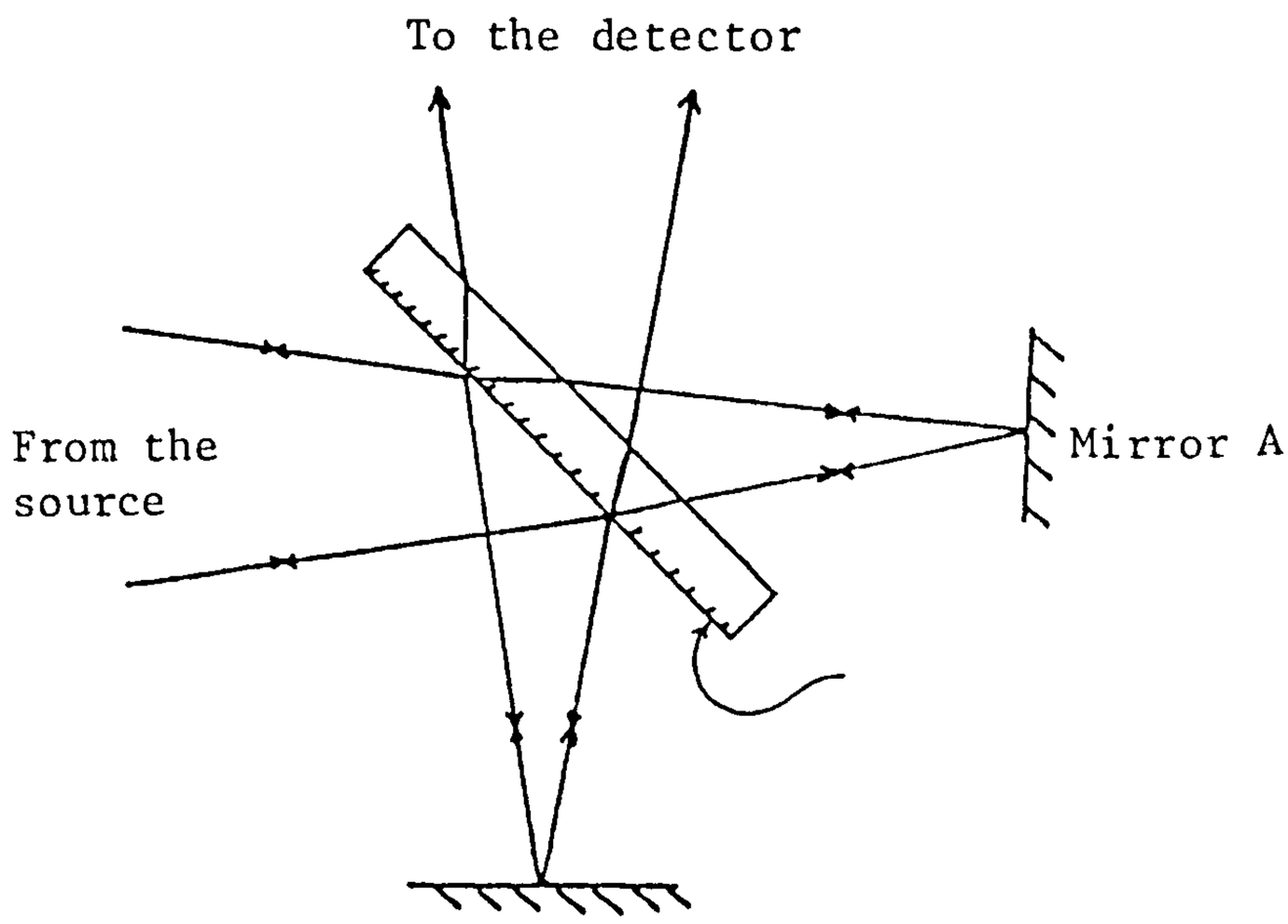

Figure 38: The beamsplitting arrangement in an uncompensated Michelson interferometer.

in interferometers such as that depicted in Figure 37 are in general gas discharge lamps. These are low power and as such result in poor device sensitivity.

In order to remove the problems of spatial incoherence and low light power the light source selected for use in the interferometer is a continuous wave laser. The form of the Michelson interferometer then becomes that shown in Figure 11. The laser beam is first expanded and then focussed onto the two mirrors. This procedure means the size of the laser spot imaged onto the mirrors is smaller than would be the case if the laser beam was focussed directly without previous expansion. The reflected light is collected by a lens and imaged onto a photodetector.

III.1.1 The intensity patterns generated by a Michelson interferometer.

III.1.1i) Experimental Michelson interferometer intensity patterns.

The form of the intensity pattern generated by an interferometer as depicted in Figure 11 depends on several factors. These factors are the path difference between the two interferometer arms, the tilt of the mirrors, the positions with respect to the mirrors at which the laser is focussed and finally the astigmation introduced by any assymetry in the beamsplitter.

The experimental interferometer was built as follows: A 2mW polarized Helium-Neon laser (Hughes Corporation 3222-PC) provided the light power. The beam was expanded by using

a microscope objective in reverse (magnification 60X, numerical aperture 0.85). This focussed the beam onto a 50μm spatial filter which removed diffraction effects from imperfections in the focussing optics. The intensity pattern was therefore more uniform. Two types of collimating lens were used. The first was a simple bi-convex lens of focal length 100mm and diameter 50mm and the second a 135mm, f 3.5 camera lens (Carl Zeiss Jena manufacturers). As will be shown the simple lens had undesirable properties and was not used apart from these initial intensity pattern studies. The beamsplitting was performed initially by using a partially reflecting glass plate with a fully transmitting compensator plate in the reference arm. This generated slight astigmation and was therefore replaced by a beamsplitter cube. The light from the interferometer was collected using a simple lens only as the photodetector sensitive area was large enough to make spherical aberrations unimportant for this application. The photodetector will be discussed later. The patterns found for different combinations of the beamsplitting method and the focussing lens will now be discussed.

a) 135mm, f3.5 camera lens as the focussing lens.

Beamsplitter formed of one partially reflecting plate with no compensating plate.

Figure 38 shows the beamsplitting arrangement. Light reflected from mirror A passes through the angled plate 3 times whilst that reflected from B passes through only once. There is then clearly asymmetry between the two interferometer

arms. When the mirrors are both perpendicular to the optic axis then the patterns shown in Figure 39 are observed. These are exactly as expected from an interferometer with a plate beamsplitter and no compensating plate[102].

It can be shown that the highest sensitivity of the pattern to small disturbances of one mirror occurs for zero path difference. However, even in this situation the sensitivity is poor, because the pattern (Figure 39) is composed both of areas of constructive and of destructive interference. The "uncompensated" interferometer should therefore not be used as an ultrasonic detector.

b) 135mm, f3.5 camera lens as the focussing lens. Beamsplitter formed of one partially reflecting plate with a compensating plate in the reference arm.

A compensated interferometer is shown in Figure 40. When the two plates are identical and parallel then both interferometer arms are the same and the hyperbolic fringes in Figure 39 should be replaced by a uniform intensity over the entire field of view.

Unfortunately, it is very difficult to achieve the necessary conditions of identical, parallel plates and some residual astigmation usually occurs. This is the case here with the pattern for zero path difference being that shown in Figure 41. For this reason the preferred method of beamsplitting is to use a beamsplitter cube. This cube will therefore be used in the final form of the interferometer when it is being employed to detect ultrasound.

(a)

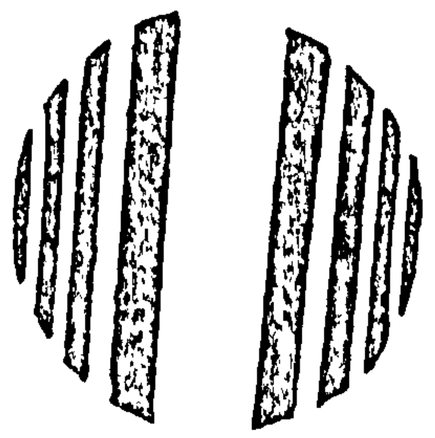

(b)

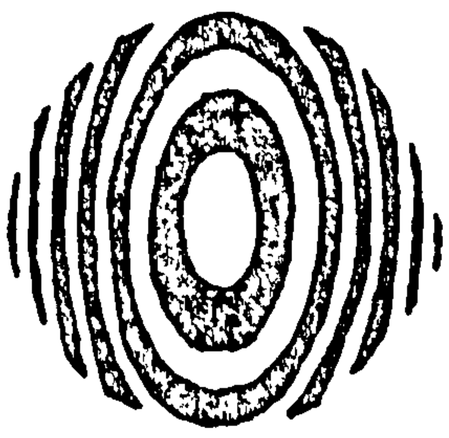

(c)

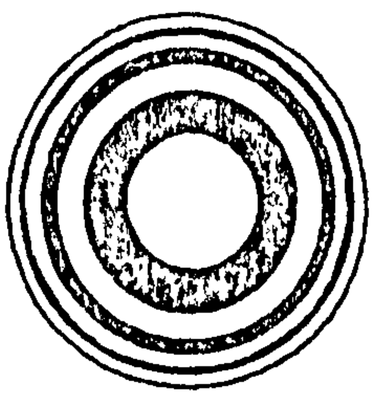

(d)

Figure 39: The patterns seen in the uncompensated Michelson interferometer given in Figure 38. (a) → (d) are the patterns for increasing path length differences between the interferometer arms starting with zero difference in pattern (a).

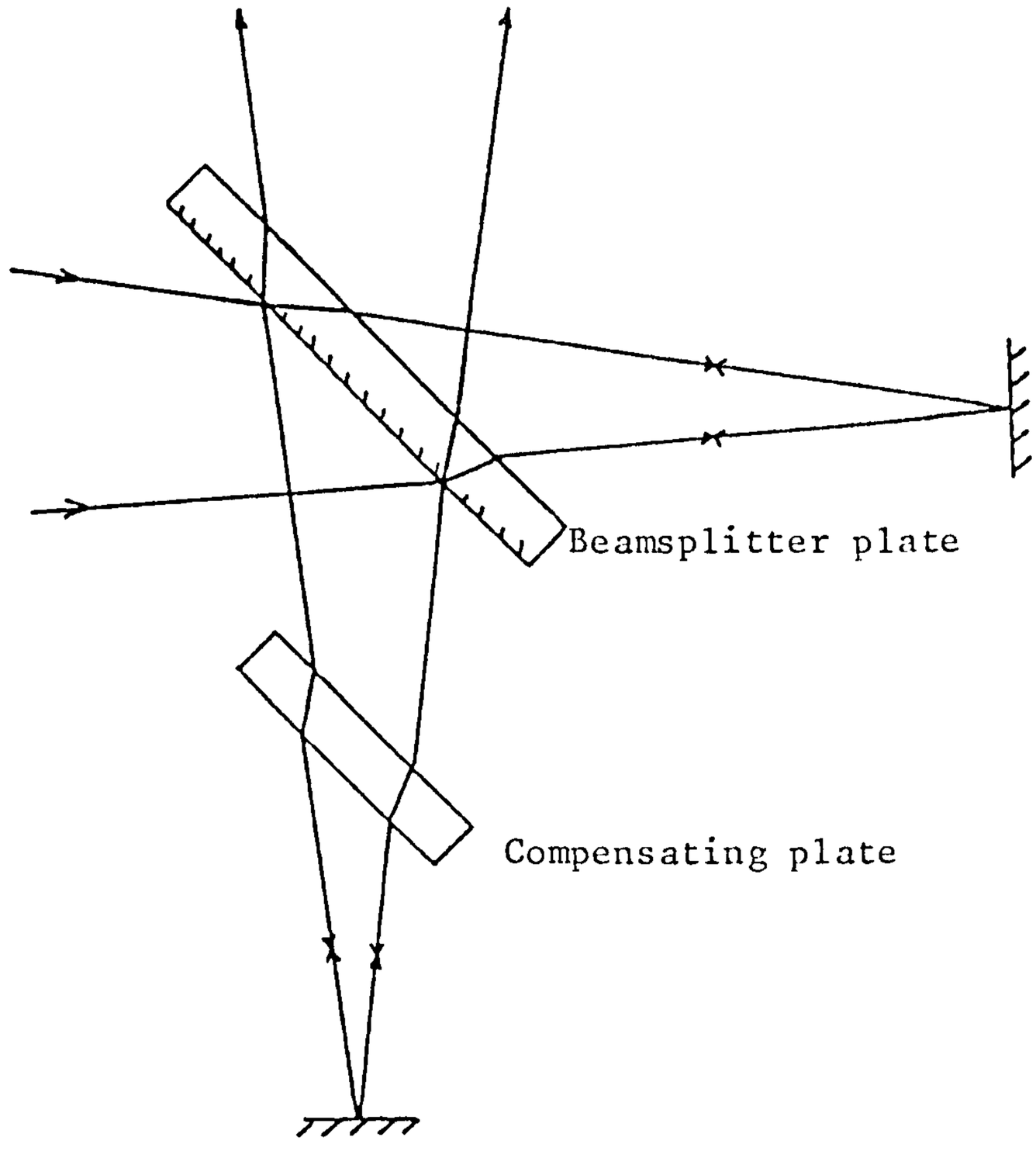

Figure 40: The compensated Michelson interferometer.

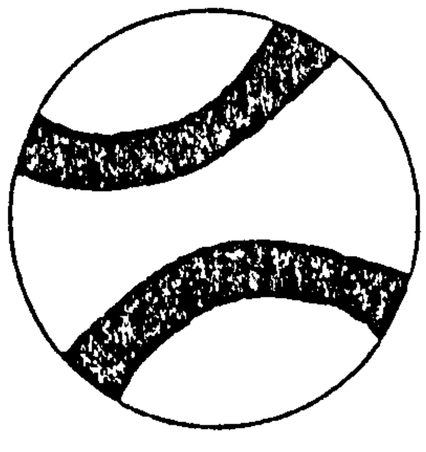

Figure 41: The intensity pattern achieved for zero path length difference in the 'compensated Michelson interferometer'. The hyperbolae occur due to residual astigmation arising from imperfect compensation.

c) Simple lens (f = 100mm, diameter = 50mm) as the focussing lens. Beamsplitter cube to perform the beamsplitting.

The first obvious effect of using the simple lens rather than the camera lens to focus the laser light is that the focus becomes much less distinct, containing a substantial amount of scatter around the main focal point.

The arrangement of specific interest for detecting ultrasound is when the laser is focussed onto the mirrors and the path length to each mirror is the same. The effect of mirror tilt in this arrangement is then the most important factor and must be considered. This is shown in Figure 42. The results are different to those obtained with a camera lens (see next section) in place of the simple lens. This difference is in fact quite severe and is thought to arise because of spherical aberrations in the simple lens. The sensitivity of the interferometer using the simple lens to mirror tilt is very high with the patterns in Figure 42 being created by very small tilt angles compared to those given for the camera lens in the next section. Measurements of the total intensity (via the photo-detector) confirm that the interferometer using the simple focussing lens suffers much greater distortions in the intensity pattern as a result of tilt than the same interferometer using a camera, or other high quality, lens.

Aperturing the focussing lens reduces the spherical aberration and hence the sensitivity to tilt. However to approach the results for a camera lens given in the next section the aperture necessary reduces the light power by 80%

Negative mirror tilt of ∿0.02 radians

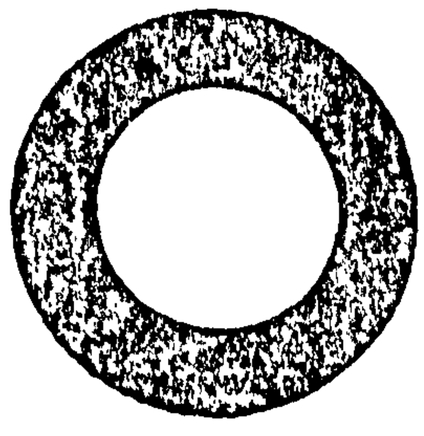

Zero mirror tilt

Positive mirror tilt of ∿0.02 radians

Figure 42: The sensitivity of the Michelson interferometer to mirror tilt when the focussing lens in the interferometer is a simple bi-convex lens. The patterns are obtained for zero path length difference when the laser is focussed onto the mirrors as accurately as possible.

d) 135mm, f3.5 camera lens as the focussing lens.

Beamsplitter cube to perform the beamsplitting.

For the reasons outlined above this is the best choice for the experimental arrangement of an interferometric ultrasound transducer. Two sets of intensity patterns are of particular interest. The first set occurs as a result of tilt on a fairly well focussed/symmetrical arrangement whilst the second arises for non-zero path length differences when both the mirrors are perpendicular to the optic axis.

The results of the first experiment described above are shown in Figure 43 whilst for the second experiment the patterns are those in Figure 44. It can clearly be seen that the patterns in Figure 43 are more uniform than the corresponding ones in Figure 42 even though the mirror tilt for the former (Figure 43) is much more severe.

The figure of greatest interest in terms of using the device to monitor ultrasound is that of total output intensity. As above, this is measured by monitoring the photodetector output. Total intensity is governed by tilt and focussing errors, astigmation and by path length differences. Astigmation cannot be avoided when the mirrors are tilted with respect to one another if finite thickness beamsplitters are used. This accounts for the appearance of a hyperbola in the well focussed results from Figure 43a). It should be realised, however, that a hyperbola is not seen unless some tilting occurs. In this respect the result in Figure 43a is different to the corresponding one in Figure 41.

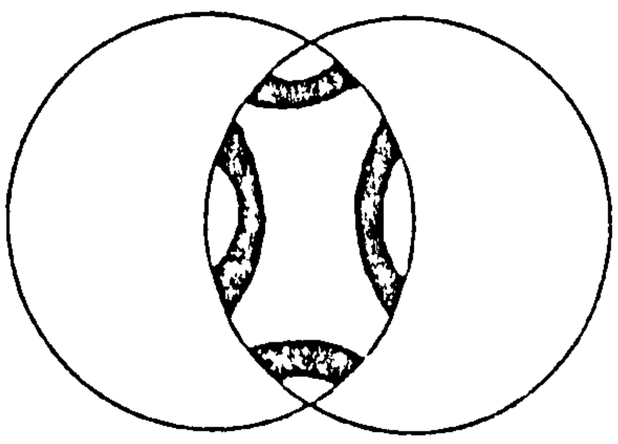

Negative mirror tilt
of ∿ 0.1 radians

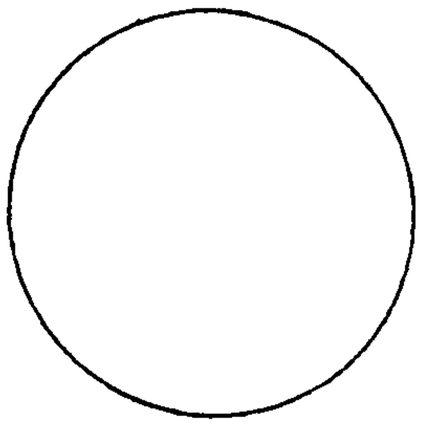

Zero mirror tilt

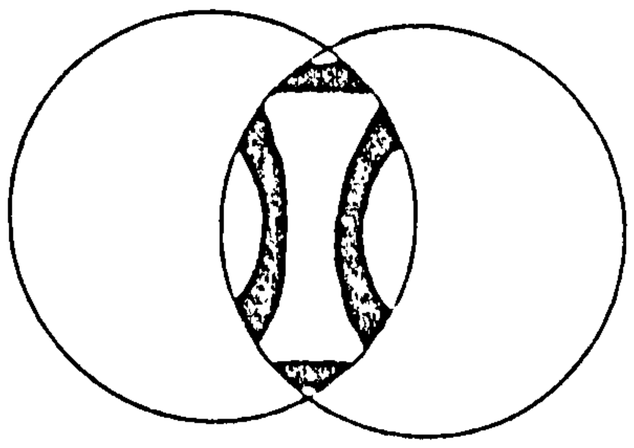

Positive mirror tilt
of ∿ 0.1 radians

(a)

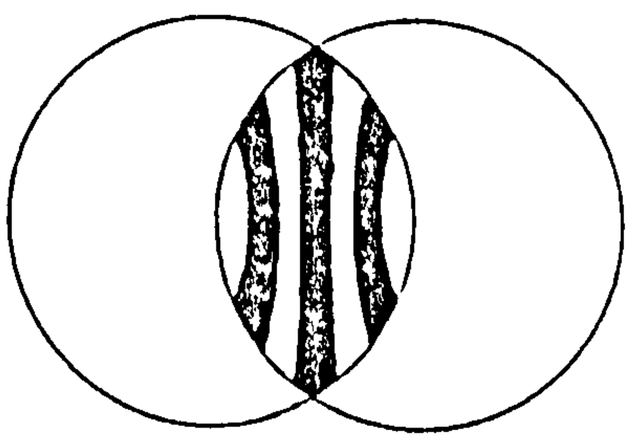

Positive mirror tilt
of ∿ 0.1 radians

(b)

Figure 43: The effect of mirror tilt in a Michelson interferometer employing a high quality focussing lens and a good cube beamsplitter. The three patterns in (a) are when the laser is focussed as accurately as possible onto the interferometer mirrors for zero path length difference between the interferometer arms. The pattern in (b) is when the focussing accuracy is reduced but all other parameters are held constant. The hyperbolae in figures (a) are due to the unavoidable astigmation that arises due to mirror tilt in an interferometer with a finite thickness beamsplitter.

The major factor contributing to mirror tilt is the flexing of the multimorph element. When this bending is as large as possible then the modulation of the total intensity output falls by 7½%, which is acceptable.

The final effect of path length difference depends on the numerical aperture of the device. For a large numerical aperture then small path length differences introduce many rings into the intensity pattern (cf Figure 44) thus altering the pattern modulation. These effects may be readily demonstrated by vibrating the reference mirror on the end of a long multimorph crystal (long so that tilt is insignificant) giving results as shown in Figure 45.

The theoretical basis for the observations above will now be discussed.

III.1.1ii) Theoretical Michelson interferometer intensity patterns.

The results in this section will be restricted to an interferometer with a point spatially coherent source, focussing optics free of aberrations and a beamsplitter free of astigmation. Such a device is, as mentioned above, the one of practical interest and the practical results that will be analysed are those in Figures 43b, 44 and 45. The interferometer output may be treated analytically to derive the results of Figures 44 and 45. However, to the author's knowledge this is not possible when mirror tilt is introduced and so the theoretical results corresponding to Figure 43b have to be evaluated numerically. To the author's knowledge such work has not been published previously.

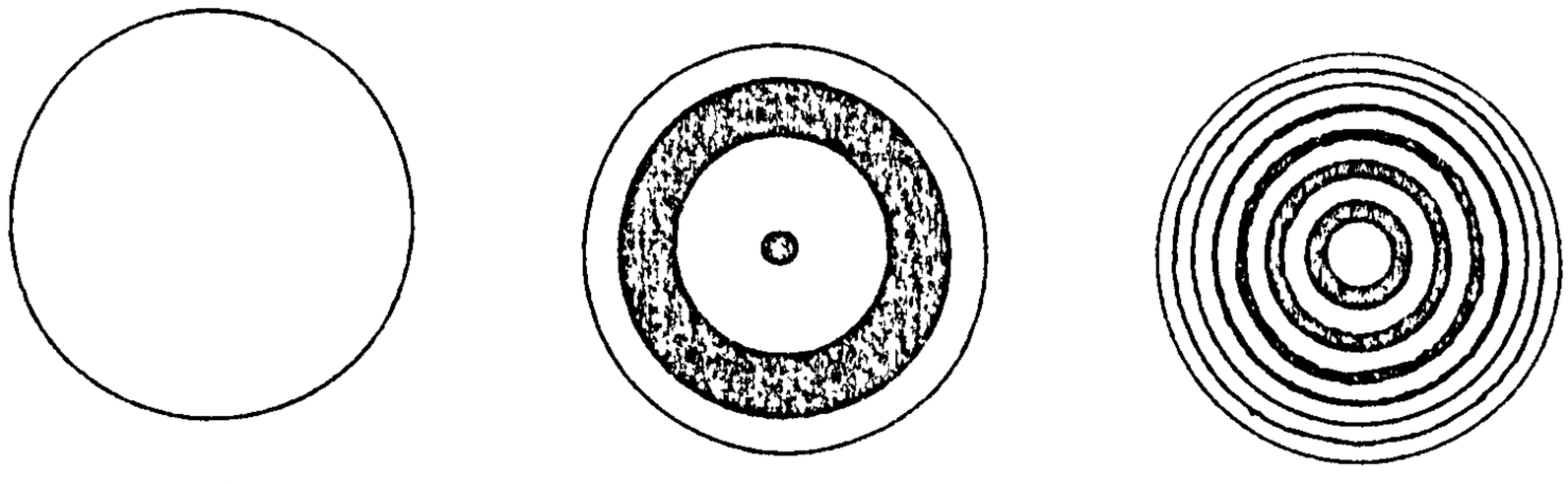

(a) (b) (c)

Figure 44: The intensity patterns seen in a Michelson interferometer, when both mirrors are perpendicular to the optic axis, as the path length difference between the interferometer arms is changed. (a) is for zero path difference, whilst (b) and (c) are for larger and larger differences.

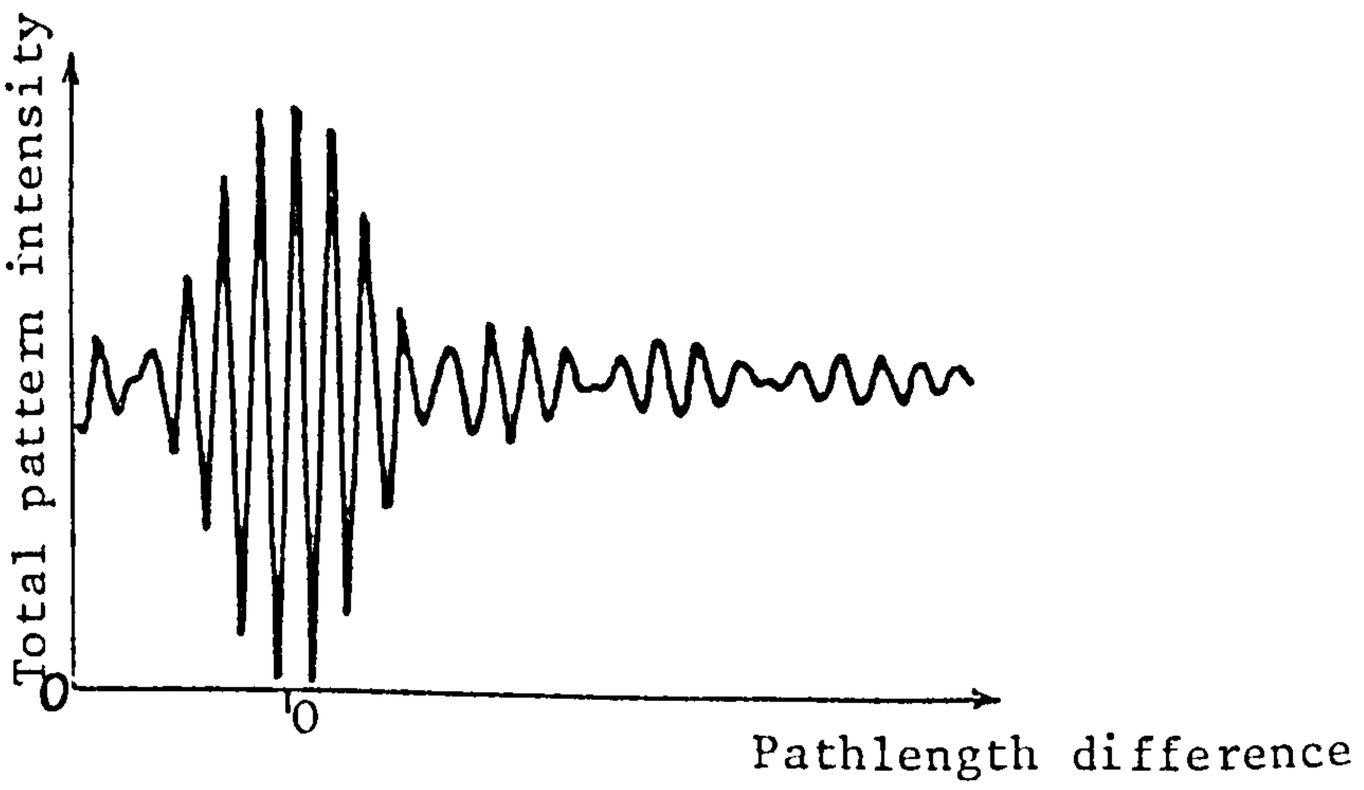

Figure 45: The total intensity of the interference pattern seen in a Michelson interferometer as a function of path length difference. The output shown above was determined experimentally by vibrating one mirror on the end of a long piezoelectric multimorph crystal.

The interferometer in Figure 11 may be drawn in line as shown in Figure 46. The laser light originates at S and is focussed by the collimating lens to the image point I. (Geometrical optics are assumed throughout the calculation). I therefore is a spatially coherent point source. The light from I is reflected off mirrors M_1 and M_2 which thus form images of I at I_1 and I_2. So far the interferometer has been reduced down to two coherent point sources at I_1 and I_2. These sources are focussed by the collecting lens L_2 to positions V_1 and V_2. The intensity pattern on some plane P may then be derived.

At the centre of plane P (OP) then the path length difference from I_1 and I_2 may be found by considering the coaxial rays. Hence:

$$\begin{matrix}\text{Path length from } I_2 \\ \text{to OP}\end{matrix} - \begin{matrix}\text{Path length from } I_1 \\ \text{to OP}\end{matrix} = 2x \qquad (24)$$

where x is the relative mirror separation.

Consider rays converging on V_1. The phase along the wavefront C_1C_2 is a constant as the laser is spatially coherent. Hence the path length from I_1 to C_1 is shorter than from I_1 to OP by the distance y where

$$(y + (v_1-p))^2 = R^2 + (v_1-p)^2 \qquad (25)$$

Consider now rays converging on V_2 and in particular the ray I_2AV_2. The path length of this ray at C_1 is less than the path length from I_2 to OP by the distance z where

$$(z + (v_2-p))^2 = R^2 + (v_2-p)^2 \qquad (26)$$

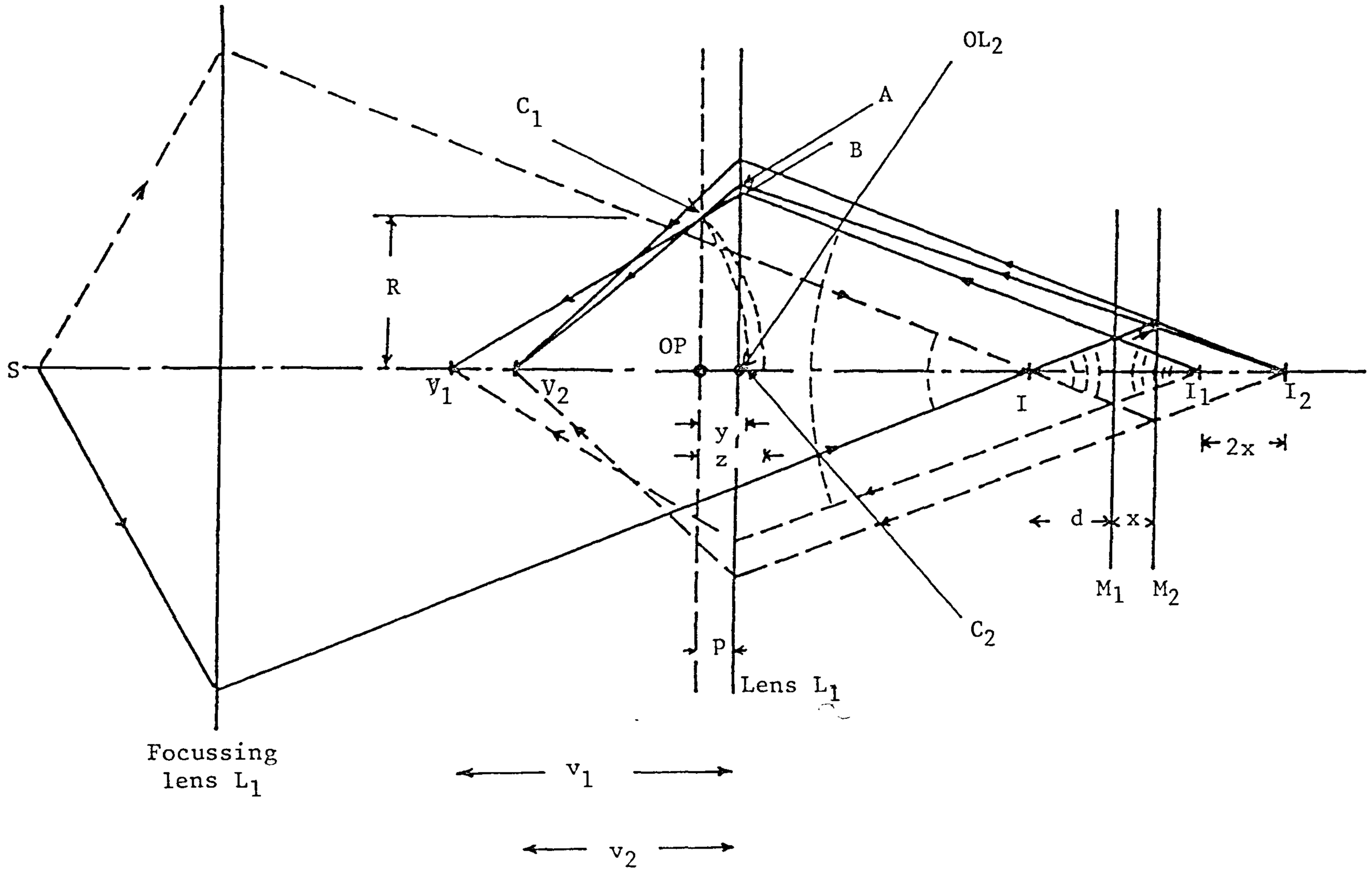

Figure 46: Schematic in-line representation of the Michelson interferometer used to derive the theoretical intensity pattern.

The path length difference to C_1 for the rays I_2AV_2 and I_1BV_1 is therefore:

$$I_2AV_2 - I_1BV_1 = I_2OP - z - (I_1OP - y) \quad (27)$$

$$\therefore \quad I_2AV_2 - I_1BV_1 = 2x - z + y \quad (28)$$

The rays passing through C_1 have electric fields varying as:

$$E_{I_1}\exp(i(\omega t - kX_{I_1} + \phi)) \text{ and } E_{I_1}\exp(i(\omega t - kX_{I_2} + \phi + \gamma)) \quad (29)$$

where E_{I_i} is the electric field strength per square root of unit area from the source I_i, ω is the angular frequency of the light, t time, X_{I_i} the path length, k the wavenumber, ϕ an arbitrary starting phase and γ a phase lag introduced by the beamsplitter. The two fields add to give:

$$E_{C_1} = \exp(i(\omega t + \phi))\left(E_{I_1}\exp(-ikX_{I_1}) + E_{I_2}\exp(i(-kX_{I_2} + \gamma))\right) \quad (30)$$

The intensity at C_1 is then

$$c\varepsilon|E_{C_1}|^2$$

$$\text{or} \quad I = c\varepsilon E_{C_1}E_{C_1}^* \quad (31)$$

$$\text{therefore} \quad I = c\varepsilon\left(E_{I_1}\exp(-ikX_{I_1}) + E_{I_2}\exp(i(-kX_{I_2} + \gamma))\right) \cdot \left(E_{I_1}\exp(ikX_{I_1}) + E_{I_2}\exp(i(kX_{I_2} - \gamma))\right) \quad (32)$$

$$\text{and} \quad I = c\varepsilon\left(E_{I_1}^2 + E_{I_2}^2 + E_{I_2}E_{I_1}\exp(i\gamma)\exp(ik(X_{I_1} - X_{I_2})) + E_{I_2}E_{I_1}\exp(-i\gamma)\exp(-ik(X_{I_1} - X_{I_2}))\right) \quad (33)$$

$$\text{Now as} \quad \cos(x) = \tfrac{1}{2}(e^{+x} + e^{-x}) \quad (34)$$

then equation (33) may be rewritten as:

$$I = c\varepsilon \left[E_{I_1}^2 + E_{I_2}^2 + 2E_{I_1}E_{I_2}\cos(k(X_{I_1} - X_{I_2}) + \gamma)\right] \qquad (35)$$

γ then merely gives a non-zero starting value for the phase angle and is subsequently dropped. As cosine is an even function, then equation (35) may be rewritten using equation (28) as:

$$I = c\varepsilon \left[E_{I_1}^2 + E_{I_2}^2 + 2E_{I_1}E_{I_2}\cos\left(\frac{2\pi}{\lambda}(2x - z + y)\right)\right] \qquad (36)$$

where k has been replaced by $\left(\frac{2\pi}{\lambda}\right)$. All that remains now is to determine z,y in terms of the focal length of L_2, (f_{L_2}), R, and the positionsof I, M_1 and M_2. From equation (25) then:

$$y^2 + 2y\,(v_1 - p) = R^2 \qquad (37)$$

If the numerical aperture of lens L_2 is not too large, then $y << v_1 - p$ and

$$y \simeq \frac{R^2}{2(v_1 - p)} \qquad (38)$$

and

$$z \simeq \frac{R^2}{2(v_2 - p)} \qquad (39)$$

The thin lens formula may be used to determine $v_{1,2}$ as follows:

$$\frac{1}{f_{L_2}} = \frac{1}{OL_2I_1} + \frac{1}{v_1} \qquad (40)$$

and

$$\frac{1}{f_{L_2}} = \frac{1}{(OL_2I_1 + 2x)} + \frac{1}{v_2} \qquad (41)$$

Combining equations (38-41) leaves (for $2x << f_{L_2}, (OL_2I_1), \frac{f_{L_2}(OL_2I_1)}{p}$):

$$y - z \simeq \frac{-R^2(2x)}{2(f_{L_2}(OL_2I_1) - p(OL_2I_1) + pf_{L_2})} \qquad (42)$$

or $$y - z \simeq - \frac{R^2(2x)}{2F^2} \qquad (43)$$

Equation (36) may now be written as

$$I = c\varepsilon\left(E_{I_1}^2 + E_{I_2}^2 + 2E_{I_1}E_{I_2}\cos\left(\frac{4\pi x}{\lambda}\left(1 - \frac{R^2}{2F^2}\right)\right)\right) \qquad (44)$$

This is now the intensity as a function of radius R on a given observation plane, provided that overlap between the reflections from both mirrors occurs. The maxima for the pattern occur when

$$\frac{4\pi x}{\lambda}\left(1 - \frac{R^2}{2F^2}\right) = 2n\pi \qquad (n \text{ integral}) \qquad (45)$$

For x = 0 the entire pattern is a maxima whilst for non-zero x then

$$R = \sqrt{2}\, F \left(1 - \frac{n\lambda}{2x}\right)^{\frac{1}{2}} \qquad (46)$$

When F is small the radii at which maxima occur are also small. Equation (46) describes the patterns in Figure 44 very well.

A solution will now be sought for the total intensity. This is obtained easily by integrating equation (44) over the range of R which covers the aperture of the photodetector. The integral to be evaluated is:

$$\text{Total } I = \int_{R=0}^{R=R_A} I.2\pi R\,dR \qquad (47a)$$

$$\text{Substituting } v = \frac{4\pi x}{\lambda}\left(1 - \frac{R^2}{2F^2}\right)$$
$$\text{and } dv = \frac{4\pi x}{\lambda}\left(-\frac{R}{F^2}\right)dR \qquad (47b)$$

allows this integral to be calculated and results in:

$$\text{Total } I = \varepsilon c\left[(E_{I_1}^2+E_{I_2}^2)\pi R_A^2+2E_{I_1}E_{I_2}\frac{\lambda F^2}{x}\cos\left(\frac{4\pi x}{\lambda}\left(1-\frac{R_A^2}{4F^2}\right)\right)\sin\frac{\pi x R_A^2}{\lambda F^2}\right] \quad (47c)$$

This then explains Figure 45. In Figure 45, the value of (R_A/F) was approximately $^1/_2$, implying that the first minima in the modulation occurs at approximately $d = 2\lambda$ or 4 fringes. (1 fringe occurs for a relative mirror movement of $\lambda/2$ which is that which causes one cycle of oscillation in the cosinusoidal term in equation 47c).

The next problem to be solved is the one for which experimental results are given in Figure 43b. The method to be used to solve this is similar to the previous calculation, except that a full analytical solution is not attempted.

Referring to Figure 47 then, the laser source S creates an image I via lens L_1 (geometrical optics are again assumed). The beamsplitter and mirrors create images of I at I_1 and I_2 which are now two coherent sources. As in the previous calculation these are now focussed by the collecting lens L_2 at V_1 and V_2 respectively. The positions of I_1 and I_2 are best seen in Figure 48. The values a and b which determine the position of I_1 as shown in Figure 48 are derived using the simple geometry indicated in this figure. The angle of tilt in this diagram is exaggerated. In reality the angle of tilt is always less than 0.1 radians and so within a 1% error, a may be neglected with respect to the distance 2d when I_1 is displaced parallel to the axis from I.

The difference in the path lengths $I_2OL_2V_2$ and $I_1OL_2V_1$

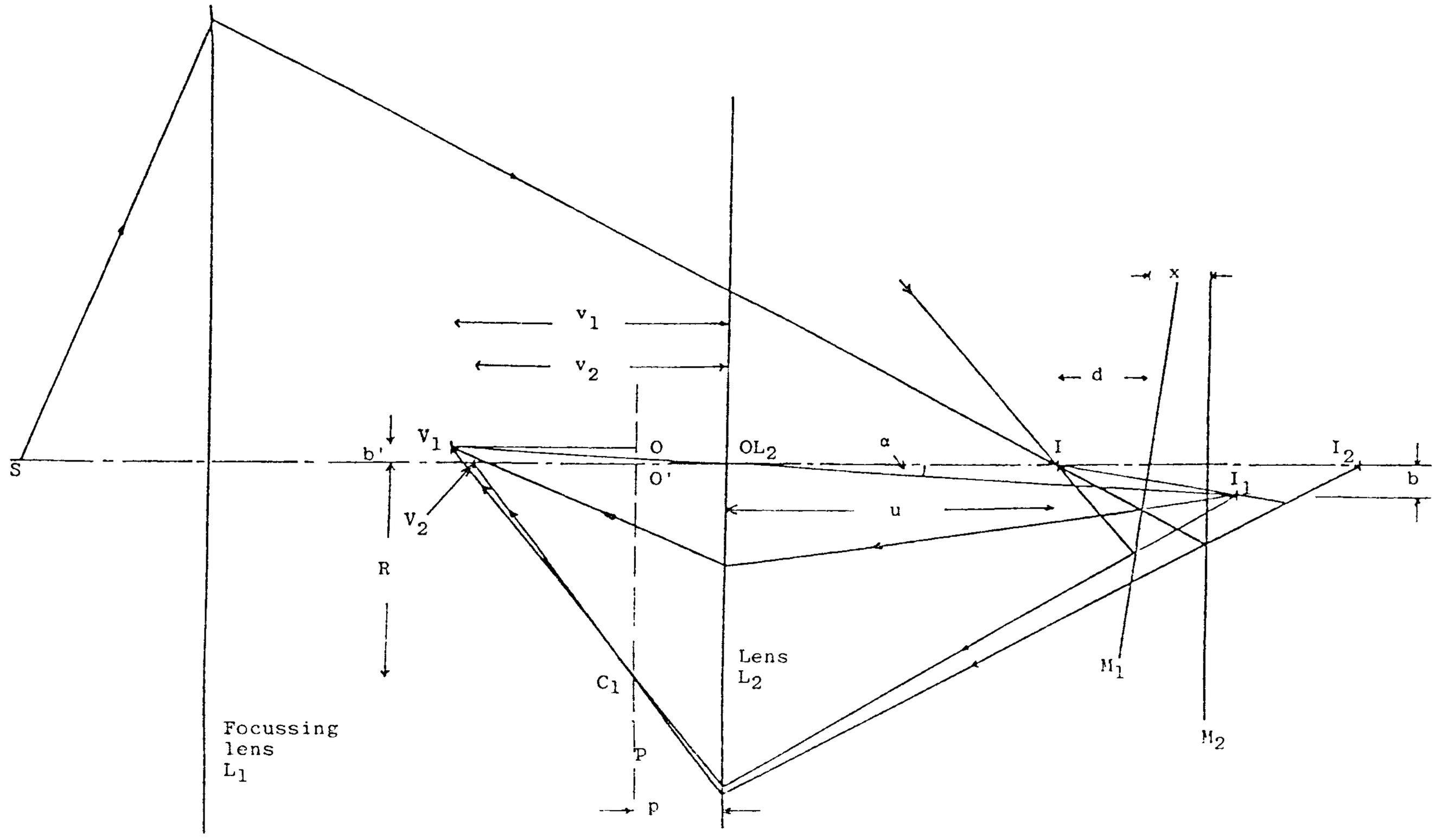

Figure 47: Schematic in-line representation of a Michelson interferometer used to derive the theoretical intensity distribution of the interferometer pattern when the mirrors are non-parallel.

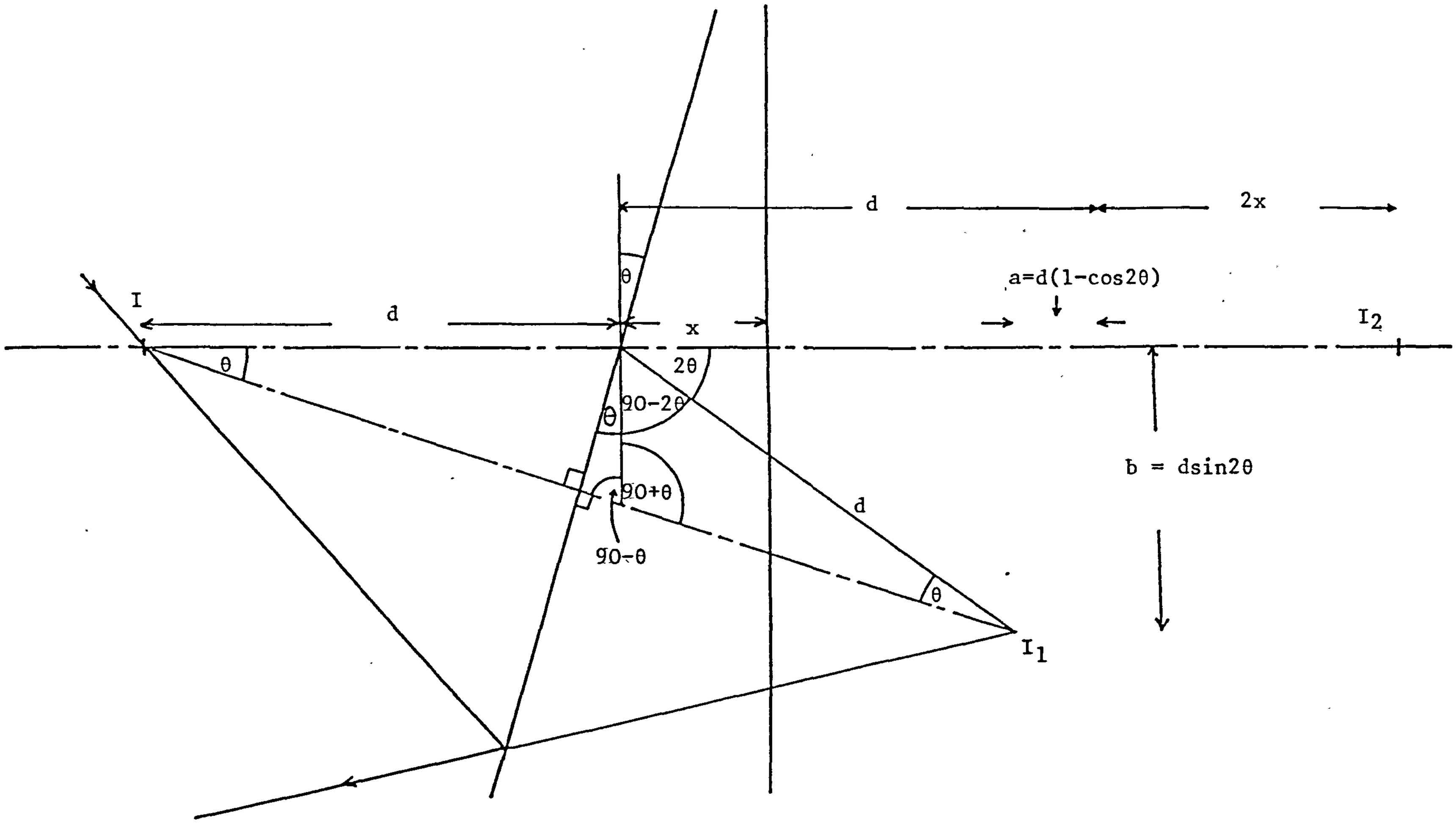

Figure 48: Expanded view of the interferometer mirror geometry used to derive the intensity pattern for an interferometer with non-parallel mirrors.

may be calculated easily. Consider an extended object extending across the optic axis on one side of lens L_2. An image is formed on the far side of L_2 which, when lens aberrations are ignored, is a scale replica of the original object. Therefore the phase relationship between on axis rays (such as $I_2OL_2V_2$) and off axis rays (such as $I_1OL_2V_1$) is maintained. In determining the path difference ($I_2OL_2V_2 - I_1OL_2V_1$) the lens may therefore be neglected.

The displacement (b') of V_1 off axis is related to b (see Figure 48) via the magnification which is given as (using the thin lens formula):

$$\text{Magnification} = \frac{b'}{b} = \frac{v_1}{u+2d} \qquad (48)$$

where v_1 may also be determined using the thin lens formula as

$$\frac{1}{f_{L2}} = \frac{1}{v_1} + \frac{1}{u+2d} \qquad (49)$$

(v_2 may be derived similarly). Using these results then (for $u >> b$, $v_1 >> b'$, $x,d << u$)

$$I_2OL_2V_1 - I_2OL_2V_2 = 2x\left\{1 - \frac{f^2}{(u-f)^2}\right\} - \frac{b^2(u-2f)}{2u(u-f)} \qquad (50)$$

The image point V_1 is the centre for a set of converging spherical waves. The plane, P, cuts this pattern in such a way that on the plane the contours of constant phase are circles centred at O. The path length from V_1 to O,(g),is indicated in Figure 49, and is given simply by

$$g = v_1 - p \qquad (51)$$

and similarly the path length from V_2 to O' is $v_2 - p$.

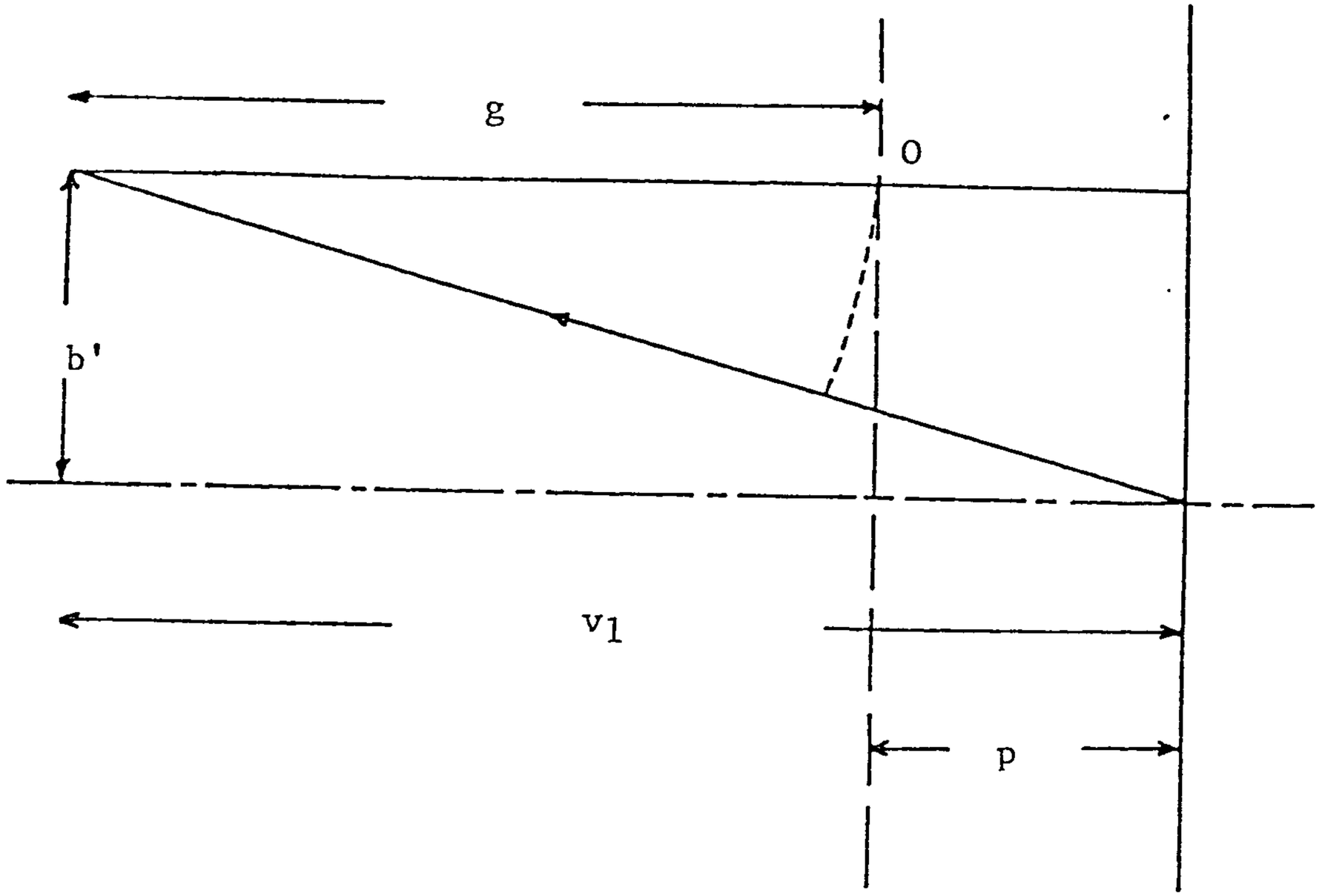

Figure 49: The path length difference to the left of lens L_2 for reflections from the mirrors M_1 and M_2 in Figure 47.

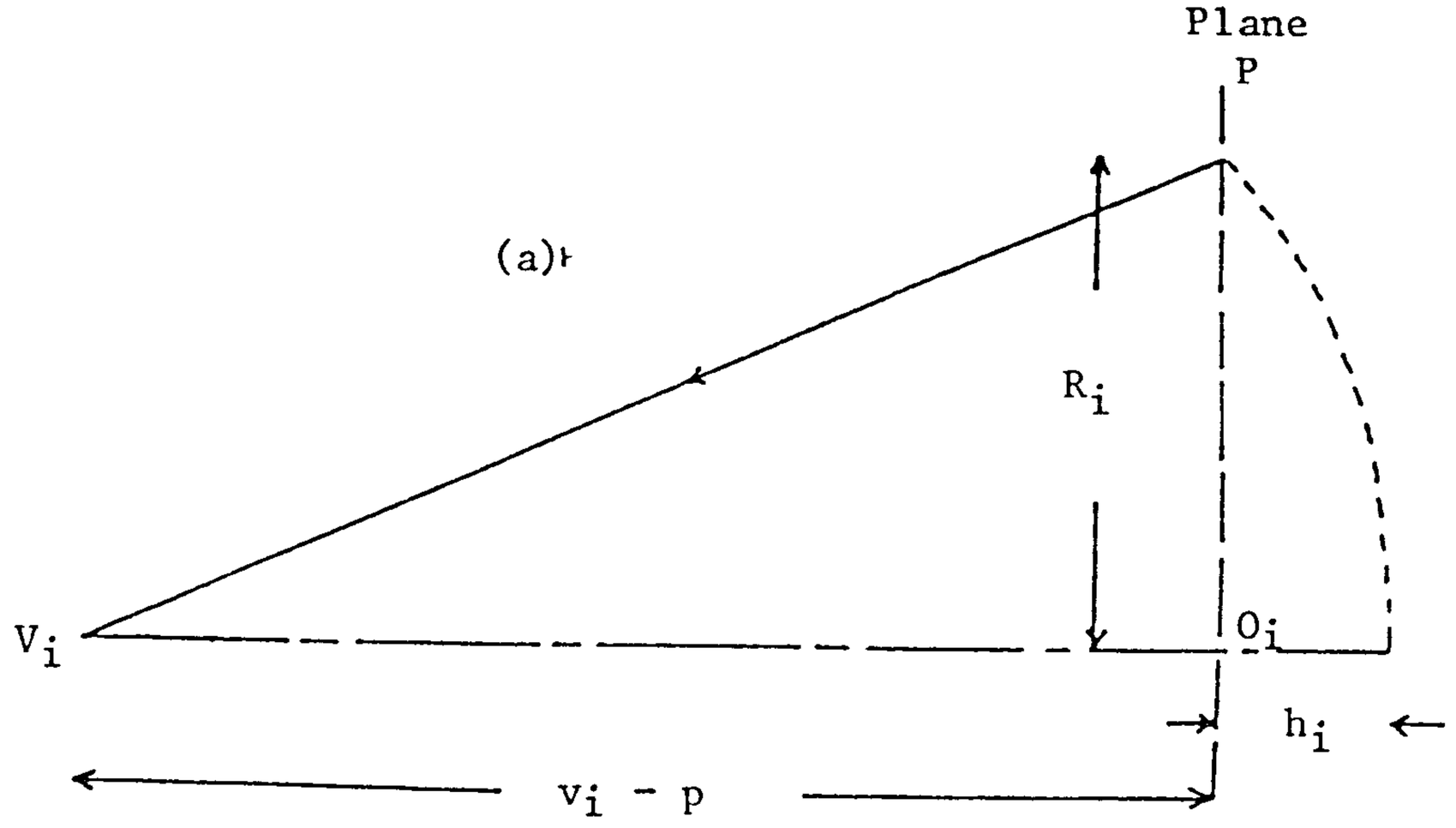

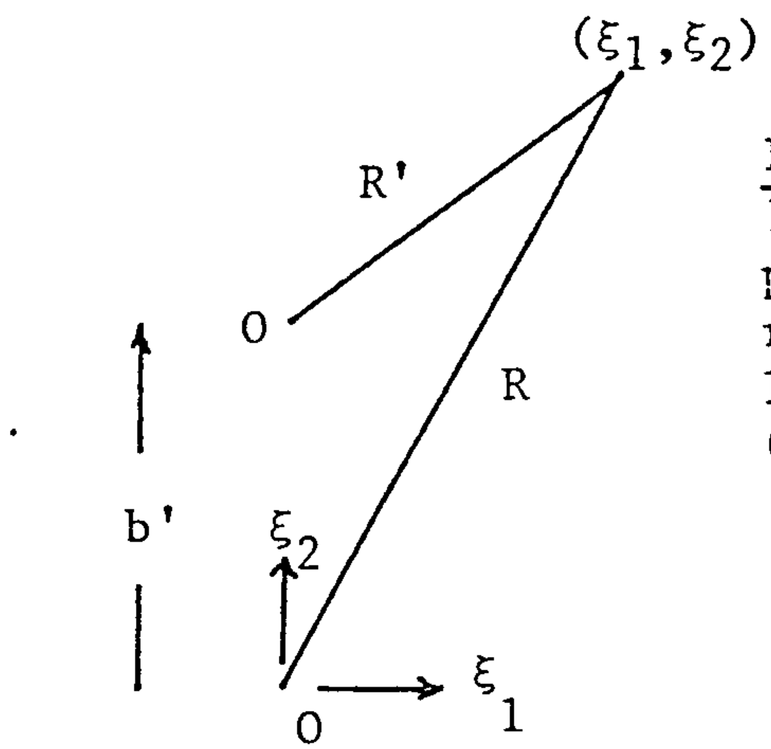

Figure 50: The path length as a function of position on plane P relative to the path length at either O or O' (see Figure 47).

(b)

$$(R')^2 = \xi_1^2 + (\xi_2 - b')^2$$

The final path length to be determined is the path length to the point C_1 (for instance) in the plane P. To do this it is convenient to set up a cartesion co-ordinate system in the plane P where the ξ_2-axis is in the plane of the paper (Figure 47) and the ξ_1-axis perpendicular to this plane. The point O is therefore at the position (O,b'). Figure 50 shows how this path difference may be evaluated. For a set of waves converging at V_i then in some plane P_i the phase contours are circles centred at O'. The path difference at X is retarded relative to O_i by h_i where

$$h_i = (R_i^2 + (v_i-p)^2)^{\frac{1}{2}} - (v_i-p) \qquad (52)$$

The path lengths to a point (ξ_1,ξ_2) with respect to the centres of the two sets of circular phase images at O and O' may now be written as follows. First for the pattern centred at O. The path length at (ξ_1,ξ_2) relative to the centre O is retarded by

$$h = (\xi_1^2 + (\xi_2 - b')^2 + (v_1 - p)^2)^{\frac{1}{2}} - (v_1 - p) \qquad (53)$$

and for the image centred at O' then

$$h' = (\xi_1^2 + \xi_2^2 + (v_2 - p)^2)^{\frac{1}{2}} - (v_2 - p) \qquad (54)$$

Equations (50), (51), (53) and (54) may now be combined to yield the difference in path length between the paths from I_2 to the point (ξ_1,ξ_2) and from I_1 to the point (ξ_1,ξ_2). This distance is termed $\Gamma(\xi_1,\xi_2)$ and

$$\Gamma(\xi_1,\xi_2) = I_2OL_2V_2 - (v_2-p) - h' - (I_1OL_1V_1 - (v_1-p) - h) \quad (55)$$

Equations (48) and (49) may be used to calculate b', v_1 and v_2 whilst the value of b may be taken from Figure 48. Once this is done the resulting equation is (replacing f_{L_2} by f for simplicity)

$$\Gamma(\xi_1,\xi_2) = 2x\left(1-\frac{f^2}{(u-f)^2}\right) - \frac{b^2(u-2f)}{2u(u-f)} + \left(\xi_1^2 + \left(\xi_2 - \frac{fb}{(u-f)}\right)^2 + \left(\frac{fu}{u-f} - p\right)^2\right)^{\frac{1}{2}} - \left(\xi_1^2 + \xi_2^2 + \left(\frac{fu}{u-f} - \frac{2f^2x}{(u-f)^2} - p\right)^2\right)^{\frac{1}{2}} \quad (56)$$

The contours of constant $\Gamma(\xi_1,\xi_2)$ may be derived from this equation to be roughly parabolic in shape.

Using equations (29), (30), (31) and (56) allows the intensity pattern to be calculated. This calculation was performed on a micro-computer due to the complexity of equation (56) and because this equation may not be integrated. The impetus behind developing this theory was twofold. The first reason was to explain the experimental results shown in Figure 43b whilst the second was to determine the effect of tilt introduced by the multimorph crystal.

Figure 51 shows the predicted intensity output corresponding to such an experiment as shown in Figure 43b, when the distance from the light focus to the mirrors (the distance d in Figures 46, 47 and 48 is 1mm, the mirror separation (x) is zero, the angle of tilt Φ (Figure 48) is 0.1 radians, the focal length of L_2, (f_{L_2}), is 100mm, the radius of L_2 is 7.2mm and the distance p (Figure 47) is zero.

8	8	8	8	7	7	7	7	7	7	7	7	7	7	7	8	8	8	8
58	58	57	57	57	56	56	56	56	56	56	56	56	56	56	57	57	57	58	58
98	98	98	98	98	98	98	98	98	98	98	98	98	98	98	98	98	98	98	98
81	81	82	82	82	82	82	82	82	82	82	82	82	82	82	82	82	82	81	81
27	27	27	27	28	28	28	28	28	28	28	28	28	28	28	28	27	27	27	27
0	0	0	0	0	0	0	0	0	0	0	0	0	0	0	0	0	0	0	0
33	33	33	33	33	33	33	33	33	33	33	33	33	33	33	33	33	33	33	33
87	87	86	86	86	86	86	86	86	86	86	86	86	86	86	86	86	87	87	
96	96	96	96	96	96	96	96	96	96	96	96	96	96	96	96	96	96	96	
60	60	60	60	60	60	60	60	60	60	60	60	60	60	60	60	60	60	60	
4	4	4	4	4	4	4	4	4	4	4	4	4	4	4	4	4	4	4	
14	14	14	14	14	14	14	14	14	14	14	14	14	14	14	14	14	14	14	
67	67	67	67	68	68	68	68	68	68	68	68	68	68	68	68	67	67	67	67
AA	AA	AA	AA	AA	AA	AA	AA	AA	AA	AA	AA	AA	AA	AA	AA	AA	AA	AA	AA
73	72	72	72	72	72	72	72	72	72	72	72	72	72	72	72	72	72	72	73
18	18	18	18	18	17	17	17	17	17	17	17	17	17	17	18	18	18	18	18
2	2	2	2	2	2	2	2	2	2	2	2	2	2	2	2	2	2	2	2
43	43	44	44	44	44	44	45	45	45	45	45	45	44	44	44	44	44	43	43
92	93	93	93	93	93	93	93	93	93	93	93	93	93	93	93	93	93	92	
92	91	91	91	91	91	90	90	90	90	90	90	90	90	91	91	91	91	91	92

Figure 51: The predicted intensity pattern of the Michelson interferometer when one mirror is tilted with respect to the optic axis. The interferometer parameters are given in the text.

The scale on the pattern is from 0 to 100 (the 100 being replaced by AA) with 100 corresponding to total constructive interference and 0 to total destructive interference. It can be seen that the pattern consists of four maxima with the maxima exhibiting slight curvature away from the pattern centre. Considering the change in aperture shape and lack of astigmatism compared with the experimental pattern in Figure 43b the agreement is good.

In addition to predicting results as above the computer program also, as mentioned above, predicts the effect of tilt of the multimorph element in the stabilising system. This system will be described in greater detail later but for now it is sufficient to realise that in translating the reference mirror the multimorph crystal also tilts this mirror with respect to the optic axis. Two results are of particular interest. The first (Figure 52) predicts the output of the interferometer as the multimorph element is vibrated, when the stabilisation feedback loop is disconnected. The actual form of the oscillations are shown schematically as the curve of interest is the envelope of the pattern. Clearly in this situation, corresponding to the parameters shown in Figure 52, then the peak to peak intensity drops (by 8.4%). The values of all but one of these parameters are taken from measurements on the experimental interferometer. The exception is d which is very difficult to measure directly. An estimate may be made of its value by monitoring the movement of the collimating lens which causes no detectable change in the

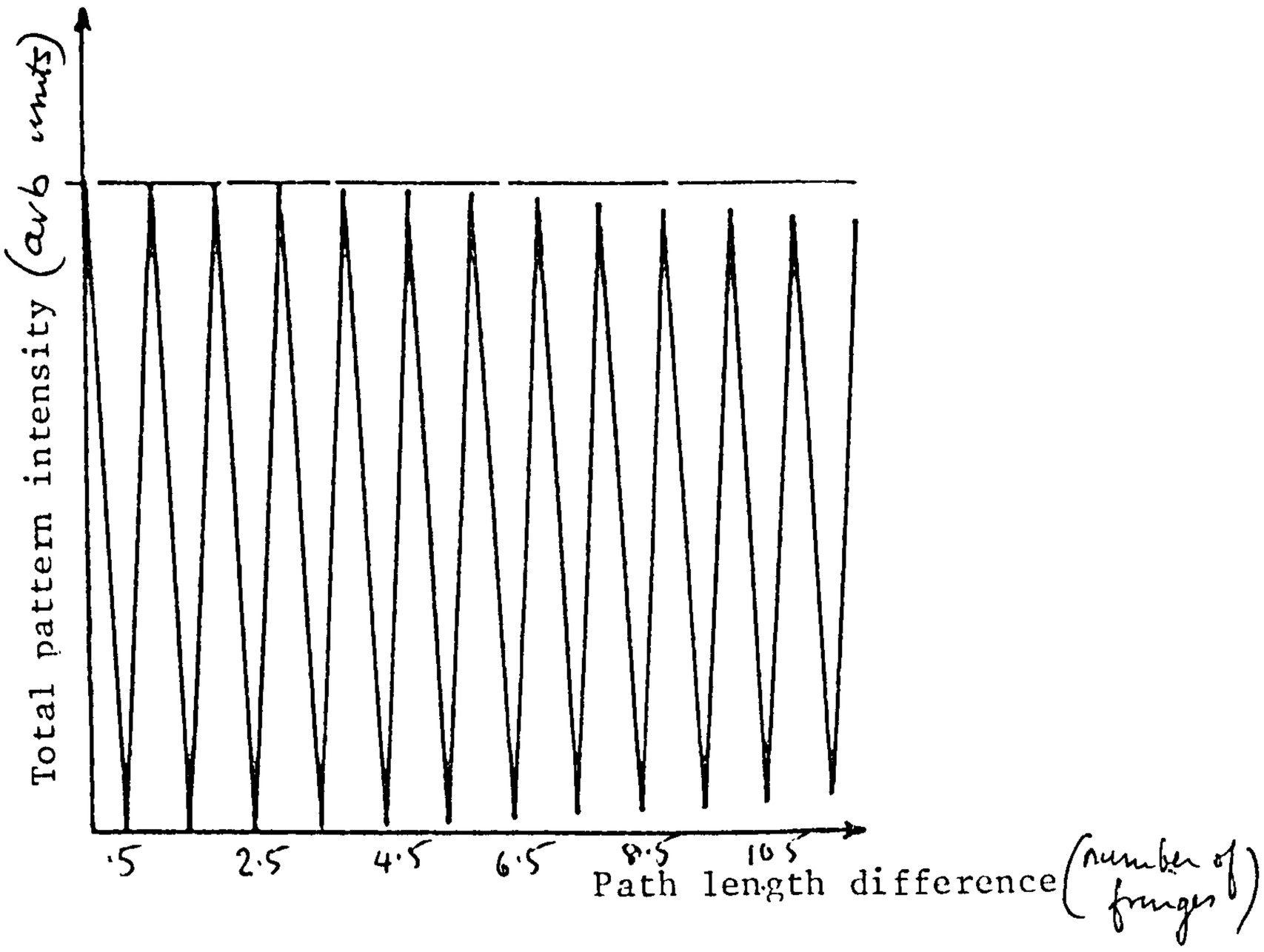

Figure 52: The total intensity output of the Michelson interferometer as one mirror is vibrated freely on a piezoelectric multimorph element of length 2.8mm. The initial path length difference and mirror tilt were zero. The collimating lens L_2 has a focal length of 100mm and an aperture of 7.2mm. The distance of the mirrors off focus (d in Figure 47) is 0.4mm.

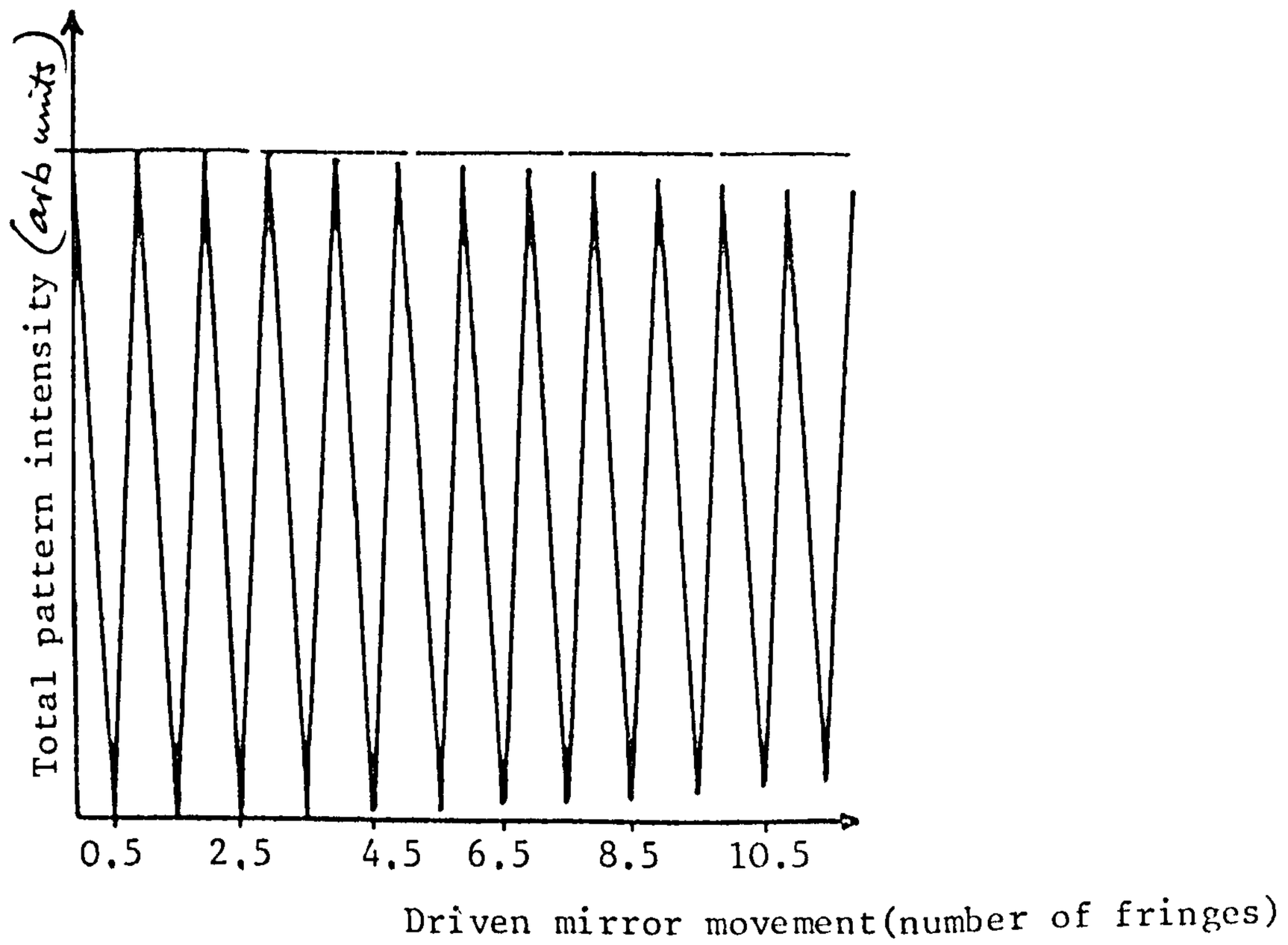

Figure 53: The effective intensity variation in a Michelson interferometer as one mirror is moved along the optic axis and the other mirror is driven on a piezoelectric multimorph element to stabilize thus keeping the path length difference zero. Parameters are as given in Figure 52.

intensity pattern when the tilt angle Φ is approximately 0.1 radians. Such measurements yield a value of d of approximately 0.4mm, which is therefore used to obtain the results for Figure 52.

This focussing range is assumed to be created by spherical aberrations in the system. Changing from the simple lens to the camera lens for the collimator L_1 improves the situation somewhat. However, most of the aberrations are thought to arise in the beam expanding lens, rather than the collimator. Measurements of the spot size to be made later also indicate spherical aberrations much larger than would be expected from the high quality camera lens.

The results indicated in Figure 52 will be investigated experimentally later.

The final situation of interest to be modelled on the computer is the effective peak to peak intensity change occurring when the multimorph crystal is vibrated over its full stabilisation range (in its stabilisation mode). It will be shown that Figure 52 predicts the experimental results very well and so all these parameter values are retained. Figure 53 shows the result of this final prediction. The fall in peak to peak intensity is found to be 10.4% when the vibration being stabilised against has an amplitude of 3.17μm. This is therefore the error on the system calibration if such a large vibration has to be stabilised against.

The computer program itself is given in Appendix 5.

III.2 Electrical noise arising in the photodetector circuits used in the interferometer

III.2.1 Theoretical noise considerations for a photodetector circuit

Noise is unavoidable in any detection and amplification circuit. Its occurrence in photodetector circuits has been studied by Kwaaitaal et al[18]. The basic photodetector circuit shown in Figure 54 has three fundamental sources of noise. The first is Johnson or thermal noise in both the photodetector and the resistor R. The second is the amplifier noise in the amplifier A (this will be due to various causes, one of which will also be Johnson noise). The third cause of noise is shot noise in the photodetector which has been briefly discussed in the introduction. Johnson noise arises due to the random thermal excitation of electrons (Millman and Halkias[103]) and has the following value for its root mean square (r.m.s.) value in a resistor R:

$$\langle V_{nJ} \rangle = (4kTR\Delta f)^{\frac{1}{2}} \qquad (57)$$

where $\langle V_{nJ} \rangle$ is the r.m.s. noise value, k Boltzman's constant, T absolute temperature, R the resistance and Δf the bandwidth of the system. Evaluating this gives

$$\langle V_{nJ} \rangle = 12.5\ \mu V \qquad (58)$$

when $k = 1.38 \times 10^{-23}$, $T = 293$, $R = 1000\Omega$, $\Delta f = 10MHz$.

The Johnson noise in the detector will be discussed overleaf.

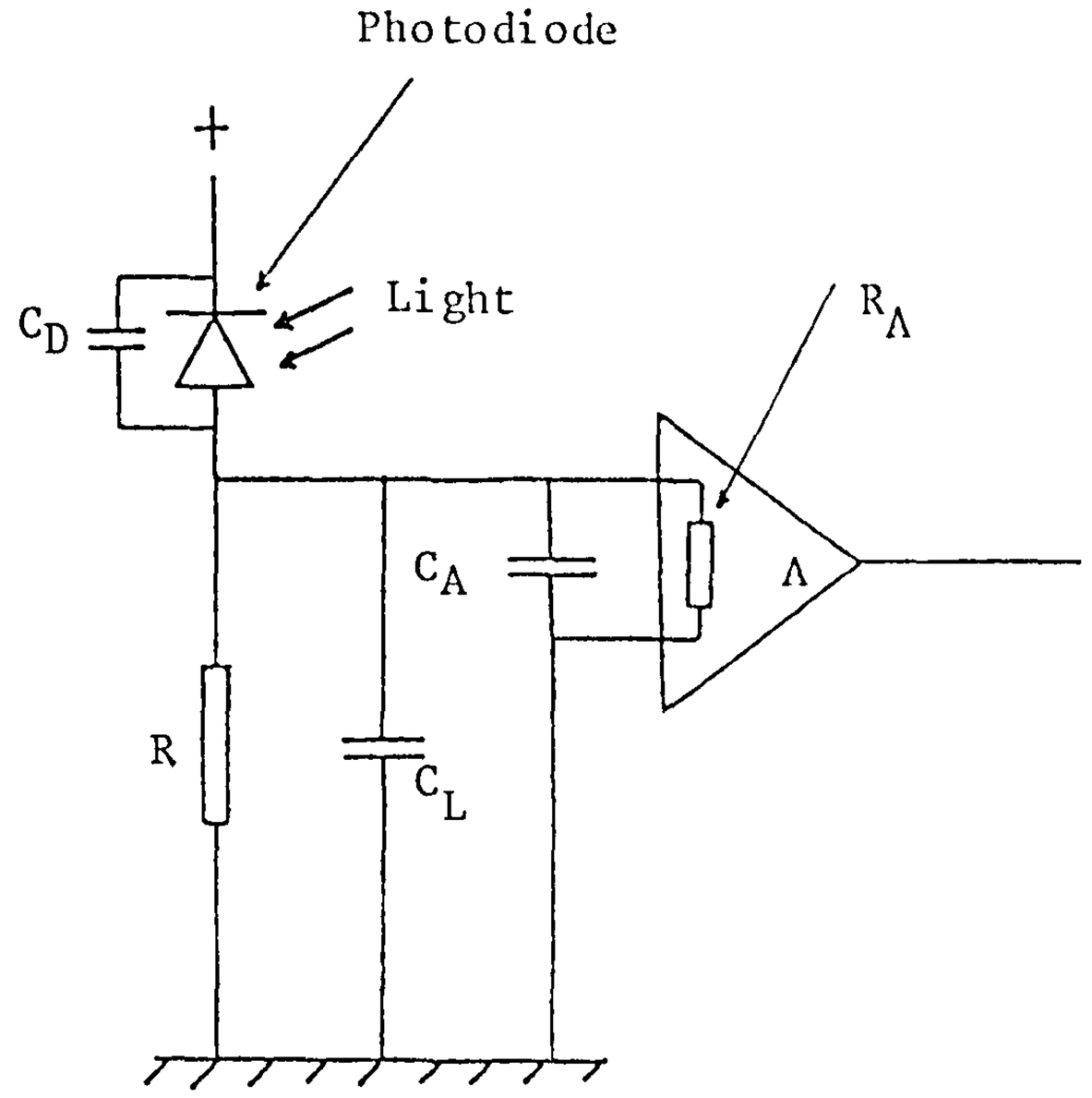

Figure 54: The basic photodetector circuit used in the Michelson interferometer.

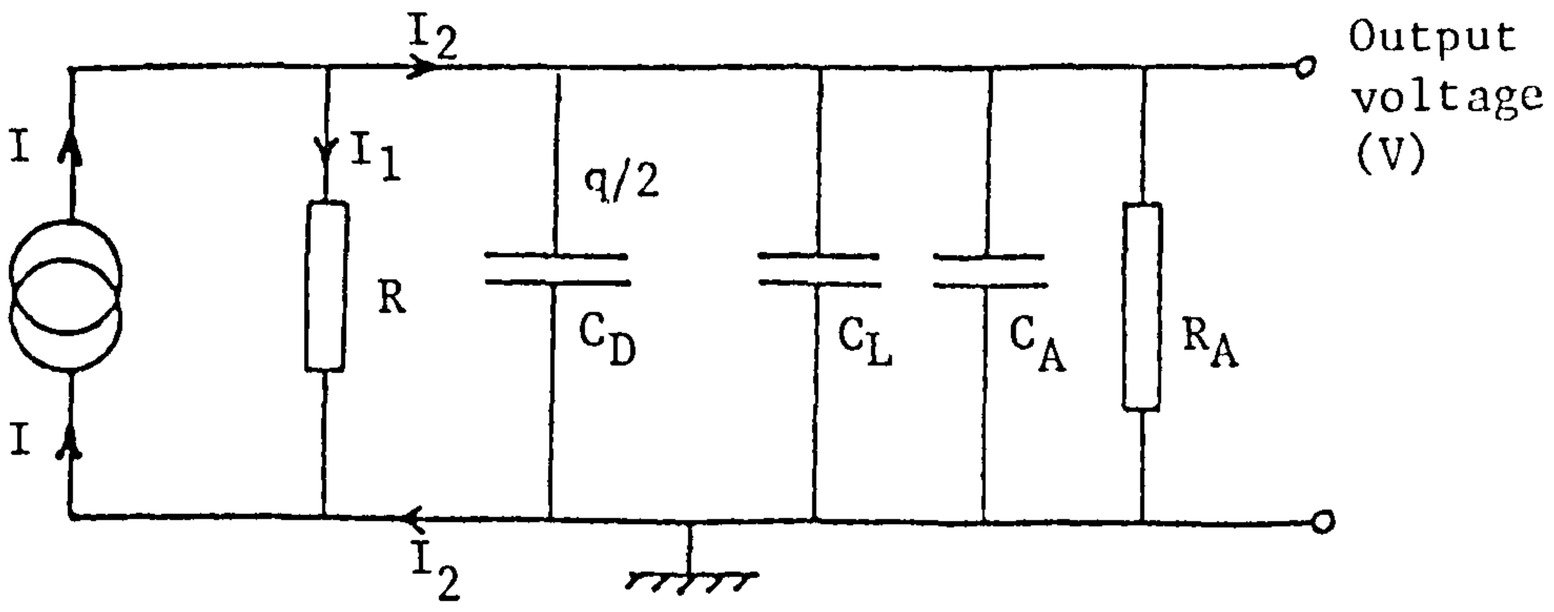

Figure 55: An equivalent circuit for the photodiode detection circuit given in Figure 54.

Amplifier noise is usually given in terms of an input equivalent value. Typical values are 10 to 20μV r.m.s.[104] for a 10MHz bandwidth, the noise being proportional to the square root of the bandwidth). In general then this value is of the same order as or larger than the Johnson noise. It should be realised that even though amplifier noise is not a fundamental limitation it must always be considered in a practical situation.

The final source of noise, shot noise, occurs because of the finite energy of each photon falling on the detector. In a stabilised interferometer the sensitivity is held constant by operating at the mid-point of a fringe (A, B, C, D etc in Figure 12). Therefore light is constantly falling on the detector. The finite energy of each photon means this light flux has a random fluctuation about some mean value[105]. This fluctuation leads to the shot noise, the form of which depends on the type of detection device used and is derived below for a photodiode.

A photon incident on a detector will create an electron with a probability or quantum efficiency η. If the incident light power (of frequency ν) is P then the flux of photons δ is P/(hν) creating a flow of electrons of charge (-e) which form a current i_s:

$$i_s = \frac{e\eta P}{(h\nu)} = \alpha P \qquad (59)$$

(where h is Planck's constant and α the device responsivity in amps per watt of radiation).

The fluctuations in P yield the r.m.s. shot noise $\langle i_{ns} \rangle$ for a bandwidth Δf:

$$\langle i_{ns} \rangle^2 = 2\eta e^2 \frac{P}{(h\nu)} \Delta f \qquad (60)$$

In addition to this incident light generated noise there is also a dark current noise. Any photodetector has a dark current flowing through it. This current also generates shot noise (which can alternatively be considered as thermal noise). In general the dark current noise is very low and will be ignored.

For the circuit of Figure 54 the shot noise in equation (60) creates a voltage across the resistor R of

$$\langle V_{ns} \rangle^2 = 2\eta e^2 \frac{P}{(h\nu)} \Delta f \, R^2 \qquad (61)$$

which may be rewritten using equation (59) as:

$$\langle V_{ns} \rangle^2 = 2ei_s \Delta f \, R^2 \qquad (62)$$

thus reproducing equation (8). The signal to noise ratio (SNR) may be derived by dividing equation (59) by the square root of equation (60) leaving:

$$SNR = \left(\frac{\eta P}{2h\nu\Delta f} \right)^{\frac{1}{2}} \qquad (63)$$

This is the signal to noise ratio for a photodiode. Other types of detectors might also be used in the interferometers. These are photomultipliers and avalance photodiodes. Photomultipliers have quantum efficiencies of around 0.05 and consequently a poor SNR compared to silicon p.i.n. photodiodes which have quantum efficiencies

of 0.85. Avalance photodiodes, being made of the same type of material as the p.i.n. photodiodes have very similar quantum efficiencies. At first sight then they should have the same signal to noise ratios. However, extra shot noise occurs in the avalance multiplication effect and this reduces the SNR by a factor of between 1.4 and 10. Silicon p.i.n. photodiodes are therefore the best detector to use in situations where their shot noise exceeds amplifier noise.

Typical values of the shot noise may be calculated by assuming a laser power L_o and an interferometer efficiency of 10%. In this situation

$$P = 0.05\ L_o \qquad (64)$$

and

$$\langle V_{nS} \rangle = 11.7\ \mu V \qquad (65)$$

where $\Delta f = 10MHz$, $R = 1000\Omega$, $L = 2mW$ and $\eta = 0.85$.

If the three contributions to noise (thermal, amplifier and shot) are assumed to be independent then a total noise figure ($\langle V_{nT} \rangle$) may be calculated:

$$\langle V_{nT} \rangle^2 = \langle V_{nS} \rangle^2 + \langle V_{nJ} \rangle^2 + \langle V_{nA} \rangle^2 \qquad (66)$$

where $\langle V_{nA} \rangle$ is the r.m.s. amplifier noise. Using the figures in equations (58), (65) together with $\langle V_{nA} \rangle$ as 10μV yields:

$$\langle V_{nT} \rangle = 19.8\mu V \qquad (67)$$

To derive the minimum detectable displacement the

device sensitivity has to be considered. For a stabilised interferometer the sensitivity is taken from equation (47) as (for $R << F$):

$$\delta I \simeq \varepsilon c\left(2E_{I_1}E_{I_2}\pi R_A^2 \frac{4\pi}{\lambda} \sin\left(\frac{4\pi x}{\lambda}\right)\right)\delta x \qquad (68)$$

If $E_{I_1} = E_{I_2}$ and the light efficiency of the interferometer is α then for a laser power intensity I_o:

$$\delta I = \frac{\alpha I_o}{2} \cdot \frac{4\pi}{\lambda} \sin\left(\frac{4\pi x}{\lambda}\right)\delta x \qquad (69)$$

the maximum sensitivity being

$$\delta I = \frac{\alpha I_o}{2} \cdot \frac{4\pi}{\lambda} \delta x \qquad (70)$$

With $\alpha = 0.05$, $I_o = 2mW$ and $\lambda = 632.8nm$ this becomes

$$\frac{\delta I}{\delta x} = 1.0 \times 10^{-6} W\ nm^{-1} \qquad (71)$$

With a photodiode of reponsivity $0.43 Aw^{-1}$ and a bias resistor of $1k\Omega$ then

$$\delta V = 0.43.1000\ \delta I \qquad (72)$$

and hence

$$\frac{\delta x}{\delta V} = 2.3 \times 10^3\ nmV^{-1} \qquad (73)$$

Using the noise figure of equation (67) this gives a minimum detectable displacement of

$$\delta x_{min} = 46pm \qquad (74)$$

Calculations such as those above clearly depend on the values of the parameters chosen. The four variable parameters being I_o, Δf, R and the photodiode quantum

efficiency η. As discussed previously, η is optimised by choosing to use a silicon p.i.n. photodiode as the detector. The only variable parameters are then I_o, Δf and R. I_o determines the size of δx_{min} in that δx from equation (70) is inversely proportional to I_o, whereas i_{ns} in equation (60) is inversely proportional to the square root of P and hence I_o. Therefore the minimum detectable displacement is inversely proportional to the square root of the laser power ($\delta x_{min} \propto I_o^{-\frac{1}{2}}$). By merely increasing the laser power an interferometer is made more sensitive. Laser noise in terms of laser intensity variations may then become a problem. Methods are available though to remove this noise and are outlined in section II.4.2ii for a stabilised interferometer or Appendix 2 for a quadrature interferometer.

The two remaining parameters, Δf and R, govern the speed of response of the circuit. This clearly is an important consideration and will now be looked at in more detail.

An equivalent circuit may be drawn of the one in Figure 54 which for AC currents is that shown in Figure 55, where the power supply is assumed a short for AC and the photodiode is replaced by a current generator. R_A will always be much greater than R and is therefore effectively infinite. The response of this circuit to a stepwise (Heaviside function time dependency H(t)) current (I_o) generated in the current generator (photodiode) may easily be calculated. To perform the calculation C_D, C_L and C_A are added together to give a total capacitance C. The

currents must add at each function yielding:

$$I = I_1 + \frac{d}{dt}(VC) \qquad (75)$$

as $$I_2 = \frac{dq_2}{dt} = \frac{d}{dt}(VC)$$

The voltage dropped over the resistor R should also equal that dropped over the capacitor C and hence:

$$I_1 R = \frac{q^2}{C} = V \qquad (76)$$

Writing I as $I_o H(t)$ allows equations (75) and (76) to be combined which upon integration gives

$$V = I_o H(t).R(1-e^{-t/RC}) \qquad (77)$$

A result may also be derived in the frequency domain by assuming the current to vary as $I_o e^{i\omega t}$. The voltage V as a function of frequency is then

$$V = \frac{I_o R e^{i\omega t}}{1+i\omega RC} \qquad (78)$$

or $$V = \frac{I_o R}{(1+(\omega RC)^2)^{\frac{1}{2}}} .\exp(i\omega t - i \tan^{-1}\omega RC) \qquad (79)$$

A result which will be of interest later may be derived at this stage. This links the rise time (t_r) of equation (77) that is the time to rise from 10% to 90% of the final value, to the 3dB frequency point ω_{3dB} or f_{3dB} in equation (79). The relationship is

$$t_r = \frac{2.20}{\omega_{3dB}} \qquad \left(\omega_{3dB} = \frac{1}{RC}\right) \qquad (80)$$

or $$t_r = \frac{0.35}{f_{3dB}} \qquad (81)$$

where ω_{3dB} is the 3dB point in terms of angular frequency

and f_{3dB} the corresponding point in cyclic frequency.

It can clearly be seen that the speed of response (or bandwidth) depends on the values of R and C. The experimental practicalities covering their choice will now be discussed.

III.2.2 Experimental studies of electrical noise arising in photodetector circuits and the speed of response of these circuits

The input noise equivalent values of most recording instruments (screen storage oscilloscopes, digitisers etc) are of the order of 100 or 200μV. This figure fixed by the recorder's input amplifier is far too large when considered next to the figures quoted in the previous section. To produce a sensitive laser interferometer therefore requires preamplification. The first question to be answered is what frequency bandwidth is required. The results given by Scruby et al[10] and Rouby et al[11] suggest, as mentioned previously, a bandwidth range from around 1kHz to 10MHz would be appropriate. Operational amplifiers with gain-bandwidth products of 600MHz exist[106] thus allowing amplification of around 50 times. However such devices are noisy and in fact cannot be used.

Other possibilities exist. One method available is to use a preamplifier built from discrete components. A preamplifier built by Dunegan/Endevco corporation (model number 1801) was one such device tested experimentally. The frequency bandwidth of 2MHz quoted (and experimentally

verified) is really too low, but the experiments highlight the problems associated with such an approach.

The input capacitance was measured by driving the amplifier from a voltage generator through a large series resistor and measuring the amplifier output as a function of frequency. This figure is then compared to the output without a series resistor. The capacitative loading effect of any measuring leads must be carefully considered, which is why the amplifier output is measured and not the amplifier input voltage. These measurements gave a value of 38pF for the input capacitance. This includes the small capacitance of the correctors to and from the series resistor (probably around 1 or 2pF) and compares well with the quoted value of 30pF.

In order to utilise all the available bandwidth of the preamplifier this value of the input capacitance determines that the bias resistor (R in Figure 54) should be less than or equal to 2.1kΩ, yielding a shot noise value for a 2MHz bandwidth of 11.0μV. The measured output noise however gave an input equivalent value of 25μV which thus exceeded the shot noise limit indicating that amplifier noise dominated.

Other amplifiers were tested but all suffered from this problem that R must be small to make the system fast which meant that the shot noise fell below the amplifier input noise.

The solution to the problem was found to be a hybrid silicon p.i.n. photodiode/preamplifier module. (RCA device number C30816). This device has a bandwidth from

DC to 10MHz. The noise out of this hybrid was measured at approximately 100μV which matched the quoted noise figure. Using the response figures given then the shot noise calculated from equations (60) and (64) of 12.7nA yields an output noise of 200μV. This is therefore greater than the amplifier noise with the combined noise being calculated to be only 220μV. Noise is therefore effectively determined by shot noise which was measured as being equivalent to 25pm in most of the following experiments. (The Johnson noise is included in the quoted background noise of the preamplifier).

The use of a variable power Argon Ion laser and a root-mean-square (r.m.s.) meter allowed the shot noise dependency of the total noise figure to be verified. In this experiment the r.m.s. noise in an arbitrary bandwidth was measured as a function of laser intensity. The total noise $\langle V_{nT} \rangle$ is related to the shot noise $\langle V_{nS} \rangle$ and amplifier noise $\langle V_{nA} \rangle$ via equation (66). As the square of the shot noise is proportional to the laser intensity (I) then the following is also true:

$$\langle V_{nT} \rangle^2 = \langle V_{nA} \rangle^2 + (\text{Constant}).I \qquad (82)$$

Figure 56 shows that this equation is followed where the measured noise is plotted against I the nominal laser power. The intensity actually falling on the photodetector is only proportional to and not equal to I.

The detector bandwidth has been verified by measuring the response of the hybrid detector to the pulse from a Q-switched Nd-YAG laser. This laser produced a pulse with

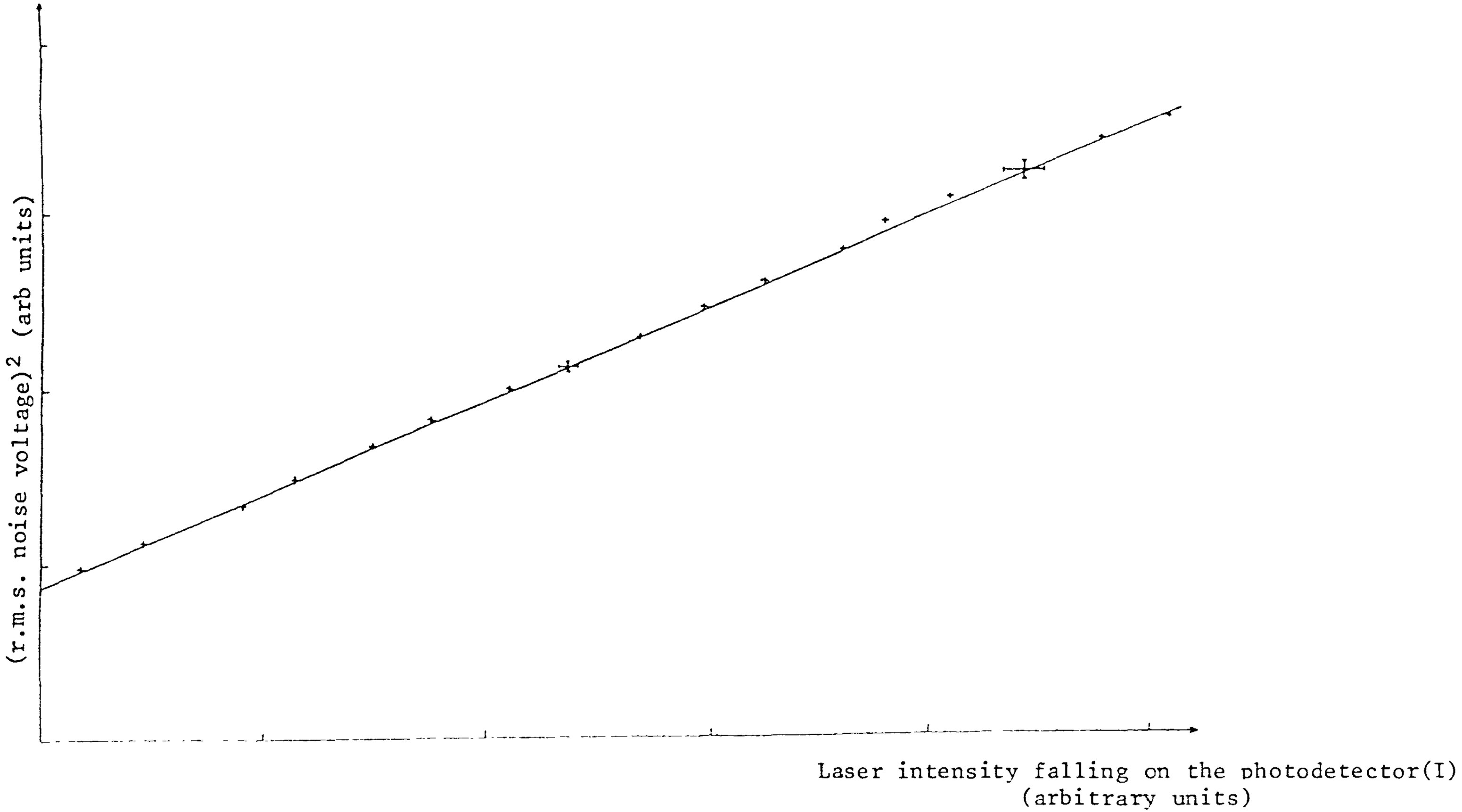

Figure 56: The r.m.s. noise voltage squared out of a photodetector as a function of the light power striking the detector.

a temporal half width of approximately 20ns and the detector responded with a rise time (10% to 90%) of 25ns. Such a figure means that the hybrid device actually has a bandwidth in excess of 10MHz. However slight ringing in the response was noted implying that the useful frequency range is only up to the quoted 10MHz.

Further partial verification of the bandwidth was carried out by measuring the scattered light from the edge of a variable speed rotating turntable. When the light was scattered almost tangentially to the turntable circumference large Doppler shifts resulted. This enabled the device frequency response to be plotted up to 2.6MHz which was shown to be flat.

III.3 Determination of the size of the laser image spot on the interferometer mirrors

III.3.1 Theoretical spot size

The beam out of the Helium-Neon laser has a Gaussian cross-section due to the fact that the laser operates in the TEM_{00} mode. This laser is designed as a hemispherical resonator[107] with a planar mirror at the output. The waist of the output beam is therefore at the mirror and has a diameter of 0.64mm[40] measured at the $1/e^2$ intensity points.

Assuming that gaussian beam optics apply throughout the system (this is so if the lenses do not significantly aperture the beam) then the image spot size on the interferometer mirrors may be calculated using a method

given by Self[108]. Adopting the real is positive sign convention then the magnification produced by a lens of focal length f focussing a gaussian object at distance s to an image at distance s' is given by

$$m = \frac{w_O'}{w_O} = \frac{1}{((1-(s/f)^2+(Z_R/f)^2)^{\frac{1}{2}}} \qquad (83)$$

where w_O is the object beam-radius, w_O' the image beam radius and Z_R the Rayleigh range of the object beam. Z_R is depicted in Figure 57 and is given by

$$Z_R = (\pi w_O^2/\lambda) \qquad (84)$$

The first lens in the system is a microscope objective with a magnification of 60X and a numerical aperture (N.A.) of 0.85 where the numerical aperture for a lens focussed in a medium of refractive index n is given by[107]

$$N.A. = n \sin(\Phi) \qquad (85)$$

with Φ the angular radius of the cone of light the lens accepts. Numerical aperture is related to the diffraction limited spot size of the lens by[107]

$$r_d = \frac{1.22\lambda s'}{2(N.A.)} \qquad (86)$$

or

$$r_d = \frac{1.22\lambda s'}{nD} \qquad (87)$$

where D is the lens diameter (N.A. = D/2s'). The focal length of the microscope objective is determined by its magnification because it is designed for use in microscopes which all have the same tube length. This focal length is 3mm. It should be mentioned that the objective is

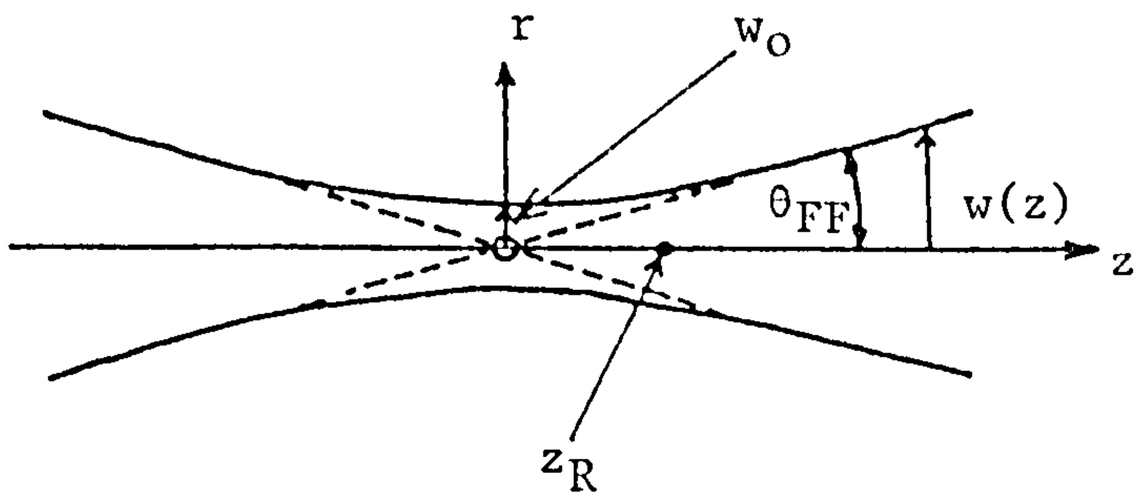

Figure 57: The geometry of the focus point of a spherical Gaussian laser beam to show the Rayleigh range z_R (After Self[108]).

Figure 58: (below). The experimental apparatus used to measure the size of the laser spot on the interferometer mirrors in situ.

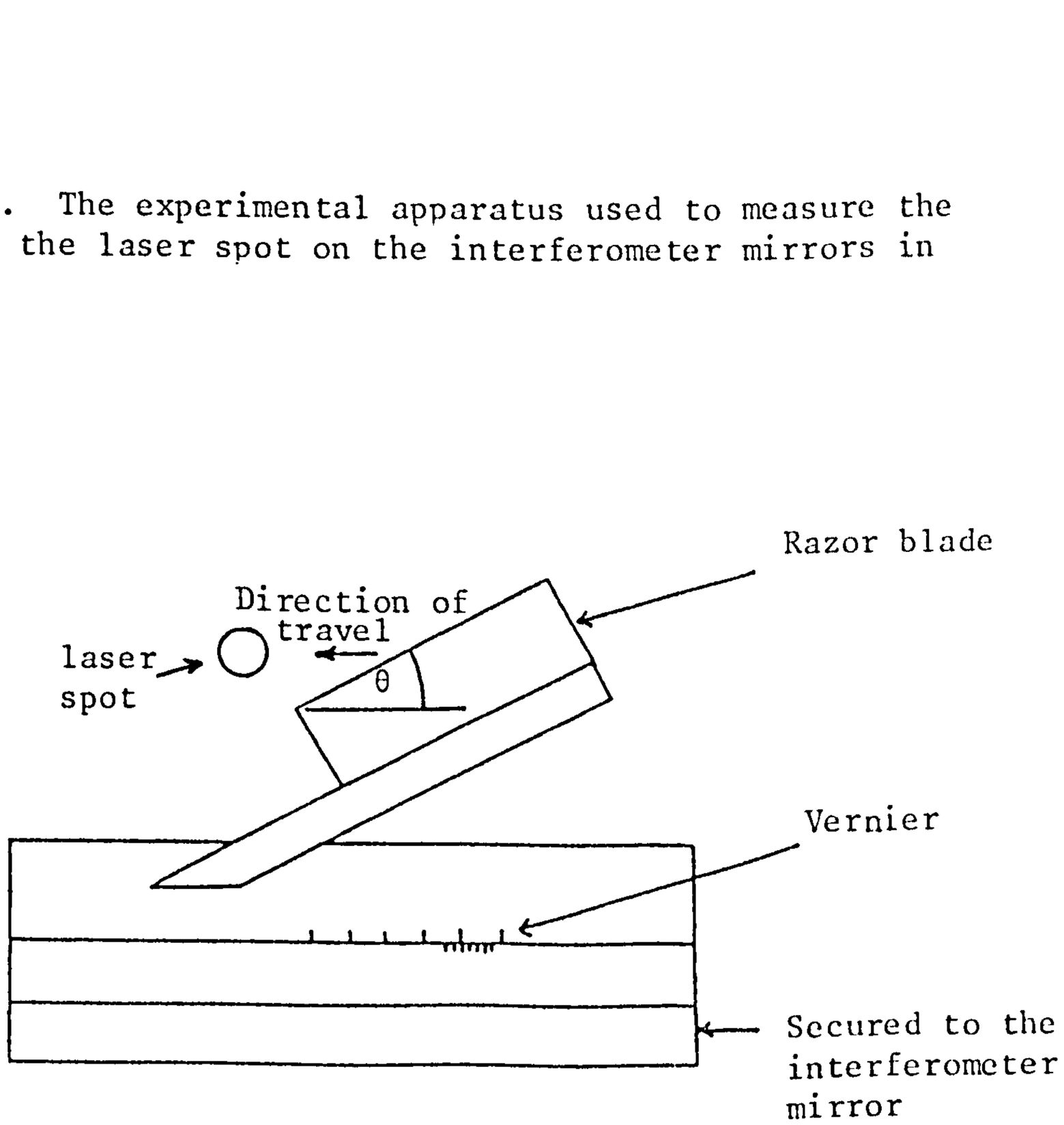

optimised for the object and image distances arising in microscopes which in this case are approximately 3.05mm and 183mm, aberrations will increase when the lens is used in other conjugate ratios. The lens diameter may be determined knowing the N.A. and is found to be 5.2mm.

It is now possible to calculate the size of the spot produced by the microscope objective assuming gaussian optics. First Z_R is calculated at the laser output mirror to be:

$$Z_R(\text{output of laser}) = 5.08 \times 10^5 \mu m \qquad (88)$$

The distance from the output mirror of the laser to this microscope lens is approximately 60mm. Equation (83) may now be evaluated to give

$$\frac{w_o'}{w_o} = 5.87 \times 10^{-3} \qquad (89)$$

and so

$$w_o' = 1.9\mu m \qquad (90)$$

Zn' may now be calculated for this image and is

$$Z_R' = 17.9\mu m \qquad (91)$$

This image now forms the object for the camera lens, which has an f-number of 3.5 and a focal length of 135mm. Now f-number is defined as the ratio of the focal length to the clear aperture diameter[107]. The diameter of this camera lens is therefore 38.6mm. The measured object distance to it was 183mm. Using equation (83) again yields

$$\frac{w_o'}{w_o} = 2.81 \qquad (92)$$

and so $$w_o' = 5.35\mu m \qquad Z_R = 142\mu m \qquad (93)$$

The final spot diameter is therefore calculated to be 10.7μm ($1/e^2$ points) assuming gaussian optics.

The question of beam aperturing will now be considered. As the laser output beam has a Rayleigh range of 508mm then the beam diameter at the first (microscope) lens is 0.64mm. This lens is then not apertured. The diameter at the camera lens is calculated easily as the distance to this lens is much greater than the new Rayleigh range and is found to be 37mm. Slight aperturing may therefore occur. Using equation (87) then the final beam radius at focus would be, assuming pure diffraction:

$$r_d = 10.3\mu m \qquad (94)$$

The final spot size will be found by some convolution process between the diffraction limit, the gaussian limit and the limit due to aberrations. An estimate of the contribution from the first two factors being given by:

$$r_{g+d}^2 = (w_o)^2 + r_d^2 \qquad (95)$$

$$r_{g+d} = 11.6\mu m \qquad (96)$$

III.3.2 Experimental spot size

The calculations shown above neglect lens aberrations in the system. It was mentioned earlier that when a simple lens was used as the collimating lens focussing aberrations were apparent and as a consequence this lens was not used. The final interferometer system employing the camera lens

may still be subject to aberrations and so the spot size was measured directly in this case.

The experimental arrangement for this measurement, shown in Figure 58, was used on the interferometer in situ. The razor blade edge was held flush with the subject mirror surface and slowly moved across the laser spot. The amount of laser light reflected from the spot into the optical system, which depends on the blade position, was measured by removing the reference mirror and monitoring the photodetector output.

The solid angle for light acceptance into the photodiode from the mirrors is approximately 1.2×10^{-2} sterradian. Now the razor blade is a diffuse scatterer of radiation which means that the laser power reflected from the blade is scattered isotropically. The laser power entering the optical system when the blade entirely covers the spot is therefore only 0.2% of that which would be reflected from a perfect specular reflector. Unfortunately, the mirrors are not perfect reflectors and reflect around 25% specularly. Therefore the scattered radiation from the blade represents 0.8% of the specular reflection from the mirror. It can be assumed then that the blade effectively stops the light returning from the mirror.

The voltage from the photodetector is plotted against position from the vernier scale, (see Figure 59). Some estimate of the spot diameter is required and is taken to be the distance between 10% and 90% of the full excursion. The distance from the graph (x) (Figure 59) is related to

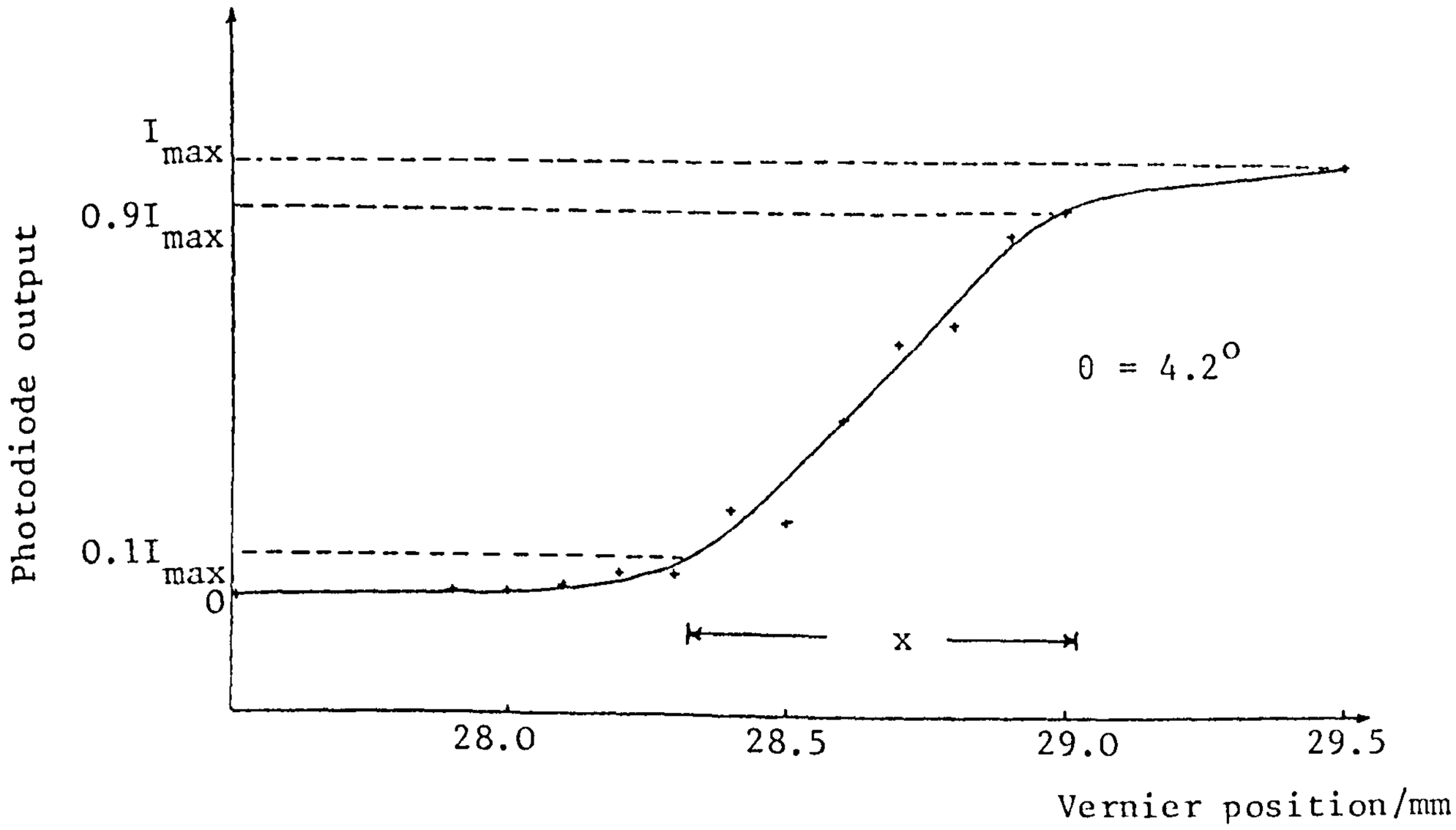

Figure 59: The output voltage of the photodiode versus the vernier position in the device given in Figure 58 as used to measure the laser spot size.

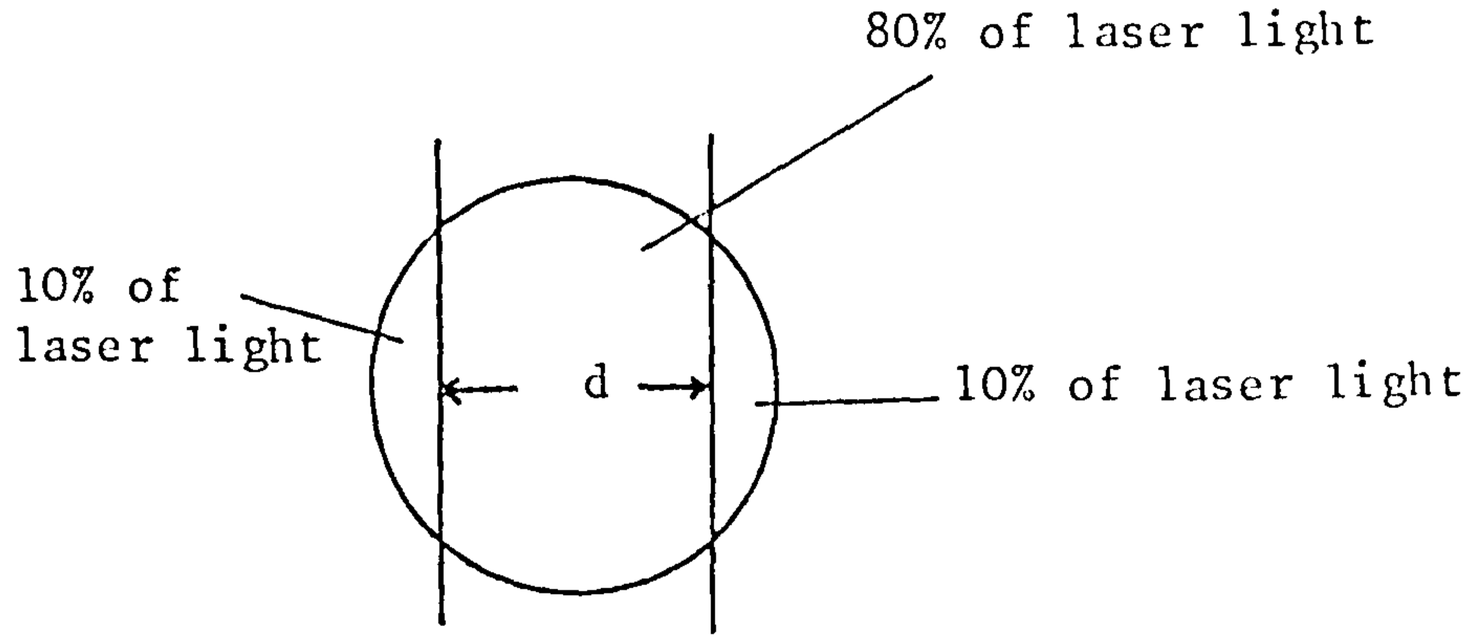

Figure 60: Definition of the laser spot diameter determined in Figure 59.

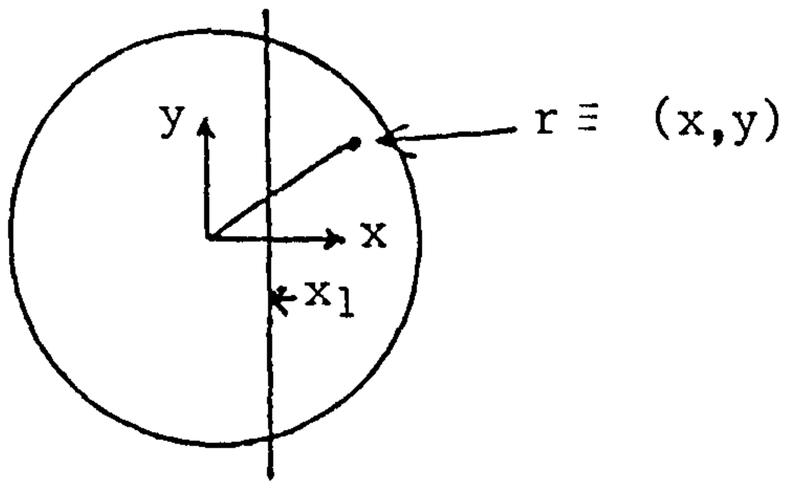

Figure 61: The geometry used to link the spot diameter (d) measured above to that determined in theoretical calculations. (see equations 94-96).

the corresponding real size (d) (Figure 60) by

$$d = x \sin \theta \qquad (97)$$

where θ is given on Figure 58.

The experiment was performed four times and the resulting distance d (see Figure 60) found to be:

$$d = 43 \pm 5\mu m \qquad (98)$$

A step Rayleigh pulse travelling over the surface of the mirror will affect between 10% and 90% of the light in the laser interferometer spot over this distance d. Assuming a Rayleigh wave velocity of 2.906 mm μs^{-1} for aluminium then the rise time (10% to 90%) of the interferometer response to this wave will be (15 ± 2)ns. Using equation (81) this corresponds to an upper frequency limit of (23 ± 2)MHz. Therefore the electronics in fact limit the system frequency response.

The distance d should now be related to the spot diameters quoted in the theoretical calculations of the previous section. Assuming that the spot has a Gaussian profile on the mirror then the intensity as a function of radius r and angle θ is

$$I(r,\theta) = I_o\left(\frac{2}{\pi w^2}\right)e^{-2(r/w)^2} \qquad (99)$$

where w is the radius at which the intensity falls to $1/e^2$ and I_o is the total beam intensity. This may be written in cartesion co-ordinates as

$$I(x,y) = I_o\left(\frac{2}{\pi w^2}\right)e^{-2\left(\frac{x^2+y^2}{w^2}\right)} \qquad (100)$$

The intensity to the right of the line passing through x_1 is then I_R(Figure 61):

$$I_R = \int_{y=-\infty}^{y=+\infty} dy \int_{x=x_1}^{x=+\infty} I_o \frac{2}{\pi w^2} e^{-2\left(\frac{x^2+y^2}{w^2}\right)} dxdy \qquad (101)$$

This is a double integral and may be written:

$$I_R = I_o\left(\frac{2}{\pi w^2}\right) \int_{-\infty}^{+\infty} e^{-\frac{2y^2}{w^2}} dy \int_{x_1}^{+\infty} e^{-\frac{2x^2}{w^2}} dx \qquad (102)$$

The y-integral is easily evaluated by considering the integral of equation (99)[109] and leaves:

$$I_R = I_o\left(\frac{2}{\pi w^2}\right)^{\frac{1}{2}} \int_{x_1}^{+\infty} e^{-2x^2/w^2} dx \qquad (103)$$

This problem is often found in statistics as it is the normal distribution function. Substituting $\frac{1}{2}u^2 = \frac{2x^2}{w^2}$ in equation (103) leads to:

$$I_R = I_o \int_{u'=\frac{2x_1}{w}}^{+\infty} \frac{e^{-\frac{1}{2}u^2}}{\sqrt{2\pi}} du \qquad (104)$$

which is the normalised normal distribution. The value of u' for which $I_R = 0.1I_o$ is 1.28 and so

$$x_1 = 0.64w \qquad (105)$$

Therefore the value of d in a Gaussian beam is related to the $1/e^2$ radius (w) by

$$d = 1.28w \qquad (106)$$

Equation (96) gives d as

$$d_{Gaussian + diffraction} = 14,8\mu m \qquad (107)$$

Clearly then some aberration effects do occur in the lenses resulting in a larger spot size than would be expected for either diffraction limited optics or Gaussian beam optics. However the spot size is still small enough to ensure that the electronics are the limiting factor in the speed of response of the interferometer. The measured spot size is 2.9 times longer than the calculated size. A similar scaling factor might be expected on the calculated Rayleigh range which leads to a longitudinal spherical aberration of 4.1×10^{-4}m.

III.4 The development of a stabilisation technique

III.4.1 Experimental work performed on the stabilisation

The basic concept for the stabilisation is that of a negative feedback controlled servo loop controlling some type of translator upon which the reference mirror is mounted.

Preliminary work carried out on the problem of stabilisation followed the work of Palmer and Green[17]. The mirror translator was in this case a transverse expansion mode piezoelectric crystal with a small piece of silvered glass glued on to form the mirror. It was found that the background vibrations occurring in the laboratory were sufficiently large to cause the loop to continually jump out of stabilisation. This occurs because of the limited range of movement possible with the available drive voltage of ±450V. With an expansion

coefficient of around 0.5μm/kV this voltage range of 900V could only stabilise 0.45μm. A study of the amplitude of the background disturbances indicated a stabilisation of 3 - 4μm was necessary. Such a figure would require a voltage of 6 - 8kV. As the piezoelectric crystal represents a large capacitative load the amplifier power required would be large.

One solution to the stabilisation problem then would be to develop a high voltage high power amplifier and a piezoelectric crystal to go with it. Such a crystal would have to be quite thick to avoid electrical breakdown and possibly also quite wide to avoid distortion of the crystal faces due to edge effects of the electric fields.

Another solution is to change the type of translation mechanism. A possible choice for this new mirror translator is the piezoelectric multimorph element mentioned earlier. This second solution is preferred as the multimorph crystal offers potentially a very large stabilisation range.

The multimorph crystal described above is effectively composed of two piezoelectric crystals poled in opposite directions and secured back to back (in reality the device is made of one piece of piezoelectric ceramic and poled so as to appear as described). The assembly works in a manner similar to that of a bimetallic strip. A voltage applied across the composite results in the expansion of one side of the element and contraction of the other. A multimorph element therefore produces large

transverse displacements of its tip by bending. The mirror consisting of a small piece of aluminised milar was glued on the tip of the cantilever. Such a mirror was used because its small mass did not signficantly overload the multimorph crystal which could only generate a fairly small force.

The intensity pattern in a Michelson interferometer is a function of path length, mirror tilt and the position of the focus of the laser light with respect to the interferometer mirrors. If the multimorph is to be used as a mount for one of the interferometer mirrors then the tilt as mentioned before which the mirror suffers, as a result of bending of the stabilising element, must be taken into account. The maximum displacement of the multimorph is limited by the maximum mirror tilt which can be tolerated. This then defines a maximum range of stabilisation.

In order to assess the stabilisation some definition of adequate stabilisation is required. A Michelson interferometer when perfectly aligned gives rise to an intensity at the detector which is a function of the relative separation of the mirrors (x), equation (47). This equation may be approximated by equation (1) when $E_1 = E_2$ and $R << F$ and is depicted in Figure 12. The differential sensitivity is then given by equation (3) when $\delta I_o = 0$ and $\delta\lambda = 0$.

If I (Figure 12) is constrained to lie within the range

$$\frac{4I_o}{5} < I < \frac{6I_o}{5} \qquad (108)$$

corresponding to the middle 20% on Figure 12, then $\partial I/\partial x$ will lie within the range

$$0.98 \frac{4\pi I_o}{\lambda} < \frac{\partial I}{\partial x} < \frac{4\pi I_o}{\lambda} 1.02 \qquad (109)$$

As the conditions in equation (108) are relaxed then the calibration errors indicated in equation (109) rapidly become greater. Clearly some decision has to be made on what calibration error may be tolerated. In the system studied the limits as set out above of ± 2% have been adopted.

III.4.1i) Experimental arrangement

The stabilisation system for which results are given is shown in Figure 62. The parameters of interest are:

(i) ℓ - the free length of the multimorph crystal,

(ii) The type and order of the filters used in the feedback electronics,

(iii) The roll-off point for these filters,

(iv) G_o - the DC gain of the feedback loop, controlled by ℓ and the filter responses.

The action of each element in Figure 62 is as follows. Light from the interferometer falls on the hybrid detector mentioned earlier which converts this information into an electrical signal. The electrical signal is passed into a differential amplifier, which removes the DC offset produced by the hybrid detector as well as the DC offset produced in the intensity pattern. The output of the differential amplifier is centred about zero, which now becomes the reference voltage. The high frequency

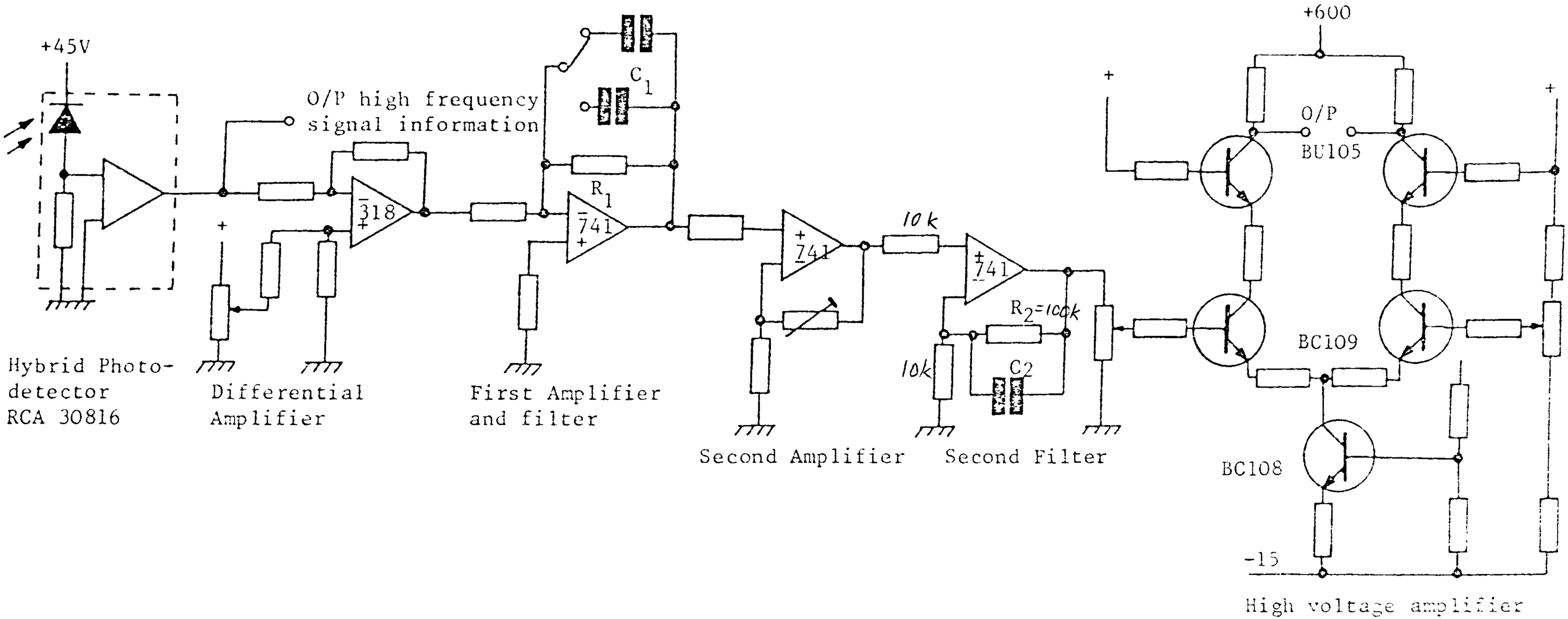

Figure 62: Basic feedback loop

signal information is also taken from the output of the hybrid detector to separate recording instrumentation. The voltage from the differential amplifier is fed into the first filter which reduces the system gain at the resonance frequency of the crystal in order to suppress system oscillation. The second amplifier in the chain is to increase the DC system gain. This capability could, of course, be built into the first filter. However, the DC gain and roll-off point of this filter would then be interdependent. This is undesirable in this experimental arrangement. The DC gain of the differential amplifier must not be increased to such a value that the output of this second amplifier becomes saturated. A second filter is employed to further reduce the system gain at the crystal resonance frequency, but without either introducing any significant phase lag at high and intermediate frequencies or reducing the gain in the region of stabilisation. This filter is therefore designed to roll-off at approximately 200Hz and have a high frequency gain of unity.

The final amplifier is a high voltage amplifier to drive the piezo element. The maximum displacement of the multipmorph is ideally determined by some maximum angle of tilt. However, in order to reach this fundamental limit the voltage applied to the crystal must be moderately high, of the order of a few hundred volts.

The stabilising properties of the system were assessed using a second multimorph element in the other arm of the interferometer in place of the mirror which would normally

be the subject. This element was approximately one centimetre in length and thus easily produced large excursions of the test mirror without introducing significant tilt.

III.4.1ii) Results of the stabilisation tests

III.4.1ii)a) Change of filtering

A variety of changes were implemented in the filter characteristics for one fixed length of crystal as the active stabilising element. The length of the crystal was 3.6 ± 0.2mm.

The first test is a change in $(RC)_1$, the time constant, for the first amplifier shown in Figure 62. Two values of $(RC)_1$ are given, that is $(RC)_1 = 0.79 \pm 0.05s^{-1}$ and $(RC)_1 = (0.79 \pm 0.05) \times 10^{-3}s^{-1}$. The stabilisation results (Figure 63) for vibration frequencies below 200Hz are improved by the use of a larger value of $(RC)_1$, whereas the results are identical for frequencies much greater than 200Hz. The maximum disturbance against which the system will stabilise is $|x_3 - x_2|_{max}$ or the stabilisation. The half power point for a filter with $(RC) = 0.79 \times 10^{-3}s^{-1}$ is 200Hz. The interferometer itself did not, in general, suffer from DC or very low frequency vibrations (less than 5Hz) and so no improvements are found by using very large values of $(RC)_1$, $((RC)_1 < 1)$. The upper limit on the stabilisation is provided by the voltage produced by the high voltage amplifier as defined by equation (133).

The second test made was to replace the second filter shown in Figure 62 with one identical to the first filter,

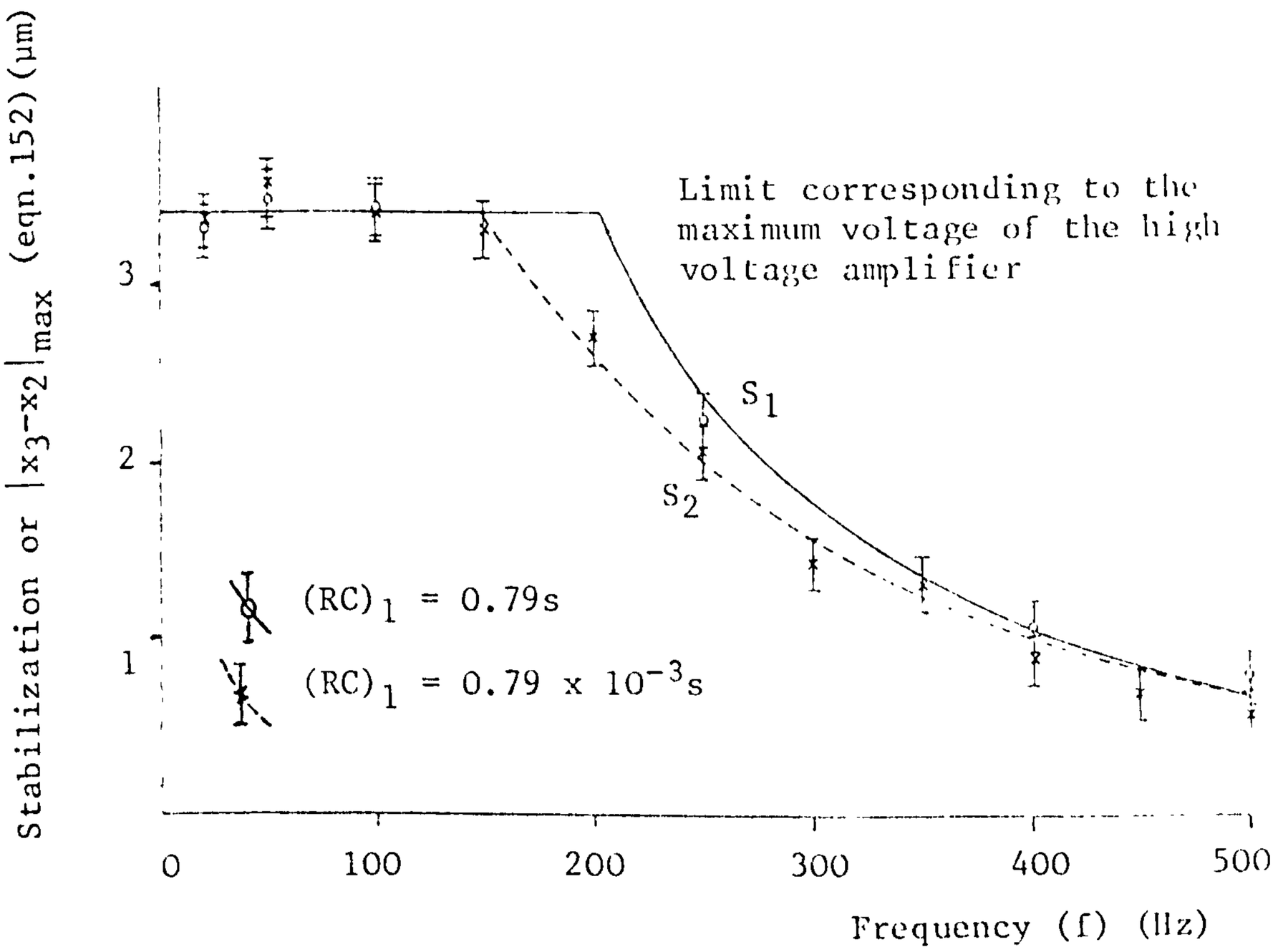

Figure 63: The change in stabilization brought about by a change in $(RC)_1$. The two curves are given by equation (152) and scaled at points S_1 and S_2.

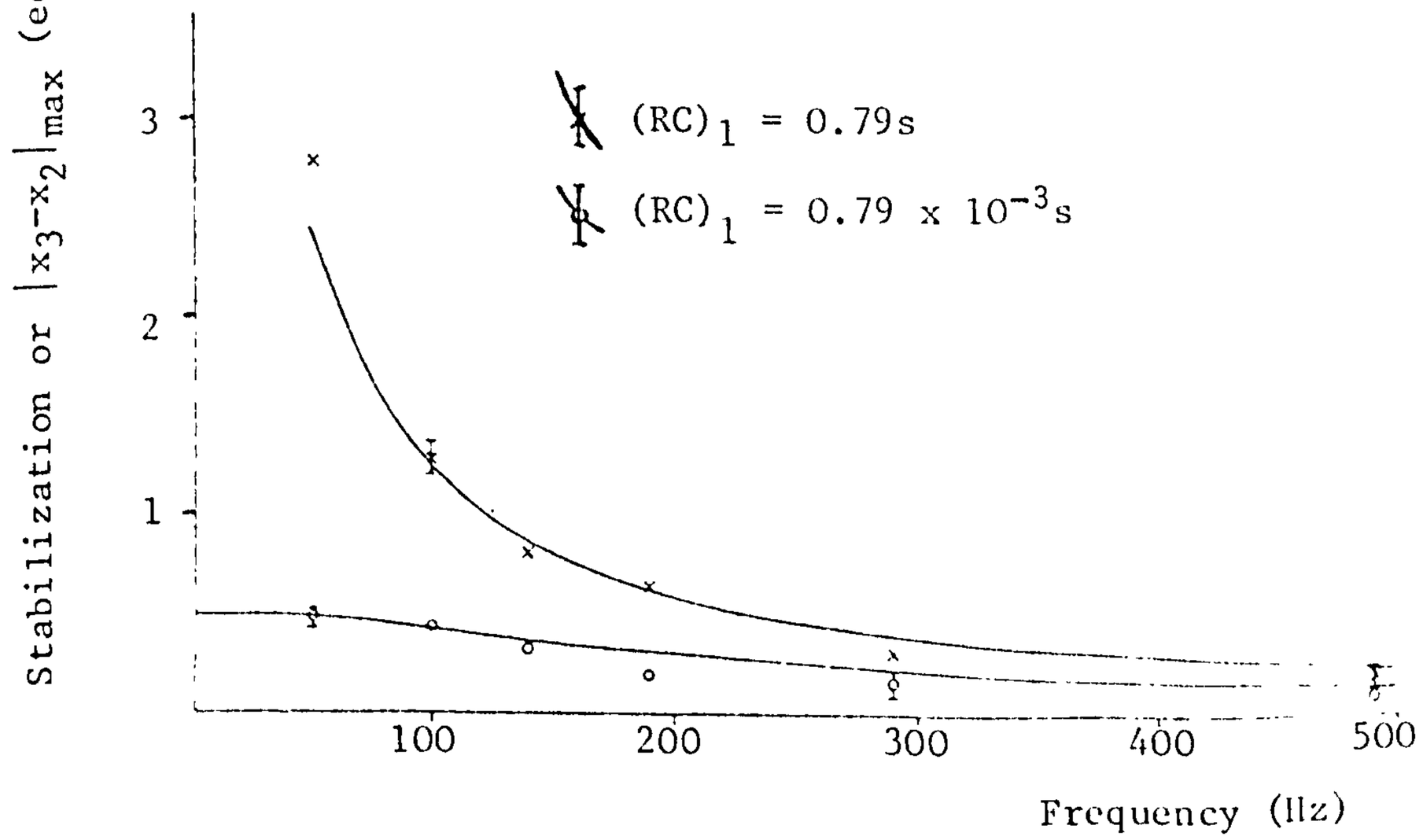

Figure 64: The effect of removing the second filter shown in Figure 62. The curves are derived from equation (142). When the second filter is introduced the response of the feedback loop is further modified by equation (144) giving the results in Figure 63. An error exists in experimentally determining the maximum feedback loop gain which causes no oscillation. This appears as a scaling error.

both filters having a time constant RC = 1. The high voltage amplifier is also a first order filter with a half power point at 4.8kHz. This is a result of driving the capacitative load presented by the piezo-electric element. These three filters together produce a phase lag which is too large to enable successful stabilisation to be achieved. Calculations in the next section suggest the phase lag should be less than 180^{o} at all times and that the best possible stabilisation at 100Hz is 0.04μm. This is below background disturbances at this frequency thus explaining why stabilisation fails.

The final test was to remove the second filter. The removal of this filter required the DC gain to be reduced, thus reducing the effectiveness of the stabilisation. This effect is illustrated by the results shown in Figure 64 for $(RC)_1$ values of $0.79 \times 10^{-3}s^{-1}$ and $0.79s^{-1}$. The reduction in stabilisation is consistent with the reduction in gain necessitated by removal of the filter. The magnitude of the gain for the second filter is

$$\frac{1}{11} \cdot \frac{((11 + \omega^2 X_2{}^2)^2 + (10\omega X_2)^2)^{\frac{1}{2}}}{1 + \omega^2 X_2{}^2} \qquad (110)$$

where $X_i = (RC)_i$.

Under the condition that the high frequency imaginary gain (see next section) is constant the ratio of stabilisation amplitudes at 100Hz is calculated to be 9.7, whilst the measured values taken from Figures 63 and 64 were 7.5 and 10.4. (The two values correspond to a time constant for the first filter of $(RC)_1 = 0.79s^{-1}$ and $(RC)_1 = 0.79 \times 10^{-3}s^{-1}$ respectively.

III.4.1ii)b) Change of crystal length

The experimental arrangement shown in Figure 62 was used with two different free lengths of multimorph crystal, ℓ, as the active stabilising element. The (RC) of the first filter was again changed between $(RC)_1 = 0.79s^{-1}$ and $(RC)_1 = 0.79 \times 10^{-3}s^{-1}$. The two different lengths of crystal used were (3.6 ± 0.2)mm and (6.6 ± 0.2)mm with corresponding resonance frequencies of 13.51 ± 0.02 and 2.94 ± 0.02kHz. The theory of vibrations of thin cantilever beams shows that the resonance frequency is inversely proportional to the square of the length. However, the theory is not entirely valid in this case. This is because the multimorph cantilever has been loaded by attaching a mirror to it. It is also a broad cantilever rather than the thin cantilever considered in the theory.

The results shown in Figure 65 show the stabilisation as a function of frequency. Clearly, the longer crystal will, if $(RC)_1 \approx 1$, stabilise far better at very low frequencies. However, at frequencies above 100Hz where saturation of the high voltage amplifier does not occur the longer crystal will stabilise to only approximately 10% of the value attained by the short crystal. Calculations in the next section verify this change in performance. Equation (152) is given in the next section as:

$$|x_3 - x_2|_{max} = \frac{11\lambda}{10\pi Q} \quad \omega_{cr}X_1 \frac{(1+\omega_{cr}^2 X_3^2)}{(1+\omega^2 X_1^2)^{\frac{1}{2}}} \qquad (111)$$

(this corresponds to the maximum value of the stabilisation $|x_3 - x_2|$ before available voltage and tilt are taken into

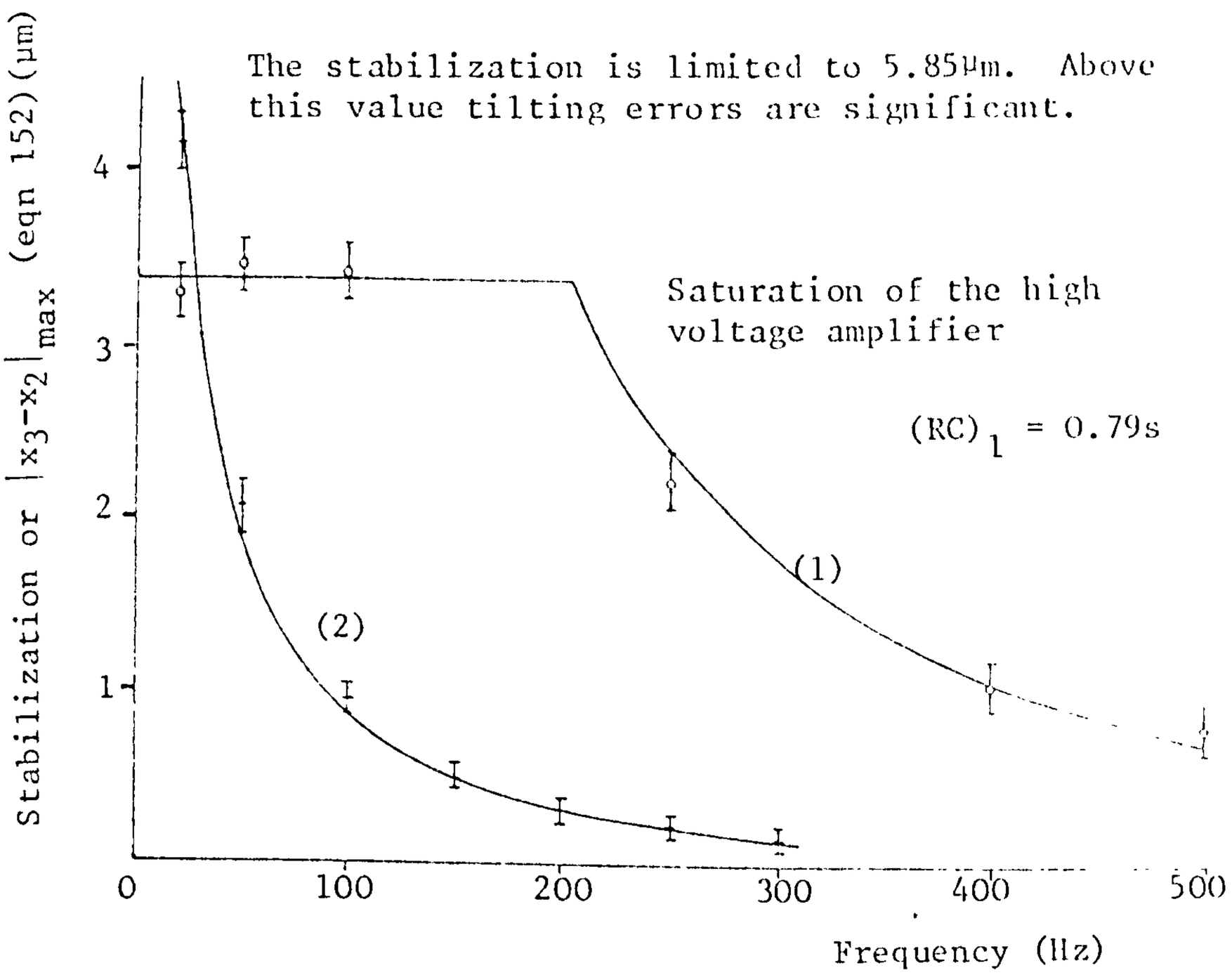

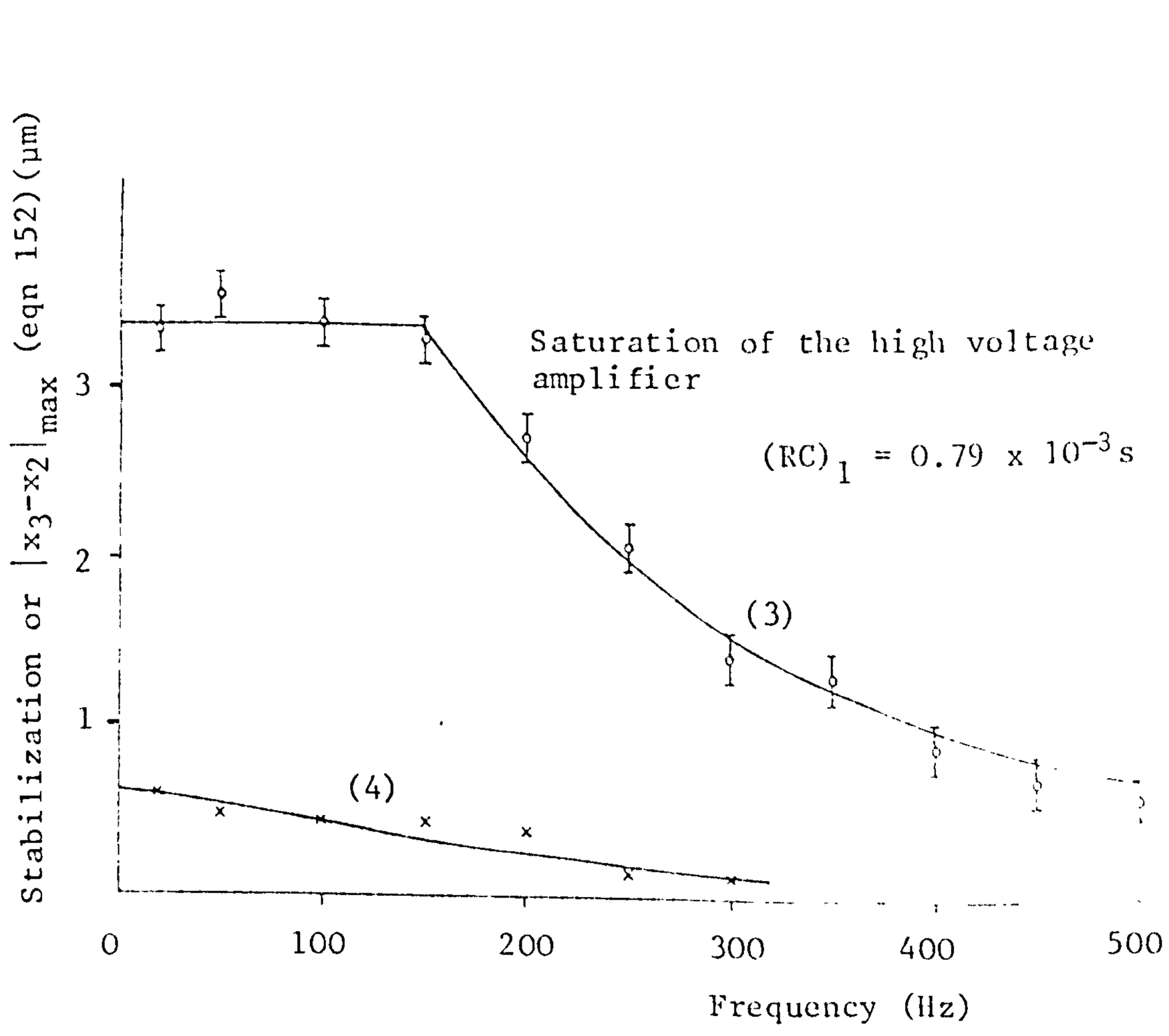

Figure 65: The curves represent the stabilization response for two different lengths of multimorph crystal. Curves (1) and (3) represent the response for a crystal length of 3.6mm and curves (2) and (4) that for a crystal length of 6.6mm. The curves are all given by equation (152).

consideration).

Calculations based on this equation suggest a ratio of stabilisation results for the two crystals, for frequencies where neither the saturation of the high voltage amplifier nor excessive tilting of the mirror occurs, is 7, whereas the measured ratio is 11.

It is shown in the next section that for a given length of crystal there exists a critical frequency (ω_c) of the disturbance against which the system is stabilising. Above this value (ω_c) the stabilisation limit is determined by equation (111). Below this value the maximum stabilisation is governed by one of the following equations. These are all independent of ω.

$$|x_3 - x_2|_{max} = \ell^2 BV_{max}$$
$$|x_3 - x_2|_{max} = \ell^2 \frac{10x6.33x10^{-7}}{(3.6)^2} \quad (\mu m) \qquad (112)$$

and

$$|x_3 - x_2|_{max} = \frac{\ell\theta}{2}max$$
$$|x_3 - x_2|_{max} = \ell\frac{10x6.33x10^{-7}}{(3.6)} \quad (\mu m) \qquad (113)$$

For a crystal shorter than 3.6mm, equation (112) applies as the stabilisation is limited by the voltage available. For crystals longer than 3.6mm, equation (113) applies as the stabilisation is limited by the angle of tilt of the bimorph crystal.

III.4.1iii) Discussion of the stabilisation results

III.4.1iii)a) Choice of filtering

The experimental results support the belief that the

optimum choice of filters is that shown in Figure 62 and when RC for the first filter is equal to approximately 1. Calculations, outlined in the next section, suggest that the optimum choice of filter is for the first filter is

$$\omega(RC)_1 \quad > \quad 1 \qquad (114)$$

where ω is the angular frequency of the disturbance and $(RC)_1$ is the time constant of the first filter. As DC and very low frequency (< 5Hz) were not excessive in the apparatus then $(RC)_1 = 1$ would seem to be the best choice for this particular parameter. However, as can be seen from the results, the maximum stabilisation for low frequencies is limited by the output of the high voltage amplifier (Figure 63) for a multimorph length of 3.6mm). If ω_c is the highest angular frequency at which saturation occurs, then the condition for optimum stabilisation becomes:

$$\omega_c(RC)_1 \quad > \quad 1 \qquad (115)$$

The stabilisation ratio for the two experimental choices of $(RC)_1 = 0.79$ and $0.79 \times 10^{-3}s^{-1}$ is, in the notation of the next section, for no saturation of any amplifier, given by:

$$\frac{|x_3-x_2|_{(RC)_1=0.79}}{|x_3-x_2|_{(RC)_1=0.79\times10^{-3}}} = \frac{(0.79)}{(0.79\times10^{-3})}\left\{\frac{1+(\omega(0.79\times10^{-3}))^2}{1+(\omega(0.79))^2}\right\}^{\frac{1}{2}} \qquad (116)$$

The calculated ratios agree well with the experimental results, thus supporting the theoretical calculations and the conclusion that $(RC)_1 \simeq 1$ is the optimum choice of

filter time constant.

There is one class of unwanted motion of the mirrors that has not so far been considered. This is the response of the system to disturbances large enough to produce a relative motion of the mirrors, whilst the stabilisation is active, in excess of $\lambda/8$. If this situation does arise then the interferometer becomes unstable. It will eventually settle down to another stable state. This may be at any of the positions A, B, C etc (see Figure 12). Experimentally it was found that if $(RC)_1 < 2\pi/\omega$, where ω is the angular frequency of the disturbance, then this final position will be quite close to the original one. However, if $(RC)_1 > 2\pi/\omega$, then the final position may be a significant departure from the original. This choice of $(RC)_1$ agrees with qualitative theoretical considerations. As the stabilisation operates between two bounds, fixed either by mirror tilt or amplifier rail voltages, then any large excursions will severely limit the performance of the stabilisation loop by introducing a bias voltage and tilt. Therefore, if such disturbances are regularly encountered a smaller value of $(RC)_1$ should be chosen to minimise the use of any resetting mechanism.

III.4.1iii)b) Length of crystal and angle of tilt

It appears at first that it is desirable to have the crystal as long as possible to minimise tilt and required voltage. However, the crystal resonance frequency (f_{cr}) when held in a simple cantilever position (see Figure 66) decreases as its length is increased. Stabilisation cannot

Output from the high voltage amplifier shown in Figure 62

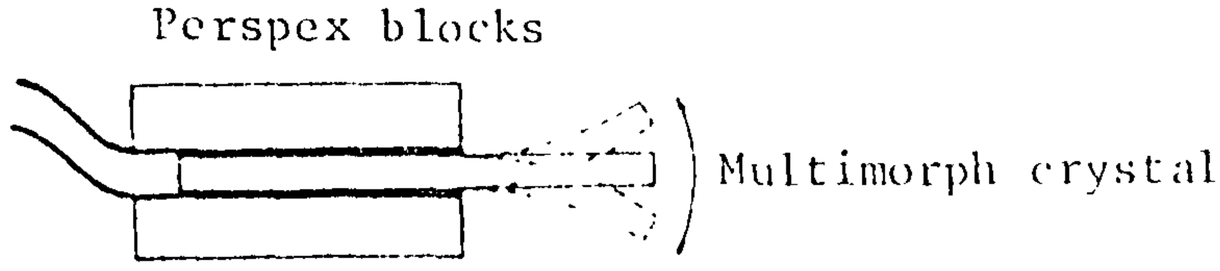

Figure 66: The multimorph crystal held in a simple cantilever position.

$$\theta = \frac{\ell}{R} = B\ell V$$

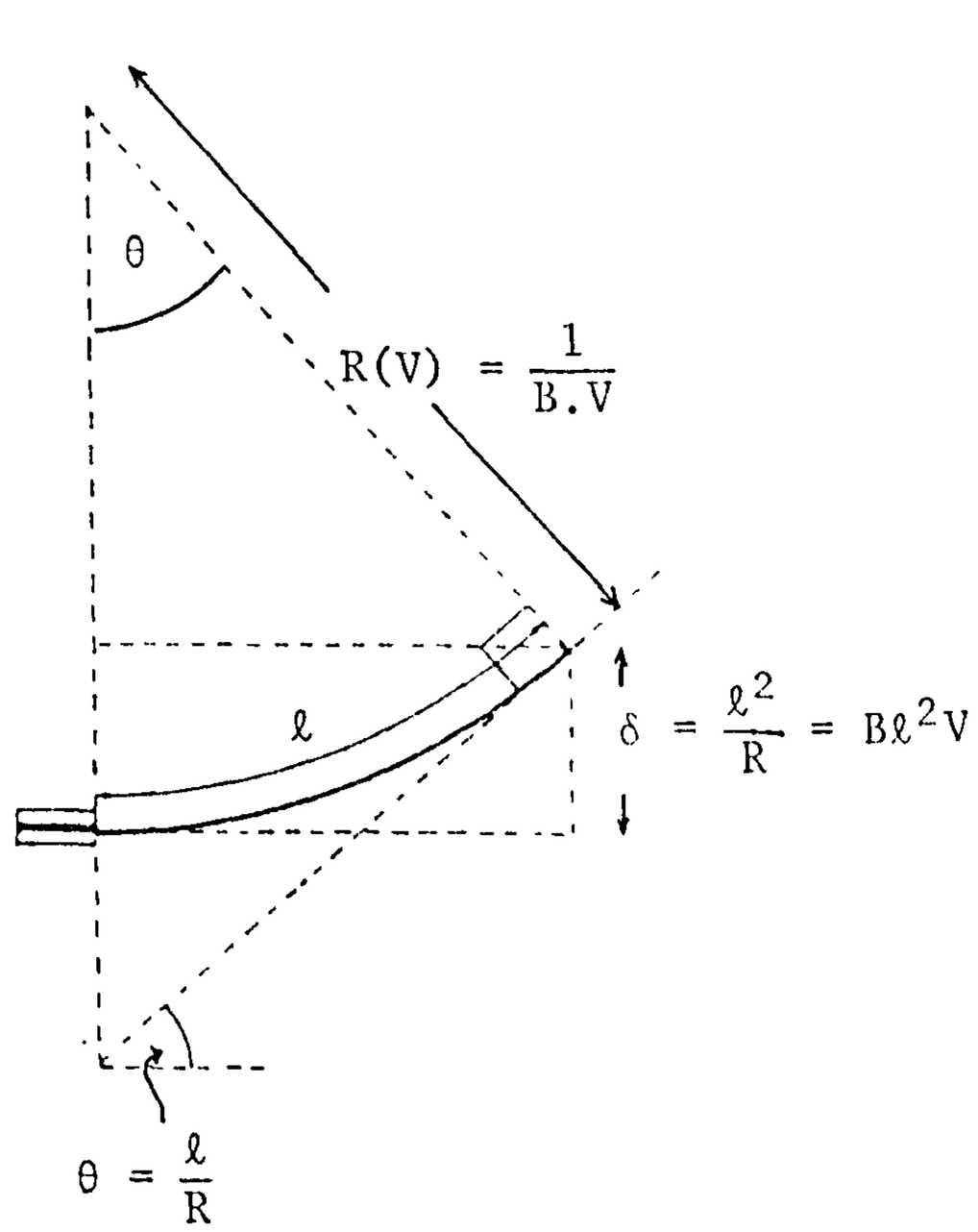

Figure 67: Exaggerated diagram of the form of the deformation of the multimorph element of length ℓ caused by the application of voltage V. The crystal flexes to form an arc of a circle as shown.

be properly achieved if this resonance frequency lies in the range of frequencies at which disturbances occur. Furthermore, to remove the possibility of the feedback system oscillating f_{cr} must be sufficiently above the frequency range of stabilisation to allow a filter to be used to suppress the oscillation.

A voltage applied to the crystal results in the cantilever deforming in the pure bending mode. The crystal then forms part of an arc of a circle with radius inversely proportional to the voltage, Figure 67. The 3.6mm crystal when subjected to the maximum voltage available in the system, produces a tilt which reduces the amplitude of the light intensity pattern by 7½%, when the camera lens is used for focussing, as shown in Figure 68. (This figure matches the theoretical predictions of Figure 52). When the camera lens is replaced by the simple lens, this percentage change becomes unacceptable and is the reason why the camera lens is preferred over the simple lens. The actual error at any one time may be found by monitoring the voltage applied to the crystal which dictates the displacement and tilt. The corresponding result for the 6.6mm crystal produces an error at maximum voltage which is of the order of 95% and quite unacceptable. Therefore, for crystals larger than 3.6mm maximum movement is given by the tilt introduced and is not limited by the available output of the high voltage amplifier.

The tip of a long crystal will clearly move a long way

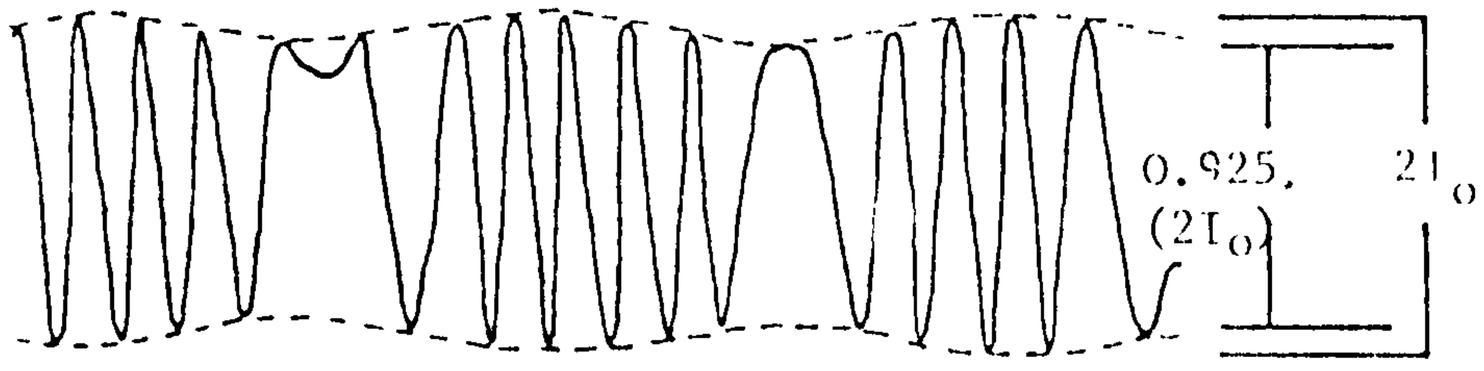

Figure 68: Schematic diagram of the intensity from the unstabilized interferometer caused by vibrating the multimorph crystal in the reference arm over the maximum voltage available from the high voltage amplifier. The crystal length is 3.6mm. The shape of the envelope of the pattern modulation above matches well the theoretical prediction given in Figure 52.

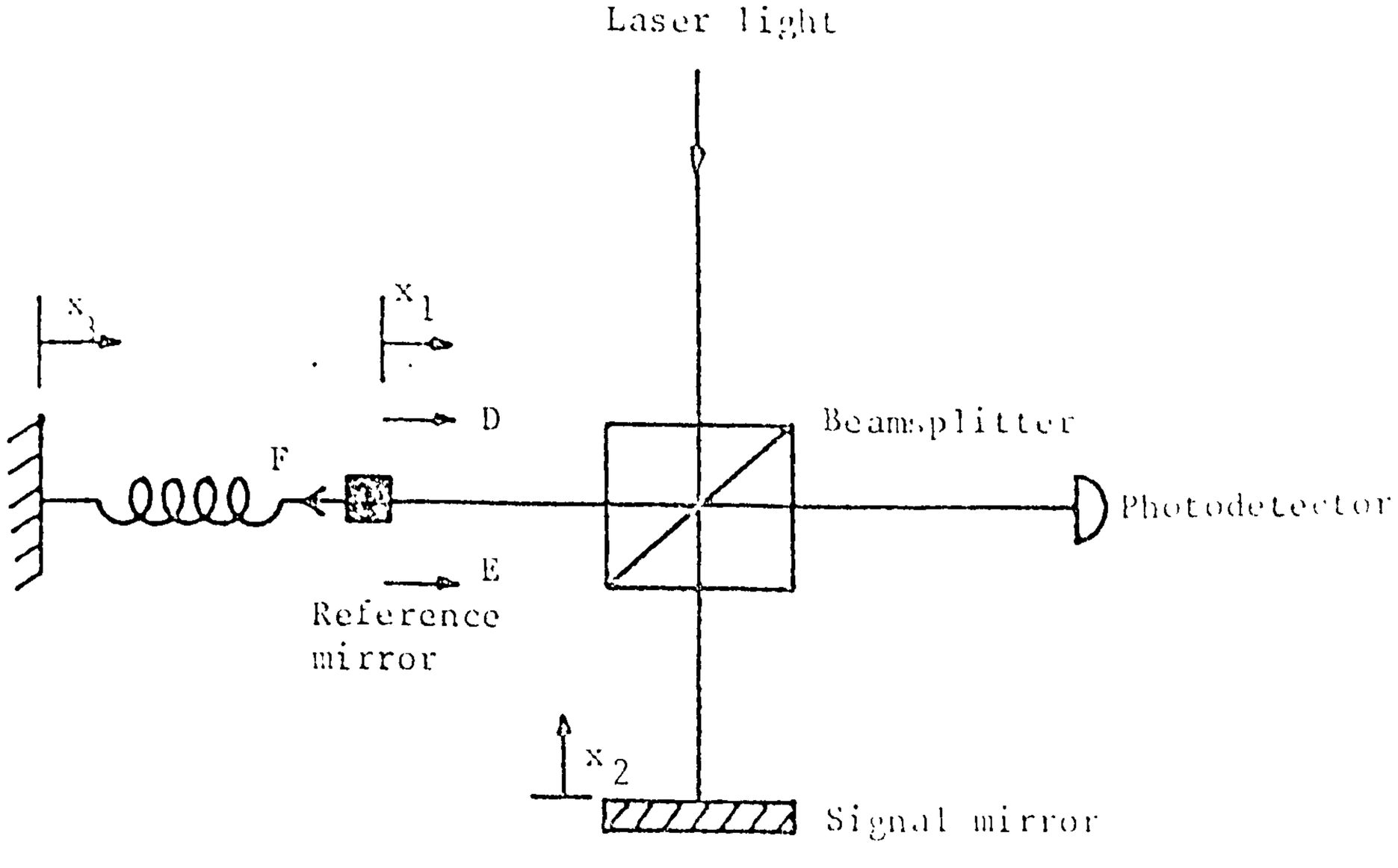

$$F = k^2(x_3 - x_1)$$
$$\text{Damping force} = D = -\gamma \dot{x}_1$$
$$\text{Electrical force} = E = \beta V/\ell$$

Figure 69: The forces acting on the multimorph crystal, here represented as a simple harmonic oscillator of spring constant k^2 and mass m.

for quite a modest voltage. However, the low value of (the crystal resonance frequency) f_{cr} will require a lower system gain and in order to keep the frequency response the same then the DC gain must be reduced. The two effects do not cancel and as the calculations referred to earlier show, the better choice of crystal is in general the 3.6mm one.

III.4.2 Theoretical treatment of the stabilisation problem

The stabilising system works by means of a negative feedback loop. Any negative feedback loop may become unstable if the gain of the loop, when the phase lag is 180^{o}, is too large. All amplifiers introduce a phase lag at high frequencies and so the problem of instability must be carefully considered. In addition to this problem, introduced by the amplifier roll-off, the piezoelectric bimorph itself is capable of oscillation and has a natural resonance frequency. The aim of this section is to study the problem of loop stability.

The stabilising element may be considered as a simple harmonic oscillator. There are three forces acting upon it as shown in Figure 69. These are:

a) electrical force[57]

$$F = \beta V/\ell \qquad (117)$$

where F is the force, V is the applied voltage, ℓ the length of the piezoelectric bimorph and β a constant for the type

of multimorph element used.

The voltage V is derived initially from the light intensity information via the photodetector and is then modified by the response of the filters and amplifiers in the feedback loop. Therefore the voltage is

$$V = K(\omega)\sin\,(4\pi(x_2 - x_1)/\lambda) \qquad (118)$$

where $K(\omega)$ is the response of the photodetector, amplifiers and filters in the feedback loop and x_1, x_2 are the positions of the mirrors.

The region in which these calculations are of interest is the region in which $(x_2 - x_1)$ is much less than $\lambda/8$ where the stabilisation is working and hence

$$V = K(\omega)\,\frac{4\pi}{\lambda}\,(x_2 - x_1) \qquad (119)$$

$$\text{therefore} \quad F = \frac{\beta}{\ell\lambda}\,K(\omega)\;\;4\pi\;\;(x_2 - x_1) \qquad (120)$$

b) movement of the support of the multimorph

A simple harmonic oscillator may be described by its resonance frequency, ω_{cr}, its force constant k^2 and a Q-value, Q. From these we may define an effective mass of the multimorph element, m.

The displacement of the holder of the multimorph crystal is given as, x_3, hence the force acting on the mirror is:

$$F = k^2\,(x_3 - x_1) \qquad (121)$$

where k^2 is the force constant of the simple harmonic oscillator as described above.

c. damping force

If no damping is introduced then any transient introduced into the system will cause the crystal to oscillate continuously. The damping is assumed to be proportional to velocity. This then maintains the system as linear. The damping force is taken as

$$F = -\gamma \dot{x}_1 \qquad (122)$$

Once the forces have been derived then the equation of motion as given by Newton's second law of motion is

$$m\ddot{x}_1 + \gamma \dot{x}_1 + x_1 \left(\frac{4\pi\beta}{\ell\lambda} .K(\omega) + k^2\right) = x_3 k^2 + \frac{4\pi\beta}{\ell\lambda} K(\omega) x_2 \qquad (123)$$

The particular integral solution of this, for low frequencies of x_3 and x_2 ($\omega <$ the resonant frequency of the system) wich are taken as sinusoidal functions of frequency ω, is given by

$$(x_1 - x_2) = \frac{k^2 \lambda \ell}{4\pi\beta K(\omega)} (x_3 - x_2) \qquad (124)$$

In addition to the assumptions above, the following assumptions are necessary to derive equation (124):

$$|4\pi\beta K(\omega)| >> |k^2|$$

$$|4\pi\beta K(\omega)| >> |\gamma\omega|$$

All light information is governed by $x_1 - x_2$ which becomes the important variable. Let this variable be x. Now x must lie within the bounds defined by equation (108).

Using equation (124) we may write:

$$|(x_3 - x_2)_{max}| = \left|\frac{4\pi\beta K(\omega)}{k^2\lambda\ell} (x)_{max}\right| \qquad (125)$$

Assuming in the region defined by equation (108) that sin x ≈ x then x_{max} is given by

$$|x_{max}| = \frac{\lambda}{20\pi} \qquad (126)$$

This allows equation (125) to be rewritten as

$$|(x_3 - x_2)_{max}| = \left|\frac{\beta K(\omega)}{5k^2\ell}\right| \qquad (127)$$

Equation (127) then defines an upper limit to the possible stabilisation. Two further limits exist in the instrument as previously mentioned. These other limits are firstly the maximum voltage available from the high voltage amplifier and the maximum angle of tilt. From Figure 67it can be seen that the angle of tilt θ is given by

$$\theta = \frac{2}{\ell} (x_3 - x_2) \qquad (128)$$

This assumes that the loop gain is large. These conditions are met within the range of stabilisation.

Experimentally it has been found that when the stabilisation $(x_3 - x_2)$ is equal to 10λ for a crystal length of 3.6mm the angle of tilt θ is a maximum which corresponds to a fall in I_o of 7½%. These figures agree with theoretical calculations performed on the intensity pattern taking into account the angle of mirror tilt and focussing error (the latter being dominated by spherical

aberration in the interferometer lenses).

Therefore the following may be written

$$\theta_{max} = \frac{2}{3.6} \times \left(\frac{10}{2}\right) \times 6.33 \times 10^{-6} \text{ (radians)} \qquad (129)$$

where $\lambda = 6.33 \times 10^{-6}$ mm

The angle of tilt condition may, therefore, be written as

$$\frac{2}{\ell} (x_3 - x_2) \leq \theta_{max} \qquad (130)$$

The final condition any solution must satisfy is that the voltage required to move the crystal be less than the saturation voltage of the high voltage amplifier. The displacement caused by a voltage V applied to the crystal is given by

$$(x_3 - x_2) = B\ell^2 V \qquad (131)$$

where B is a constant for the type of multimorph used.

Again the limit on the voltage in terms of a crystal length ℓ has been found experimentally. The result, shown earlier, is that for a multimorph crystal length of 3.6mm then $(x_3 - x_2)$ is 10λ when the applied voltage is the maximum possible. Therefore if V_{max} is this voltage

$$V_{max} = \frac{10\lambda}{B(3.6)^2.2} \qquad (132)$$

This final condition may therefore be written as

$$(x_3 - x_2) \leq B\ell^2 V_{max} \quad (\ell \text{ in mm's}) \qquad (133)$$

or $$(x_3 - x_2) \leq \frac{\ell^2.10\lambda}{(3.6)^2.2}$$

Returning now to the solution of equation (123). Solutions of equation (123) contain a transient or complementary function part. This is given by

$$x_1 = a \exp(\alpha_1 t) + b \exp(\alpha_2 t) \quad (134)$$

or $$x_1 = a \exp(j\omega_{or} - \Gamma + \omega_{oi})t + b \exp(-j\omega_{or} - \Gamma - \omega_{oi})t \quad (135)$$

where α_1, α_2 are roots of the equation

$$m^2 + \gamma\alpha + \frac{4\pi\beta}{\ell\lambda} K(\omega_{or}) + k^2 = 0 \quad (136)$$

with ω_{or} and ω_{oi} the real and imaginary parts of the system oscillation frequency, and

$$K(\omega_{or}) = K_r(\omega_{or}) + jK_i(\omega_{or}) \quad (137)$$

and $$\Gamma = \gamma/2m \quad (138)$$

or $$\Gamma = Q \quad (139)$$

Q is a Q-value of the simple harmonic oscillator.

ω_{or} and ω_{oi} are then:

$$\omega_{or} = \frac{1}{2m}\left(4k^2m + \frac{16\pi\beta}{\ell\lambda} K_r(\omega_{or})m - \gamma^2\right)^2 + \left(16\pi K_i(\omega_{or})\frac{\beta}{\ell\lambda}m\right)^2\Big)^{1/4}$$
$$\cdot\cos\left\{\tfrac{1}{2}\tan^{-1}\left\{\frac{16\pi\beta K_i(\omega_{or})m/\ell}{4k^2m + \frac{16\pi\beta}{\ell\lambda} K_r(\omega_{or})m - \lambda^2}\right\}\right\} \quad (140)$$

$$\text{and } \omega_{oi} = \frac{1}{2m}\left(\left(4k^2m + \frac{16\pi\beta}{\ell\lambda} K_r(\omega_{or})m - \gamma^2\right)^2 + \left(16\pi K_i(\omega_{or})\frac{\beta}{\ell\lambda}m\right)^2\right)^{1/4}$$
$$\cdot\sin\left\{\tfrac{1}{2}\tan^{-1}\left\{\frac{16\pi\beta K_i(\omega_{or})m/\ell\lambda}{4k^2m + \frac{16\pi\beta}{\ell\lambda} K_r(\omega_{or})m - \gamma^2}\right\}\right. \quad (141)$$

The solutions above depend on the multimorph crystal parameters k^2, m, ℓ, Q and on the filtering as determined by K_r and K_i. In order to obtain useful results filter

characteristics must be approximated thus allowing ω_{or} to be determined from the transcendental equation (140). Knowing the value of ω_{or} allows the value of ω_{oi} to be calculated from equation (141). This value then determines whether equation (135) is stable or not.

The solutions of these equations are now considered. The filter responses required are those of the filters shown in Figure 62.

First filter:

$$K(\omega) = \frac{1}{1 - jX_1\omega} \qquad (142)$$

$$X_1 = (RC)_1 \qquad (143)$$

Second filter:

$$K_2(\omega) = \frac{1}{11} \frac{11 + \omega^2 X_2{}^2 - j10X_2\omega}{1 + X_2{}^2\omega^2} \qquad (144)$$

$$X_2 = (RC)_2 \qquad (145)$$

High voltage amplifier:

$$K_3(\omega) = \frac{K_O}{1 - jX_3\omega} \qquad (146)$$

$$X_3 = (RC)_3 \qquad (147)$$

The frequency response of all other amplifiers is assumed to be flat. The overall system gain has been incorporated in equation (146). The condition for a stable solution for equation (135) is

$$\omega_{oi} < \Gamma \qquad (148)$$

Knowing these responses allows us to calculate the entire responses of the filter set shown in Figure 62.

Therefore a set of solutions may be obtained corresponding to various filtering combinations. These are now derived.

a. Solution 1

First and second filter and high voltage amplifier in series (cf. Figure 62). The graphical solution of equation (140), (141) and (142) is indicated in Figure 70. The analytical solution may be approximated by assuming

$$\frac{4\pi\beta}{\ell\lambda} K_i (\omega_{or})m << k^2 m \qquad (149)$$

and

$$\frac{4\pi\ell\lambda}{\ell\lambda} K_r (\omega_{or})m << k^2 m \qquad (150)$$

Equations (148) and (140) then reduce to:

$$1 > \frac{Q.K_j(\omega_{cr}).\beta^2\pi}{k^2\ell\lambda} \qquad (151)$$

where ω is the free resonance frequency of the crystal. Using the filter responses and equations (125) and (151) leaves:

$$|x_3 - x_2|_{max} < \frac{11.\lambda}{10\ Q} \frac{\omega_{cr}X_1(1+(\omega_{cr}^2X_3^2))}{(1+\omega^2X_1^2)} \qquad (152)$$

providing that

$$X_1 >> x_2,\ \omega_{cr}X_2 >> 1,\ \omega X_2 << 1,\ \omega_{cr}X_1 >> 1$$

where ω is the frequency of the disturbing vibration. A more accurate solution may be obtained by not making the approximations on the filter responses. In this equation (152) $|x_3 - x_2|_{max}$ is the maximum disturbance against which the feedback loop will stabilise. It is clearly

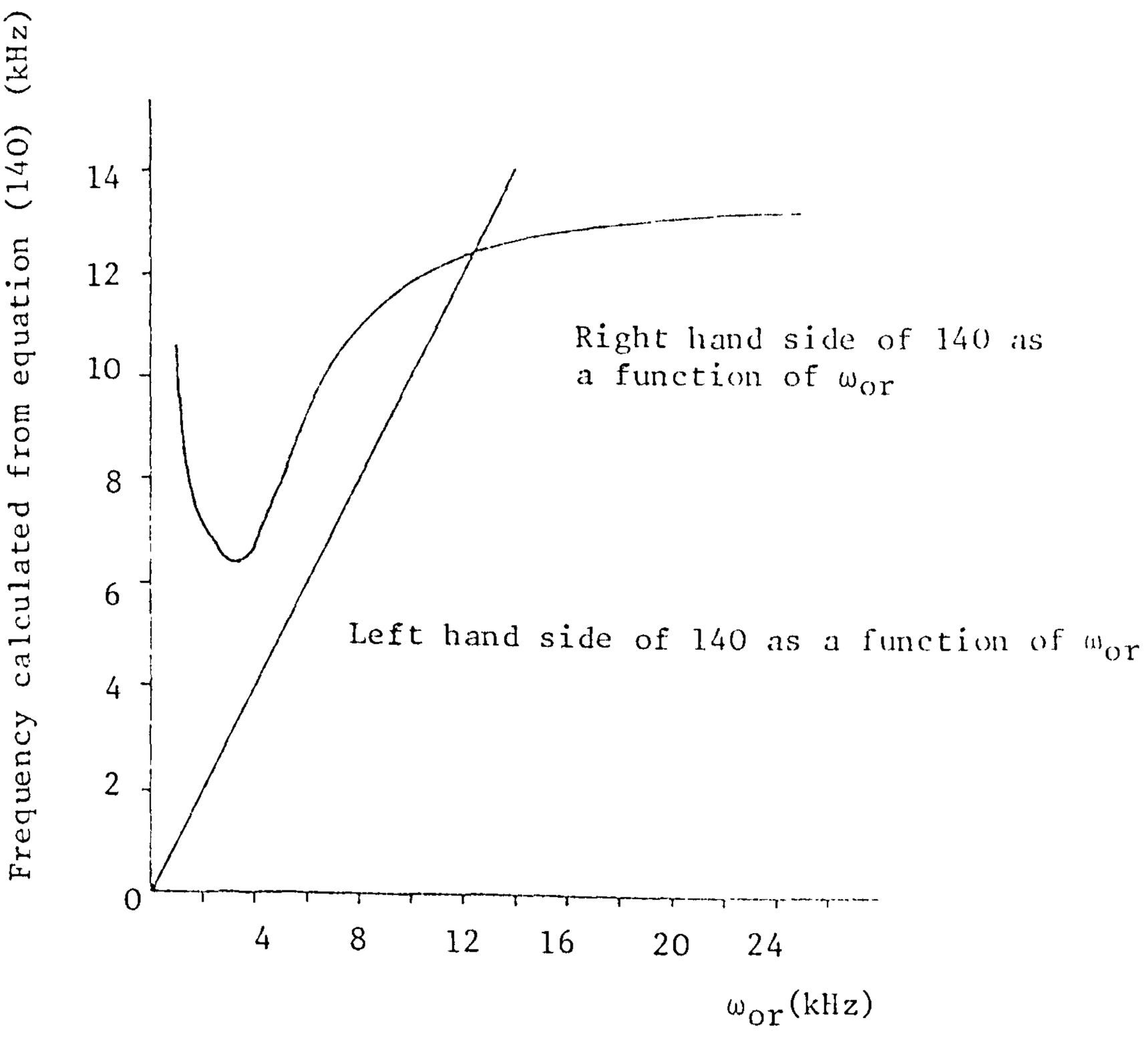

Figure 70: The numerical solution of 140 as a function of the parameter ω_{or}. The solution clearly lies at high values of ω_{or}.

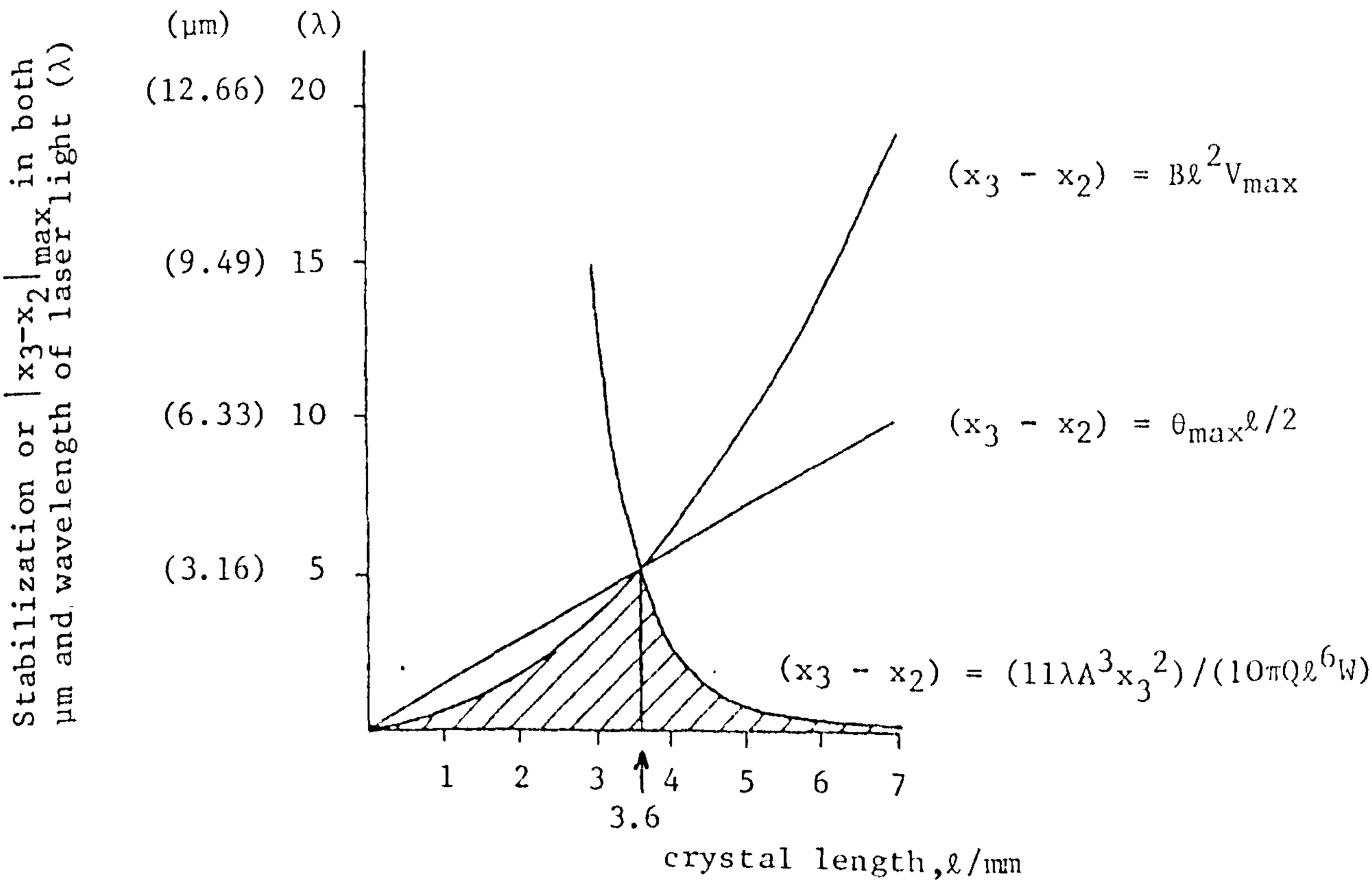

Figure 71: Graphical representation of the limits on the stabilization for a frequency $\omega = 2\pi.200$ (radians s^{-1}) as a function of the multimorph crystal length (ℓ).

affected by the filtering parameters and the crystal parameters (in the latter case via ω_{cr}).

It should be recalled that the criteria used to derive equation (152) are merely that no oscillation should occur in the feedback loop and that the light intensity should remain in a band as defined in equation (108). From equation (152) the optimum parameter values may be obtained and these are

$$\omega X_1 >> 1 \qquad (153)$$

$$\omega_{cr} \to \infty \qquad (154)$$

It is not possible to let $X_3 \to \infty$ as the approximations to equations (140) and (141) then break down. It can be shown that if X_3 and X_1 tend to infinity then the stabilisation is not as efficient as the system considered above. To obtain this result numerical solutions to (140) and (141) are required.

Equation (154) must, therefore, now be considered in view of equation (130) and (131). The resonance frequency of a beam held in a cantilever position is inversely proportional to the square of its length. Therefore

$$\omega_{cr} = A/\ell^2 \qquad (155)$$

Condition (154) for the maximum solution of equation (152) now becomes

$$\left.\begin{array}{rcl} \frac{A}{\ell^2} & \to & \infty \\ \text{or} \qquad \ell & \to & 0 \end{array}\right\} \qquad (156)$$

Writing equation (152) in terms of the crystal length ℓ for $(\omega_{cr}X_3)^2 >> 1$ then

$$|x_3 - x_2|_{max} < \frac{11.\lambda}{10\pi Q} \cdot \frac{\Lambda^3}{\ell^6\omega} \cdot X_3^2 \qquad (157)$$

Experimentally it has been found that for $\omega = 2\pi.200$ and a crystal length of 3.6mm then $|x_3 - x_2|_{max} = 5\lambda$. The three conditions of (130), (133), (157) may be represented graphically in Figure 71.

The region in which $|x_3 - x_2|_{max}$ may exist is shaded. The optimum value is, therefore, 5λ at ℓ = 3.6mm.

Consider now decreasing the frequency (ω) of the disturbance as shown in Figure 72. In this case, the stabilisation is improved by use of a longer crystal. The limit is now governed by the maximum angle of tilt. The optimum choice of crystal length is then ℓ_{opt} where

$$\theta \frac{max}{2} \qquad \ell_{opt} = \frac{11.\lambda}{10\pi Q} \cdot \frac{A}{\ell^2_{opt}\omega} \cdot \left(1 + \left(\frac{X_3 A}{\ell^2_{opt}}\right)^2\right) \qquad (158)$$

As ℓ increases then ω_{cr} will decrease and the approximation $(\omega_{cr}X_3)^2 > 1$ is no longer valid).

If the frequency of the disturbance is increased the plot becomes that of Figure 73.

The optimum crystal length is now decreased. The limit is now given by

$$B\ell^2_{opt}V_{max} = \frac{11\lambda\Lambda^3 X_3^2}{10\pi Q\ell_{opt}{}^6\omega} \qquad (159)$$

It should be pointed out that once a crystal length has been chosen then there exists a lower frequency (ω_c)

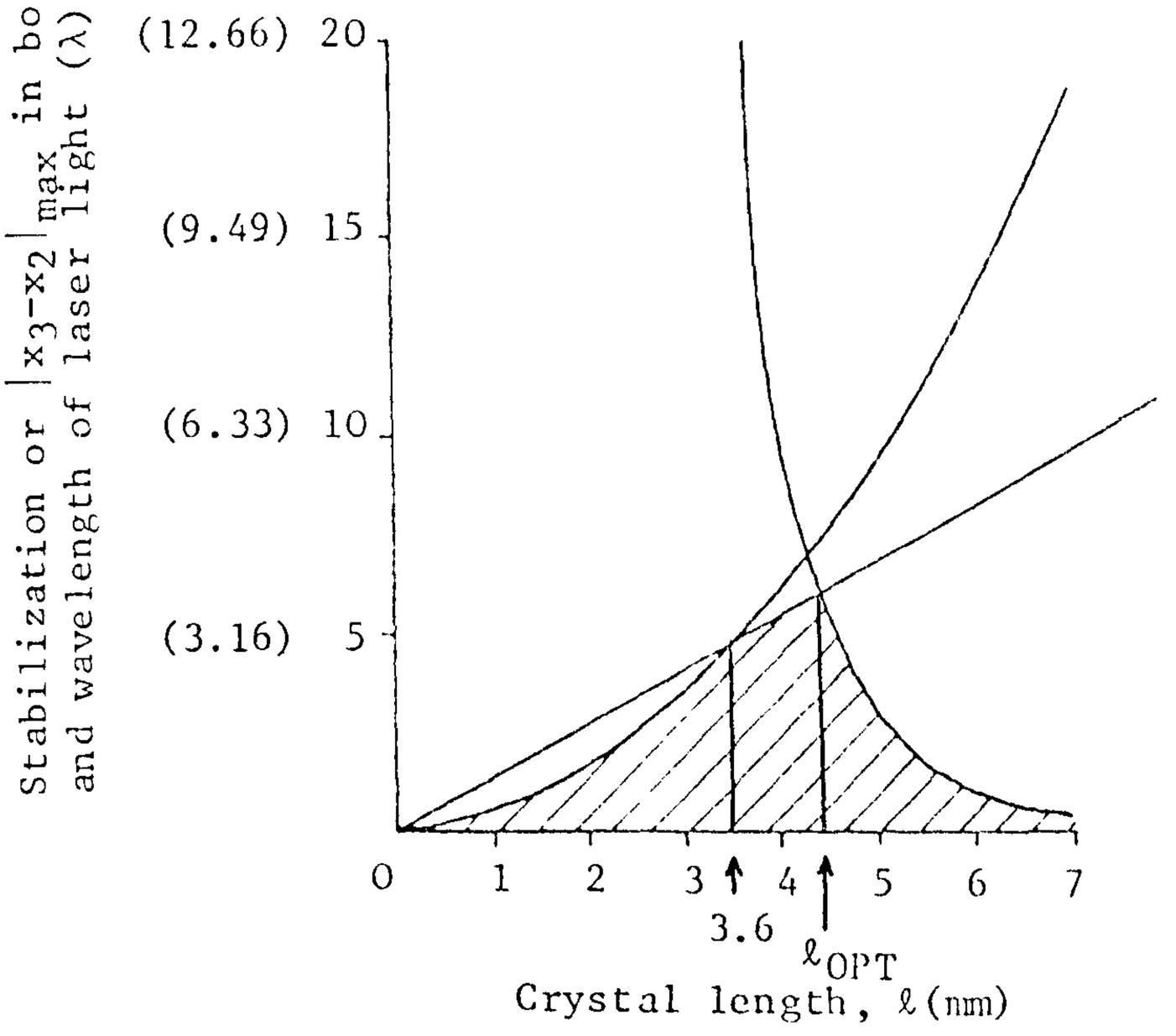

Figure 72: Graphical representation of the limits on the stabilization for $\omega < 2\pi.200$ (radians s^{-1}) as a function of the multimorph crystal length (ℓ).

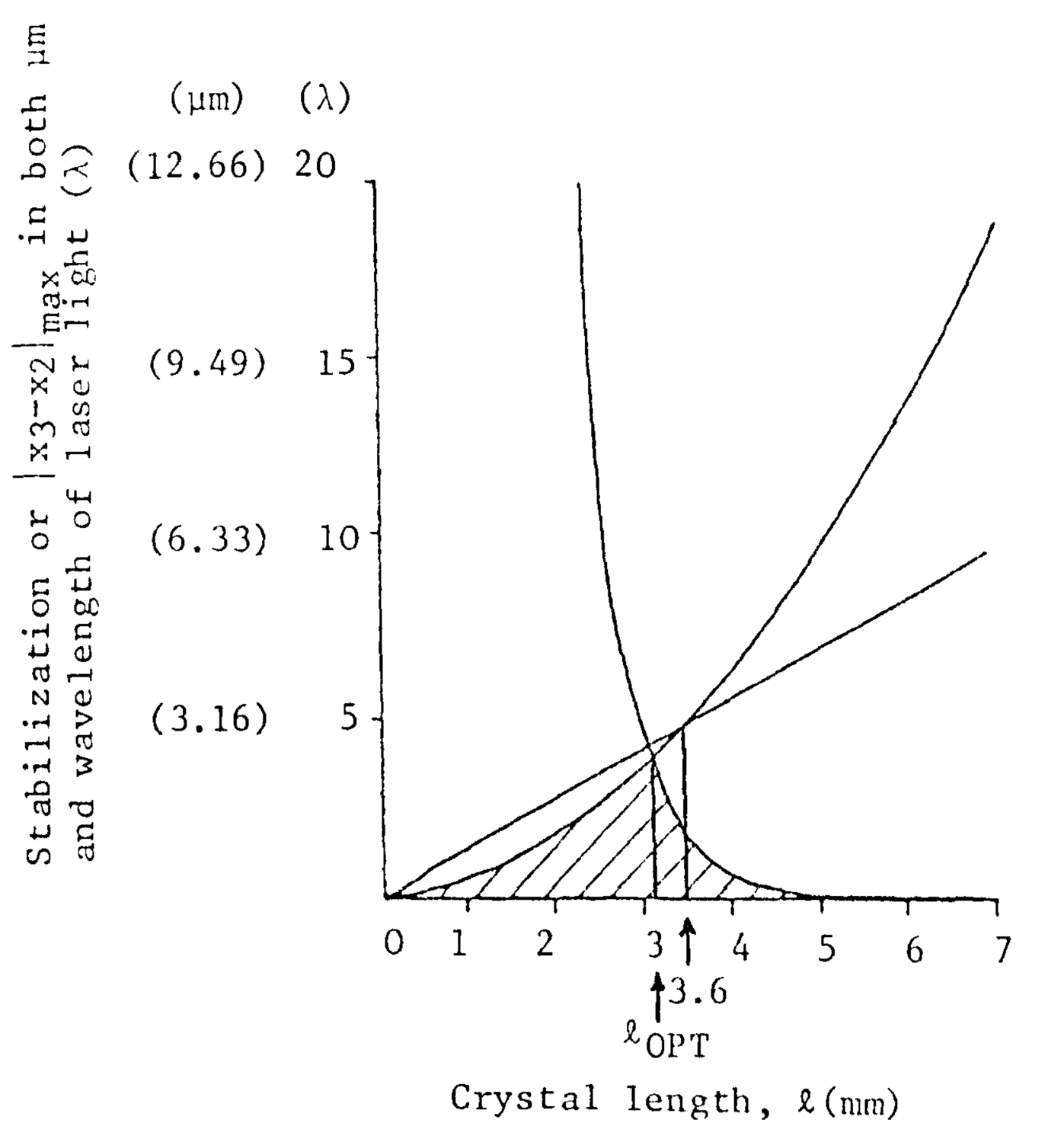

Figure 73: Graphical representation of the limits on the stabilization for a frequency $\omega > 2\pi.200$ (radians s^{-1}) as a function of the multimorph crystal length (ℓ).

below which stabilization is fixed by either the angle of tilt (if $\ell > 3.6$mm) or by the maximum voltage available (if $\ell < 3.6$mm). For example for the 3.6mm crystal the $\omega_c = 2\pi.100$, whereas for the 6.6mm crystal then equation (158) may be used to determine (ω_c) where

$$\left.\begin{aligned} \omega_c &= \frac{22\lambda.}{10\pi Q} \quad \frac{\Lambda}{\theta_{max}\ell^3} \cdot \left(1 + \left(\frac{X_3\Lambda}{\ell^2}\right)^2\right) \\ \omega_c &= \frac{22\lambda.}{10\pi Q} \cdot \frac{(\omega_{cr})^{3/2}}{\theta_{max}\Lambda^{\frac{1}{2}}} \cdot (1 + (X_3\omega_{cr})^2) \end{aligned}\right\} \quad (160)$$

The existence of a critical frequency may be described in an alternative way. As the stabilization $(x_3 - x_2)$ depends on the frequency ω then a critical frequency (ω_c) may be described by a maximum value of $(x_3 - x_2)$. In other words for a given length of crystal the stabilization $(x_3 - x_2)$ is described by equation (152) up to some critical value of $(x_3 - x_2)$. At this point $(x_3 - x_2)$ is then limited to a constant value for a given ℓ from either equation (130) if $\ell > 3.6$mm or equation (133) if $\ell < 3.6$mm. The critical value is found by solving equation (152) with the value of ℓ obtained from either equation (158) or (159). It is interesting to consider what happens as different lengths of crystal are chosen. The problem may be illustrated for crystal lengths less than 3.6mm by the use of equations (159), (133) and (152).

Combining these a relation between ω_c and the maximum value of $(x_3 - x_2)_{max}$ may be obtained. This relation is

$$\text{Maximum } |x_3 - x_2|_{max} = \left(\frac{11\lambda A^3 X_3^2 B^3 V_{max}^3}{10\pi Q}\right) \quad \frac{1}{\omega_c^{1/4}}$$

This defines the value of frequency (or value of $|x_3 - x_2|_{max}$) at which equation (133) replaces (152) or

vice versa. The following family of curves may be drawn for different lengths of crystal (Figure 74).

Having dealt with the solution to the filter choice of Figure 62 the solution to two other filter combinations will now be briefly treated.

The first new combination is given by two filters of the first type in Figure 62 in series with the high voltage amplifier.

The graphical solution for ω_{or} is shown in Figure 75. Using the numbers obtained the solutions become:

a) For $(RC)_1 = 1$; $|x_3 - x_2| < \frac{5.2 \times 10^4}{(1 + (\omega.1)^2)}$ (162)

$\therefore$ for $\omega = 2\pi.100$ (163)

then $|x_3 - x_2| < 0.04\mu m$ (164)

The value of $|x_3 - x_2|$ is much less than the background disturbances indicating why no experimental stabilization could be achieved with this arrangement.

b) For $(RC)_1 = 10^{-3}$; $|x_3 - x_2| < \frac{54}{(1+(\omega.10^{-3})^2)}$ (165)

at $\omega = 2\pi.100$ then $|x_3 - x_2| < 0.82\mu m$ (166)

which is not as useful a response as obtained for the experimental set-up shown in Figure 62. The limits defined by (130) and (133) are not important in this case because of the poor response.

The final filtering combination is the first filter in series with high voltage amplifier.

The high frequency gain is increased by a factor of 11

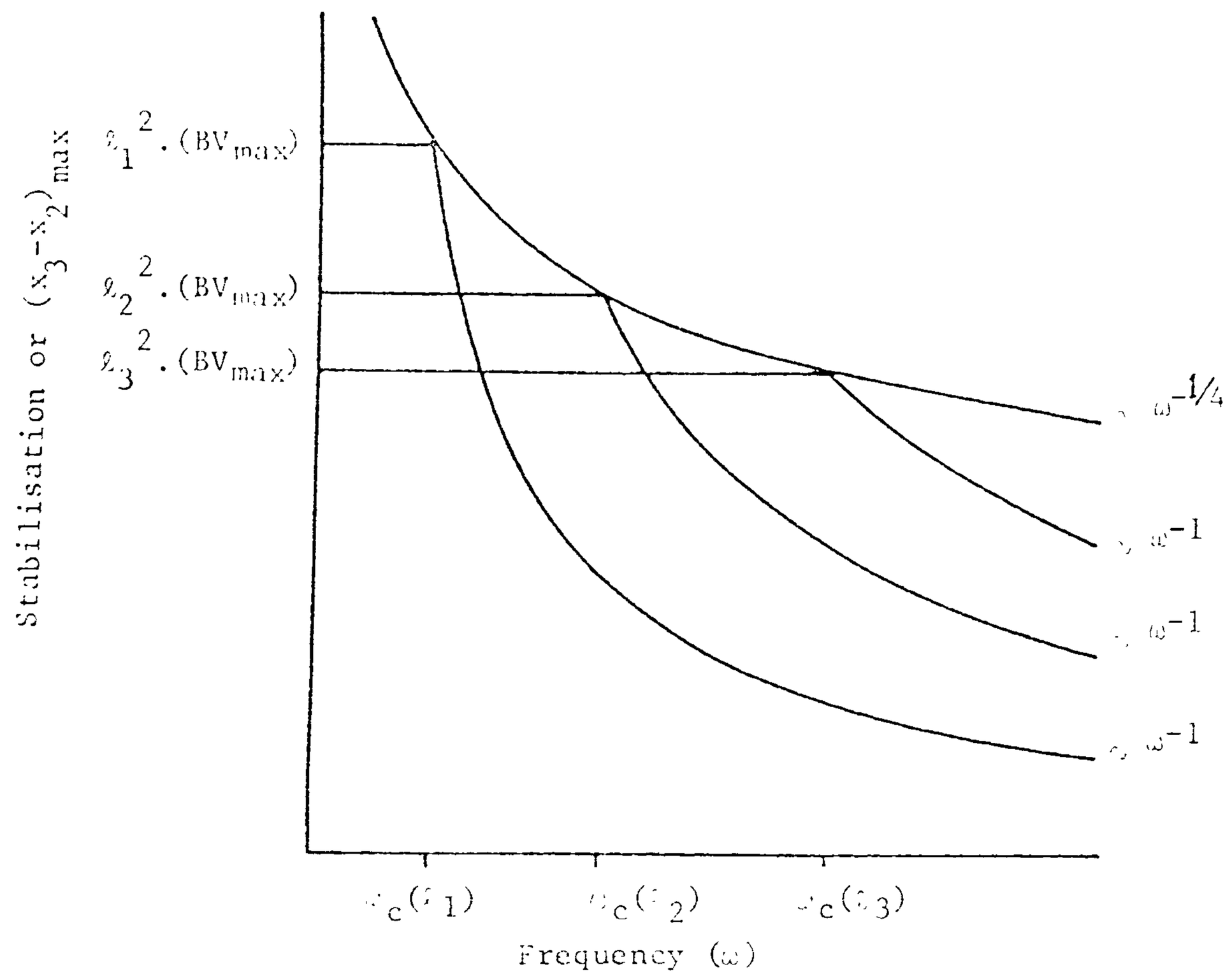

Figure 74 : Stabilisation versus the frequency of disturbance for various lengths of multimorph crystal (= 3.6mm)

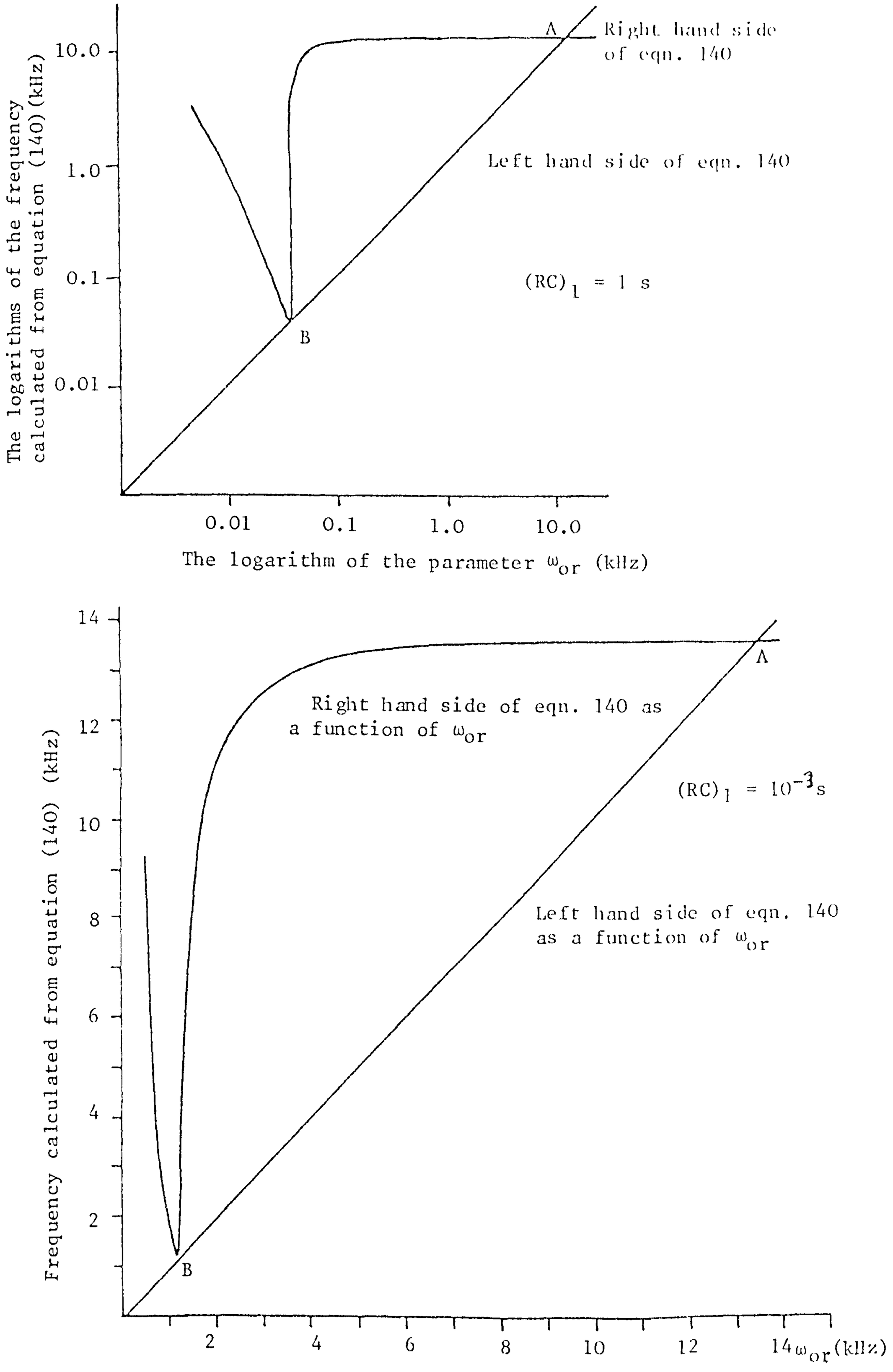

Figure 75: The numerical solution of equation 140 for two filters of the first type in series with the high voltage amplifier. The optimum value of the force gain and hence stabilization is found to occur when the solution lies at A and not B. These optimum values of gain are used to evaluate eqn. 164 and 166.

via equation (144) thus reducing equation (157) to

$$|x_3 - x_2|_{max} = \frac{\lambda}{10Q\pi} \frac{\omega_{cr}X_1(1+(\omega_{cr}X_3)^2)}{(1+(\omega X_1)^2)^{\frac{1}{2}}} \quad (167)$$

This value for the stabilization is subject to the same constraints as equation (152) and is derived under identical approximations. As the value of the maximum disturbance which may be stabilized against is largest in the first solution considered, then this clearly is the filtering combination which must be adopted as producing the optimum system performance.

The theory above successfully predicts all the experimental phenomena from the previous section and the stabilized interferometer should therefore be considered well characterized. This interferometer was then used to perform the calibration of ultrasonic transducers and to characterize various ultrasonic propagation problems.

III.5 The miniaturization of the stabilized interferometer

The interferometer described earlier in this chapter was formed of conventional laboratory optical components. For calibration and laboratory experiments the size of such a device is of no consequence. However, if an optical transducer is to be used in the field some sort of miniaturization would be beneficial. It should be remembered that due to an interferometer's inherent lack of sensitivity over piezoelectric detectors any in field use would be restricted to certain controlled situations.

A miniature optical interferometer has been built and tested[110,111]. Vickers instruments provide various interferometric microscope objectives for use in surface finish examinations. One such device is based on the Michelson interferometer where the interferometer is built inside the objective resulting in an objective of size approximately 30mm x 30mm x 50mm. Obviously this interferometer is not stabilized and is therefore of no use in ultrasonic measurements as it stands. To produce a stabilized instrument the reference mirror was replaced by a multimorph crystal supporting an aluminized milar mirror as in the laboratory device described earlier. The modified objective, now forming the stabilized interferometer head, is shown in Figure 76. Due to the limited space available in the objective the multimorph crystal was found to be the only possible choice for the reference mirror translator. A thick, high voltage expansion mode piezoelectric crystal would have been too bulky for this application.

Having built the stabilized interferometer head the problem remained to introduce light power. The system initially adopted for this utilised a Helium-Neon laser and is shown in Figure 77. The single transverse mode Helium-Neon laser has a beam diameter of 0.64mm and the 10X objective expands this beam to fill the interference objective. It is immediately obvious that ¾ of the available laser power is wasted by the use of the second beam splitter. This was, however, not of specific interest in the preliminary evaluation of the miniature interferometer.

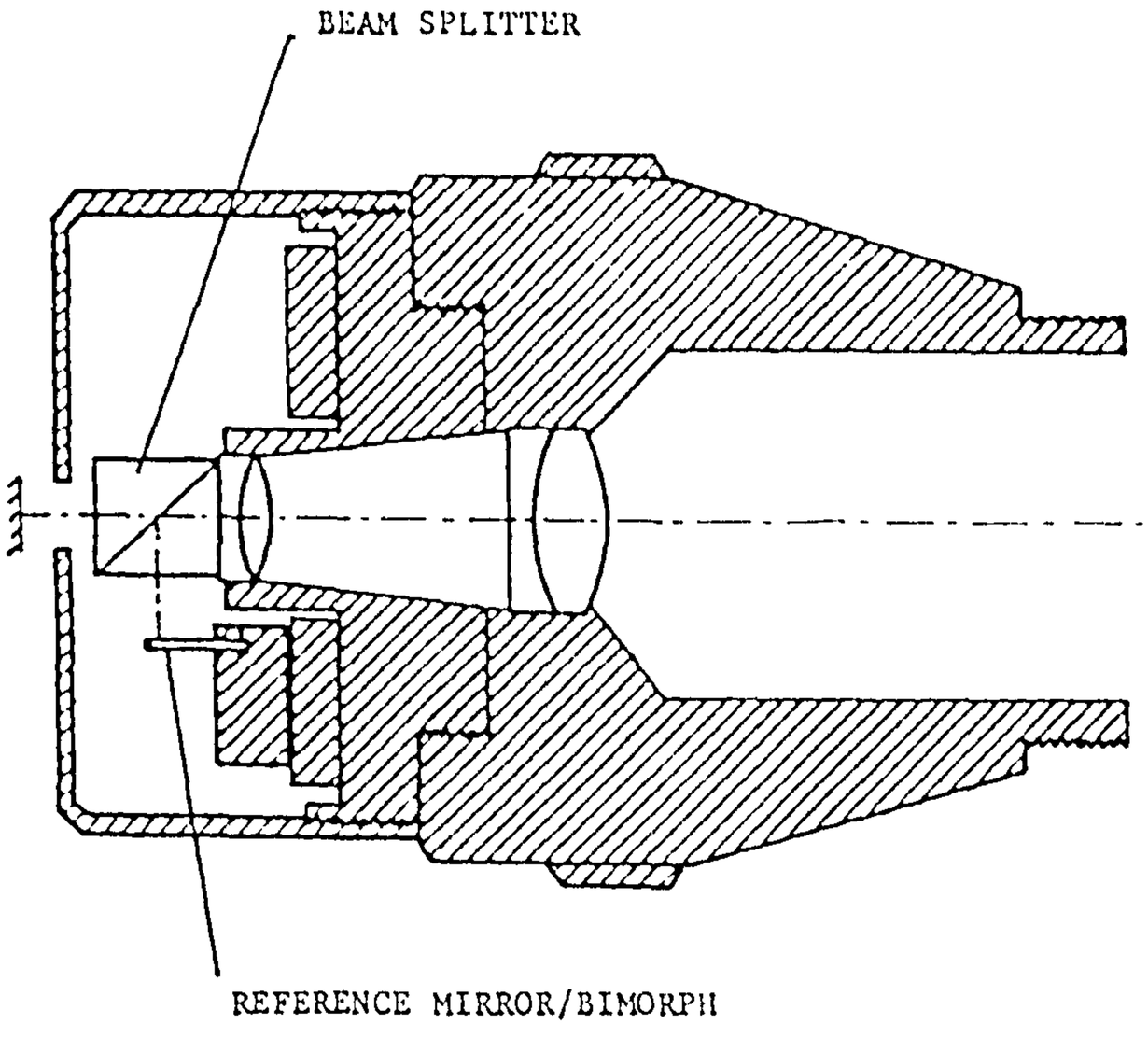

Figure 76: Modified interferometer microscope objective.

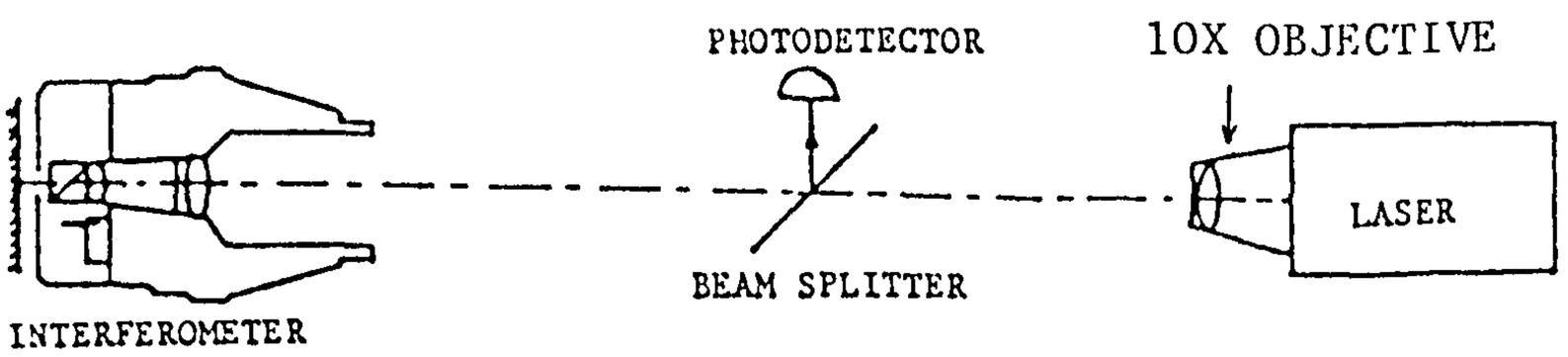

Figure 77: Instrument layout shown diagramatically.

The photodetection circuitry was not optimised either and employed a single silicon p.i.n. photodiode operating in the photoconductive mode followed by pre-amplification with a readily available (LM318) operational amplifier.

A minimum detectable displacement of 50pm (r.m.s.) over a bandwidth of 1kHz to 500kHz was achieved with both these figures being amplifier limited. The use of the RCA C30816 hybrid detector described earlier would immediately improve the figures to 50pm r.m.s. over a bandwidth of 1kHz to 10MHz. Further improvement could be made by placing the hybrid photodiode adjacent to the unused side of the main beamsplitter cube and removing the second beamsplitter. Such a modification would lead to the 25pm/10MHz bandwidth figure of the laboratory interferometer.

Using a Helium-Neon laser as in Figure 77, unfortunately makes the final device somewhat bulky with dimensions of approximately 50mm x 50mm x 400mm. If the laser could be removed to some remote position, or replaced by a smaller laser, then the interferometer head (or full interferometer) could be mounted directly onto a prepared specimen surface, thus ensuring that the unwanted background disturbances were sufficiently small to enable them to be countered by the available stabilization.

One small laser that might be used is a solid-state laser diode. These devices are certainly small with the entire package including support and mount being less than 10mm in any one dimension. A drawback of solid state lasers

is that the light is emitted over a very large angle, the angular radius being approximately 50^{o}. To capture all this light requires a numerical aperture of around 0.75. This is certainly possible and would form an interesting area of work.

Removing the Helium-Neon laser to some remote position requires that the laser light be introduced into the objective from some distance. Simply directing the beam through the atmosphere is unlikely to be successful as the amount of power entering the objective along the optic axis would vary as the laser and interferometer head vibrated with respect to one another. This variation in source power would then mean a variation in calibration. An alternative method would be to direct the laser power down an optic fibre. Such an approach has been used successfully by Garg and Claus[41]. Again problems may arise with the numerical aperture of the emitted laser light but these problems must clearly be solvable. Again this would form an interesting area of work.

III.6 The quadrature interferometer

III.6.1 Theoretical considerations in the quadrature interferometer

In addition to the stabilized interferometer being a possible ultrasound detector the quadrature interferometer discussed in section II.4.2i) and shown schematically in Figure 14 may also be used for such measurements. As shown

earlier the quadrature interferometer is basically two interferometers built into one and produces two outputs in quadrature ($\pi/2$ out of phase). The two signals are similar to that in equation (1) and may be written as

$$I_c = \frac{\alpha I_o}{2} \cos^2 \left[\frac{2\pi}{\lambda} (x)\right] \qquad (168)$$

$$\text{and} \quad I_s = \frac{\alpha I_o}{2} \cos^2 \left[\frac{2\pi}{\lambda} (x - \frac{\lambda}{8})\right] \qquad (169)$$

where the laser intensity I_o has been divided into the two polarizations in the interferometer. These equations may be rewritten using

$$2\cos^2 x = 1 + \cos 2x \qquad (170)$$

$$\text{leaving} \quad I_c = \frac{\alpha I_o}{4} \left[1 + \cos \left[\frac{2\pi}{\lambda} (2x)\right]\right] \qquad (171)$$

$$\text{and} \quad I_s = \frac{\alpha I_o}{4} (1 + \cos \left[\frac{2\pi}{\lambda} (2x - \frac{\lambda}{4})\right] \qquad (172)$$

As $\cos (y - \pi/2) = \sin y$, then (171) and (172) becomes (writing $A = \alpha I_o/4$):

$$I_c = A(1 + \cos \frac{4\pi x}{\lambda}) \qquad (173)$$

$$I_s = A(\sin \frac{4\pi x}{\lambda}) \qquad (174)$$

These are therefore the basic operating equations of the quadrature interferometer.

To demonstrate how the technique works from this point consider the displacement x to be composed of a low frequency (ω_1) and a high frequency (ω_h) component with amplitudes a_i and a_h. Hence

$$x = a_1 e^{i\omega_1 t} + a_h e^{i\omega_h t} \qquad (175)$$

therefore
$$I_c = A\left(\cos \frac{4\pi a_l e^{i\omega_l t}}{\lambda} . \cos \frac{4\pi a_h e^{i\omega_h t}}{\lambda} - \sin \frac{4\pi a_l e^{i\omega_l t}}{\lambda} . \sin \frac{4\pi a_h e^{i\omega_h t}}{\lambda}\right) \quad (176)$$

and
$$I_s = A\left(\sin \frac{4\pi a_l e^{i\omega_l t}}{\lambda} \cos \frac{4\pi a_h e^{i\omega_h t}}{\lambda} + \cos \frac{4\pi a_l e^{i\omega_l t}}{\lambda} . \sin \frac{4\pi a_h e^{i\omega_h t}}{\lambda}\right) \quad (177)$$

If $\frac{4\pi a_h}{\lambda} < \frac{\pi}{10}$ then to within a 5% error

$$I_c = A\left(\cos \frac{4\pi a_l e^{i\omega_l t}}{\lambda} - \left(\sin \frac{4\pi a_l e^{i\omega_l t}}{\lambda}\right) \frac{4\pi a_h e^{i\omega_h t}}{\lambda}\right)$$

$$I_s = A\left(\sin \frac{4\pi a_l e^{i\omega_l t}}{\lambda} + \cos\left(\frac{4\pi a_l e^{i\omega_l t}}{\lambda}\right) \frac{4\pi a_h e^{i\omega_h t}}{\lambda}\right)$$

(178), (179)

The signals may be hi-pass filtered to produce

$$I_c = - \frac{4\pi A}{\lambda} (a_h e^{i\omega_h t}) \sin \left(\frac{4\pi a_l e^{i\omega_l t}}{\lambda}\right) \quad (180)$$

$$I_s = + \frac{4\pi A}{\lambda} (a_h e^{i\omega_h t}) \cos \left(\frac{4\pi a_l e^{i\omega_l t}}{\lambda}\right) \quad (181)$$

A second order approximation is given in appendix 6. The results of this calculation show that the following condition

$$a_h \lesssim 55 \text{ Å}$$

must be satisfied if the calibration error of 5% or less indicated above in the approximation leading to equations (178) and (179) is required.

The information produced by the quadrature interferometer, outlined by the equation above, must now be processed in some way. This is investigated overleaf.

III.6.1i) Processing of the information on the quadrature interferometer

The two equations (178) and (179) represent the information received by the electronics if $a_h \lesssim 55\mathring{A}$. Before any information can be extracted, the signals represented by these equations must be high pass filtered producing equations (180) and (181). The reason for this is that the ratio of the magnitudes of the low and high frequency components is such that to maintain a good signal to noise ratio then a dynamic range is required that is in excess of any signal capture devices known of. This is very unfortunate as simply dividing leads to

$$\frac{4\pi}{\lambda}\ (a_1 e^{i\omega_1 t} + a_h e^{i\omega h t}) = \tan^{-1}\left(\frac{I_s}{I_c}\right) \qquad (182)$$

Although this would have led to problems of noise etc. when I_c was small, these problems could possibly have been removed by use of a computer. It may be possible by use of a four channel recording system to implement this idea. It is shown in appendix 7 that in the worst case in terms of frequency the first term may be replaced approximately by

$$\sin\ (\frac{4\pi a_1 \omega_1 t}{\lambda})$$

$a_1 e^{i\omega t}$ has been replaced by $a_1 \sin\omega_1 t$ and $a_h e^{i\omega h t}$ by x_h.

Therefore

$$I_c = A\left(\cos\ \frac{4\pi a_1 \omega_1 t}{\lambda} - \sin\ \left(\frac{4\pi a_1 \omega_1 t}{\lambda}\right)\ \frac{4\pi x_h}{\lambda}\right) \qquad (183)$$

and

$$I_s = A\left(\sin\ \frac{4\pi a_1 \omega_1 t}{\lambda} + \cos\ \left(\frac{4\pi a_1 \omega_1 t}{\lambda}\ \ \frac{4\pi x_h}{\lambda}\right)\right. \qquad (184)$$

The high pass analogue filter will reduce the magnitude of the first terms. Let this reduction be represented by $G(\omega)$. The equations above now become:

$$I_C \approx A\left[G(\omega_2)\cos\omega_1 t - \sin(\omega_1 t)\ \frac{4\pi x_h}{\lambda}\right] \qquad (185)$$

$$I_S \approx A\left[G(\omega_2)\sin\omega_1 t + \cos(\omega_1 t)\ \frac{4\pi x_h}{\lambda}\right] \qquad (186)$$

$$\text{where } \omega_2 = \frac{4\pi a_1 \omega_1}{\lambda} \qquad (187)$$

Two approaches have been adopted in the experimental work to process the quadrature interferometer signals. These have been to square and add the signals or to determine the phase of $\cos(\omega_1 t)$ or $\sin(\omega_1 t)$ by the ratio of the signals. Consider the first technique. Squaring and adding leaves

$$I_C^2 + I_S^2 = A^2\left[G^2(\omega_2) + \left(\frac{4\pi x_h}{\lambda}\right)^2\right] \qquad (188)$$

Consider the value of $\frac{4\pi x_h}{\lambda}$. This may be as low as $\sim 0.5\mathring{A}$. Then in order to allow the greatest flexibility in signal processing, for example peak height detection etc. as

$$\left(\frac{4\pi x_h}{\lambda}\right) = 10^{-3} \qquad (189)$$

then $G(\omega_1)$ must be given by

$$G(\omega_2) \lesssim 10^{-3} \qquad (190)$$

The filter response may be varied in several ways and this will be dealt with in the next section.

The constraints, as will be shown, are much more severe in the second case which will now be discussed.

In the ideal situation $G(\omega_1) = 0$ and then dividing equation (186) by (185) leaves:

$$\frac{I_c}{I_s} = - \tan \omega_2 t \qquad (191)$$

allowing $\omega_2 t$ to be determined and x_h to be extracted from either I_c or I_s. However, simply dividing these equations produces a value $\tan\alpha$ where

$$\tan\alpha = \frac{G(\omega_2)\cos\omega_2 t - \sin\omega_2 t \, 4\pi x_h/\lambda}{G(\omega_2)\sin\omega_2 t + \cos\omega_2 t \, 4\pi x_h/\lambda} \qquad (192)$$

It can be shown that the worst calibration error occurs for $\cos\omega_2 t = \sin\omega_2 t = 1/\sqrt{2}$. Similar calculations are used as were used in appendix 6. Therefore for a 5% error in the final calibration result we have

$$-1.1 = \frac{G(\omega_2) - 4\pi x_h/\lambda}{G(\omega_2) + 4\pi x_h/\lambda} \qquad (193)$$

$$G(\omega_2) \lesssim \frac{\pi x_h}{5\lambda} \qquad (194)$$

A modification of this method, which has so far been the one most extensively used in the experimental measurements, is to choose some convenient high frequency excursion (that is the displacement over a short time period) and to determine the relative phase of the two signals from these readings.

This works very well in the laboratory but calculation and consideration of problems which may appear in a real situation indicate severe difficulties would arise when this approach is used. Calculations show that if the wavform can be predicted, especially the zero displacement line

for high frequency excursions, and that the high frequency movements are measured over a time period no greater than 10μs the system produces a calibration accuracy of 5%. If the zero line is not known severe calibration errors can occur.

One final processing technique is to abandon any attempt to obtain accurately calibrated signals but to merely monitor the largest signal. In the ideal case, again, when $G(\omega_2) = 0$ the largest signal is, as determined by the value of $\omega_2 t$, always at least 70% of the largest possible value. However, non-zero values of $G(\omega_2)$ again produce confusion. This means the tolerated error must be larger. If a signal value which is only 50% of the true value can be tolerated then

$$G(\omega_2) \leq \frac{\pi X h}{\lambda} \min \tag{195}$$

So far no detailed description of $G(\omega_2)$ has been given as $G(\omega_2)$ depends on the type of filter used. The filtering requirements for the processing techniques given above will now be considered.

III.6.1ii) Filtering requirements for these techniques of processing the information on the quadrature interferometer

The four methods of signal processing considered above were:

1) square and add the signals,

2) determine the relative phase by division of the signals,

3) determine the relative phase by monitoring excursions

over a short time interval,

4) choose the largest signal and neglect accurate calibration.

There are basically three choices to be made when selecting a filter. The first is to choose the cut-off point, (ω_c), that is the frequency at which the power has fallen by 3dB. The second choice is the order of the filter which determines the rate at which the signal is attenuated in the frequency domain. The third choice is over the filter design. For example if a Butterworth filter is used the frequency response curve will be reasonably flat apart from the roll-off[112], see Figure 78, but the filter will ring slightly when subject to a step input. Alternatively a Bessel filter[113] may be used for example. This will give no ringing, but has a much weaker attenuation. Other filter types such as transitional filters[117] offer compromises between rate of roll-off and ringing problems.

Work carried out so far has utilized Butterworth filters of various orders and cut-off points. The actual magnitudes of these values will be dictated by both the amount of vibration and the frequency content of the acoustic emission of interest. Results from work done by Wadley et al[10] suggest frequencies down to 10-20kHz are of interest in acoustic emission waveforms. However it may still be possible to characterize signals when a higher frequency range is used.

The amplitudes of the unwanted vibrations in the laboratory have been given earlier and are of the order

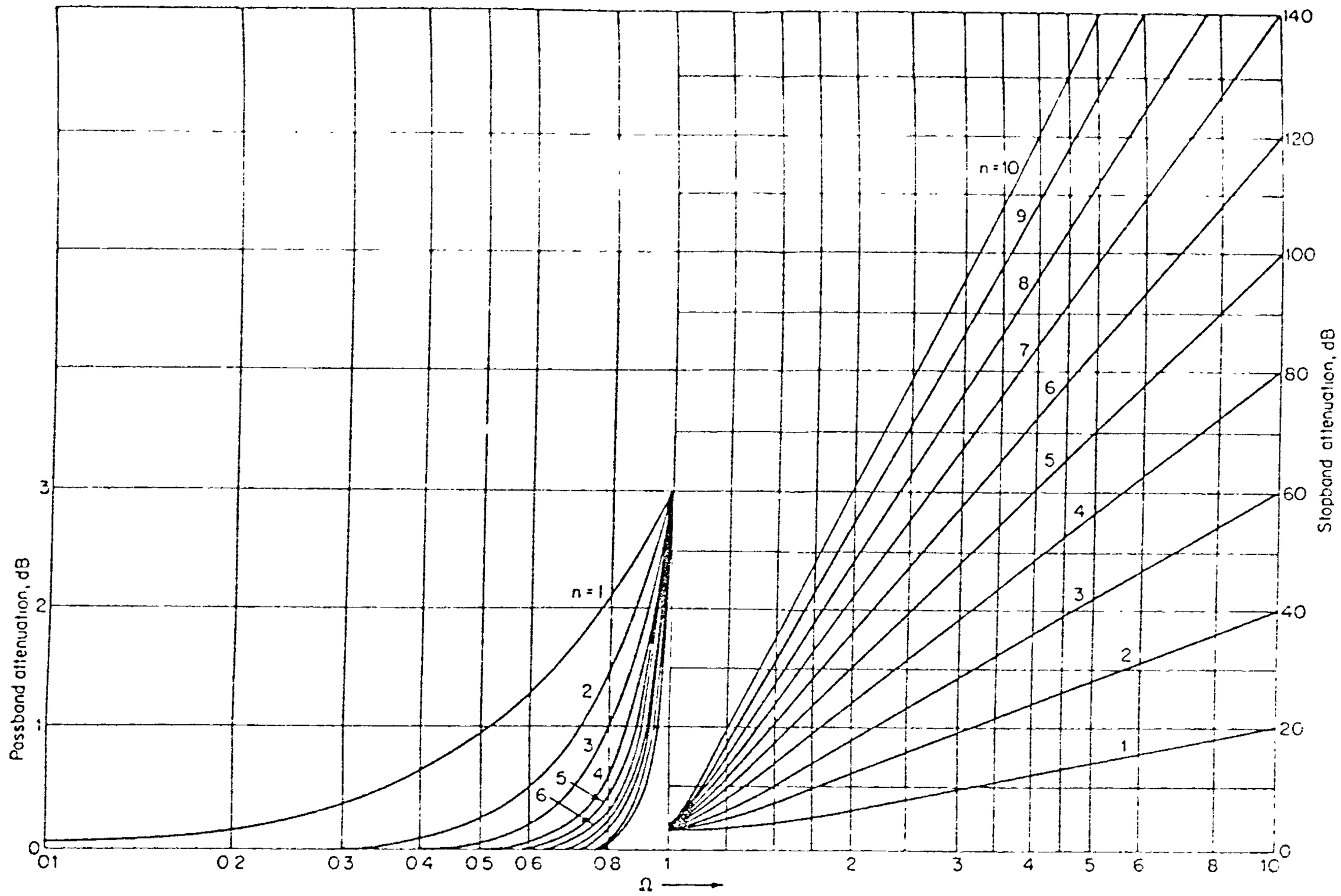

Figure 78: Attenuation characteristics for Butterworth filters. (From Anatol I. Zverev, Handbook of Filter Synthesis, John Wiley & Sons, Inc., New York, 1967).

of 3μm. Similar measurements have been made on a welding test rig at Risley Nuclear Laboratories and are given in a private communication by Mr. M.J. Beasley[113]. These show the principle vibrations on the rig occur at 30Hz and have an amplitude of 2λ (λ is the He-Ne wavelength). Therefore from equation (187):

$$\omega_2 = 2.\pi.750 \qquad (196)$$

The voltage response of a hi-pass Butterworth filter of order n at a frequency ω_2 is given by

$$\frac{V_{in}}{V_{out}} = \left(1 + \frac{\omega_c}{\omega_2}\right)^{2n}\Bigg)^{\frac{1}{2}} \qquad (197)$$

(where ω_c is the cut-off point of the filter).

The value of ω_c is chosen, because of the acoustic emission frequencies of interest indicated above, as

$$\omega_c = 2.\pi.10^4 \qquad (198)$$

Therefore
$$\frac{\omega_c}{\omega_2} = \frac{2\pi.10}{2\pi.750} \qquad (199)$$

$$= 13.3 \qquad (200)$$

Applying this to the methods mentioned for the processing of information:

1) Square and add the signals.

From equations (197) and (200):

$$\frac{V_{out}}{V_{in}} = \frac{1}{(1 + (13.3)^{2n})^{\frac{1}{2}}} \qquad (201)$$

From equation (190) the largest value of V_{out}/V_{in} is

given in the limit as:

$$\frac{1}{(1 + (13.3)^{2n})^{\frac{1}{2}}} = 10^{-3} \qquad (202)$$

therefore $n = 2.7$ (203)

This method therefore requires a 3rd order filter.

2) Determine the relative phase by division of signals.

Equation (194) is

$$G(\omega_2) \lesssim \frac{\pi x_h}{5\lambda} \qquad (204)$$

In the limit $x_h = 0.5\mathring{A}$ and

$$G(\omega_2) = 5 \times 10^{-5} \qquad (205)$$

Following the calculation above this produces a value of the filter order of:

$$n = 3.8 \qquad (206)$$

Therefore a 4th order filter is required for this method of signal processing.

3) Determine the phase by monitoring excursions over a short time interval.

Choosing the time interval correctly is the same as using a high-pass filter. As was mentioned before the major difficulty is knowing the shape of the high frequency pulse. If this can be overcome then a filter is required which brings the signal within the measuring range of any instrument. In the experiments performed a recording

instrument is used which requires

$$G(\omega_2) \simeq 0.02 \qquad (207)$$

This type of experiment requires a second order filter.

4) Choose the largest signal and neglect accurate calibration.

Equation (195) is:

$$G(\omega_2) < \frac{\pi x_h}{\lambda} \qquad (208)$$

therefore $$G(\omega_2) < 2.5 \times 10^{-4} \qquad (209)$$

which yields n = 3.2 requiring a fourth order filter.

The response of these filters to step impulses are indicated qualitatively in Figure 79.

III.6.2 Experimental measurements of the performance characteristics of the quadrature interferometer

A quadrature interferometer has been built and used to verify the results obtained from the stabilized device as well as producing results which it was not possible to obtain, or at least very difficult to obtain, with the stabilized interferometer.

The polarization of the laser (see Figure 14) sets the polarization axis of the entire interferometer. The polarizing beamsplitter is then set at 45^{o} to the axis resulting in the same average light intensity being deflected to each photodetector. If the beamsplitter is not at 45^{o} then the two intensities are not equal. This

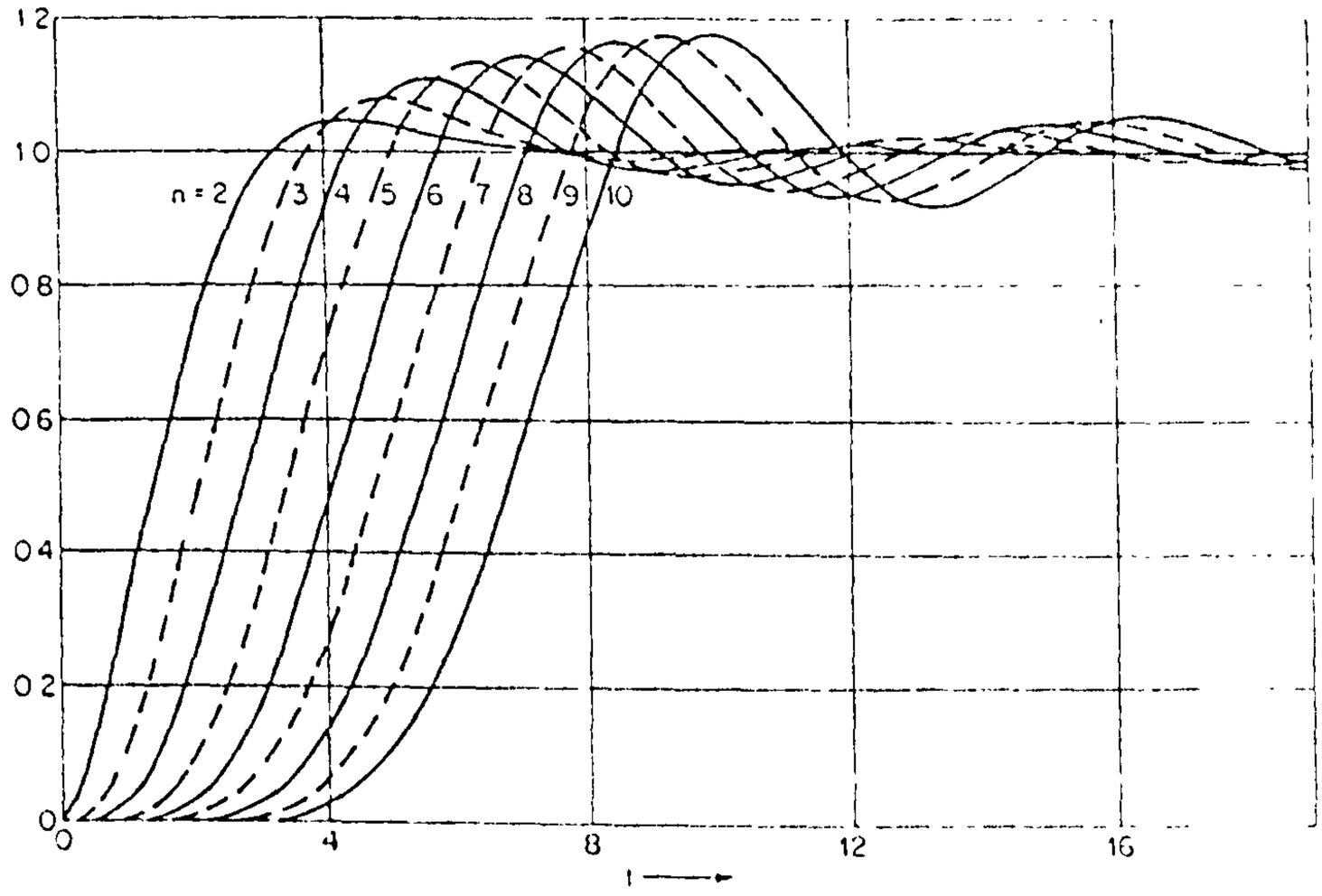

Figure 79: Step response for Butterworth filters (From Anatol I. Zverev, Handbook of Filter Synthesis, John Wiley & Sons, Inc., New York, 1967).

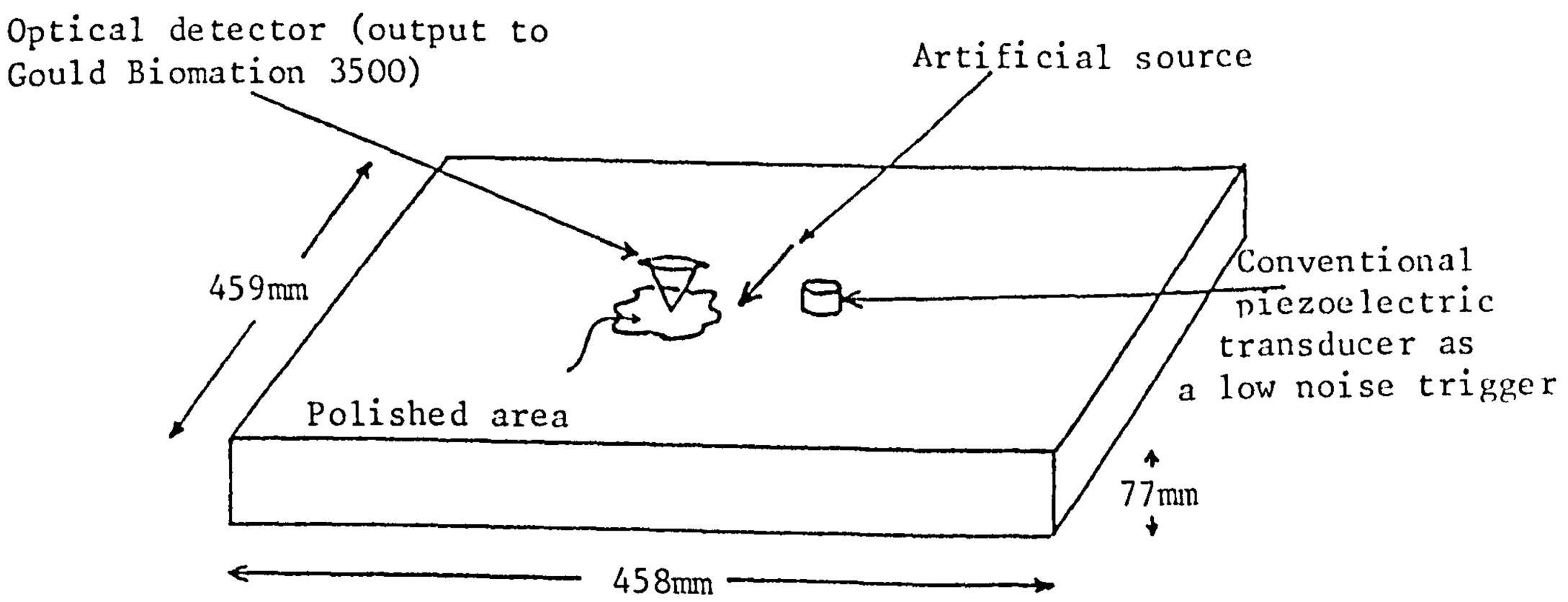

Figure 80: Schematic representation of the system used to monitor artificial sources of acoustic emission at a distance.

is not a problem as the outputs of the detectors may be balanced by suitable amplification.

The $\lambda/8$ plate is also set at 45^{o} to the laser polarization. Errors in the setting of the axis of this plate result in the two interferometer outputs not being in exact quadrature. Slight inaccuracies in the thickness of the mica plate and difficulties in setting the axis resulted in a quadrature error of 4^{o}. For the quantitative measurements given later this results in an error of 4% and being less than the other combined measurement uncertainties is neglected.

The photodetection circuitry was identical to the final choice for the stabilized device given earlier; a hybrid silicon p.i.n. photodiode and preamplifier (RCA C30816). The minimum detectable displacement was $0.5\mathring{A}$ over a bandwidth of 1kHz to 10MHz. If shot noise were the only source of noise this figure would be $\sqrt{2}$ times larger than the corresponding stabilized interferometer figure.

Unfortunately, some contribution from amplifier noise is encountered as the laser power loss factor (α) is increased with the addition of extra optical components. The quadrature minimum detectable displacement is therefore around twice as large as the stabilized minimum detectable displacement.

It was found that if care was taken to reduce the background vibrations a single stage 1kHz RC high pass filter was sufficient to keep the measured signal within

the dynamic range of recording instrumentation. Other Butterworth filters of order n = 5 (19kHz high pass) and n = 3 (100kHz high pass) were also tested and shown to work. Quantitative measurements were however only taken using the first (single RC) filter given above.

Signal processing was carried out using two different methods. As the shapes of the waveforms measured were known then the zero positions could accurately be determined. By measuring high frequency excursions from these zero lines the phase angle of the interferometer could be determined accurately (see section III.6.1) compared with measuring uncertainties. This method was the one most extensively used in the signal processing, being used exclusively when quantitative measurements were taken.

A second processing method was briefly investigated which involved high pass filtering the signals and then squaring them in a 4MHz analogue squaring device. Problems were encountered due to the temperature and frequency dependence of the squaring process in the device, therefore the method was not pursued and quantitative measurements were made in the way described earlier.

Recent developments in fast analogue squaring devices indicate that such problems as those described above may be solvable and this would form an interesting area of work.

The quadrature interferometer as it stands has been used in various experimental measurements. These will be discussed later.

IV THE CHARACTERIZATION OF ULTRASONIC SYSTEMS

Ultrasonic systems are in general complicated. The series of events leading for instance to the detection of an acoustic emission signal as outlined in Figure 19 involves ultrasonic pulse generation and propagation and transduction of this pulse into a usable electrical signal. This chapter is concerned with the experimental study of all the various aspects of this problem. The optical ultrasound detectors described in the previous chapter form the basis for the absolute measurements given. Individual facets of the ultrasonic system characterization will now be considered separately.

IV.1 The study of artificial sources of acoustic emission

Many ultrasonic systems are unique and exist only in a given specialised practical situation. Such systems still require calibration. Obviously it is not sensible to try to model these arrangements in the laboratory and proceed with a characterization on the simulation. A preferred approach would be to perform the calibration in situ. One possible approach to the problem is to measure the in situ system response to a known artificial stimulus. This approach has been discussed before in chapters I and II and is the one studied here.

The problem therefore comes down to measuring and characterizing one or several ultrasonic sources. In the field of acoustic emission these are often termed artificial acoustic emission sources. Two methods may be adopted for such a study. The first involves measuring the response

of a simple well understood ultrasonic system at some point remote from the source. The source function is then determined by deconvolution with the theoretical Green's function for the system. This approach has been used widely by other workers (see chapter II) but relies on the Green's function being correct. Previous work has suggested these functions are in fact correct. This method has been extensively used in the experiments detailed later.

The alternative approach is to try to measure the generating source function directly. Coupled with the other results outlined above such measurements allow a verification of the Green's functions as well as producing the required results for the source. This method has also been studied experimentally and will be detailed in due course.

IV.1.1 Artificial acoustic emission sources studied at a distance

IV.1.1i) Experimental arrangement

Several workers have carried out experimental work concerned with the detection of ultrasonic pulses at the source epicentral position on thick plates. However little work has been performed on the measurements of surface pulses. Such work has been discussed in chapter II. The experimental work outlined below is therefore concerned mainly with the study of surface pulses.

The experimental arrangement for this study is very simple. The source is applied to some position close to the centre of a large aluminium block (77mm x 459mm x 458mm). A small area is polished on the same surface which therefore comprises the signal mirror for either a stabilized interferometer or a quadrature interferometer. The output of the interferometer is taken via a simple RC 1kHz hi-pass filter to a Gould Biomation 3500 transient recorder. This device then forms a digitized signal of the analogue interferometer output, the maximum digitizing rate being one point every 10ns. A conventional piezoelectric transducer is sometimes used to provide a low noise trigger for the optical detection. The arrangement is shown schematically in Figure 80.

IV.1.1ii) Experimental results

A variety of sources have been studied and each considered in view of its potential as a useful tool for in situ system characterization. These will now be discussed separately.

IV.1.1ii)a) The mechanical impact of solid objects

A useful artificial source must contain a wide range of frequency components. This range must be large enough to cover the frequencies which might be encountered in subsequent practical experiments on any ultrasonic system the artificial source is used to characterize. As pointed out by Hsu and Hardy[8] the frequencies of the ultrasonic

waves produced by mechanical impact, of for example ball bearings, are limited by the finite size of the impact objects. The time of contact for the collision of two spheres was treated by Hertz in 1881[114] and is shown to be of the order of one or two microseconds for ball bearings of a few millimeters diameter giving an upper frequency of only one or two hundred kilohertz.

The surface ultrasonic pulse is shown in Figure 81 resulting from the impact of a thin needle approximately 6cm in length. This trace was captured on the stabilized optical interferometer. The rise time is given by the time taken for an ultrasonic wave to travel the length of the needle and back. Clearly this is a low frequency event.

A similar event is shown in Figure 82. This is the impact of a 4mm diameter ball bearing captured by a broadband piezoelectric sensor. At such low frequencies this sensor will be shown (chapter VI) to reproduce accurately the vertical surface displacement on a plane surface as used here. The rise time is again slow , being given approximately by the time taken for an ultrasonic pulse to traverse the ball bearing diameter twice. (This is in fact only an approximation due to the spherical nature of the bearing - Hertz[114]). The ultrasonic velocity in the ball bearing is unknown thus making quantitative deductions difficult, however the event is again clearly low frequency. Consequently, the mechanical impact of a solid object does not represent a useful artificial acoustic emission source.

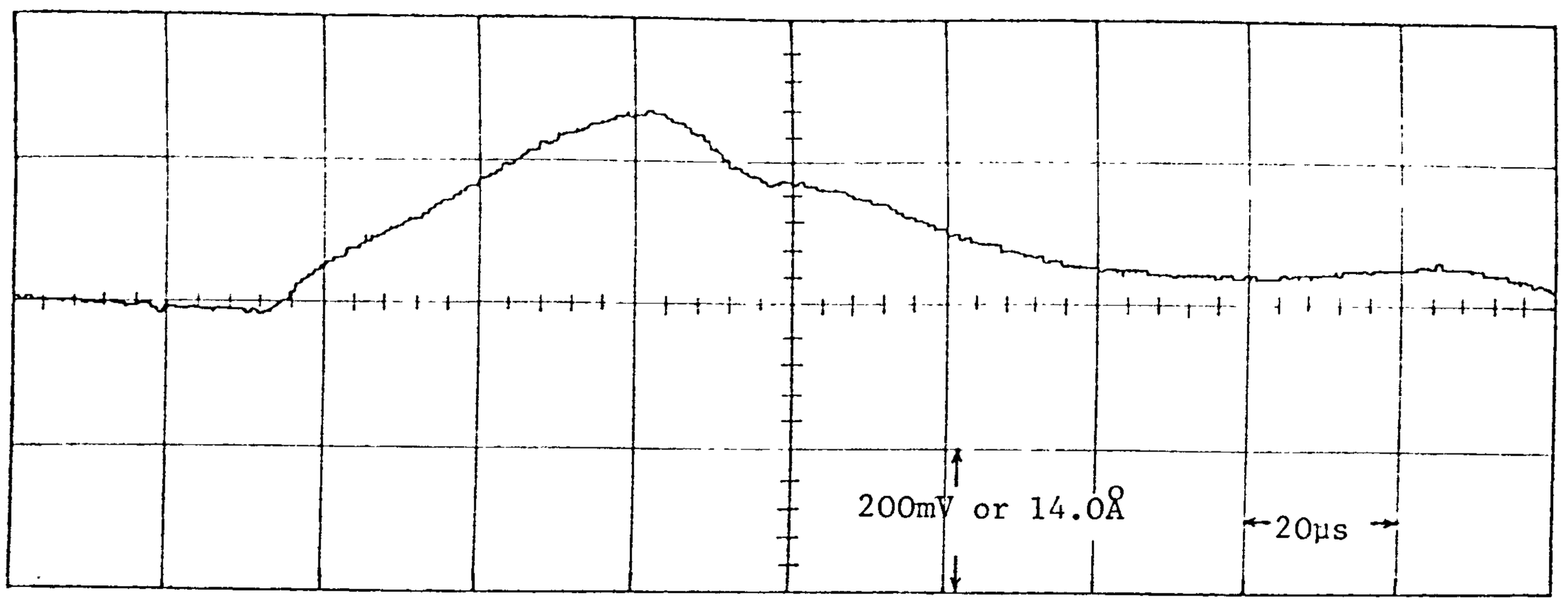

Figure 81: The vertical surface displacement created by the impact of a 60mm long steel needle as measured by the stabilized optical interferometer at a distance of 35mm from the impact point.

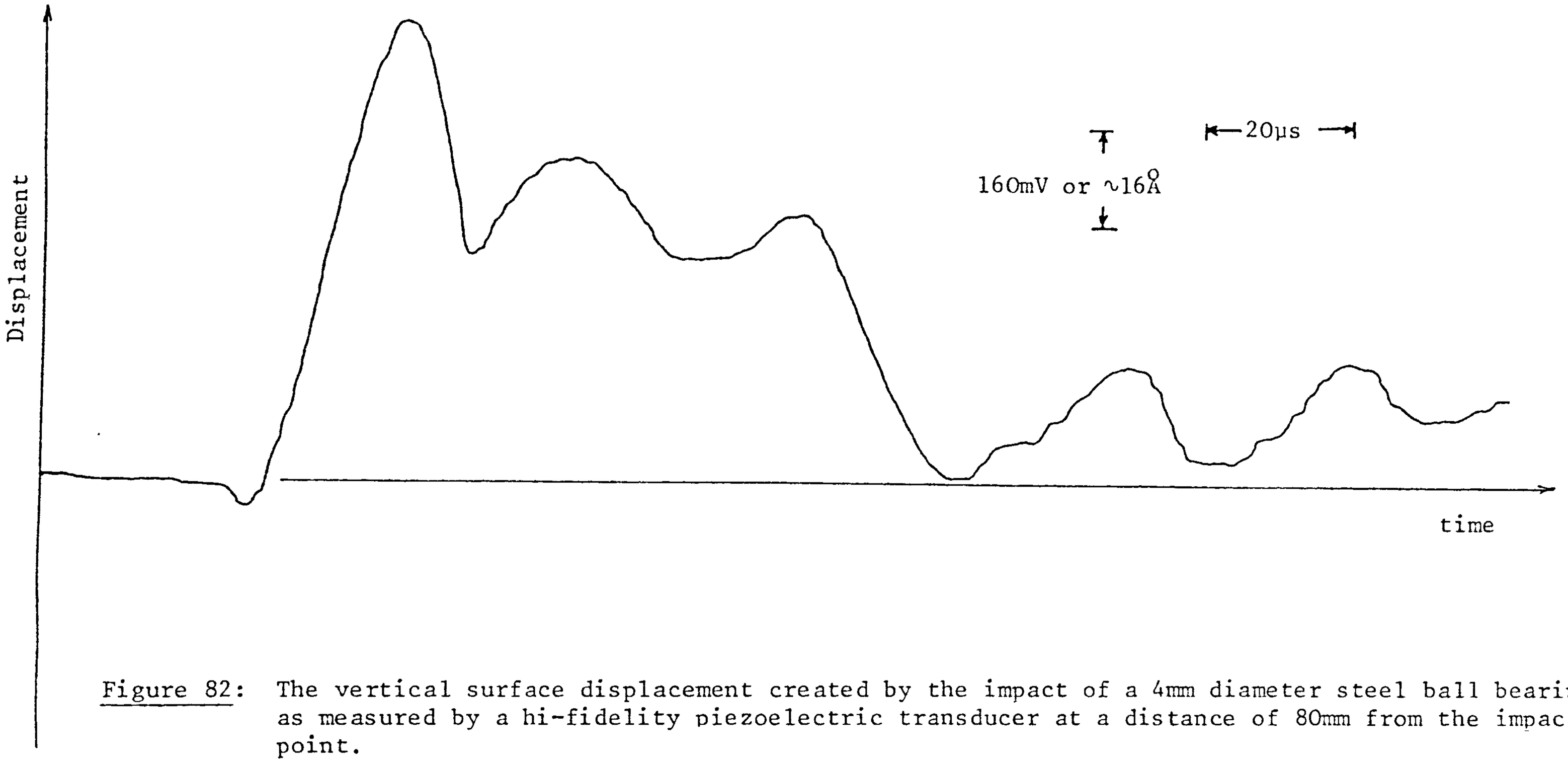

Figure 82: The vertical surface displacement created by the impact of a 4mm diameter steel ball bearing as measured by a hi-fidelity piezoelectric transducer at a distance of 80mm from the impact point.

IV.1.1ii)b) The brittle fracture of ceramic pencil leads

As mentioned in chapter II, a common artificial source is the fracture of a ceramic pencil lead held in a normal propelling pencil. This source was first suggested independently by both Hsu[115] and Nielson[116]. The surface of the test specimen, in this case the aluminium block, is quasi-statically loaded as the tip of the lead is pushed onto the material. As the pencil is pivoted about the attached collar then the extended section of lead is subjected to higher and higher stresses (Figure 83) until it eventually fractures. Stresses built up in the material surface are then rapidly released producing an ultrasonic pulse. This source is usually termed a Hsu/Nielson source.

Previous studies of this source reviewed in chapter II have not been comprehensive leaving several questions unanswered. For example: where does the negative pulse preceeding the main release (Micheals et al[71]) originate from? What effect does the length and thickness of the lead have? What is the frequency domain reproducibility of the source? What happens if the angle of contact between the lead and the surface is changed?. Various experiments have been performed to attempt to answer these questions and the results will now be given.

IV.1.1ii)b)i) Propagation effects for the surface pulse generated by the fracture of a 0.5mm diameter 2H ceramic pencil lead on an aluminium block

The theoretical surface pulse shown in Figure 5 for

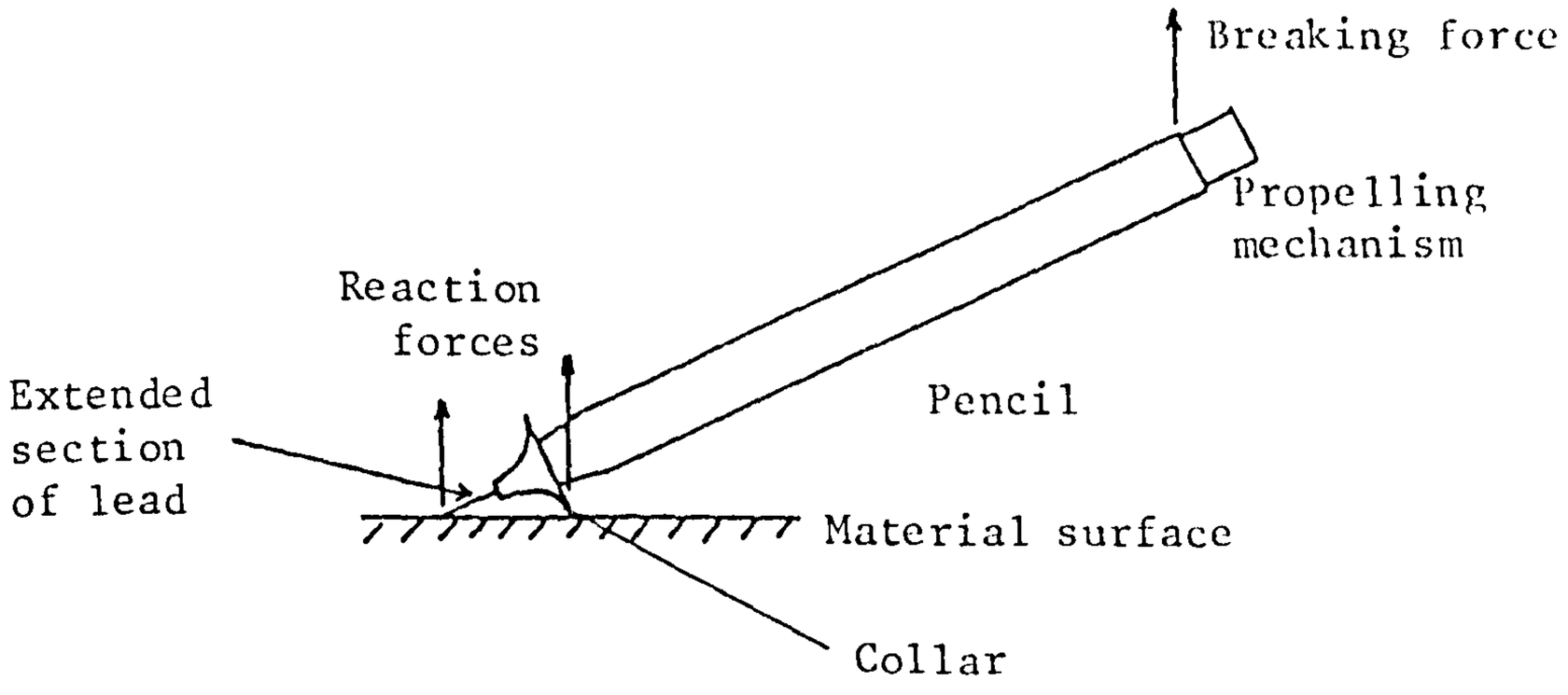

Figure 83: Schematic representation of the method by which ceramic pencil leads are broken to create an artificial acoustic emission source.

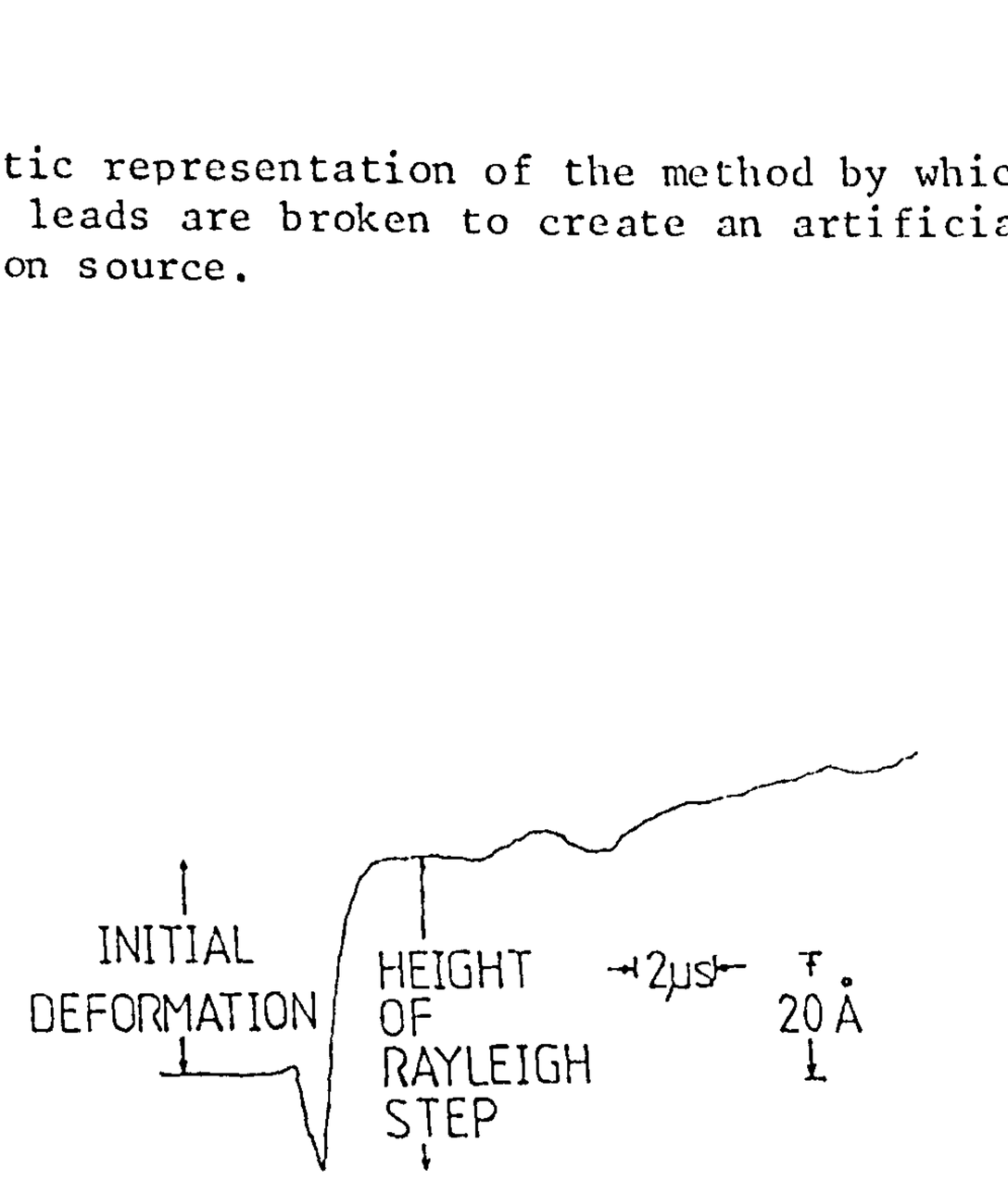

Figure 84: Typical waveform obtained when a ceramic pencil lead is broken by the method indicated in Figure 83. Extended lead length was (2.24±0.02)mm (4 clicks of the propelling mechanism).

the step point unloading of a semi-infinite solid maintains a constant relative profile as it propagates over the surface. The absolute size of the pulse is inversely proportional to the distance travelled whilst the absolute arrival times of the individual waves are proportional to the distance travelled.

For any real source then the rise time will be finite and consequently the discontinuity at the Rayleigh wave arrival should disappear.

In order to carry out a propagation study the distance between the source and the optical detector was varied. The first experiment employed the stabilized interferometer as the transducer and the length of the extended lead was maintained at around 2mm. This length was fixed by the propelling mechanism of the pencil, 4 clicks of this mechanism producing an extension of around 2mm. The true length was, including its reproducibility, in fact (2.24 ± 0.02)mm

The actual force with which the pencil breaks is found to vary somewhat and so several fractures are taken at each separation distance between source and detector. Typical waveforms are shown in Figure 84[117]. Two parameters may easily be extracted from these traces which are the initial static deformation caused by the loading process and the height of the Rayleigh step as shown. Boussinesq in 1885 calculated the deformation created by a point load on the surface of a semi-infinite solid[118]. This deformation (w) was found to be:

$$w = F(1 - \nu^2)/\pi E r \qquad (210)$$

where F is the force, ν Poisson's ratio for the material, E the Young's Modulus and r the distance from the load to the observation point. Therefore plotting the deformation against 1/r should yield the value of F as ν and E are known. Such a plot is shown in Figure 85[117].

Rayleigh waves are a surface wave and as such propagate in two dimensions only. The height of the Rayleigh step should therefore be inversely proportional to the square root of the propagated distance, Figure 86[117] shows a graph of the height of the Rayleigh step versus $1/r^{\frac{1}{2}}$.

The slope of the graph in Figure 85 is $(9 \pm 1 \times 10^{-12})m^2$ yielding a value of the force F as 2.3 ± 0.2N.

A similar experiment was performed using a different extended lead length of (3.50 ± 0.02)mm corresponding to 6 clicks of the lead propelling mechanism. The measuring instrument used here was the quadrature interferometer with the two quadrature outputs being captured on the Gould Biomation transient recorder. The relative phase could then be calculated by considering the relative amplitudes of the two traces knowing the zero position (see section III.6.1i). The use of the quadrature interferometer also enabled the results from the stabilized version to be checked. Excellent agreement was found as expected.

Again the initial deformation and the height of the Rayleigh step are plotted against 1/r and $1/r^{\frac{1}{2}}$ respectively (Figures 87 and 88). The use of the quadrature interferometer allowed the source to be moved very close to the detection

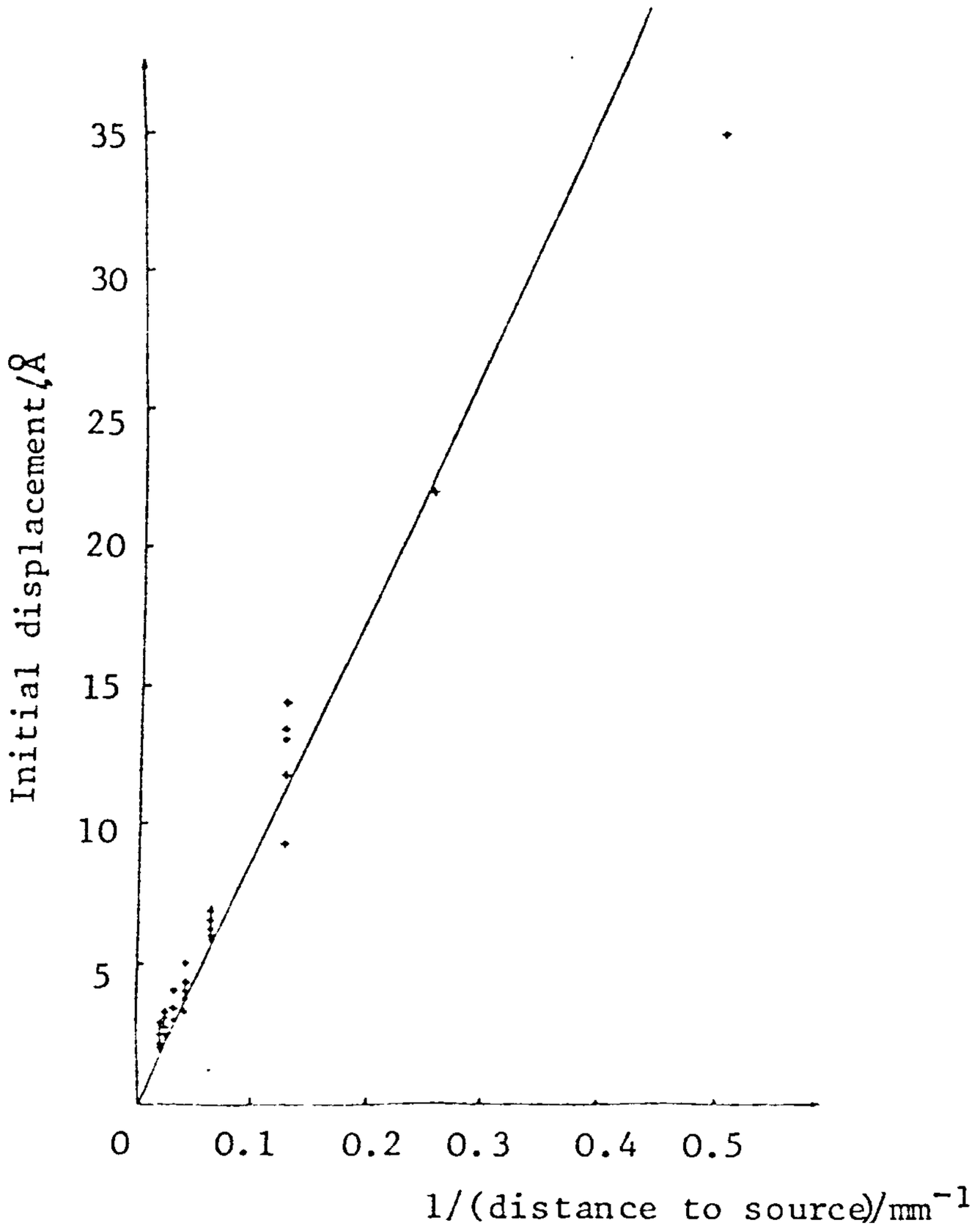

Figure 85: The variation of the initial deformation (Figure 84) with the inverse of the propagation distance for a breaking ceramic pencil lead of length (2.24±0.02)mm.

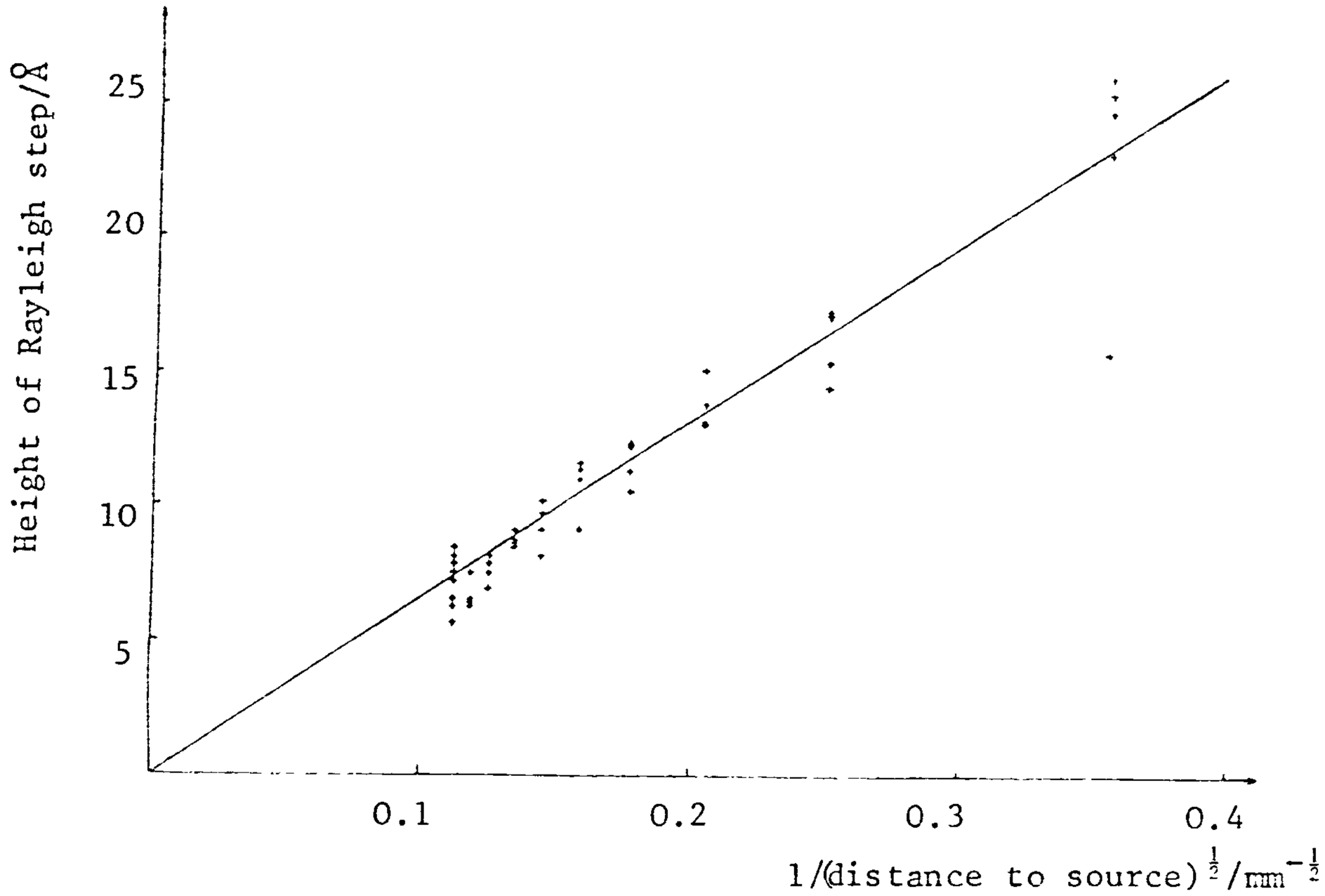

Figure 86: The variation of the Rayleigh step height (Figure 84) with distance for a breaking ceramic pencil lead of length (2.24±0.02)mm.

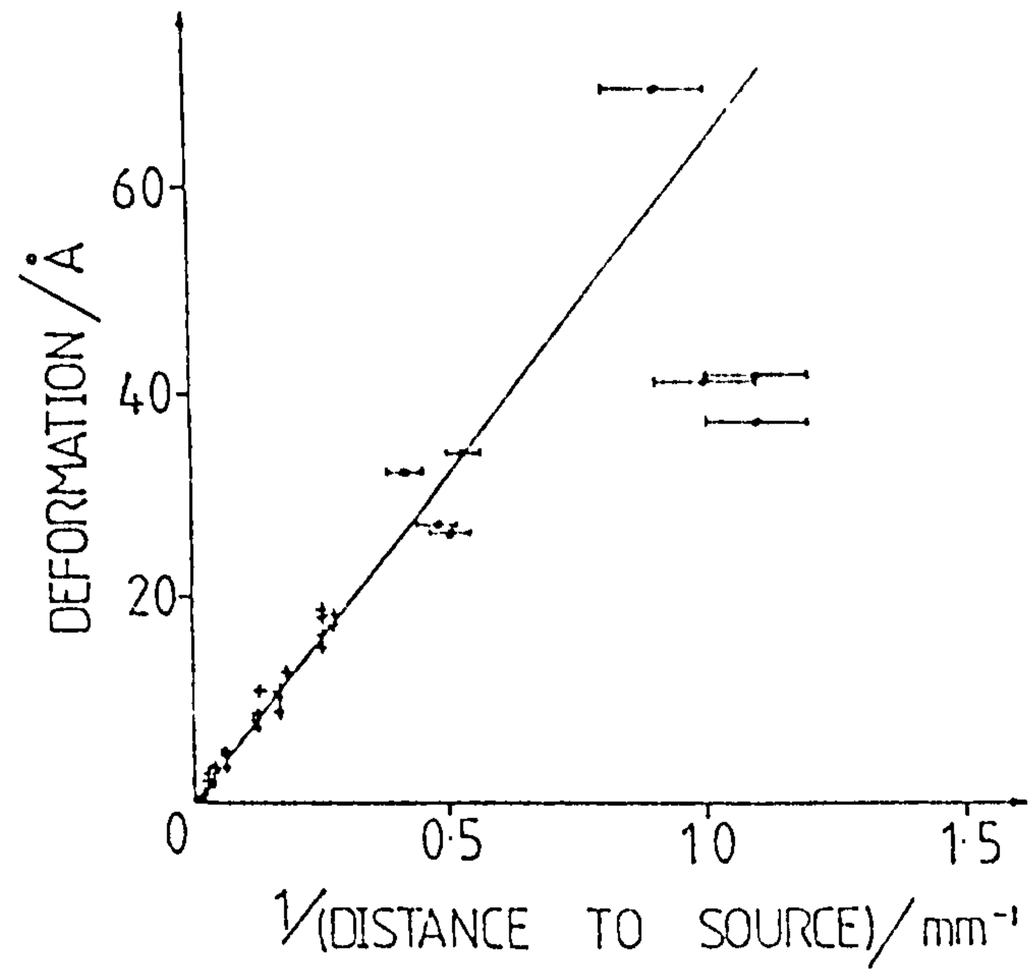

Figure 87: The variation of the initial deformation (Figure 84) with the inverse of the propagation distance for a breaking ceramic pencil lead of length (3.50±0.02)mm.

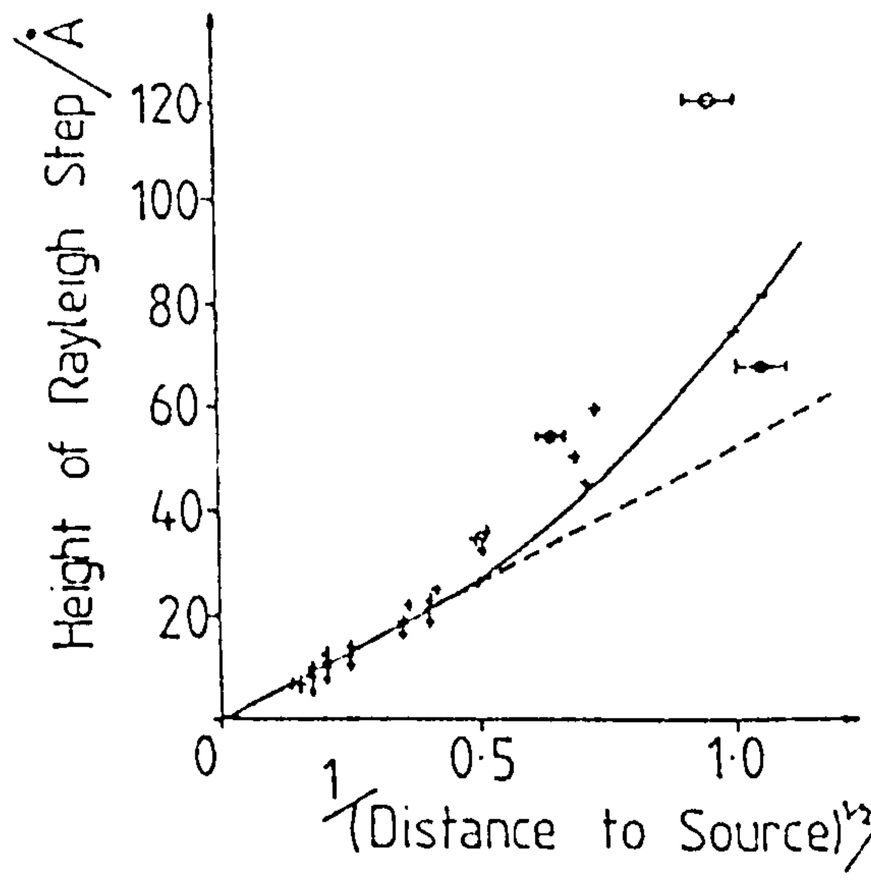

Figure 88: The variation of the Rayleigh step height (Figure 84) with distances for a breaking ceramic pencil lead of length (3.50±0.02)mm.

point as setting up difficulties associated with interruption of the laser light were greatly reduced. The force released was found in this case to be (1.55 ± 0.15)N.

The form of Figure 88 for the Rayleigh step shows a deviation from the expected inverse square root behaviour. It is shown in Figure 89 that a dip precedes both the theoretically predicted longitudinal (p) and shear (s) wave arrivals. This suggests that the pencil source is not merely a release but contains a preliminary compressive component. This component must also affect the Rayleigh wave being most noticeable when the time between the shear and Rayleigh wave arrivals is comparable to the source rise time. Such effects will be investigated more thoroughly later.

Although the existence of this compressive component in the source causes the height of the Rayleigh step to deviate from its expected variation the initial deformation should not be affected. Therefore the two forces deduced above should be connected both to the actual forces generated by the sources and to each other.

The actual forces generated were measured directly by the method outlined in Figure 90. The force gauge was calibrated and an average of 10 breaks taken. The forces required to break the pencil leads when the leads were extended by 4 and 6 clicks respectively were (2.37 ± 0.02)N and (1.47 ± 0.01)N. These therefore match the values taken earlier from Figures 85 and 87. It should be remembered

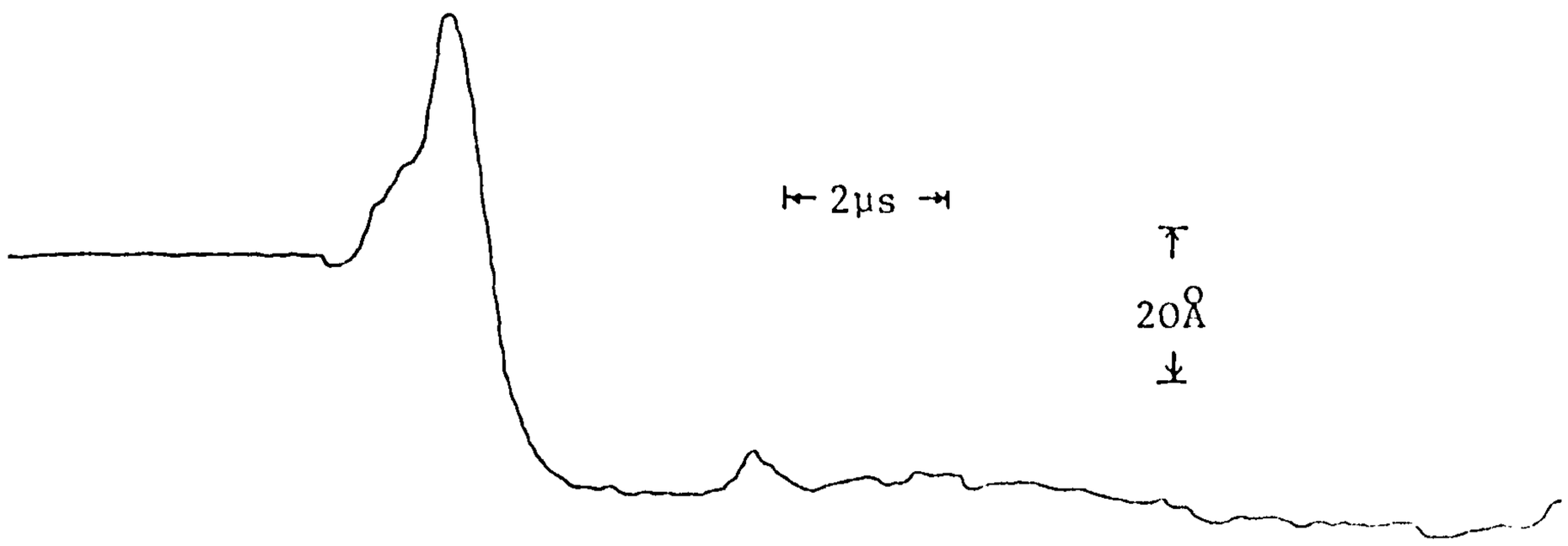

Source detector distance ∿1.9mm

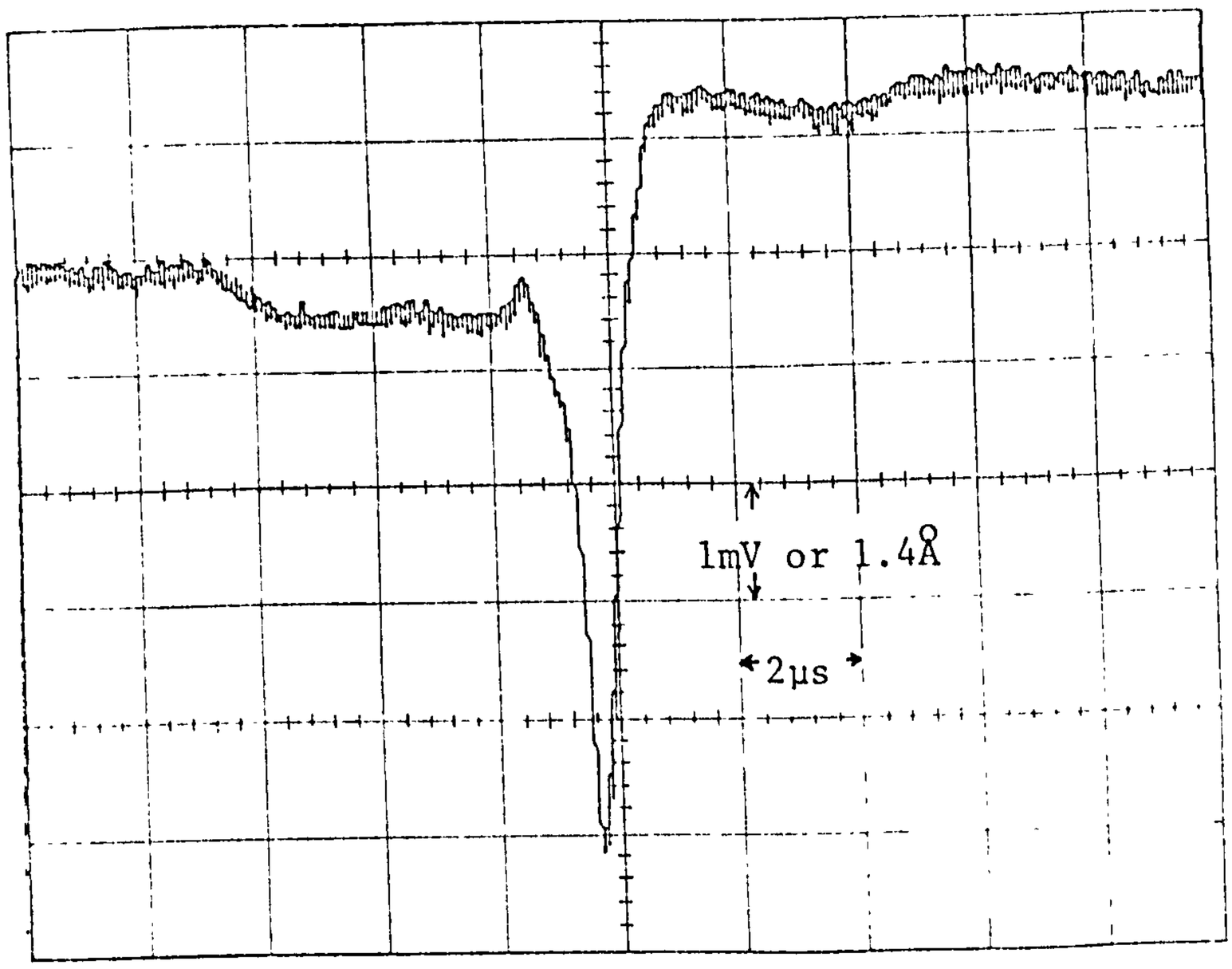

Source detector distance ∿35mm

Figure 89: Typical waveforms obtained when a ceramic pencil lead is broken by the method indicated in Figure 83. Extended lead length (3.50±0.02)mm.

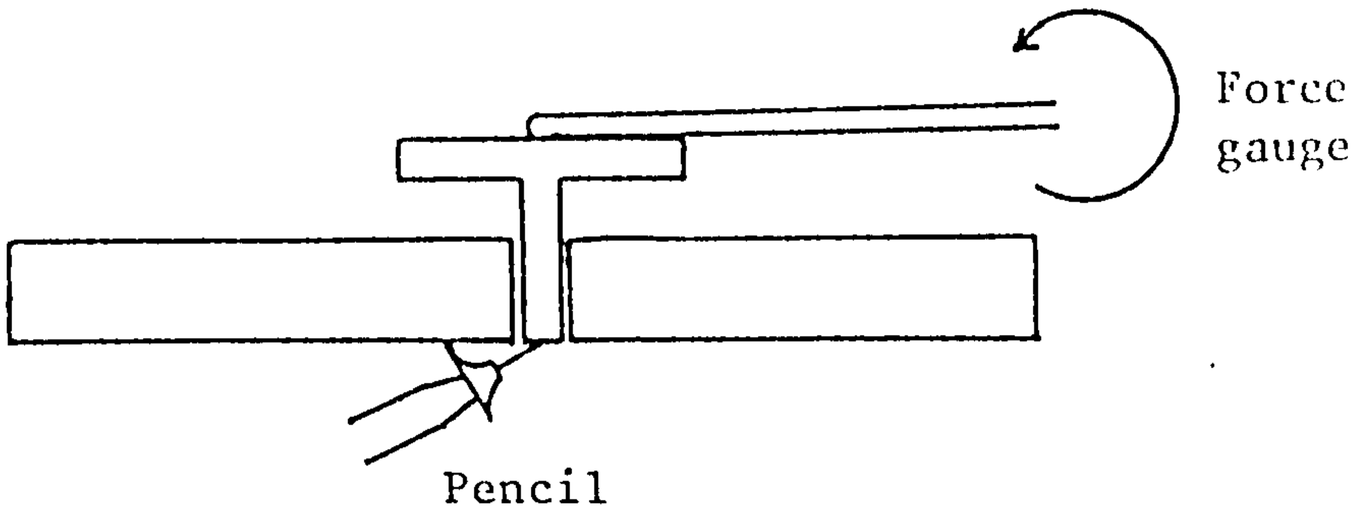

Figure 90: Schematic representation of the method used to measure the breaking force of the ceramic pencil lead.

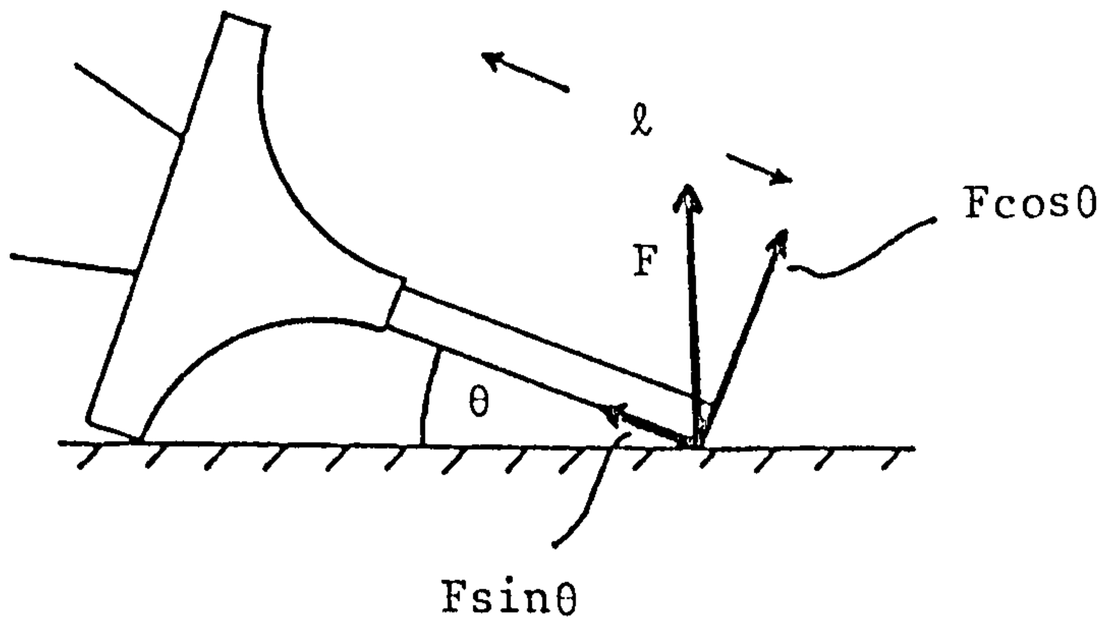

Figure 91: Forces acting on the extended pencil lead in the artificial source shown in Figure 83.

that the aluminium block is not actually a semi-infinite half-space and results are only valid if the Rayleigh wave reaches the detector before any reflections from the lower face of the block. This yields a maximum source-detector separation of around 60mm.

A relation may be derived between the expected breaking force required from leads extended by 4 and 6 clicks. Referring to Figure 91 then the free lead of length ℓ will fracture at a given bending moment ($M = F\ell\cos\theta$). For the case of 4 clicks $\cos\theta = 0.88$ whilst for 6 clicks the value is 0.91. Using the values of ℓ given earlier as 2.24mm and 3.50mm then the ratio of these moments is

$$\frac{M_6}{M_4} = \frac{F_6\ell_6(\cos\theta)_6}{F_4\ell_4(\cos\theta)_4} \qquad (211)$$

when $M_6 = M_4$ (the condition for fracture) then:

$$\left.\frac{F_4}{F_6}\right)_{CALC} = 1.62 \qquad (212)$$

The measured value for this force ratio is:

$$\left.\frac{F_4}{F_6}\right\}_{MEAS} = \frac{2.37 \pm 0.02}{1.47 \pm 0.01} \qquad (213)$$

giving

$$\left.\frac{F_4}{F_6}\right\}_{MEAS} = (1.61 \pm 0.03) \qquad (214)$$

The two ratios therefore agree.

Before the problem of surface pulse propagation is left then the question of the finite spatial extent of the source should be investigated. The theoretical waveforms given in Figure 5 are for a point source as is the

deformation given in equation (210). When the lead fractures then it leaves a small mark on the aluminium surface due to very slight crushing of the tip. This mark has been measured under a travelling microscope to be roughly circular in shape with a diameter of (0.14 ± 0.02)mm. The time taken for the Rayleigh wave to traverse the radius is therefore 23ns. In terms of the time of fracture of the source this contact area is therefore effectively a point. The contact area may be calculated[120] assuming the tip of the pencil to act as a sphere of diameter equal to the diameter of the lead, 0.5mm). This produces a circular contact area of diameter approximately 0.06mm in rough agreement with the measured area above. The calculation involves several approximations and so is not expected to yield an accurate solution.

Equation (120) may now be replaced by a better approximation for the deformation. This improved approximation assumes the load is evenly distributed over the contact area and results in the following[118] for a circular contact area of radius a:

$$r \leqslant a \qquad w = \frac{4(1-\nu^2)}{\pi E} qa \int_0^{\pi/2} \sqrt{1-\left(\frac{r\sin\theta}{a}\right)^2}\, d\theta \qquad (215)$$

$$r \geqslant a \qquad w = \frac{4(1-\nu^2)}{\pi E} qr \left\{ \int_0^{\pi/2} \sqrt{1-\left(\frac{a^2}{r^2}\right)\sin^2\theta}\, d\theta - \left(1-\frac{a^2}{r^2}\right) \cdot \int_0^{\pi_2} \frac{d\theta}{\sqrt{1-\left(\frac{a^2}{r^2}\right)\sin^2\theta}} \right\} \qquad (216)$$

where q is the load per unit area.

The result of this calculation is plotted in Figure 92.

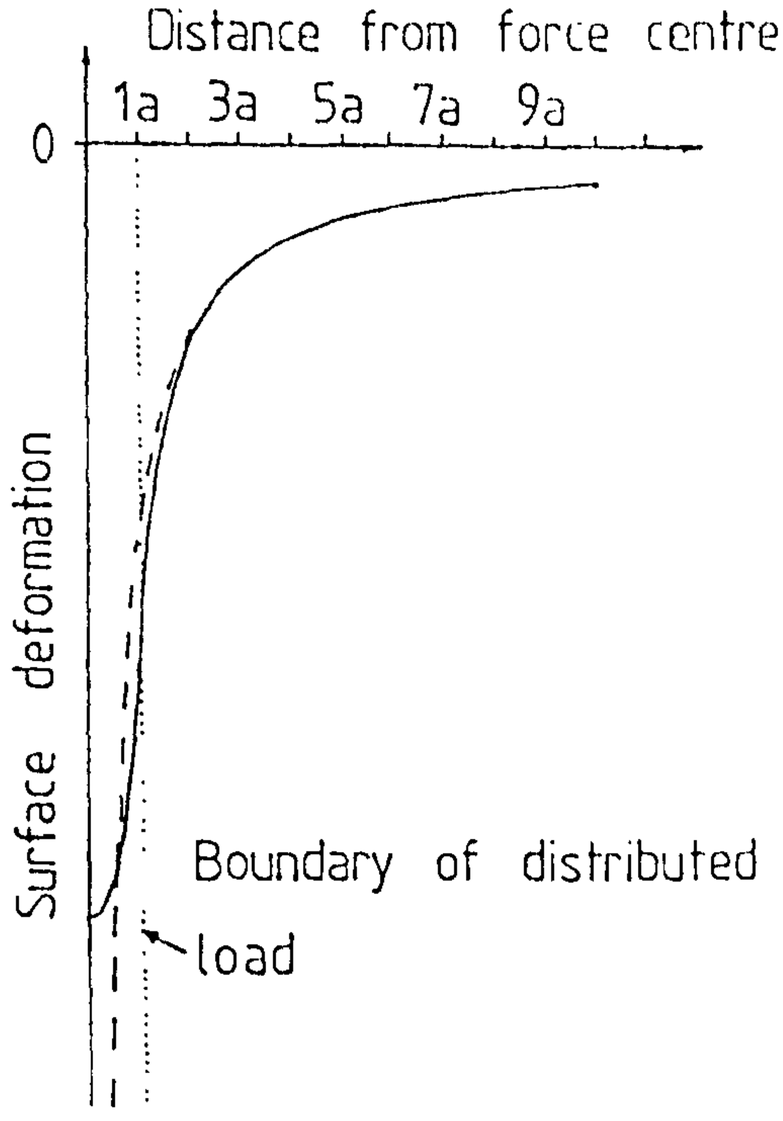

Figure 92: The surface deformation due to a distributed load (solid line) or a point load (broken line).

It can be shown that for r = 5a the error in using the Boussinesq solution of equation (210) is 1.3%, whilst at r = 7a the error is only 0.2%. Experimental measurements above were only taken for distances greater than 0.9mm. In this case r/a = 13 and so the error in using the Boussinesq approximation is negligible.

The pseudo-static displacement at the centre of the pencil contact area before fracture may now be roughly calculated. For 4 clicks assuming a contact area of radius 0.07mm and a displacement at a source detector separation of 1mm of 90Å, then the displacement at the centre is 0.252μm. This result is only approximate as it depends strongly on the actual contact area.

Once the solution for the deformation has been derived then the energy stored in this deformation may also be calculated. The energy stored in creating a deformation w(r) with a force F(r) is

$$U(r) = \int_0^{w(r)} F(r)\, dr \qquad (217)$$

The force in the calculation above acts over an area πa^2 with $F = q\pi a^2$. Hence between r and (r + dr) the force is $2\pi rqdr$. Therefore from equation (217):

$$U(r,r+dr) = \int_0^{w(r)} 2q\pi r dr dw \qquad (218)$$

From equation (215) then $q = \alpha(r)\, w(r)$ where $\alpha(r)$ is some function of r and so:

$$U(r,r+dr) = \int_0^{w(r)} 2\alpha(r)\pi w(r) r dr dw \qquad (219)$$

which can be integrated to give

$$U(r,r+dr) = 2\pi\alpha(r)\frac{w^2(r)}{2} rdr \qquad (220)$$

leading to a total potential energy of

$$U = \pi q \int_o^a r.w(r)dr \qquad (221)$$

This may be numerically integrated using equation (215) to give U ≈ 350nJ which is then the energy introduced into the aluminium by the pencil break (lead diameter 0.5mm extended by 4 clicks). This value of 350nJ agrees reasonably well with an estimate of the energy contained in the travelling elastic waves. The energy in these waves may be calculated from the amplitudes and profiles of the waves (see Appendix 8) and is determined to be 200nJ.

In summary then, the initial deformation is well described by Boussinesq's solution (equation (210)) but the actual form of the fracture event, in containing a compressive component, means that it is very difficult to extract other parameters from the observed waveform. The general form of the pulse as it propagates over the surface appears to be given accurately by the convolution of the theoretical waveform given by Pekeris[19] with a source of finite rise time containing a compressive preliminary component.

IV.1.1ii)b)ii) The effect of changing the length of the protruding lead in the Hsu/Nielson source

In the previous section it was shown that when the

lead length was 3.50mm then the height of the Rayleigh step deviated from its expected $1/r^{\frac{1}{2}}$ behaviour. This was explained by the fact that the source was not a simple release but probably had a compressive component indicated by a dip before the s and p-wave arrivals. This dip was more evident for the 6 click extensions than for the 4 click extension. In order to investigate this more thoroughly a series of experiments were performed in which the extension length and angle of contact θ (see Figure 91) were varied.

For the first experiment the number of clicks used to extend the lead was varied whilst the collar about which the pencil was pivoted remained unchanged. The results of these experiments are shown in Figure 93 in terms of the surface displacement at a distance from the source of 35 ± 1mm.

Clearly as the extended lead length becomes greater then the traces in Figure 93 resemble the theoretical solution for a step input less and less. Two parameters are being varied in this experiment. The first is of course the free length of lead whilst the second is the angle of contact. To remove some of the ambiguity caused by varying both these parameters together then a further experiment is necessary.

This second experiment was to vary the angle of contact for some of the lead lengths shown in Figure 93. To do this the collar was removed and the angle of contact reduced down to an approximately constant 10^{o}. Figure 94

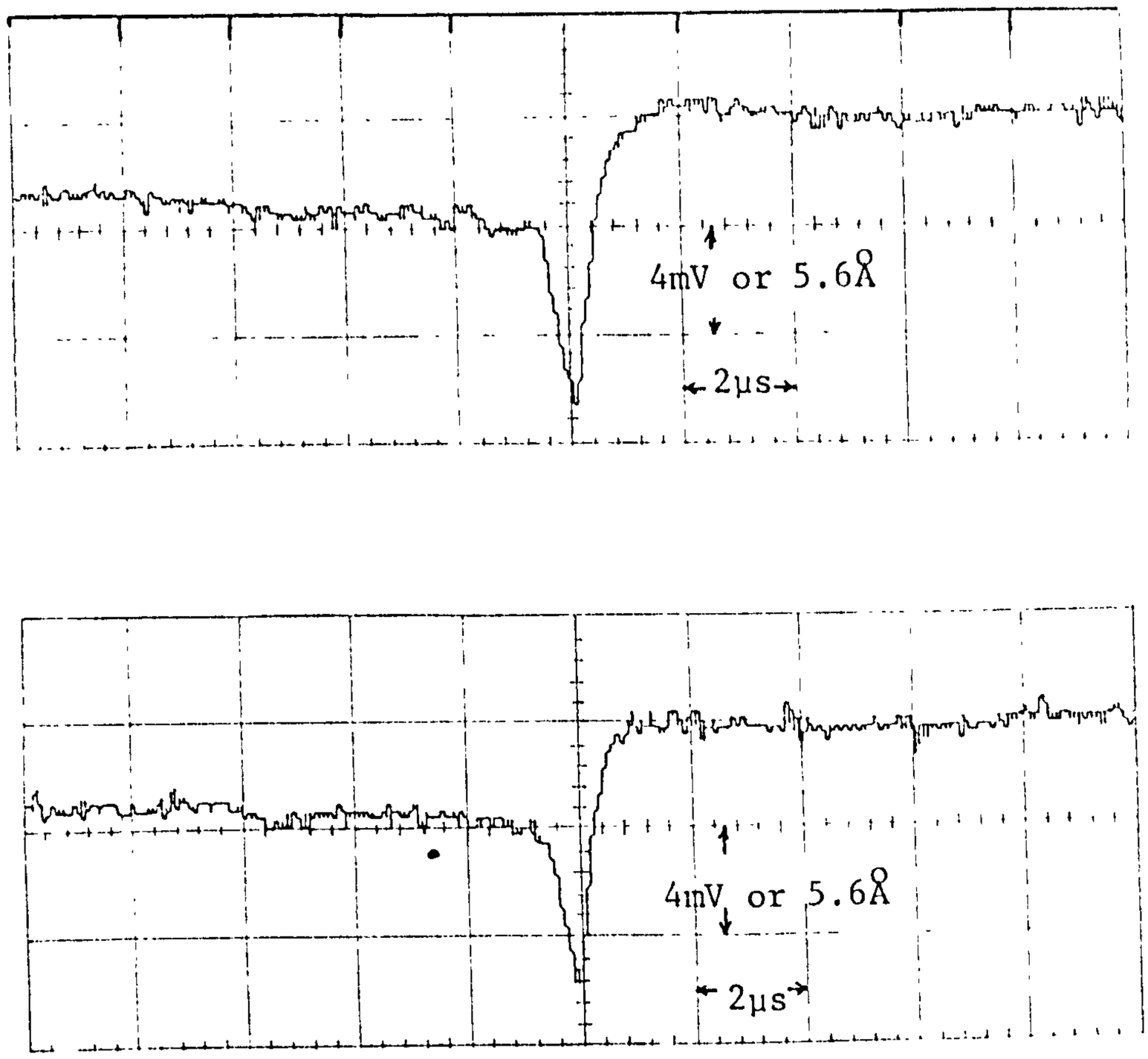

(a)

(b)

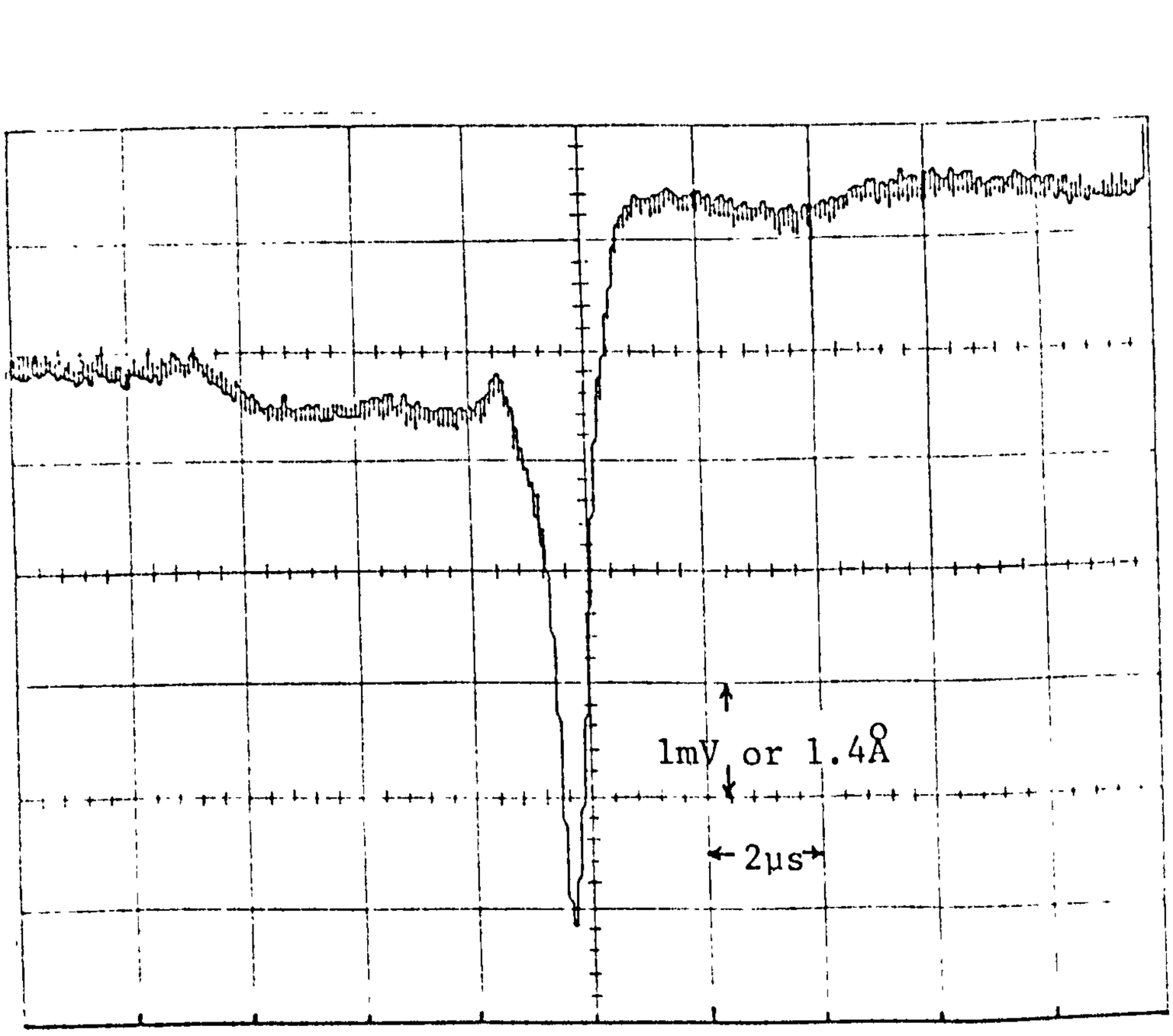

(c)

Figure 93: Part 1. (Part 2 overleaf).

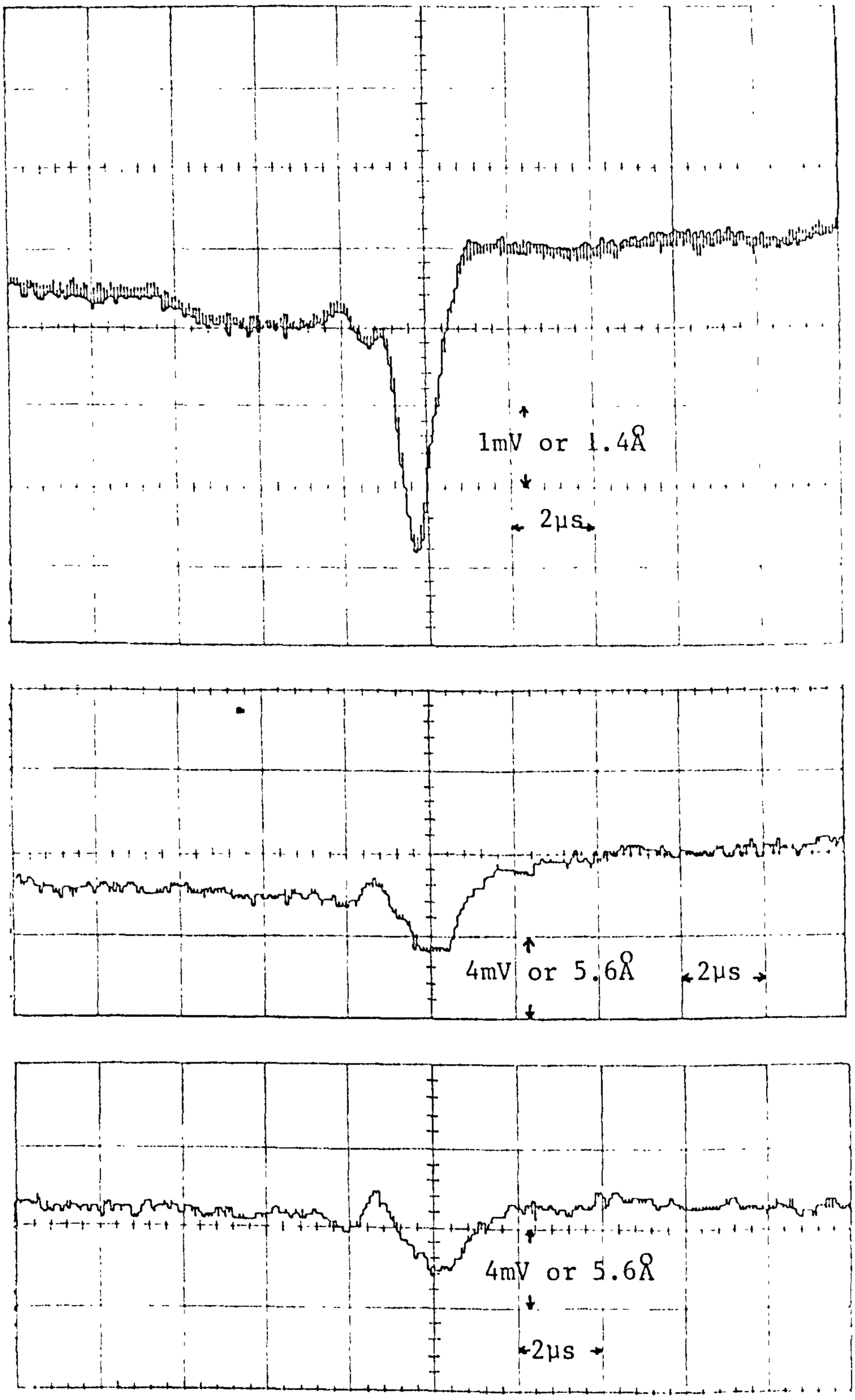

Figure 93: The variation in ultrasonic waveform produced when different lengths of extended lead are broken in the Hsu/Nielson source. The changes in lead length were brought about by varying the number of clicks of the propelling mechanism. The lengths are as follows: (a) 3 clicks (1.8mm); (b) 4 clicks (2.3mm); (c) 6 clicks (3.5mm); (d) 8 clicks (4.6mm); (e) 10 clicks (5.8mm) and (f) 12 clicks (7.0mm). Traces (c) and (d) are averaged over 16 events.

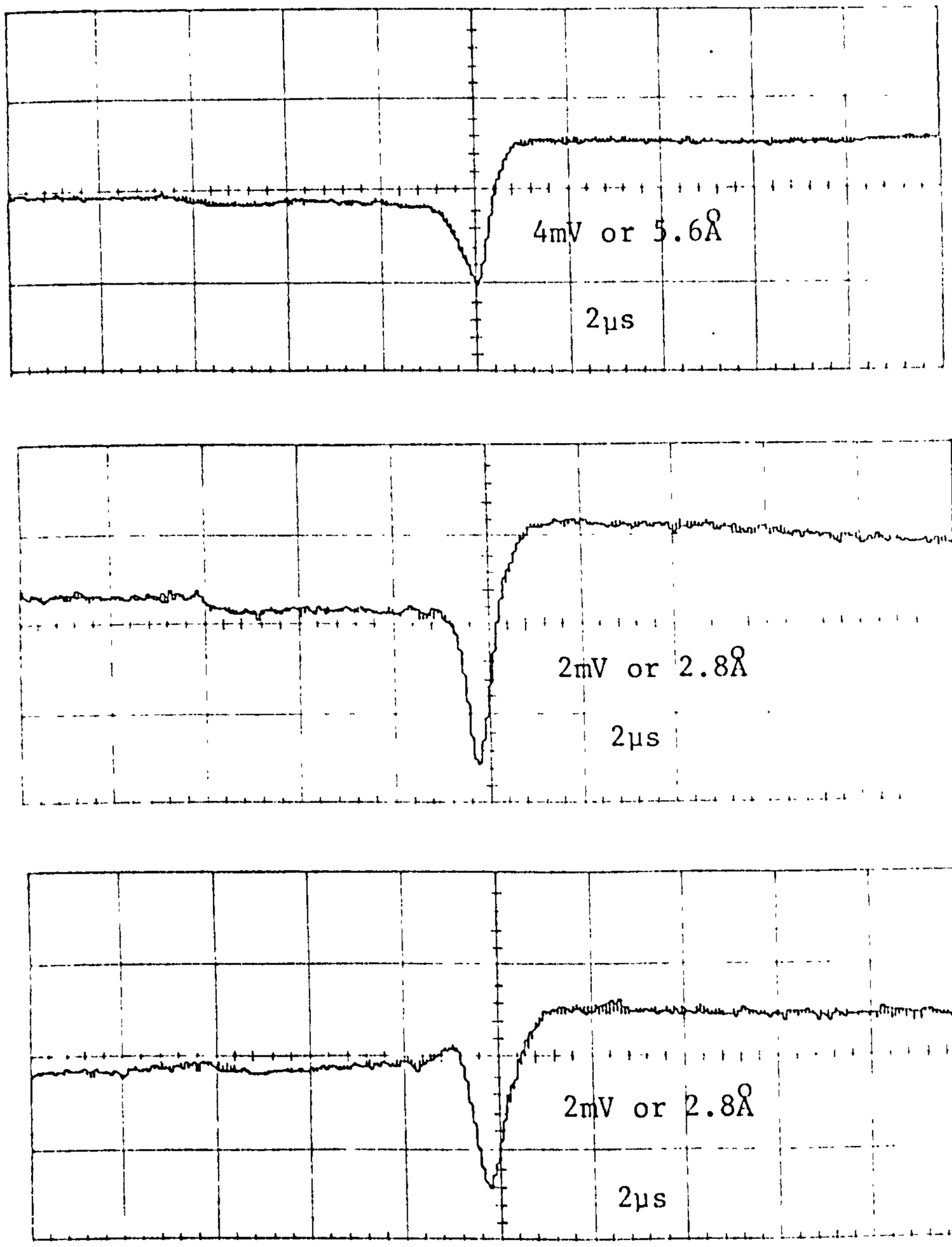

Figure 94: The variation in the ultrasonic pulse generated by a Hsu/Nielson source as the length of the extended lead is changed. The propagation distance is a constant (35±1)mm and the contact angle between the lead and surface is roughly fixed at 10^{o}. The lead lengths are as follows:
(a) 4 clicks of the propelling mechanism (2.3mm);
(b) 6 clicks, (3.5mm); (c) 8 clicks (4.7mm).
An average of 16 events is taken for each trace.

shows the results of such experimentation. In each case the deviations from the predicted waveform for a step release are reduced.

The results given above resolve the discrepancies in the literature about the compressive dip before the main release. This dip does indeed exist. The fact that this dip varies in form according to the angle of contact and length of lead has not however been previously reported. It is not possible therefore to compare the results shown in Figures 93 and 94 with those of other workers.

It would be desirable to be able to explain the form of the waveforms shown above in terms of the actual mechanism of the generating source. The source is a fracturing cantilever with forces acting on it prior to fracture as shown in Figure 95. Calculations in appendix 9 show that the deformation of the free length of lead prior to fracture is governed almost entirely by the force $F\cos\theta$ and that this force is also responsible for the stresses actually causing fracture (for $\theta < 45^{o}$). The calculations also indicate that the lead flexes by an angle α which depends on the square of the length of the extended lead. Therefore for a constant angle θ a long length of lead produces a poorer approximation to a simple release than does a short piece of lead. This therefore explains the results of Figure 94.

When the angle θ is varied up to about 45^{o} these calculations however indicate that the deformation and state of stress at fracture is effectively unchanged. This leads

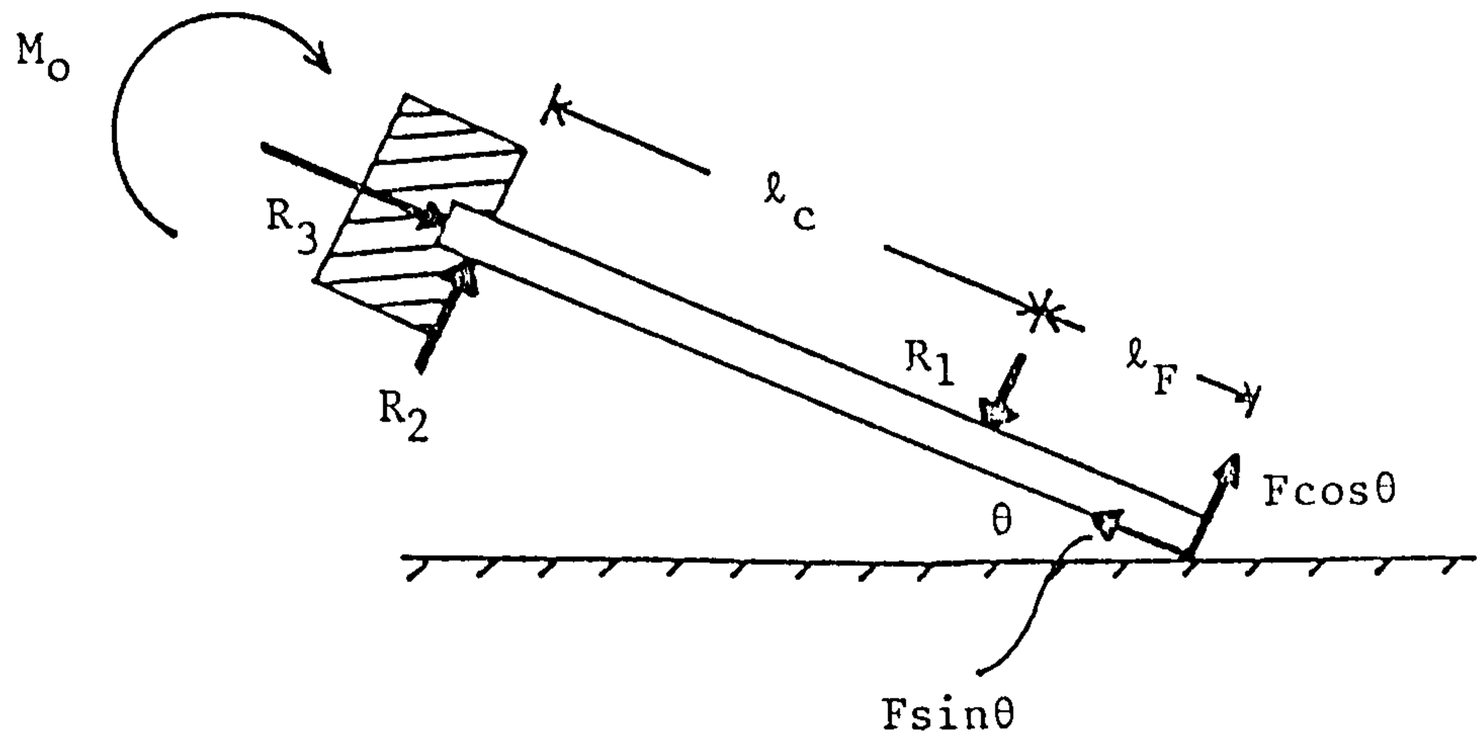

Figure 95: The forces acting on the extended length of ceramic lead in the Hsu/Nielson source.

to the conclusion that the increased departure from a pure step release noted in Figure 93 with larger angles 0 for a given lead length must be due to an increased coupling of the flexural and compressional release waves, from the fracture process, into the surface onto which the lead is being pushed.

The type of release which is most useful as an artificial source of acoustic emission will be that most closely resembling a pure release. Such a source allows simple parameters such as system rise time etc. to be more easily extracted without the need for full deconvolution. This would suggest a pencil length given by 4 clicks of the propelling mechanism and a contact angle less then 10^{o}.

IV.1.1ii)b)iii) The effect of changing the diameter of the protruding lead in the Hsu/Nielson source including source deconvolution using a fast Fourier transform

The time taken for a crack to propagate across the thickness of the pencil lead should determine the release time for this source. Clearly this ought to be made as short as possible. In order to test this hypothesis three different thicknesses of lead have been used: 0.3mm, 0.5mm and 0.7mm.

Figure 96 shows typical waveforms detected at a distance of 35 ± 1mm using the stabilized detector. The minimum detectable displacement being 25pm (r.m.s.) which agrees with the theoretical shot noise limit (see chapter III). Varying the length of the lead produced the effects

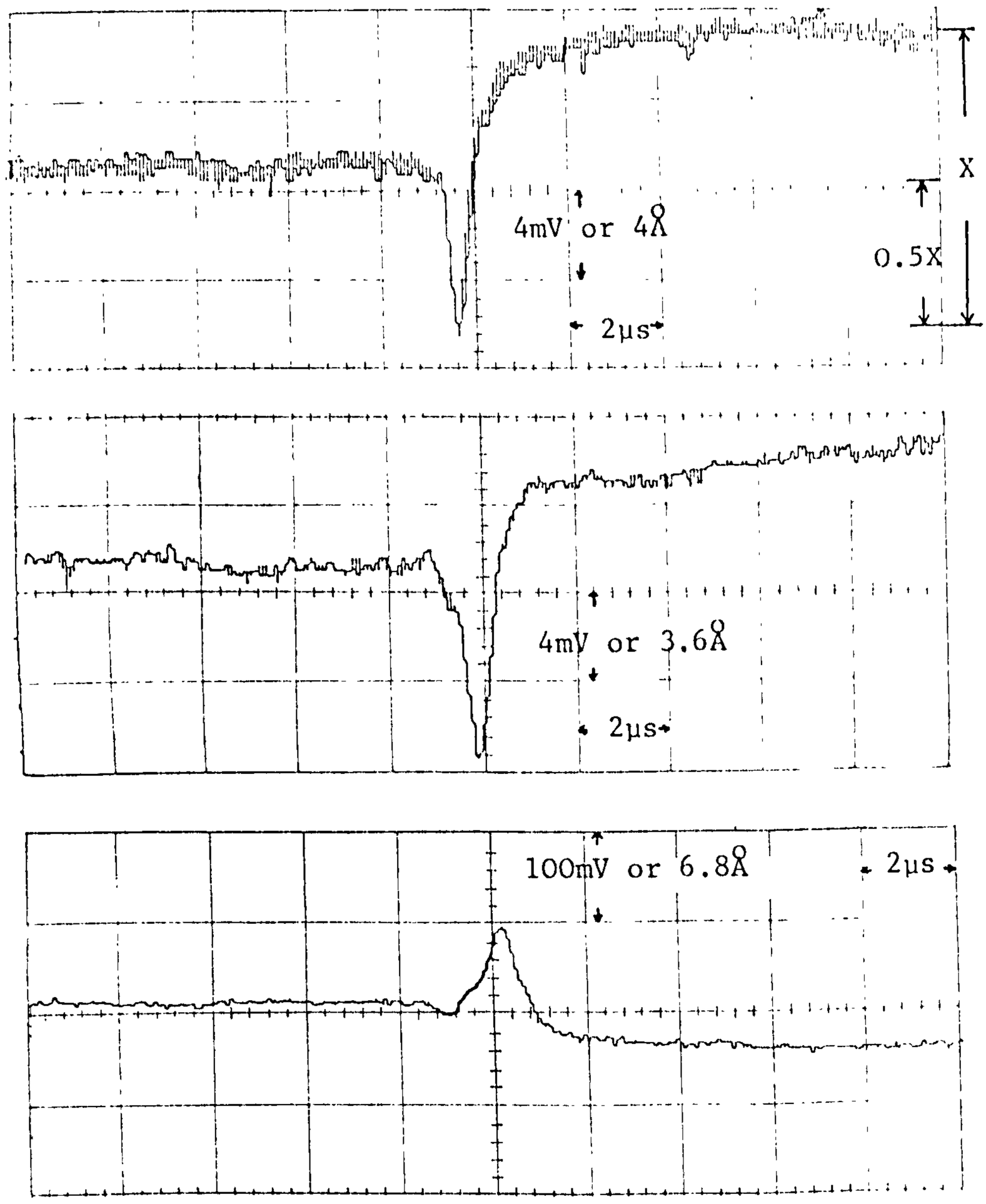

Figure 96: Typical waveforms detected 35mm away from a Hsu/Nielson artificial acoustic emission source. The three traces are for lead thicknesses of (a) 0.3mm, (b) 0.5mm and (c) 0.7mm. The voltage output of the photodiode in trace (c) is amplified by -12.75.

described in the previous section which noticeably changed the rise times of the Rayleigh waves. In order to get a valid comparison for this rise time traces which are similar in overall shape are therefore chosen. It was unfortunately not possible to maintain exactly the same shape and so some errors might be expected.

For the three traces shown the rise times have been calculated on the time taken to rise from the minimum value on the trace to 50% of the final value (0.5X on Figure 96) and are found to be:

0.3mm diameter: rise time 320ns

0.5mm diameter: rise time 430ns

0.7mm diameter: rise time 511ns

These results are in the ratio of 3.0:4.0:4.8.

Although the thinner diameter lead produces the fastest trace merely using the rise time of the Rayleigh appears not to give a complete answer concerning the source rise times. This occurs as the minimum peak in the trace arises really from a convolution of the source and the propagation function and as such it is not merely pure Rayleigh wave beyond this peak, but a combination of shear and Rayleigh due to the finite source time.

Some sort of deconvolution should therefore be performed to provide a better estimation of the source rise time. Equation (20) in seciton II.6.1 is given as:

$$\underline{S}(\underline{x}_o,\omega) = \underline{U}(\underline{x},\omega)/\underline{G}(\underline{x},\underline{x}_o,\omega) \qquad (20)$$

where $\underline{S}$ is the source force function at $\underline{x}_o$, $\underline{U}$ the displacement at $\underline{x}$ and $\underline{G}$ the propagation function. In terms of the modulus only this becomes (dropping the tensor representation):

$$|S(\underline{x}_o,\omega)| = |U(\underline{x},\omega)| \,/\, |G(\underline{x},\underline{x}_o,\omega)| \qquad (222)$$

It is not easy to obtain numerical values for G but the Heaviside Green's function $G^H(\underline{x},\underline{x}_o,\omega)$ is readily available. Now G^H is given by the convolution of G with the Heaviside function H:

$$G^H(\underline{x},\underline{x}_o,t) = \int_o^t G(\underline{x},\underline{x}_o t - \tau)H(\tau)\, d\tau \qquad (223)$$

The Fourier transform of equation (223) is

$$\int_{-\infty}^{+\infty} G^H(\underline{x},\underline{x}_o,t)e^{-i\omega t}dt = \int_{\infty} e^{-i\omega t}\left(\int_o^t G(\underline{x},\underline{x}_o,t\ -\tau)H(\tau)d\tau\right)dt \qquad (224)$$

therefore

$$G^H(\underline{x},\underline{x}_o,\omega) = G(\underline{x},\underline{x}_o,\omega).H(\omega) \qquad (225)$$

and

$$H(\omega) = \int_{-\infty}^{+\infty} H(t)e^{-i\omega t}\, dt \qquad (226)$$

To make the solution physically sensible a factor $e^{-t/\tau}$ is introduced where τ is very large compared to the time scales of interest. Equation (226) becomes

$$H(\omega) = \int_{-\infty}^{+\infty} H(t)e^{-t/\tau}\, e^{-i\omega t}\, dt \qquad (227)$$

$$H(\omega) = \frac{-1}{i\omega+1/\tau} \qquad (228)$$

or approximately

$$H(\omega) = \frac{i}{\omega} \tag{229}$$

Substituting equation (229) into equation (225) and then into equation (20) gives

$$\underline{S}(\underline{x}_o,\omega) = U(\underline{x},\omega)(i/\omega)/_{G^H(\underline{x},\underline{x}_o,\omega)} \tag{230}$$

Again in terms of the modulus equation (230) can be rearranged to yield

$$\omega|S(\underline{x}_o,\omega)| = |U(x,\omega)| \,/_{|G^H(\underline{x},\underline{x}_o,\omega)|} \tag{231}$$

The only problem remaining is how to obtain numerical values for $|G^H(\omega)|$. It will be shown later that the fracture of a glass capilliary produces a waveform which is almost identical to theoretical predictions given by Mooney[25]. If the theoretical waveform is correct then this experimental result could be used. Results given later in this chapter will verify the theoretical waveform, therefore the experimental waveform obtained from the glass capilliary fracture is taken as $G^H(t)$.

A fast Fourier transform (FFT)† computer program is used to determine $G^H(\omega)$. A fast Fourier transform calculates the Fourier series expansion for a given waveform. The waveform, of finite time interval T, is assumed to be a repetitive signal of the period T. If there is a shift in level between the start and end of the time period T then repeating the signal would cause spurious effects. These problems are usually overcome by the use of a window. This window is a smoothly varying function which decays to

† This was adapted for use on an Apple IIe microcomputer by Mr. M.W. Godfrey

zero at each end of the time period T. Multiplying the original waveform by this window function therefore removes most of the problems associated with the repetition process (see Appendix(C). The window used in the experiments in this and subsequent chapters is a Hanning window given by

$$f(t) = 0.5\ (1 - \cos(2\pi t/T)) \qquad (227)$$

The waveform is of course digitized and so the integrals required in the Fourier series expansion are replaced by finite sums. It can be shown that many of the multiplications needed to evaluate such sums occur more than once. Multiplications take a relatively long time for computers to perform and so a fast Fourier transform saves time by calculating only the minimum number of multiplications and then using these results in the various summations[121]. Results given in Appendix 10 show that the FFT algorithm used produces quite accurate results for the Fourier series when no noise is present. However when fairly high noise does occur the results contain significant errors in the phase. These errors arrive because of the use of divisions involved in determining the phase together with the manner in which the phase results are later manipulated.

As this FFT produces good results for the modulus of the Fourier series then it can be used to evaluate equation (231). The results of the calculation of $|U(\omega)|/|G^H(\omega)|$ are given in Figure 97a. In each case the result is found to fall off at some point. The

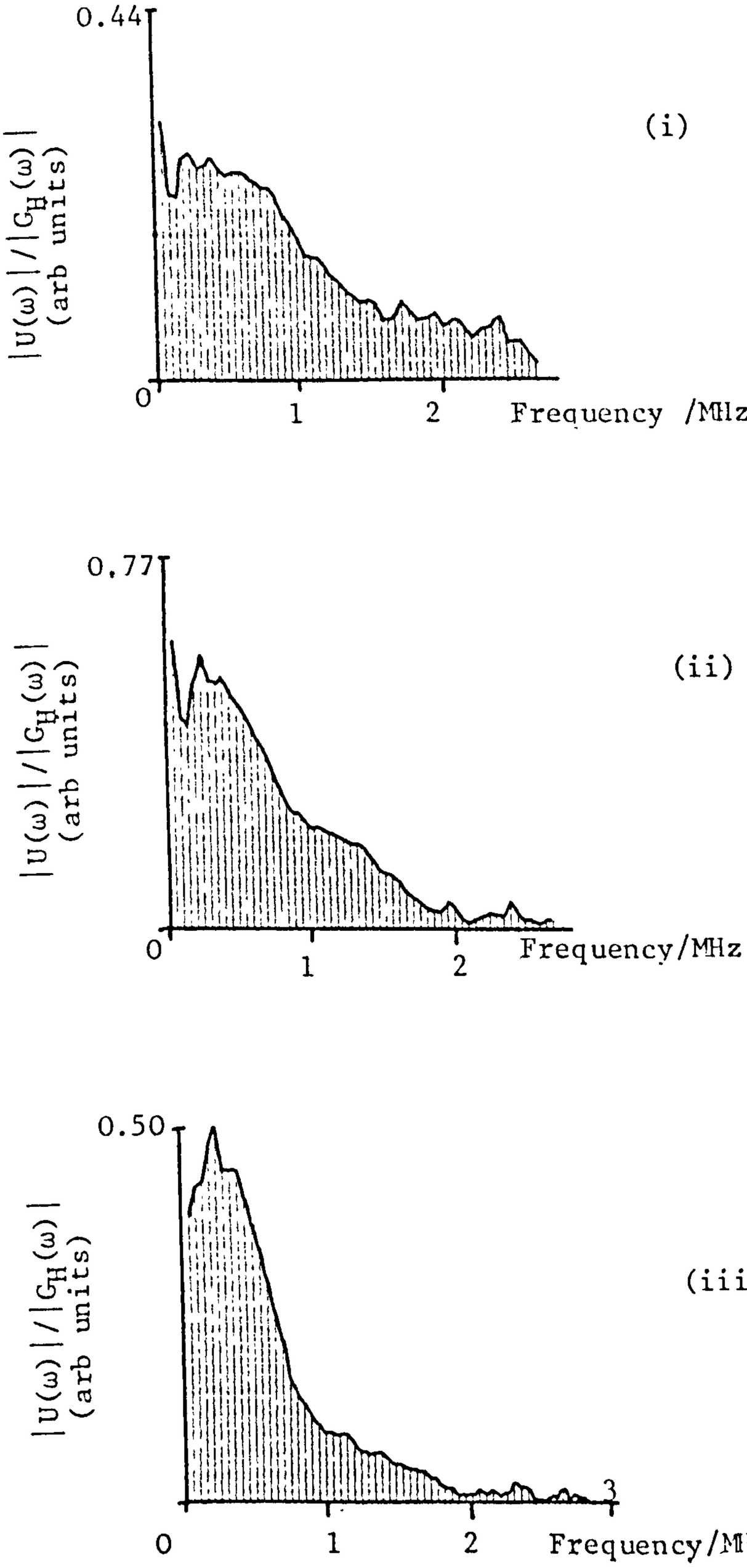

Figure 97a): The results of the calculation $|U(\omega)|/|G_H(\omega)|$ where $U(\omega)$ is the frequency domain surface displacement due to a Hsu/Nielson source at a distance of 35mm. The three traces (i), (ii) and (iii) are for lead diameters of 0.3, 0.5 and 0.7mm respectively.

approximate frequencies (f3dB) at which the values of the division is found to fall to 70% of its maximum are as follows for the three lead thicknesses

0.3mm diameter lead: f3dB = 950 ± 20kHz

0.5mm diameter lead: f3dB = 680 ± 20kHz

0.7mm diameter lead: f3dB = 560 ± 20kHz

the ratio of these being 1.7:1.2:1.0. This ratio does not agree exactly with the ratio of the diameters. This discrepancy may arise due to the different extended length to diameter ratios. It is virtually impossible to maintain the ratio constant with varying lead diameter and consequently the severity of the dip noticed before the shear wave does in fact alter. Alternatively, the fracture velocity may be stress-dependent with the higher velocities occurring in the more highly stressed wider diameter leads.

When a different length to diameter ratio and contact angle is used with the 0.5mm diameter lead (4 clicks with a contact angle of $\sim 0^{o}$ rather than 6 clicks with a contact angle of 24.5^{o}) then the half power frequency point becomes 610 ± 20kHz as shown in Figure 97b. Therefore the variation in the ratios of the half power frequency points from that of the lead diameters is probably mainly due to changes in length to diameter ratios and in contact angles and not due to variations in the fracture velocity.

In section IV.1.2i)b) the waveform generated by a Hsu/Nielson source, employing a 0.5mm diameter pencil lead extended by 6 clicks, is captured at the origin. The product of the frequency and the modulus of the fourier

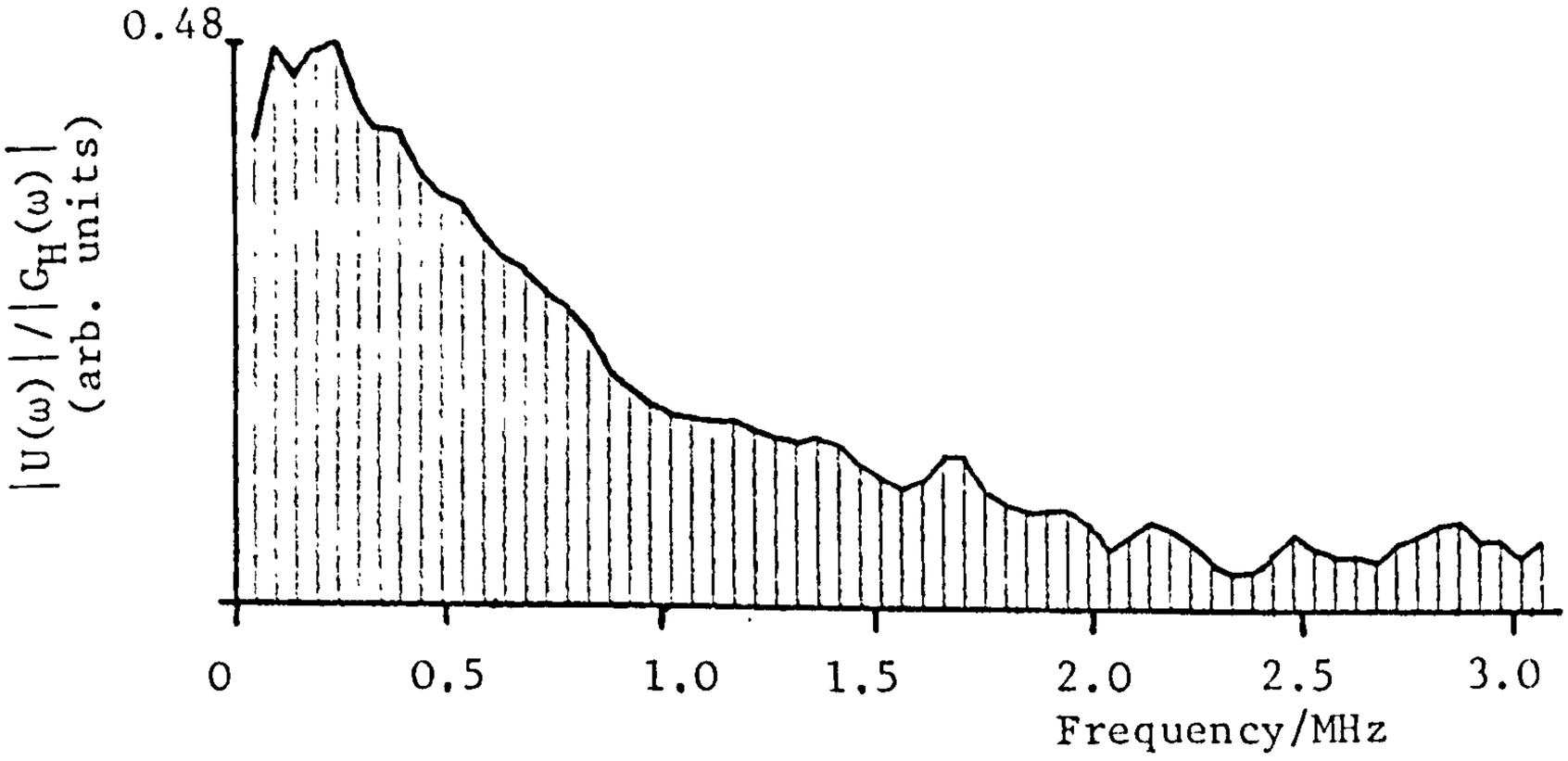

Figure 97b): The effect of varying the length of the extended lead and angle of contact in the Hsu/Nielson source on the calculation $|U(\omega)/|G_H(\omega)|$. This result above is nominally identical to trace (ii) in Figure 97a), but yields a different half power frequency point.

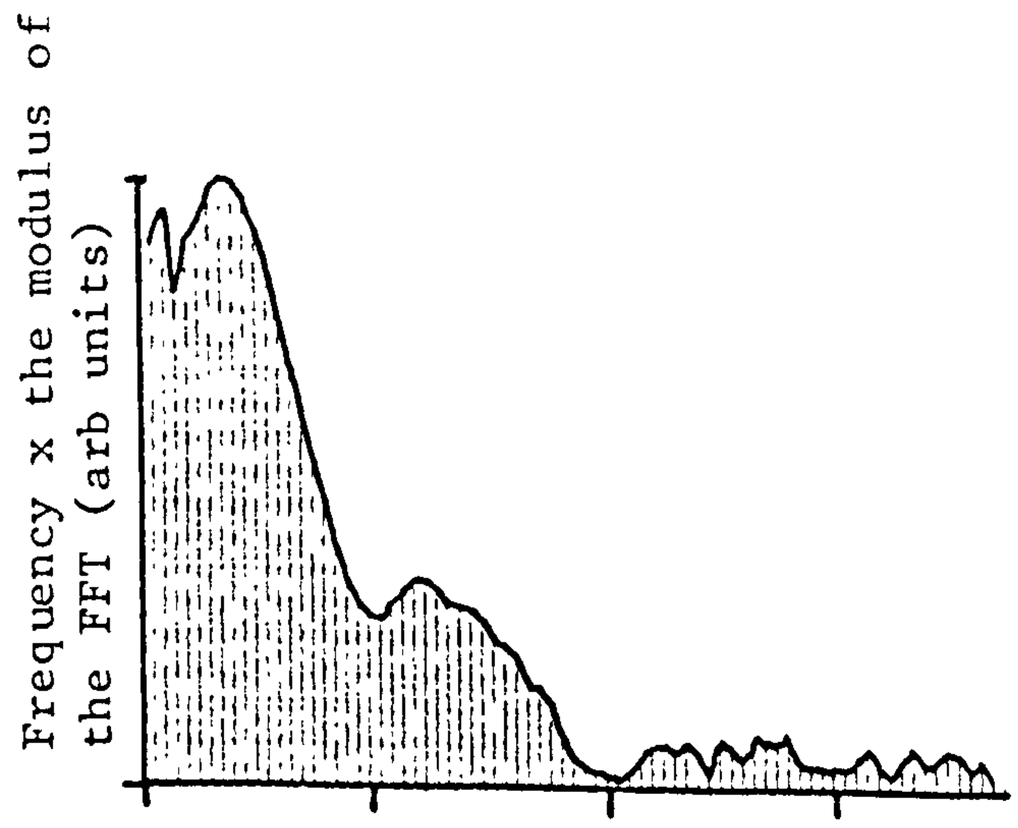

Figure 97c): The result of the calculation: frequency times modulus of the Fourier transform for a Hsu/Nielson source measured at the origin. This trace is nominally identical to trace (ii) in Figure 97a).

transform of this trace should therefore reproduce the corresponding result in Figure 97a. This product is shown in Figure 97c. The agreement is fair, certainly up to f3dB, but with some obvious discrepancies. These discrepancies arise because of the noise or the detected waveform. This noise does not allow the source function to be accurately deconvoluted from the detected waveform using the inverse propagation function thus leading to various errors.

In summary then it appears that the source rise time is probably determined by the time taken for a crack to propagate across the lead diameter. Using $f_{3dB} = 0.35/t_r$, where t_r is the rise time, then the source rise times for the three diameters 0.3mm, 0.5mm and 0.7mm are 0.37, 0.52 and 0.63μs respectively. Therefore none of these sources produce high enough frequency components to be of general use as artificial acoustic emission sources.

IV.1.1ii)b)iv) The frequency domain reproducibility of the Hsu/Nielson source

An important attribute of any artificial source is its ability to generate reproducible events. To be reproducible then not only must the total force released be the same each time but the time history must also be identical from event to event. A test of the reproducibility would be to compare the FFTs of the waveforms, generated by a series of different fractures, at a given constant distance. Ideally, the FFTs would give both phase and modulus information,however as discussed in the previous section

the phase information is somewhat unreliable and so only a comparison of the modulus is possible.

Experiments were performed using a 0.5mm diameter pencil extended by 3 clicks with waveforms recorded by the stabilised interferometer at a distance of 29 ± 1mm. The minimum detectable displacement was 0.4Å which corresponded to the shot noise limit for the optical power available. Four traces were taken in all (Figure 98). These were Fourier transformed and the moduli of the transforms averaged. (Variations in the trigger position affects only the phase of the transform). Each individual transform was then divided by this average to determine the reproducibility. One such result is given in Figure 99 together with the averaged transform.

It can be seen that there is an overall error of ∿ 20% (in terms of the average value between 0 and 1MHz) together with an additional ∿ 10% error about this mean value. A great deal of noise occurs on these traces and so comparisons are difficult. The reproducibility will be further considered when the source-detector separation is much less (see section IV.2.1i)b)).

IV.1.1ii)c) The fracture of glass capilliaries

A common event used as an artificial acoustic emission source is the fracture of a glass capilliary. To create this fracture the capilliary may be either placed in a pencil (that is it replaces the ceramic lead) or may be layed on the material surface and loaded with a knife edge (see Figure 100).

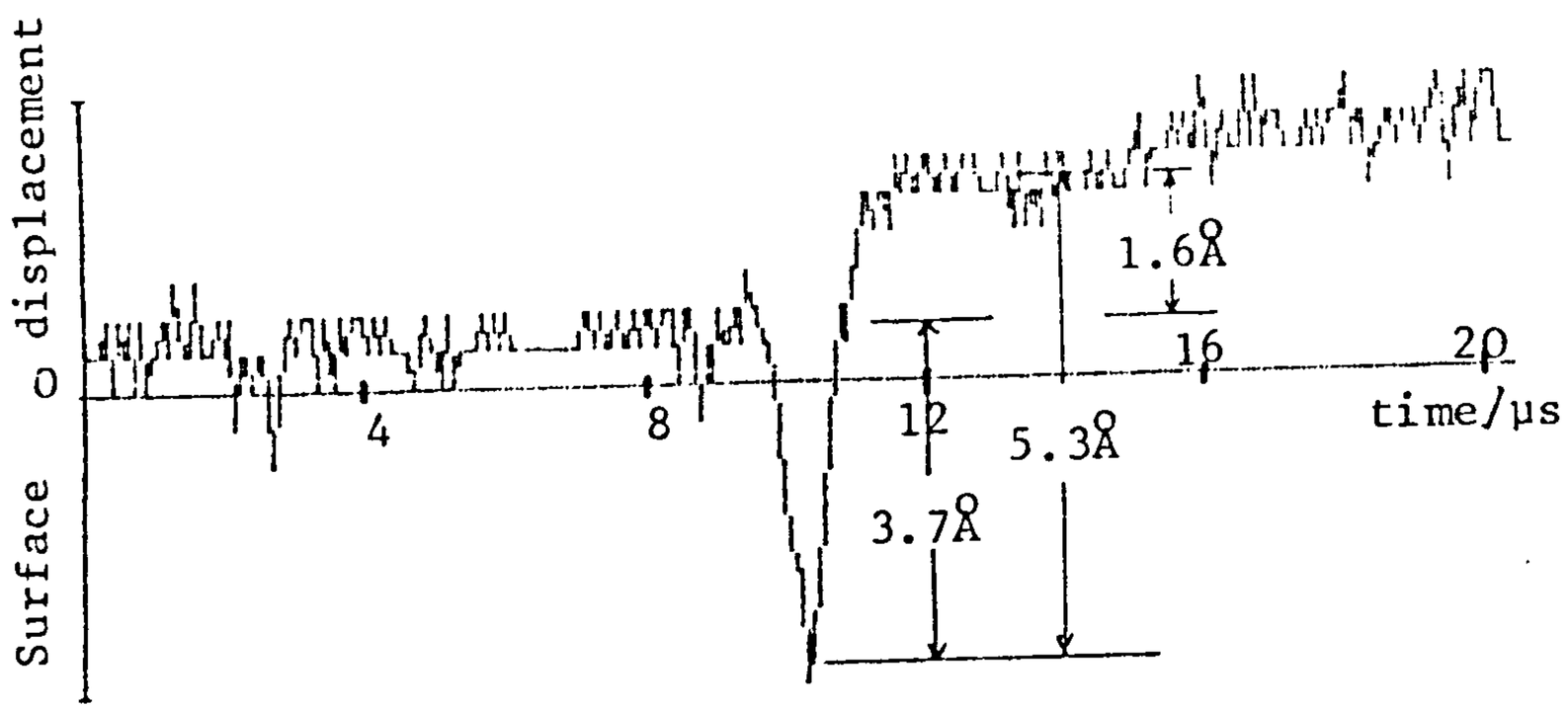

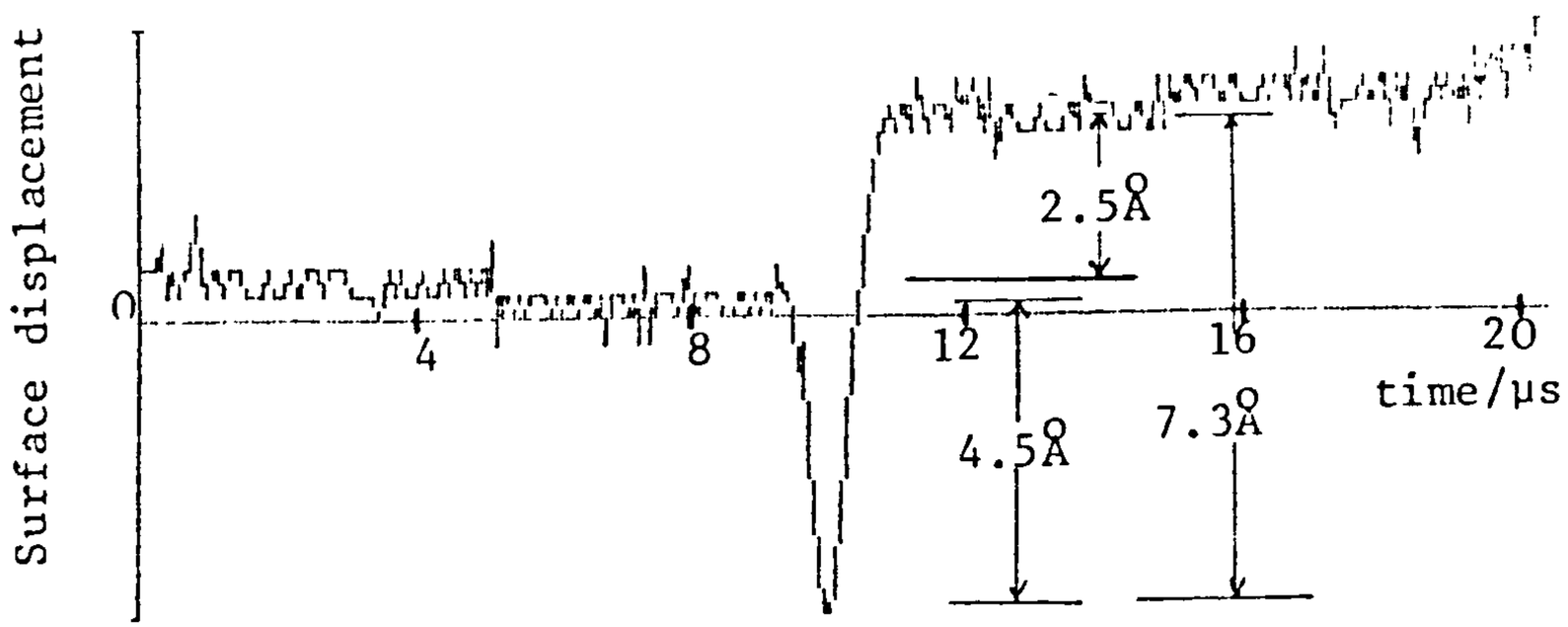

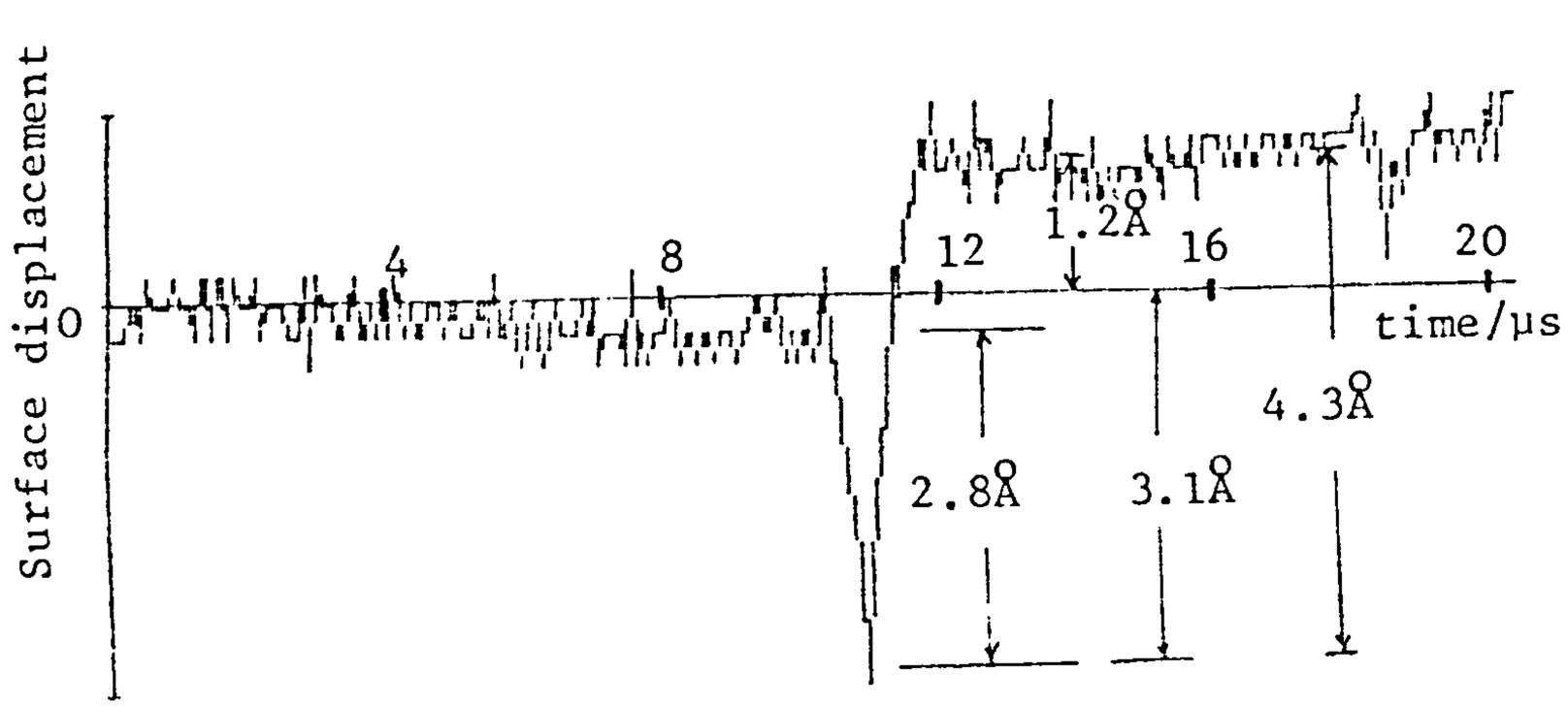

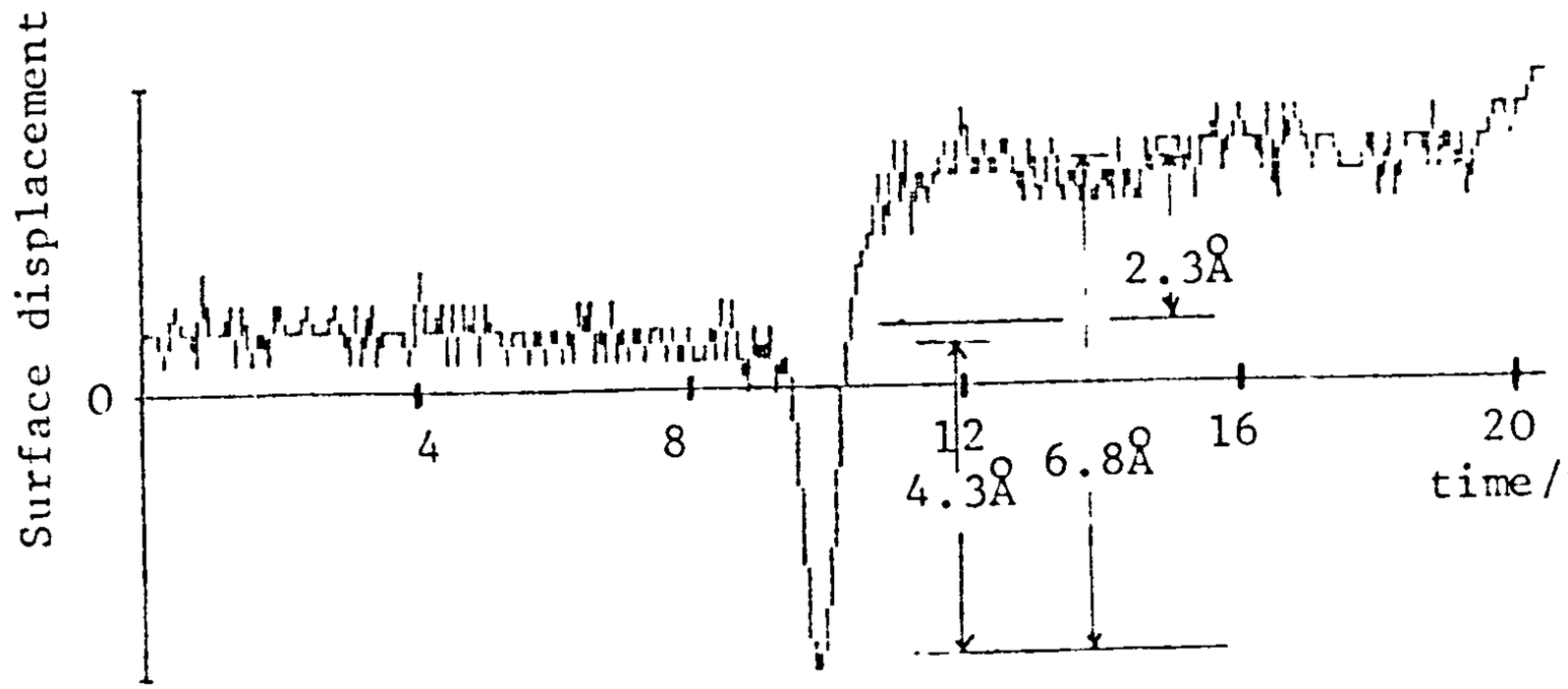

Figure 98: Four nominally identical artificial acoustic emission events generated by a Hsu/Nielson source. The variations between these traces indicates the reproducibility of the source.

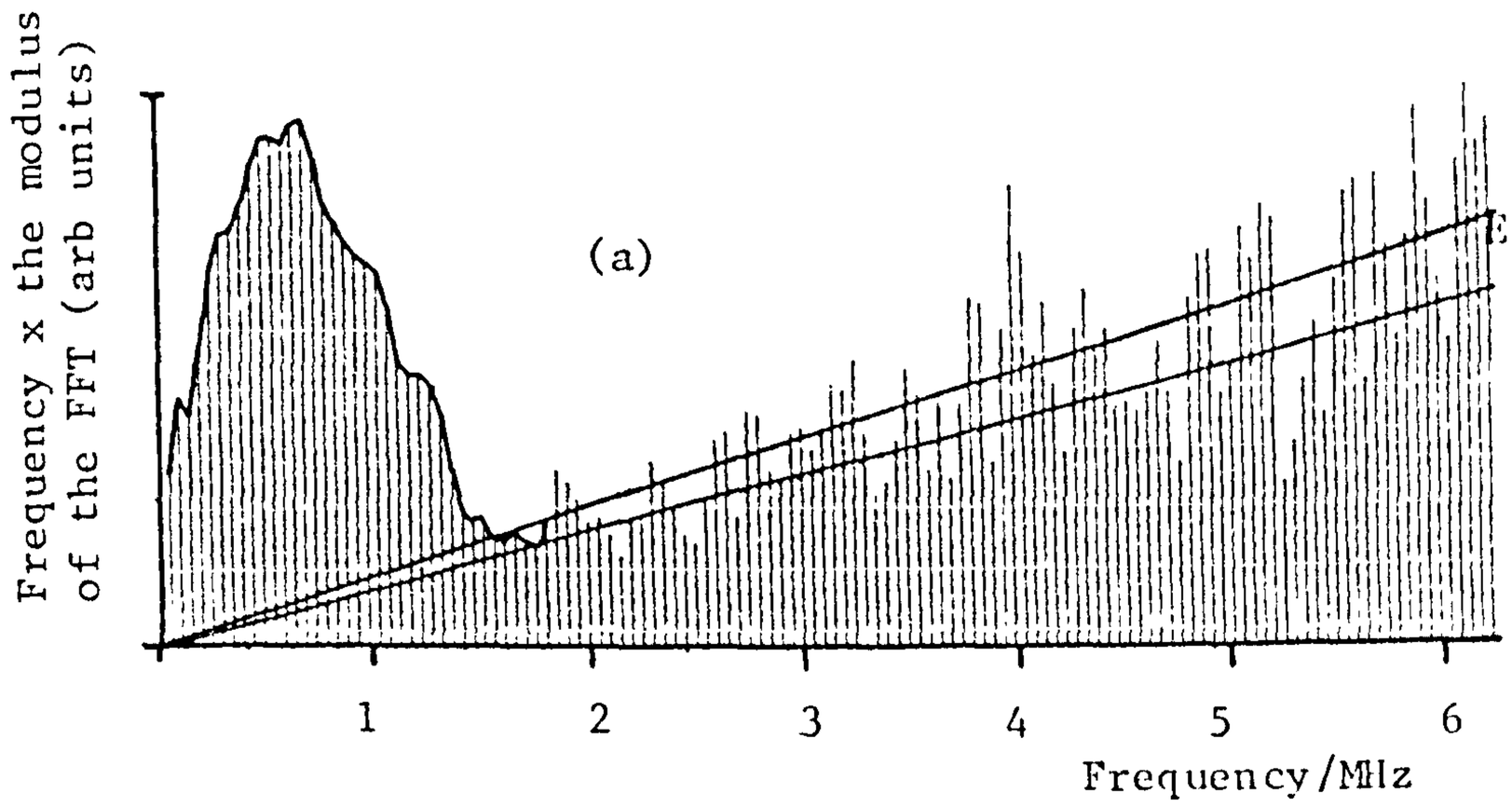

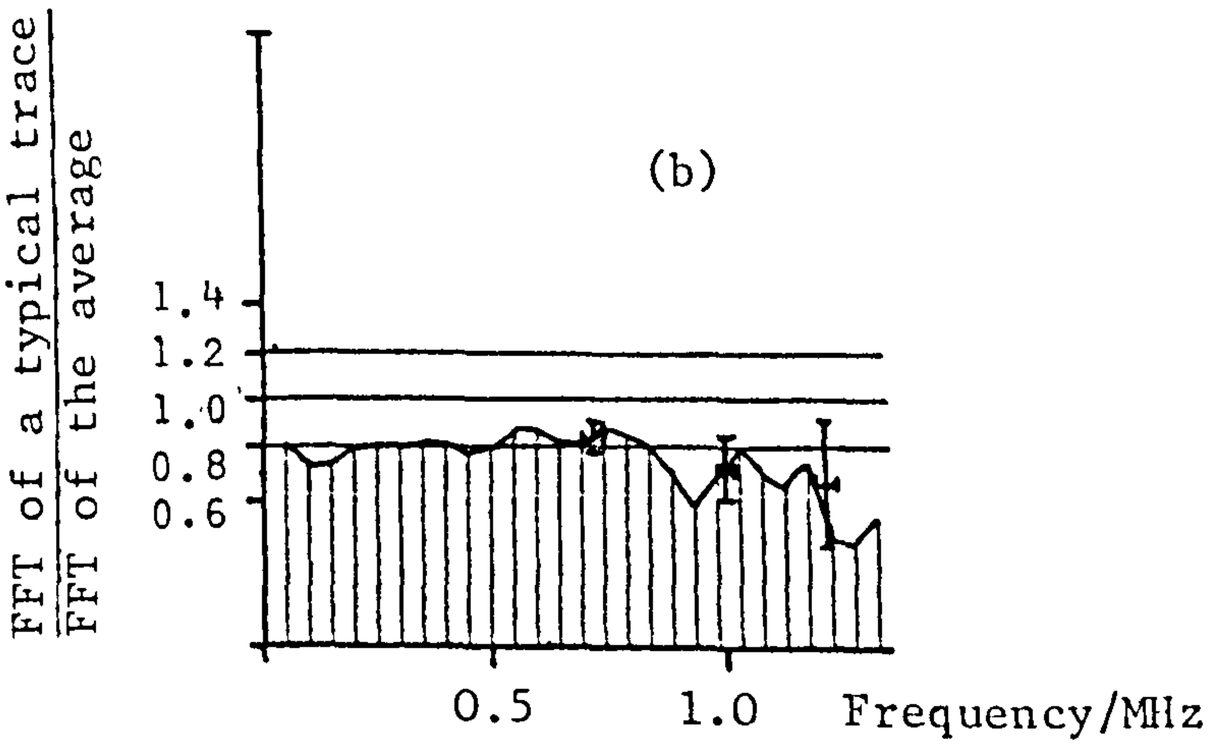

Figure 99: Trace (a) shows the average of the frequency x the modulus of the FFT for the traces shown in Figure 98. Trace (b) shows the transform of one of these waveforms divided by the average transform. As such trace (b) gives the frequency domain reproducibility of the Hsu/Nielson source. The error bars indicate uncertainties in this division.

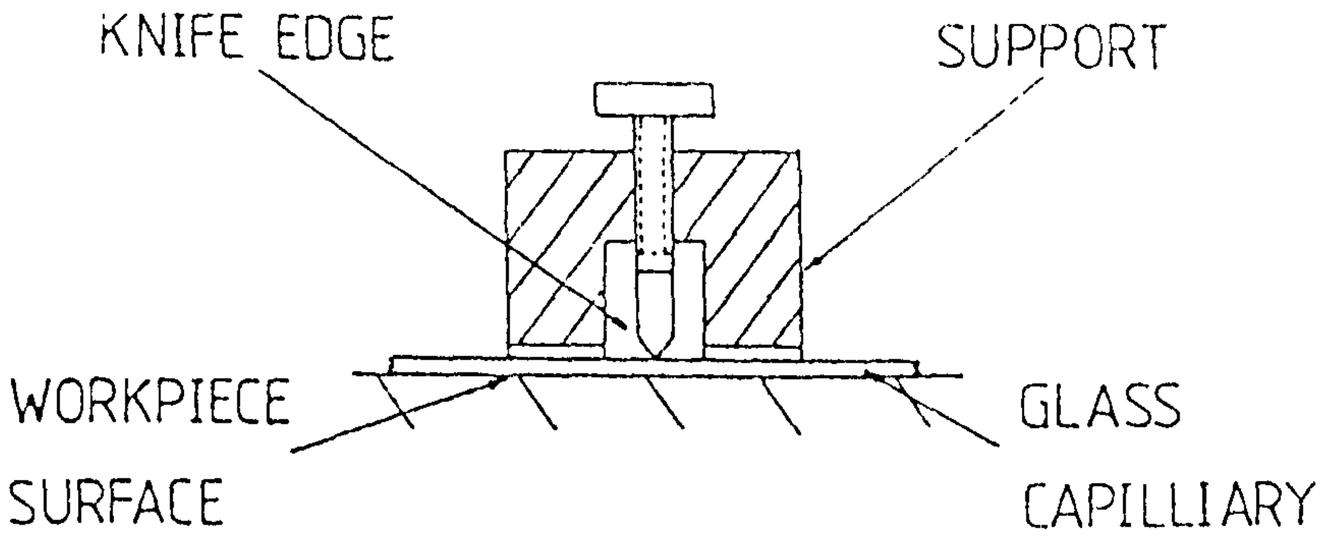

Figure 100: Schematic representation of one method by which capilliaries may be fractured on a material surface.

The first method outlined turns out to be highly irreproducible[122] presumably due to the fact that high stresses are formed in the capilliary where it contacts the surface. This contact point is in general of an irregular shape and so the stress at fracture and the method of fracture will vary.

However, the second fracturing technique produces events all of which are superficially similar. Figure 101 shows typical events for two capilliaries of differing dimensions. The first two traces being for capilliaries of outside diameter (0.27 ± 0.02)mm and a wall thickness of (0.038 ± 0.002)mm whilst the second two are for capilliaries of outside diameter (0.44 ± 0.02)mm and wall thickness (0.062 ± 0.003)mm. The source transducer separation being 39.5 ± 1.0mm.

Similar reproducibility calculations to those outlined in section IV.1.1ii)b)iv) have been performed on the frequency domain results. The error for a single event, from capilliaries of fixed dimensions, in terms of a low frequency average value is 32% whilst the variation from this average is 10% at 1MHz, 25% at 2MHz, 28% at 3MHz and 54% at 5MHz. Measuring errors were not significant. The low frequency average value being not very reproducible leads to large uncertainties in the absolute values of high frequency components. A capilliary fracture then is best used as an artificial source, for in situ calibration, not on its own but in conjunction with another low frequency reproducible source (for instance the Hsu/Nielson source). The reproducibility of the overall shape of the frequency

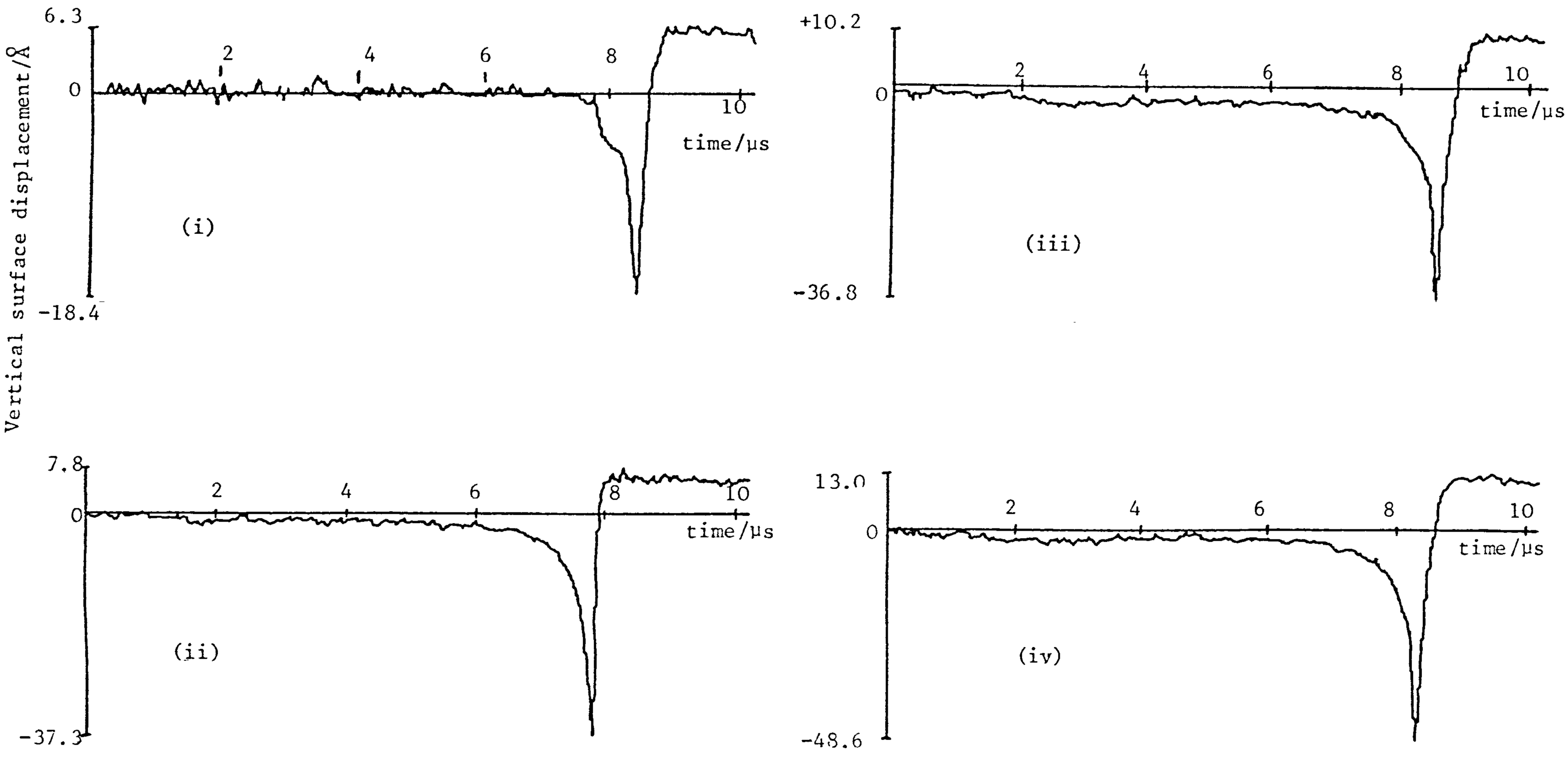

Figure 101: Typical ultrasonic waveforms detected at 39mm from a breaking glass capilliary source. The capilliary was fractured by the device shown in Figure 100. Traces (i) and (ii) are for capilliaries of outside diameter (0.27±0.02)mm and wall thickness (0.038±0.002)mm whilst traces (iii) and (iv) are for capilliaries of outside diameter (0.44±0.02)mm and wall thickness (0.062±0.003)mm.

spectrum is then adequate to allow calibration up to $\sim$ 2MHz.

The results detailed above are the event to event variations arising from the fracture of capilliaries of constant dimensions. Changing the capilliary dimensions alters both the overall average size of the waveforms and also the upper frequency limit. This upper frequency limit appears to be inversely proportional to the wall thickness. Such a relationship appears reasonable as the fracture time is probably given by the time taken for a crack to propagate across the capilliary wall as shown in Figure 102. Assuming this hypothesis to be correct the crack velocity becomes approximately (0.038/0.22) = 0.17mm μs^{-1}. (The fracture time is roughly estimated as being the rise time of the Rayleigh step). Such a figure is approximately 0.05 times the shear wave velocity (v_S) and is therefore similar to the figure of $0.07v_S$, given by Wadley et al[10].

Difficulties in producing large quantities of capilliary of effectively identical dimensions coupled with the variation from shot to shot of the fracture mean that it has not been possible to produce accurate relationships between the capilliary sizes and the shape of the frequency spectrum of the events produced by their fracture.

Further work along these lines would be of interest. If relationships outlined above do exist then a knowledge of them would allow the glass capilliary to be used as a

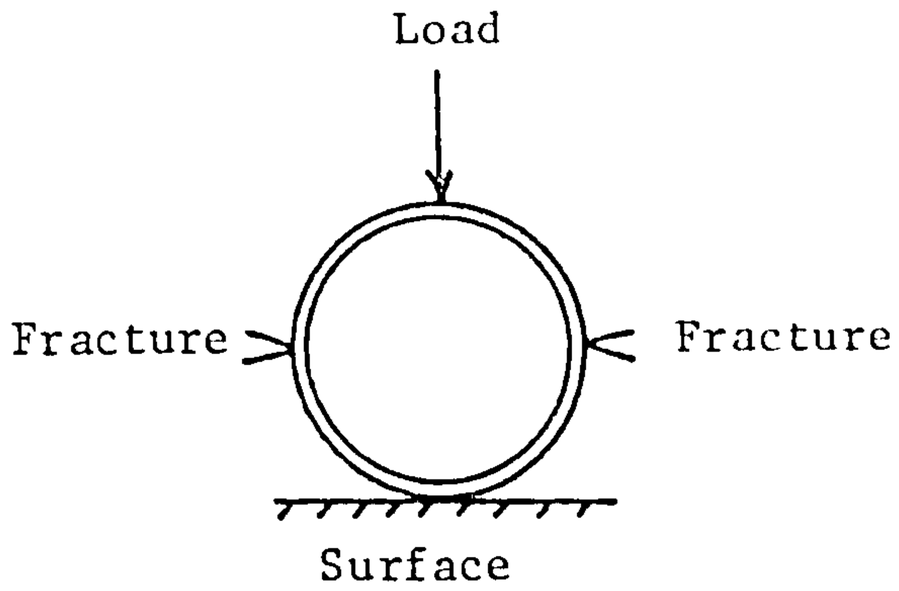

Figure 102: Assumed failure mode for the glass capilliaries broken by the method shown in Figure 100.

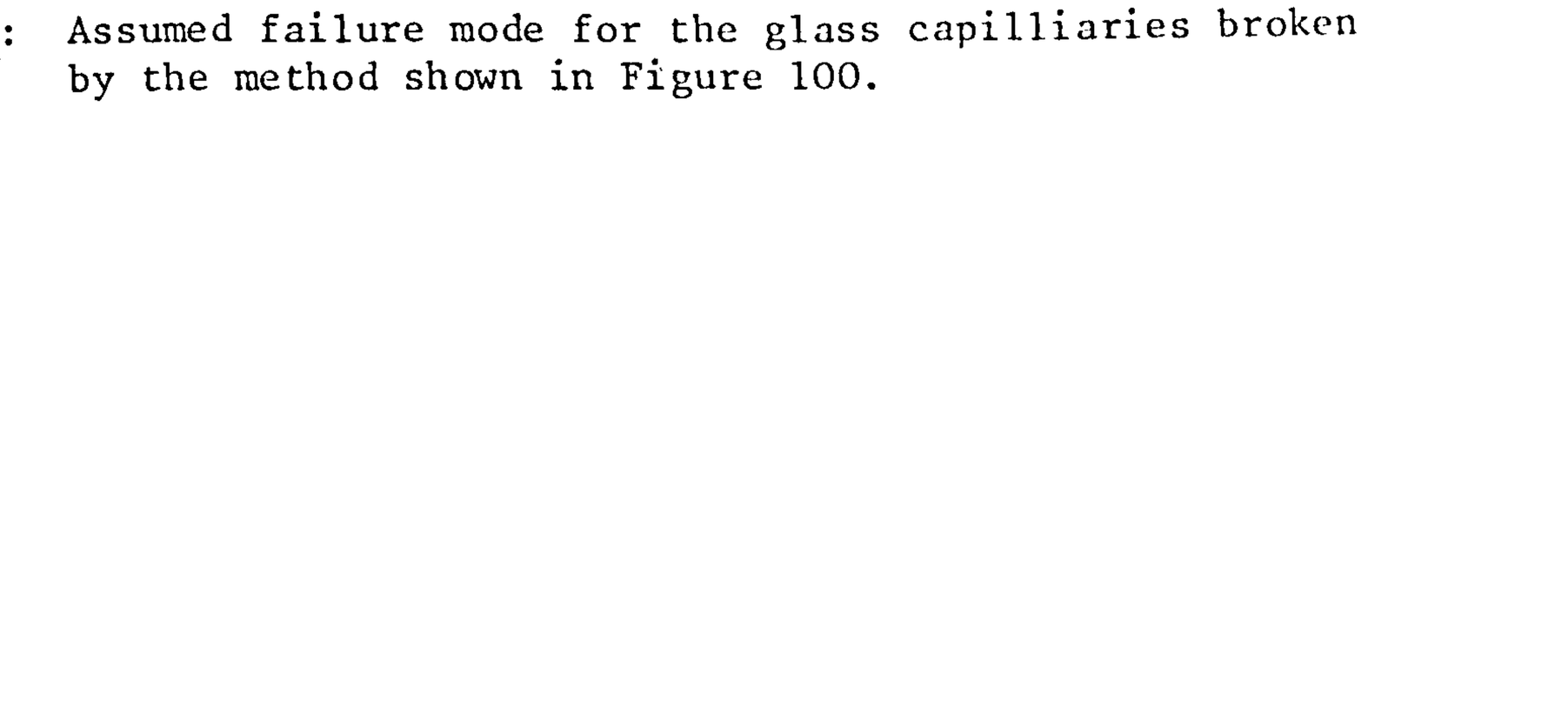

Figure 103: A typical waveform captured at 35mm from an artificial acoustic emission source when the source is the fracture of glass balatini. The detector was the stabilized interferometer.

high frequency artificial source in conjunction with another low frequency source.

IV.1.1ii)d) The fracture of glass balatini

Glass balatini is composed of a great number of small hollow glass spheres with outside diameters of the order of 50 or 100μm. It is used in a variety of applications including laser fusion studies and as an additive to various foodstuffs. As such it is readily available. Fracturing such spheres on a surface should produce a rapid step unloading of the surface[123]. Preliminary investigations have been carried out into this potential source and will now be detailed.

A typical waveform captured at a distance of 35mm is shown in Figure 103. Unfortunately, even though the noise level of the stabilized interferometer used to detect this was shot noise limited at 0.25Å the event amplitude was such that the signal to noise ratio was in fact low. Despite this, certain parameters may still be taken from the traces and are shown in Figure 103. The following values being obtained:

$$A = (1.06 \pm 0.17)\text{Å} \quad (16\% \text{ variation})$$

$$B = (3.45 \pm 1.0)\text{Å} \quad (8\% \text{ variation})$$

Rise time of the Rayleigh wave = (70 ± 20)ns (30% variation)

Scaling each trace to a constant value of A, which gives approximately the DC frequency component, leads to:

$$A = (1.06 \pm 0)\text{Å} \quad (0\% \text{ variation})$$

$$B = (3.45 \pm 0.44)\text{Å} \quad (13\% \text{ variation})$$

The rise time of the Rayleigh wave suggests an upper frequency limit for the source of around 5 ± 1MHz whilst the other results indicate a reproducibility in the shape of the Fourier transform spectrum towards the upper limit of this frequency range of around 13%. This is the error for a given high frequency component from a given scaled value. The reproducibility of lower frequency components when scaled should be much better than this upper limit of 13%. The reproducibility of the scaling factor itself was 16%. Therefore even though it may not be possible to use the balatini on its own as an artificial source it should be possible to use it in conjunction with other low frequency sources.

Further work on this source would be of interest. By producing events very close to the optical detector then the problem of poor signal to noise ratio could be overcome allowing a detailed study of the source to be carried out. A method by which the source-detector separation may be greatly reduced will be shown later.

IV.1.1ii)e) The impact of a Nd-YAG laser

As the review of chapter II indicates an alternative choice for an artificial acoustic emission source is the impact of a Nd-YAG laser. Extensive work has been carried out by other workers on the epicentral waveform created by such an event. However little work has been performed on the surface pulse mainly because of the lack of a suitable absolute high frequency detector. The work

reported here will therefore be restricted to the study of high frequency surface sources.

To produce a high frequency surface source then the size of the Nd-YAG laser impact on the material should be small. For a Rayleigh wave velocity on aluminium of 2.906mm μs^{-1} then for an upper frequency of 10MHz the impact area diameter should be 0.10mm. The Nd-YAG laser used for the experiments produced a $\sim$ 13mJ pulse with a temporal half-width of $\sim$ 15ns. When all of the available energy is focussed into a circle of radius 0.10mm the energy density is $\sim$ 165Jcm^{-2} and the power density 1.1×10^{10}Wcm^{-2}. This is in excess of the vaporization threshold of aluminium and so a plasma would be produced. To avoid this plasma the energy out of the laser could be reduced for example by the use of neutral density filters. However, to ensure that the elastic pulse was of sufficient amplitude to allow it to be easily detected then the full laser power was used. In fact the sensitivity of the stabilized interferometer detector was such that a thermoelastic pulse generated by a focussed low power beam can be detected and would form an interesting area of work. The only thermoelastic sources reported here are for unfocussed and partially focussed laser beams.

The first result obtained was the thermoelastic impact of the unfocussed laser using the full 13mJ of energy at a source/detector distance of 90 $\pm$ 5mm. The shear and Rayleigh waves produced the trace shown in Figure 104. Even though the laser beam was not Gaussian, but contained

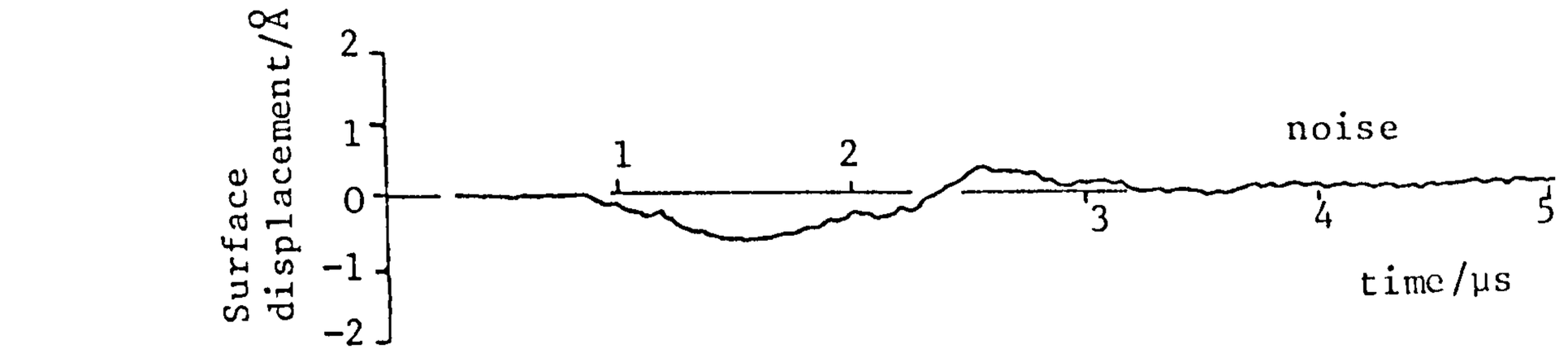

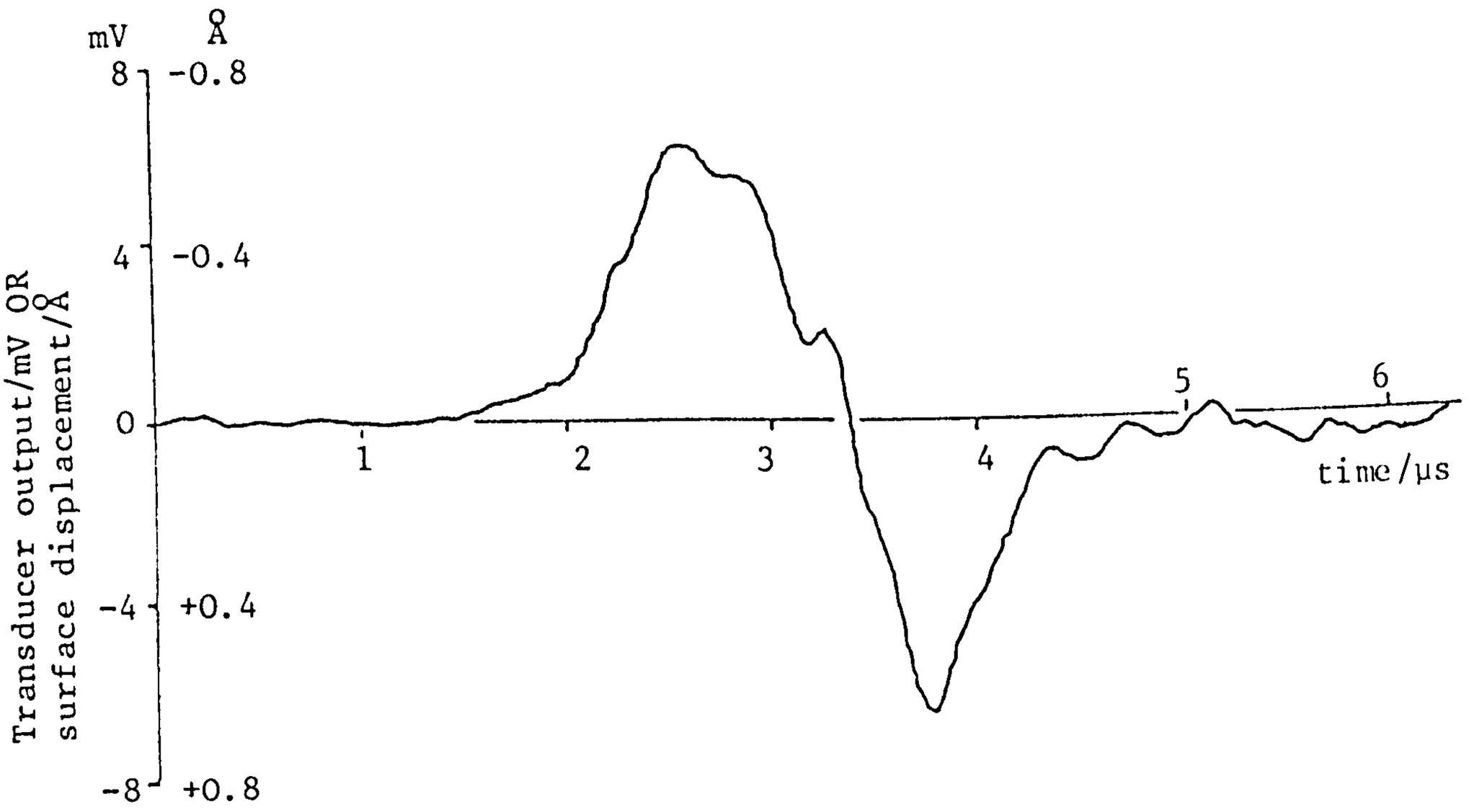

Figure 104: The surface displacement due to the impact of a Nd-YAG laser onto an aluminium plate of thickness 77mm detected at a distance of 90mm. The upper trace is captured on a stabilized optical interferometer and the lower on a broadband piezoelectric detector. The laser impact was thermoelastic with a spot diameter of ∿3mm. An average of 16 shots were taken giving a minimum detectable displacement of 0.07Å on the interferometer.

a good deal of structure, the trace did not have much high frequency in it and could be adequately followed by a broadband piezoelectric transducer whose output is also given in Figure 104.

The optical results in Figure 104 are the same, within the experimental noise, to both the theoretical and experimental traces given by Aindow et al[15]. However, the second peak in the waveform detected by the broadband piezoelectric sensor appears to be too large. This discrepancy is assumed to be due to a slight ringing in this transducer.

The optically detected trace given in Figure 104 has only a poor signal to noise ratio. In order to improve this figure the source is both brought closer to the detector and also mildly focussed. These measurements were made possible by placing a Helium Neon interference filter in front of the photodetector to reduce Nd-YAG laser light pick-up. The source/detector separation is now 11.7mm and the resulting trace is shown in Figure 105. The minimum detectable displacement for the interferometer in this new arrangement was shot noise limited at 0.5Å. However the peak height of the trace was only 2.2Å and so to enhance the SNR (4 for the peak value) an average of 64 shots were taken leading to a minimum detectable displacement of 0.06Å. The modulus of the Fourier transform is also shown in this figure.

The focussing used to generate this trace was, as mentioned above, only mild, and so this thermoelastic laser impact had an overall spot diameter

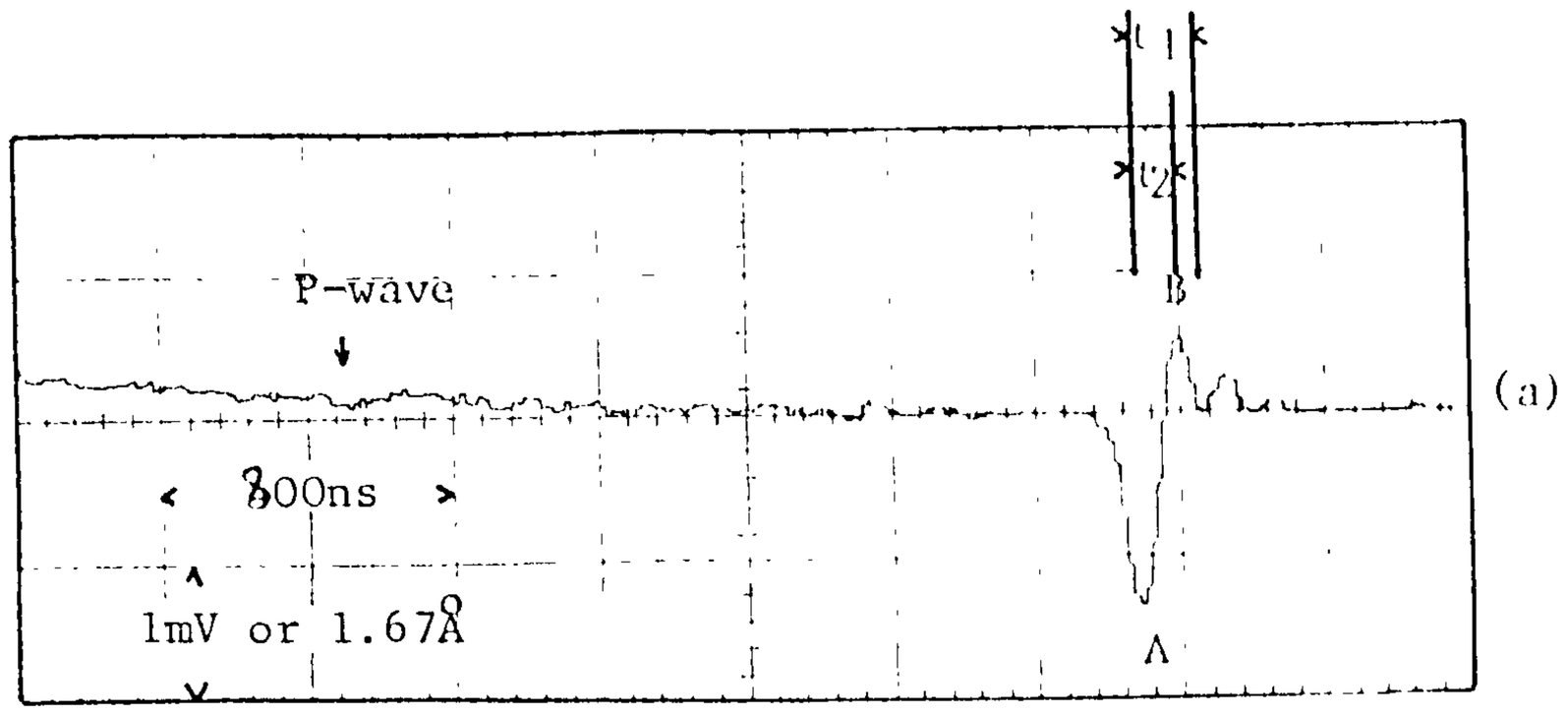

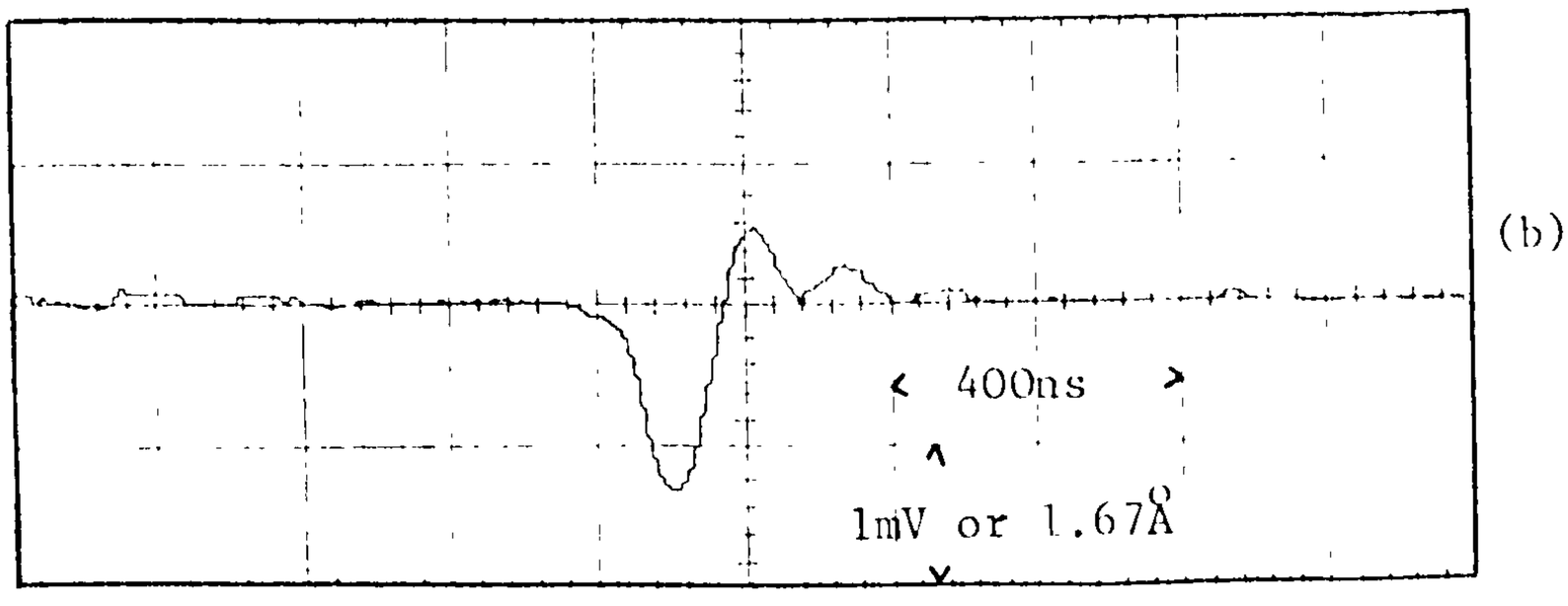

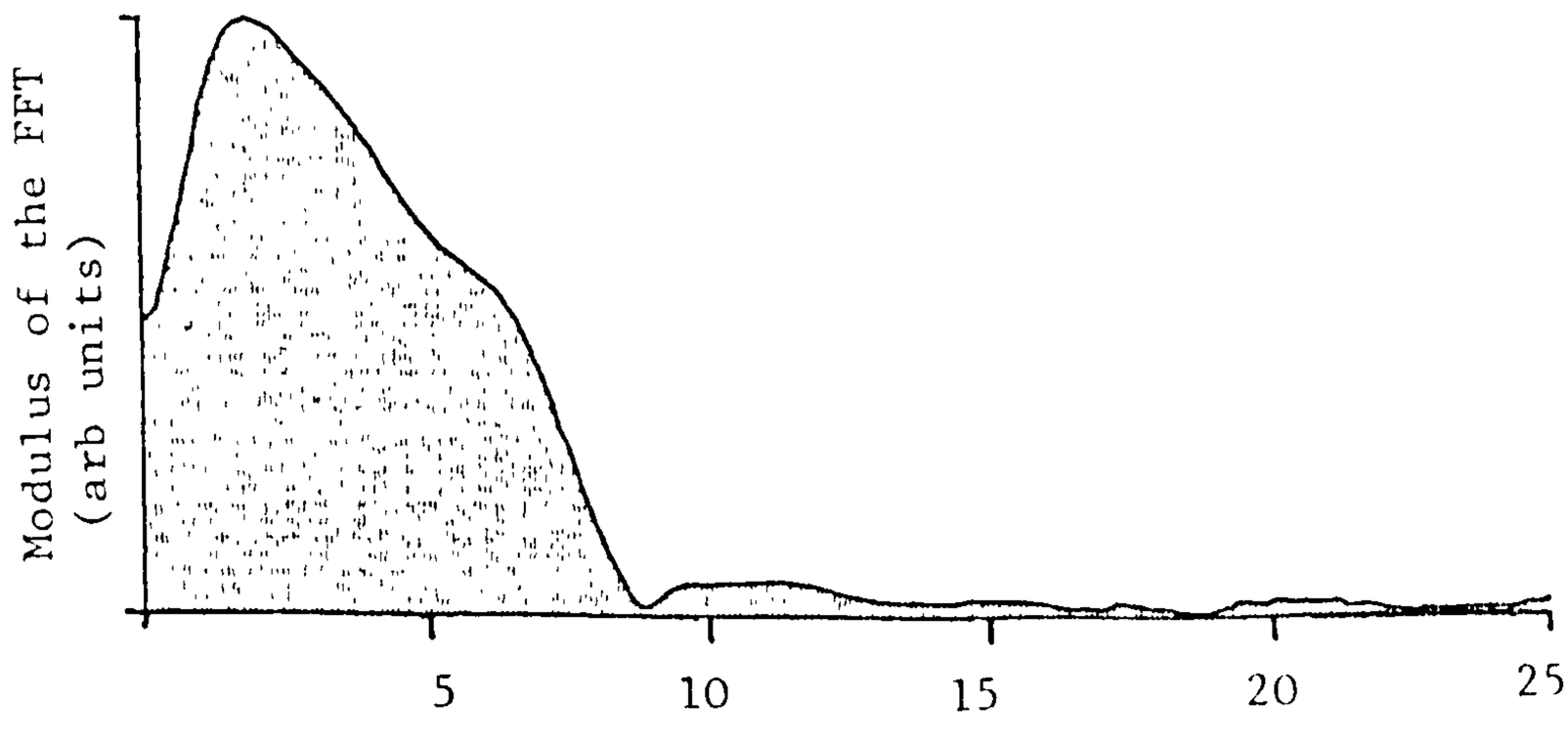

Figure 105: The surface acoustic pulse generated by the thermoelastic impact of a mildly focussed Nd-YAG laser (traces a and b) together with the FFT of this trace. The waveforms were detected by a stabilized optical interferometer 11.7mm away.

of approximately 1mm. The mode structure in the laser was such that there were two distinct peaks within this spot. It is these peaks which are assumed to create the oscillations occurring after the main peak in Figure 105. The time t_1 is measured to be 170ns which corresponds to a distance of travel, for a Rayleigh wave, of 0.5mm and as such would appear to arise from the mode structure in the laser impact. The rise time, t_2, of 63ns suggests the first pulse is generated by a source of diameter $\sim$ 0.2mm, which again ties up with the observed impact.

Apart from this ringing the pulse follows the theoretical waveform given by Aindow et al[15] very well with the ratio between the height of peaks A and B being (2.6 ± 0.1) compared with the theoretical ratio of 2.7. However the corresponding experimental trace given by Aindow et al[15] has this ratio as (4.1 ± 0.2). The discrepancy between the two experimental results is thought to arise because of the limited bandwidth of the capacitor detected used by Aindow et al.

The size of the impact spot is now further reduced to 0.4 ± 0.1mm with the energy density rising to a point where a plasma is created each shot. Figure 106 shows a waveform detected when the source/detector separation is 4.25mm. The general slope on this trace is due to the photodetector recovering from the residual pick-up of the Nd-YAG light and appears to be of no consequence. Measuring the ratio of B to A yields a

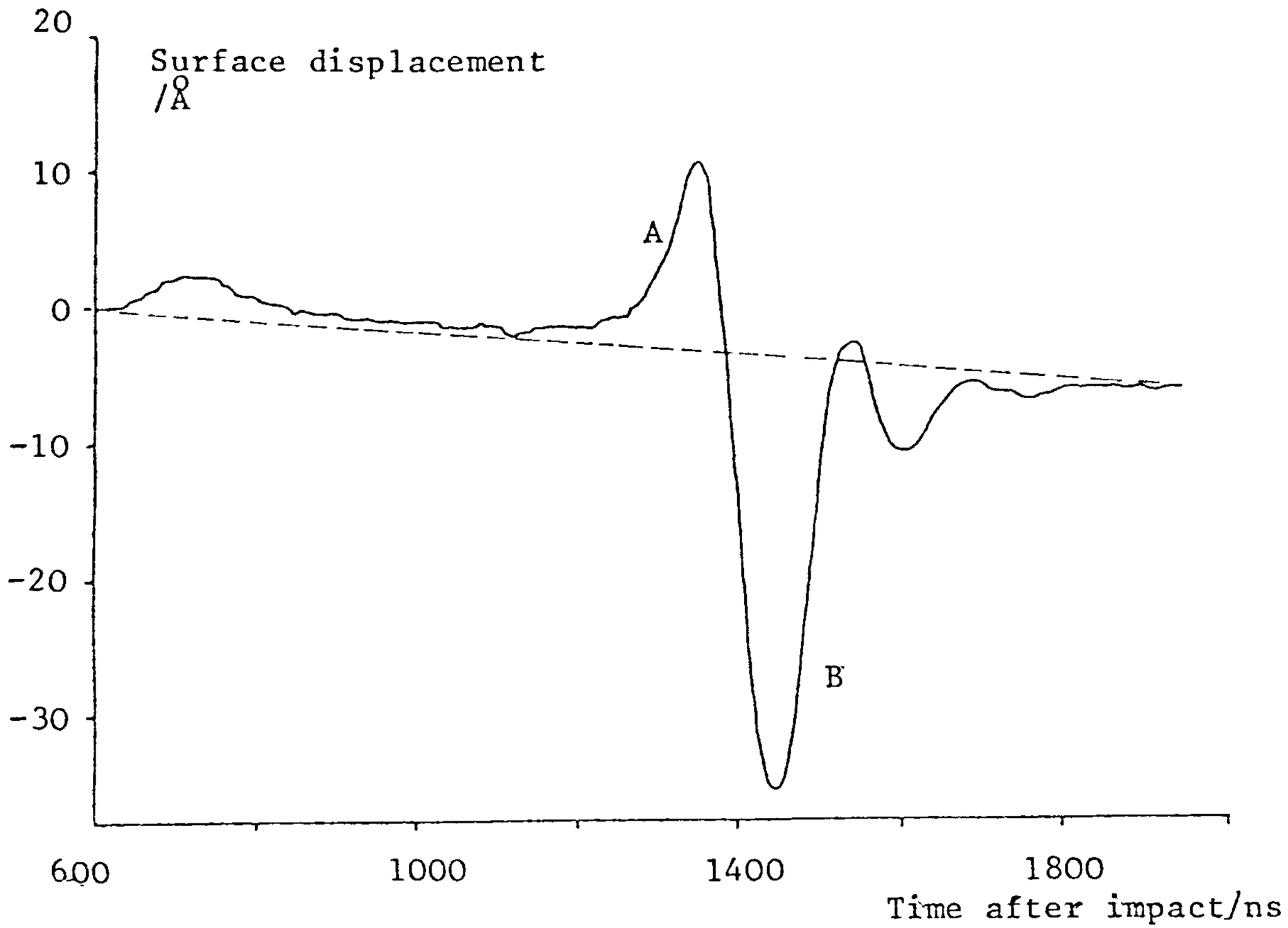

Figure 106: The surface displacement measured by the stabilized optical interferometer due to the impact of a Nd-YAG laser in the low temperature plasma region on the surface of an aluminium semi-infinite half space. Source detector separation 4.25mm.

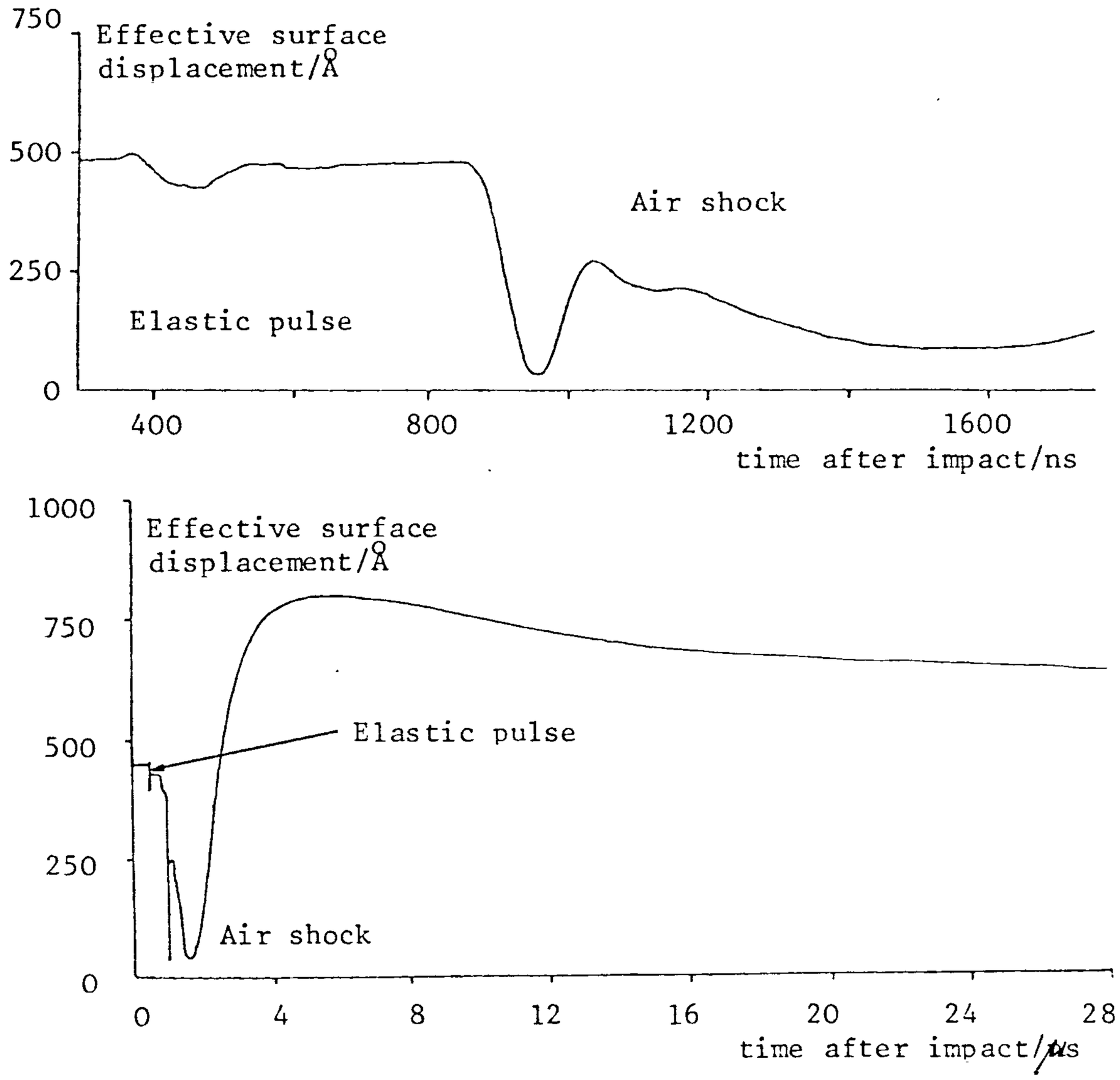

Figure 107: The interferometer path length change caused by the surface displacement of a surface elastic wave and an air shock both created by the impact of a Nd-YAG laser in the plasma region (Source/interferometer distance 1.38mm).

figure of 2.4 ± 0.1. The theoretical waveform given by Aindow et al[15] also has this ratio as 2.4. Again the experimental results given by Aindow et al[15] differ from the theoretical figure in that this ratio is only 2.1 ± 0.2.

As the source/transducer distance is reduced further an interesting effect occurs which can be seen in Figure 107. The second pulse is in fact an air shock wave produced by the plasma. The high pressure in the shock wave changes the refractive index of the air and hence the path length in the interferometer arm. This change is sufficient to create a path length variation in excess of $\lambda/8$ (corresponding to a phase change of $(4\pi/\lambda)\lambda/8 = \pi/2$) resulting in the output of the interferometer passing over the fringe peak. Therefore the path length change for the shock is actually that given in Figure 108. The mach number and form of this shock wave are similar to that given in previous work by Emmony[124].

An expanded version of the elastic pulse shown in Figure 107 is virtually identical to the elastic pulse given for the similar event at a greater distance (Figure 106).

When the source/detector distance is further reduced two problems occur. The first is that the trace due to the elastic pulse becomes buried in the Nd-YAG laser light pick-up. This problem is not a fundamental one as the pick-up levels are reasonably low. The use of a second interference filter together with shielding designed to ensure that light can only fall perpendicularly onto this

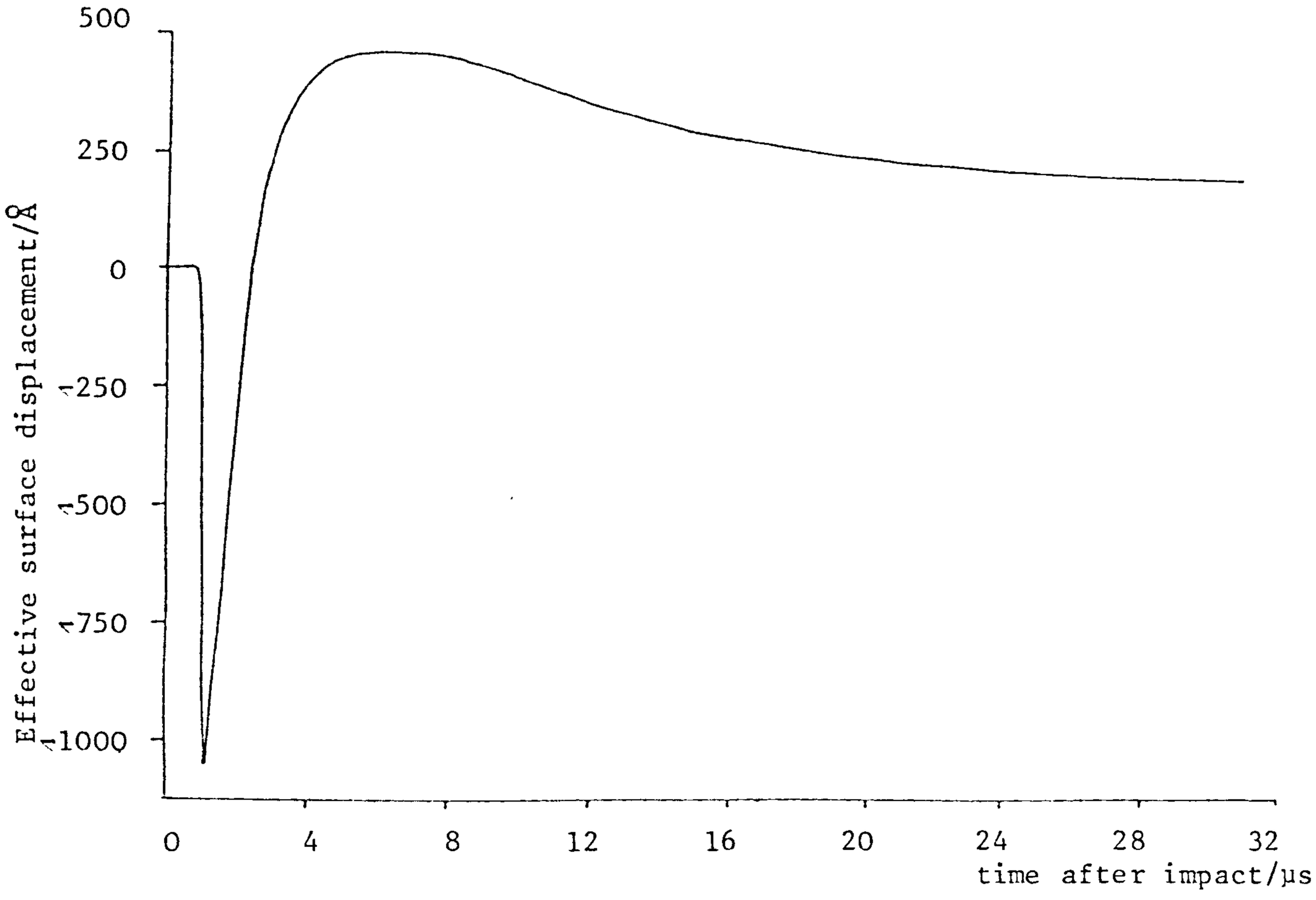

Figure 108: The deconvoluted interferometer path length change created by the air shock generated by the Nd-YAG laser impact described in Figure 107.

filter would then reduce the pick-up to insignificant levels.

The second problem is that when the source/detector separation is very small the excursions produced by the plasma and by the elastic pulse overlap making evaluation difficult. If the laser impact was however thermoelastic in nature no such problem would occur. It would be interesting to try to detect the thermoelastic pulse at the origin. Even though stress dipoles in the plane of the surface create most of the elastic waves the vertical surface displacement would allow certain assumptions about the source to be verified, for example the time dependency of the laser heating.

A second variation in the experimental arrangement which is of interest would be the use of a Nd-YAG laser operating in the TEM_{OO} mode. This would allow the ringing indicated in Figures 105 and 106 to be further investigated.

In summary the use of a laser interferometer transducer to detect the ultrasonic pulse from a Nd-YAG laser impact has indicated that the theoretical waveforms given by Aindow et al[15] appear to be correct. The uncertainties in the experimental measurements of Aindow et al arising from a possible system bandwidth limitation have also been resolved. Finally it would seem that the interferometer could be used to monitor the laser heating at the origin and in so doing verify some of the theoretical predictions associated with the phenomena.

IV.1.1ii)f) The use of piezoelectric ultrasonic transmitting transducers as an artificial acoustic emission source

So far all of the sources investigated have been monitored by detecting the surface ultrasonic pulses they generate. To enable the various calibration assumptions connected with the mode uncoupling approximations outlined in section II.6.1 to be tested, it is desirable to have a source placed in such a position with respect to the detector that surface waves do not predominate, the ideal position being epicentral to the detector.

Forces with a step function time dependency produce only low amplitude events at epicentral positions on thick plates. Some examples of these will be given later. A force with a delta function time dependency, however, will give a large vertical surface displacement at such a point. An ultrasonic transmitting transducer should generate roughly a delta function force output and hence would appear to be a suitable choice for an epicentral artificial acoustic emission source.

This transmitting transducer which had a front face diameter of 16mm was placed at the centre of one face of the large aluminium block described earlier (Figure 80). The stabilized interferometer was focussed at the epicentral position to this within 5mm. Theoretical results given by Pekeris and Lifson[20] indicate this positioning error is not significant.

The detected vertical surface motion as determined by

the interferometer is shown in Figure 109. Two sets of waveforms are given. The first set is for single events where the shot noise limited minimum detectable displacement was 0.25Å and the second set is for an average of 256 events where 0.02Å could be monitored. Slight triggering uncertainty produces some broadening on the averaged results compared to the unaveraged traces. However, as the number averaged is large then this trace is, like the single shot case, reproducible.

The elastic waves appear to be generated by a force with an approximately delta function time dependency but containing some undershoot. The traces are similar to a corresponding event given by Hsu et al[60] which is shown in Figure 22.

As the source is reproducible it allows the optical detector to be replaced by some other transducer thus enabling this to be calibrated if the conditions of section II.6.1 are met.

IV.1.2 Artificial acoustic emission sources studied at the source origin

An optical transducer may probe inside transparent materials and so if one side of a glass block is coated with a thin layer of aluminium (by evaporation) the movement of this face may be monitored either directly or through the block (Figure 110). The block used is 11.452mm x 64.48mm x 18.87mm with one large face being silvered.

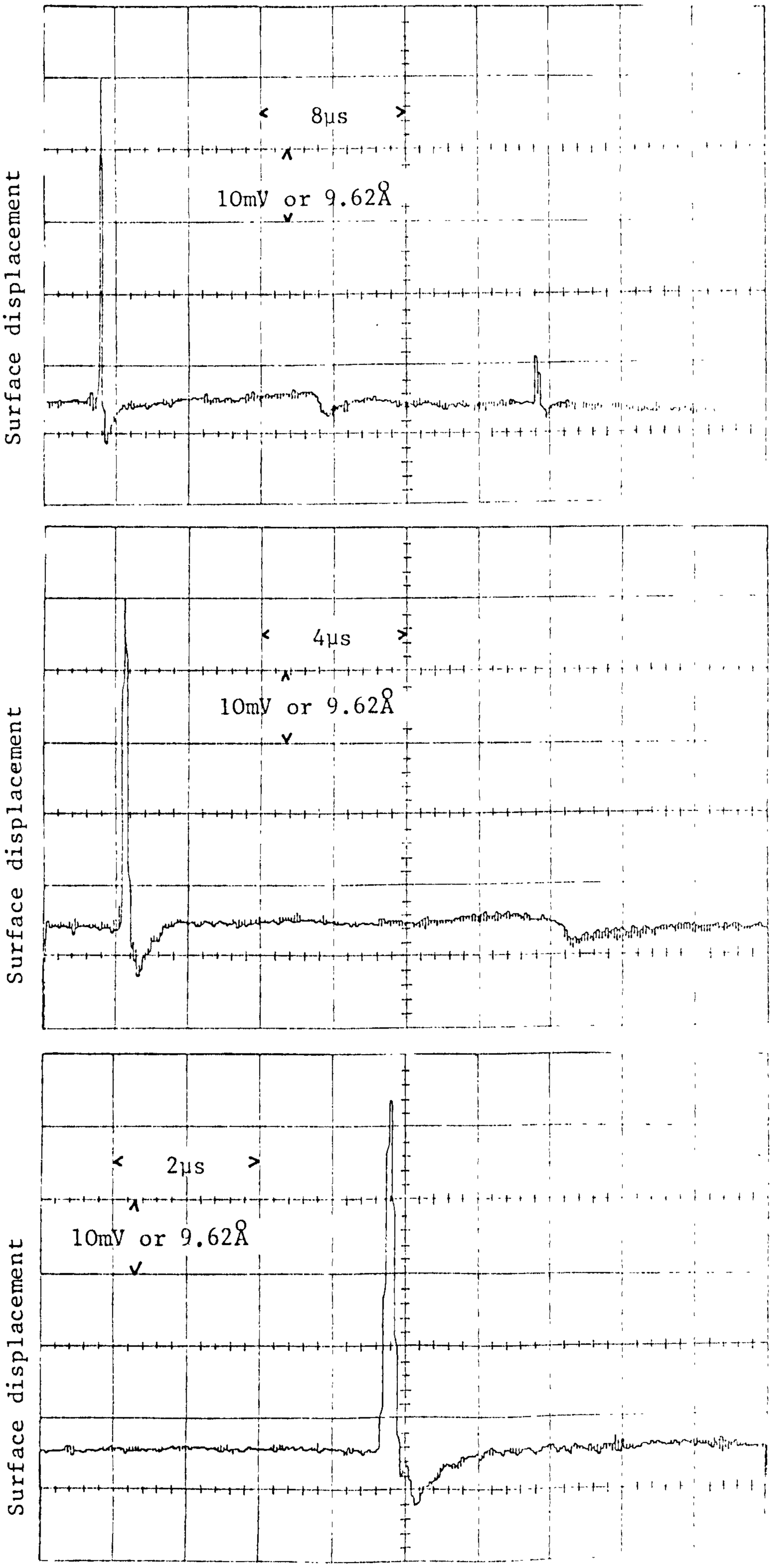

Figure 109: (Part 1). The vertical surface displacement at the epicentre of an ultrasonic transducer. These are single events.

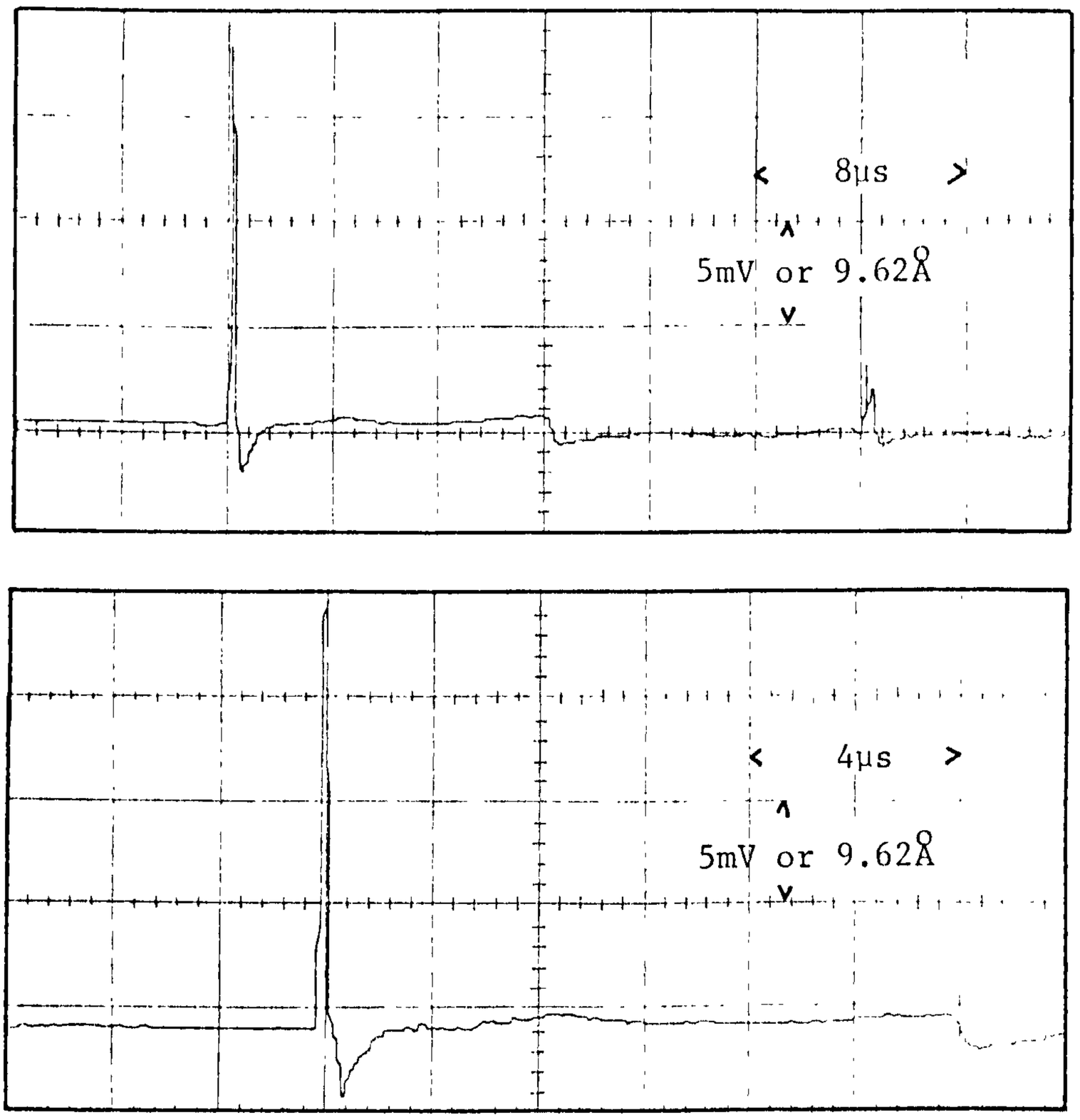

Figure 109: (Part 2). The vertical surface displacement at the epicentre of an ultrasonic transducer. These traces are averaged over 256 shots. The displacements are very similar to those reported by Hsu et al[60] and shown in Figure 22.

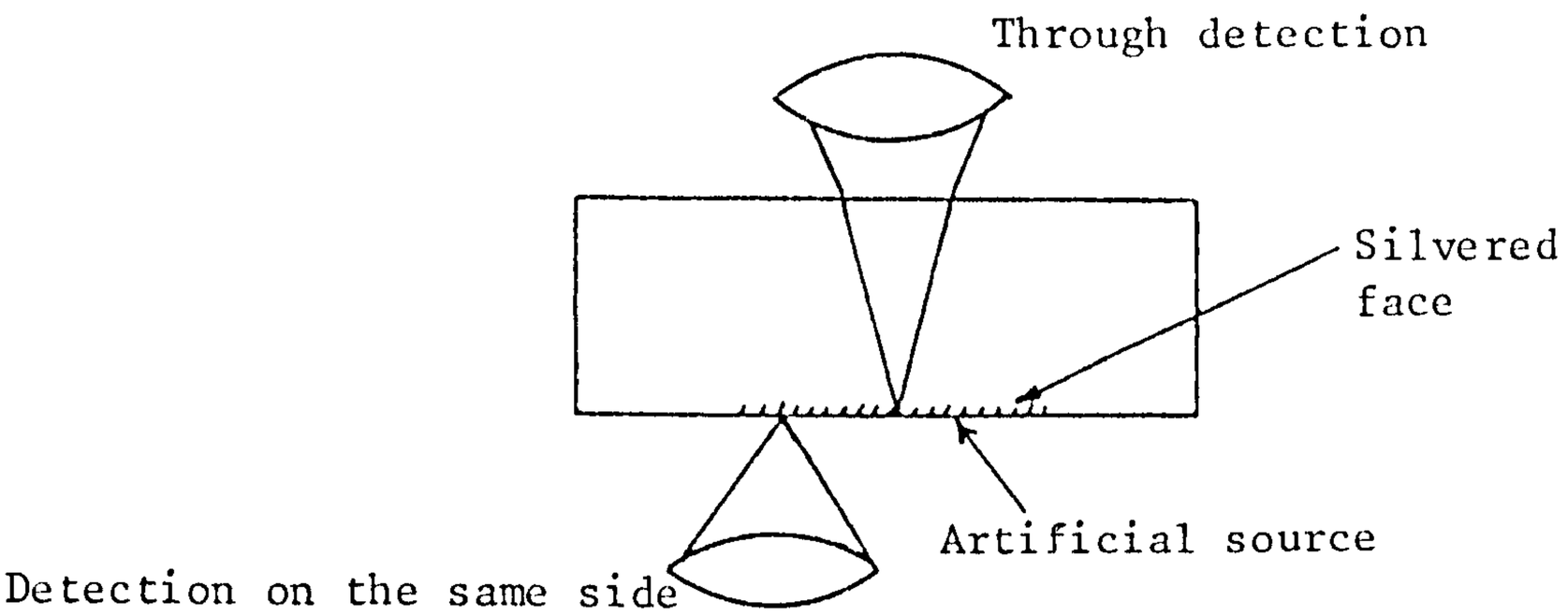

Figure 110: The two methods by which the surface displacement due to an acoustic pulse may be measured with an interferometric detector.

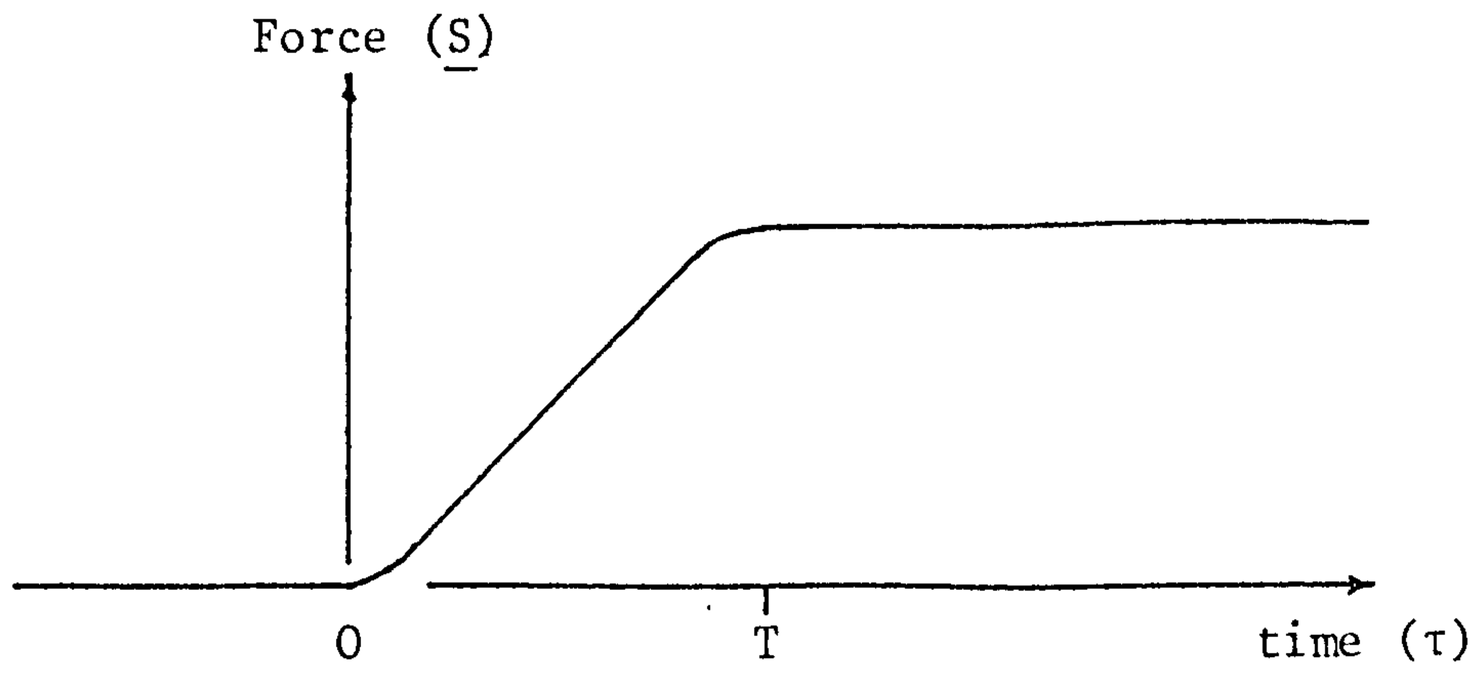

Figure 111: The assumed time dependency of a step artificial source. Using this dependency allows calculations to be performed to determine at what source/detector separation the surface displacement ceases to be that of the source (as measurable with the optical interferometer).

Two problems might arise with the through block measurements. The first of these is whether the aluminium coating affects the transmission and propagation of ultrasonic waves. Considerations of the bandwidths of the detectors and of the thickness of the aluminium suggest this should not be a problem.

The second area of uncertainty is the change in refractive index of the glass resulting from the pressure changes brought about by the ultrasonic waves. Calculations based on the magnitude of these pressure changes and on the size of the refractivity/pressure dependency indicate this should not be a problem either.

To test whether either of the effects above are significant some event should be viewed both through the block and directly. The event chosen to make this comparison is the ultrasonic surface pulse generated by a Hsu/Nielson source at a distance of 10mm from the source. Within the limits of experimental error no difference could be discerned showing that the effects outlined above are indeed insignificant.

Two sources have been viewed at their origin. These are the Hsu/Nielson source and the ultrasonic transmitting transducer which will now be discussed in more detail.

IV.1.2i) The Hsu/Nielson source monitored at the origin

IV.1.2i)a) Theoretical considerations

The question which must first be answered is what

constitutes the origin. Now the diameter of the focussed laser spot is (43 ± 5)μm whilst the diameter of the contact area for the pencil is (140 ± 20)μm. Referring to Figure 92 it can be seen that if the laser spot is focussed to within 50μm of the correct dead centre of the pencil source the displacement will be 85% of the true centre displacement. This would be sufficient for these measurements but the positioning tolerance of 0.05mm might be difficult to achieve. A better estimate of the positioning tolerance will now be given.

It will be recalled that the surface pulse given in Figure 5 is plotted on dimensionless axes where the vertical axis is scaled to the force divided by the distance travelled and the horizontal axis to a shear wave arrival at t = 1. In other words the time duration of the pulse will be short when the source/monitoring distance is small. At a distance of 0.3mm on glass the trace duration is only 46ns with the major part of the displacement occurring between the shear and Rayleigh waves over a time period of approximately 12ns. The pencil source contains rise times of the order of 700ns which effectively means the pulse in Figure 5 is integrated with time.

This integral may be numerically evaluated. As shown previously the surface displacement at a detector position $\underline{x}$ due to a source force function at $\underline{x}_o$ $\underline{S}(\underline{x}_o,t)$ is given as equation (17):

$$\underline{U}(\underline{x},t) = \int_o^t \underline{G}(\underline{x},\underline{x}_o,t-\tau)\underline{S}(\underline{x}_o,\tau)d\tau \qquad (17)$$

The source is assumed to have the time dependency given in Figure 111 and act perpendicularly to the surface. Therefore only part of the Green's function tensor ($\underline{G}$) is required if the vertical surface motion at the detector is monitored. This is usually termed G_{33}. All other terms G_{31}, G_{32} and zero. The time dependency shown in Figure 111 is approximated by

$$\begin{aligned} \underline{S}(\underline{x}_o,\tau) &= 0 && \tau \leqslant 0 \\ \underline{S}(\underline{x}_o,\tau) &= \alpha\tau && 0 \leqslant \tau \leqslant T \\ \underline{S}(\underline{x}_o,\tau) &= \alpha T && \tau \geqslant T \end{aligned} \qquad (232)$$

where the force acts in direction 3 at point $\underline{x}_o$. Equation (17) above may therefore be written as

$$U_3(\underline{x},t) = \int_o^t G_{33}(\underline{x},\underline{x}_o,t-\tau)\alpha\tau \; d\tau \qquad (233)$$

$$t - \tau \leqslant T$$

and

$$\begin{aligned} U_3(\underline{x},t) = &\int_o^T G_{33}(\underline{x},\underline{x}_o,T-\tau)\alpha\tau \; d\tau \\ &+ \int_o^t G_{33}(\underline{x},\underline{x}_o,(t-T)-\tau)\alpha T \; d\tau \end{aligned} \qquad (234)$$

$$t - \tau \geqslant T$$

Substituting $u = t - \tau$ into equation (233) leads to

$$U_3(\underline{x},t) = \int_o^t G_{33}(\underline{x},\underline{x}_o,u)\alpha(t-u)du \qquad (235)$$

which may be integrated by parts to yield:

$$\begin{aligned} U_3(\underline{x},t) = &\left[\alpha(t-u)\left(\int_o^u G_{33}(\underline{x},\underline{x}_o,u')du'\right)\right]_o^t \\ &+ \alpha\int_o^t\left(\int_o^u G_{33}(\underline{x},\underline{x}_o,u')du'\right)du \end{aligned} \qquad (236)$$

Consider

$$I = \int_o^u G_{33}(\underline{x},\underline{x}_o,u')du' \qquad (237)$$

by substituting $\xi = u - u'$ this becomes

$$I = \int_o^u G_{33}(\underline{x},\underline{x}_o,u-\xi)d\xi \qquad (238)$$

which may be written as

$$I = G_{33}^H(\underline{x},\underline{x}_o,u) \qquad (239)$$

Now the first term in equation (236) is zero and so this equation becomes

$$U_3(\underline{x},t) = \alpha\int_o^t G_{33}^H(\underline{x},\underline{x}_o,u)du \qquad (240)$$

and writing u = t-v then:

$$U_3(\underline{x},t) = \alpha\int_o^t G_{33}^H(\underline{x},\underline{x}_o,t-v)dv \qquad (241)$$

$$(t - v \leqslant T)$$

The surface pulse in Figure 5 is in fact $G_{33}^H(\underline{x},\underline{x}_o,u)$ and so the numerical integration may be performed on this. Having reduced equation (233) to a calculable numerical integration, then the same may be done for equation (234). Following a similar procedure this reduces to:

$$U_3(\underline{x},t) = \alpha\int_o^T G_{33}{}^H(\underline{x},\underline{x}_o,t-v)dv + \alpha T\int_T^t G_{33}(\underline{x},\underline{x}_o,(t-T)-\tau \qquad (242)$$

$$(t - \tau \geqslant T)$$

The case of interest is when the time T is greater than the time taken for the Rayleigh wave to travel from the source at $\underline{x}_o$ to the detector $\underline{x}$. In this case the solution is most

easily seen by considering the force as the sum of two forces (see Appendix 12).

A problem arises from the infinity at the Rayleigh wave arrival when the surface pulse (G^{H}_{33}, Figure 5) is integrated. This infinity occurs because of the time dependency of the source. To remove this discontinuity a finite rise time step should be used in the initial calculations. An approximation may be made for the result of such a change and this is indicated in Figure 112. Here the fall time of the Rayleigh step has been limited to the source rise time. Of course the finite source rise time will also affect the shear wave but such effects are ignored. This waveform may now be digitized. Digitizing is performed at the points shown in Figure 112 so as to avoid further distortion of the waveform. In fact the digitizing should be performed with a narrower sampling rate of approximately 1 sample every $\delta t/4$. Unfortunately this leads to a very large calculation which would take far too long to evaluate.

Using results given by Mooney[25] for $\nu = 0.25$ together with a δt of 0.8ns then at a distance of 0.3mm the force of Figure 111 produces a displacement as shown in Figure 113.

In a time T the force at the origin decreases from the pencil lead breaking force of 1.47N for 6 clicks to zero. Therefore α(equation (232) → (242)) is 1.47/T. Using values for E and ν as $7.0 \times 10^{10} Nm^{-2}$ and 0.26 respectively allows Figure (113) to be dimensioned.

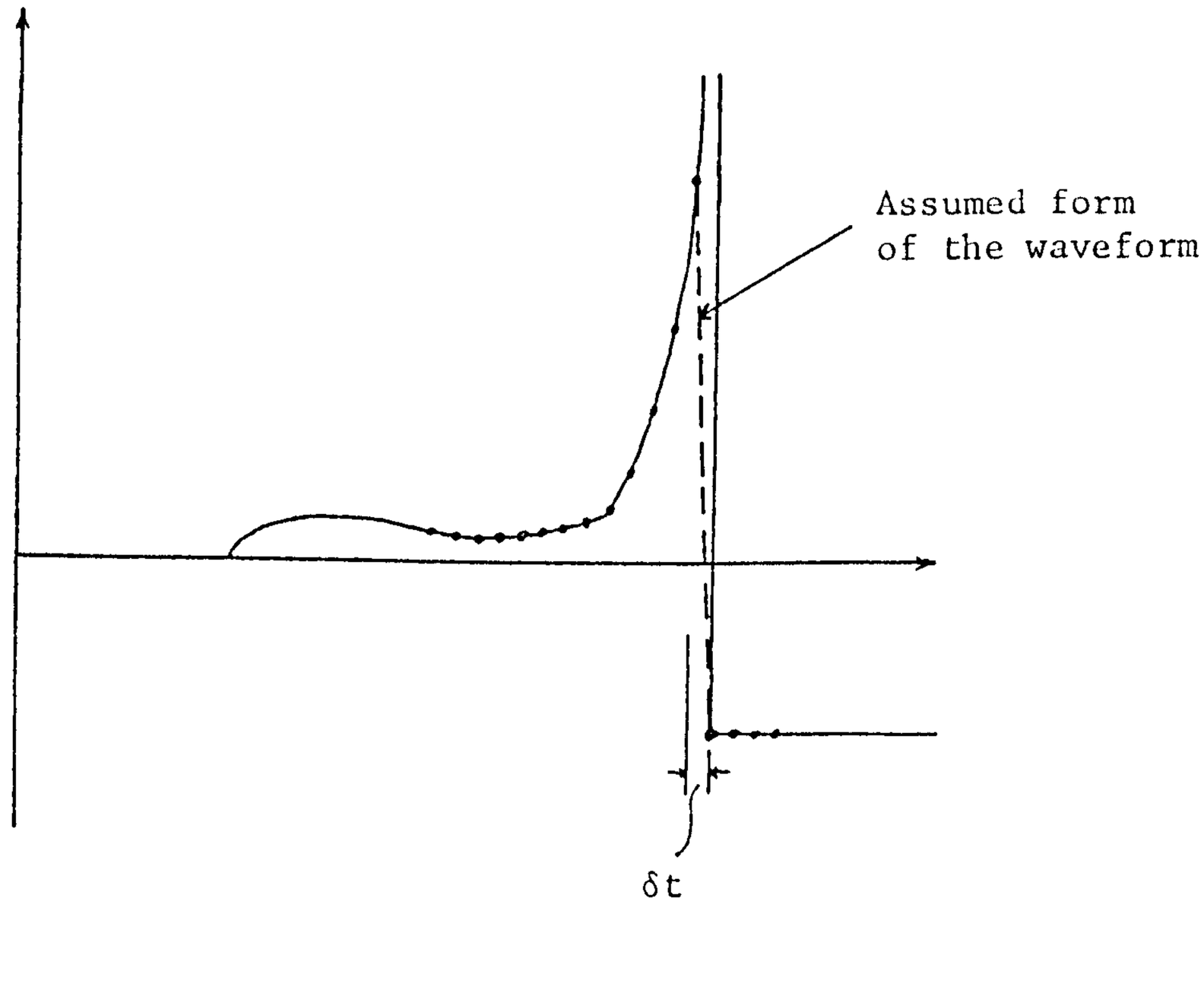

Figure 112: The schematic representation of the digitizing of $G_{33}{}^{H}$ used to calculate convolution integrals. The Rayleigh infinity is removed by the effective bandwidth introduced by the digitizing.

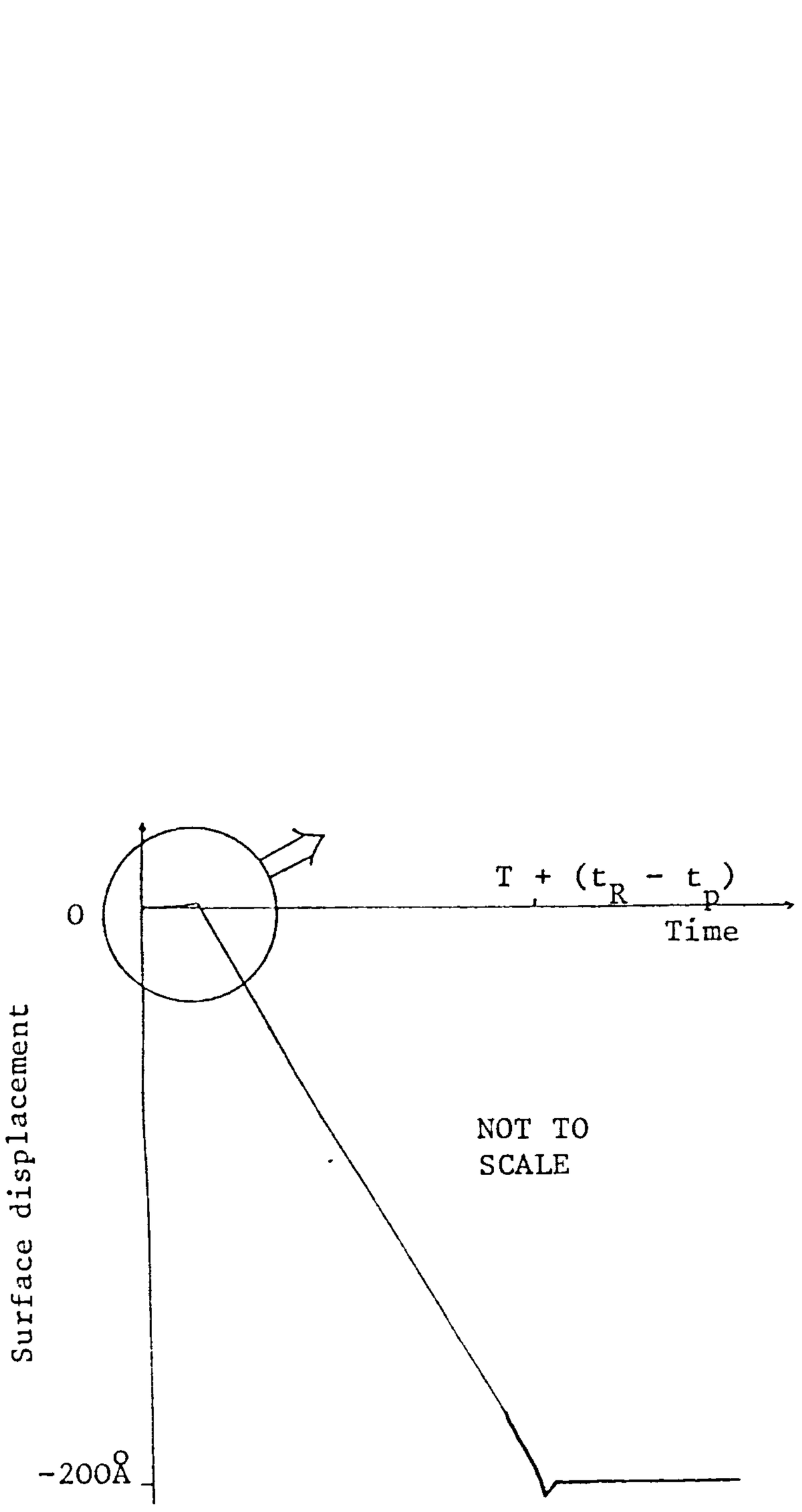

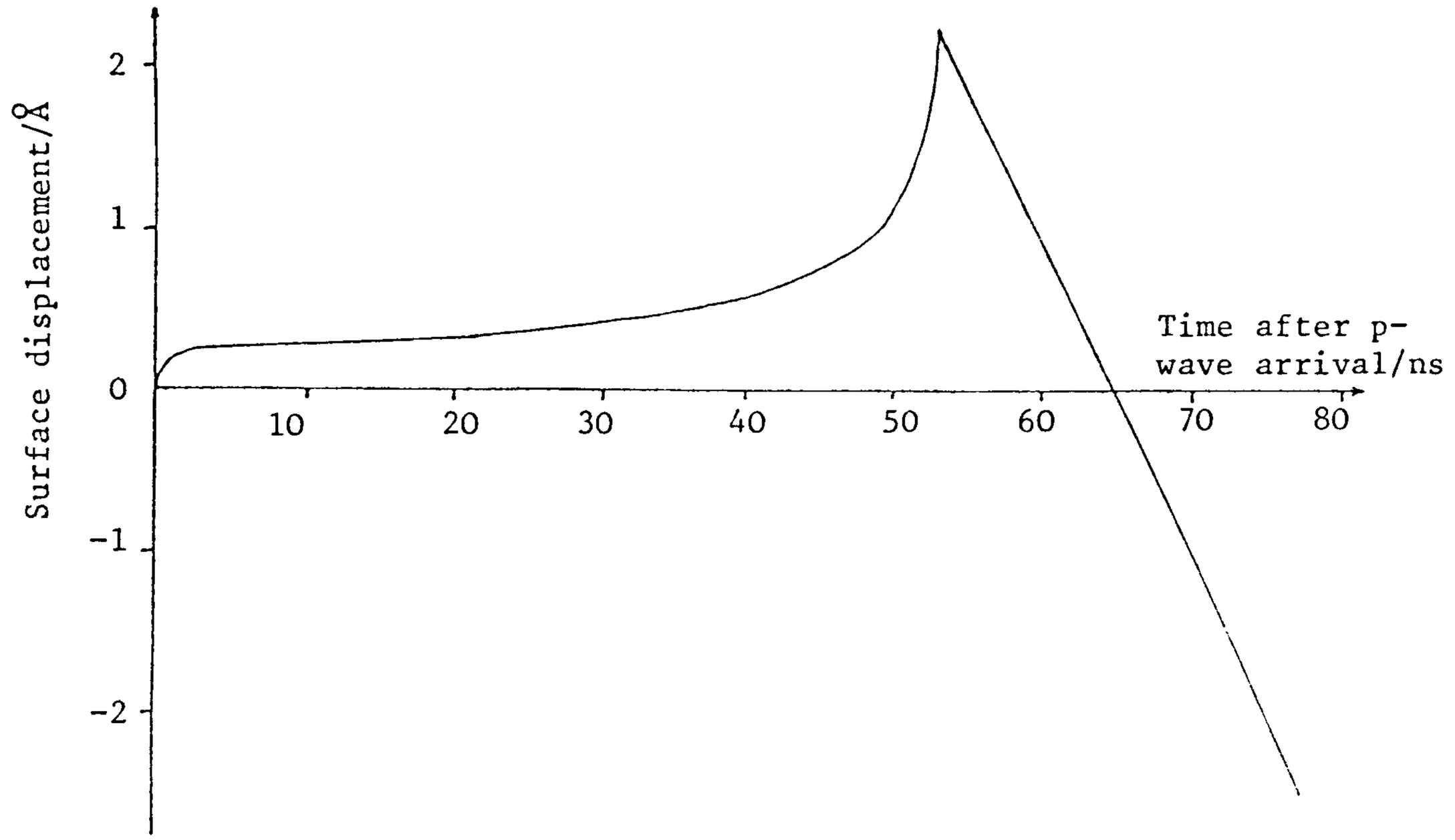

Figure 113: The result of the calculation outlined in equations (232) and (233). Here t_p and t_R are the arrival times of the ṗ-waves (longitudinal) and Rayleigh waves respectively. Source/detector separation 0.3mm.

When the distance from the source to detector is 0.06mm then Figure 113 changes to that given in Figure 114. For both Figures 113 and 114 the positive peak has a very fast rise time. As the rise time of the stabilized optical detector is only 35ns then in both instances this peak will only be partially followed by the optical detector. For the case depicted in Figure 113 then the optical detector will rise to only about $^1/_3$ of the true height of this first peak, that is $\sim$ 0.6Å. This will be almost entirely lost in the noise. Therefore for a source/detector distance less than $\sim$ 0.3mm the detected pulse will have the time dependency of the source at the origin. The size of the trace will then depend on the propagation distance.

Having determined how close to the source the detector should be the experimentally measured waveforms will now be given.

IV.1.2i)b) Experimentally measured waveforms generated by the Hsu/Nielson source and detected at the source origin

Using the experimental arrangement outlined above the waveform (in terms of the vertical surface movement) generated by a Hsu/Nielson source was measured through the glass block at a selection of distances. The Hsu/Nielson source employed a 0.5mm 2H pencil lead extended by 6 clicks. The results of these measurements are shown in Figure (115) as a function of the estimated source/detector distance. As this distance becomes small it is difficult to

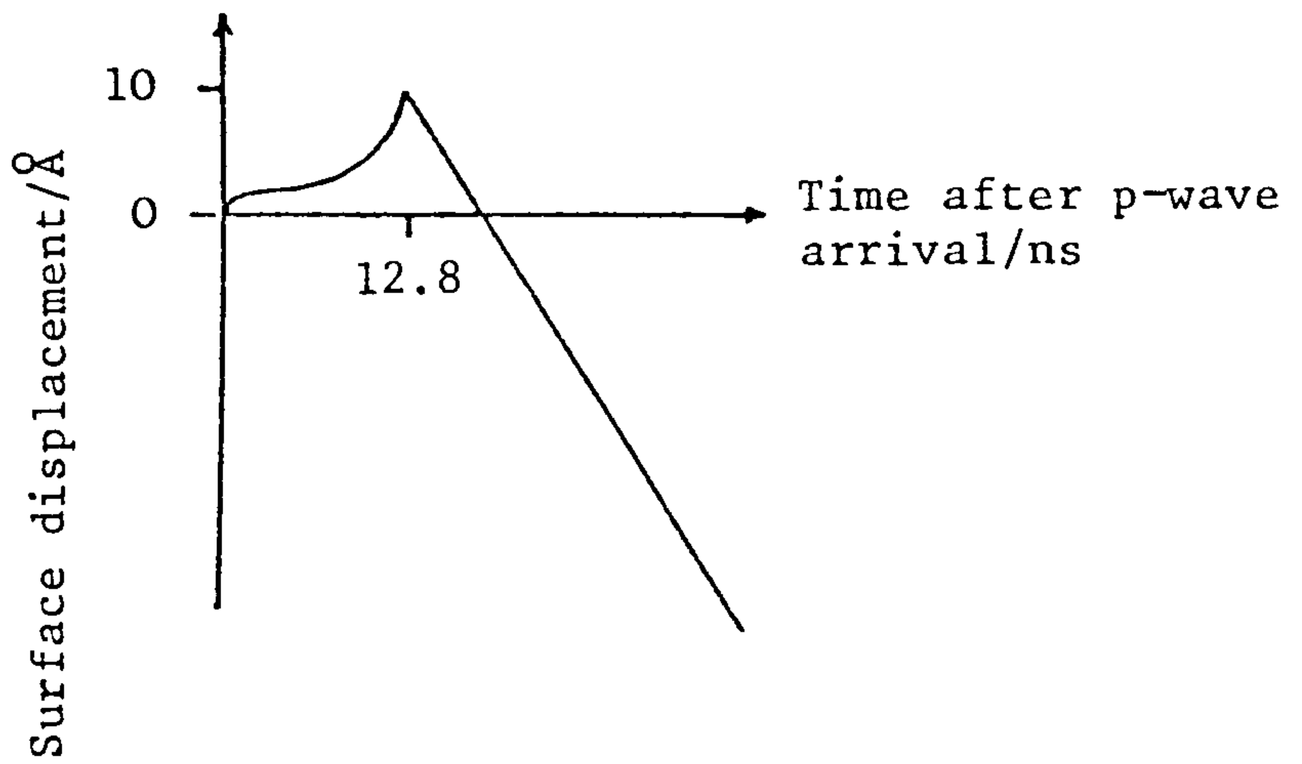

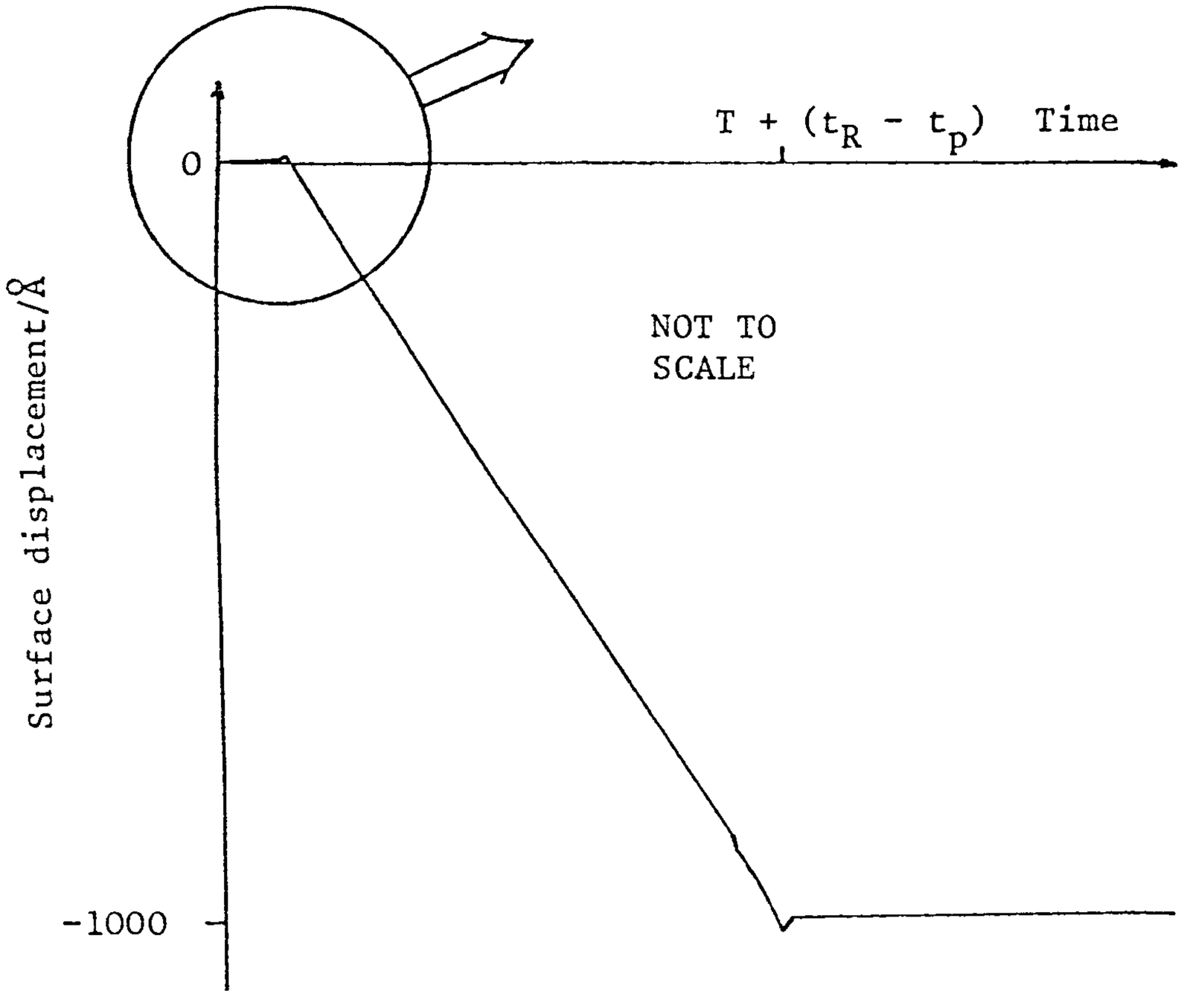

Figure 114: The result of the calculations outlined in equations (232) and (233) for a source-detector separation of 0.06mm. t_p and t_R and the arrival times of the p-waves (longitudinal) and Rayleigh waves respectively.

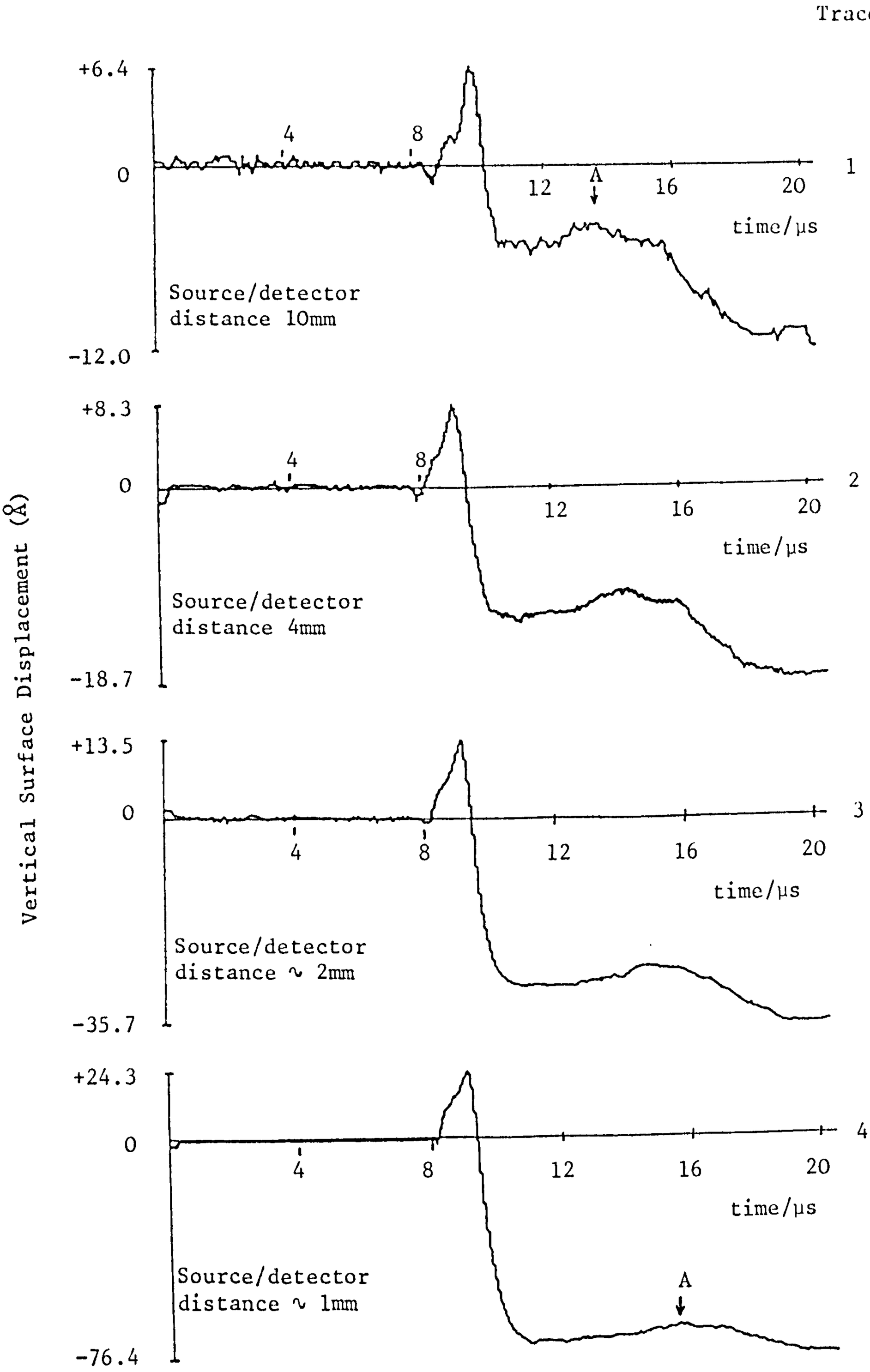

Figure 115: (Part 1). The displacement due to a surface pulse from a Hsu/Nielson source measured through the glass block (see figure 110) as the source/interferometer detector distance is varied.

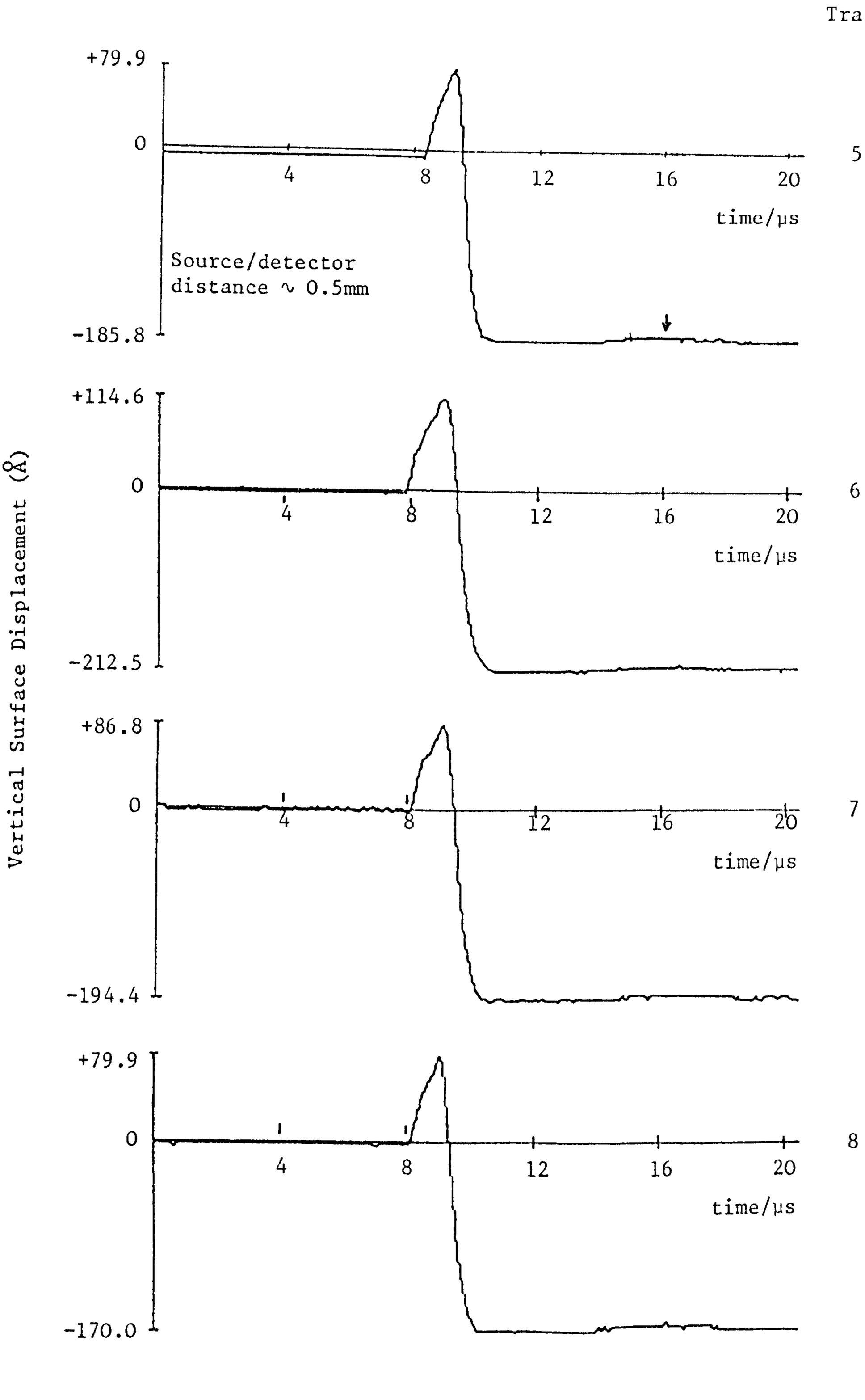

Figure 115: (part 2)

Traces

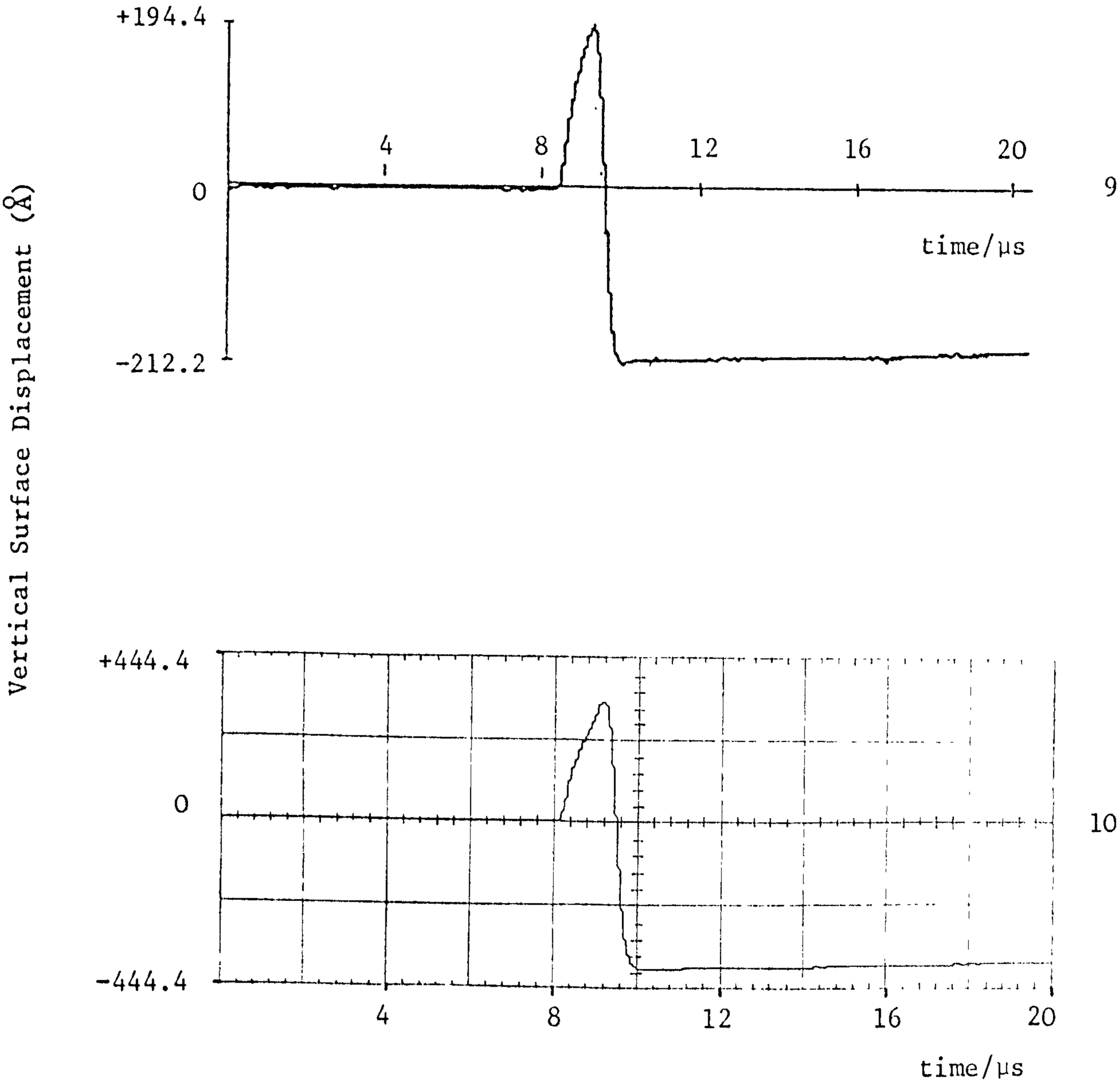

Figure 115: (part 3)

estimate.

Two points should be noted about these traces. Firstly the jog at A corresponds to the reflection of the longitudinal wave off the back wall of the glass, with the time delay within experimental errors being that expected. Secondly for all traces where the estimated propagation distance is zero there is no dip at the beginning of the trace. An expanded view of trace 9 in Figure 115 shows this well (Figure 116)

The Rayleigh step height may be measured in all cases and is given in Table IV.1 below. The first two traces are used to calculate a scaling factor for the theoretically

Trace (Figure 114)	Nominal propagation distance/mm	Rayleigh step Height/Å	Deduced propagation distance/mm
1	10.0±0.3	7.6±0.2	9.8±0.5
2	4.0	18.4±0.5	4.1±0.2
3	2.0	45±2	1.66±0.08
4	1.0	108±5	0.69±0.08
5	0.5	270±10	0.28±0.01
6	0.0±0.3	350±20	0.21±0.01
7	0.0	310±20	0.24±0.01
8	0.0	270±10	0.28±0.01
9	0.0	330±20	0.23±0.01
10	0.0	710±40	0.118±0.005

Table IV.1: The variation of Rayleigh step height for the traces in Figure 115

predicted pseudo-static depression created by the pencil lead as shown in Figure 92. It will be recalled that the

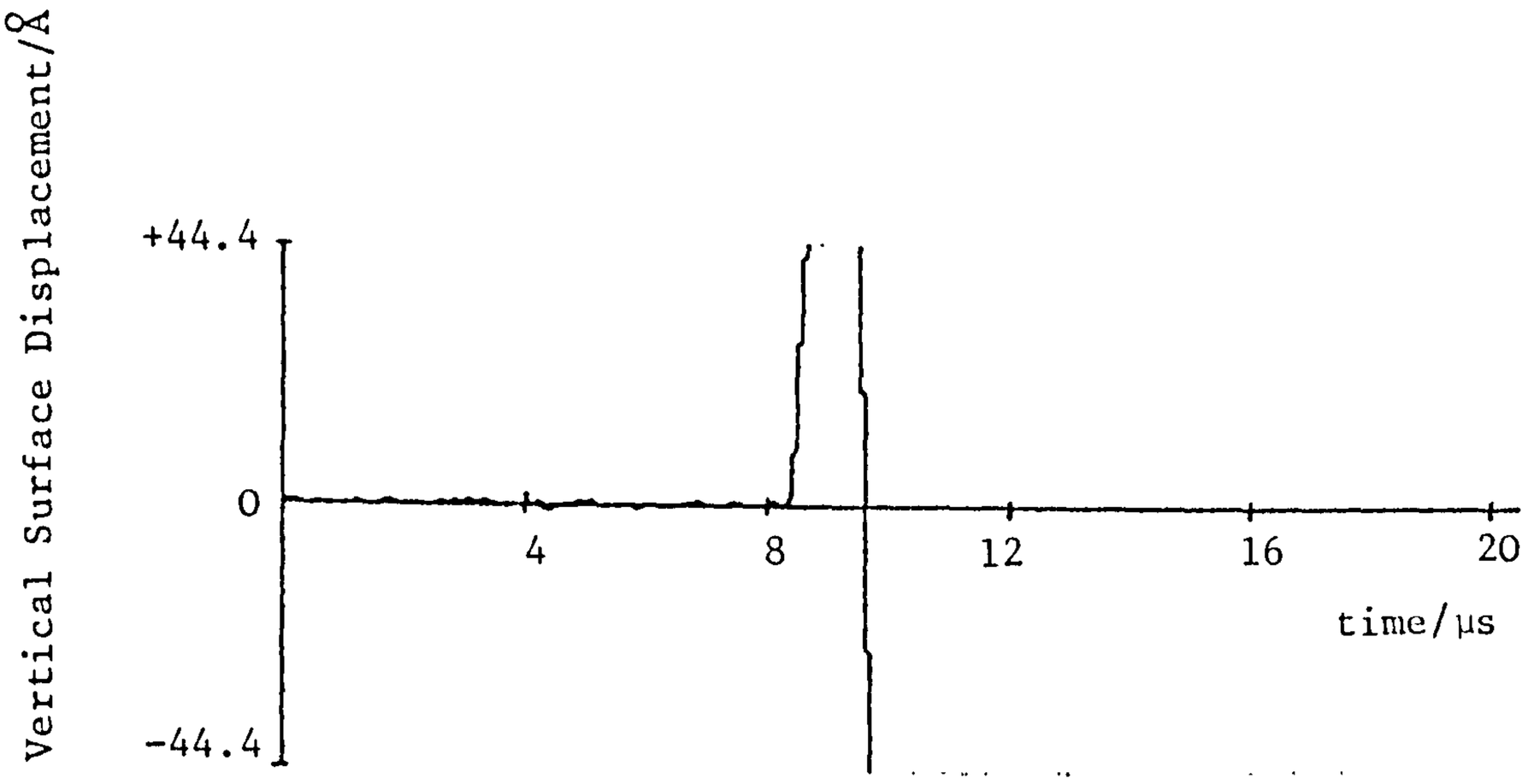

Figure 116: An expanded view of the surface displacement shown in trace 9 of figure 115. The waveform clips. No dip is evident before the first positive pulse even though it is captured on the most sensitive recorder setting.

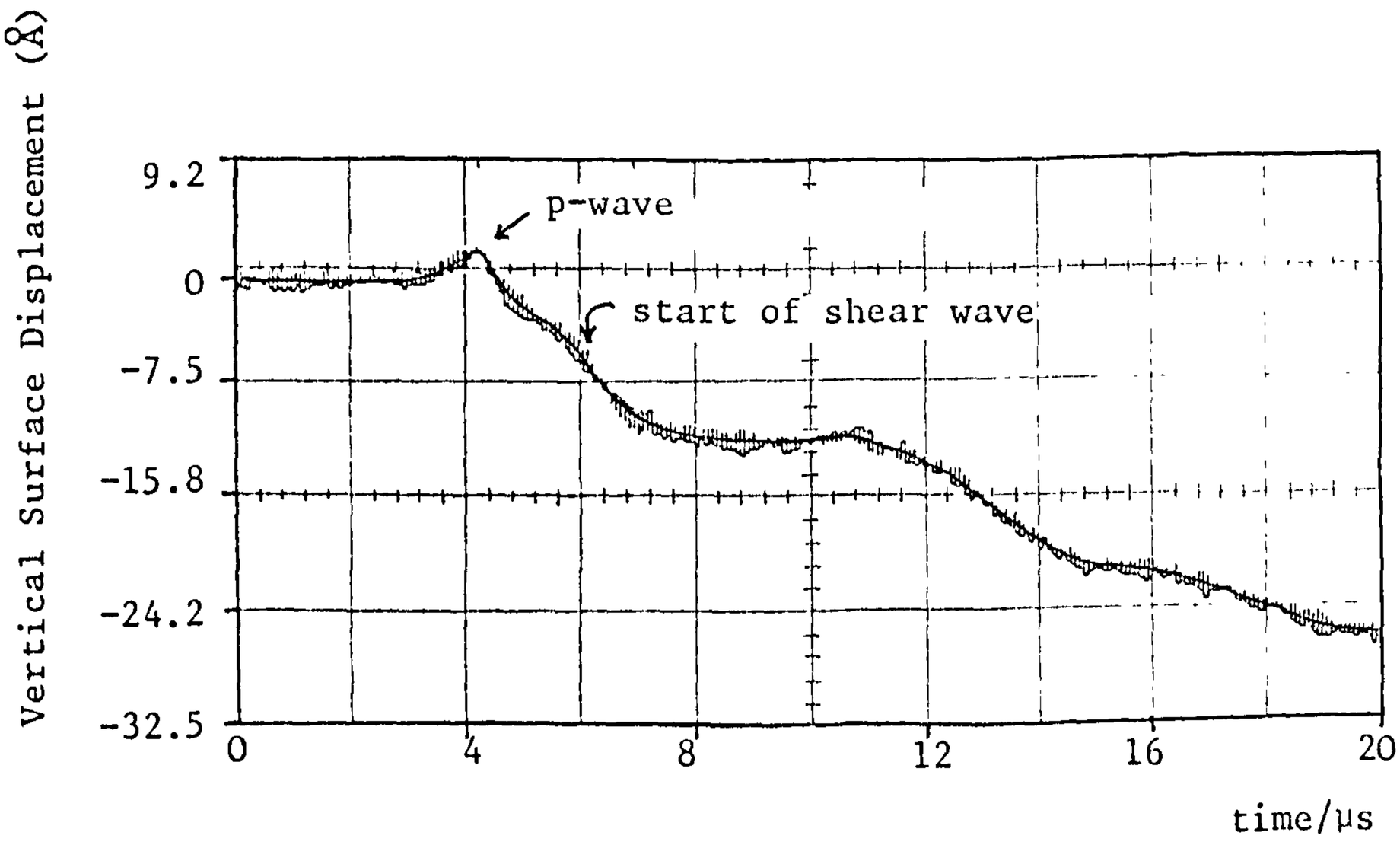

Figure 117: The ultrasonic waveform measured at the epicentre of a Hsu/Nielson source on the glass block. The trace exhibits the shape expected from a source such as that given in traces 6 → 10 of figure 115.

results of Figures 85 and 87 verified this theoretical solution as far as possible.

. It can clearly be seen that the general shapes of the traces 5 to 10 in Figure 115 are all the same thus confirming the conclusions in the previous section. This also indicates that traces 5 to 10 have the same time dependency as the artificial source at the origin. Knowing this allows the appropriate Green's function to be verified if the tangential force is assumed to be zero. Such work will be reported in section IV.2.2 later.

As a final check on those results the ultrasonic waveform measured at an epicentral position is captured (Figure 117). The pulse at the p-wave arrival is seen to be very similar to the source waveform, thus reinforcing the belief that the traces indicated above are in fact scaled versions of the source waveform. Work on the large aluminium block at epicentre also gives similar results although the signal to noise ratio in this case is much poorer.

The reproducibility of the Hsu/Nielson source may now be determined using the methods outlined previously. These results are summarized in Table IV.2 where the standard deviation gives the error about some scaled value. The standard deviation in the scaling factor was determined in section IV.1.1ii)b)iv) to be $\sim$ 20%. It can be seen that above 500kHz the pencil is not very reproducible and could not be used as an artificial source for higher frequencies than this.

Frequency/kHz	Standard deviation about a scaled value at this frequency/%
200	5 ± 1
500	21 ± 4
700	39 ± 8
1000	32 ± 10
1200	36 ± 15
1500	65 ± 20
2000	63 ± 30

Table IV.2: The reproducibility of the modulus of the frequency spectrum of the Hsu/Nielson source

IV.1.2ii) The ultrasonic transmitting transducer monitored at the origin

Using identical methods to those outlined above measurements were made of the movement of the lower force of a glass block in contact with an ultrasonic transducer, the transducer being coupled to the glass using silicone grease.

It would be expected that the vertical movement of the transducer face at some point from the centre of the transducer would be different. Measurements made using a broadband piezoelectric transducer placed directly on top of the transmitting transducer verify this belief. Unfortunately the present arrangement did not lend itself to making such measurements. Such work, however, would be of interest because in order to verify theoretical propagation predictions the movement of all points of the

source should be known.

The movement of the face of the glass block in contact with the centre of the transmitting transducer is shown in Figure 118. Peak A is due to the initial impulse from the transducer electrical pick-up being insignificant. As the p-wave from this pulse arrives at the upper face of the glass block the path length change produces the peak B. Reflection of this p-wave then generates C whilst the shear wave generated at the upper face leads to D. The initial impulse at A is very similar to a deconvoluted waveform given by Hsu et al[60] for a similar transmitting transducer. This waveform is shown in Figure 22.

By turning this glass block over, the movements of the upper face may be more easily seen, Figure 119. Various arrival times may be calculated. Each reflection at the lower face generates both p and s waves, presumably due to the grease coupling and finite curvature of the wavefront. An arrival time denoted by t_{pps} indicates a time which is the combination of two traversal times of a p-wave and one of an s-wave. The arrival time of the first reflection from the edge of the glass block is also shown.

Clearly the pulse evolves as the effective distance to the source and the number of reflections increases. Each part of the transducer face generates ultrasonic waves. The final pulse is formed from a sum of these waves. As the distance from the transducer increases the phase and magnitude of these contributions alter. A detailed

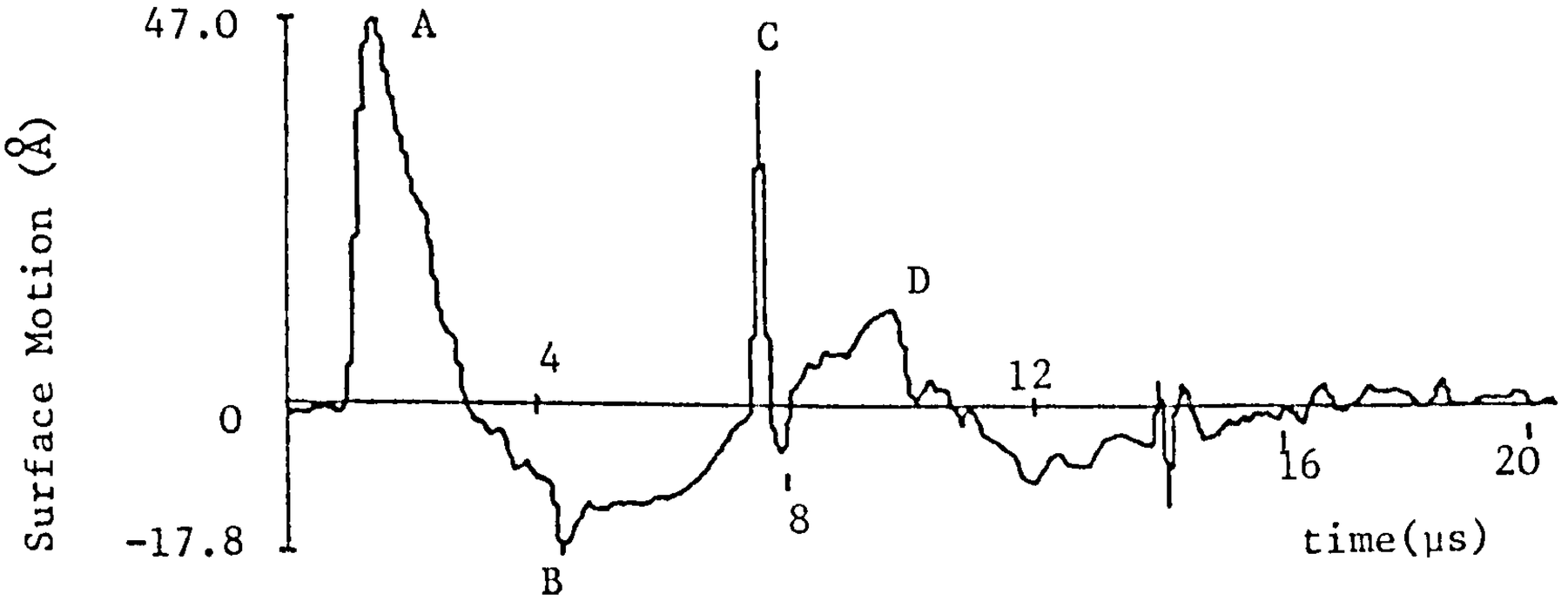

Figure 118: The vertical surface motion of the silvered face of a glass block in contact with the face centre of an ultrasound transducer. Measurements are taken with the optical interferometer as shown in figure (110).

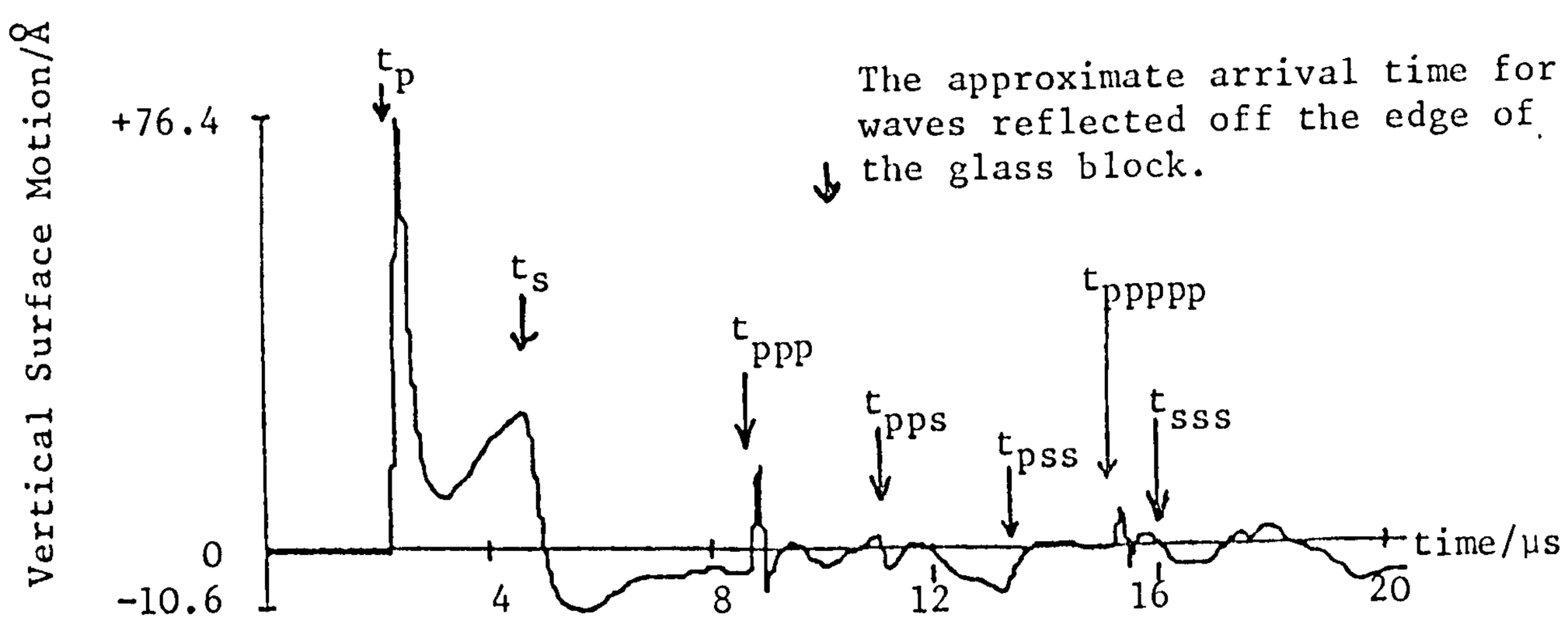

The approximate arrival time for waves reflected off the edge of the glass block.

Figure 119: The movement of the surface of a glass block at the epicentre of an ultrasound transducer. This motion corresponds to an event identical to that described in figure 118. The arrival times of various waves are calculated and shown.

calculation based on such effects may be made only if the movement of each point on the transducer face is known. This calculation, although of interest, is not possible with the present results.

It should be remembered that the source monitored here is the transmitting transducer in combination with a coupling layer of silicone grease.

IV.2 The study of ultrasonic pulse propagation

The propagation of surface pulses from point artificial sources has already been discussed in section IV.1.1. However, this included results only made at a distance and the accuracy of various propagation functions could only be inferred. To allow a fuller verification of the propagation function then, both the input function and the displacement at a distance must be measured. Having made measurements of the waveforms generated by a Hsu/Nielson artificial source both at a distance (section IV.1.1ii)b)) and at the origin (section IV.1.1i)b)) then this may now be done. However, before this is done the propagation functions of other geometries will be considered.

IV.2.1 The propagation functions for various simple geometries

The ability of the optical detector to probe inside transparent objects may be further employed to make the measurements necessary to determine a propagation function.

Some simple and well-characterized input pulse is preferred when making these measurements. It was shown in the preivous section (IV.1.2ii) that the near field from an ultrasonic transmitter is complicated and as yet not characterized. However the ultrasonic pulse generated by this source at epicentre on the large aluminium block described earlier is well-characterized.

This pulse has been measured over a circle of radius 3mm and found not to vary within this area. Therefore such a pulse is preferred for making propagation measurements.

To actually make the measurements the geometries of interest are first of all fashioned in glass. One face of the glass block is then silvered (following flame polishing in some cases). This glass piece is then coupled to the large aluminium block at the epicentre of the transmitting transducer described above. The coupling is performed using either silicone grease or water. Initial measurements are made with the silvered face in contact with the large aluminium block thus allowing the movement of the lower face to be detected. After inverting the glass the upper (now silvered) end is monitored. Therefore measurements are made of both the input and output ultrasonic pulses.

The propagation in various geometries is now discussed separately.

IV.2.1i) The propagation of an ultrasonic pulse in a large glass block

The first geometry tested is a glass block of dimensions 114.52 x 64.48 x 18.87mm. Initially this was coupled to the surface of the aluminium by silicone grease. With the silver side down the trace given in Figure 120 was found. Clearly this bears only a superficial relationship to the traces shown in Figure 109.

The ringing was assumed to be due to multiple reflections within the grease coupling. When the block is pushed down with much greater force the grease spreads out and the resulting waveform is shown in Figure 121. The ringing is now of higher frequency thus reinforcing the view given above. Due to the high viscosity of the grease and the large surface area of the glass in contact with it, then the viscousforces are large and a thin layer cannot be produced.

Changing the couplant to water greatly reduces the viscosity and the pulse corresponding to that shown in Figures 120 and 121 is now given in Figure 122. There is still evidence of pulse spreading in this case but the ringing, if it exists which it is assumed to do, is of too high a frequency to be resolved by the input ultrasonic pulse.

The peak A is due to the input pulse. The transmission of a plane ultrasonic wave across an interface is given by:

$$\frac{U_2}{U_0} = \frac{2\rho_1 v_1}{\rho_1 v_1 + \rho_2 v_2} \qquad (243)$$

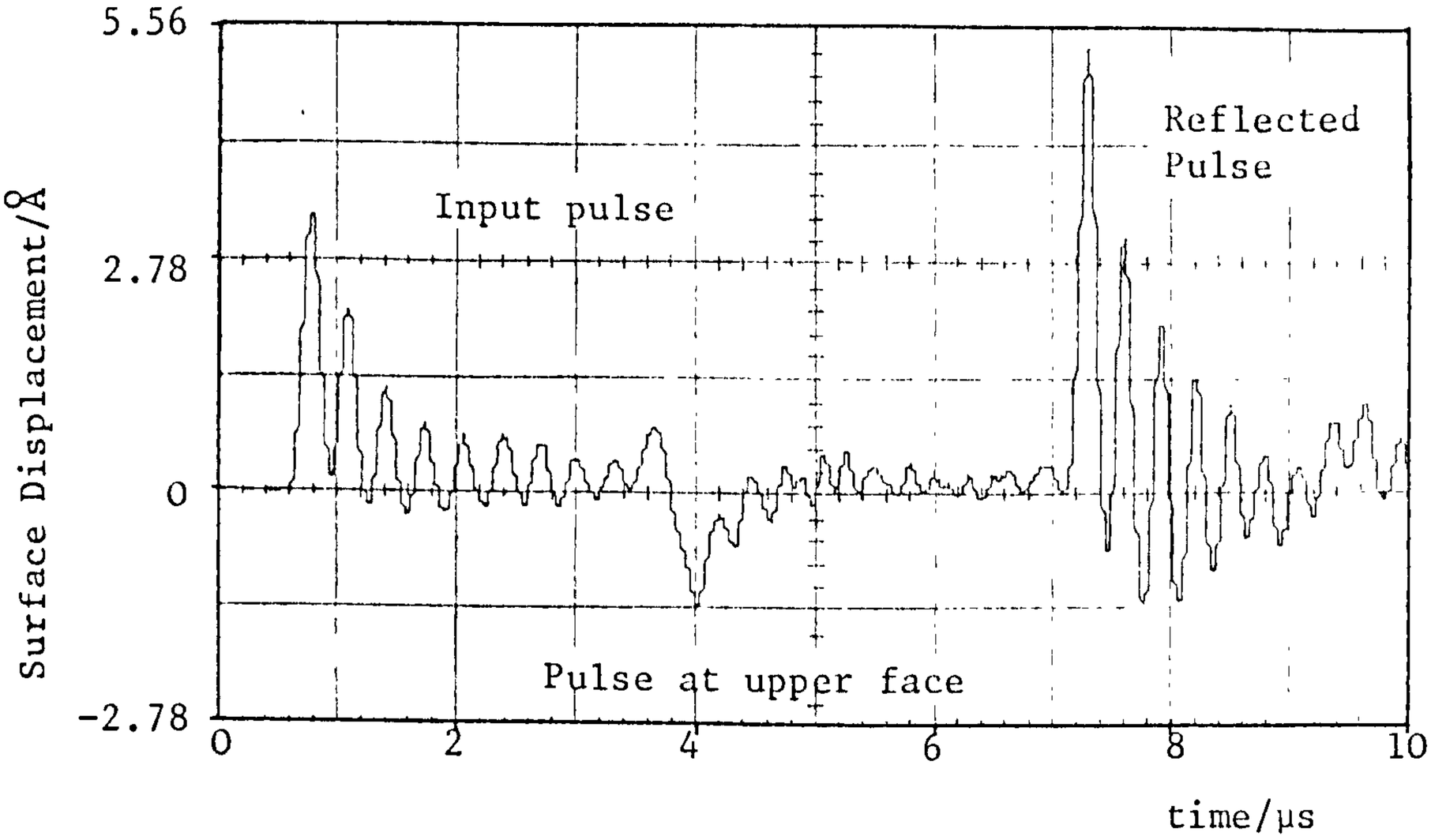

Figure 120: The displacement of the face of a glass block placed at the epicentral point on the large aluminium block of the transmitting ultrasound transducer. Coupling was performed with silicone grease.

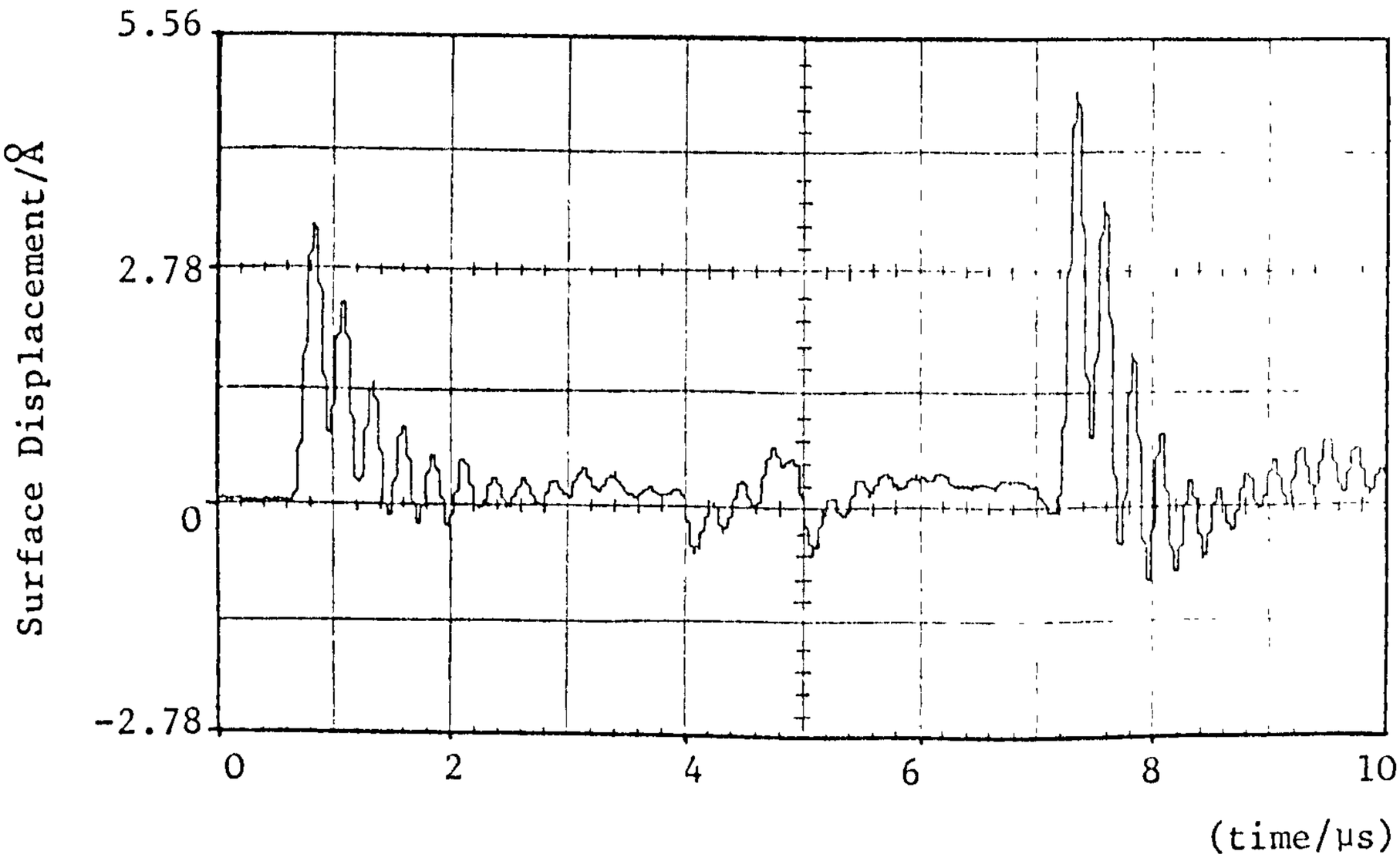

Figure 121: The surface displacement of the face of a glass block measured in an identical manner to figure 120 except the coupling layer of silicone grease is now thinner.

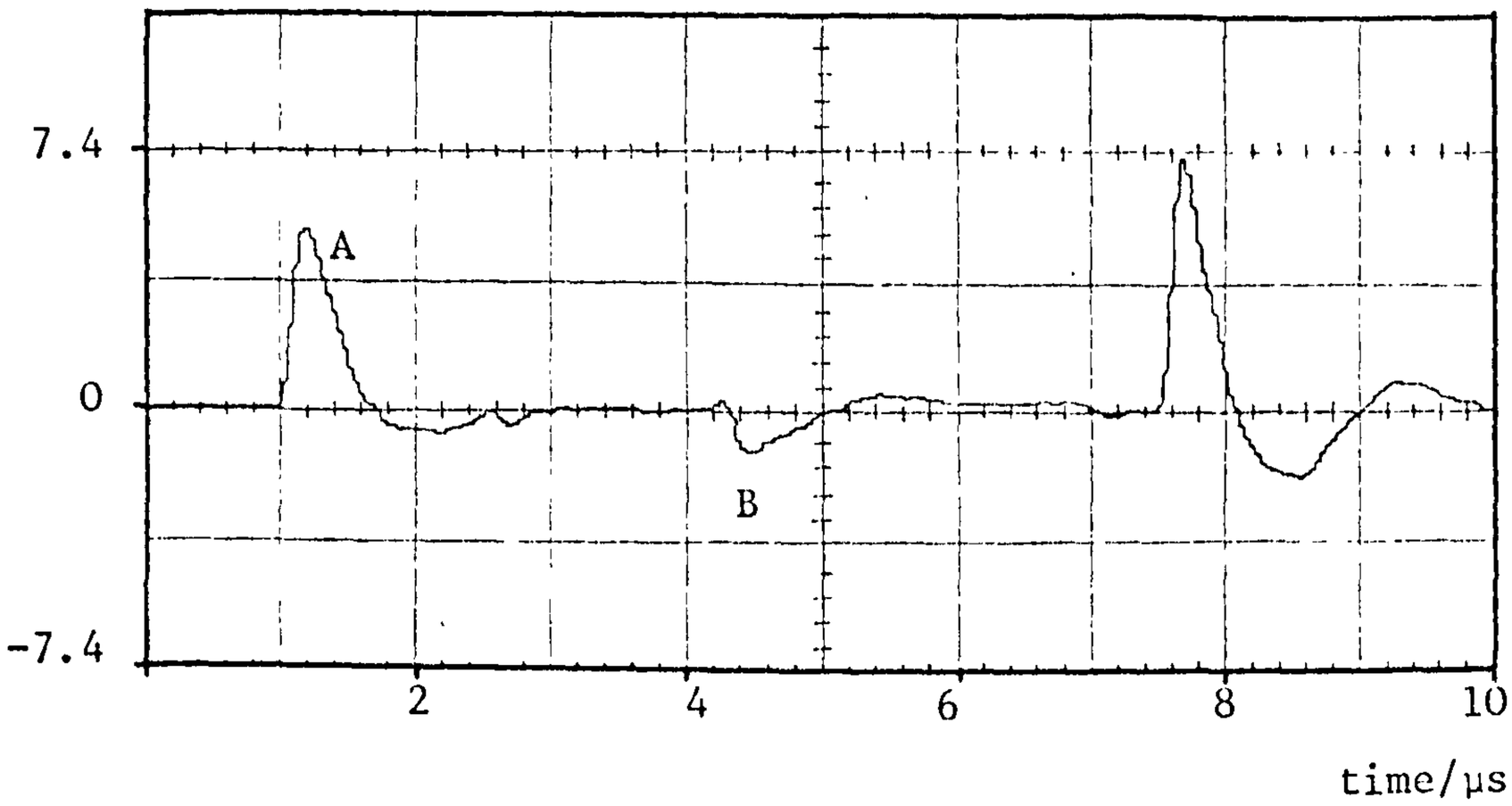

Figure 122: The same event as that given in figures (120) and (121) except that now the coupling is effected by a layer of water.

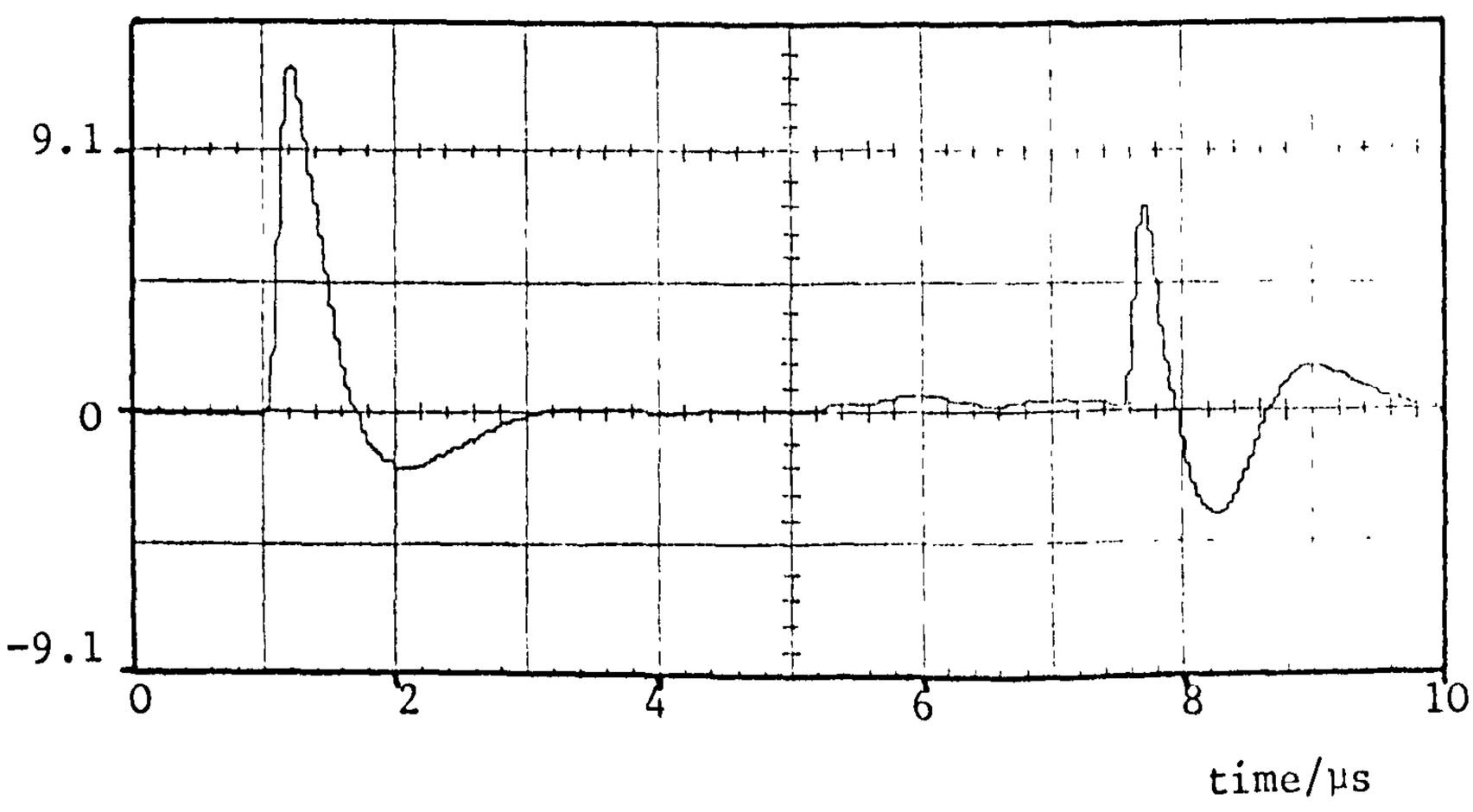

Figure 123: The surface displacement of the upper face of a glass block due to the first arrival and the first reflection of an ultrasonic pulse. The pulse is introduced by coupling the glass with water at the epicentral position on the large aluminium block of the transmitting ultrasound transducer.

where ρ_1 and v_1 are the density and velocity of the wave in the first (input) medium and ρ_2, v_2 the corresponding variables in the second (output) medium. The value U_2 is the amplitude of the wave in the second medium and U_0 the value in the incident medium. The density of the glass block is measured to be 2476kgm^{-3} and the velocity of longitudinal waves to be 5900ms^{-1}. Therefore taking the density of aluminium to be 2700kgm^{-3} and the velocity of longitudinal waves to be 6374ms^{-1}, equation (242) may be evaluated to give

$$\frac{U_2}{U_0} = 1.08 \qquad (244)$$

The free surface displacement on the surface of the aluminium is 30.3Å whilst that of the lower face of the glass block when in contact with the aluminium is 5.1Å (assuming a refractive index of 1.5 for the glass). The free surface displacement of aluminium (in contact with air in fact) is $2U_0$ and so the measured value of U_2/U_0 is 0.34. Clearly the water coupling is having an effect. It is possible to calculate the transmission of an aluminium, water, glass interface. However, this transmission depends on the thickness of the water and as this is not known then the theoretical transmission cannot be determined.

The second peak (B) is caused by the arrival of the pulse at the top of the glass block.

Turning the block over so the silvered side is now away from the aluminium gives the trace of Figure 123. The first peak is identical in shape to peak B on Figure 122. After two more reflections the pulse shape has changed to

that of the second peak in Figure 123. This evolution is assumed to be due to a combination of two causes. The first part is an aperture effect arising because the input wave is not plane but spherical. Therefore the wave entering the glass block has a range of phases and magnitudes. The second contribution is assumed to be the ringing in the couplant. This ringing should exaggerate the aperture effect by creating a wave-front with a broadened range of phases.

Testing this hypothesis would require measurements to be made over a large area of the base of the glass block to check for phase variations. Unfortunately insufficient time was available to do this.

In summary, the transmission of an ultrasonic pulse into a glass block and then through this block depends initially on the couplant. The subsequent propagation of the pulse within the block is assumed to be simple plane wave propagation. However this simplicity is masked by the fact that a large aperture effect exists due to the contact area of the glass block and the thickness of the aluminium block used to couple ultrasound from the transmitter to the glass.

IV.2.1ii) The propagation of an ultrasonic pulse in a (16.9 ± 0.1)mm diameter glass cylinder

Following on from the work on the large glass block (section IV.2.1i)) then some sort of aperture effect and also some sort of coupling effect might be expected with

this cylinder of diameter 16.9mm. The coupling effect is apparent with ringing occurring when silicone grease is used as a couplant. However due to the smaller contact area the effect is greatly reduced. With water as a couplant the couplant effect is not noticable. The cylinder length is 30.6mm. The first trace is taken with the cylinder placed epicentrally over the transmitting transducer and the silvered face in contact with the aluminium via a water coupling layer. Figure 124 then shows the movement of the centre of the lower face. The first peak in the trace is almost the same as that in Figure 109 for the movement of the free surface of the aluminium. The couplant effect is therefore negligible.

Consideration of the width of the cylinder and face and of the thickness of the aluminium block show that the time delay between the input ultrasonic pulse reaching the centre of the cylinder face and its circumference is only 60ns. This time is only just resolvable taking into account the input pulse width.

Therefore to a first approximation the end of the cylinder receives a uniform displacement over its entire surface. The time dependency of this impulse being given in Figure 109. The boundary condition at the input end is the glass rod in intimate contact with aluminium.

The pulses arriving after the first pulse is due, it is believed, to reflections from the sides of the cylinder.

Turning the rod over allows the movement of the centre of the upper face to be measured. This movement is shown in Figure 125. Clearly many reflections occur. Some of

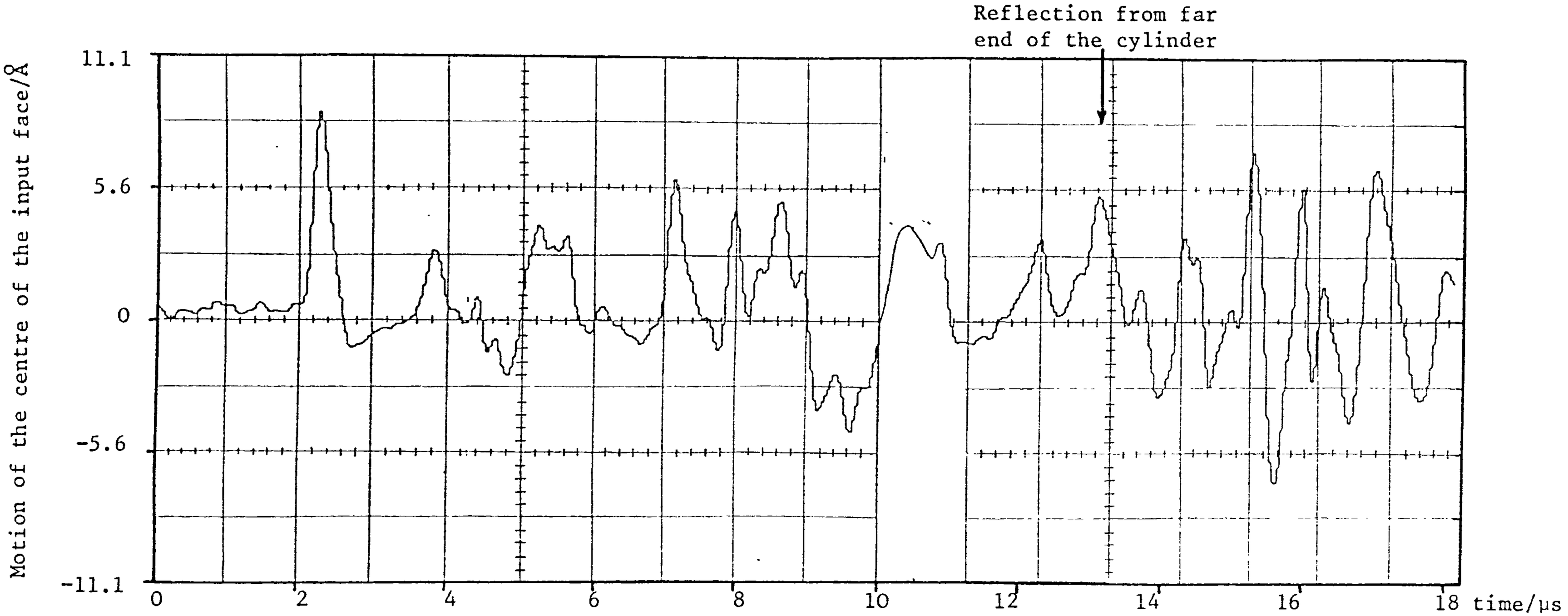

Figure 124: The movement of the centre of the input face of a 16.9mm diameter glass rod in contact with the large aluminium block at the epicentre of the ultrasonic transducer.

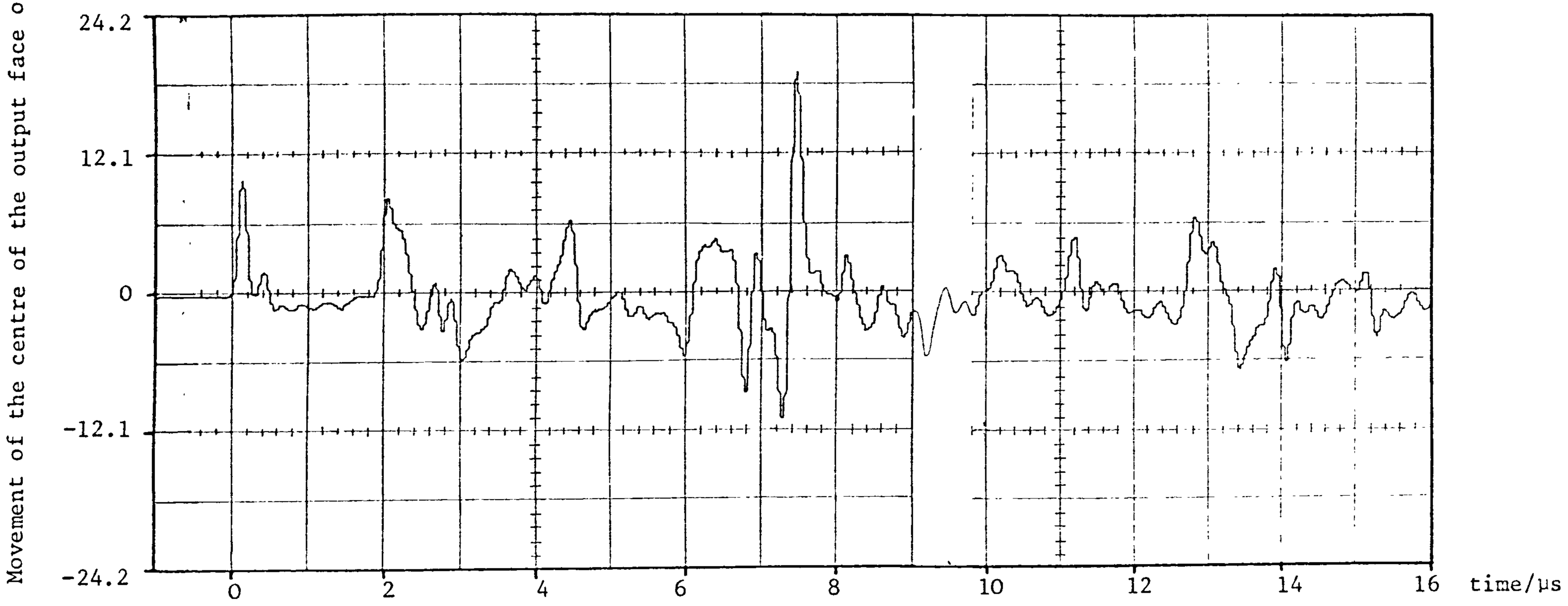

Figure 125: The movement of the centre of the far face of a 16.9mm diameter glass rod. The input ultrasonic pulse is introduced by coupling the glass rod with water to the epicentral point on the large aluminium block of the ultrasonic transmitting transducer.

these reflections have similar time delays behind the first peak as certain of the peaks in Figure 124 and as such may arise from similar reflections.

In summary Figure 125 gives the movement of the centre of the far end of a glass rod as a result of the near end receiving a plane ultrasonic pulse uniformly over its entire area. The time history of the input pulse being that given in Figure 109. The boundary conditions for the glass rod being intimate contact with aluminium at the near end with the far end being free.

These results now await a theoretical model, based on the initial and boundary conditions given above, to which they may be matched. Such theoretical work would be of great interest as the propagation function for a solid cylinder has, to the author's knowledge, never been derived, either experimentally or theoretically.

IV.2.1iii) The propagation of an ultrasonic pulse in a (6.87 ± 0.03)mm diameter solid cylinder

Similar results to those obtained above have been obtained on this cylinder of length 36.5mm. The error (± 0.5mm) in centering the laser probe in the glass rod is more significant, in this case due to the smaller cylinder diameter. Nonetheless reasonable pulses are obtained and are shown in Figure 126. The couplant here is water but no difference is observed when a grease couplant is used (Figure 127).

From these results it appears the boundary and initial conditions are the same as for the 16.9mm diameter rod.

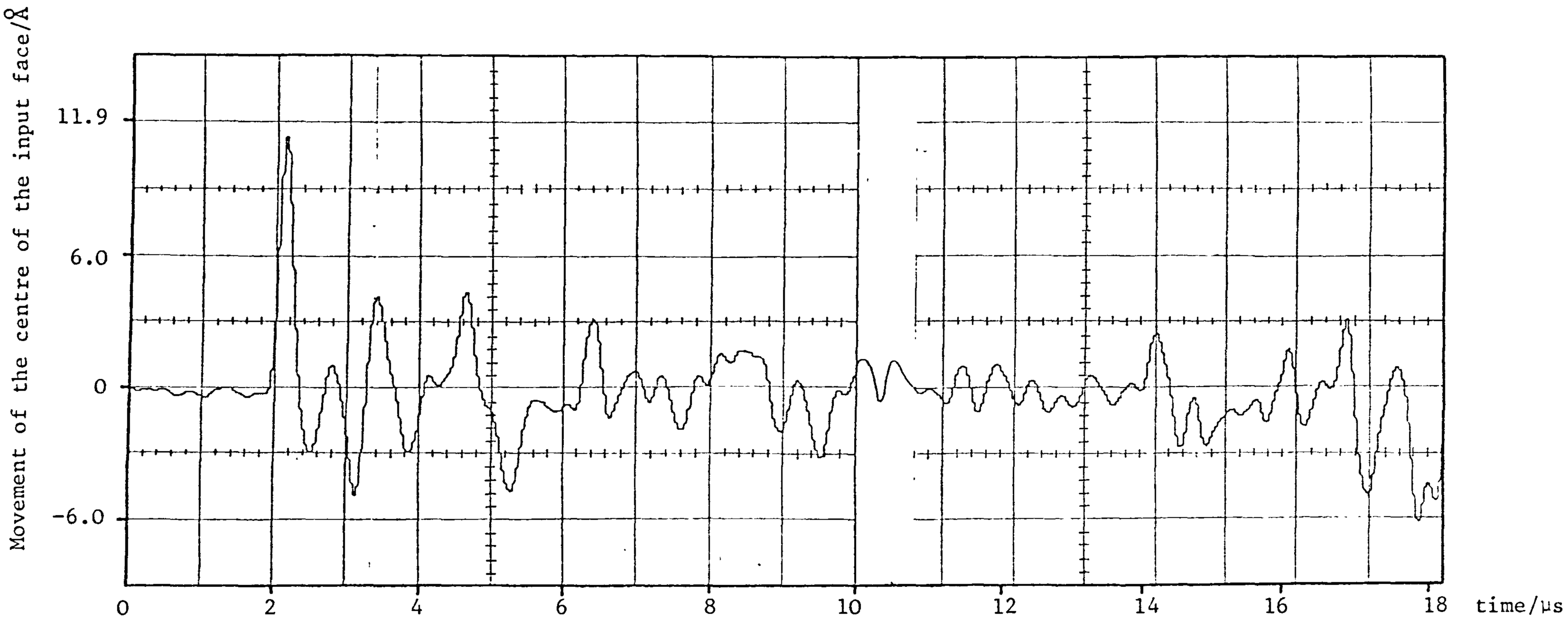

Figure 126: (part 1) The movement of the centre of the input face of a 6.87mm diameter glass rod generated by the ultrasonic pulse arriving at the epicentre of the ultrasound transmitting transducer on the large aluminium block. Coupling performed with water.

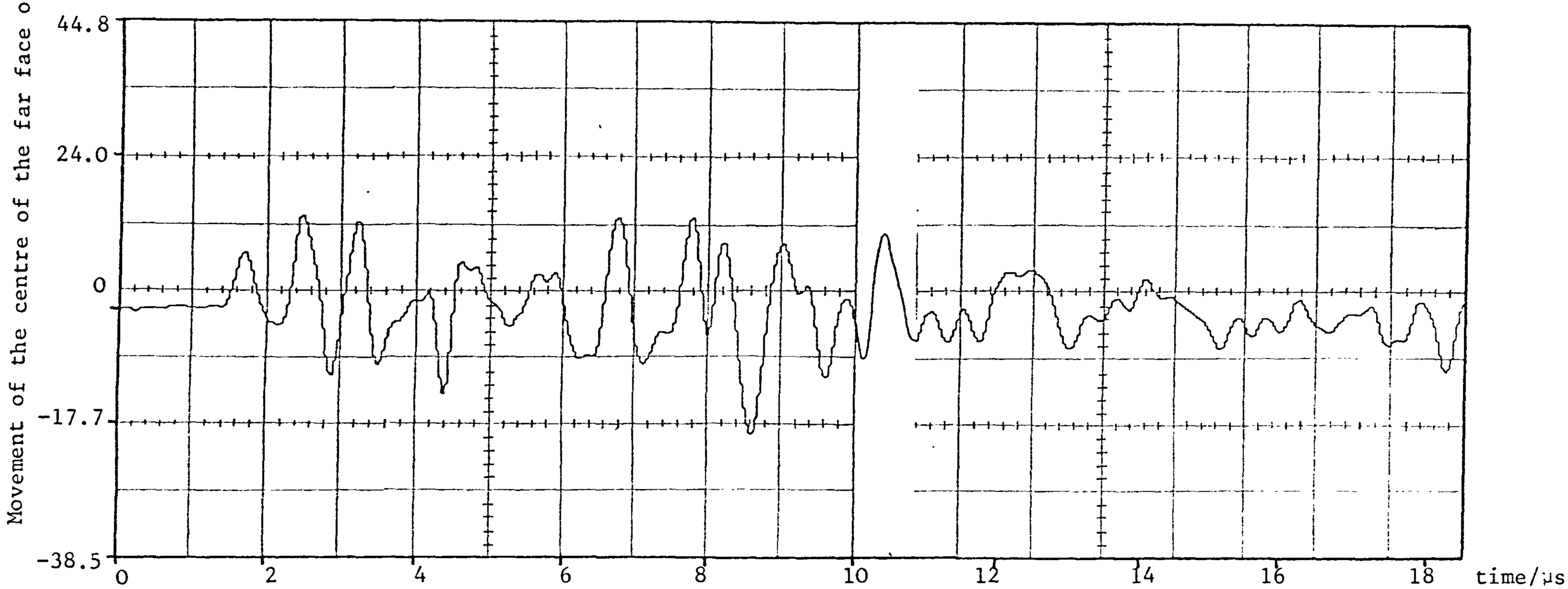

Figure 126: (part 2) The movement of the centre of the far face of the glass rod when the opposite end is subjected to the ultrasonic pulse outlined in figure 126 (part 1).

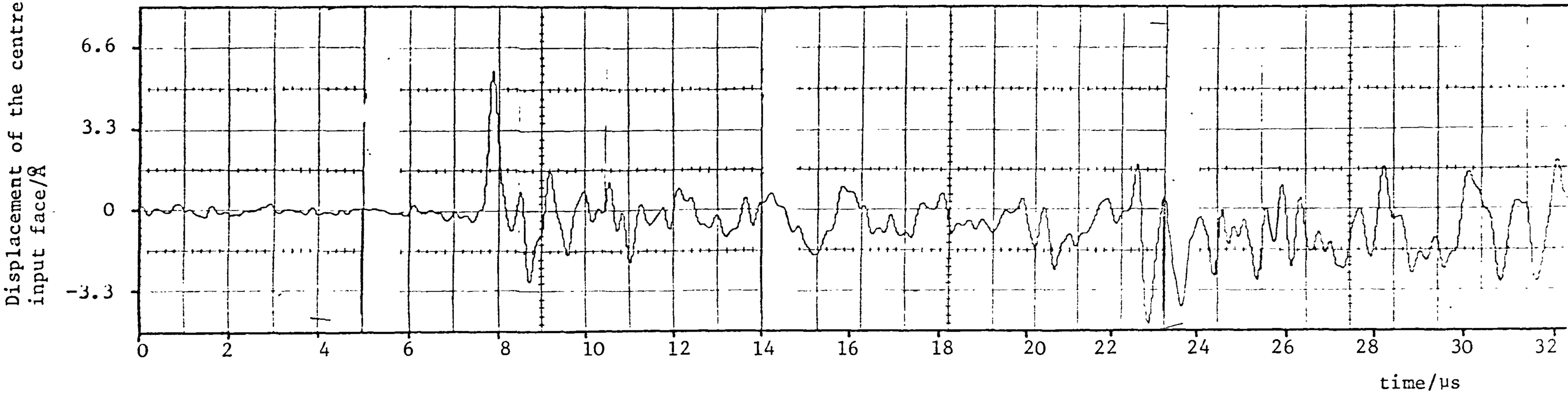

Figure 127: (part 1) The results of an identical experiment to that outlined in figure 126 (part 1) except the coupling medium is now silicone grease. Very little difference is noted between the traces as the grease thickness is small due to the small contact area of the glass rod.

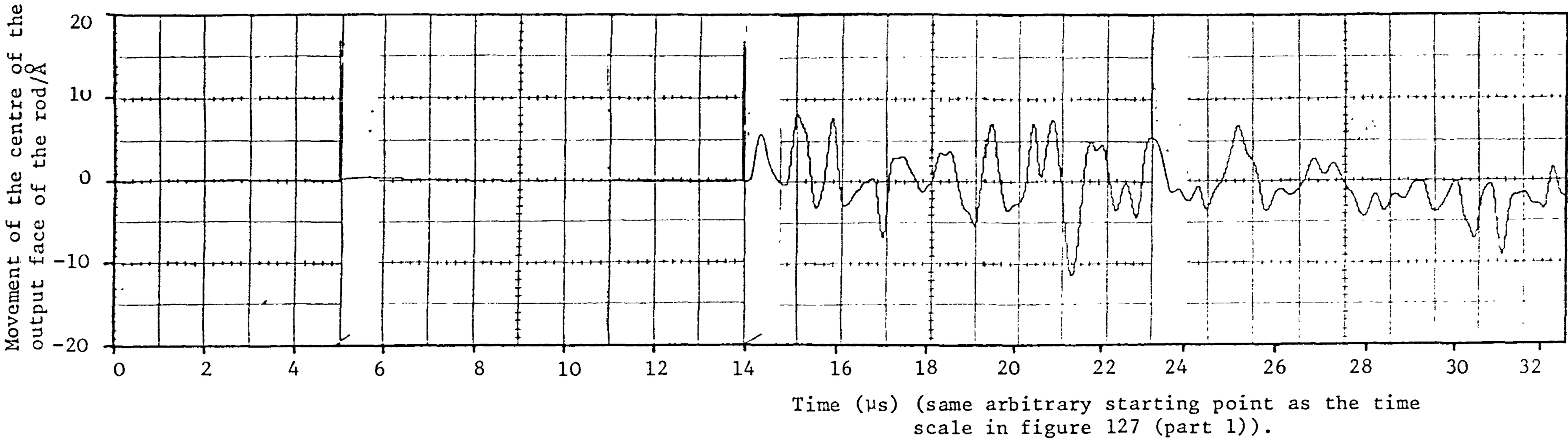

Figure 127: (part 2) The results of an identical experiment to that outlined in figure 126 (part 2) except that the coupling is performed here with silicone grease.

Indeed the time difference due to the aperture effect is now only 12ns.

The ringing seen now in the trace for the silvered end upwards (output end) is clearly much more severe than the corresponding trace for the 16.9mm diameter rod given in Figure 125. This is obviously due to the increased length to diameter ratio.

These results again require theoretical comparisons. It is felt that with the reduced aperture of this thinner rod these results may well match the theory better than those for the wider cylinder.

IV.2.2 The convolution of the measured Hsu/Nielson source function with theoretical Green's functions

As mentioned above now that the waveform generated by a Hsu/Nielson artificial source has been measured at both the source origin and at a distance then a fairly rigorous test of theoretical Green's propagation function is possible. Such a test involves convoluting the Green's function with the source function.

The first assumption to be made is that there is no tangential force in the surface due to the source. Due to the low frictional force between the ceramic pencil lead tip and the aluminium coating on the glass this appears to be a valid assumption. Once this assumption is made then various forms of the Green's functions may be verified.

The choice of which one to verify depends to some extent on the accuracy of the waveforms measured at a

distance. An epicentral waveform exists (Figure 117) but this has a fairly low signal to noise ratio. However several surface pulses have been captured and these have in general a reasonable signal to noise ratio. Indeed above 2MHz surface waveforms may only be accurately detected by an interferometer. Capacitor detectors on the other hand, although not suited to the detection of high frequency surface waves, produce excellent results at epicentre. Therefore the theoretical results for the surface pulse shown in Figure 5 derived by Pekeris[19] will be tested.

The final waveform to which the convolution is to be compared was detected on the large aluminium block at a distance of (35.0 ± 0.5)mm. Poisson's ratio for this particular aluminium is 0.343 and so the Green's function should be calculated for this ratio. Mooney[25] has given results for $\nu = {}^1/_3$ and these will be used. Following from equation (17) the convolution of interest is given by:

$$U_3(\underline{x} \equiv (35,0,0),t) = \left\{ \int_0^t G_{3,3}(\underline{x} \equiv (35,0,0)\,\underline{x_0} \equiv (0,0,0), t-\tau) \right.$$
$$\left. .S(\underline{x_0} \equiv (0,0,0),\tau)d\tau \right\} \qquad (245)$$

Putting $t = n\Delta t$ and $\tau = m\Delta t$, then this becomes (dropping $\underline{x}$ and $\underline{x_0}$)

$$U_3(n\Delta t) = \sum_{m=0}^{m=n} G_{3,3}(n\Delta t - m\Delta t).S(m\Delta t)\Delta t \qquad (246)$$

As $G_{3,3}$ is not generally available this sum may not be evaluated. Returning to equation (245) and substituting $u = t - \tau$ then (with subscripts dropped):

$$U(t) = \int_o^t G(U)S(t - u)du \qquad (247)$$

which upon integration by parts yields

$$U(t) = \left[S(t-u)\left(\int_o^u G(u')du'\right)\right]_o^t$$

$$- \int_o^t \left(\int_o^u G(u')du'\right) \frac{\partial S(t-u)}{\partial u}\, du \qquad (248)$$

From equation (237), (238) and (239) then

$$\int_o^u G(u')du' = G^H(u) \qquad (249)$$

also

$$\frac{\partial S(t-u)}{\partial u} = \frac{\partial S(t-u)}{\partial (t-u)} \cdot \frac{\partial (t-u)}{\partial u} \qquad (250)$$

Therefore equation (248) becomes (as the first part of (248) is zero):

$$U(t) = -\int_o^t G^H(u) \frac{\partial S(t-u)}{\partial (t-u)} \frac{d(t-u)\partial u}{\partial u} \qquad (251)$$

Substituting $\xi = t - u$ allows equation (251) to be rewritten as:

$$U(t) = \int_o^t G^H(t-\xi) \frac{\partial S(\xi)}{\partial \xi}\, d\xi \qquad (252)$$

where $\partial(t-u)/\partial u = -1$.

Equation (252) above may be transformed into a sum where with $\xi = m\Delta t$ and $t = n\Delta t$

$$\frac{\partial S(\xi)}{\partial \xi} = \frac{S(\xi_{m+1}) - S(\xi_m)}{\Delta t} \qquad (253)$$

therefore

$$U(n\Delta t) = \sum_{m=0}^{m=n} G^H(n\Delta t - m\Delta t).(S((m+1)\Delta t)-S(m\Delta t)) \qquad (254)$$

It is possible now to evaluate this sum as G^H is known and so G^H ($n\Delta t - m\Delta t$) may be determined.

The displacements caused by the p-wave in G^H are in general small and so only a partial sum is evaluated. Δt is taken as 0.1μs with the infinity at the Rayleigh wave arrival being dealt with in the manner described earlier in section IV.1.2i)a). With Δt = 0.1μs then digitizing errors may occur for two reasons. Firstly, some rise times in the source function are around 0.3μs and secondly the Rayleigh step in G^H now has a rise time of 0.1μs. The results from Mooney's[25] work and the source function (trace 10 in Figure 115) are now digitized and equation (254) evaluated (see appendix 11).

The result of this convolution is shown in Figure 128 together with four traces captured on the aluminium block with the same source and at the same separation of 35mm as the convolution.

The agreement is very good although some errors still occur with the two traces not being perfectly identical. There are a variety of reasons for this.

Firstly only one source function was digitized. There will be some variation in this function as indicated both by the frequency domain reproducibility and by inspection of the traces in Figure 115. This would introduce a discrepancy. However of all the waveforms measured at 35mm none produces a perfect fit to the convolution which suggests this is not the problem.

The second source of error is linked with the size of the source function. The size of the initial displacement

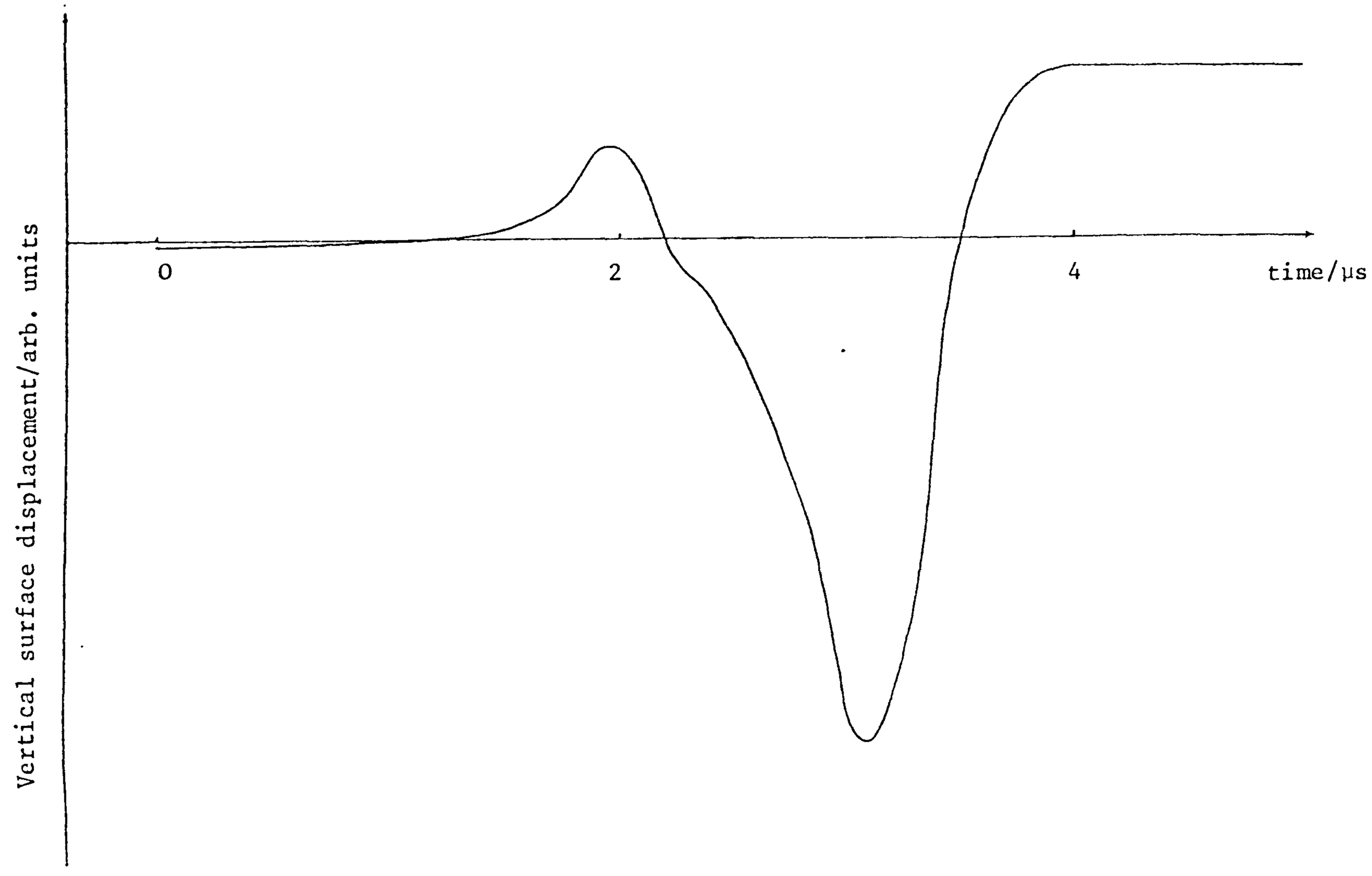

Figure 128: (part 1) The result of the convolution of a directly measured Hsu/Nielson source function (trace 10 in figure (115)) with the theoretical Green's function for a surface pulse on an aluminium semi-infinite half space taken from Mooney[25]. Only the latter part of the pulse if given.

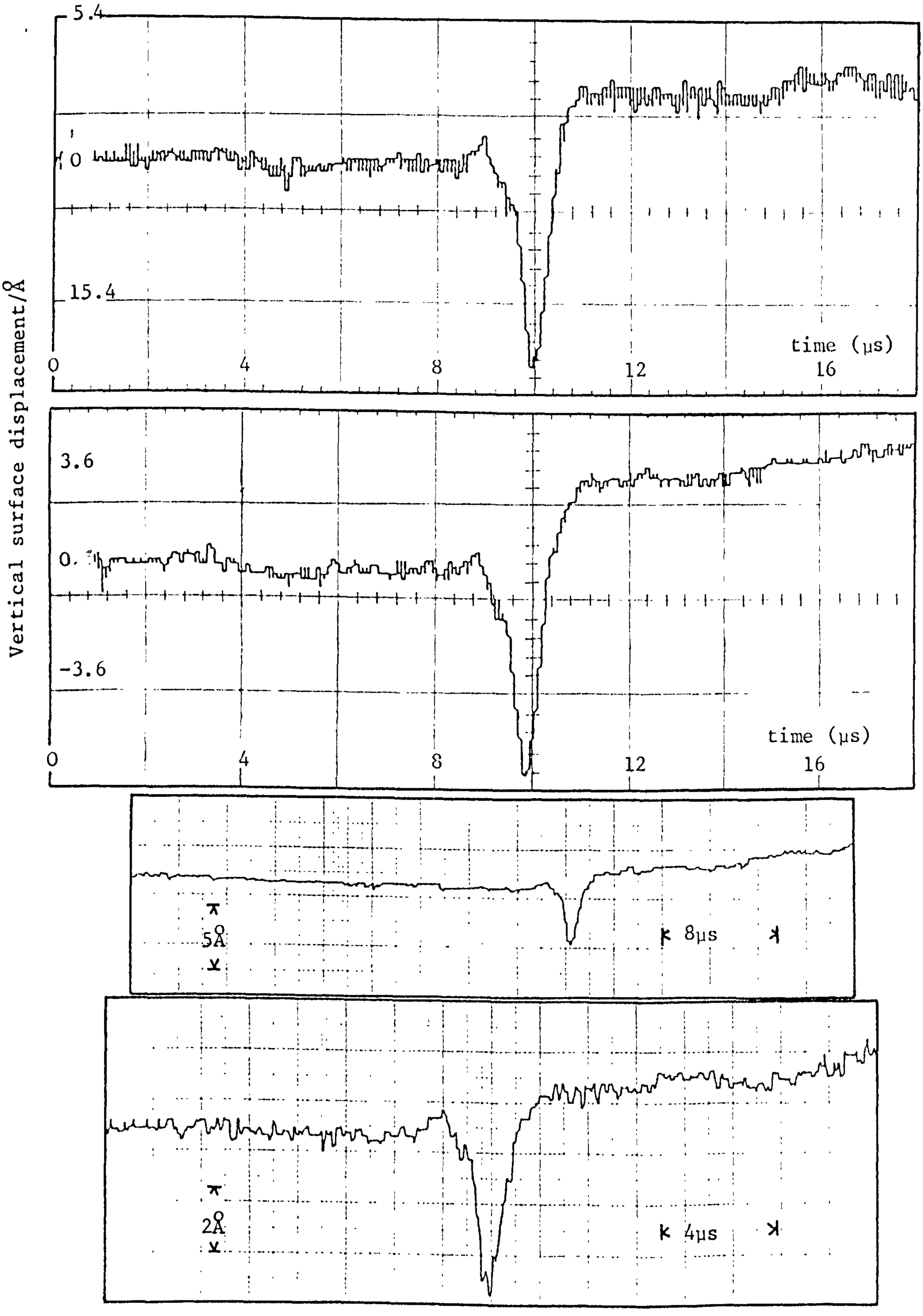

Figure 128: (part 2) Four surface pulses from a Hsu/Nielson source measured at a distance to be compared with the convolution given in (part 1).

is so large that the output from the interferometer approaches the top of the fringe. At this point the error in the peak height of the fringes becomes more significant leading to an error of ∿ 8% in the value for the displacement. Even though this is quite large it is felt this is still not enough to cause the discrepancies seen.

The third source of error is that caused by both the finite digitizing interval of 0.1μs and by the method used to remove the Rayleigh infinity. It is difficult to determine the extent of these errors without performing another calculation.

The final error source is caused by errors in digitizing the theoretical Green's function. Only small scale graphs existed of this function and ideally the original numerical values should be used.

In summary the convolution of a theoretical Green's propagation function with an experimentally measured artificial source function produces a waveform which is in fair agreement with experimentally measured versions. Considerations of the possible sources of error indicate that the propagation function is probably correct although further work is desirable. To the author's knowledge, this is the first such verification performed.

IV.3 The laboratory calibration of ultrasonic transducers

IV.3.1 Surface pulse calibration

Once a high frequency artificial source is available

then it may be used to calibrate transducers in the laboratory. This was done for surface pulses by placing the artificial source symmertrically between the stabilized optical interferometer and the transducer under test (see Figure 129). All of the sources described above produce spherically symmetric pulses and so each detector responds to the same surface motion.

The output of the stabilized interferometer is then compared with the output of the uncalibrated transducer. Following the methods outlined in sections II.6.1 and II.6.3i)a) the transducer may be calibrated either taking the fourier transforms of each output and performing a complex division or by determining the inverse of the interferometer output (by matrix inversion) and then computing a time domain convolution. Equations (22) and (23) are:

$$V_O(\omega) = \alpha.U(\omega) \qquad (255)$$

and

$$V_T(\omega) = T_T(\omega).U(\omega) \qquad (256)$$

where $V_O(\omega)$ and $V_T(\omega)$ are the frequency domain outputs from the optical and uncalibrated transducers respectively, $T_T(\omega)$ is the transfer function for the uncalibrated transducer and $U(\omega)$ is the frequency domain surface displacement.

Dividing these gives

$$T_T(\omega) = \alpha.V_T(\omega)/V_O(\omega) \qquad (257)$$

or

$$T_T(\omega) = \alpha.V_T(\omega)V_O^{-1}(\omega) \qquad (258)$$

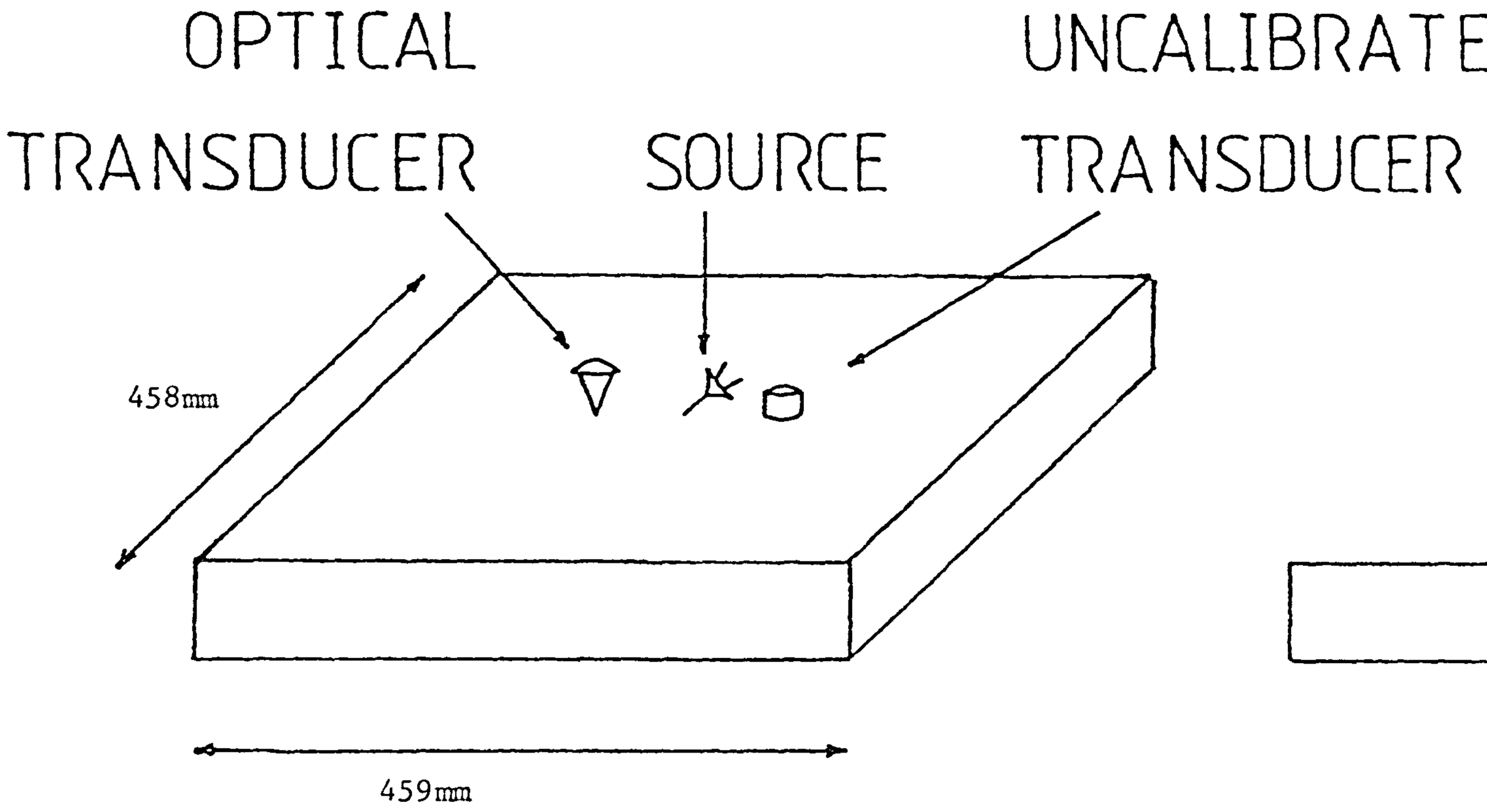

(a)

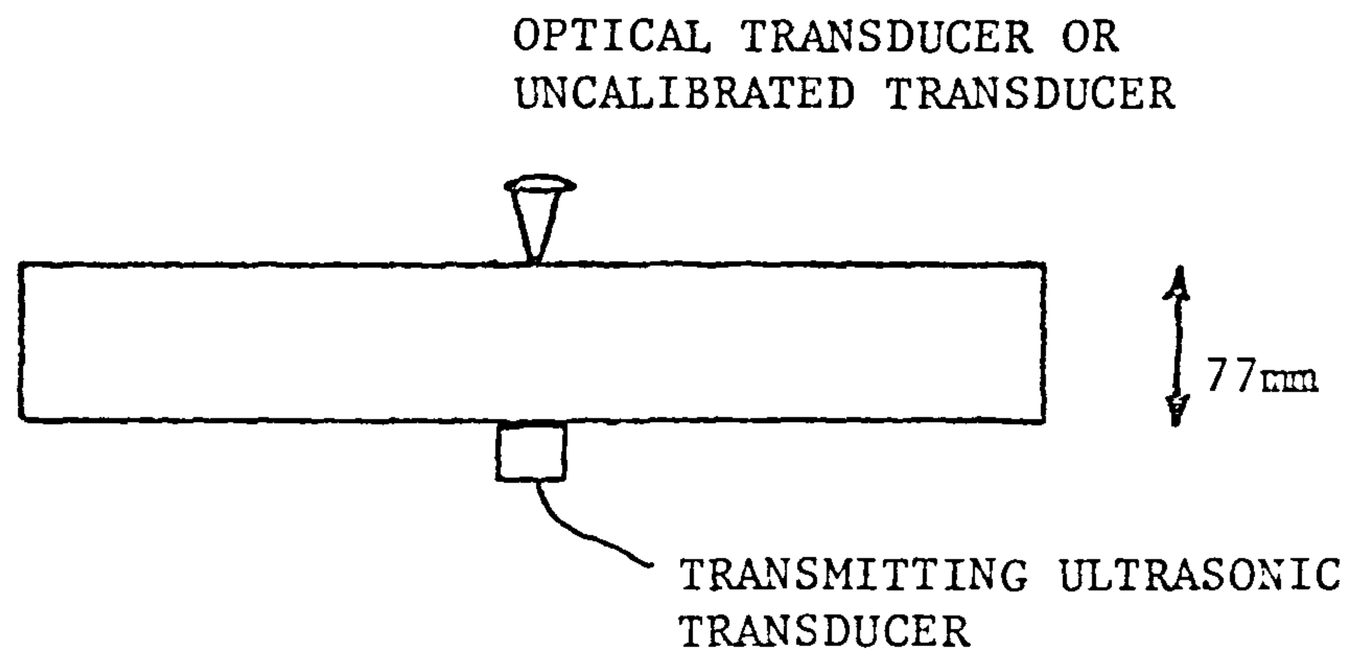

(b)

Figure 129: The schematic arrangements for (a) surface pulse calibrations and (b) epicentral calibrations.

leading to:

$$T_T(t) = \alpha \int_o^t V_T(t-\tau) V_O^{-1}(\tau) d\tau \qquad (259)$$

where $V_O^{-1}(\tau)$ is derived from $V_o(\tau)$ by matrix inversion (see appendix 3).

IV.3.2 Epicentral pulse calibration

For this calibration the repeatable ultrasonic transmitter is placed under the large aluminium block so that the stabilized interferometer can detect the epicentral pulse (see Figure 129).

$V_o(t)$ is first measured. The optical detector is then replaced by the uncalibrated transducer and $V_T(t)$ determined. Experiment shows that the interchange of transducers does not affect the repeatability of the source.

This epicentral calibration together with the surface pulse calibration then allows various assumptions made in the calibrations to be verified (see section II.6.1).

Results obtained using these methods will be discussed in the next two chapters together with various developemental work carried out on the transducers tested.

V. THE DEVELOPMENT AND CHARACTERIZATION OF MAGNETO-STRICTIVE TRANSDUCERS

Several materials, when subjected to external stress, suffer a change in magnetization. This phenomena is often termed inverse magnetostriction and the possibility clearly exists of being able to use this effect to transduct ultrasonic signals into initially magnetic and then electric signals. The reverse process is also possible. When a magnetostrictive material is placed in a magnetic field the magnetic field causes the material to strain, if it is free, or to become stressed if it is clamped. A great deal of work has been performed on this latter effect. However to the author's knowledge no previous work has been carried out on the development of high bandwidth inverse magneto-strictive (IMS) ultrasound detectors. The work that has been done of ultrasonic transducers has been performed on lower frequency devices often with a view to developing pulse echo techniques[98]. Such work will form a starting point for the work described in this chapter.

V.1 Preliminary development of the inverse magnetostrictive detector

Before preliminary work may be carried out on the effects of magnetic field variation etc., some consideration should be given to the final transducer configuration. In order to remove transducer resonances to frequencies below the ranges of interest then ideally all the dimensions

of the detector should be large. Unfortunately, this is not possible as a consideration of aperture effects quickly indicates that at least the transducer contact area must be small.

Once ultrasonic waves have been coupled into the IMS detector then the magnetic field variation they produce must be monitored. A simple and efficient way of doing this is to wind a coil around the magneto-strictive material resulting in the creation of electrical signals via Faraday's induction law. A magnetic disc recorder head was tried, but found to have a poor signal to noise ratio. This was unfortunate as it offered the possibility of being able to detect the magnetic field variations over very small sections of material.

Consideration of all the points above indicates the final detector will probably best be fashioned as a long thin rod. This is therefore the configuration on which preliminary investigations will be carried out.

The prototype transducer actually used for the initial tests is shown in Figure 130. Here the measuring coil is a simple coil wound around the bar. A magnet coil generates a biasing magnetic field and pressure impulses were introduced at one end of the bar. Two different methods were employed to produce the pressure pulses in the bar: the standard Hsu/Nielson source, or a piezoelectric pulser. For the latter the trigger pulse for the recording device, a storage oscilloscope, was taken from the exciting voltage waveform. However, for the case of pencil excitation, the triggering coil shown in Figure 130 was used with the

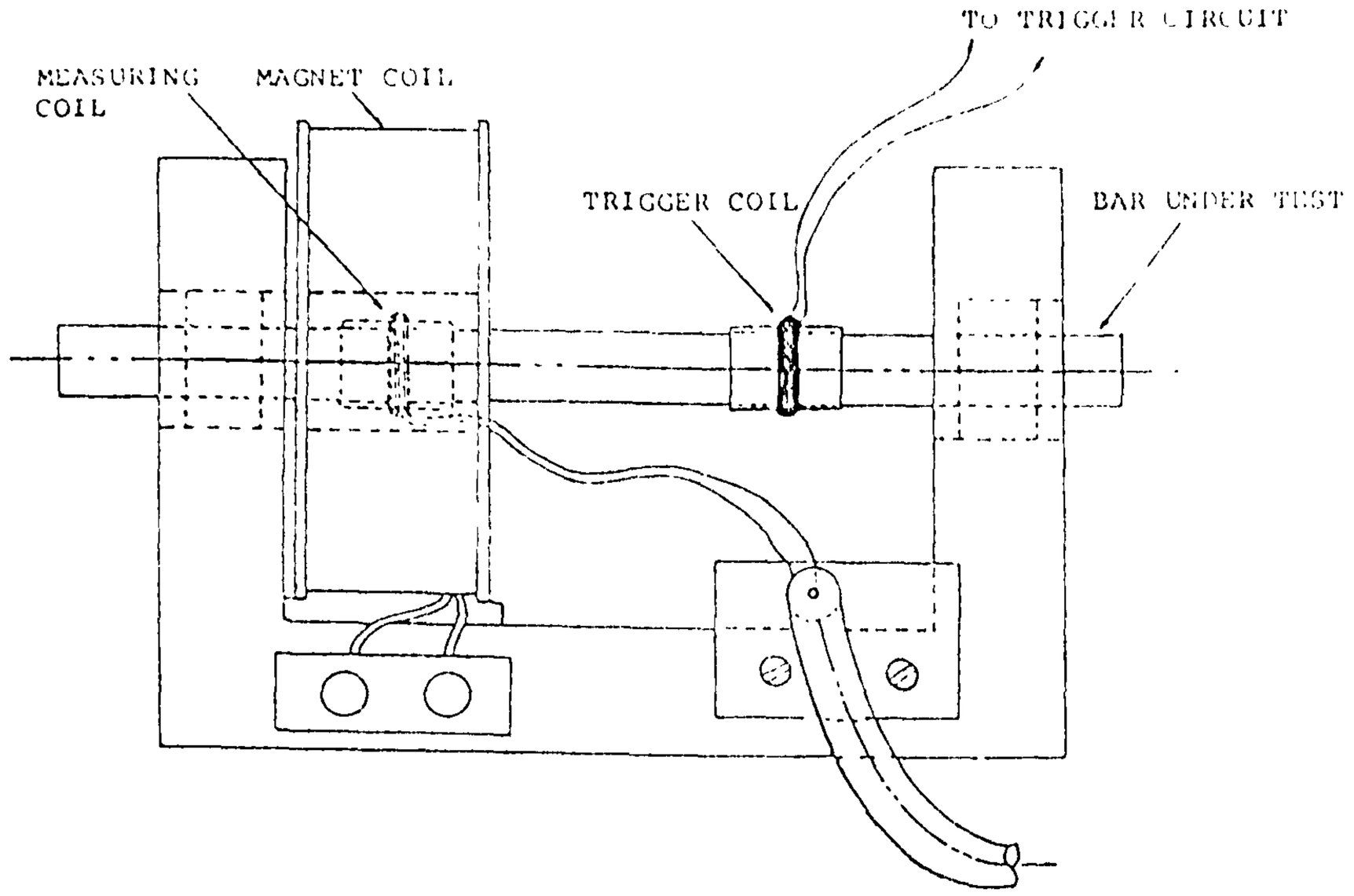

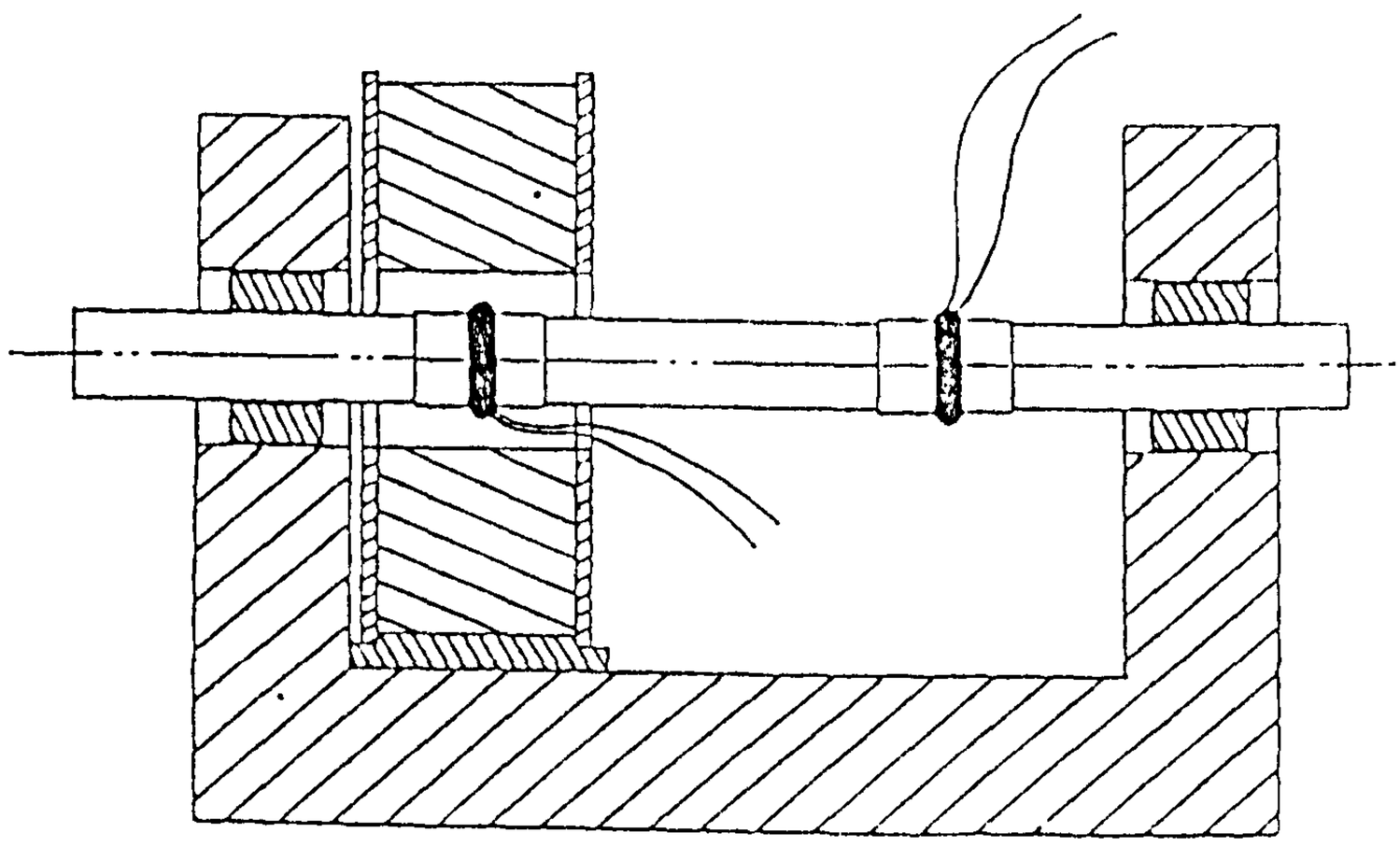

Figure 130: The prototype transducer used for initial investigations of the inverse magnetostrictive effect. Approximately one quarter scale. The lower diagram is a sectional view of the upper one.

associated electronics given in Figure 131. It was found that the filter removed mains noise and greatly improved the reliability of the trigger. Typical device responses are shown later in Figure 136.

The response of the measuring system to these pressure pulses was determined as a function of several different parameters which will now be discussed separately.

V.1.1 Development of the measuring coil and associated detection circuitry including optimum signal to noise ratio

Obvious variables in the detection circuitry are associated with the measuring coil itself and the preamplifier following it. Such variables are for example the dimensions and number of turns (N) of the coil and the input impedance of the preamplifier.

Now a detecting coil having a large N has a large inductance and hence large high frequency impedance. Therefore if N is to be increased then so must the input impedance (R_{in}) of the amplifier, if the high frequency response is not to be reduced. From Figure 132 it is obvious the voltage across the input impedance of the amplifier is given by

$$\frac{VR_{in}}{R_{in} + j\omega L} \qquad (260)$$

Experiments indicate this to be the case.

The experimentally measured signal to noise ratio for the leading pulse resulting from a Hsu/Nielson excitation

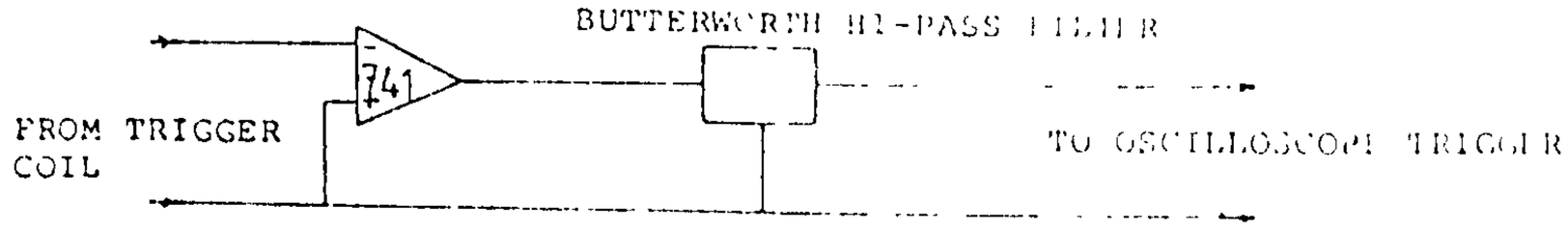

Figure 131: The triggering circuit (upper trace) and measuring circuit (lower trace) electronics used with the inverse-magnetostrictive prototype transducer.

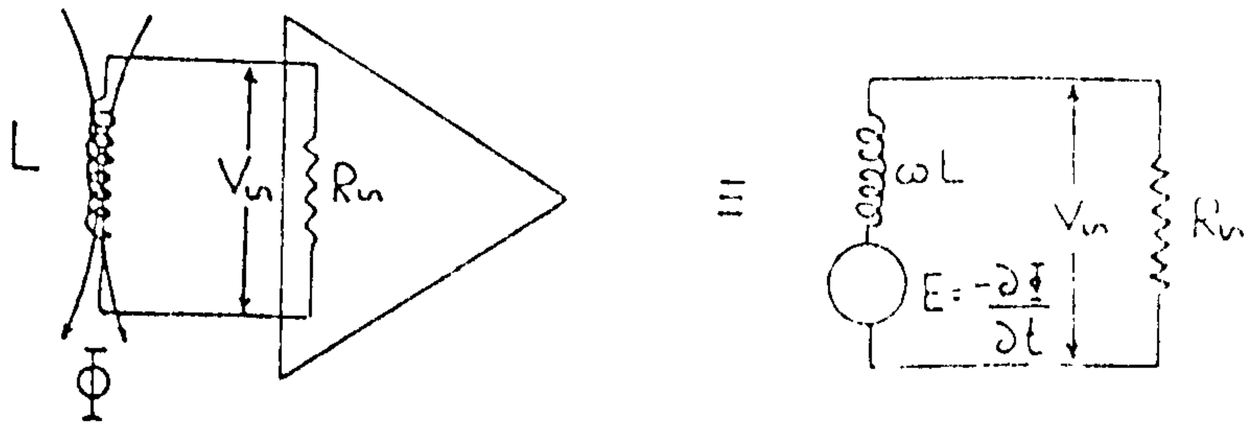

Figure 132: The equivalent circuit for the measuring coil on the prototype transducer.

is given versus (N/R_{in}) in Figure 133, whilst the relative response of the system to subsequent high frequency components is shown in Figure 134 as a function of (N/R_{in}) and as a function of frequency for given (N/R_{in}) in Figure 135.

Figures 134 and 135 indicate that equation (260) is obeyed once the parameter L is determined. In order to explain the results in Figure 133 then the various sources of noise in the detecting circuitry should be determined.

Three sources of noise can be identified. The first of these is the amplifier base level of noise created by fluctuations in charge flow within components such as transistors. The value of this when referred to the input was 5μV for the preamplifier used. However, this noise is overwhelmed if the input resistance is increased by Johnson noise in the input impedance[103]. At room temperature the contribution to the noise figure for Johnson noise is

$$V_{nJ} = 0.13 \times 10^{-6} R_{in}^{\frac{1}{2}} \qquad (261)$$

The final source of noise occurs for very large values of N (the number of turns of the coil) where any shielding becomes ineffective and pick-up of the measuring coil becomes the dominating factor. This is written as:

$$V_{np} = A_p N \qquad (262)$$

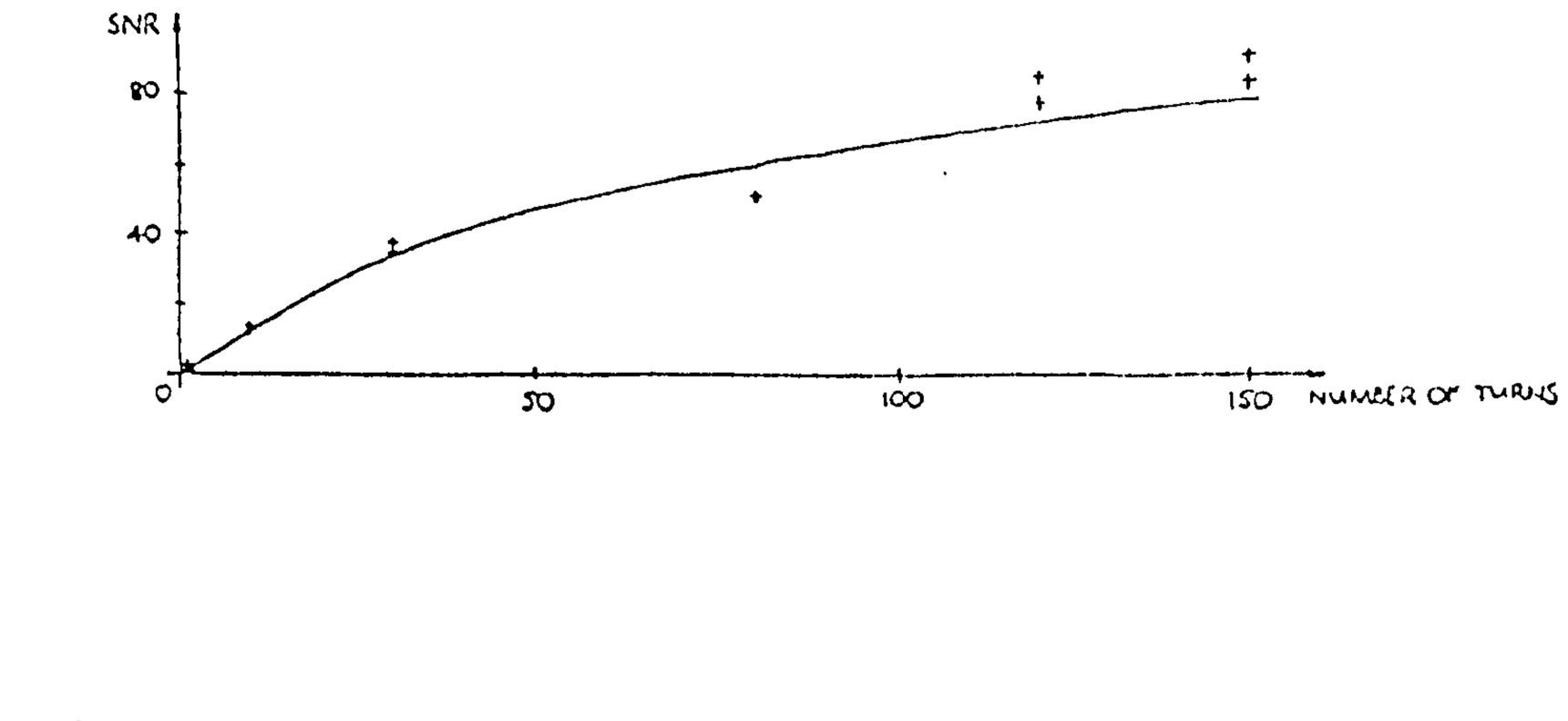

Figure 133: The signal to noise ratio in the prototype transducer for a Hsu/Nielson source (0.5mm diameter lead extended by six clicks) as a function of the number of turns (N) on the measuring coil (R_{in} = 100Ω) (upper trace) and as a function of input impedance (lower trace - N = 80).

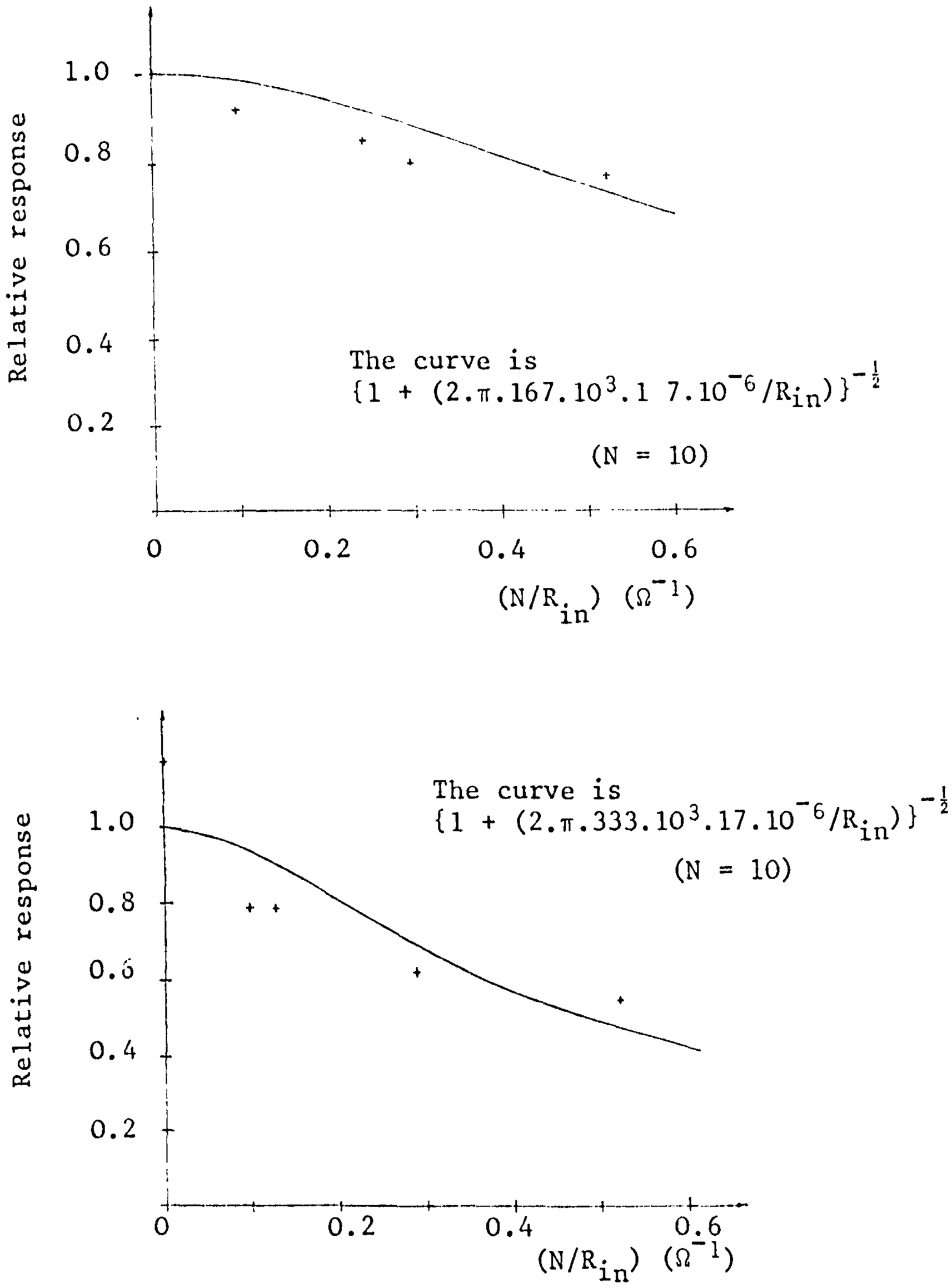

Figure 134: The relative system response as a function of (N/R_{in}) for two different frequencies. Upper curve f = 167kHz, lower curve f = 333kHz. Number of turns on the coil (N) = 10.

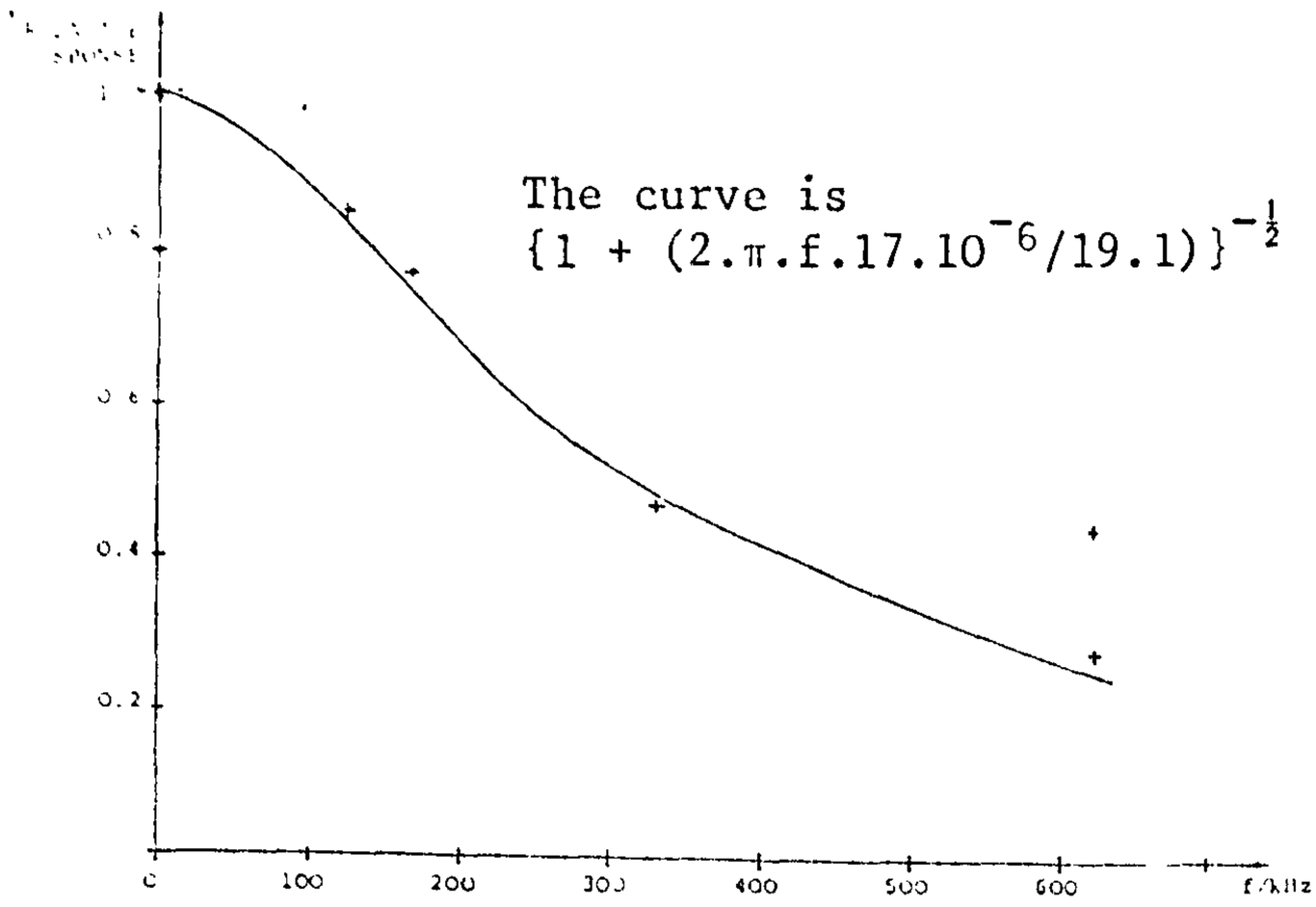

The curve is
$\{1 + (2.\pi.f.17.10^{-6}/19.1)\}^{-\frac{1}{2}}$

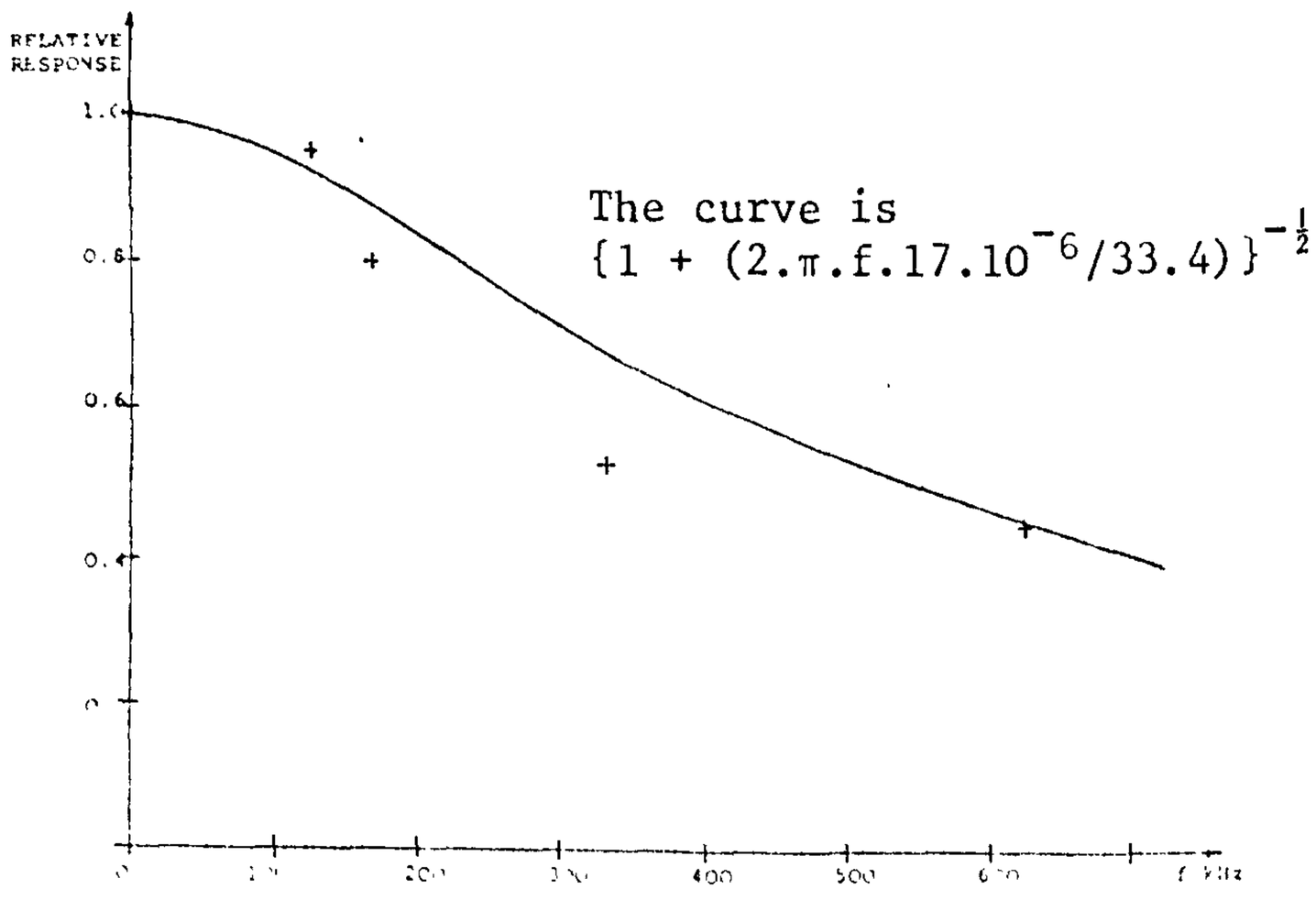

The curve is
$\{1 + (2.\pi.f.17.10^{-6}/33.4)\}^{-\frac{1}{2}}$

Figure 135: The relative system response as a function of frequency for two different values of R_{in}. Upper curve R_{in} = 19.1Ω, lower curve R_{in} = 33.4Ω. N = 10.

The total noise figure is therefore the sum of these three contributions and is:

$$V_{nT}^2 = \left(5 \times 10^{-6}\right)^2 + \left(0.13 \times 10^{-6} R_{in}^{\frac{1}{2}}\right)^2 + \left(A_p N\right)^2 (\text{Volts})^2 \qquad (263)$$

As the work outlined above indicates the choice of R_{in} and N determines the upper frequency limit of the device. For example, for an upper half power point of 2MHz then from equation (260):

$$1.3 \times 10^7 L = R_{in} \qquad (264)$$

The value of the inductance is proportional to N^2 and is approximately given, for a coil wound on a 19mm diameter rod made from Permendur, by:

$$L = 2.6 \times 10^{-8} N^2 \qquad (265)$$

N are R_{in} are linked via equation (264) and (265) and the relationship is therefore:

$$0.34N^2 = R_{in} \qquad (266)$$

Experimental measurements indicate the signal from a IIsu/ Nielson source (0.5mm diameter lead extended by 6 clicks - see chapter IV), in terms of the first peak to arrive at the measuring coil, in a 19mm Permendur bar is:

$$N.2.1 \times 10^{-5} \left(\frac{1}{1 + (\omega L/R_{in})^2}\right)^{\frac{1}{2}} \qquad (267)$$

The experiments carried out to produce the graphs of Figure 133 were however not designed to produce a frequency

bandwidth of 2MHz. Figure 133a) has in fact $R_{in} = 100\Omega$. The signal to noise ratio (SNR) is then given by equations (267) and (263) and is:

$$SNR = \left(\frac{(2.1 \times 10^{-5}N)^2}{(5.2\times 10^{-6})^2+(A_pN)^2}\right)^{\frac{1}{2}}\left(\frac{1}{1 + (\omega L/R_{in})^2}\right)^{\frac{1}{2}}$$

(268)

This equation has the same form as Figure 133a), because $(\omega L/R_{in})$ is constant.

Figure 133b) has, on the other hand, N = 80 which leads to a signal to noise ratio of

$$SNR = \left(\frac{(1.7 \times 10^{-3})^2}{(5\times10^{-6})^2+(A_p80)^2+(0.13\times10^{-6}R_{in})^2}\right)\left(\frac{1}{1+(\omega L/R_{in})^2}\right)^{\frac{1}{2}}$$

(269)

Now the upper frequency of the leading pulse is approximately 65kHz and so for $R_{in} > 200\Omega$ then the factor $(1+(\omega L/R_{in})^2)^{-\frac{1}{2}}$ should be negligible giving a signal to noise ratio which has the form of $\frac{A}{(B+R_{in})^{\frac{1}{2}}}$. However, for small values of R_{in} the opposite is true and

$$SNR \simeq \frac{1.7 \times 10^{-3}R_{in}}{((5 \times 10^{-6})^2+ (A_p80)^2)^{\frac{1}{2}}} \frac{1}{\omega L} \qquad (270)$$

Therefore the form of the graph in Figure 133b) is adequately explained by the theory outlined above.

To determine now the optimum choice of R_{in} and N then the result of equation (264) is used giving a signal to noise ratio of

$$SNR = \frac{2.1 \times 10^{-5}}{((5\times10^{-6}/N)^2+(7.6\times10^{-8})^2+A_p^2)^{\frac{1}{2}}}\left(\frac{1}{1+(\omega/2\pi.2.10^6)^2}\right)^{\frac{1}{2}}$$

(271)

If A_p can be made zero then this gives, over the frequency range from 0 to 2MHz for N = 150:

$$SNR = 190 \tag{272}$$

This result should be compared to the SNR for a piezoelectric transducer mounted on the far end of the bar. This was measured to be five times greater. It would appear then that the IMS transducer is worth pursuing considering the various advantages it offers in terms of being able to be attached to hot surfaces (for example by welding) or rotating surfaces.

The final question to be answered concerning the coil is its shape. If N is increased the physical dimensions of the coil become larger. This will affect the high frequency response of the system as shown in Figure 136. Clearly the high frequency ($\sim$ 1MHz) components have approximately doubled in amplitude.

In summary, the signal to noise ratio and the electrical frequency response of the magnetic field detection system are controlled by a combination of the number of turns on the coil and the input impedance of the preamplifier. These have been shown to vary as expected and indicate the optimum number of turns is around 250 with an input impedance of 20kΩ. It has been found that a coil of this size can be constructed in such a way that high frequency information is preserved.

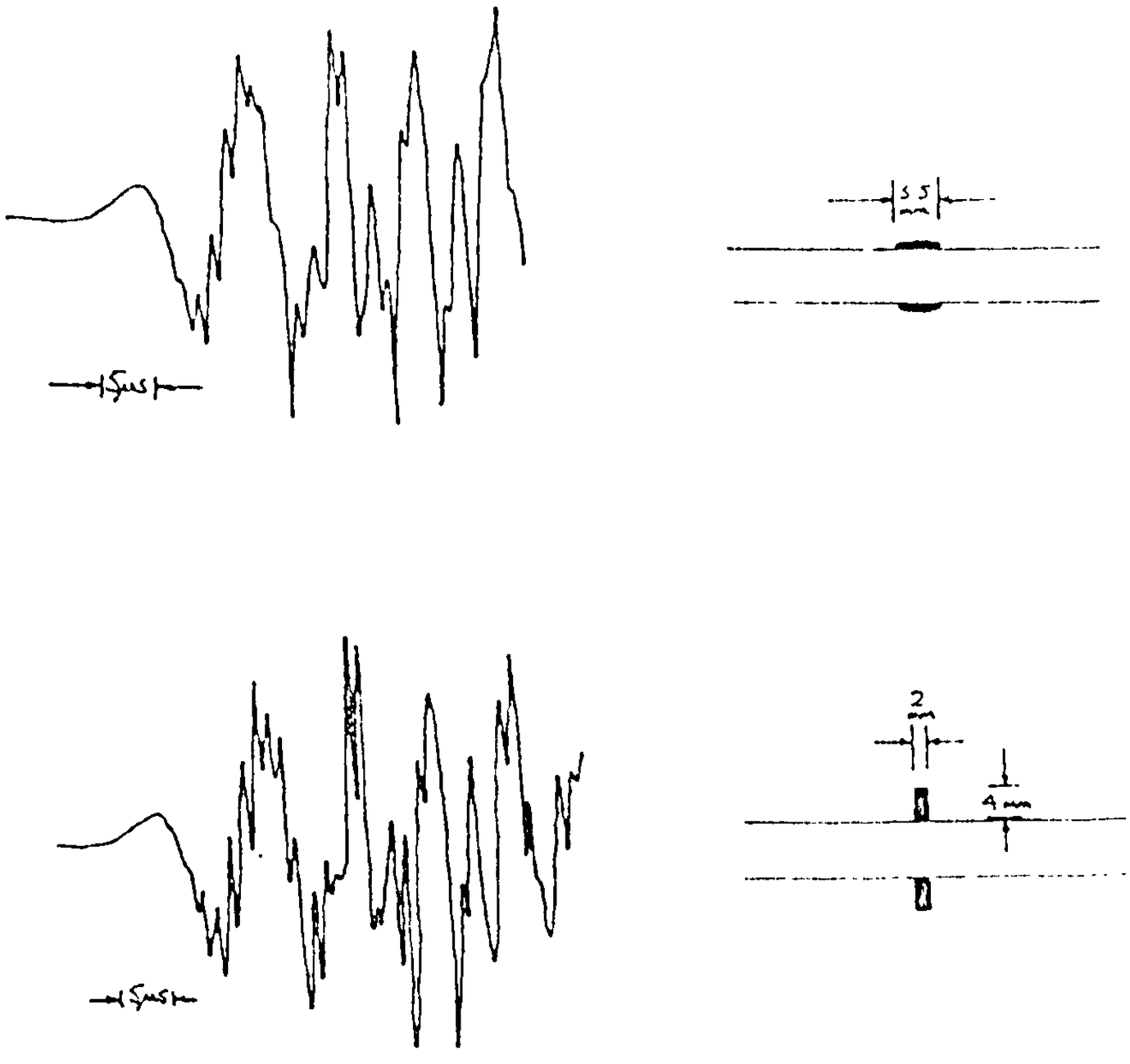

Figure 136: The change in signal shape as a result of altering the coil dimensions (given on the right).

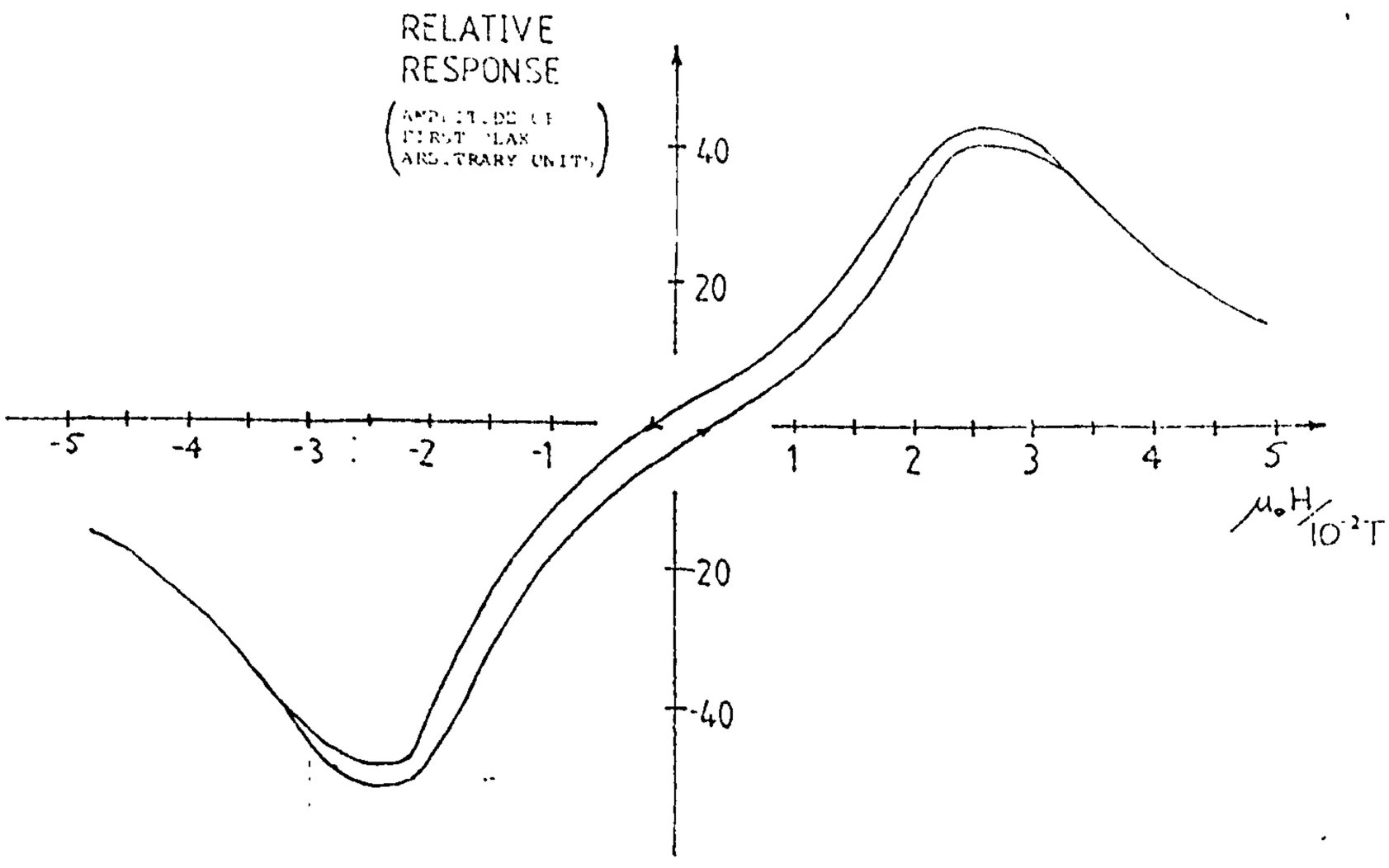

Figure 137: (part 1) The response of the Permendur bar as a function of applied magnetic field strength (H). The vertical scale is given in the same arbitrary units as the next two materials.

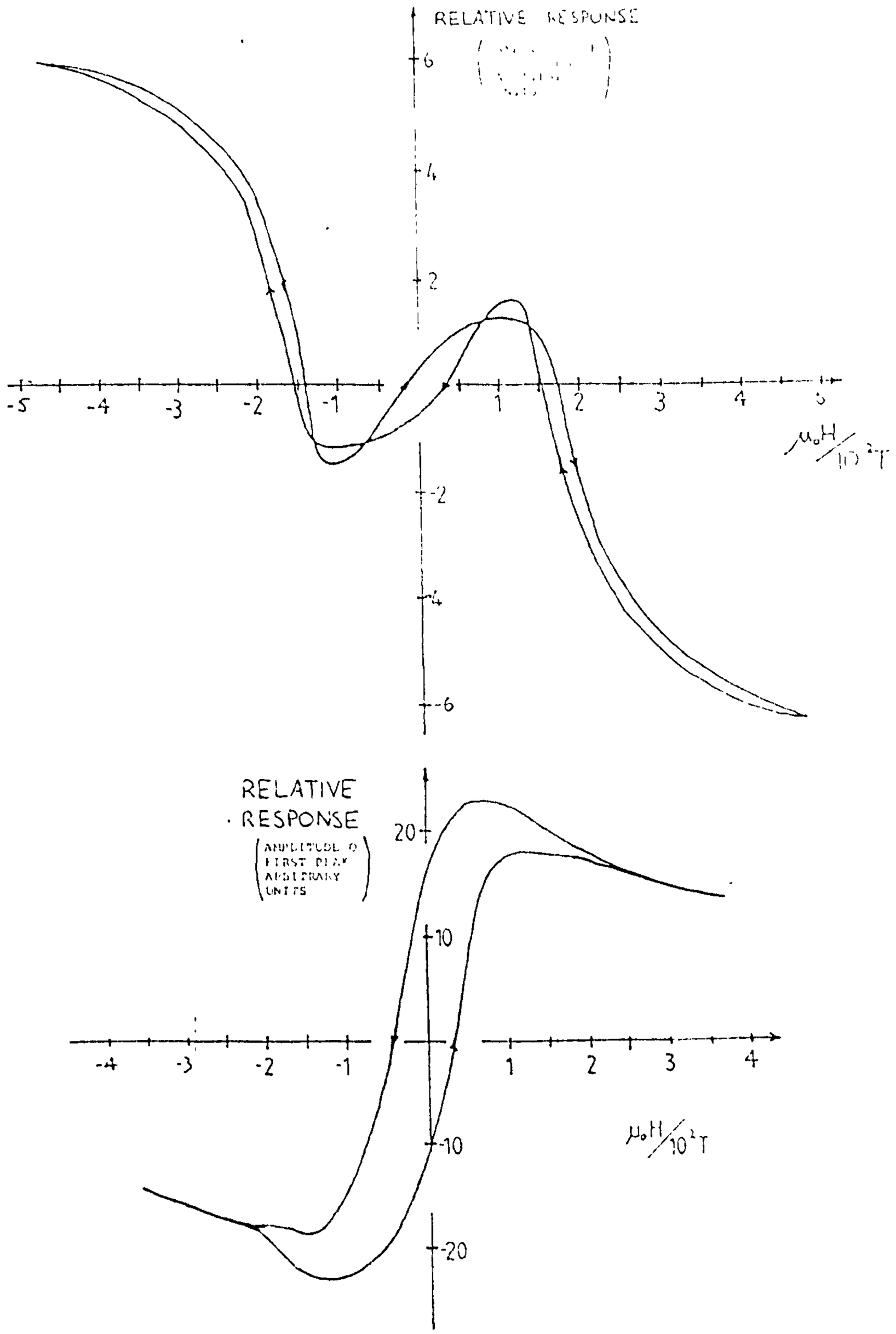

Figure 137: (part 2) The response of the mild steel bar (upper trace) and nickel bar (lower trace) as a function of the applied magnetic field strength (H). The vertical scale is in the same arbitrary units for all traces in this figure.

V.1.2 The choice of the magnetostrictive material and the dependence of the inverse response on the biasing magnetic field

It is found that several materials have usable magnetostrictive coefficients with the most promising being 49-Permendur (49% cobalt, 49% iron, 2% vanadium). The magnetostrictive coefficient itself is defined as the strain developed in a free specimen at magnetic saturation. This coefficient is given as $+70 \times 10^{-6}$[126] for Permendur compared with the nickel value of -33×10^{-6}[126].

Three materials have been tested and their response determined as a function of the biasing magnetic field[127]. The results in terms of the amplitude of the first detected pulse are shown in Figure 137. Clearly Permendur offers the best response when biased although nickel gives a reasonable response even when unbiased.

Using a piezoelectric pulser as a reproducible source the variation in pulse shape versus biasing field becomes apparent (Figure 138). It appears that at larger fields the ratio of the response at high frequencies to the response at low frequencies is increased. However the absolute value of the high frequency excursions seems to peak at the same value of $\mu_o H$ as does the size of the initial peak.

Certain rare earth compounds have very high magnetostriction coefficients but their nature (being non-metallic) does not allow them to be shaped easily nor to be easily attached by welding to ferrous surfaces and

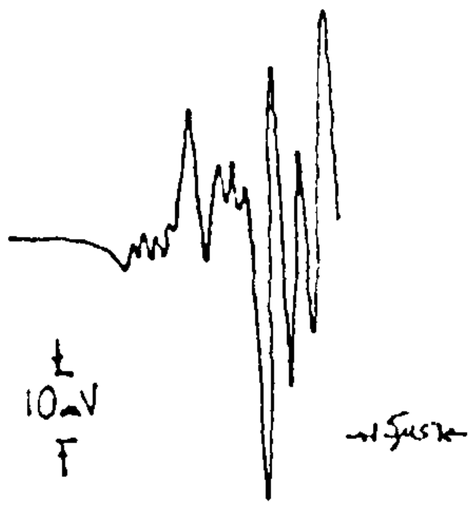

$\mu_o H = 2.2 \times 10^{-2} T$

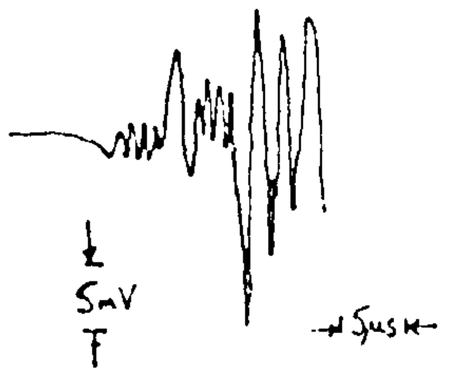

$\mu_o H = 4.4 \times 10^{-2} T$

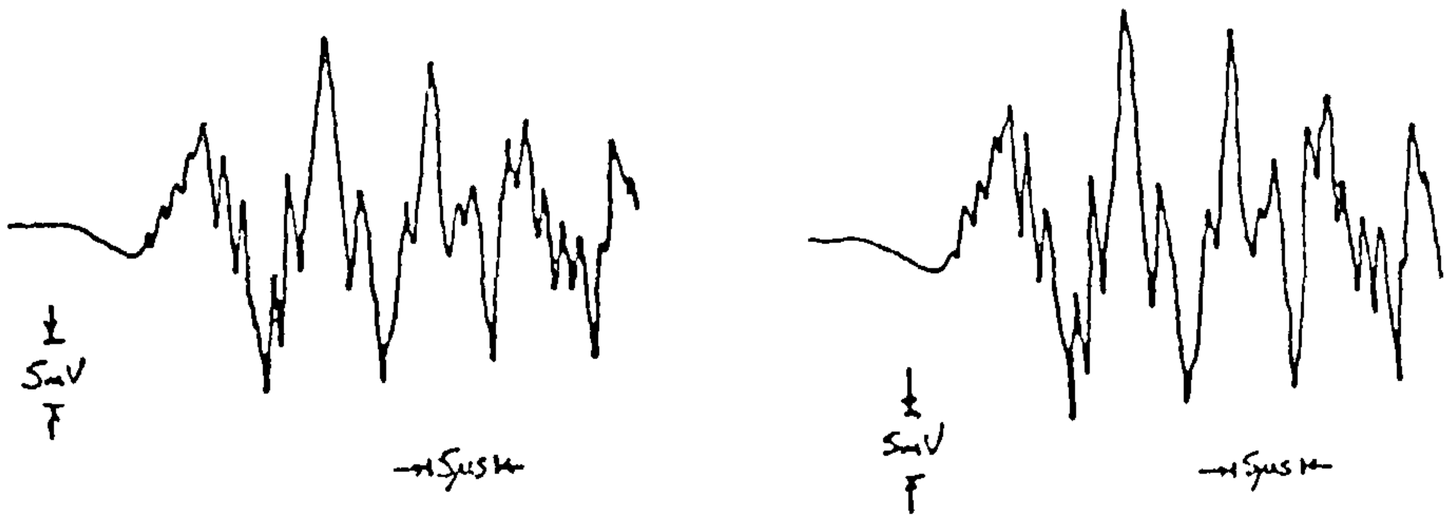

Figure 138: The change in response as a function of applied field. Upper traces are for a permendur bar whilst the lower traces are for a mild steel bar.

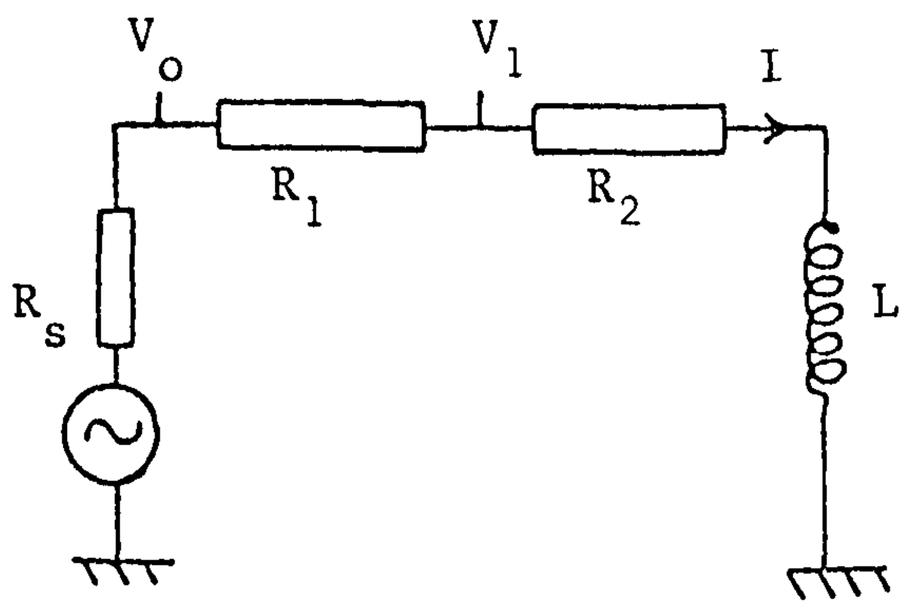

Figure 139: A simple method of measuring the inductance of a permendur linked coil.

consequently they offer no advantage over piezoelectric transducers. Therefore it appears that the best choice for the magnetostrictive material is 49-Permendur which should be biased at $\mu_o H = 2.5 \times 10^{-2} T$.

V.1.3 Eddy current effects: Inductance as a function of frequency

When a ferromagnetic material is subjected to an alternating magnetic field then eddy currents flow in the material surface. If the rate of change of the field is high then these currents create a magnetic field of sufficient strength to shield the remaining material from the external influence. In terms of the reciprocal effect then if a magnetic field is generated inside the specimen (via inverse magnetostriction) then similar eddy currents are generated in the surrounding material thus reducing the externally measured effect. The size of this effect is clearly important and should be determined.

A simple method of estimating this magnitude is to measure the inductance of the simple measuring coil. This was done by driving the coil through a series resistor as shown in Figure 139. Using Kirchoff's circuital laws and Faraday's induction law then

$$V_o - V_1 = IR_1 \qquad (273)$$

and

$$V_1 = IR_2 - \frac{\partial \Phi}{\partial t}(H,\omega) \qquad (274)$$

where R_1 is the series resistance, R_2 is the DC resistance of the coil and Φ the flux linked in the coil.

Now
$$\frac{\partial}{\partial t} = \frac{\partial I}{\partial t} \cdot \frac{\partial}{\partial I} \qquad (275)$$

and also as $H = k.I$ then $\frac{\partial}{\partial I} = k.\frac{\partial}{\partial H}$ therefore:

$$V_1 = IR_2 - k.\frac{\partial I}{\partial t} \cdot \frac{\partial \Phi}{\partial H}(H,\omega) \qquad (276)$$

$\Phi(H,\omega)$ is the commonly encountered hysteresis curve for, in this case, 49-Permendur. As H has only a small maximum value then the saturation point of the hysteresis curve is not reached and so the maximum value of the second term in equation (276), as a function of time, is assumed to occur at the maximum of $\frac{\partial I(t)}{\partial t}$, because $\partial\Phi/\partial H$ will not be a strongly varying function. Writing

$$I = I_o e^{j\omega t} \qquad (277)$$

allows equation (276) to be written as

$$V_1 = I_o e^{j\omega t} \left(R_2 - kj\omega\frac{\partial \Phi}{\partial H}(H,\omega)\right) \qquad (278)$$

and as the maximum of $k\frac{\partial I}{\partial t} \cdot \frac{\partial \Phi}{\partial H}$ is assumed to occur with the maximum of $\frac{\partial I}{\partial t}$ then the resulting function has the phase of $\frac{\partial I}{\partial t}$ with the phase lag of π given by the $(-j)$.

Therefore

$$|V_1| = |I_o|\left(R_2^2 + k^2\omega^2\left(\frac{\partial \Phi}{\partial H}(H=0)\right)^2\right)^{\frac{1}{2}} \qquad (279)$$

and from equation (273)

$$|I_o| = \frac{|V_o - V_1|}{R_1} \qquad (280)$$

leading to

$$\left(R_2^2 + k^2\omega^2\left(\frac{\partial \Phi}{\partial H}(H=0)\right)^2\right)^{\frac{1}{2}} = \left|\frac{R_1|V_1|}{V_o - V_1}\right| \qquad (281)$$

If, therefore, the peak values of V_1 and of (V_o-V_1) are measured then the differential permeability at H=0 may be determined. This is defined as

$$\mu_r = \frac{1}{\mu_o} \frac{\partial B}{\partial H} \qquad (282)$$

and as

$$\frac{\partial \Phi}{\partial H} = \int_A \frac{\partial B}{\partial H} \cdot dA \qquad (283)$$

then an effective area dependent on the angular frequency, ω, may be defined so that with $\partial B/\partial H$ (H=0) $= \mu_r \mu_o$ then

$$\frac{\partial \Phi}{\partial H} = \mu_o \mu_r A_{eff}(\omega) \qquad (284)$$

The flux linking a coil is usually defined in terms of an inductance (L) where

$$\Phi = LI \qquad (285)$$

and

$$\frac{\partial \Phi}{\partial I} = L \qquad (286)$$

In the absence of magnetic materials then this may be written as

$$\frac{\partial \Phi}{\partial I} = L_o \qquad (287)$$

Introducing the magnetic material then gives

$$\frac{\partial \Phi}{\partial I} = \left(\mu_s \frac{A_{eff(\omega)}}{A_1} \right) L_o \qquad (288)$$

where A_1 is the true area of the coil.

The measurement of the peak voltages yields the inductance results shown in Figure 140a for a 6 turn coil on a 19mm diameter Permendur bar. Assuming a skin depth Δr where $\Delta r = \alpha\omega^n$ then equation (288) becomes upon taking logarithms:

$$\ln\left(\frac{\partial\Phi}{\partial I}\right) = \ln\left(\frac{2(\mu_r)\alpha L_o}{r_o}\right) + n\ln(\omega) \qquad (290)$$

where $A_1 = \pi r_o^2$ and $A_{eff} = 2\pi r_o \Delta r$ with r_o the true radius of the coil. The graph of $\ln\left(\left(\partial\Phi/\partial I\right)/1.5 \times 10^{-6}\right)$ versus $\ln\left(\frac{\omega}{2\pi.10^3}\right)$ shown in Figure 140a) yields $n = 0.45 \pm 0.07$.

A detailed treatment of eddy current effects is given by Bozorth[128]. The theory given suggests that at high frequencies $n = 0.5$. Therefore the inductance measurements above show that there is indeed a strong effect due to eddy currents which effectively limits the volume of magnetostrictive material in use. The actual part in use being roughly the outer 10μm at a frequency of 1MHz. It may be possible to increase the volume of material used by introducing laminations as shown in Figure 140b). This should then increase the signal to noise ratio by a factor given as roughly twice the number of laminations. This information now enables the effect of change of bar diameter to be considered.

V.1.4 The effect of changing the diameter of the bar in the prototype detector

Two effects are important as far as the bar diameter is concerned. The first of these is the variation in the

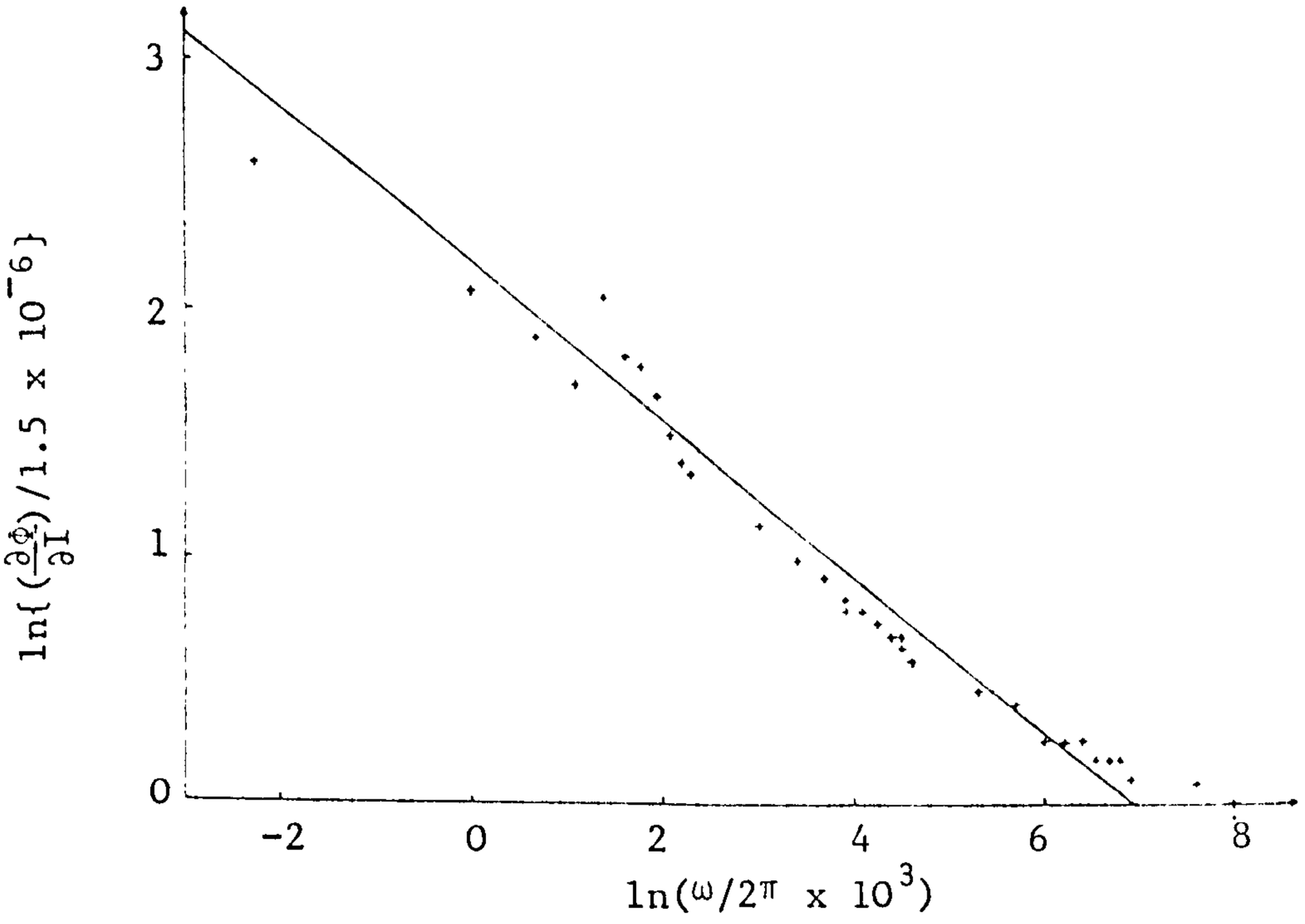

Figure 140a: The inductance of a permendur linked coil as a function of the frequency of the applied voltage.

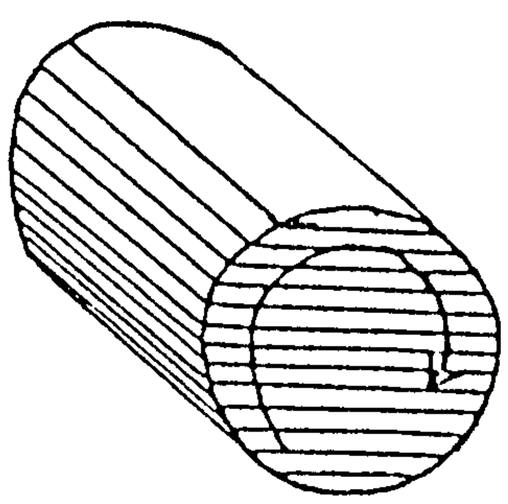

Figure 140b: Laminar construction suggested for the inverse magnetostrictive transducer. Eddy currents as indicated by the arrow cannot exist but must follow paths within the laminations.

magnitude of the response of the system to a standard input whilst the second effect is the change in the rise time of the first pulse (see for example Figures 136 and 138). The latter is in fact associated with frequency based dispersion in the bar which will change the complexity of any deconvolution. The two effects are dealt with independently.

V.1.4i) The change in the magnitude of the response of the inverse magnetostrictive detector as a function of bar diameter

Consider Figure 130. If the diameter of the entire bar is varied, then clearly the initial stress conditions, introduced by a force function applied at one end of the bar, would vary. The system response is then a combination of this effect and the effect on the detection mechanism of changing the bar diameter. If the end of the bar received a given displacement over its entire cross-section then the variations in the input would be removed provided the system is linear.

By varying either the length of the lead, and hence breaking force, in the Hsu/Nielson source, or by varying the voltage drive on the piezoelectric pulser, the output of the IMS transducer has been shown to be proportional to the displacement of the end of the bar. Therefore merely some sort of uniform displacement of the bar end is required for tests involving changes in bar diameter.

The development of the ultrasonic transmitting transducer as an epicentral source beneath the large

aluminium block (see chapter IV) would allow such work as described above to be performed. Unfortunately, this system was not developed until after the preliminary investigations of the IMS prototype transducer were carried out. An alternative and similar method was used. This involved taking a 19mm diameter bar and turning down a section of this bar to some smaller diameter. The piezoelectric pulser was then attached to the 19mm end. Therefore the displacement at the interface of the two cross sections should be constant provided this displacement does not vary with radius (see Figure 141).

The assumption of invariance of displacement with radius may be checked theoretically or experimentally. Kolsky[129] gives the theory of elastic wave propagation in an infinite cylinder (the finite cylinder does not have an analytical solution) and shows that in a cylinder of radius a, then waves propagating in the first vibrational mode (most common) and with wavelength λ have, for $a/\lambda = 0.375$, a nodal cylinder at the surface. Although the 19.1mm diameter section is not infinite its length to diameter ratio is 4.8 which allows the theory for the infinite bar to be used as a reasonable approximation. The pulse whose height is to be used as a measure of the system response will be the first pulse. Now it is assumed that the input from the pulser, being driven by a step generator, is itself a step. The height of the first pulse should therefore be independent of the rise time.

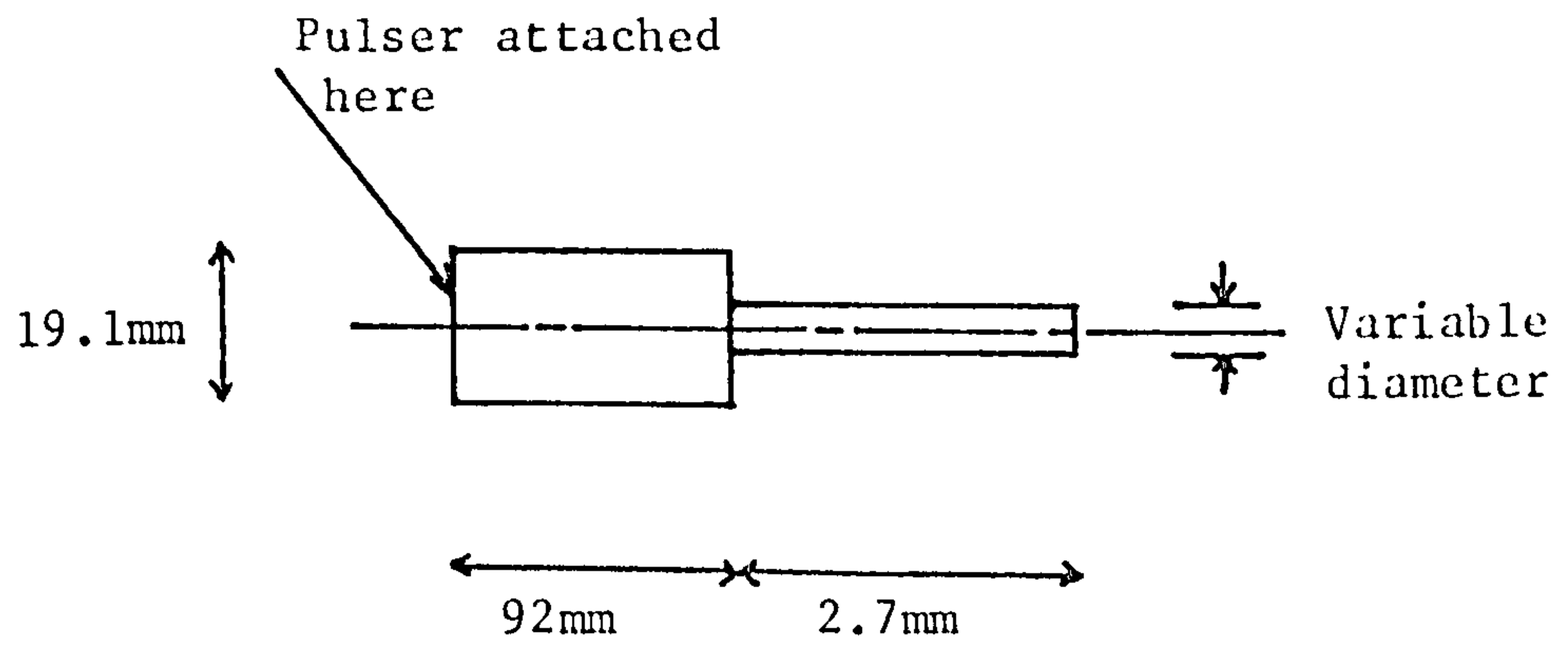

Figure 141: The stepped bar used for studying the variations in the inverse magnetostrictive response with bar diameter.

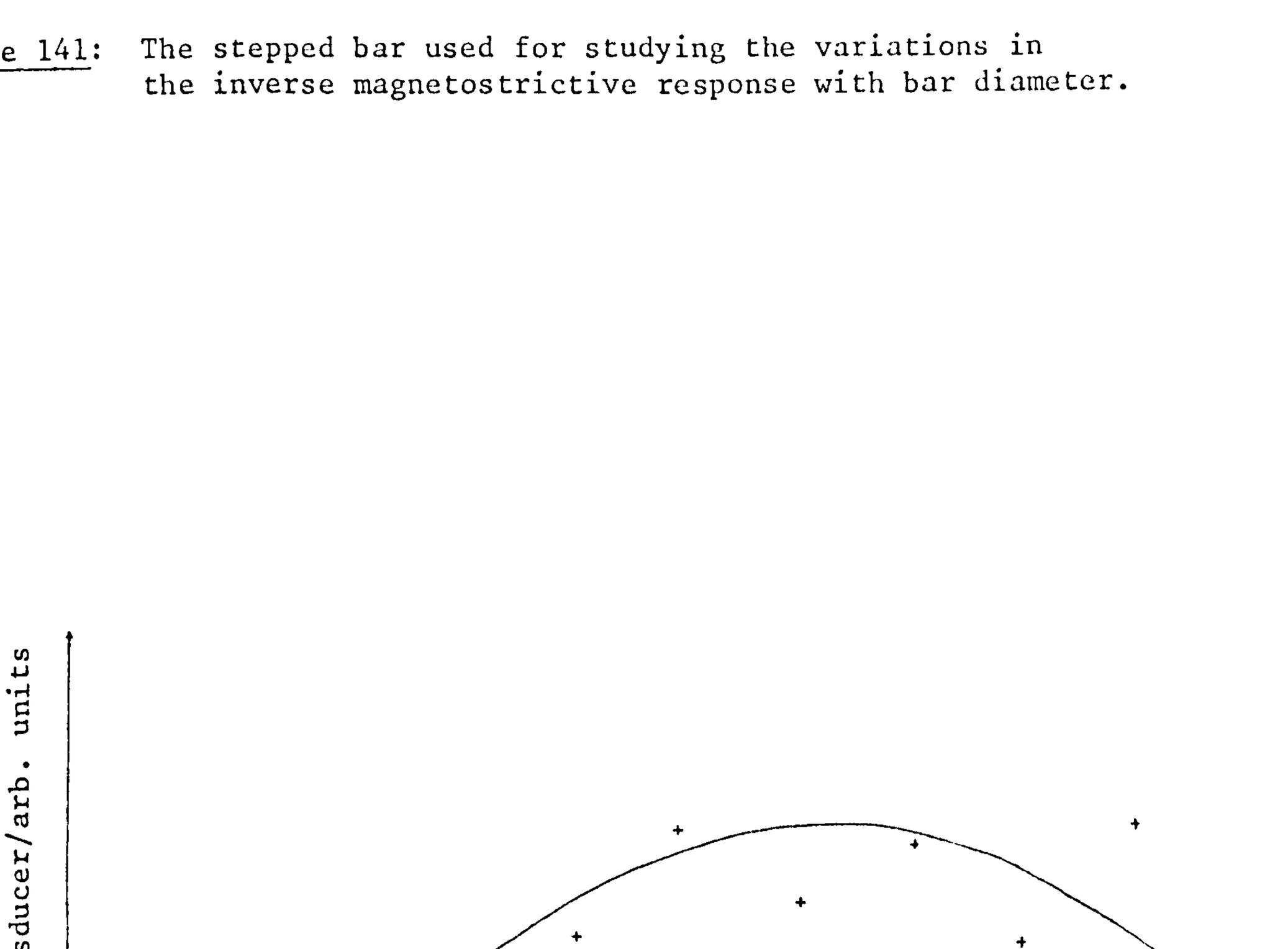

Figure 142: The output of the IMS transducer formed on the variable diameter portion of the stepped bar shown above. The curve is $ArJ_o(0.185r)$ which has a zero at r = 13.00mm or r = 1.36 x r_o where r_o is (19.1/2)mm. (A is arbitrary).

The rise time of the first pulse is 5.5μs corresponding to an upper frequency of around 65kHz and a wavelength of 80mm. For a/λ to equal 0.375 then a must be 29mm which is three times the actual radius. The variation of elastic wave amplitude with radius in an infinite cylinder has the form of a sum of two Bessel functions, $AJ_o(\alpha r) + \frac{B}{r}\frac{\partial}{\partial r}(rJ_1(\beta r))$. This has various zeros and so the movement at the edge of the cylinder will be only a fraction of the movement at the centre.

Experimental results to be given later confirm that there is a variation in amplitude with radius of this order.

The result on the system response of varying the cross section is now given in Figure 142. It can be seen that the graph is linear to begin with (for small radii) and then begins to turn over. The work in the previous section indicated that the only detectable effect from the inverse magnetostriction would occur in a thin outer layer of the cylinder. Now from Faraday's induction law then

$$V = \frac{\partial \Phi}{\partial t} \qquad (291)$$

and

$$V = \frac{\partial B}{\partial t} \cdot A_{eff} \qquad (292)$$

where A_{eff} is an effective area possessing a field change ∂B. The theory to be given later shows that

$$\partial B \propto \frac{\partial \xi}{\partial x} \qquad (293)$$

where ξ is the elastic wave amplitude and $\partial \xi/\partial x$ the strain.

The effective area may be written as:

$$A_{eff} = 2\pi r_o \Delta r \qquad (294)$$

where r_o is the radius of the cylinder and so

$$V \alpha \partial\xi . r_o \qquad (295)$$

For small radii $\partial\xi$ is constant and so

$$V \alpha r_o \qquad (296)$$

but for larger radius the displacement along the surface of the cylinder is less being given, as mentioned earlier by $AJ_o(\alpha r) + \frac{B}{r}\frac{\partial}{\partial r}(rJ_1(\beta r))$. Using the formula for the differential of a Bessel function then $\frac{B}{r}\frac{\partial}{\partial r}\left(rJ_1(\beta r)\right) = B\beta J_o(\beta r)$. The sum of these two will be approximated by a single Bessel function giving:

$$\partial\xi \alpha J_o(\alpha r_o) \qquad (297)$$

The curve shown in Figure 142 is given by:

$$V = \beta . r_o J_o(\alpha r_o) \qquad (298)$$

where β is arbitrary and $\alpha = 0.185 mm^{-1}$. Considering the approximations made in the theory the agreement is good. The curving over of the theoretical curve for large values of r is thought to arise because $AJ_o(\alpha r) + B\beta Jo(\beta r)$ was approximated by $Jo(\alpha r)$.

Having invesigated the variation in the height of the first pulse as a function of bar diameter, the variation of the rise time of this first pulse will now be considered.

V.1.4ii) The variation in the rise time of the inverse magnetostrictive detector as a function of bar diameter

As only the time dependence of the system response is required in this investigation then considerations of the energy introduced into the system and changes in initial stress conditions at the input are not important. Therefore simple bars of uniform cross sections are used. These bars were excited by using a Hsu/Nielson source and the rise time of the first peak measured. The results are shown in Figure 143. It appears that this rise time is proportional to the bar diameter for large rise times but for small rise times this tends to a constant value.

The existence of this limiting rise time is assumed to be due to the rise time of the Hsu/Nielson input source. Measurements given in the previous chapter of the Hsu/Nielson source at the origin show the event lasts approximately 1 to 2μs which then corresponds to the limiting rise time here. It should also be recalled that variations occur in the source rise time.

Measurements made on the stepped bar in the previous section show that the rise times on the reduced diameter part are nearly independent of radius. This is assumed to be because the rise time in the 19.1mm section is long compared to the system rise time in the other sections. Such a result verifies the assumption above about the Hsu/Nielson source as well as suggesting that the waveform in the reduced portion is proportional to the waveform incident on the shoulder which was assumed in

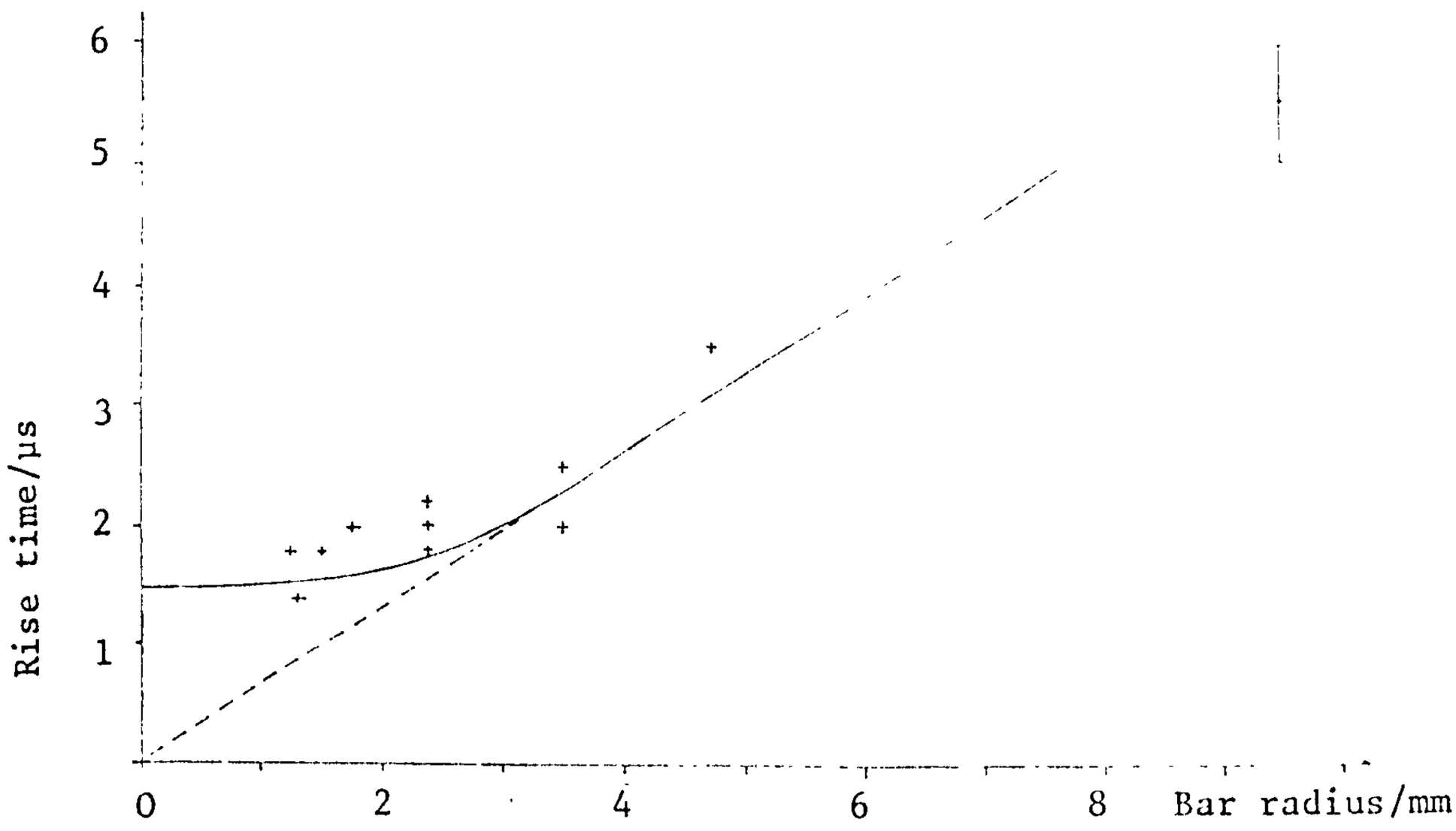

Figure 143: The rise time of the first peak as a function of bar diameter in mild steel. The results are taken on simple (uniform) bars using the Hsu/Nielson source as the excitation.

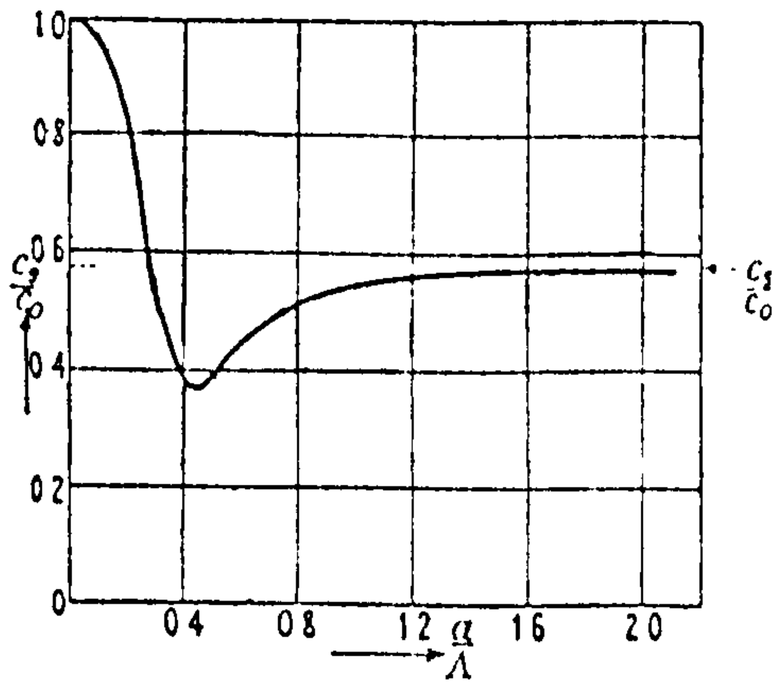

Figure 144: The group velocity Cg of the first mode of elastic waves in an infinite bar (after Kolsky [129]) as a function of a/Λ. a is the bar radius, Λ the wavelength of the ultrasound, $C_0 = (E/\rho)^{\frac{1}{2}}$ (the velocity of infinitely long waves in a bar) and C_s is the velocity of Rayleigh waves.

section V.1.4i).

The variation in the rise time for the large radii bars above occurs because of a frequency dependent group velocity of elastic waves in cylindrical bars. The theory for infinite bars[129], to which these simple bars approximate quite well, shows that the group velocity varies with a/λ (radius of the bar/wavelength), see Figure 144, falling from a maximum of v_L for $\lambda \to \infty$, passing through a minima at $\lambda/a = 0.45$ and finally tending to a constant level of $0.5764v_L$. Therefore to a first approximation the rise time of a square pulse should be given by the frequency corresponding to a wavelength derived from $a/\lambda \simeq 0.17$. The velocity when $a/\lambda = 0.17$ being $(1/\sqrt{2})(v_L - 0.5764V_L)$. For $v_L = 5.94 mm.\mu s^{-1}$ the rise time is therefore $t_r \simeq (0.35a)\mu s$. The experimental result from Figure 143 is $t_r = (0.33a)\mu s$. The agreement is therefore very good.

V.1.5 Other experiments carried out to characterize the prototype inverse magnetostrictive detector

Various results have been touched upon in the preceeding section, such as the direct measurement of the propagation of elastic pulses in bars and the variation of the pulse with bar diameter. These results together with some other effects will now be reported.

V.1.5i) Propagation effects in simple bars

An elastic pulse introduced at one end of a bar will evolve, due to multiple reflections, as it propagates

towards the far end. This has already been shown to affect the rise time of the magnetostrictive first pulse as well as the size of the magnetostrictive response due to the variation of displacement with radius in the bars.

It would be expected therefore that moving the detecting coil along the bar would change the form of the output. Such an effect is shown in Figure 145. The changes that occur are not severe because the ratio of the bar diameter to the position of the measuring coil along the bar is 8.7 for the first trace. At such a distance the pulse shape will be quite well set. It should be noted that measurements indicate the B field in the bar does not vary by more than 7% over the middle 60% of the bar and as such the biasing is effectively constant for both traces shown in Figure 145.

When the elastic pulse reaches the end of the bar then the displacement it causes may be measured. A convenient method of doing this is to use a broadband piezoelectric sensor (see chapter VI). Such a sensor is a good approximation to a displacement transducer. Measurements were taken on a 19.1mm diameter mild steel bar of length 300mm. The bar was excited at the centre of one end face using a Hsu/Nielson source with an extended lead length produced by 3 clicks of the propelling mechanism. The displacement was measured at r = 0 on the far end and r = 5mm (Figure 146) where r is the radial position, using a 20kHz hi-pass filter.

In addition to those high frequency excursions there

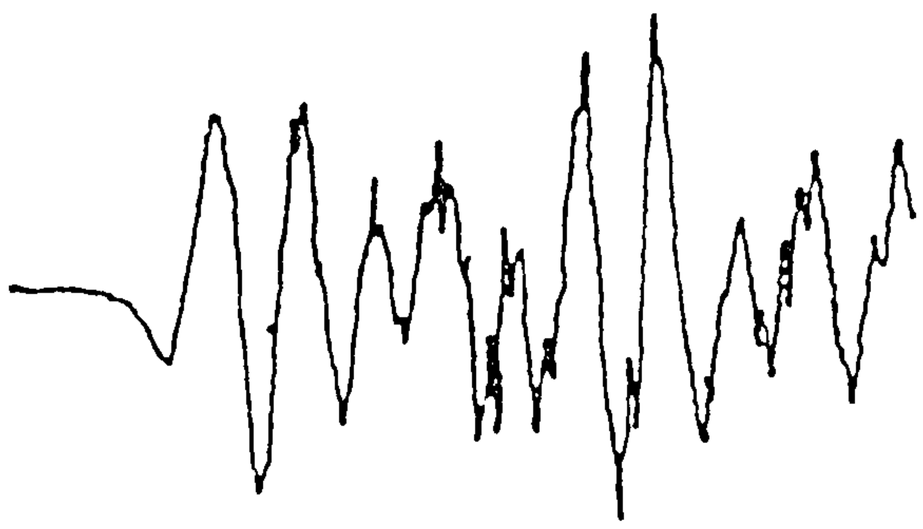

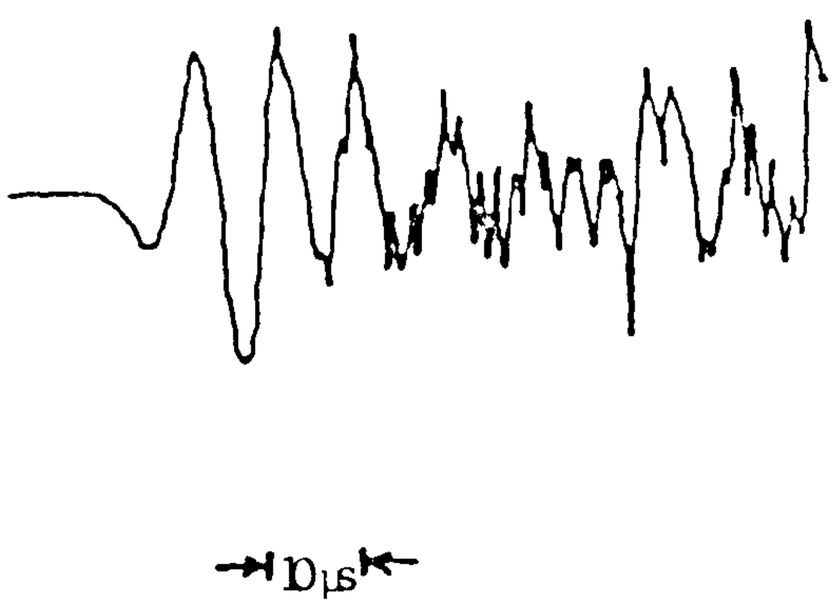

Figure 145: The evolution of the pulse, as detected by inverse magnetostriction, as it travels along a simple bar.

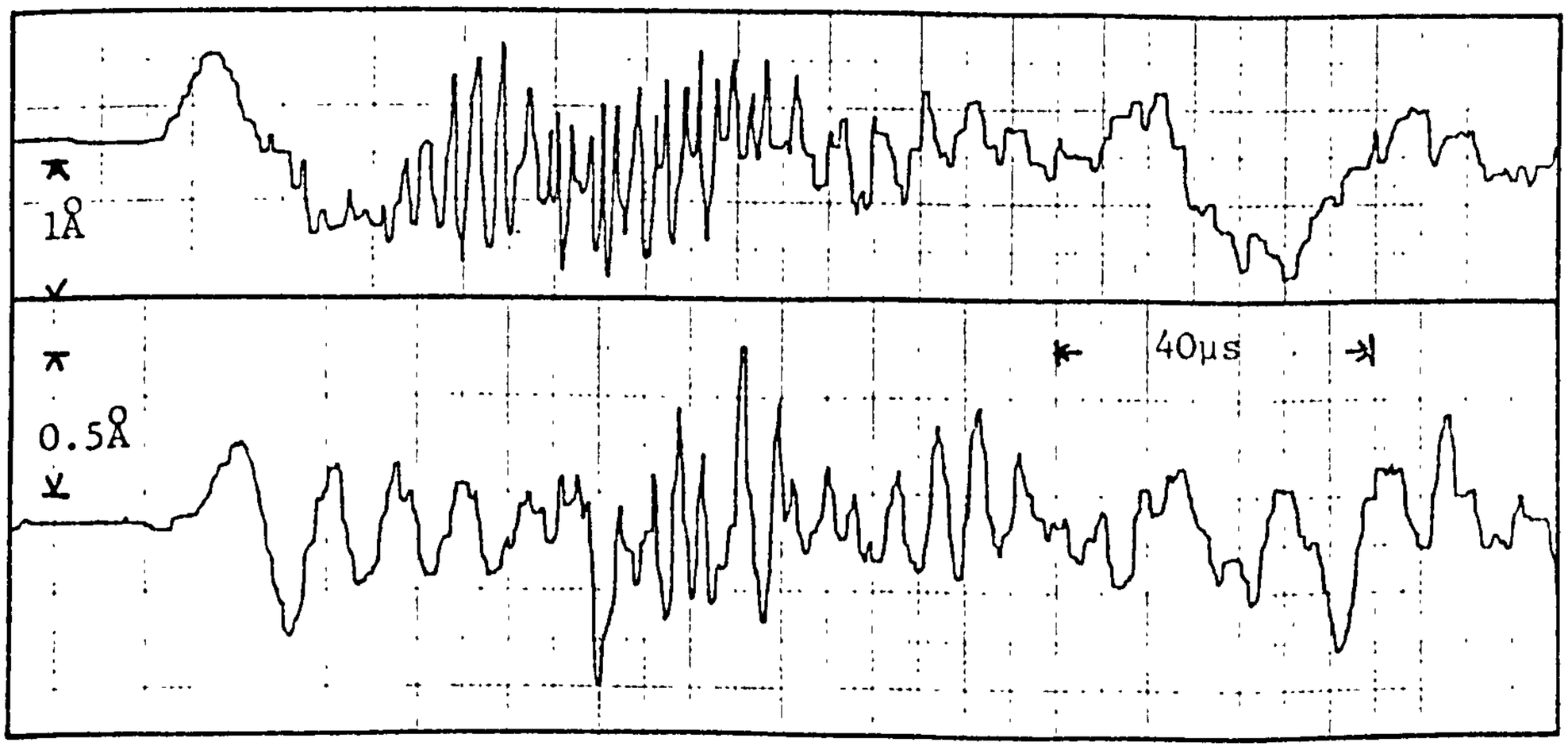

Figure 146: The movement of one end face of a 19.1mm diameter steel bar when the far end is excited with a Hsu/Nielson source. Trace (a) is measured at r = 0 whilst trace (b) is measured at r = 5mm. Measurements are taken with a broadband piezoelectric detector.

were also oscillations at a much lower frequency of $\sim$ 8.4kHz. Calculations show that the angularly invarient radial mode of oscillation has a frequency of $\sim$ 310kHz whilst the longitudinal vibration frequency is $\sim$ 8.3kHz. Therefore these large amplitude oscillations are due to the fundamental longitudinal bar vibration and are shown in Figure 147.

This trace was captured using the stabilized optical interferometer. The interferometer was also used with 20kHz hi-pass filtering to check the trace of Figure 146b) and this is shown in Figure 148. Clearly the two traces are very similar.

The peak output on Figure 147 is approximately 280Å giving a displacement amplitude for the elastic wave inside the material of 140Å. Knowing this amplitude allows a rough calculation to be made of the energy in the bar. It can be shown that for plane, uniform, longitudinal waves in a bar of radius a, the energy, U, in the waves is given by:

$$U = \int_{\text{all } x} \tfrac{1}{2}\pi a^2 \left(E\left(\frac{\partial \xi}{\partial x}\right)^2 + \rho\left(\frac{\partial \xi}{\partial t}\right)^2 \right) dx \qquad (299)$$

where ξ is the wave displacement, E Youngs modulus and ρ the density. Evaluating this integral for the high frequency trace of Figure 146a) gives $U \simeq 2 \times 10^{-2}\mu J$, whilst for the low frequency trace in Figure 147 then $U \simeq 0.2\mu J$. This figure is therefore similar to that calculated in chapter IV for the energy introduced into a specimen by a Hsu/Nielson source.

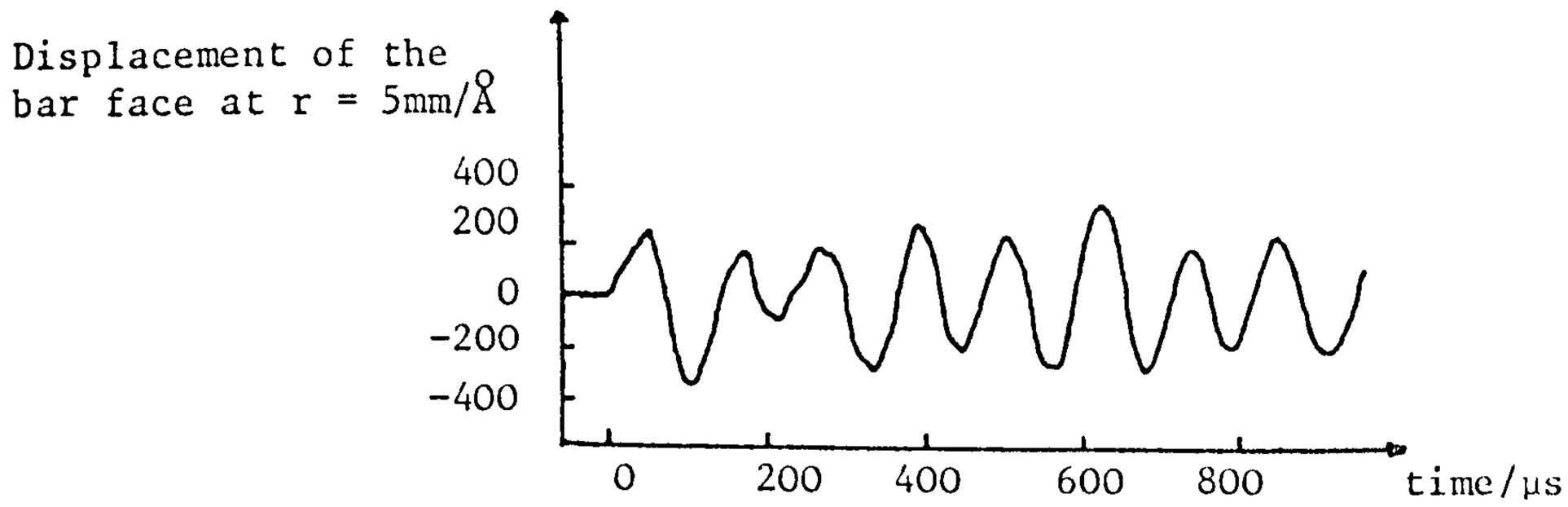

Figure 147: The vibration of a steel bar at its fundamental longitudinal frequency as a result of excitation with a Hsu/Nielson source.

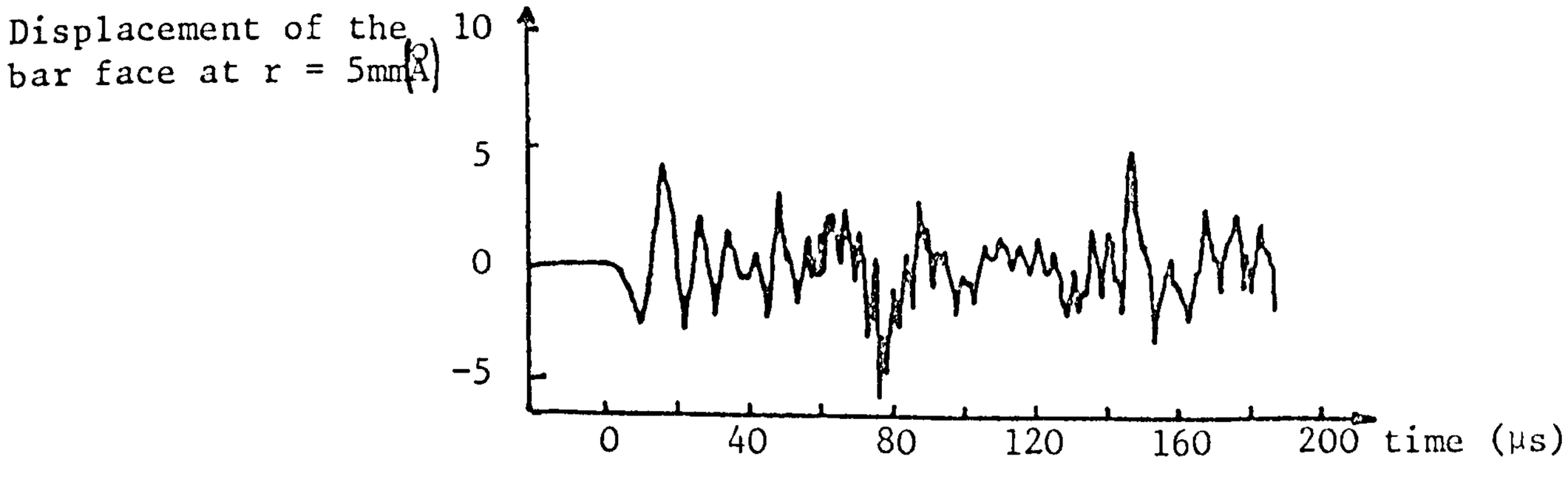

Figure 148: The output of the interferometer detector used to monitor the high frequency vibrations of one face of a 19.1mm diameter steel bar of length 30cm as the other end is excited with a Hsu/Nielson source. Measurements are taken at r = 5mm to check the results obtained with a broadband piezoelectric detector given in figure (146b).

One final point of interest connected with propagation effects is the change in IMS response resulting from changing the input force function. The sensitivity to such changes is easily demonstrated by the use of the Hsu/Nielson source. Two variations are easily introduced. The first involves changing the angle of contact of the lead (see Figure 149) whilst the second involves moving the position of application of the lead tip from the centre of the end face of the 19mm bar to the edge of this face. The results from these two changes are shown in Figure 150. It can clearly be seen that the IMS detector is sensitive to variations in the force function, a necessary result if the transducer is to be of much use. As well as this the detector is likely to be affected by compounded aperture effects as different responses result when different portions of the bar end face are excited.

These results on pulse propagation suggest that the IMS response is dominated mainly by propagation effects in solid elastic cylinders. The effects, such as the slow rise time of the initial pulse with the high frequency excursions following and the variation in wave displacement across the cylinder diameter, may all be explained using the theoretial results derived for the solid infinite cylinder given by Kolsky[129].

V.1.5ii) Magnetic effects associated with the simple measuring coil

Electromagnetic interactions depend fairly critically on the distances between the source position and measuring

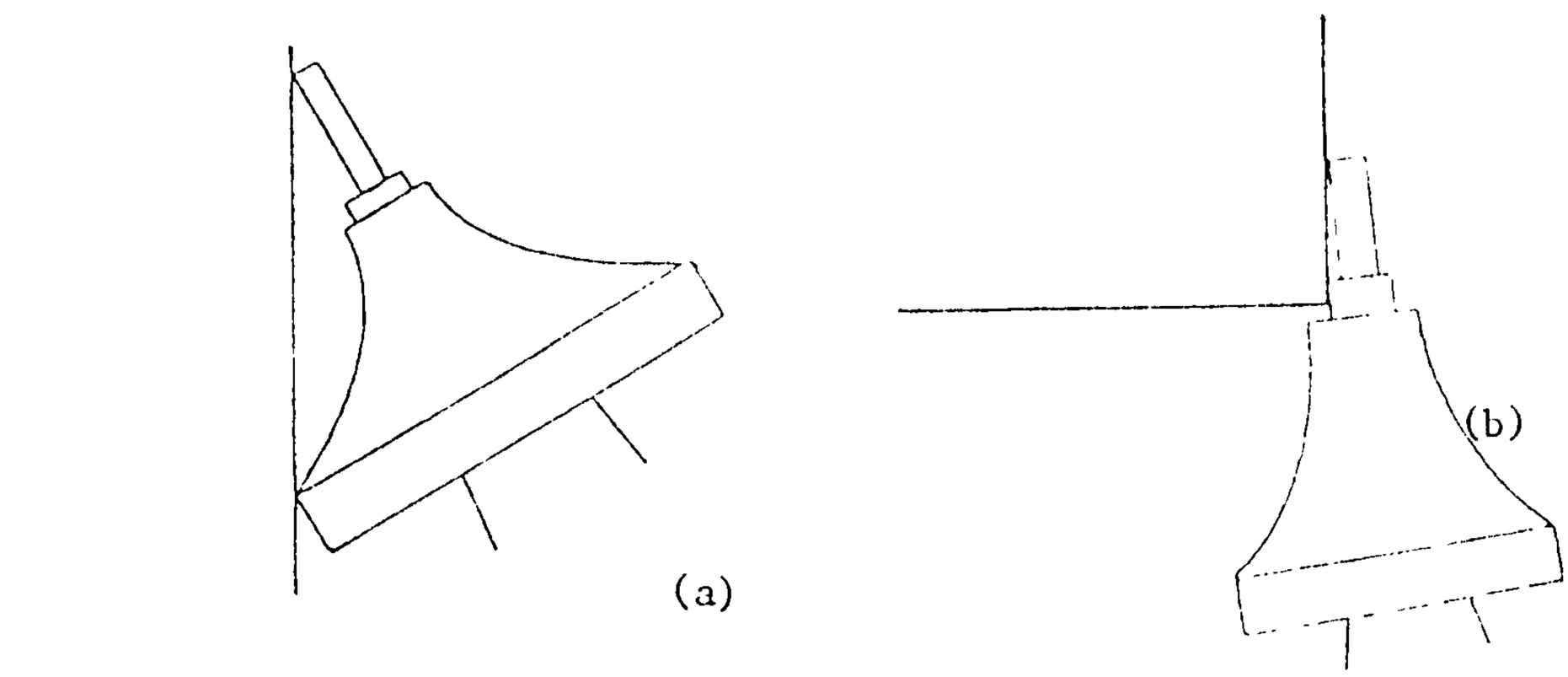

Figure 149: The two types of loading method used to break the pencil leads in the Hsu/Nielson source resulting in a change of contact angle.

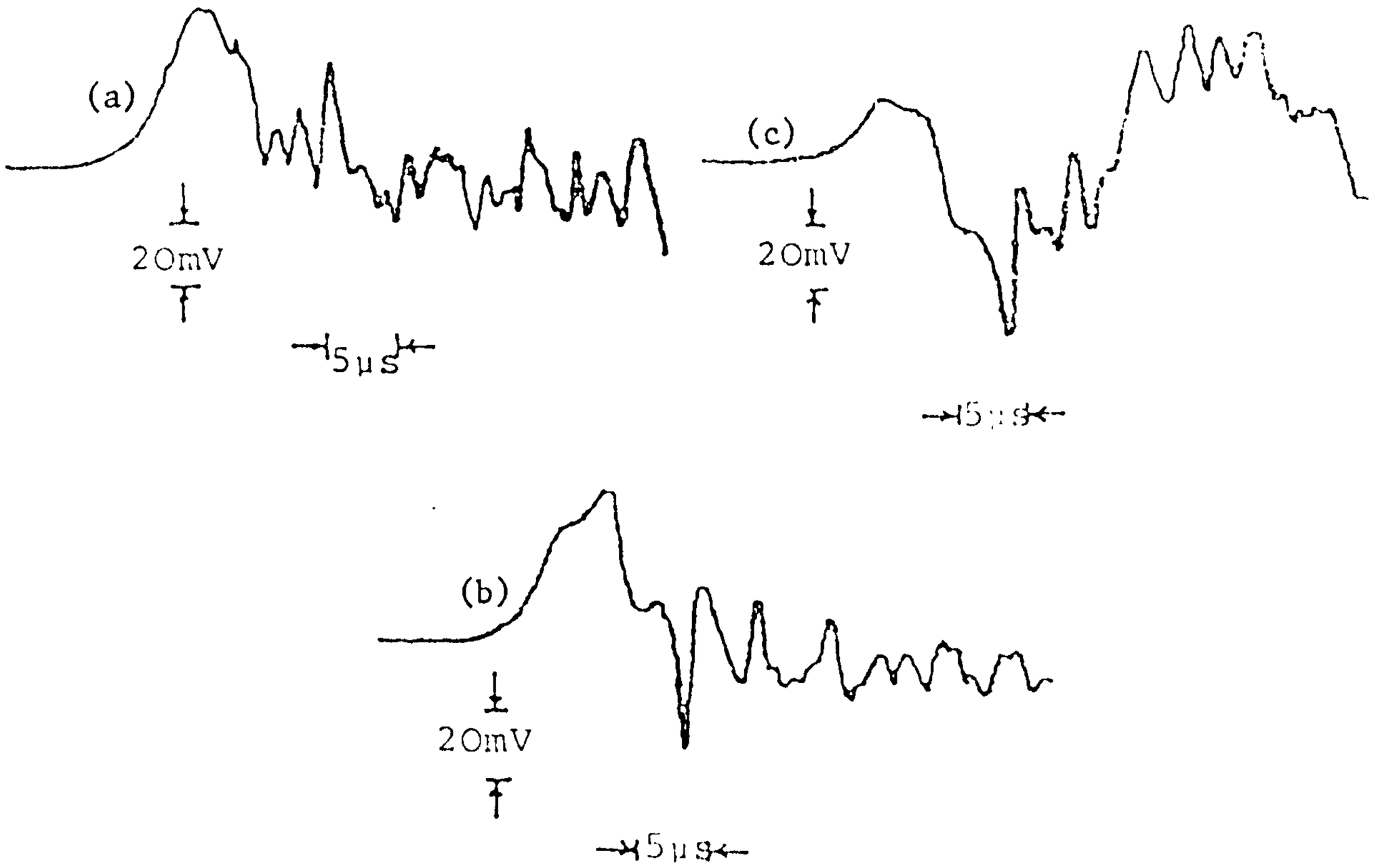

Figure 150: The change in IMS response as a result of varying the type of loading produced by and the position of a Hsu/ Nielson source on the end of a permendur bar.

(a) loading method given in figure (149a) at the centre of the end face of the bar

(b) loading method given in figure (149a) at the edge of the end face of the bar

(c) loading method given in figure (149b) at the edge of the end face of the bar.

position. The distance (x) between the surface of a ¼" mild steel bar and a measuring coil was varied. The distance from the centre of the source to the detector is then (B + x) where B is some constant. In an approximately two dimensional system the response, R, might be expected to vary inversely with this distance and so:

$$R = \frac{A}{B + x} \qquad (300)$$

or

$$\frac{1}{R} = \frac{x}{A} + \frac{B}{A} \qquad (301)$$

The results taken are plotted as V_R against x (Figure 151) yielding A = 2.4 ± 0.4 and B = (2.5 ± 0.6)mm The radius of the steel bar is 3.18mm and so the value of B appears to correspond to this value of the radius especially considering there is probably a zero error on the measurement of x.

Another facet of the operation of the measuring coil is that of its inherent finite rise time. If a magnetic current loop with its axis parallel to the detector coil axis passes through the latter then the voltage generated will not simply be a delta pulse but will have a considerable time duration. The theoretical analysis of this will be dealt with later but an experimental model of part of the IMS system will now be discussed.

The theory given later suggests that it might be possible to model stress pulses in a bar as a series of small magnets moving through free space. A case which lends itself to some sort of calculation is when the stress is a

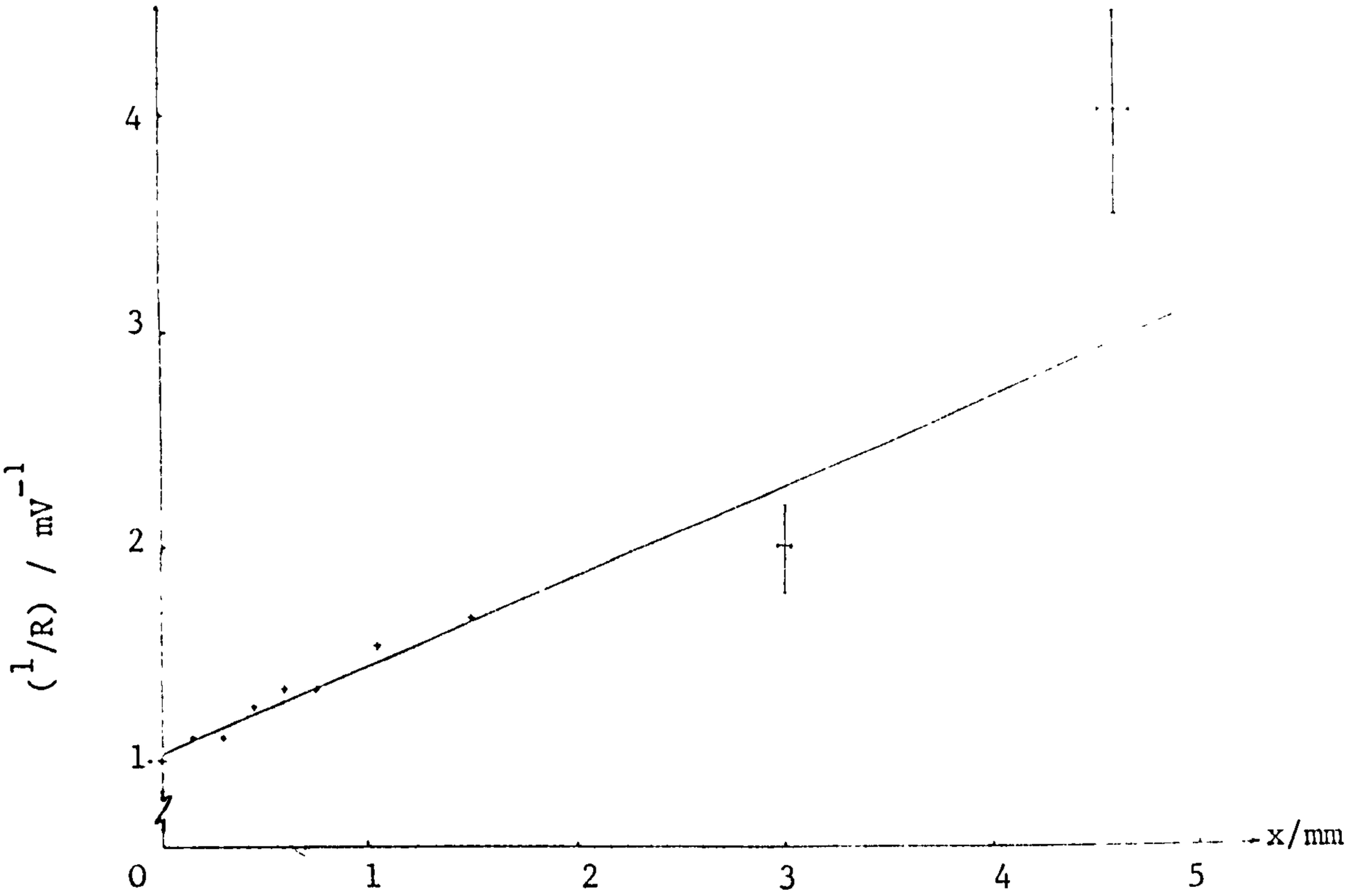

Figure 151: The variation of the inverse of the IMS response ($^1/R$) as a function of the separation between the surface of a mild steel bar and a measuring coil (x).

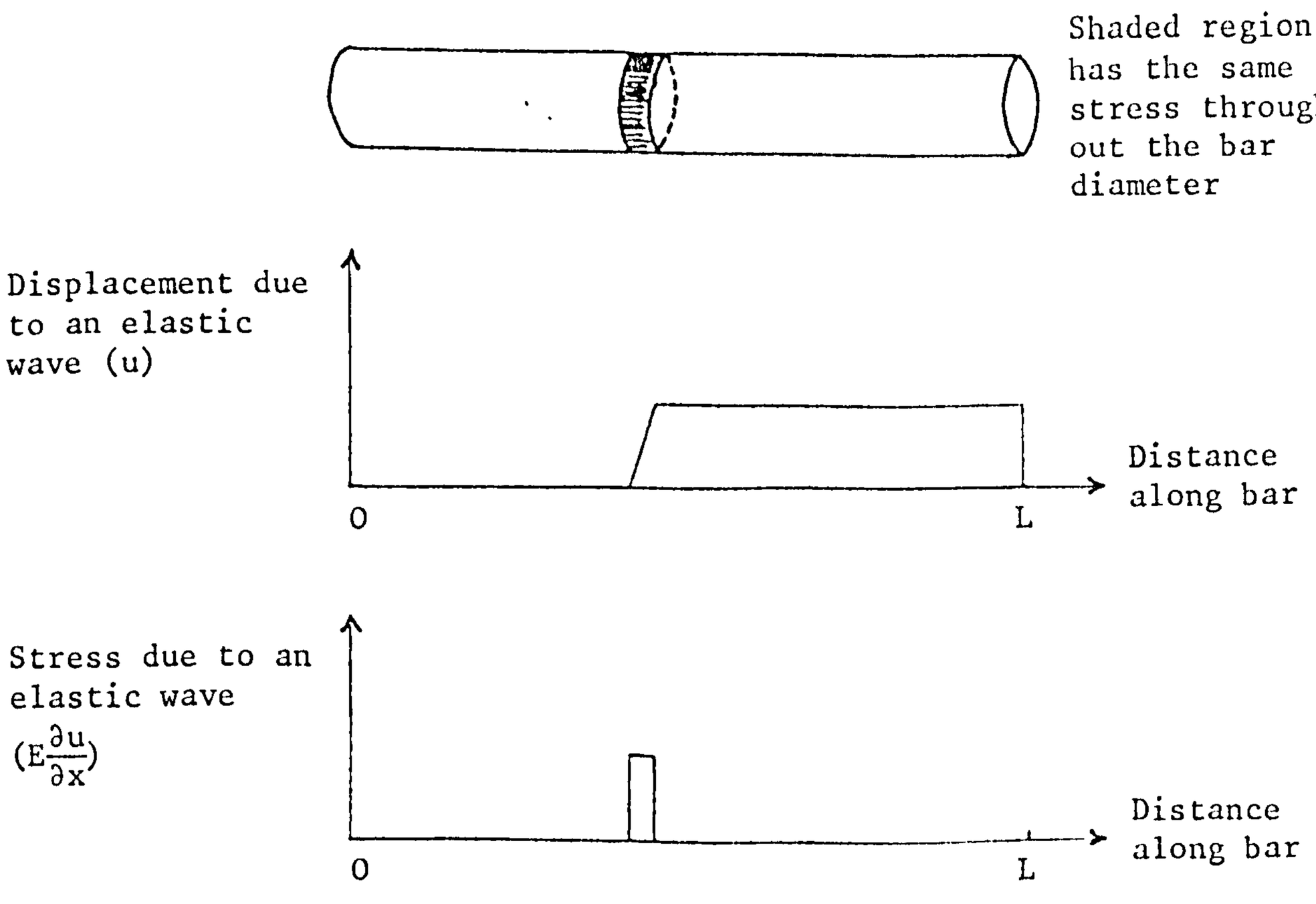

Figure 152: The uniform stress pulse described in the discussion of the theory of the IMS response.

simple square pulse extending uniformly over the width of the bar. This is indicated in Figure 152. In the case of a short pulse the theoretical results given in Figure 153 are obtained when Eddy currents are neglected. These will be derived later.

The experiment derived to test these calculations is shown schematically in Figure 154, and consists basically of a coil through which a magnet, or short solenoid, is passed (the two being equivalent[130]). Typical results are given in Figure (155). In the case of a solenoid being passed through the detecting coil the peak height was found to be proportional to the solenoid current in agreement with the theory. This is one parameter that appears to be of importance. A second parameter is the rise time of the pulse. It was found that this rise time was inversely proportional to the velocity. Referring to Figure 156, then the measured points on the waveform, the 10% and 90% values for the rise time occur when the separation (x) between the coils is 2mm and 17mm. These values correspond to angles θ as shown of $\theta = 84^{o}$ and 47^{o}. The theory indicates that θ is the important parameter. Calculations of the rise time can then be made for an IMS transducer formed as a long cylindrical bar. These may be summarized as follows:

Velocity/ms^{-1}	Bar diameter/mm	Rise time/μs
5000	20	3.0
5000	15	2.3
5000	10	1.5
5000	5	0.8

By modifying the shape of the detecting coil it should

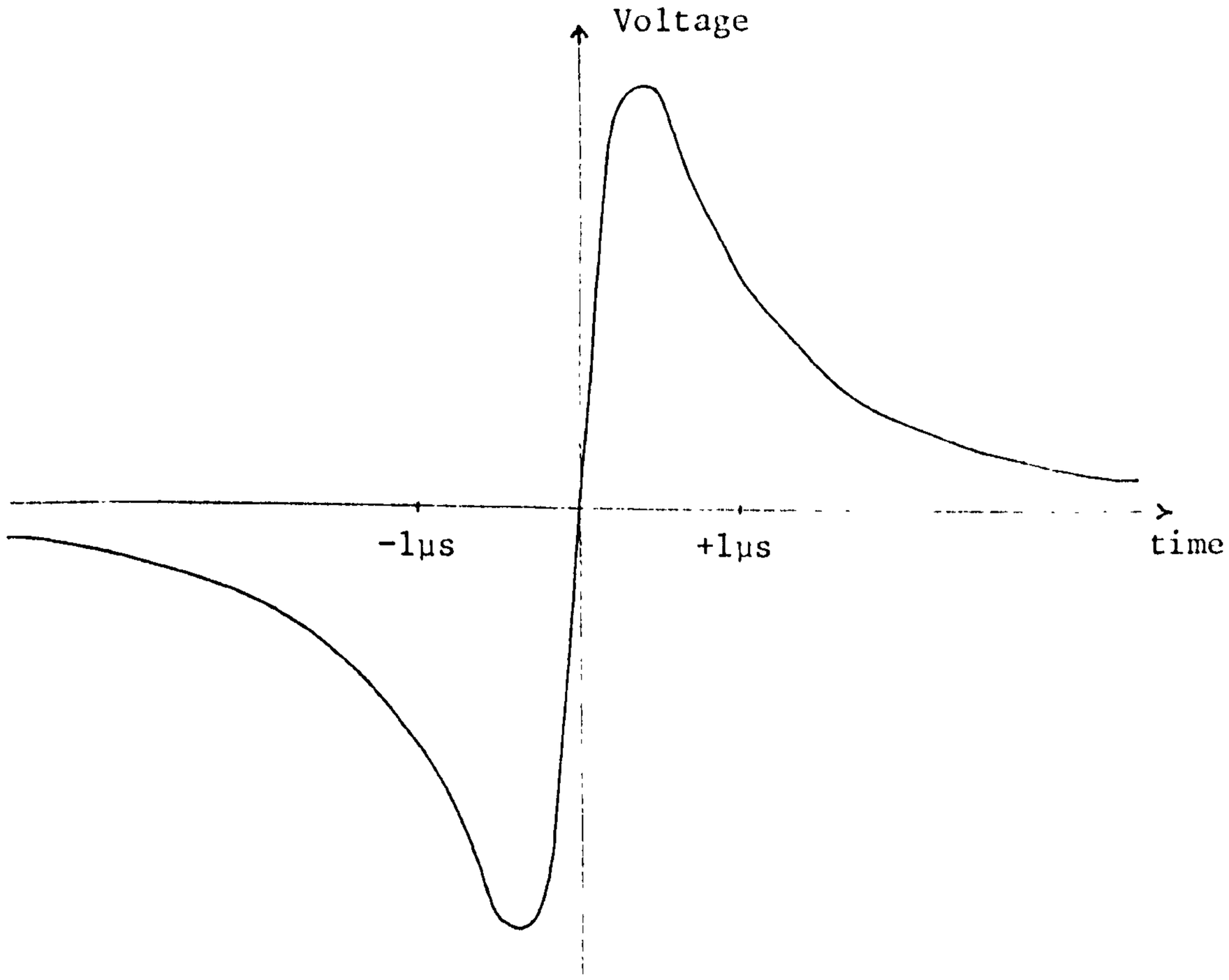

Figure 153: The result of the calculation given in section V.2 for the IMS system response to a stress pulse whose shape is given in figure 152. Eddy currents are neglected and the entire pulse is assumed to interact with the measuring coil. The time scale is for a bar diameter of 20mm and an elastic wave velocity of $5mm\mu s^{-1}$.

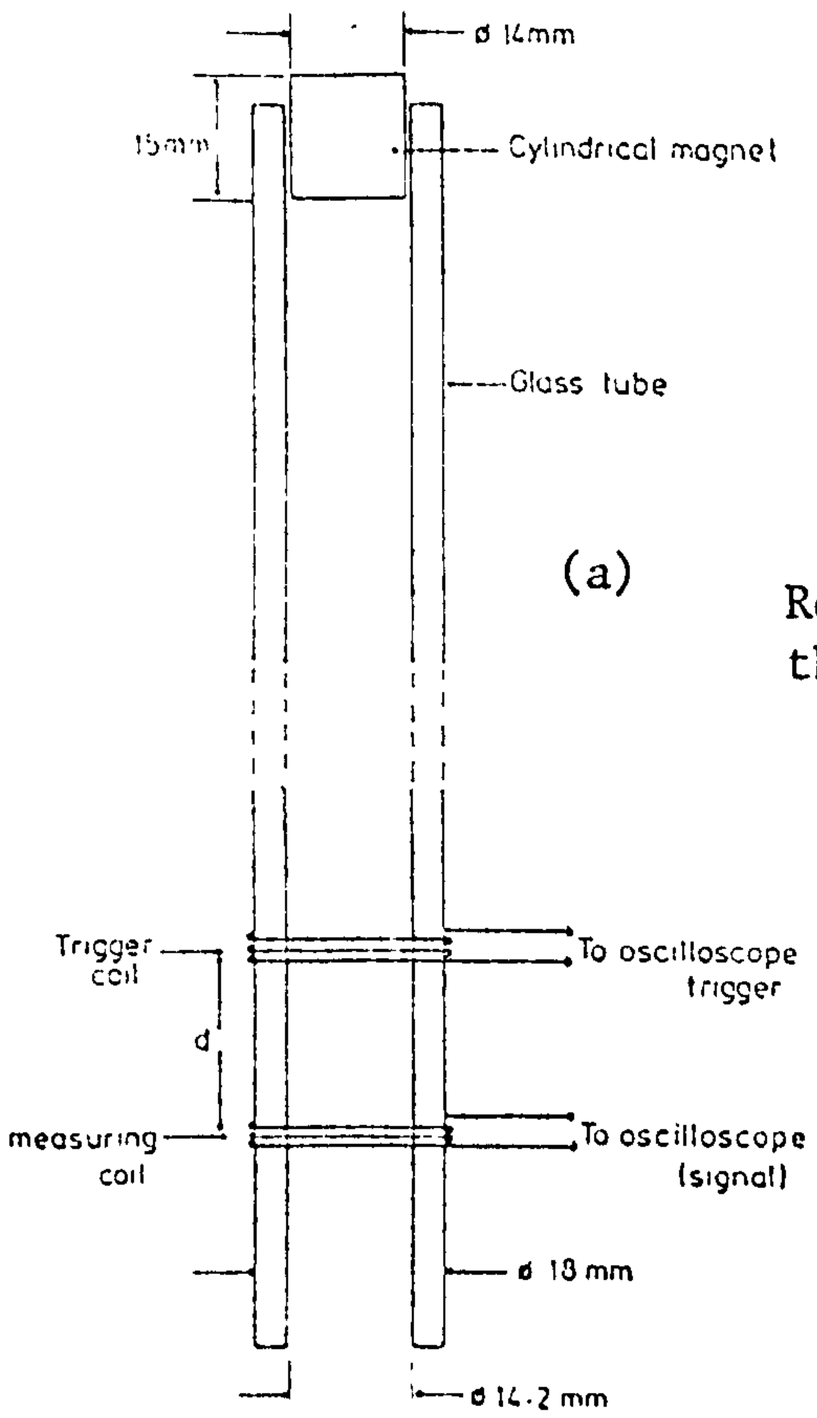

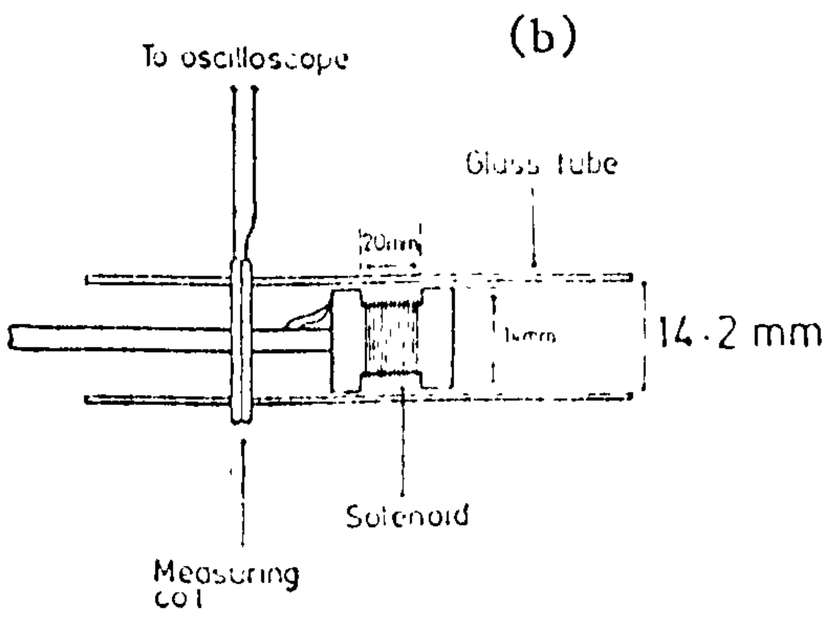

Rod to move the solenoid

Figure 154: Schematic diagrams of the apparatus used to verify the calculations in figure 153. In (a) the stress pulse is modelled as a short bar magnet whilst in (b) it is modelled as a short solenoid.

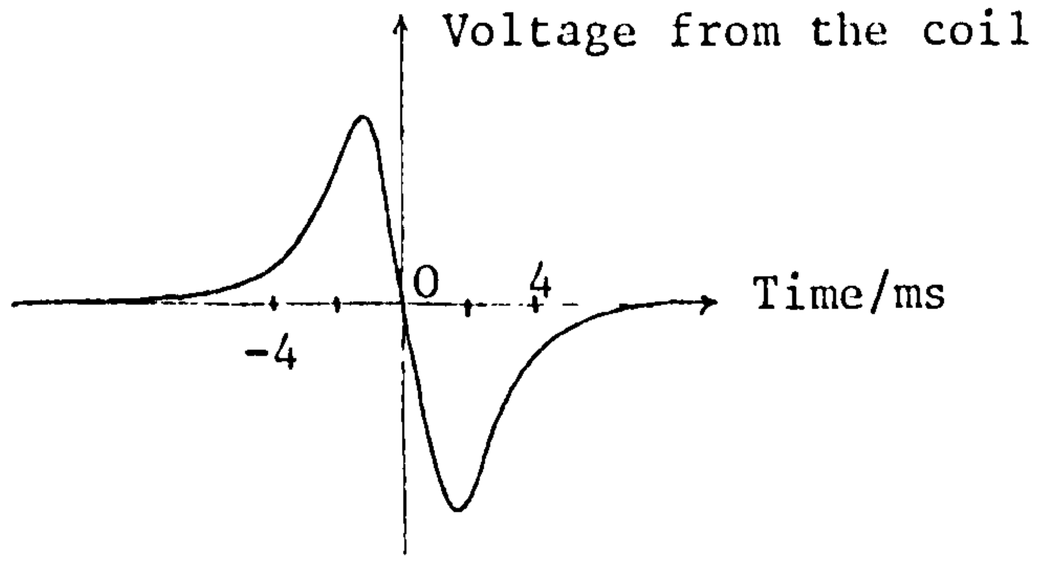

Figure 155: A typical result obtained from the apparatus shown in figure (154a). The magnet velocity was $5ms^{-1}$. The slight assymetry is due to the use of the AC coupling on the oscilloscope. This trace is very similar to that shown in figure 153.

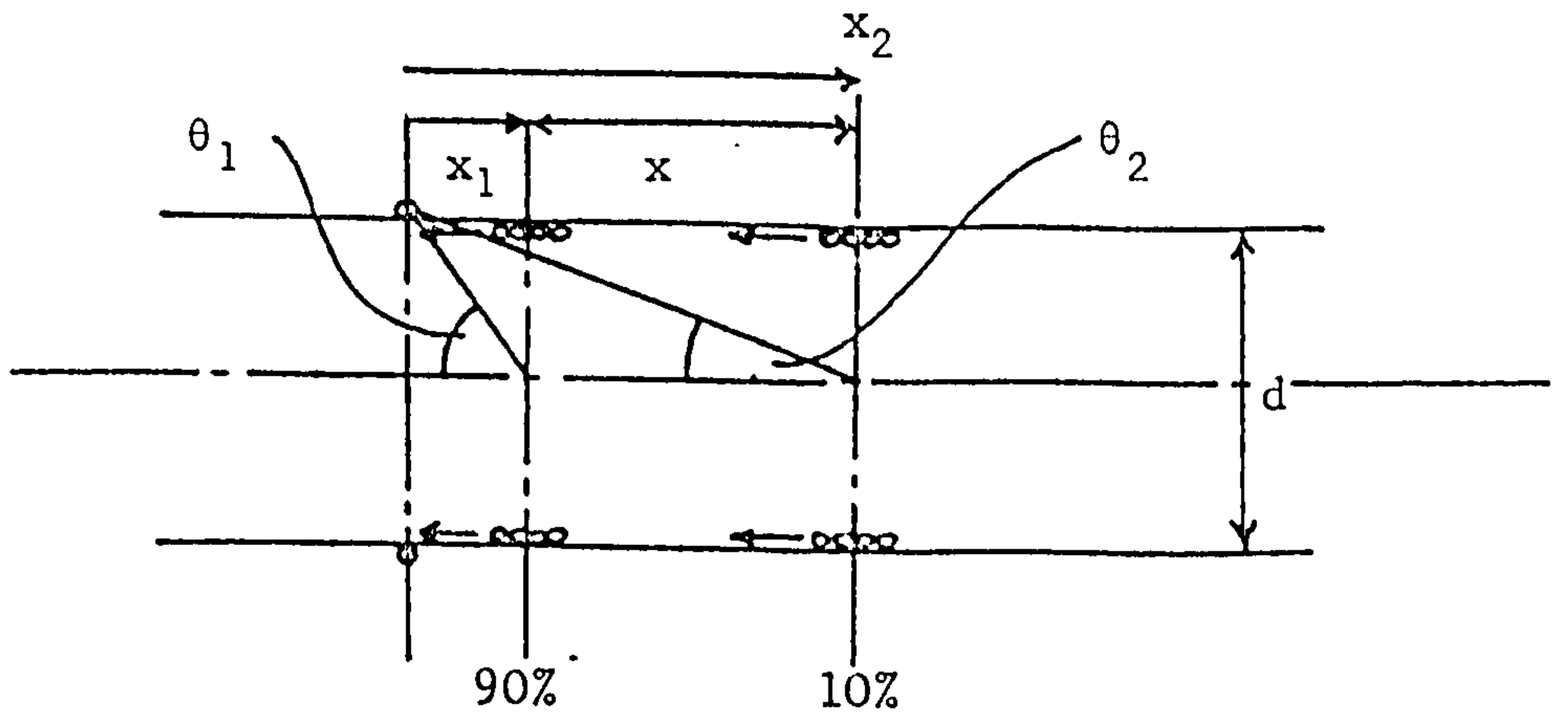

Figure 156: The relative positions of the measuring coil and the short solenoid (figure 154b) corresponding to voltage outputs at 10% and 90% of peak output. When d = 18mm the following are true

$$x_1 = 2mm, \quad \theta_1 = 84^o$$
$$x_2 = 17mm, \quad \theta_2 = 47^o$$

be possible to extract information from the IMS detector in a different form. Such variations may be investigated with this experimental set-up. The coil shape was altered to that shown in Figure 157. It was found that if the width, d, was small compared to the length of the magnet then this new coil configuration produced a voltage output which was the differential of the simple coil output. This again matches the theory to be given later. This may well provide better high frequency information but would not make mathematical deconvolution of the signal any easier. This new coil has been tried on the IMS transducer. The result of the work is given later in this chapter.

These results on the response of the simple coil to an approximation of a delta function stress distribution show that the final IMS response will be mainly dominated by the propagation effects of an elastic pulse in a cylinder as given in the previous section. However the smoothing effect of the simple coil will in fact itself be sufficient to introduce significant pulse modifications.

V.2 Theoretical considerations in the inverse magnetostrictive transducer. Discussion of the experimental results given earlier

A transient force applied to one end of the magnetostrictive bar sets up stress waves in the bar. These stresses generate transient changes in the magnetic induction B and as such induce voltages in coils wrapped around the bar. There are two areas of interest in this chain of events.

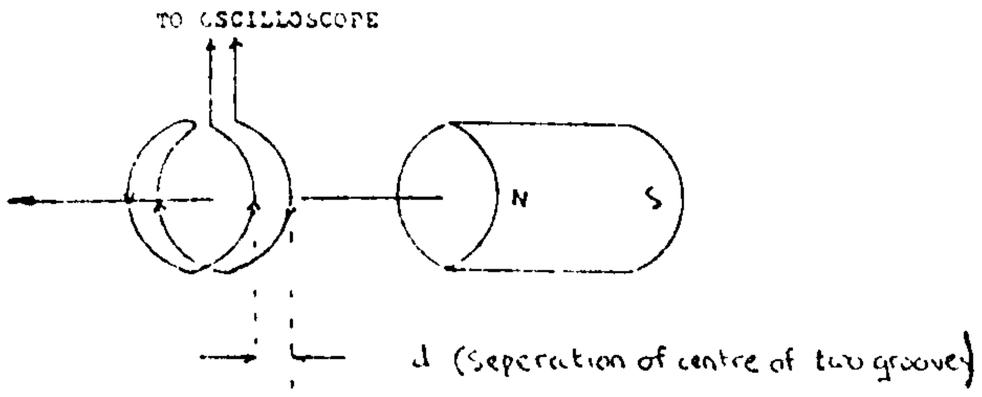

SINGLE REVOLUTION O. DIFFERENTIATING COIL IN A PLANE PERPENDICULAR TO THE MOTION OF THE CYLINDRICAL MAGNET.

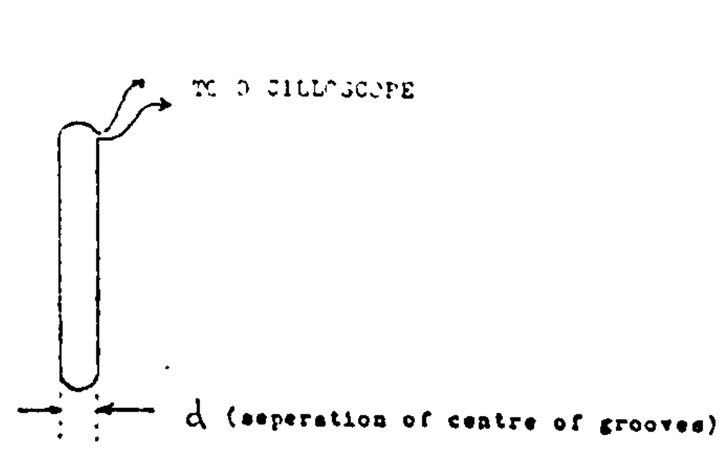

SINGLE REVOLUTION OF DIFFERENTIATING COIL IN 2 - DIMENSIONS.

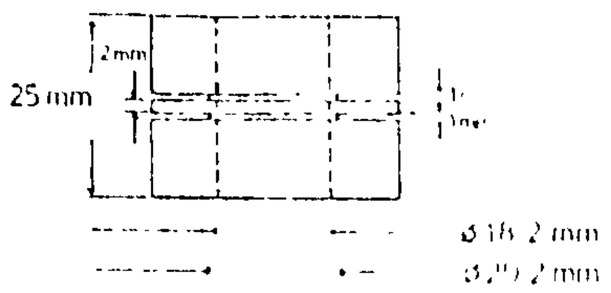

SCHEMATIC REPRESENTATION OF THE PERSPEX FORMER FOR THE DIFFERENTIATING COIL.

Figure 157: Schematic representation of the differentiating coil.

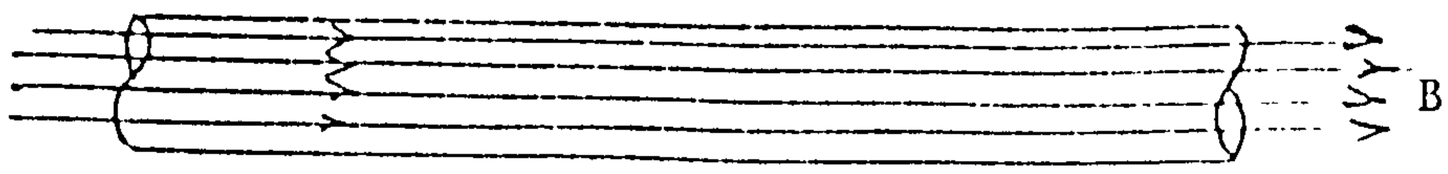

Unstressed bar

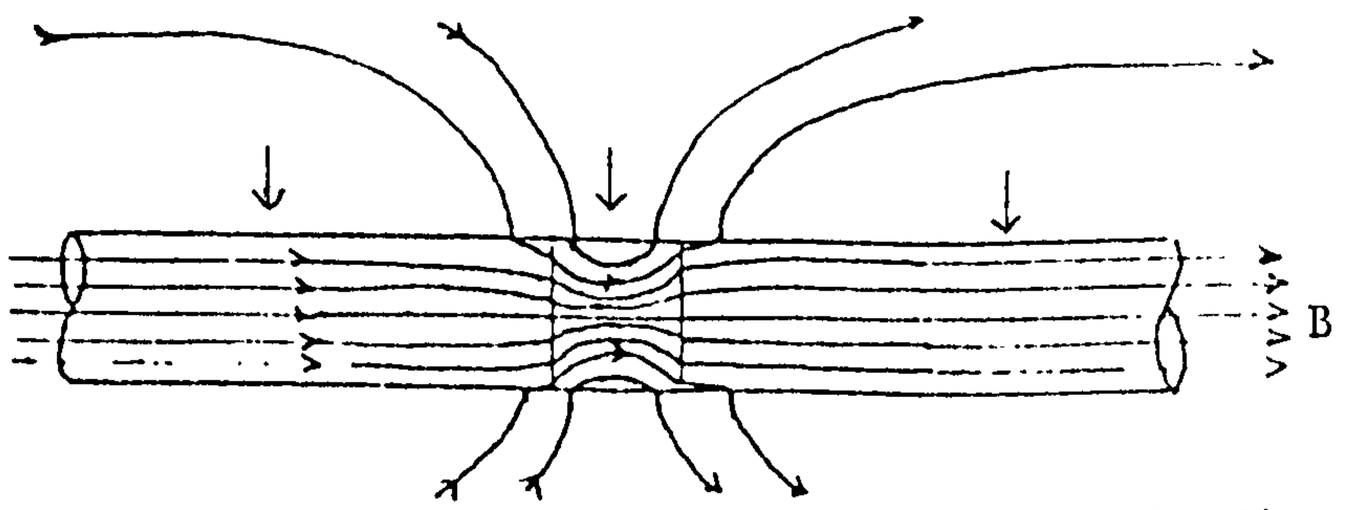

Bar stressed over a short region as in figure 152

Figure 158: The schematic representation of the B field existing in an unstressed bar and a bar stressed as in figure 152. B in the first bar is due to an external solenoid. The B field outside the bar is not shown. The case above is for a positive magnetostrictive coefficient.

The first is the propagation of the elastic pulse, whilst the second is concerned with the generation and detection of magnetic changes.

The equations governing the propagation of elastic pulses in finite solid cylinders have never been solved. However, solutions are available for an infinite cylinder, as mentioned earlier. The highlights of this theory as regards the IMS transducer are the variation in group velocity with wavelength and the existence of nodal surfaces at certain frequency dependent radii. A further point of interest for finite as opposed to infinite cylinders is the dependence of the stress waves on the initial loading conditions at the input end of the bar.

Pulse propagation in finite cylinders has been studied in chapter IV. In these studies the cylinders were excited by a force at the base of the cylinder which caused a displacement with an approximately delta function time dependency. The excitation was uniform over the end of the cylinder. The largest length to diameter ratio studied was 5.3 whereas for the IMS detector this ratio is usually around 9.

The results in Figure 126 for the output from the glass cylinder do not show any broadening of the first pulse and this pulse has in fact the same time dependency as the input pulse. However the reflections are such that there is an indication the first few pulses will eventually coalesce to form an excursion with a slow rise time of $\sim$ 1μs which compares to the predicted rise time for an infinite cylinder, of radius equal to the radius of the glass rod (3.43mm),

of 0.35 x 3.43μs = 1.20μs.

The experimental results also show that various high frequency events are building up after the initial pulse arrival. No information exists, however, concerning the variation of the amplitudes of the ultrasonic waves with radius. The results given above in section V.1.5i) suggest however that there is indeed such a variation which is similar to that predicted in the theory for an infinite cylinder.

The elastic pulse as it propagates down the IMS bar is therefore expected to be dispersed thus giving a slow rise time initial pulse followed by high frequency excursions. Such an effect is predicted by both the theory for an infinite cylinder and also approximately by the results derived in chapter IV for a finite cylinder. Radial variations are also expected with these variations being governed approximately by $J_o(\alpha r_o)$.

The elastic pulse described above generates changes in the magnetic induction which will now be considered.

Bosworth[131] shows that for stresses less than $0.32 kg.mm^{-2}$ then the change in induction B_σ due to a stress σ is given by

$$B_\sigma = \Lambda . \sigma \qquad (302)$$

Now Young's Modulus (E) is defined as

$$E = \frac{\text{Stress}}{\text{Strain}} \qquad (303)$$

and so

$$\text{Stress}(\sigma) = E.\text{strain} \qquad (304)$$

the strain being given by $\partial\xi/\partial x$ when ξ is the displacement. If ξ is the displacement of a travelling elastic wave of angular frequency ω and wavevector k, described by

$$\xi = \xi_o \sin (kx - \omega t) \qquad (305)$$

then the maximum stress (σ_{max}) is

$$\sigma_{max} = E.\frac{\omega}{v}\xi_o \qquad (306)$$

where v is the velocity of the wave.

Work described earlier in chapter IV shows that a very large value for ξ_o would be $\sim$ 10nm at a frequency of $\sim$ 500kHz. This gives a value for σ_{max} of 0.13kg.mm^{-2}. Consequently equation (302) will always be obeyed.

The magnetic induction, as described earlier, sets up eddy currents in the cylindrical bars. These currents effectively shield the measuring coil from B_σ changes occurring towards the centre of the bar. Calculations given by Bozorth[128] show that at 100kHz changes in roughly only the outer 30μm of the bar actually contribute to the voltage induced on the measuring coil. Such a figure agrees with the experimental results described earlier in section V.1.3.

Consider now then an elastic wave travelling down the bar which is a step displacement over the entire cross section with a finite rise time δt. This is the pulse described in the previous section and shown in Figure 152.

The stress generated by this is then a short square pulse of length δt (also shown in Figure 152). In reality the pulse will have an amplitude dependent on the radius, but this is unimportant. This stress distribution will set up a magnetic induction. Due to eddy current effects only the induction generated in the outer "skin" of the cylinder is considered. Only changes in the magnetic induction (B) will induce voltages in the measuring coil. The change in B is equivalent to a travelling magnet, this magnet being in the shape of a thin ring and poled approximately parallel to the axis of the ring.

Now a thin disc of material uniformly magnetized parallel to the axis of the disc is equivalent to a current loop or short solenoid[130]. Unfortunately, the disc is not uniformly magnetized as the fields $\underline{B}$ and $\underline{H}$ must satisfy the boundary conditions across all faces. This first condition is:

$$\underline{B}_1 . \hat{\underline{n}}_1 = -\underline{B}_2 . \hat{\underline{n}}_2 \qquad (307)$$

where $\hat{\underline{n}}_i$ is the unit vector perpendicular to the boundary pointing out from material i. The second boundary condition is given by:

$$H_{1t} = H_{2t} \qquad (308)$$

where H_{it} is the component of the $\underline{H}$ field tangential to the material surface. $\underline{B}$ and $\underline{H}$ are linked by the usual (SI) relationship:

$$\underline{B} = \mu_o(\underline{H} + \underline{M}) \qquad (309)$$

where $\underline{M}$ is the magnetization. These boundary conditions lead to a field structure which is shown qualitatively in Figure 158. This is clearly very complicated and would not allow further calculations to be carried out if indeed the true solution is attainable. Therefore the approximation, given above, of a uniformly magnetized disc will be retained. This is then equivalent to a current loop.

To obtain a ring rather than a solid disc then two current loops are used, one inside the other, and with the currents flowing in opposite directions. As the influence of the material external to the stressed section is ignored then these current loops are effectively in free space.

The measuring coil is now assumed to be a single thin coil and the voltage induced on it by the current loops may be calculated. To begin with the effect of one current loop is calculated. The induced voltage is given by

$$V = \frac{\partial}{\partial t} \int_A \underline{B} \cdot \underline{dA}$$

where $\underline{B}$ is the field generated by the current loop passing through the measuring coil and $\underline{A}$ is the area of this coil. Therefore to start with the field at the measuring coil is calculated. The geometry for this calculation is shown in Figure 159. The magnetic induction $d\underline{B}$ at the point P(X,Y,Z) produced by an element $d\underline{l}$ of wire carrying a current I is given by:

$$d\underline{B}(\underline{r}) = \frac{\mu_o I}{4\pi} \frac{d\underline{l} \times \underline{r_s}}{r_s^3} \qquad (311)$$

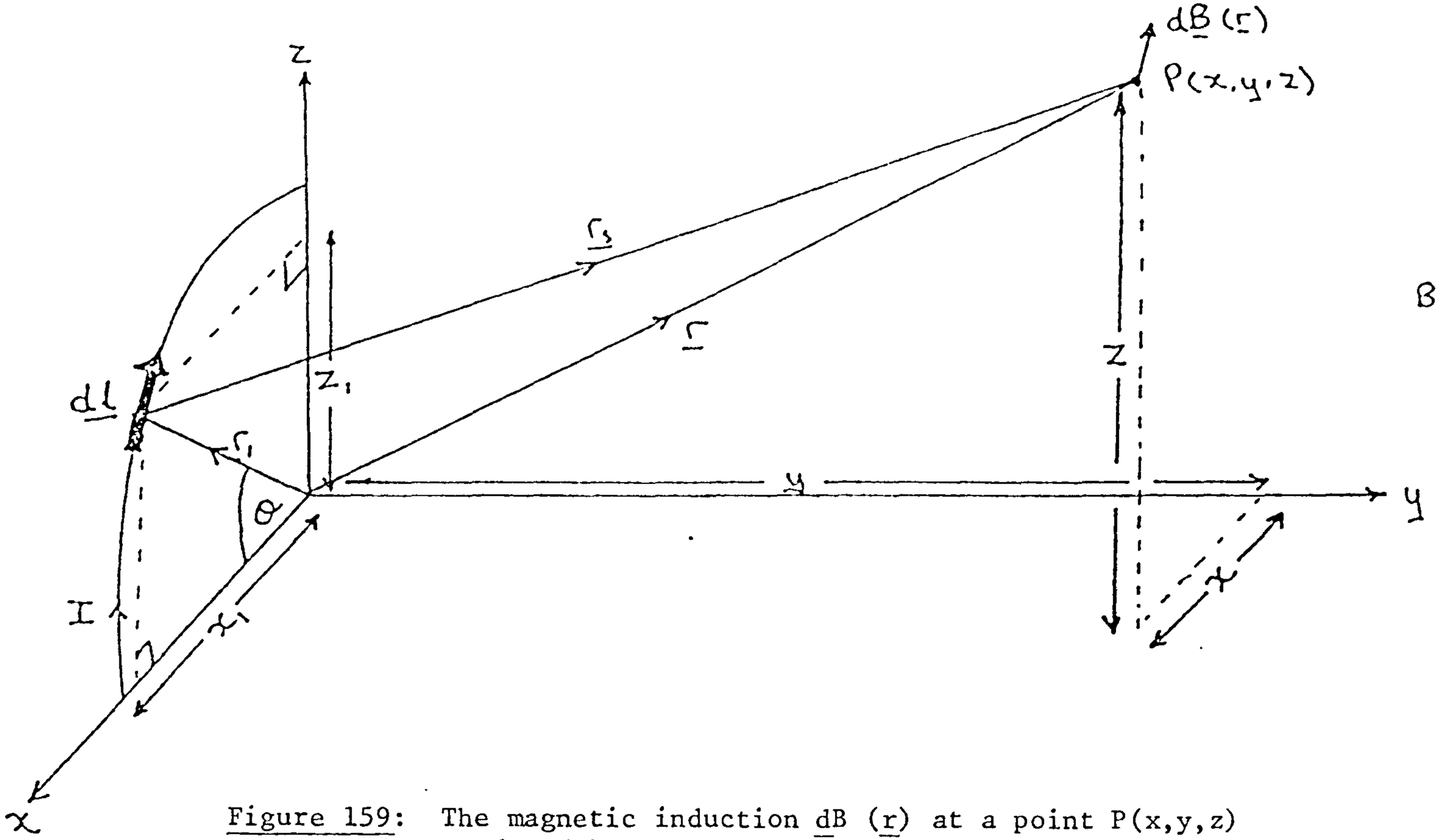

Figure 159: The magnetic induction dB (r) at a point P(x,y,z) produced by an element Idl of a current loop of radius r_1 in the x-z plane.

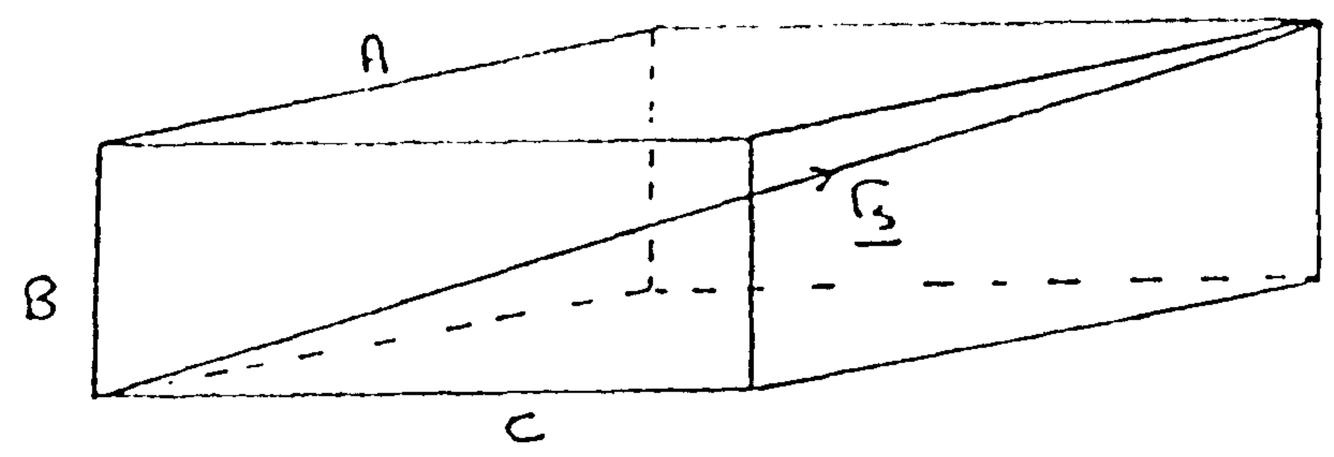

Figure 160: Parallelopiped with diagonal r_s where the lengths A,B,C are given in equation 317.

The vector $d\underline{l}$ is given by the sum of its components in the x and z directions:

$$\therefore \quad d\underline{l} = -\,dl\,\sin\theta\hat{\underline{i}} + dl\,\cos\theta\hat{\underline{k}} \qquad (312)$$

The magnitude of $d\underline{l}$ is given by:

$$dl = r_1\,d\theta \qquad (313)$$

where $d\theta$ is the angle subtended by $d\underline{l}$ at the centre of the current loop. Substituting equation (313) into equation (312) then:

$$d\underline{l} = -r_1 d\theta \sin\theta\hat{\underline{i}} + r_1 d\theta\cos\theta\hat{\underline{k}} \qquad (314)$$

The vector $\underline{r}_s$ is given by:

$$\underline{r_s} = \underline{r} - r_1$$

$$= x\hat{\underline{i}} + y\hat{\underline{i}} + z\hat{\underline{k}} - (x_1\hat{\underline{i}} + z_1\hat{\underline{k}}) \qquad (315)$$

now $x_1 = r_1\cos\theta$

and $z_1 = r_1\sin\theta$

Hence equation (315) becomes:

$$\underline{r}_s = x\hat{\underline{i}} + y\hat{\underline{i}} + z\hat{\underline{k}} - (r_1\cos\theta\hat{\underline{i}} + r_1\sin\theta\hat{\underline{k}})$$

$$= (x - r_1\cos\theta)\hat{\underline{i}} + y\underline{j} + (z - r_1\sin\theta)\hat{\underline{k}} \qquad (316)$$

The magnitude of $\underline{r}_s$ is given by the diagonal of a parallelopiped (see Figure 160) where A,B,C are given in this figure as:

$$A = x - x_1 = x - r_1\cos\theta$$

$$B = z - z_1 = z - r_1\sin\theta \qquad (317)$$

$$C = y$$

The magnitude of $\underline{r}_s$ is given by:

$$r_s = \sqrt{A^2 + B^2 + C^2} \qquad (318)$$

$$= [(x-r_1\cos\theta)^2 + (z-r_1\sin\theta)^2 + y^2]^{\frac{1}{2}}$$

hence $$r_s^3 = [(x-r_1\cos\theta)^2 + y^2 + (z-r_1\sin\theta)^2]^{3/2}$$

From equations (314) and (316) $d\underline{l} \times \underline{r}_s$ is given as the determinant:

$$d\underline{l} \times \underline{r}_s = \begin{vmatrix} \hat{\underline{i}} & \hat{\underline{j}} & \hat{\underline{k}} \\ -r_1 d\theta\sin\theta & 0 & r_1 d\theta\cos\theta \\ x-r_1\cos\theta & y & z-r_1\sin\theta \end{vmatrix}$$

therefore:

$$d\underline{l} \times \underline{r}_s = (-r_1 d\theta\cos\theta y)\hat{\underline{i}}$$
$$- (-zr_1 d\theta\sin\theta + r_1^2 d\theta\sin^2\theta - xr_1 d\theta\cos\theta$$
$$+ r_1\theta d\theta\cos^2\theta) + (-r_1 d\theta\sin\theta y)\hat{\underline{k}}$$

(319)

The component if $d\underline{B}$ in the y-direction is required since the measuring coil is also in the x-z plane.

$$(d\underline{l} \times \underline{r}_s).\hat{\underline{j}} = zr_1 d\theta\sin\theta - r_1^2 d\theta\sin^2\theta + xr_1 d\theta\cos\theta$$
$$- r_1^2 d\theta\cos^2\theta$$

$$= -r_1^2 d\theta(\sin^2\theta + \cos^2\theta) + zr_1 d\theta\sin\theta + xr_1 d\theta\cos\theta$$

$$= zr_1 d\theta\sin\theta - r_1^2 d\theta + xr_1 d\theta\cos\theta \qquad (320)$$

Substituting equation (318) and (320) into equation (311) then:

$$d\underline{B}(r).\hat{\underline{j}} = \frac{\mu_o I}{4\pi} \frac{zr_1 d\theta\sin\theta - r_1^2 d\theta + xr_1 d\theta\cos\theta}{\{(x-r_1\cos\theta)^2 + y^2 + (z-r_1\sin\theta)^2\}^{3/2}} \qquad (321)$$

Summing the contributions of all the elements $d\underline{l}$ around the loop from $0 \leqslant \theta \leqslant 2\pi$ gives:

$$\underline{B}(r).\hat{\underline{j}} = \frac{\mu_o I}{4} \int_{\theta=0}^{\theta=2\pi} \left[\frac{zr_1\sin\theta - r_1^2 + xr_1\cos\theta}{\{(x-r_1\cos\theta)^2 + y^2 + (z-r_1\sin\theta)^2\}^{3/2}}\right] d\theta \qquad (322)$$

The magnetic induction along the axis of the current loop (y-axis) i.e. when $x = z = 0$ is given by:

$$\underline{B}(r).\underline{j} = \frac{\mu_o I}{4\pi} \int_o^{2\pi} \frac{-r_1^2 d\theta}{(y^2 + r_1^2)^{3/2}} \qquad (323)$$

$$= \frac{-\mu_o I r_1^2}{2(y^2 + r_1^2)^{3/2}} \qquad (324)$$

This is in agreement with similar calculations given by Lorrain and Corson[130]. The voltage generated on the coil is given by equation (310) and in terms of the coordinates above then $\int \underline{B}.\underline{dA}$ is given as Φ where

$$\Phi = \int_A \underline{B}(r).\underline{j}.dA \qquad (325)$$

This has to be integrated over the area of the measuring

coil. It is easier to express the dimensions of the measuring coil in cylindrical coordinates as illustrated in Figure 161. Where:

$$x = \rho\cos\psi \qquad (326)$$

and $$z = \rho\sin\psi$$

Therefore equation (325) becomes:

$$\Phi = \int_{\rho=0}^{\rho=a} \int_{\psi=0}^{\psi=2\pi} \rho\, d\rho\, d\psi . \underline{j} . \underline{B}(r) \qquad (327)$$

Substituting equation (322) into (327) and putting $x = \rho\cos\psi$ and $z = \rho\sin\psi$, gives for $r_1 \simeq a$:

$$\Phi = \int_o^a d\rho \int_o^{2\pi} d\psi \int_o^{2\pi} \frac{\mu_o I \rho}{4\pi} \left\{ \frac{r_1\rho\sin\psi\sin\theta - r_1^2 + r_1\rho\cos\psi\cos\theta}{\{(\rho\cos\psi - r_1\cos\theta)^2 + y^2 + (\rho\sin\psi - r_1\sin\theta)^2\}^{3/2}} \right\} d\theta \qquad (328)$$

From equation (310) then:

$$V = \frac{\mu_o I}{4\pi} \int_o^a d\rho \int_o^{2\pi} d\psi \int_o^{\pi} \rho \frac{d}{dt} \left\{ \frac{r_1\rho\sin\psi\sin\theta - r^2 + r_1\rho\cos\psi\cos\theta}{\{(\rho\cos\psi - a\cos\theta)^2 + y^2 + (\rho\sin\psi - r_1\sin\theta)^2\}^{3/2}} \right\} d\theta \qquad (329)$$

The current loop (or magnet) is moving with a velocity (v) towards the measuring coil, therefore y is a function of t. Clearly the reverse situation where the current loop starts from the measuring coil and moves away with velocity v could be considered and so consequently the following substitution may be made:

$$y = vt$$

into equation (329) which becomes:

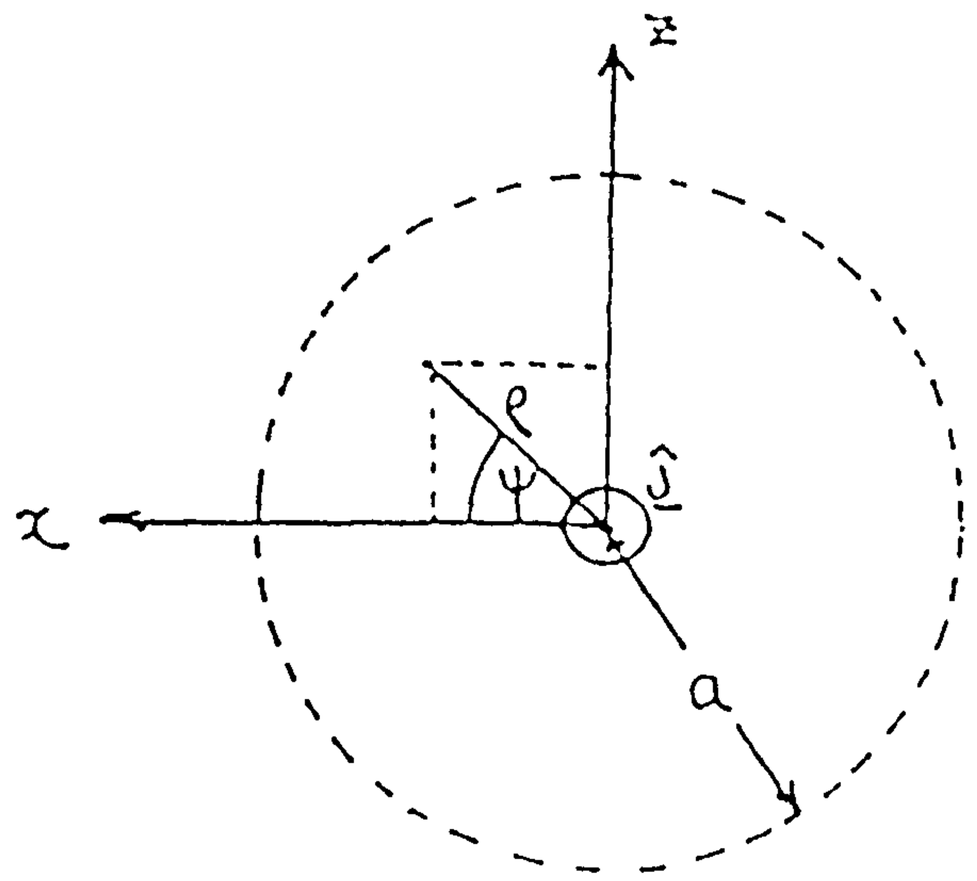

Figure 161: The cylindrical co-ordinate system used to evaluate the integral in equation (325).

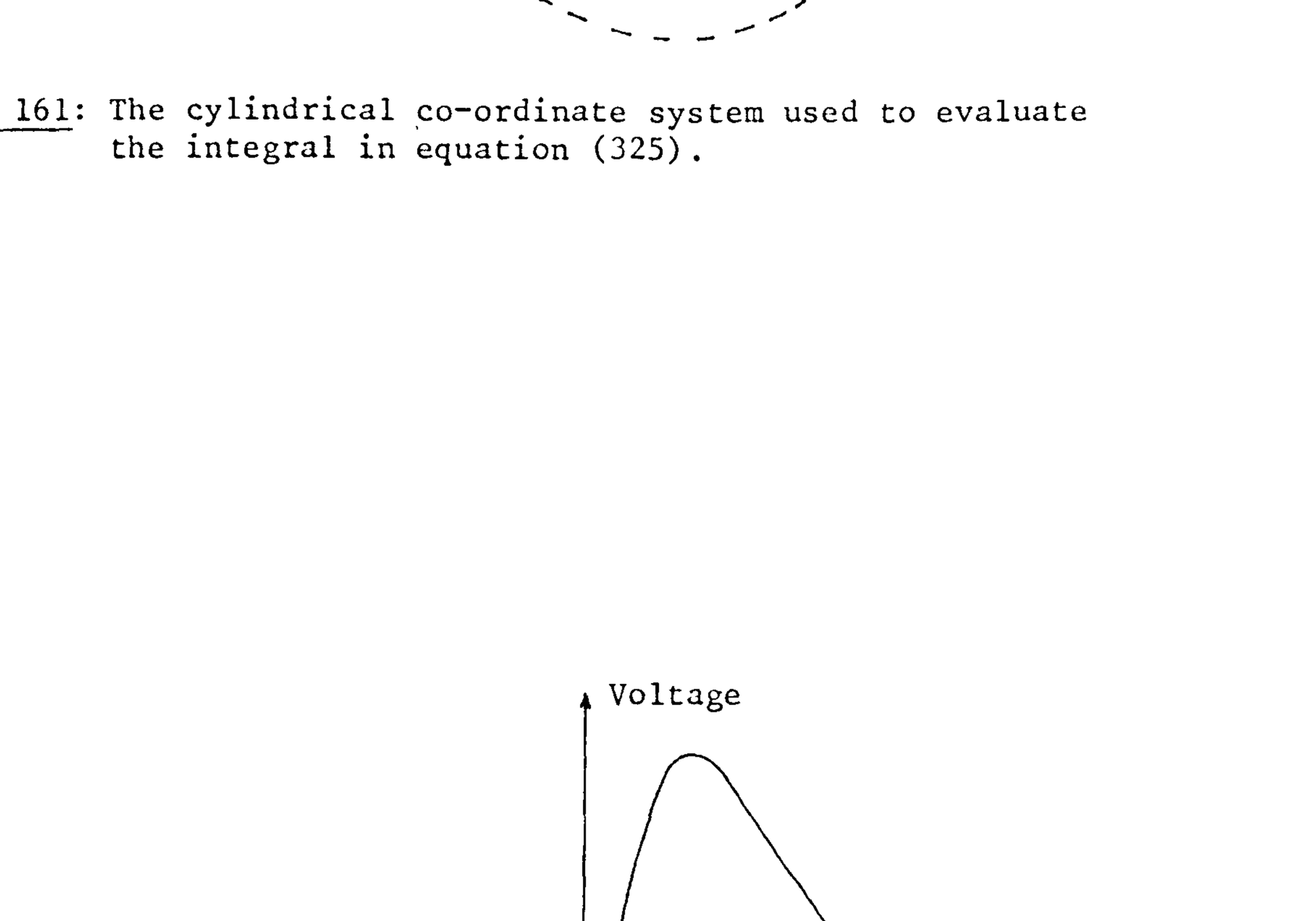

Figure 162: The final calculated response of an IMS detector to the stress pulse described in figure (152) when eddy current effects are taken into account. The time axis is scaled for a bar diameter of 20mm and an elastic wave velocity of $5 mm \mu s^{-1}$.

$$V = \frac{-\mu_o I}{4\pi} \int_o^a d\rho \int_o^{2\pi} d\psi \int_o^{2\pi} \rho \frac{d}{dt} \left(\frac{r_1 \rho \sin\psi \sin\theta - r^2 + r_1 \rho \cos\psi \cos\theta}{\{(\rho\cos\psi - r_1\cos\theta)^2 + v^2t^2 + (\rho\sin\psi - r_1\sin\theta)^2\}^{3/2}} \right) d\theta \quad (330)$$

Carrying out the differentiation in equation (330) gives the voltage at the terminals of the measuring coil as:

$$V = +\frac{N\mu_o I}{4\pi} \int_o^a d\rho \int_o^{2\pi} d\psi \int_o^{2\pi} \rho 3v^2 t \left(\frac{r_1 \rho \sin\psi \sin\theta - r^2 + r_1 \rho \cos\psi \cos\theta}{\{(\rho\cos\psi - r_1\cos\theta)^2 + V^2t^2 + (\rho\sin\psi - r_1\sin\theta)^2\}^{5/2}} \right) d\theta \quad (331)$$

Equation (331) cannot be evaluated as it stands. A numerical method is required for its evaluation.

The numerical evaluation of equation (331) has been performed with the aid of a computer and the result is that given earlier in Figure 153.

This result has previously been compared to the physical model (see section V.1.5ii)) of the IMS process and the agreement is very good. On subtracting the response for the other current loop (in the opposite direction) then the final response can be determined. This is dependent on the skin depth but is found to be very similar in shape to the result in Figure 153 and is itself shown in Figure 162.

In conclusion then the elastic waves in the bar are severely modified by the multiple reflections within the bar. This may be described as a propagation effect and is fairly well described by theoretical results for an infinite bar or by experimental results for a finite bar given in chapter IV. The waveform is then further modified by eddy current effects and finally by magnetic interactions.

The smoothing effect of the magnetic interactions is predicted to be the major smoothing contribution for the high frequency components found at the tail of the elastic pulse in the bar, but to be only of secondary importance in the first pulse. This is indeed found to be the case and can be seen in the two Figures 150a) and 146b) where the higher frequency components in Figure 146b) have been suppressed. Therefore all the features of the detection of the inverse magnetostrictive effect may be explained theoretically. The calibration of a real IMS transducer can now be carried out and is described below.

V.3 The calibration of an inverse magnetostrictive transducer

V.3.1 The design of an IMS transducer

The first decision to be made regarding the design of an IMS transducer is the shape of the bar. Now it has been shown above that due to eddy currents the amplitude of the device response is proportional to the radius of the cylinder. If a large radius is chosen then a large signal to noise ratio should result. However, for ultrasonic waves detected off epicentre this would lead to a large aperture effect. A compromise might be to form the tip of the transducer into a cone with a small flat end of radius Δr whilst retaining the rest of the transducer as a bar of radius r_o.

However it can be seen that the elastic waves emanating from the displacement at the tip will spread out with the

energy content obeying an inverse square law. Therefore the displacement at the radius r_o will be $\xi_{in}(\Delta r/r_o)$ where ξ_{in} is the displacement at the input. The detected pulse height is as described earlier proportional to the displacement and to the bar radius and is therefore given by:

$$\alpha r_o \xi_{in}(\Delta r/r_o) = \alpha \xi_{in} \Delta r \qquad (332)$$

For a uniform bar of radius r_o on the other hand the detected pulse height would be simply $\alpha \xi_{in} r_o$. These results were in fact found experimentally to be the case. The bar shape should therefore be a uniform cylinder.

The radius of this cylinder is then a compromise between the need to reduce any aperture effect and the need to maintain a reasonable signal to noise ratio. A bar diameter of 6mm is taken as this compromise.

The next question is whereabouts on the bar should the coil be placed. Ideally the detected pulse should be distorted from the original input pulse as little as possible. From the work given earlier this suggests the coil should be as near to the base of the bar as can be obtained. For calibrations carried out in terms of the modulus of the frequency response the positioning of the coil on the bar should have no effect becaused a frequency dependent dispersion affects only the phase, and not the modulus, of the Fourier transform.

A simple measuring coil is used at first with the number of turns set at 300 to ensure quite a small coil may be produced (small compared to the magnetic effects

calculated for the travelling current loops). This number also gives an induction which is sufficiently low to ensure that the input impedance of the preamplifier does not significantly affect the system frequency response. The double coil described in section V.1.5ii) is also tested to try to enhance the high frequency response.

The material chosen is obviously that with the highest inverse magnetostrictive coefficient Λ (equation (303)) and the magnetic $\underline{H}$ field is then set to make Λ as large as possible for this material. 49-Permendur is therefore used.

The completed system is shown in Figure 163 with the transducer being coupled to the aluminium block using silicone grease.

V.3.2 Epicentral calibration of the inverse magnetostrictive transducer

Following the epicentral calibration method outlined in chapter IV the modulus of the frequency response may be derived. This method implicitly assumes that the conditions outlined in chapter II regarding calibration are obeyed. The first one in doubt is thought to be that of mode uncoupling. It is assumed that the low shear modulus of the grease will result in this assumption being satisfied. The second problem is that the trace rings for a long time. Therefore the calibration will only be approximate (see chapter VI).

The surface movement of the aluminium block is shown in Figure 109 and the output of the IMS transducer

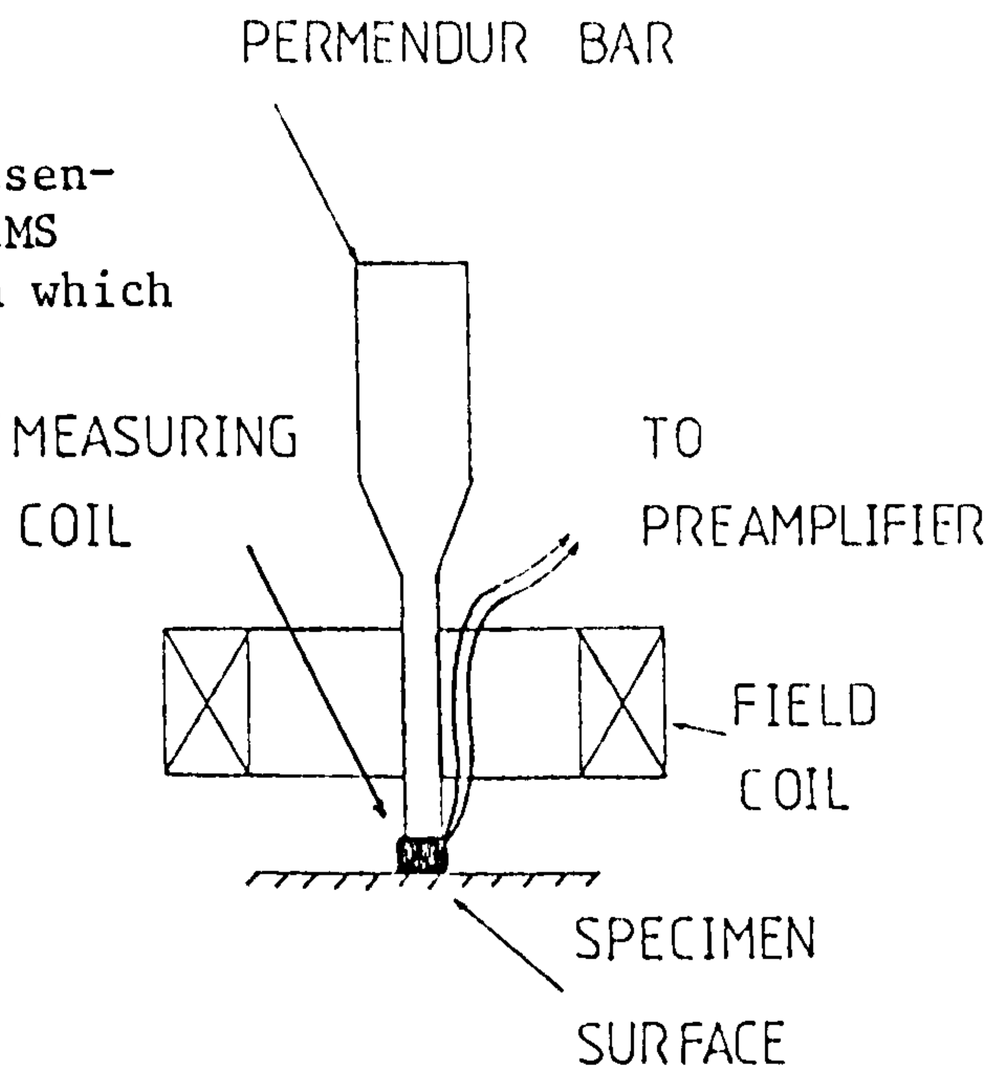

Figure 163: Schematic representation of the IMS transducer upon which calibrations were performed.

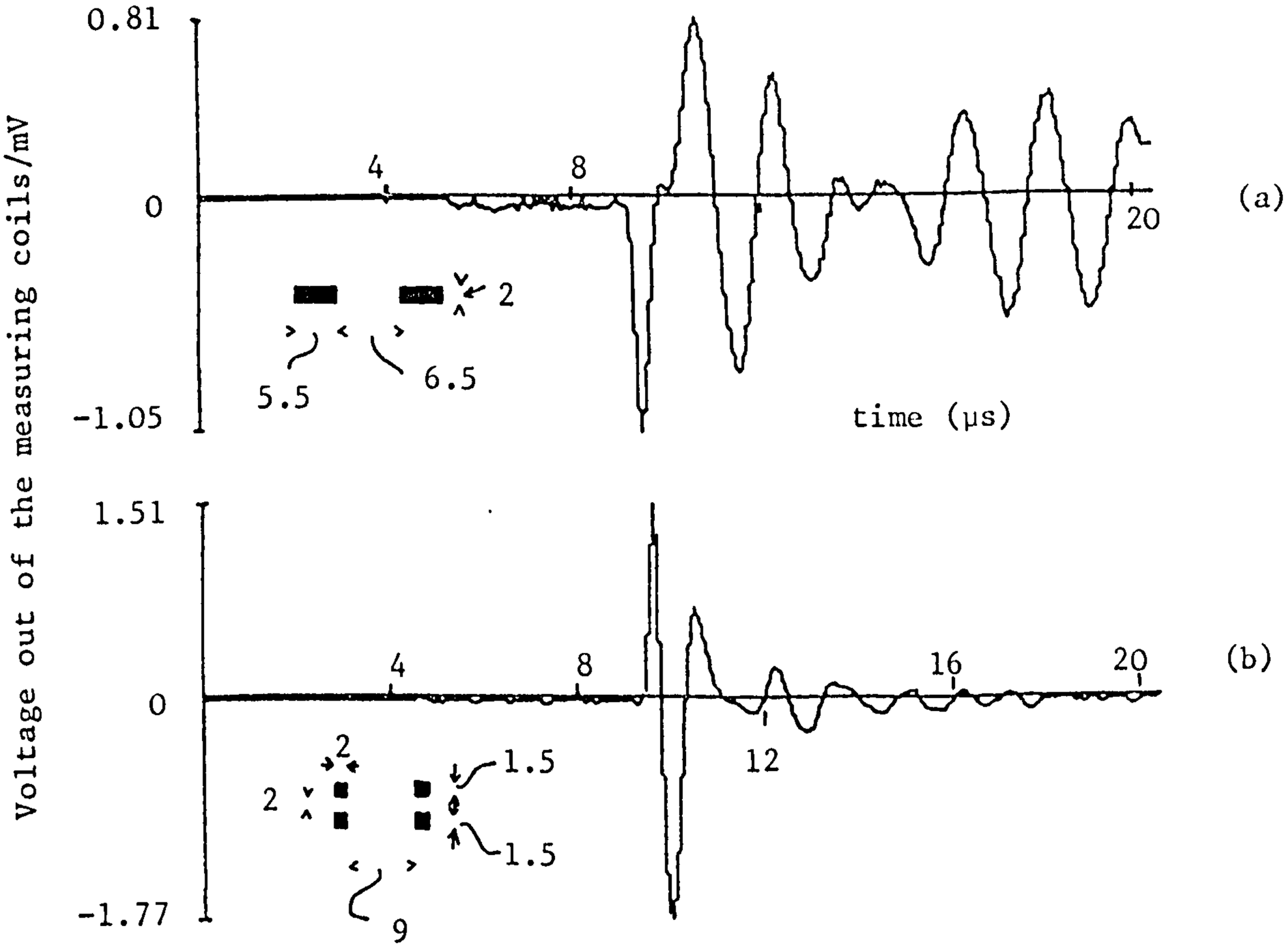

Figure 164: The voltages out of the measuring coils for epicentral calibrations of the IMS transducer shown in figure 163. Trace (a) is the output from a 300 turn simple coil whilst trace (b) is for a 150 turn double coil as shown in figure (157). The coils are shown dimensioned in millimeters by these traces.

in Figure 164 for both the simple coil and double coil. It can be seen that the first pulse in Figure 164a) has a rise time comparable to that for the movement of the unloaded surface shown in Figure 109 indicating that propagation effects are indeed negligible at the base of the cylinder.

Figure 164b) is then roughly the differential of this. However, in the former trace many of the oscillations are due to radial vibrations which affect the two "coils" in the double coil in opposite senses. In other words only the first pulse travels up the bar and is differentiated.

The frequency modulus calibrations are shown in Figure 165. The simple coil has a usable response up to about 3.7MHz whilst the double coil does as expected extend further to around 4.4MHz. It must be remembered that the calibration is only approximate due to the ringing of the transducer and finite time window used to capture the trace.

V.3.3 Surface pulse calibration of the inverse magneto-strictive transducer

Due to signal to noise problems a slight variation on the calibration method outlined in chapter IV is introduced. Instead of calibrating against the optical response the IMS transducer is compared to a broadband piezoelectric detector. This is shown in the next chapter to have a fairly flat (within 20%) frequency response up to 1.5MHz.

The two transducers were excited in a symmetrical arrangement using a Hsu/Nielson source. Due to the large aperture effect expected for the IMS device this will be of

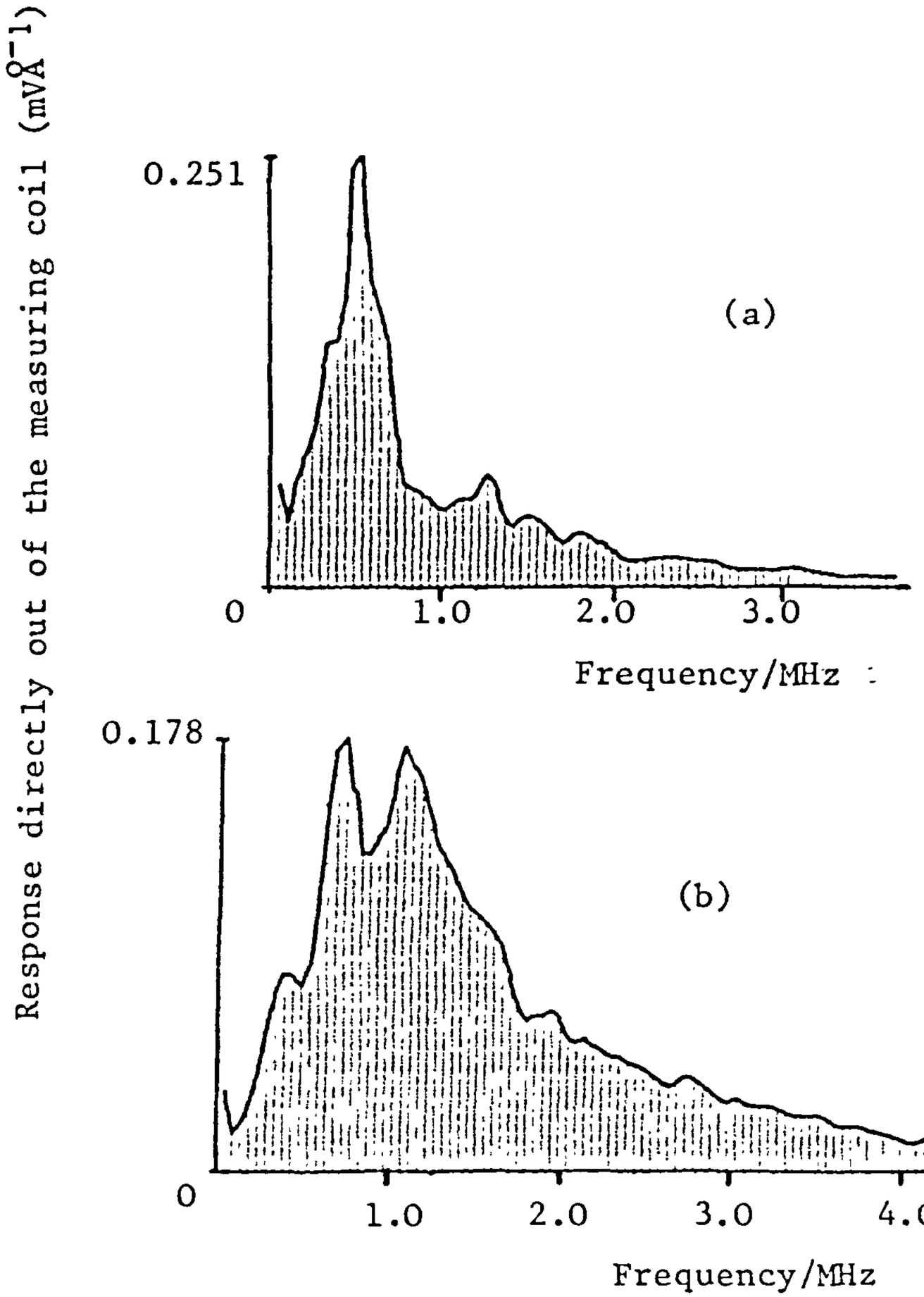

Figure 165: The frequency modulus calibrations for the two traces shown in figure 164. Figure 165(a) corresponds to figure 164(a) and similarly (b) to (b). The response is for the voltage out of the measuring coil before amplification.

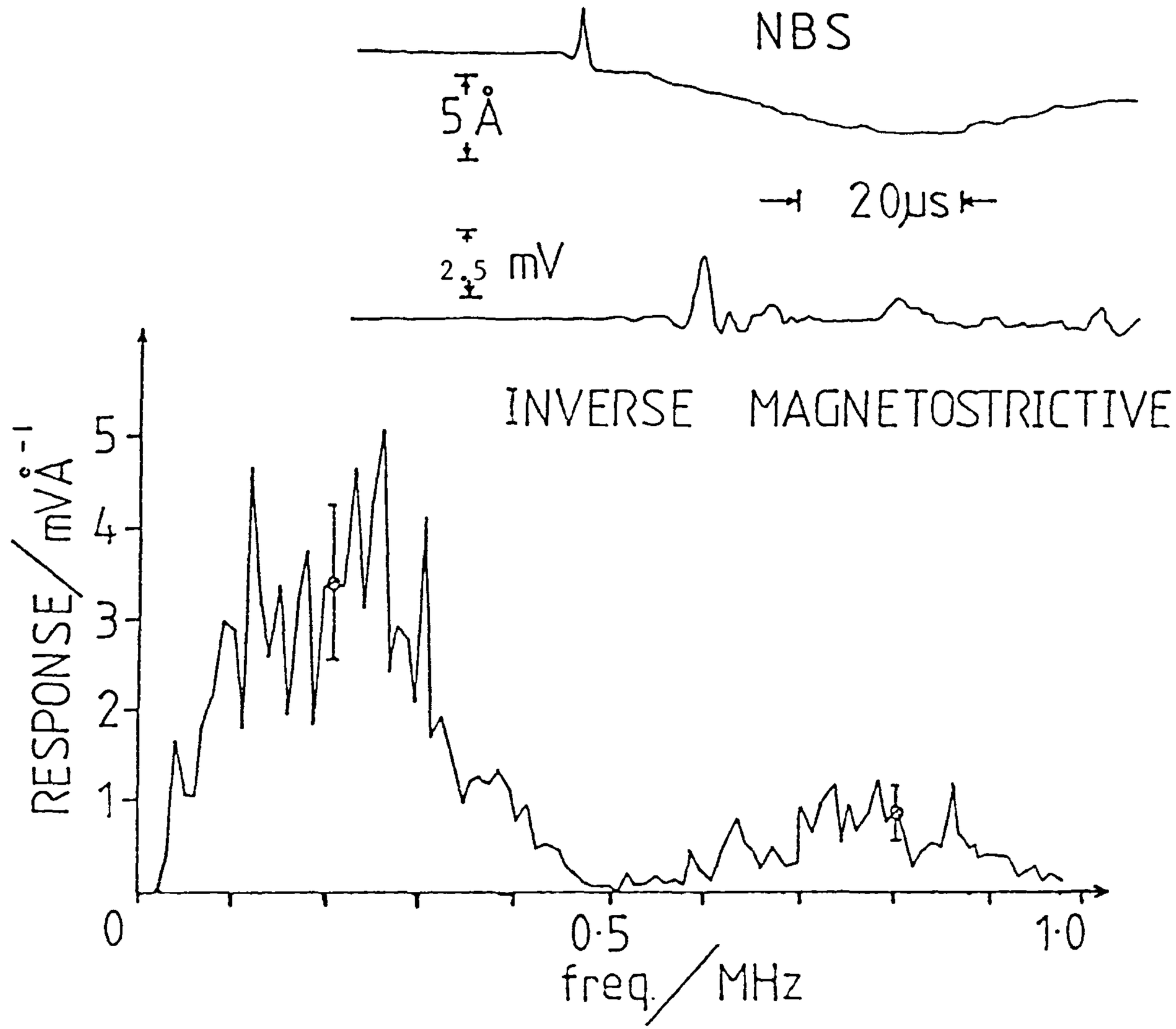

Figure 166: The surface pulse calibration of the IMS transducer.

sufficiently high frequency. For this calibration the measuring coil was a 300 turn simple coil placed 60mm up the bar.

The time domain responses for the two detectors together with the modulus calibration is shown in Figure 166. Clearly, the frequency response is modified compared to that in Figure 165a). This is thought to be due to the aperture effect. For a surface wave with a wavelength of 6mm (the bar diameter) the IMS detector should give roughly no response. This frequency is (2.906/6)MHz = 484kHz. There is a zero in the device response at 505kHz and so this zero is in fact thought to arise because of the aperture effect.

V.4 Conclusions about the inverse magnetostrictive transducer

The preliminary development work on the device showed that the transducer generated a complicated output dependent on the particular geometries of the detector. These observed effects have been explained theoretically, in some instances with the help of previous experimental results where no theoretical results were available. These observed effects are due to a combination of the change in the shape of an elastic pulse whilst it propagates in a cylinder together with various magnetic effects associated with eddy currents and detection geometries.

This development and understanding has then enabled a working transducer to be made. The frequency response is found to extend with a usable signal to noise ratio, up to $\sim$ 4.4MHz. The signal to noise ratio was only $\sim$ 5 times

down on that for a piezoelectric transducer mounted on a waveguide. It should be possible to improve this signal to noise ratio above that of the waveguide coupled piezoelectric detector by the use of a laminar construction as suggested in section V.1.3. Therefore the IMS transducer represents a useful device which should find applications in situations where either waveguides are used, for example on hot surfaces (provided the Curie point of $\sim 1000^{o}C$ is not exceeded), or where rotating machinery is being monitored. The latter being possible as the detecting coil may be made to slide easily over the IMS bar.

VI THE DEVELOPMENT AND CALIBRATION OF HI-FIDELITY PIEZOELECTRIC ULTRASOUND TRANSDUCERS

The transducers often used in acoustic emission studies, or other high resolution ultrasonic work, were originally developed essentially for pulse-echo ultrasonic investigations. This latter application only requires that reasonable sensitivity and time resolution be available and as such the transducers were not designed to monitor the movement of the test specimen surface faithfully. The design of these conventional piezoelectric ultrasound transducers therefore creates two major problems.

The first of these problems is that the devices have large apertures compared to the wavelengths of the ultrasound in the frequency ranges of interest. As discussed in chapter II these frequencies may be up to $\sim$ 5MHz and as such create wavelengths as short as 0.6mm whereas apertures are typically 10 to 20mm in diameter and are therefore far too large. The second design problem is associated with the resonant frequencies of the device. The active piezoelectric element is usually made from a piezoelectric ceramic (for example PZT-5H[132] as manufactured by Vernitron Ltd) and is formed into a disc of diameter $\sim$15mm and thickness $\sim$ 3mm. The thickness mode resonance frequency will then be $\sim$ 500kHz and due to the mismatch of acoustic impedances between the piezoelectric ceramic and the surrounding material this is easily excited. Resonances associated with other parts of the transducer are often also simultaneously excited. The device output is therefore, in general, dominated by ringing.

These two problems on their own are not critical and provided the conditions outlined in section II.6.1. are satisfied then in principle the true surface movement could be deconvoluted from the transducer output despite these resonances. Unfortunately various practical difficulties arise which make this impossible. The first is the finite noise level of any monitoring electronics which results in the low signal levels at the device antiresonances becoming immeasurable. The resonance Q's will be finite which therefore indicates the output at antiresonance is not zero. The second practical consideration is that of finite dynamic ranges in recording devices. Typical transient recorders have 8-bit precision, or occasionally 10-bit, giving ranges of 1 to 256 or 1 to 1024. These dynamic ranges are usually too low to allow the large amplitude resonances to be captured without sacrificing the absolute sensitivity required to capture information at the antiresonances.

The problems associated with a large aperture, however, are more severe. Following the discussion in section II.6.1 then clearly apertures of the order of 15mm result in a device response which, for non-epicentral sources, is highly dependent on the source-transducer separation. In addition to this problems with noise and dynamic range also occur. These are associated, in this case, with the severely reduced system response when the ultrasound wavelengths are less than approximately twice the aperture diameter.

Clearly then the first problem to be solved is that of aperture size which should be reduced to ~ 0.3mm diameter. The question of device resonance should then be dealt with. Procter[9,95] has produced a piezoelectric detector in which the aperture size and resonances have been significantly reduced. This is shown in Figure 34. The active element is a truncated right circular cone. The truncated tip forming the small contact area with the specimen surface. The cone is backed by a large brass block into which the ultrasonic energy is finally transmitted and dissipated, thus reducing resonances. Resonances are further suppressed by the cone shape itself.

As discussed in section II.8, the results given by Procter[9,95] are not complete. Calibrations have only been performed up to 1.4MHz with epicentral calibrations employing theoretical results for the surface movements rather than the true displacements generated by the actual source used (glass capilliary). Various questions associated with the principles of the device behaviour and with the effect of changing device parameters have not been fully answered.

The results given in this chapter will attempt to answer some of these questions.

VI.1 The response of hi-fidelity transducers to ultrasonic waves arriving at the epicentre of an artificial source

The effects on the system response of varying certain parameters in the transducer described earlier (Figure 34) are best investigated when the input to the system is simple.

A very simple ultrasonic pulse occurs at the epicentre of sources. Here the ultrasonic waves may be approximated as plane. Also at the exact epicentre, if the source is symmetrical, the horizontal surface movement is zero, thus further simplifying the surface motion. Therefore the first calibrations carried out on the hi-fidelity transducers will be at this epicentral position.

VI.1.1 The experimental arrangement used to perform the epicentral calibration of hi-fidelity transducers

The artificial source used in this calibration is the ultrasonic transmitting transducer (section IV.1.1ii)f)) with the calibration being performed using the method outlined in section IV.3.2. The minimum detectable displacement for the stabilized optical interferometer used was 0.3Å for a single shot, this limit being due to shot noise. However, it will be recalled that the ultrasonic pulse from the transmitter is averaged over 256 events. The shot noise limited minimum detectable displacement is therefore $0.3/\sqrt{256} = 0.02$Å.

A series of calibrations were carried out on transducers based on the design given by Procter[9,95]. Various changes were made to some of the design parameters. These are outlined in Figure 167 where the cross sections of the transducers tested are given. The transducers being approximately rotationally symmetric.

The two results of interest are, as mentioned above, the device resonances and the aperture effect. The relative severities of these two phenomena, as the design

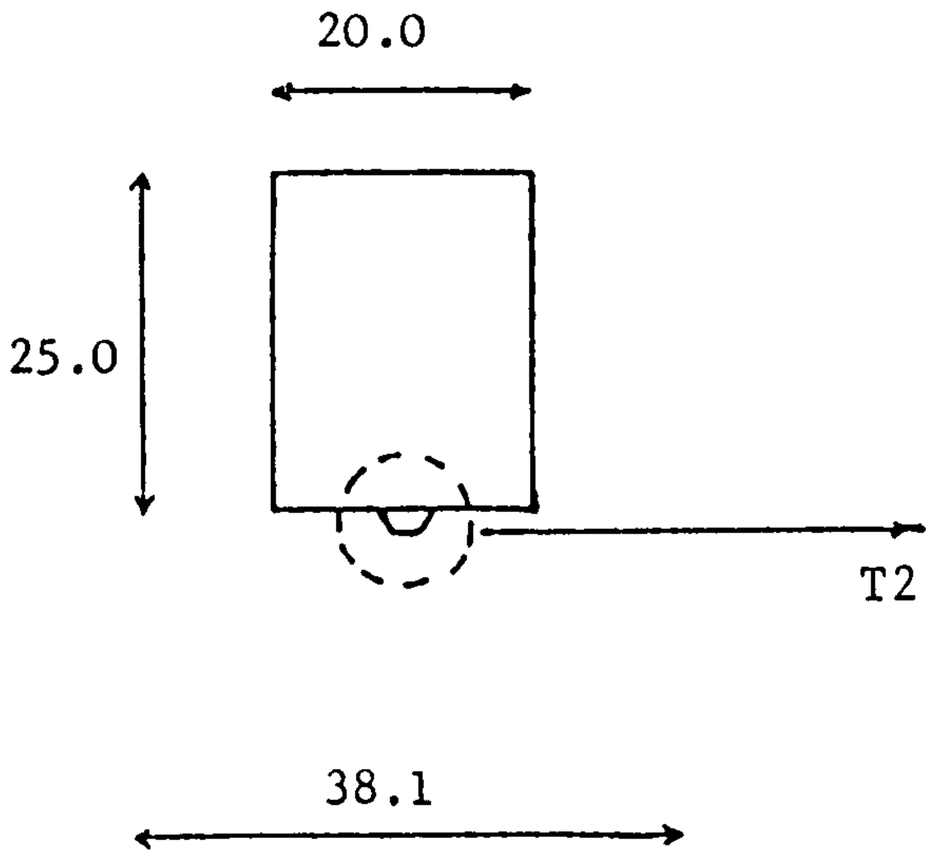

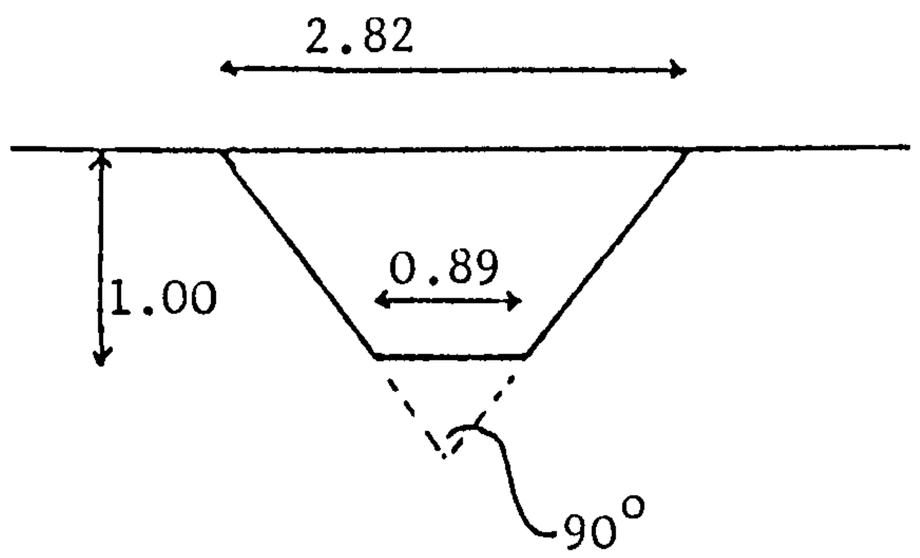

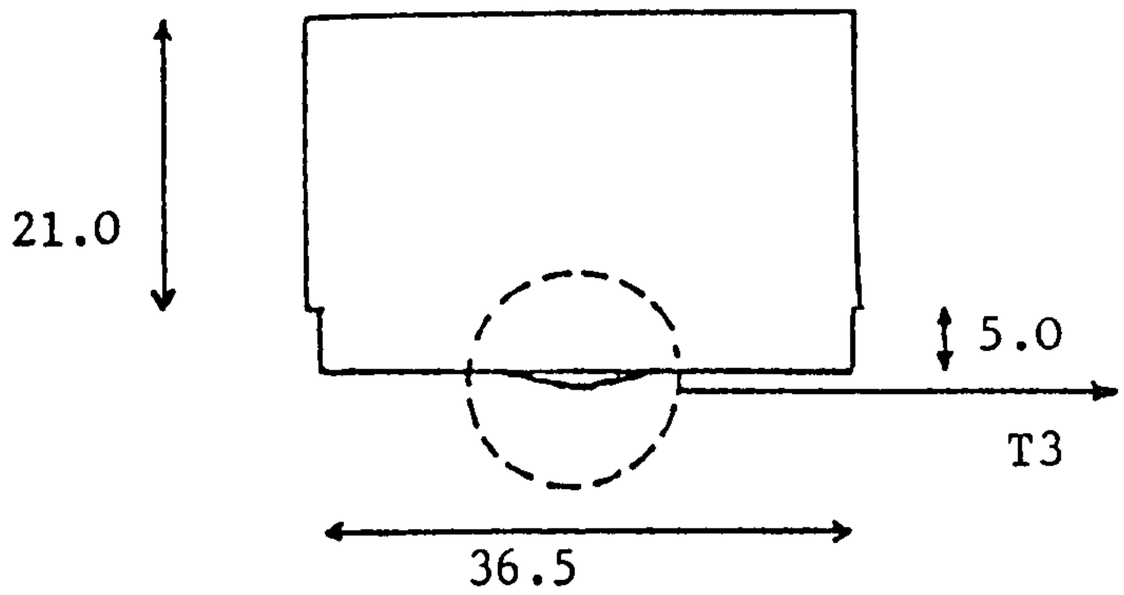

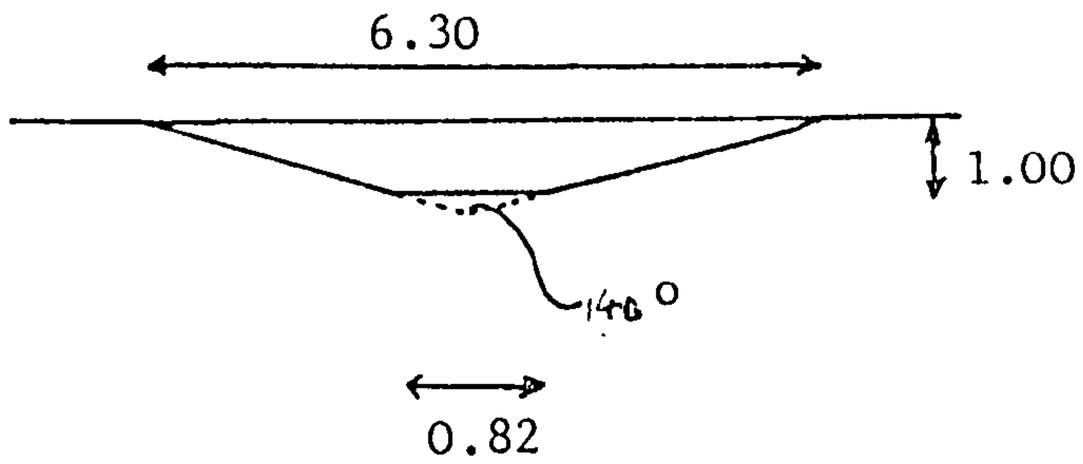

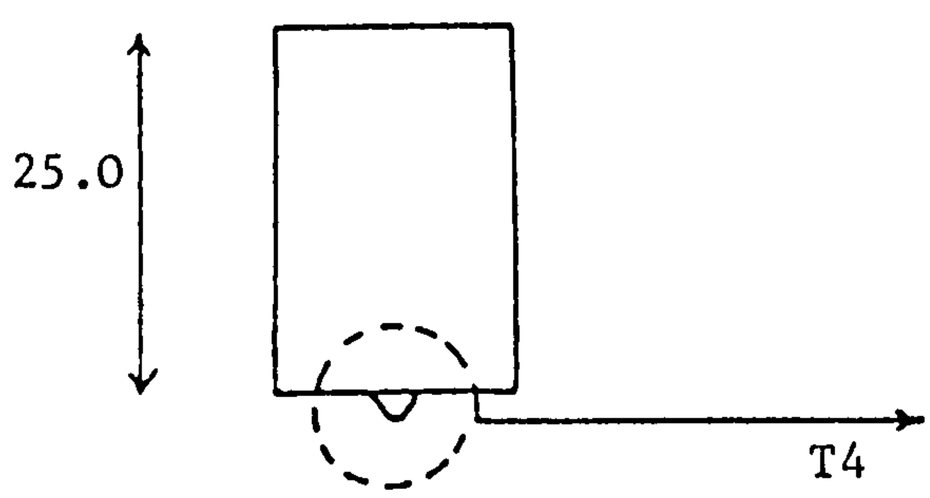

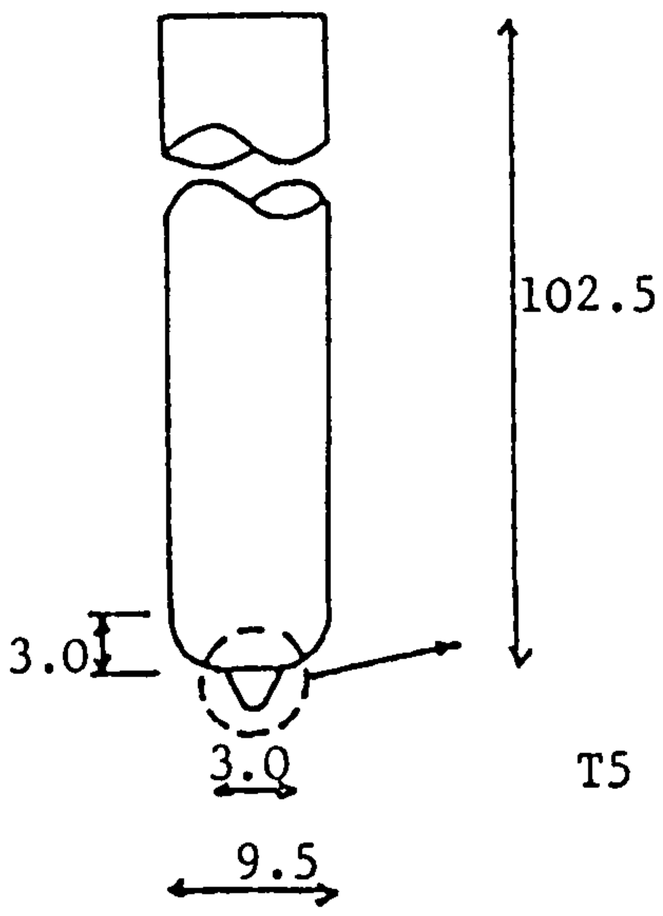

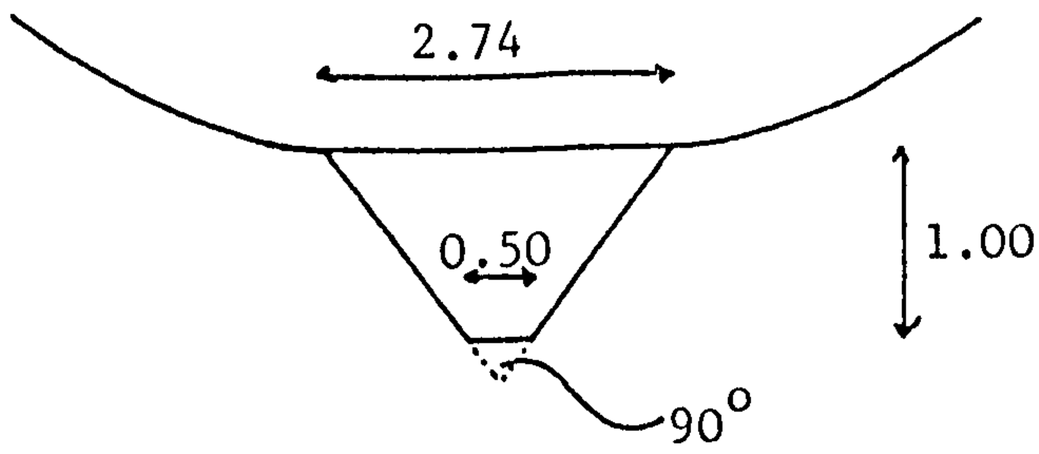

Figure 167: The cross-sections (not to scale) of the various in-fidelity transducers used in calibrations showing the change in design parameters. (All dimensions in mm.)

parameters are changed, may be seen in the magnitude of the frequency response curves. The effect of the finite aperture in this epicentral calibration may be determined by calculation. Now it will be recalled that the optical detector and hence piezoelectric transducers were not positioned at the direct epicentre but 5mm from this point. Calibrations are performed using the vertical surface movement created by the arrival of the longitudinal wave. These waves arrive at this point 26ns after they arrive at the epicentre. The largest aperture of the hi-fidelity transducers is 1mm and so the furthest point of transducer contact is 6mm from the epicentre. The arrival time at this point is 37ns with respect to epicentral arrival, giving a time difference across the device face of 11ns. Such a rise time is equivalent to 30MHz and consequently cannot be resolved by either the optical detection electronics (bandwidth 10MHz) or by the elastic pulse which contains frequencies only up to 6.8MHz. Therefore the modulus of the frequency response should yield only information about the resonances of the transducer.

The transducers are either just placed on the surface of the aluminium block (direct contact) or coupled with silicone grease. As such the finite frictional forces between the block and transducer will introduce a degree of mode coupling. However this is assumed to be very small due to the low frictional coefficient and also because the surface movement so close to the epicentre will be mainly vertical in nature. Resonances, therefore, will be those

excited by longitudinal waves, arriving at the top of the cone, rather than shear waves.

VI.1.2 The results of the epicentral calibrations on the hi-fidelity transducers

The exciting vertical surface displacement in these calibrations is shown in Figure 109a). The time domain outputs from the devices when directly coupled to the aluminium block are than as shown in Figure 168. The transducers are labelled as follows: T1 is that developed by Procter[9,95] and shown in Figure 34; T2 is that shown in Figure 167a); T3 in Figure 167b); T4 in Figure 167c); and finally T5 is shown in Figure 167d). The outputs above were found to be reproducible, within the limits of the small experimental noise, with respect to the removal and replacement of transducers.

In addition to these directly coupled responses then the effect of using siliconegrease as a couplant was also investigated. This variation was performed using transducer T1 with the time-domain output being changed from that given in Figure 168a) to the one shown in Figure 169.

Now although these time domain outputs are reasonable representations of the true surface movement given in Figure 109a), they do clearly contain some ringing. This creates a problem in that to obtain a complete calibration the output should be monitored over a long time interval with the sampling being performed quickly enough to avoid supurious effects due to the various fast rise times within

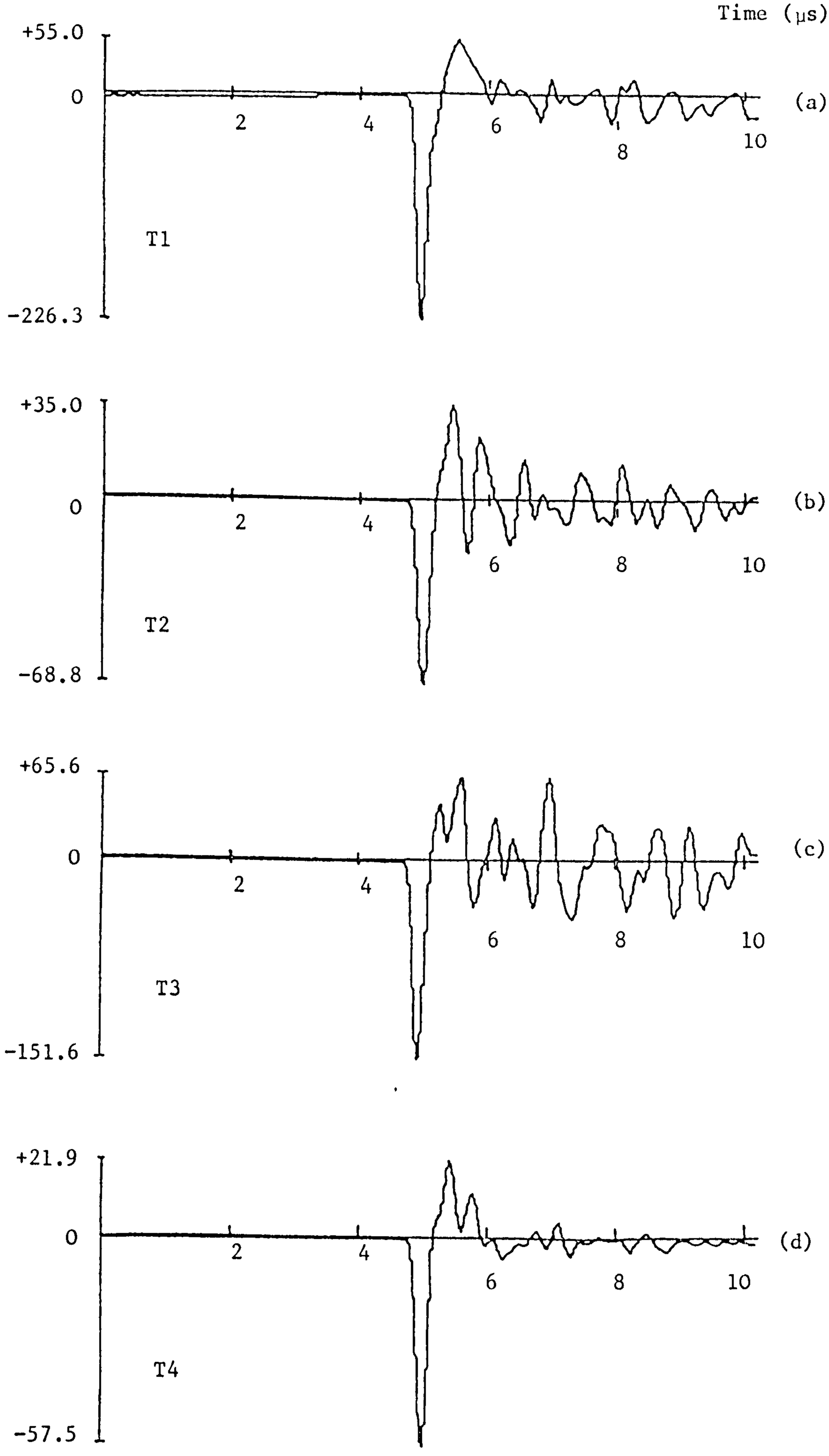

Figure 168: (part 1) (part 2 overleaf)

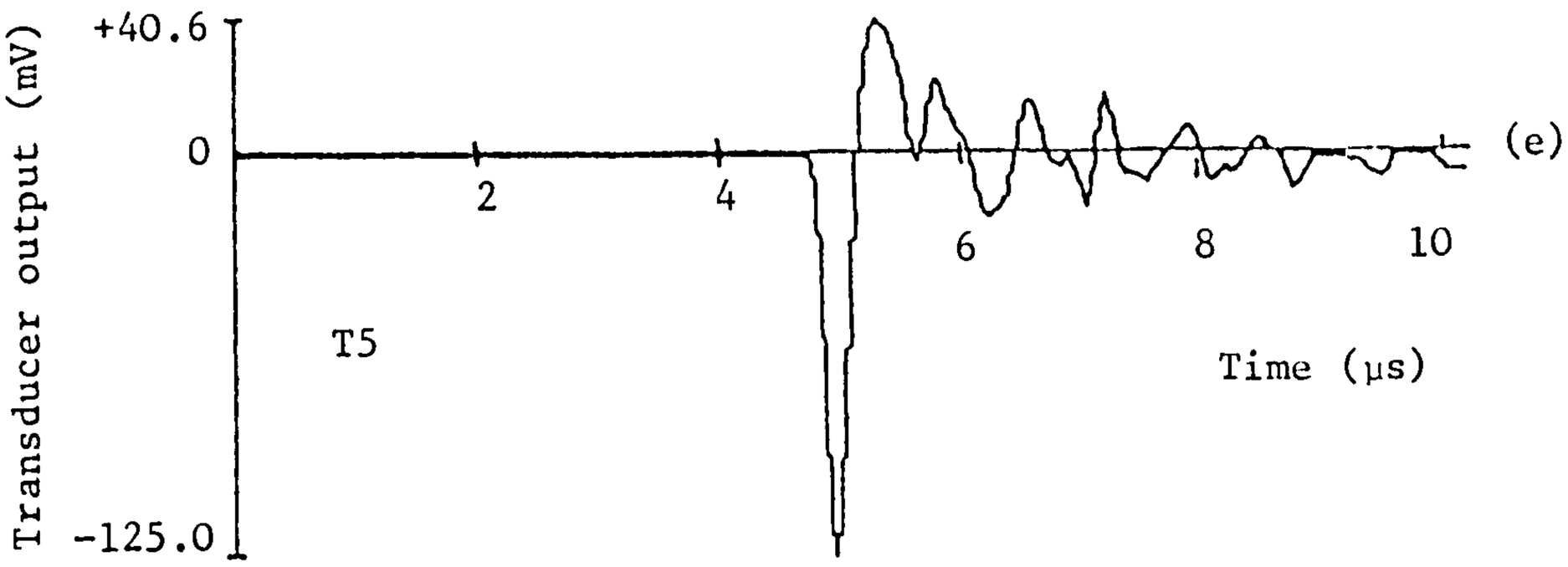

Figure 168: (part 2) The time domain traces for transducers T1 → T5 in response to the surface epicentral displacement from an ultrasonic transducer given in figure 109a.

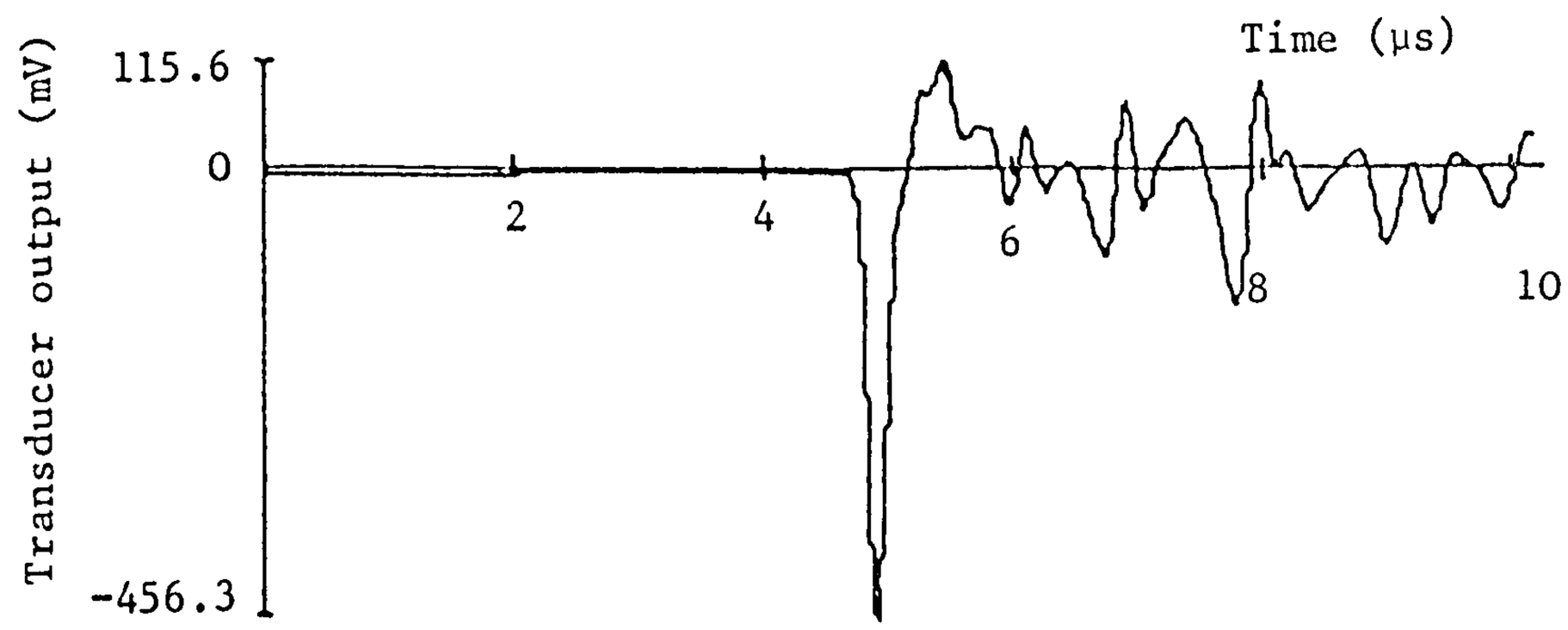

Figure 169: The change in time-domain output from figure (168a) above when silicone grease coupling is introduced rather than just direct contact.

the traces. The latter point indicates for the optically detected movement shown in Figure 109a) that the sampling rate should be at least 10ns/point. The 48k Apple IIe micro-computer used to carry out computations on the waveforms will only operate fully with a maximum of 1024 points per waveform. Therefore with a sampling rate of 10ns/point only 10.24μs of trace may be captured.

There are two consequences of having only 10.24μs of trace. The first of these is that frequencies with periods greater than 10.24μs are not detected. Now in reality the main portion of the waveform is captured in the centre of the trace to allow the use of a Hanning window if required. Therefore the minimum detectable time period is reduced to 5.12μs giving a frequency of 145kHz. Experimentation and simple calculation show this is not a major problem due to the dimensions of the devices. The second consequence of finite trace length is that the quality or Q-factors for the resonances will not be accurately determined. For comparisons between one transducer design and another this is not critical. However, if an absolute calibration is required then it is clearly important.

The magnitude of the effect may be determined by comparing the transform derived using a Hanning window

with that derived using a window with
a wider half-width. This second window merely terminates the trace oscillations at some convenient point within the last 0.3μs to make the DC shift between the trace start and trace end equal to zero. In fact the transient recorder

generates only 998 points and so the first and last 0.13μs of trace are constant leading to a loss of trace due to the termination of only 0.17μs at maximum.

This calculation has been carried out on the time-domain trace given in Figure 168a). The modulii of the two transforms are determined as above and then divided giving the result in Figure 170. The deviations from a given constant value in this division are greater than might be expected.if two nominally identical traces were transformed and then compared. Such a comparison may be made by capturing a waveform nominally identical to that shown in Figure 168a). Its transform, calculated by terminating the trace at some convenient point necessary to make the DC shift zero, is then compared to the similar transform for the actual trace in Figure 168a). Clearly some deviations occur as shown by the result of the division given in Figure 171, but these are not as large as those shown in Figure 170.

The deviations, from given constant value in Figure 170 are however not severe in themselves. This leads to two conclusions. Firstly, the use of a Hanning window in the transform has only a reasonably small effect on the transform of the trace as seen. Secondly, capturing only 9.98μs (998 points at 10ns/point) of the piezoelectric transducer output leads to a calibration result for the transducer which is a good approximation to the correct result. The correct result requiring that the output be monitored for all times when it is non-zero. These

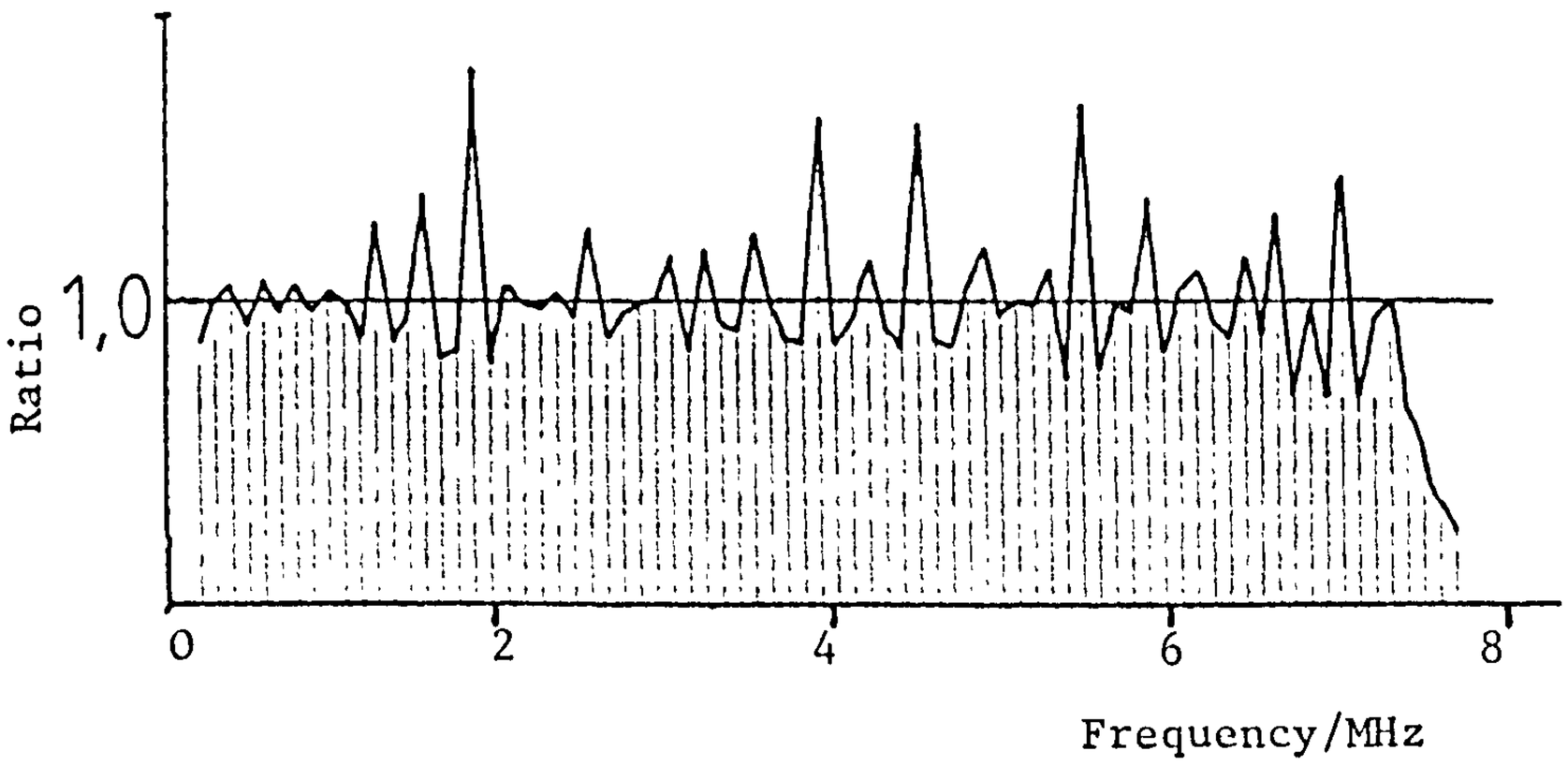

Figure 170: The result of calculating the fourier transforms of the trace in figure (168a) by either using a Hanning window or terminating the waveform as described in the text and then dividing the modulii of the transforms. The ratio is plotted here against frequency.

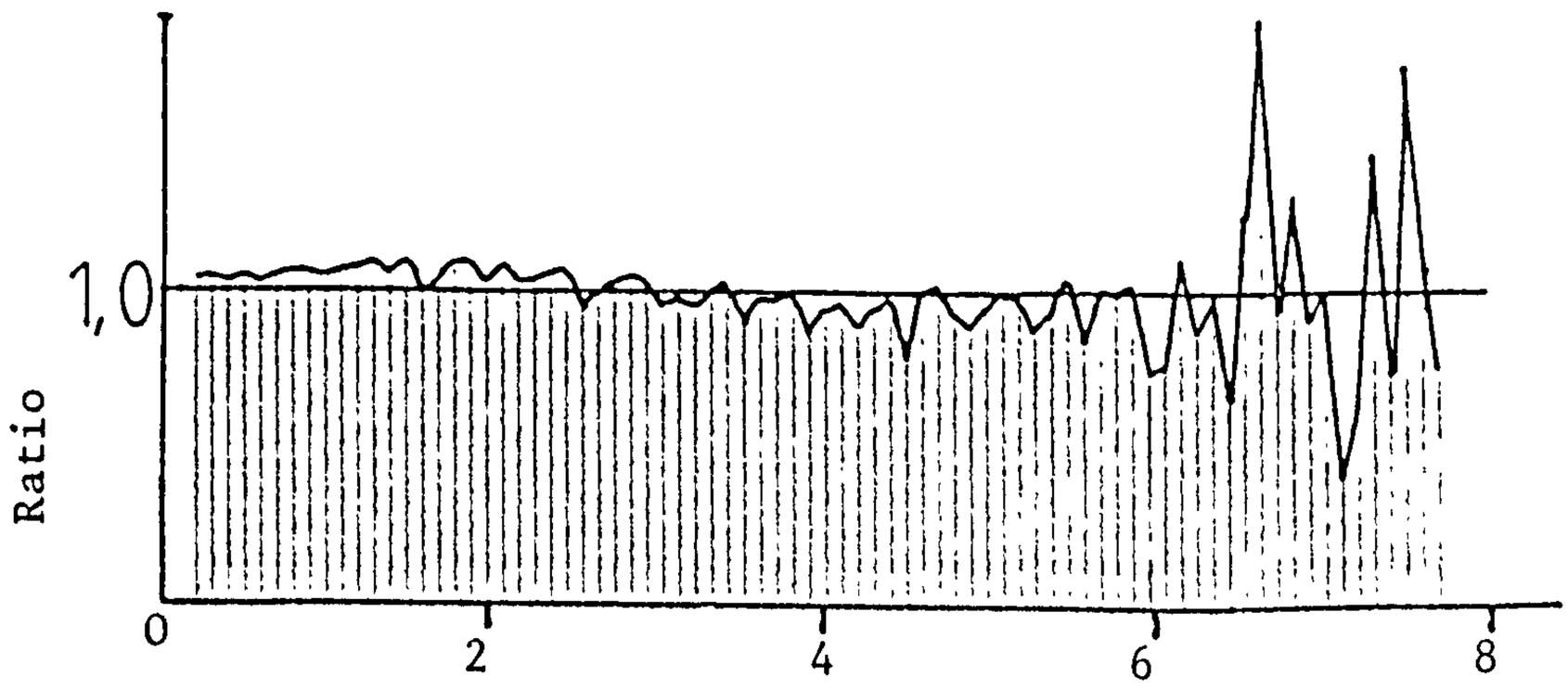

Figure 171: This ratio is the ratio of the modulii of two FFT's of nominally identical waveforms. The denominator of the division is the FFT from the trace given in figure (168a). The transforms are determined by terminating the waveforms as described in the text.

conclusions were further validated by observing traces captured over 19.96μs (998 points at 20ns/point). The longer traces show hardly any ringing beyond that which is captured above by the 9.98μs duration trace.

The relative frequency responses of the various piezoelectric transducers to that of the flat frequency response of the optical detector are shown in Figure 172. The Hanning window has been used, for ease of calculation, in all of these comparisons. It can be seen that transducer T1, the one developed by Procter, does in fact have the flattest frequency response. A further comparison is therefore performed on this trace. This involves terminating the waveform as described above so that a Hanning window is not required. Results are then given in terms of the modulus and phase of the transducer response in Figure 173. Clearly, the ringing is more pronounced than in Figure 172a) as expected. However as the traces in Figure 172 are compared against each other to determine the optimum transducer design then this effect is unimportant.

Certain points about the phase calibration are of interest. As discussed earlier, and in Appendix 10, due to the nature of the phase calibration (being a subtraction) quite large errors may be expected. These errors have been calculated by performing a reproducibility experiment, and are indicated in Figure 173. In addition to these random errors there is a shift in start position between the optically and piezoelectrically detected waveforms.

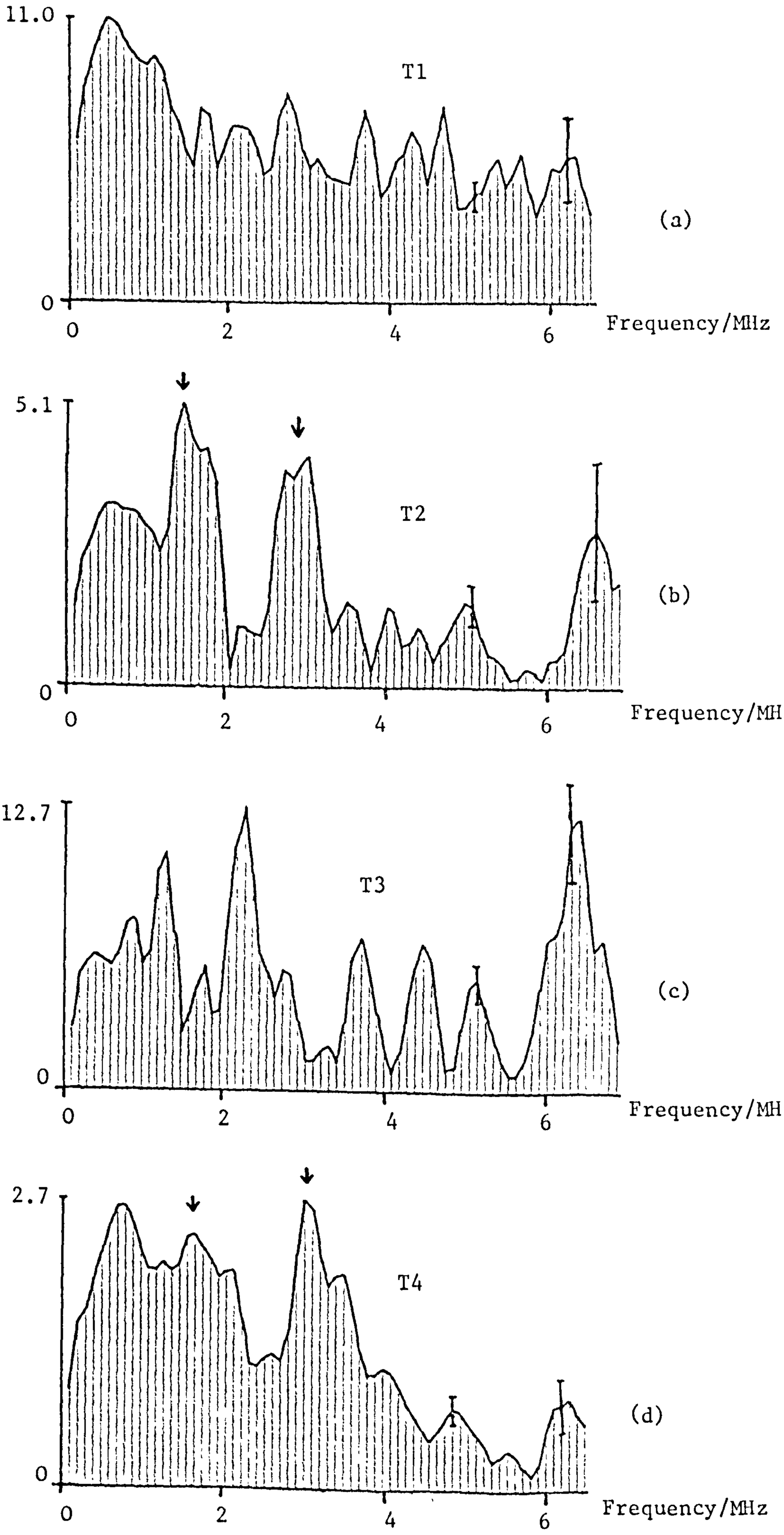

Figure 172: (part 1) See over for part 2.

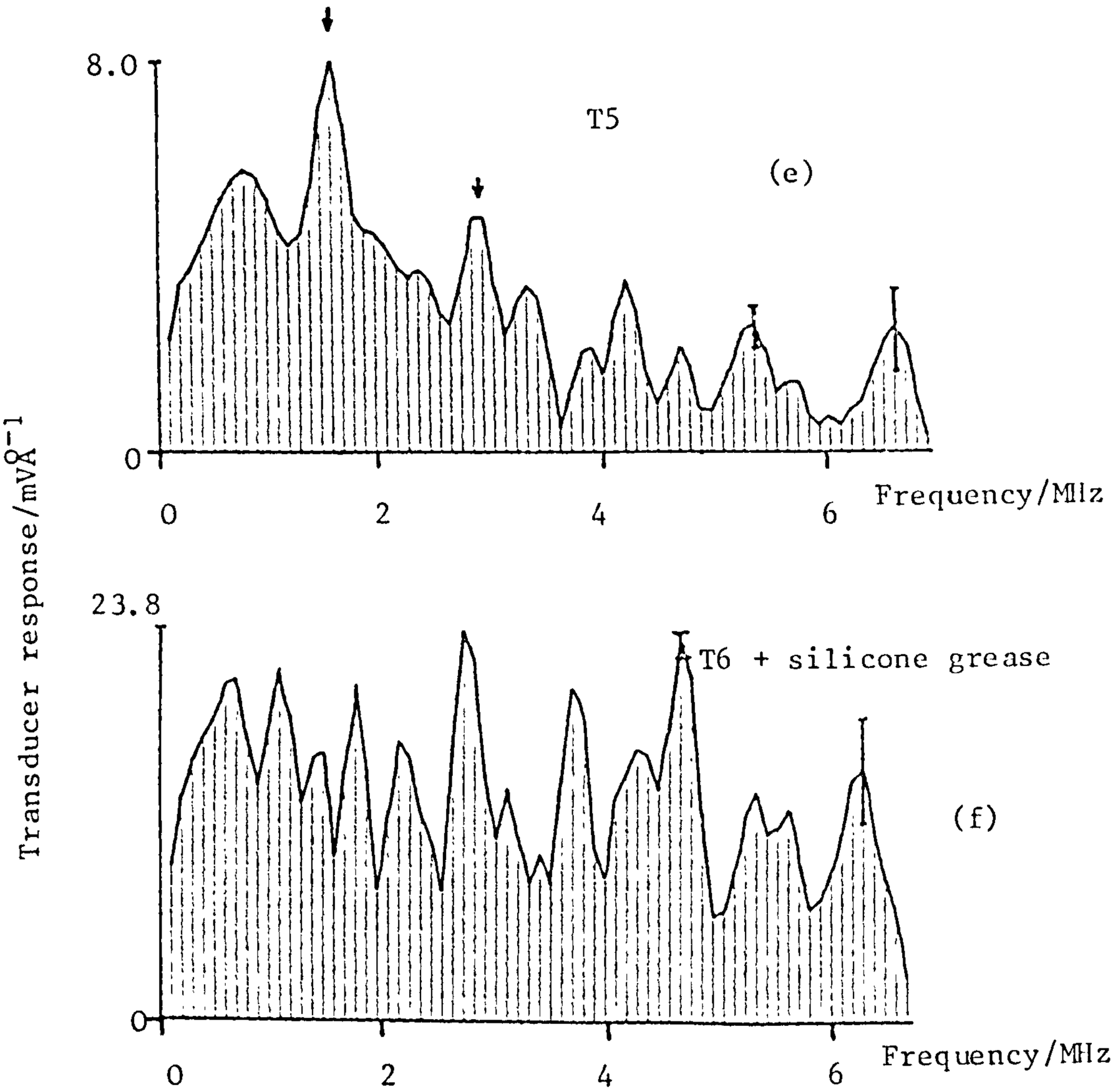

Figure 172: (Part 2). The frequency modulus calibrations of transducers T1 to T5 (a to e) whose time domain outputs are given in Figure 168. Trace (f) above is the frequency modulus calibration for the time domain trace given in Figure 169 which is obtained from transducer T1 when this is coupled with silicone grease to the aluminium block. The Hanning window is used on all the FFT's.
Transducers T2, T4 and T5 show resonances at similar frequencies (see arrows). These are thought to be the fundamental and first overtone of the longitudinal mode resonance as these then give a transducer length of (1.2±0.2)mm for a wave velocity in the PZT of 3.5mm μs^{-1}.

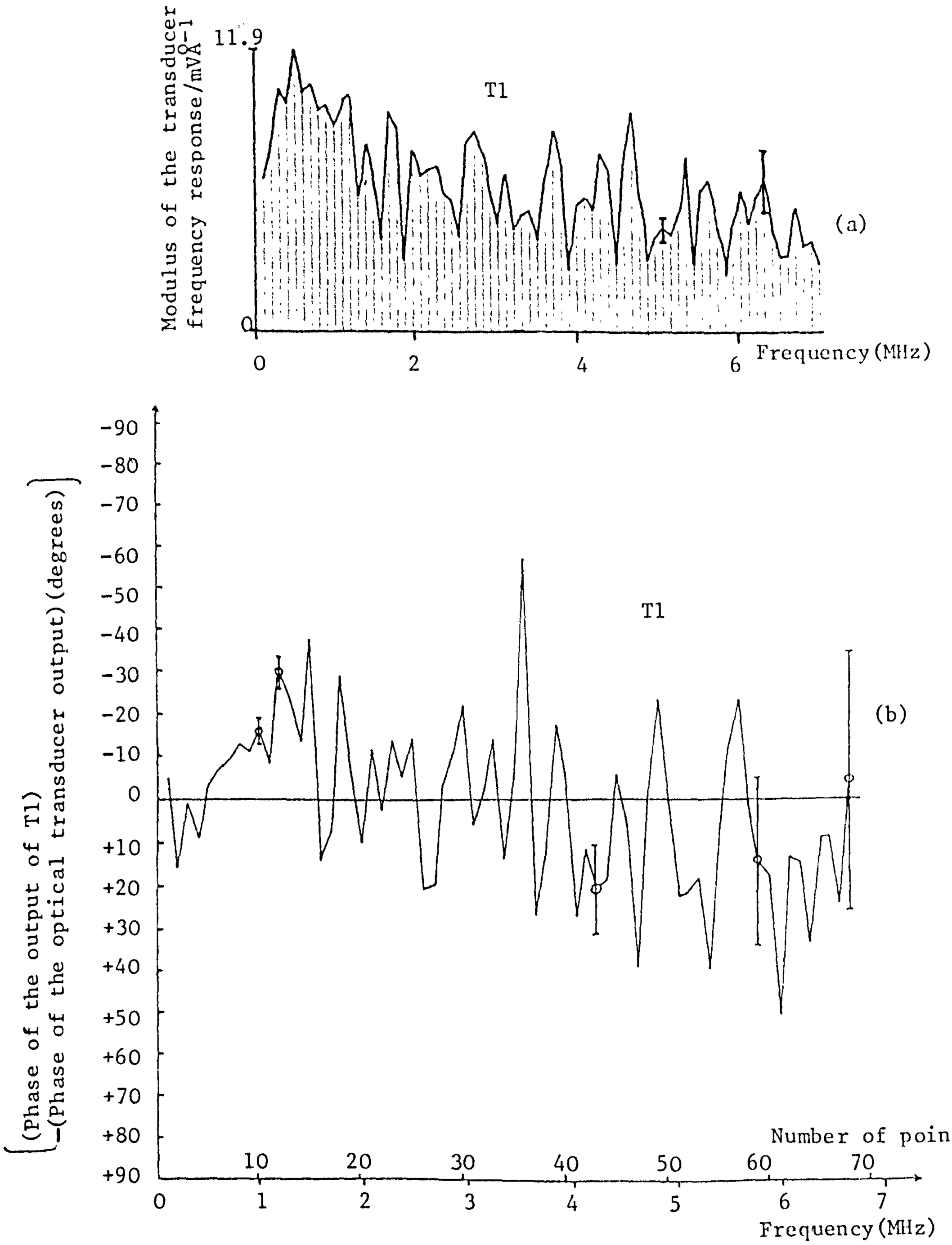

Figure 173: The epicentral calibration of transducer T1 when this is in direct contact with the aluminium block in terms of (a) the modulus and (b) the phase. The time domain trace is given in Figure 168a) and the waveform is terminated for the transform. Despite the low noise in the traces the phase calibration has large errors due to the small difference in the values of the phases for T1 and the interferometer.

This shift creates a steadily increasing phase error in the calibration. This error should and has been compensated for by measuring the initial time domain offset and then calculating the phase shift at each frequency. It should be realised that the phase calibration is only possible because of the low noise levels associated with the averaged traces.

The effect in the frequency domain of changing from direct contact to a silicone grease coupled arrangement for transducer T1 is also shown (Figure 172f)). This shows that the use of silicone grease as a couplant causes greater oscillation than when the transducer is merely directly coupled. There is however approximately an increase in the overall response by a factor of two

It is interesting to compare these calibrations with that of a conventional so-called "broadband" transducer. This is easily done by replacing the hi-fidelity transducer by the conventional type. The calibration in this case is unfortunately only approximate due to an increase in aperture size, a possible deterioration in the mode uncoupling approximation and a definite termination of the ringing.

The time domain output then of a Dunegan-Endevco transducer (D1901) is shown in Figure 174, together with the frequency domain response relative to the optical detector. This is clearly much more resonant than any of the traces given in Figure 172 and has a relatively poor high-frequency response. This indicates that

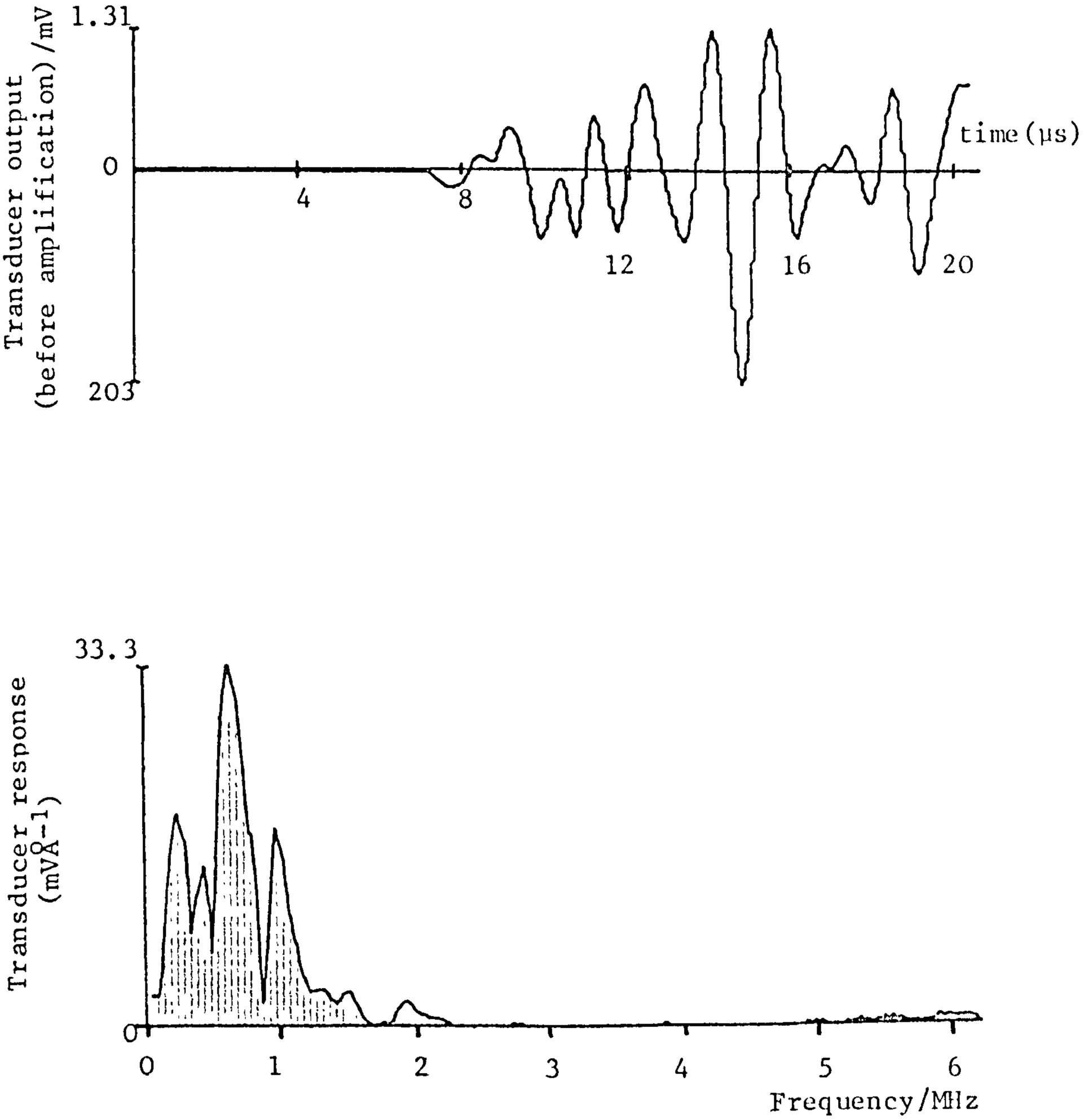

Figure 174: The time domain output and approximate frequency modulus calibration for a Dunegan/Endevco D1901 "broadband" transducer. The calibration is relative to the optically detected epicentral pulses given in Figure 109. A Hanning window is used in the calculation of the FFT which will affect the calibration. The response is relative to the voltage out of the transducer.

capturing high-frequencies would require a very large dynamic range of the recording device used.

VI.2 The response of hi-fidelity piezoelectric transducers to surface ultrasonic pulses

As previously discussed, transducers are rarely operated at the epicentre of sources except in carefully controlled situations. Therefore the transducer response to waves other than plane waves arriving normally to the detectors should be investigated. The extreme case for such a change is clearly when the ultrasonic waves being monitored arrive parallel to the transducer input face. In other words the response to surface ultrasonic waves should be determined.

VI.2.1 The experimental arrangement used to measure the response of hi-fidelity transducers to surface ultrasonic waves

This calibration follows the method outlined in section IV.3.1 where an arbitrary ultrasonic source is placed symmetrically between the transducer under test and the optical detector. As the optical detector has only a very small spatial extent ($\sim$ 50μm) then the vertical surface movement up to the electronically limited figure of 10MHz can be monitored. This movement is then compared to the output of the test transducer. It should be noted that the use of the optical detector makes such a large frequency bandwidth possible. Capacitor detectors used to monitor

surface waves have a limit of around 2MHz.

All that is required of the ultrasonic source in these calibrations is that it produce a pulse which is rotationally symmetric and one which contains high frequency components. Reviewing the sources outlined in chapter IV then, the most convenient is found to be the glass capilliary fracture discussed in section IV.1.1ii)e). Depending on the dimensions of the capilliaries the frequency spectrum of this source may be extended up to between 1.7 and 6.4MHz where at this frequency the signal to noise ratio has fallen to five (20% error). The average frequency at which this fall occurs was found to be 3.6MHz. If an average of these results is taken this upper limit is extended to around 5MHz assuming the signal to be inversely proportional to the frequency. The minimum detectable displacement, which leads to the noise discussed above, is 0.3Å being the shot noise limit.

Therefore by using glass capilliaries, with wall thicknesses of 0.038mm and outside diameters of 0.27mm, in conjunction with the stabilized optical detector, the hi-fidelity transducers' response to surface waves may be calibrated up to $\sim$ 5MHz.

It was shown in section II.6.1 that if a transducer has an aperture of $\sim$ 1mm, then in order to obtain a frequency response which is independent of the source/ detector separation the transducer must be at least 36mm away. This restraint is therefore applied to all the surface pulse calibrations.

The final point of interest is that of finite trace length. As the source used is an unbalanced monopole force then there is a DC shift between the initial zero level and the final surface position. Now the true Fourier transform of the trace is given by:

$$U(\omega) = \frac{1}{(2\pi)^{\frac{1}{2}}} \int_{-\infty}^{+\infty} U(t)e^{-i\omega t}\, dt \qquad (333)$$

In these calibrations U(t) has the following properties:

$$\begin{aligned} U(t) &= 0 && t \leqslant 0 \\ U(t) &= U_d(t) && 0 \leqslant t \leqslant T \\ U(t) &= H && t \geqslant T \end{aligned} \qquad (334)$$

where $U_d(t)$ is the detected surface movement over a time interval (0,T) and H is the final surface displacement. In reality the force is applied over a long time period which is equivalent, when a shift in DC level is made, to having U(t) for $t \geqslant T$ as $He^{-t/\tau}$ where $\tau \geqslant T$. Equation (333) may now be rewritten as

$$U(\omega) = \frac{1}{(2\pi)^{\frac{1}{2}}} \int_{o}^{T} U(t)e^{-i\omega t}\, dt + \frac{1}{(2\pi)^{\frac{1}{2}}} \int_{T}^{+\infty} He^{-t/\tau}e^{-i\omega t}\, dt \qquad (335)$$

If no Hanning window is used on the Fourier transform then the FFT calculates the first term in equation (335) at a series of discrete points due to the finite number of sample points and finite trace length T. The second term is therefore neglected. This second term may be rewritten

approximately as:

$$\frac{-i}{(2\pi)^{\frac{1}{2}}} \cdot \frac{H}{2\pi f} \qquad (336)$$

where f is one of the discrete frequencies. Clearly then information may be extracted from the entire trace if this correction is used.

An alternative method of calculation is to apply the Hanning window to the trace. It is found, as will be seen later, that the ringing of the transducers continues for only $\sim 5\mu s$. If the trace is captured over $19.96\mu s$ then the Hanning window will only reduce the average value of these oscillations by 18% which is an acceptable reduction. The use of a Hanning window offers easier calculation and is therefore the method which will be adopted.

VI.2.2 Experimental results of the surface pulse calibrations

The transducers which showed most promise in the epicentral calibration were T1 (both in direct contact and coupled with siliconegrease) T4 and T5. These transducers are therefore chosen for surface pulse calibrations.

The first point of interest is the effect of the silicone grease coupling. This is tested by calibrating T1 in both direct contact and when coupled with grease. The time domain outputs are shown respectively in Figures 175a) and 175b), together with the corresponding optical traces. Both the piezoelectric traces were found to be reproducible

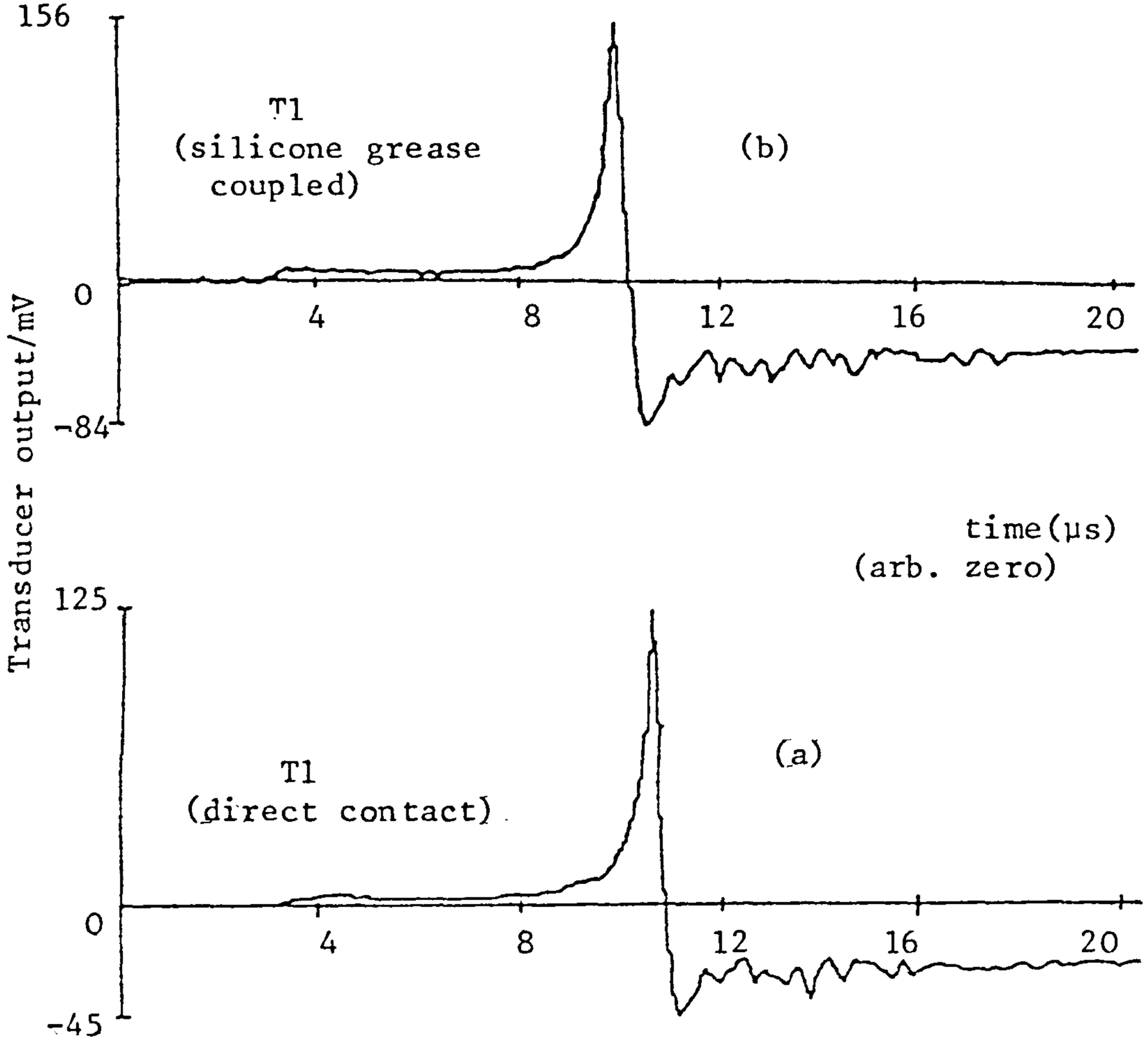

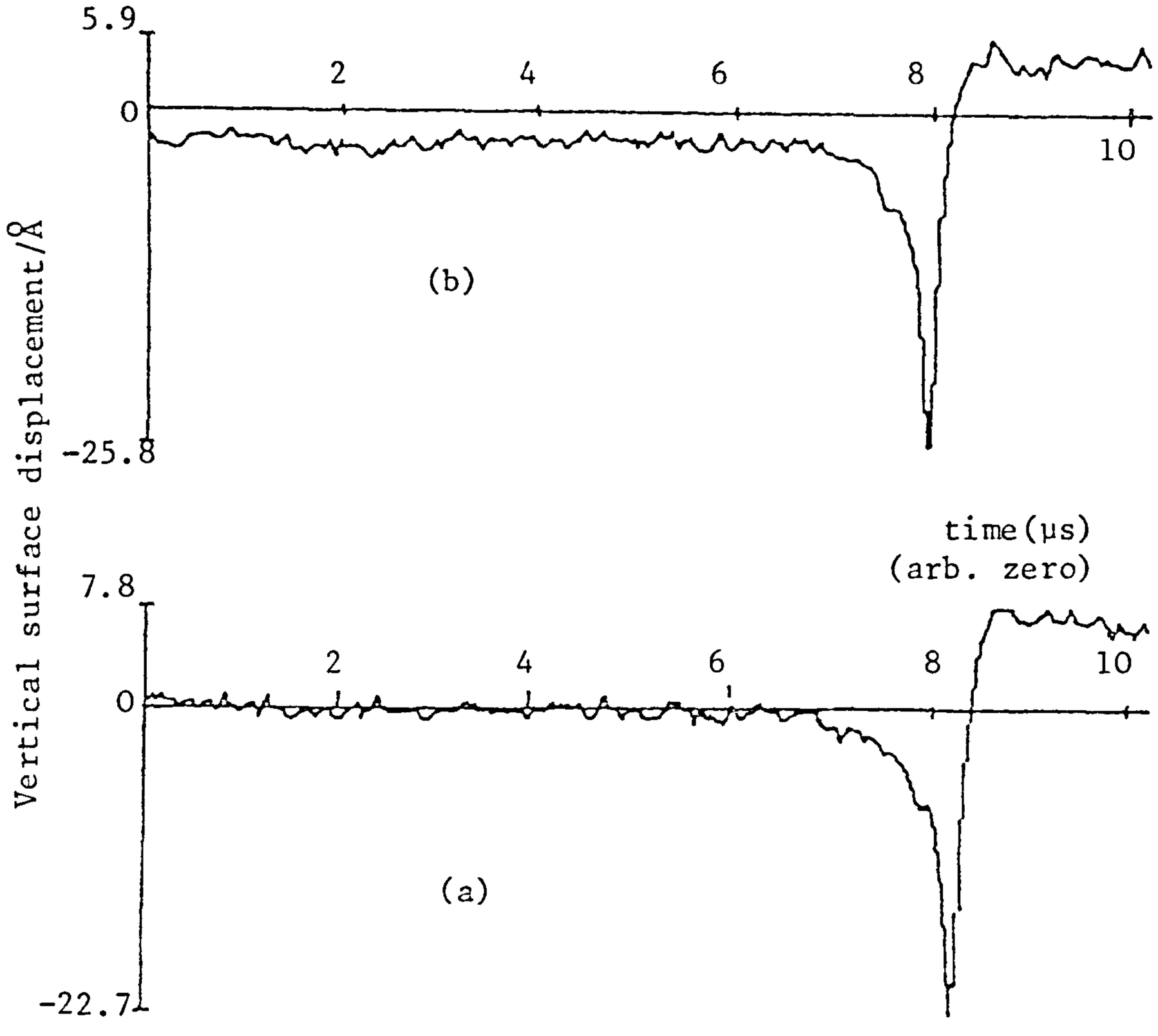

Figure 175: The vertical surface displacement (right) as measured with the optical detector and the output of transducer T1 (left) caused by the fracture of glass capilliaries of outside diameter 0.27mm and wall thickness 0.038mm. Traces (a) are for direct contact and (b) for silicone grease coupling.

as far as could be determined, both in terms of calibrations using different individual capilliary fractures and also in terms of removing and replacing the transducers. The modulus calibrations of these two arrangements are shown in Figure 176. Clearly the grease coupled trace falls off more rapidly than the directly controlled transducer. This will be discussed later.

The other two transducers, T4 and T5, were similarly calibrated with the time domain traces and frequency calibrations being shown in Figure 177. It can be seen that these two transducers contain more overshoot and a greater ringing in the time domain traces than does transducer T1. These two observations carry over into the frequency domain calibration, where clearly more resonance is evident. The probable reason for these effects will also be discussed later.

Before the various theoretical explanations for the above observed effects are discussed some consideration will be given to the Hsu/Nielson source as it applies to surface pulse calibration. It was shown earlier that although the source is quite reproducible and produces a symmetrical ultrasonic pulse its half power frequency point was only $\sim$ 600kHz for a lead diameter of 0.5mm. It does of course produce frequency components above this. The only question is whether these higher frequency components have sufficient amplitude above the noise to be of use. When the signal to noise ratio is looked at it can be seen that the use of a Hsu/Nielson source unfortunately only allows calibration up to $\sim$ 1.4MHz and as such cannot be used

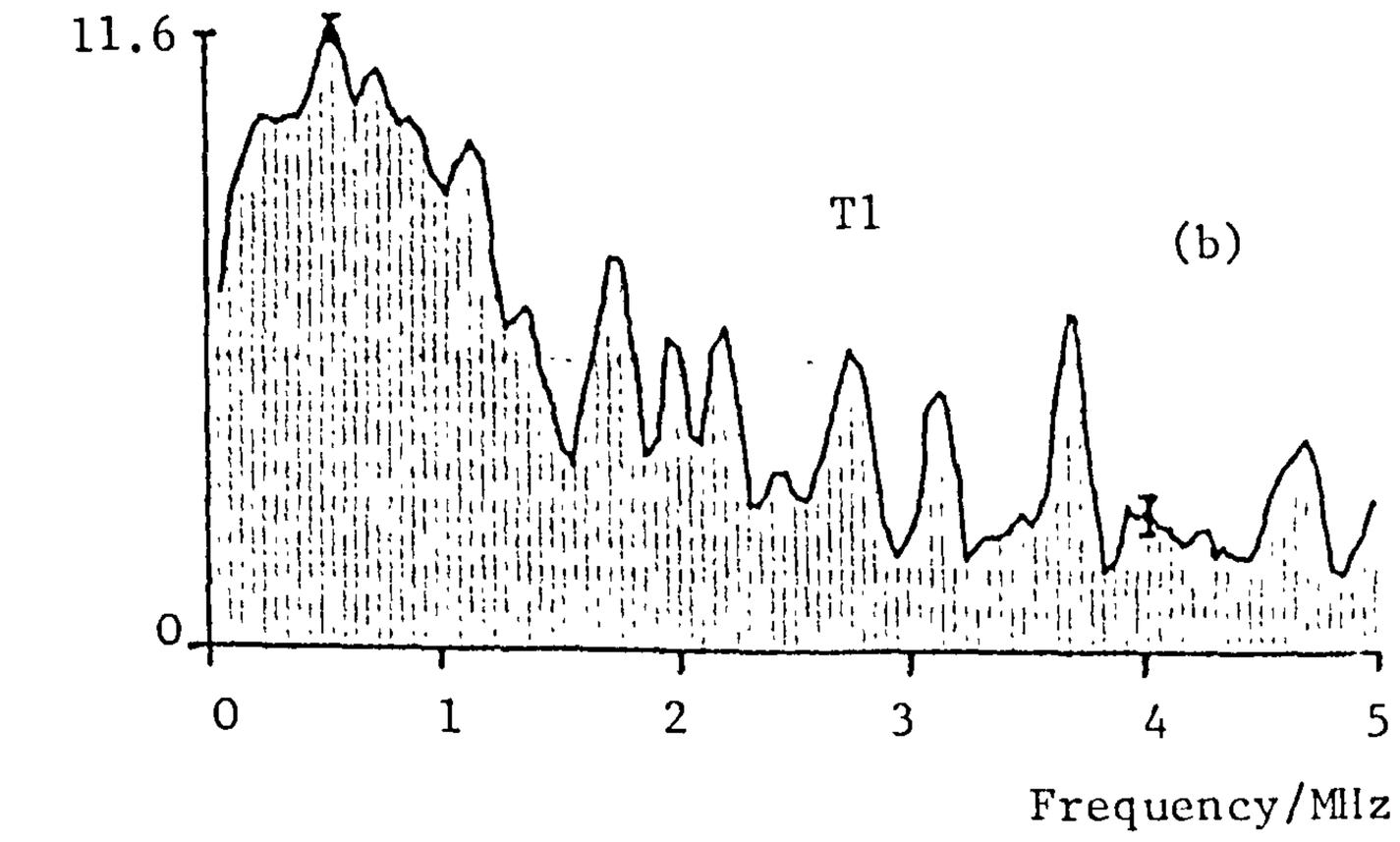

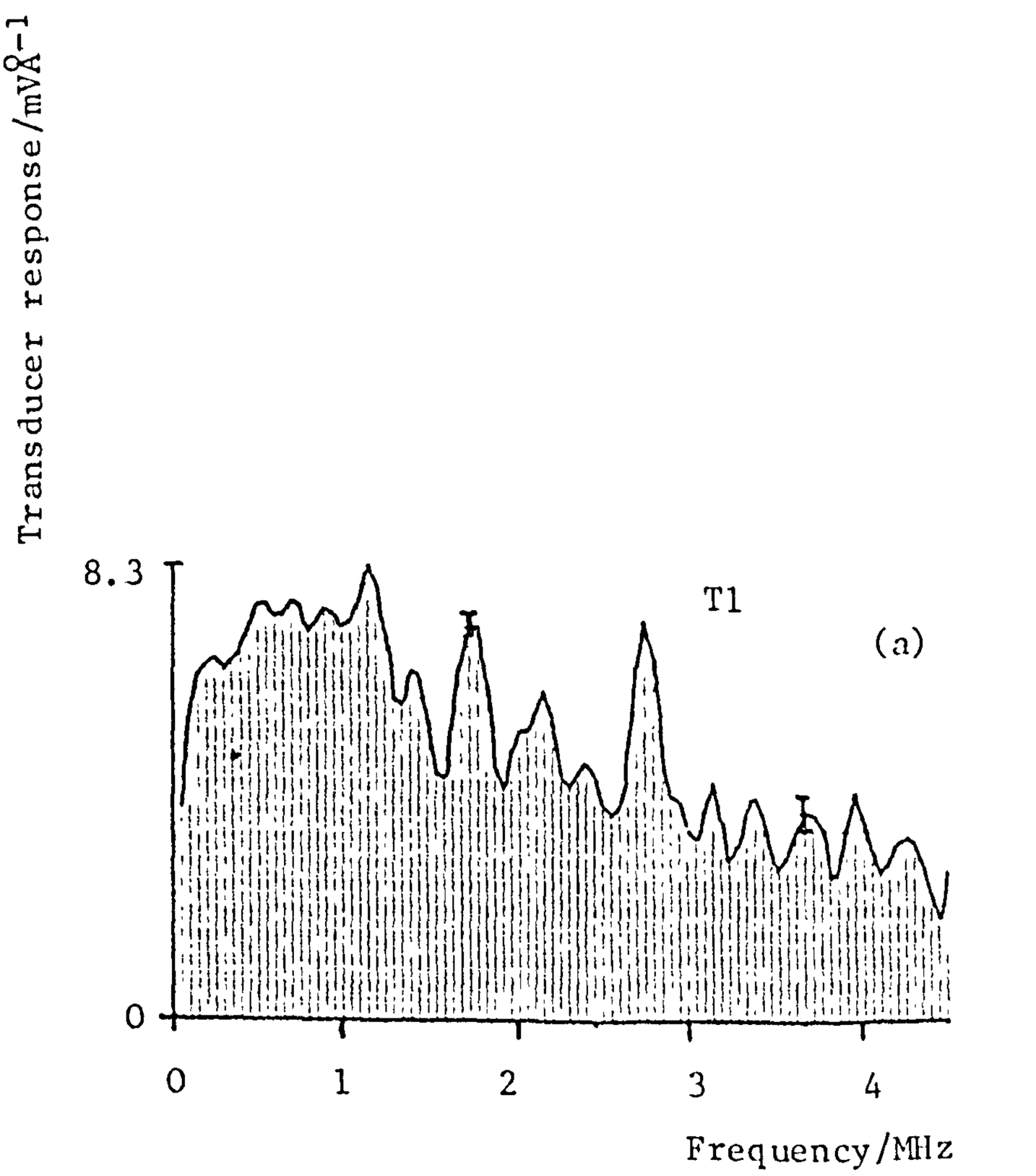

Figure 176: The frequency modulus calibrations for the two sets of traces given in Figure 175. (a) is for direct contact to the aluminium and (b) when silicone grease is used as a couplant.

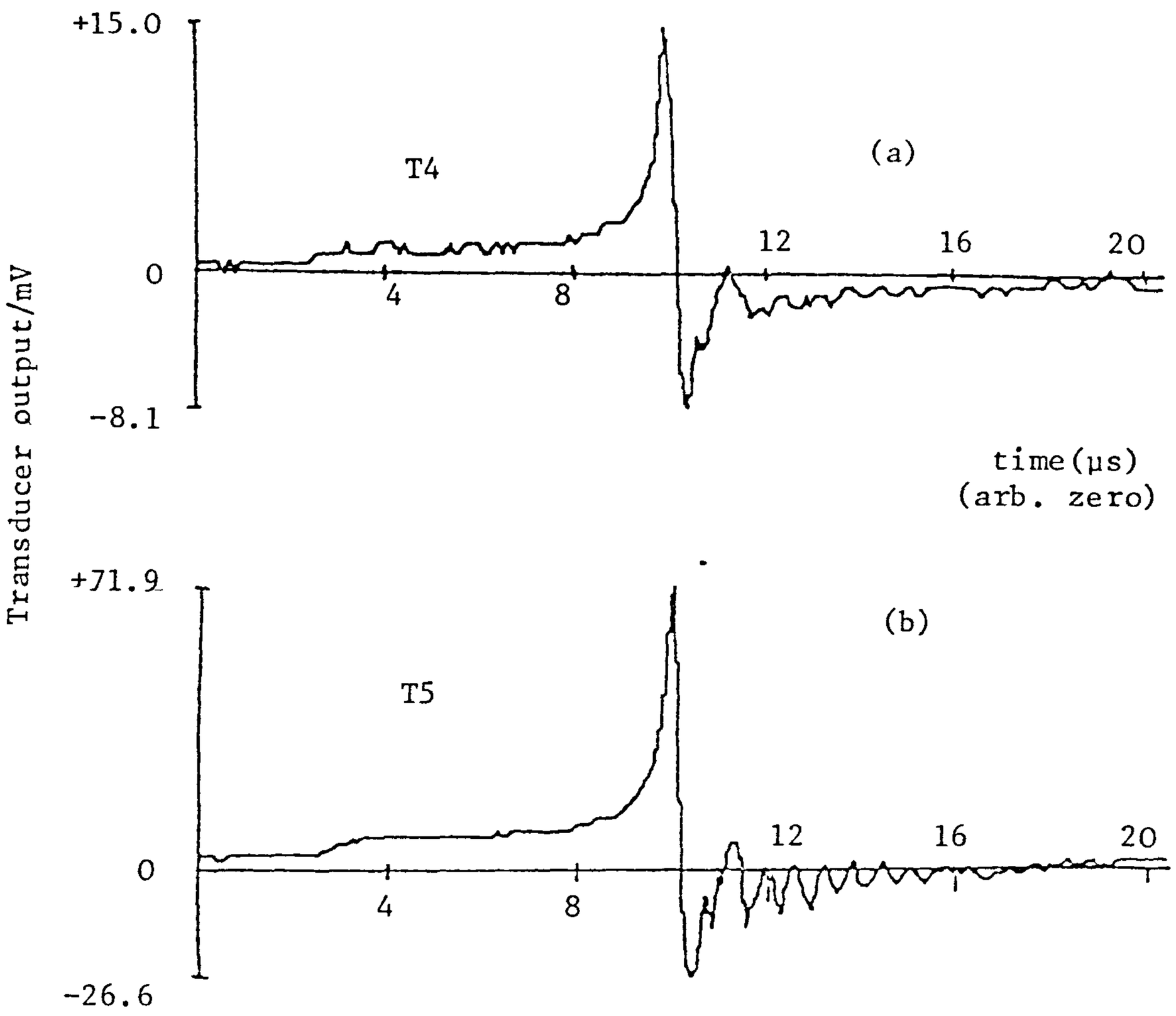

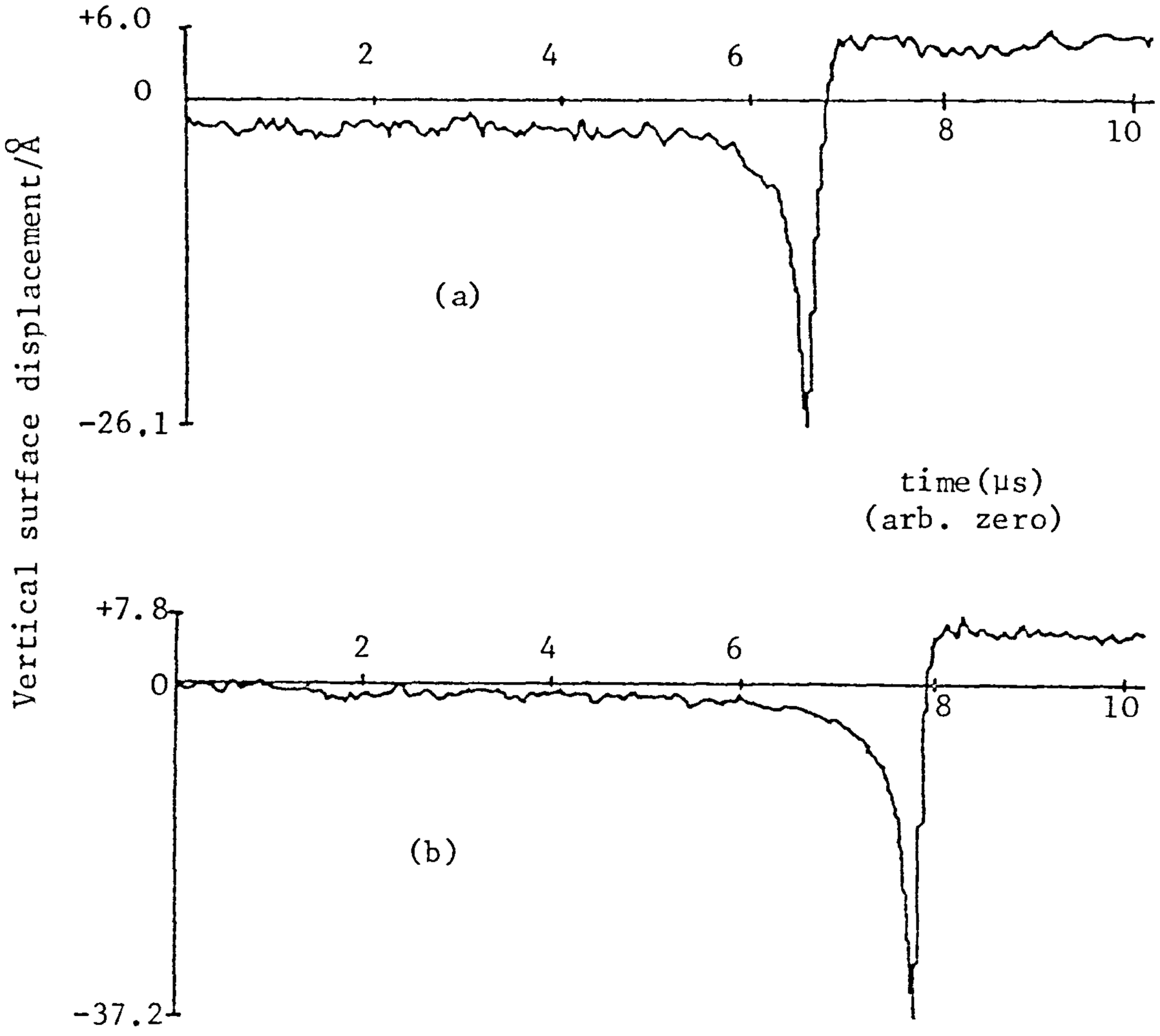

Figure 177: (Part 1). The vertical surface displacement (right) as measured with the optical detector and the output of two different transducers (left) caused by the fracture of glass capilliaries of outside diameter 0.27mm and wall thickness 0.038mm. Traces (a) are for transducer T4 and (b) for T5.

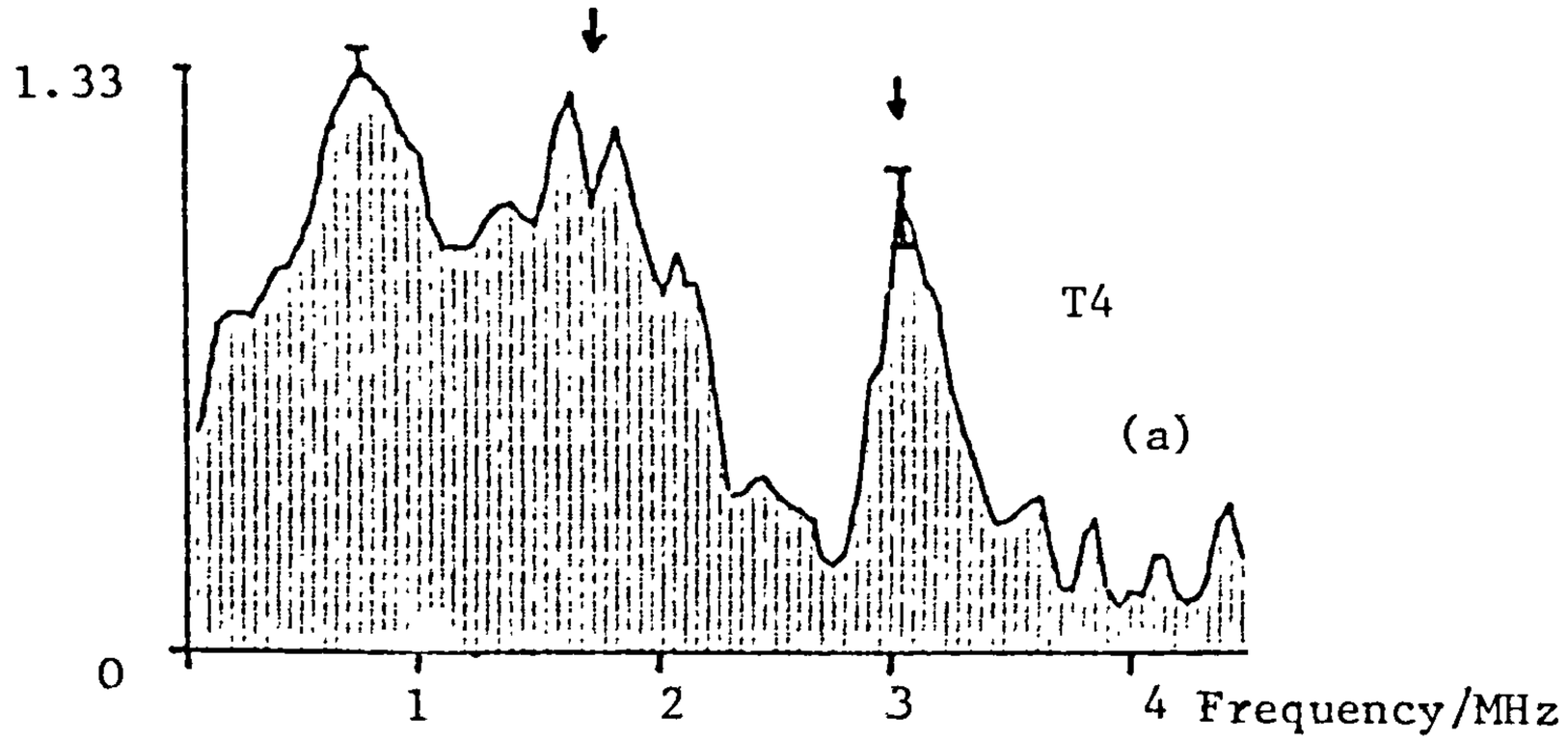

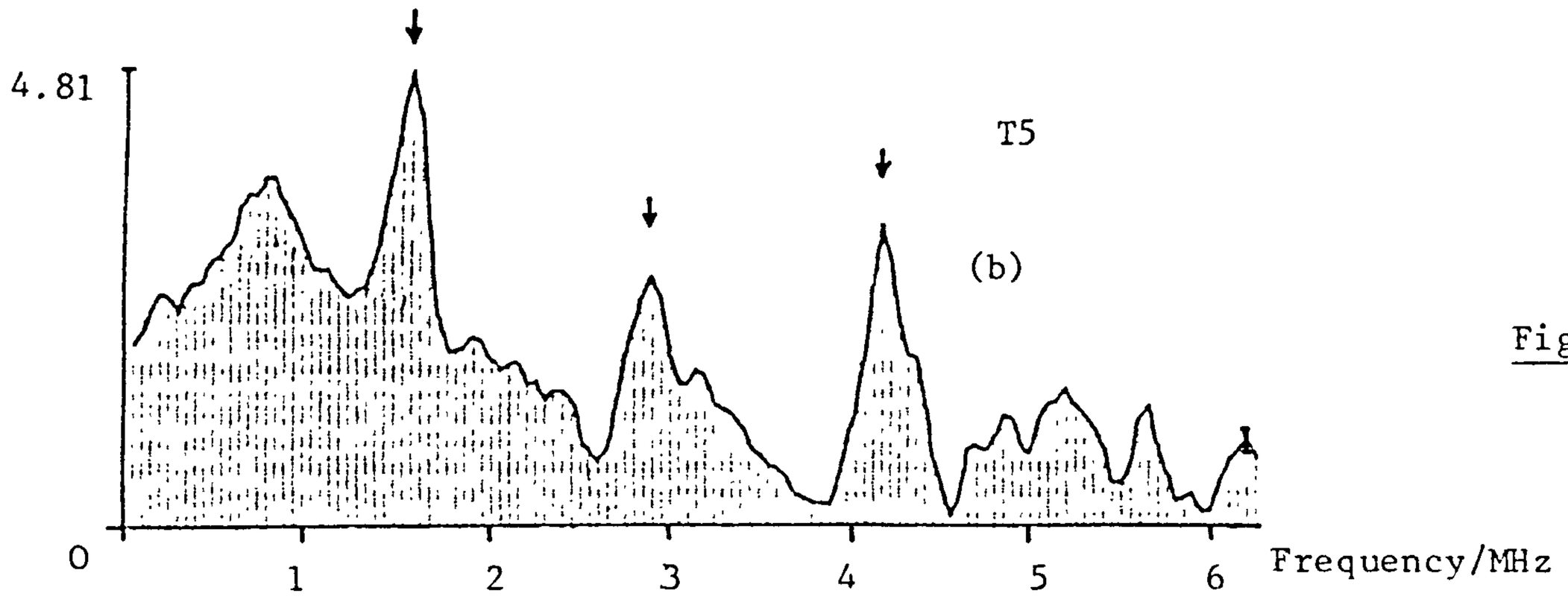

Figure 177: (Part 2). The frequency modulus calibrations for the two sets of traces given in Figure 177(part 1). (a) is for transducer T4 and (b) for transducer T5. The resonances given by the arrows suggest a resonating length of (1.2±0.2)mm.

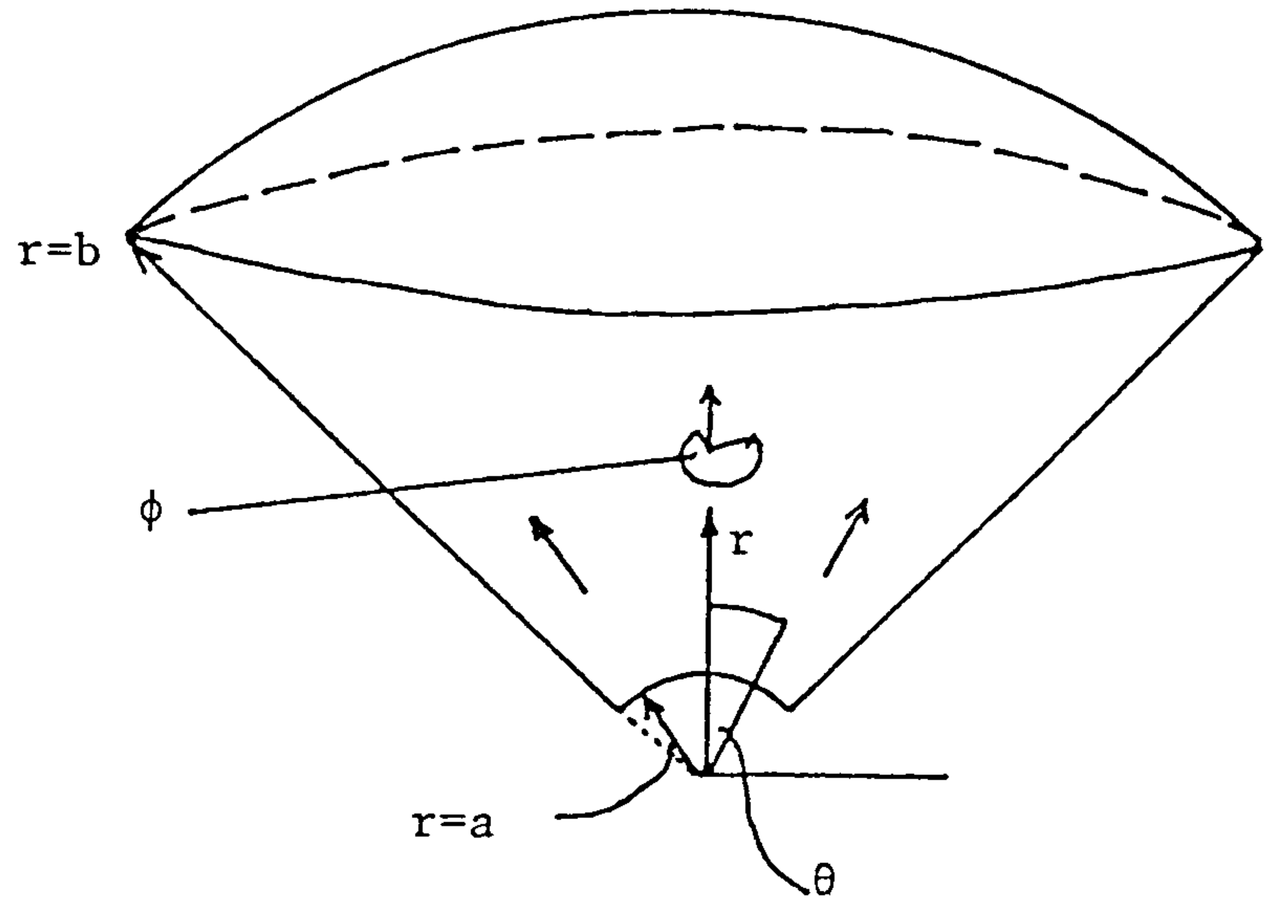

Figure 178: Schematic representation of the approximations made for the propagation of ultrasonic pulses in the piezoelectric cones of high fidelity transducers.

in these laboratory calibrations against the optical detector.

VI.3 Theoretical considerations and discussions of the experimental calibration results

The first arrangement to be discussed will be that for which the number of variables is least, that is for the epicentral calculation.

The transducer is excited in this case by a plane longitudinal wave which is incident normally to the transducer input face. As the wave strikes this face then various reflections are set up. One of these is the reflection back into the aluminium block of an ultrasonic wave. This wave does not have any further interaction with the transducer and is therefore ignored in the following discussions. Following the work in chapter IV on the transmission of ultrasonic pulses in glass rods then reflections from the edges of the transducer face might be expected. The width of the transducer faces for T1, T2 and T3 are 1mm. Therefore frequencies similar to those existing in an infinite cylinder of diameter 1mm might be expected in frequency calibrations. These may easily be calculated and are given, for the angularly invariant vibration mode as:

$$\nu = (ka) \cdot \frac{v}{2\pi a} \qquad (337)$$

where a is the cylinder radius, v the velocity of the ultrasound, and ν the frequency. The values of (ka) are

given by the solution of

$$\frac{\partial}{\partial r}\left(J_r(ka)\right) = 0 \qquad (338)$$

and are approximately

$$ka = 0,\ 3,8,\ 7.0,\ 10.15\ \ldots \qquad (339)$$

Assuming two values for the longitudinal and shear wave velocities to be $3.5mm.\mu s^{-1}$ and $1.8mm.\mu s^{-1}$ respectively then the frequencies (below 10MHz) are found to be:

$$\nu = 2.2,\ 4.0,\ 4.2,\ 5.8,\ 7.8\ MHz \qquad (340)$$

It is expected that this vibration mode accounts for some of the resonance peaks in the calibration traces for T1, T2 and T3. The corresponding frequencies for T4 and T5 will be higher due to the smaller face diameters of 0.65 and 0.50mm respectively. These increased frequencies (below 10MHz) are:

$$T4:\ \nu = 3.4,\ 6.2,\ 6.5,\ 8.9\ MHz$$

and

$$T5:\ \nu = 4.4,\ 8.1,\ 8.5\ MHz$$

Once the pulse has entered the transducer then it continues to propagate upwards towards the brass backing. The size of the entry aperture for the wave is about the same size as the wavelengths of the ultrasound in the frequency range of interest. It therefore acts as a diffraction limiting aperture. Resonances in the radial direction will therefore be set up. These will be discussed shortly. Firstly though an approximation to the equation

for the piezoelectric response will be solved.

The governing equation for the piezoelectric effect may be written as:

$$\underline{E} = g\underline{T} + \frac{\underline{D}}{\varepsilon_T} \qquad (341)$$

where $\underline{E}$ is the electric field, $\underline{T}$ the stress field, $\underline{D}$ the displacement field and g and ε_T the piezoelectric stress coefficient and the permittivity at constant stress respectively. Now $\underline{D}$ is controlled by the flow of free charge carriers and as the device is shunted by a very large resistance (effectively open circuit) this flow is zero. Therefore $\underline{D}$ must at least be constant and as no current is ever introduced into the device then $\underline{D}$ is zero. Equation (341) may be rewritten therefore as:

$$\underline{E} = -g\underline{T} \qquad (342)$$

Now an electric field may be described by a voltage (V) via:

$$\underline{E} = -\underline{\nabla}V \qquad (343)$$

The stress is related to the material strain via Young's modulus (which is termed here Y to avoid confusion with the electric field). If $\underline{S}$ is the strain, then (in one dimension only);

$$\underline{T} = Y\underline{S} \qquad (344)$$

Therefore equation (342) becomes:

$$\underline{\nabla}V = gY\underline{S} \qquad (345)$$

Approximations must now be made if this is to be solved in a simple manner. The approximations are that the cone of piezoelectric material appears as part of a sphere and the ultrasonic waves propagate in this volume in one direction only as if from a point source (Figure 178). As the face of the transducer is a diffraction limiting aperture this is a fair approximation.

Using spherical co-ordinates equation (345) may be written as:

$$\hat{\underline{r}}_1 \frac{\partial V}{\partial r} = gY \frac{\partial \xi}{\partial r} \hat{\underline{r}}_1 \qquad (346)$$

where $\hat{\underline{r}}_1$ is a unit vector in the direction $\underline{r}$, and ξ is the displacement of the ultrasonic wave. ($\partial\xi/\partial\theta$ and $\partial\xi/\partial\phi$ are zero where θ and ϕ are the spherical co-ordinate angles given in Figure 178).

Equation (346) is easily integrated to give:

$$V(r=b) - V(r=a) = gY(\xi(r=b) - \xi(r=a)) \qquad (347)$$

As the ultrasonic wave is spreading out in three dimensions then the displacement is proportional to r so that if ξ_o is the displacement at r=a, then r=b the displacement will be $\xi_o(b/a)$. This result therefore approximately describes the piezoelectric behaviour in the transducers.

One important point which is not included in the calculation above is the device capacitance. Now if the device is isolated then its capacitance has no effect on the

response as seen above. However in order to measure the voltage then a preamplifier must be coupled across the transducer. This has two effects. Firstly the input impedance of the preamplifier means that the transducer cannot hold charge indefinitely and so does not have a DC response. Secondly any charge developed on the piezoelectric cone is shared between the device capacitance (Cd) and the distributed parasitic capacitance of the preamplifier and its input leads (Cp). The voltage measured (V_m) is therefore reduced to

$$V_m = \left(V(r=b) - V(r=a)\right)\left(\frac{Cd}{Cd+Cp}\right) \qquad (348)$$

By using Gauss' law the capacitance of the part sphere ahown in Figure 178 may be calculated if edge effects are ignored. Where the half angle of the cone is taken as α then the capacitance is given by:

$$C = 2\pi(1 - \cos\alpha)\varepsilon_o\varepsilon_r\left(\frac{ab}{b-a}\right) \qquad (349)$$

where ε_r is the relative permittivity of the piezoelectric material and ε_o the permittivity of free space. For the dimensions of transducer T1 this is calculated to be 20pF (ε_r = 1700 as indicated in reference 132), whilst for T4 and T5 the value is 7pF. The input capacitance of the preamplifier used is approximately 20pF indicating that the responses of T4 and T5 should be 1.9 times smaller than that of T1. This explains the results for T5 with respect to T1 but not T4. T4 is seen to have a much lower response.

Now when the piezoelectric material is produced it is coated with silver so that electrical contact may be made to it. T4 when first produced had a good silver contact and its response was virtually identical to T5. However with use this silvering wore off and the response fell as a result. It is assumed that this wearing has some effect on the device capacitance and therefore on the measured response.

A second point not covered in the calculations leading to equation (347) is the absolute scale of the responses. Consider the device to be standing on aluminium. Now the transmission of the ultrasonic pulse from the aluminium to the piezoelectric material is governed approximately by equation (238):

$$\frac{U_p}{U_A} = \frac{2(\rho v)_A}{(\rho v)_A + (\rho v)_p} \qquad (350)$$

where U_p/U_A is the ratio of the ultrasonic waves amplitudes in the piezoelectric material and the aluminium respectively, $(\rho v)_A$ is the product of the density and ultrasonic wave velocity of aluminium and $(\rho v)_p$ the corresponding figure for the piezoelectric.

Now $(\rho v)_A = 1.73 \times 10^7 kgm^{-2}s^{-1}$ and $(\rho v)_p = 3 \times 10^7$.

This gives

$$\frac{U_p}{U_A} = 0.73 \qquad (351)$$

The response of the piezoelectric is given[132] as 2.1kV/μm and so the response in terms of the voltage output

to the surface displacement of the aluminium is $77mV\mathring{A}^{-1}$. (N.B. U_A is one half of the free surface displacement). Taking into account the capacitance effect, this becomes $38mV\mathring{A}^{-1}$, which is close to the response figure ($\sim 15mV\mathring{A}^{-1}$) derived for T1 when this is grease coupled, especially considering the approximations made on the capacitance. It should also be noted that approximations are made as well in the coupling equation (equation (350)) These arise because firstly the geometry is not simply one dimensional, that is the wave is not simply a plane wave passing between two semi-infinite half-spaces, and secondly because the coupling creates in fact a three layer system (aluminium-grease-piezoelectric). For the directly coupled case the response figure falls by a factor of ~ 1.5. This arises because only partial contact is achieved in this case giving a reduction in contact area for the piezoelectric cone thus affecting equation (350).

It can be seen then that the size of the response for all the transducers considered is adequately described by the theoretical calculations outlined above. Some of the finer details of the response will now be discussed with the help of equation (347).

So far a pulse has been considered to enter the piezoelectric cone and set up vibrations in the radial mode of the tip. Equation (347) indicates then that this initial entry into the material should create a voltage which is proportional to the ultrasonic pulse amplitude and hence also proportional to the movement of the aluminium

surface (assumed not to be significantly loaded). The reflections from the edge of the tip are expected only to be weak (as indicated by similar reflections in the glass rods studied in chapter IV). As the voltage response is integrated over the entire face then these reflections are unlikely to affect the first pulse. Experimentally this is indeed found to be the case.

As the pulse propagates in the cone it spreads out and begins to set up radial resonances. Radial resonances will be most easily set up when the sizes of the two faces of the truncated cone are similar. Therefore T2 is expected to ring more than T4 or T5, which is indeed found to be so. Once the pulse reaches the far end of the cone a voltage is again created. This voltage will be much smaller than that created from the input pulse. Such a reduction in size occurs because of the (1/r) effect described earlier due to the pulse spreading. As T1 has a deeper cone than all the others then the voltage reduction in this is greatest and so the resonance in the trace caused by this voltage output should be least in T1. This explains why T1 has lower resonances than all the other transducers.

Part of the ultrasonic pulse is now reflected from the brass setting up longitudinal vibration modes. These modes will be more easily excited if the cone appears disc like, that is it has a large half angle. T3 is therefore expected to be the most resonant device. The traces of Figure 172 indicate this to be so.

The part of the pulse entering the brass block may also

be reflected back into the piezoelectric cone. Clearly if the brass backing is approximately the same size as the cone then these reflections will be pronounced and resonances might be expected. From experiment reducing the backing size from the diameter on T4 to the diameter on T5 has negligible effect (longitudinal resonances of the brass backing are too low frequency to be noted). Therefore the size of the brass backing down to that given for transducer T5 has no measurable effect on the device responses. Further reduction in size may be possible.

The last point to be discussed concerning the epicentral calibrations is the effect of the grease coupling on the transducer resonances. Experiment shows that the introduction of the grease increases these resonances. This is assumed to arise because the grease, in unavoidably smearing out around the input end of the transducer, changes the effective shape of the active element and therefore allows vibrations to be more easily maintained.

Moving on now to the surface pulse calibrations. These are expected to vary from the epicentral pulse calibrations only as a result of the aperture effect. When a plane wave passes over a circular aperture of diameter d then the area of the aperture swept out by the wavefront may be calculated. for each position of the wave, the final area covered being of course $\pi d^2/4$. It can be shown that the wave travels a distance of 0.687d after having covered 10% of the area and before it covers 90%. For a 1mm diameter on aluminium,

the rise time for a surface pulse comprising shear and Rayleigh waves is therefore 229ns giving an upper half power frequency response of 1.5MHz.

The grease covered result of Figure 175a) is found to have a half power frequency point at 1.4MHz when compared to the epicentral calibration. This fall-off is therefore due to the aperture effect. However when transducers T1, T4 and T5 are used in direct contact then the ratio of the surface pulse calibration to that obtained at epicentre is found to be constant (within experimental error). It must be assumed therefore that the transducers in these cases are resting on the edge of the cone face in contact with the aluminium thus creating an effectively smaller aperture.

VI.4 Conclusions on the hi-fidelity transducers

The behaviour of the hi-fidelity cone transducers discussed above is found to be dominated mainly by the shape of the cone. A cone which is not greatly truncated and has a half angle of 45^{o} is found to suppress device resonances most effectively. The depth of the cone is also found to influence the resonance behaviour with a large depth giving optimum results. The aperture effect to surface waves existed as expected when the transducer was coupled with grease to the workpiece but was absent when direct coupling was used due to a reduction in contact area. The grease coupling is also found to enhance resonances.

The size of the brass backing is found not to be critical down to the dimensions considered.

The calibration results given by Procter up to 1.4MHz have been extended. These extended results which appear to vary as expected indicate the device response is still essentially resonance free even at the increased frequencies monitored.

It has been shown therefore that these transducers offer a very useful secondary standard for calibration and propagation work. It would seem that although the transducer described by Procter[9,95] (T1) produced the best results of all those tested, it could be improved upon by making both the cone deeper and the diameter of the front face smaller, although this last alteration would reduce the device capacitance.

VII SUMMARY, CONCLUSIONS AND SUGGESTIONS FOR FURTHER WORK

In the field of acoustic emission and high resolution ultrasonics a great deal of work in recent years has been concerned with developing a greater understanding of the processes involved in ultrasonic pulse generation, propagation and detection. The processes of real practical importance in the field of non-destructive evaluation are those associated with the generation of ultrasonic waves. These processes may be those connected with either acoustic emission sources or may be linked to reflections of a probing ultrasonic beam. Therefore this work has effectively been concerned with the calibration of an ultrasonic transducer with respect to the various sources of ultrasonic waves.

A review of the published literature indicated that various areas of this work had still not been covered. These included high frequency calibration of the transducer response to surface ultrasonic waves, direct verification of existing theoretical propagation functions and also the experimental determination of other commonly used propagation functions such as those for solid cylinders. An optical interferometer offered the possibility of providing a solution to all these problems. Such a device has a small probe size for ultrasonic waves and so can monitor high frequency surface ultrasonic waves. In addition it can probe inside transparent materials therefore indicating it might be able to monitor sources directly

and consequently provide information about propagation functions.

The first part of the work was therefore concerned with the development of an optical interferometric ultrasound detector. Optical interferometric detectors suffer from two significant shortcomings. The first of these is their minimum detectable displacement. This is a fundamental problem with a theoretical limit. The theoretical limit (of 0.25Å) has been attained in the device developed over a bandwidth of 10MHz and as such represents an improvement on many devices previously built. The second shortcoming of an interferometric transducer is that the sensitivity of the optical detector varies randomly between maximum and zero as a result of the detector's response to large amplitude, low frequency vibrations. These vibrations must therefore be stabilized against. The solution to the problems previously reported tended to be either complicated and expensive or to offer only a low range of stabilization.

A stabilization technique has therefore been developed which is based on moving the interferometer reference mirror by mounting it on the tip of a piezoelectric multimorph crystal. This technique is simple and has been shown to offer a good range of stabilization (3μm at 100Hz). A theoretical analysis of the stabilization circuitry, together with a study of the effect of this method of stabilization on the interferometer intensity output, has enabled the system to be optimized. Therefore a device

has been produced which is not affected by unwanted vibrations and can subsequently be used to monitor high frequency surface ultrasonic waves. This device can also measure various sources at their origin and so determine propagation functions.

A miniature version of the interferometer has also been made. Unfortunately, it was not possible to develop a miniature light source for this interferometer and so the overall device as an ultrasonic detector was somewhat bulky. Further work is therefore possible on this system. This would involve either the use of a small laser diode as the light source or the use of optical fibres to introduce light from some remote laser.

In addition to the two detectors above, a quadrature Michelson interferometer has been made and used to verify the results obtained with the stabilized device. Various methods of processing the quadrature information have been discussed indicating that it should be possible to use this interferometer in environments with large background vibrations. One of these processing methods involves the use of analogue squaring devices. Such devices are now being produced which can provide squaring over a wide bandwidth. A further development of the quadrature interferometer then might be to incorporate these squarers into some real time processing electronics and so produce a very robust optical transducer.

A method of removing laser noise in the quadrature device has been presented. To the author's knowledge, this is the first time a solution has been presented for this

problem.

The development of the optical interferometer as an absolutely calibrated ultrasound detector has enabled various methods for ultrasonic wave generation to be studied. These are usually termed artificial sources of acoustic emission.

A very common source is the fracture of a ceramic pencil lead. The reproducibility of this source in both the time and frequency domains is important but has not previously been reported. This reproducibility has therefore been studied together with the effect of changing various source parameters. Results are now available then which show what waveform could be expected when pencil leads are broken in a variety of ways. The upper half power frequency point for this source has been shown to be $\sim$ 600kHz. The work has also enabled inconsistancies in results published by different authors to be resolved. These inconsistencies were associated with the existence of a compressive component in addition to the main release, generated by the fracture process. This compressive component has been shown to exist.

A second widely used artificial acoustic emission source is the fracture of a thin glass capilliary. The reproducibility of this source has been measured as has the dependence of the source on the capilliary dimensions. The release time of the fracture appears to be proportional to the capilliary wall thickness with the fracture velocity being $\sim$ (1/20)th the velocity of the shear wave velocity in

the material. Further work needs to be done to verify this result.

A third source of ultrasound which has been quite extensively studied recently is the impact of a Q-switched Nd-YAG laser. The study of this source reported here has been restricted to monitoring surface waves, a use for which the optical detector is particularly suited. Good agreement has been obtained between experimentally measured waveforms and theoretical waveforms reported previously. The optical detector has been used to probe very close to the impact point and as a result has been able to monitor the air shock created by the laser generated plasma. It should be possible to use the optical detector further by monitoring the actual source origin for a thermoelastic laser impact. Such work would allow theoretical models associated with the laser heating process to be partially verified.

In addition to these established artificial sources a novel source has been briefly investigated. This source is the fracture of very small glass spheres usually termed balantini. Preliminary investigations have indicated this is a high frequency source, extending up to $\sim$ 5MHz, which has a fairly reproducible time dependency. The absolute scale of the waveform shape is unfortunately quite variable and therefore the source could not be used on its own to provide a calibrated ultrasonic input to a system. However it could be used in conjunction with another low frequency reproducible source. Further work is needed

to verify these results. This work would probably involve measuring the ultrasonic waveforms closer to the source in order to improve the signal to noise ratio, which was very low in the present measurements.

Having studied various sources of artificial acoustic emission it now becomes possible to study another facet of the ultrasonic wave generation and detection system. This is concerned with a study of ultrasonic pulse propagation. Now a commonly used geometry in ultrasonic work is the solid right circular finite cylinder. Such a cylinder is often used as a waveguide to couple ultrasonic waves from an inhospitable surface, for example one at a high temperature, to a monitoring transducer. To the author's knowledge, the solution to this propagation problem has never been derived either experimentally or theoretically.

Ultrasonic pulse propagation then has been studied in glass rods. These rods being transparent allowed the movement of the input face, created by an incident ultrasonic pulse, to be measured. This pulse was introduced by attaching these rods with some suitable couplant to the surface of a large aluminium block. An ultrasonic source placed beneath this block generated effectively plane waves at the far surface where the rods were positioned.

It was found that when the diameter of the rods was large and the couplant viscous then oscillations occurred

within the coupling layer. However, when the rod diameter was small and the couplant had a low viscosity, then the thickness of the couplant was reduced to such a point that these oscillations disappeared. In this case the motion of the centre of the input end of the rods was found to be initially proportional to the movement of the free surface of the aluminium block. This initial movement was followed by a series of oscillations which are assumed to arise from reflections at the cylinder walls.

As the movement of the input face follows that of the aluminium it is assumed that the rods receive a uniform input over the entire input face. The time dependency of the input is then determined by the movement of the face centre. Further work should be performed to verify this by making measurements over the entire area of this face. The movements of the upper or output faces were then measured, again at the face centre. Having determined the input ultrasonic pulses these latter measurements, together with the input pulses, provide a description of the propagation function in a finite solid cylinder.

This propagation function is dominated by a series of oscillations caused by reflections off the cylinder walls. In addition to this there is evidence that the frequency dependent dispersion predicted for an infinite cylinder is beginning to dominate the response. These results now await a theoretical model to which they may be compared.

These propagation studies have been extended to include a verification of a theoretically known transfer or Green's

function. This has been made possible by measuring an artificial source, the fracture of a ceramic pencil lead, at its origin. The measurement was made by viewing the movement of one face of a glass block, the face on which the lead was broken, through the glass block itself. This result was then convoluted with the theoretical transfer function for a surface pulse on a semi-infinite half space and compared to the experimentally determined surface ultrasonic pulse. Good agreement was found between this convolved waveform and the measured waveform. To the author's knowledge this is the first time such a verification has been made directly. All previous verifications have assumed a given form for the artificial source. This has then been compared with the result of a deconvolution using the theoretical propagation function of a waveform measured at a distance.

The verification of theoretical transfer functions is an extremely interesting area of work. The results given should be further expanded by using more accurate forms of the theoretical waveforms and also by verifying more than just the function for the surface pulse on a semi-infinite half-space.

Once the propagation functions have been determined then the final remaining unknown in the calibration problem is the interaction between the ultrasonic waves and the detectors used to monitor them. The optical detector, in providing a calibrated response, allows this detector

calibration to be performed. This calibration has been used to allow the development of two different transducers.

The first transducer was based on the inverse magnetostrictive effect. This effect can be found in metals and as such offers the possibility of direct attachment of a transducer, via welding, to, for example, hot surfaces where conventional transducers behave poorly. A theoretical and experimental study of the transducer has indicated that its response is determined by a combination of ultrasonic pulse propagation in the detector and of magnetic effects including eddy current effects. A usable transducer has been produced with an upper frequency response of ∿ 4MHz. The signal to noise ratio is only approximately five times down on that of a waveguide coupled piezoelectric transducer. (Piezoelectric transducers are usually coupled to hot surfaces via a waveguide). However, further work on the detector, involving the use of a laminar structure to reduce eddy current effects, should give a signficant improvement in the signal to noise ratio. This ratio should then be in excess of that of the waveguide coupled piezoelectric device.

The second transducer investigated was a high-fidelity piezoelectric transducer developed at the National Bureau of Standards in the United States which consisted mainly of a truncated piezoelectric cone backed by a large piece of brass. This has been previously calibrated up to 1.4MHz for both the surface and epicentral situations. However

the epicentral calibration involved a comparison not to the actual stimulating waveform, but to a theoretical approximation to it. These calibrations have been extended both by increasing the upper frequency to around 5MHz and by comparing the transducer output in the epicentral case to the actual surface movement. Even with these improvements in the calibration the transducer was determined still to be essentially non-resonant and to provide a good approximation to the true time-domain surface movement.

The optimum design of the transducer appeared to be when the truncated piezoelectric cone had a half angle of 45^{o} together with a large depth and a small front face.

APPENDIX 1

The mathematical basis behind the interferometer stabilization technique used by Speake[53].

The interferometer described by Speake[53] is shown schematically below.

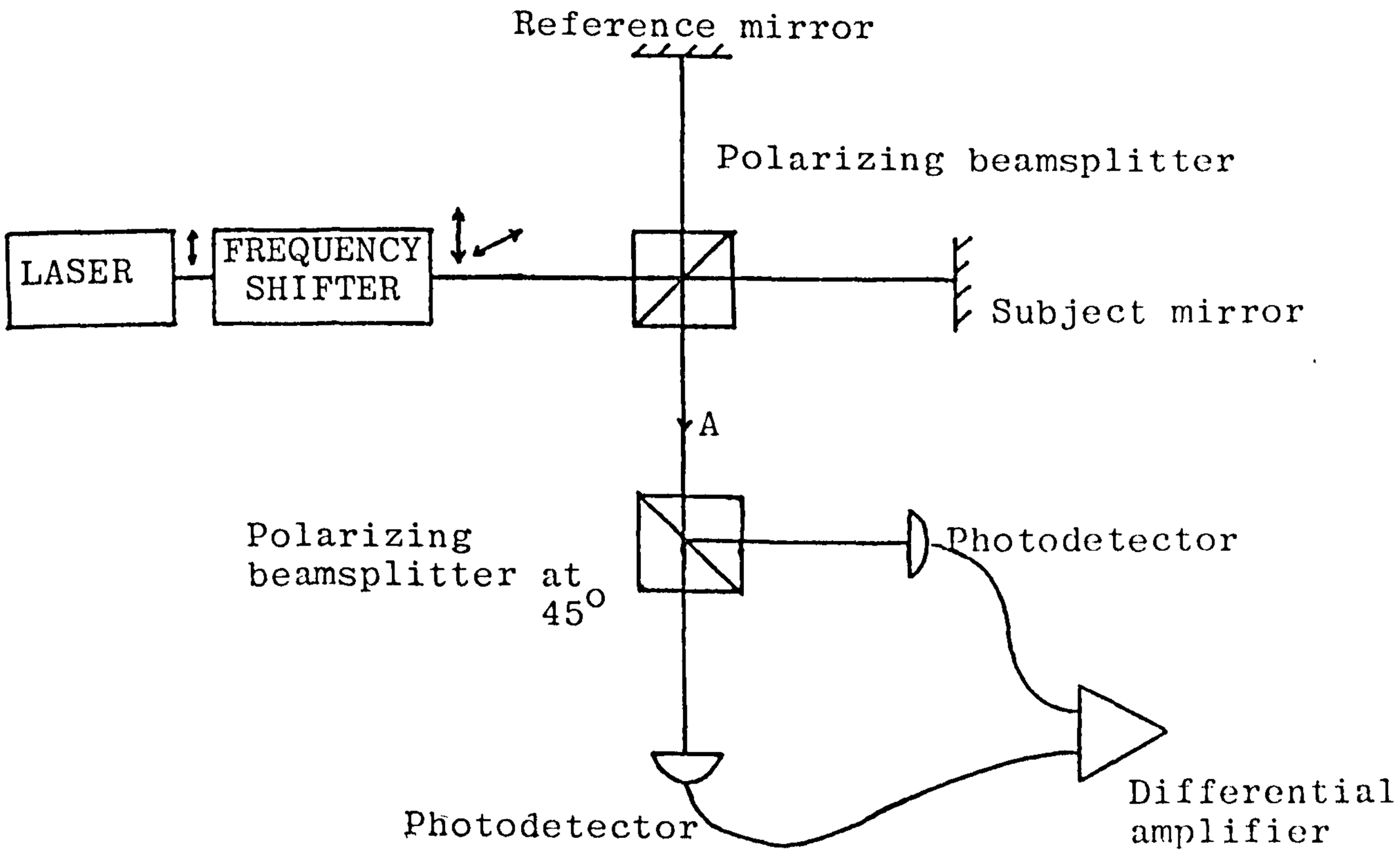

The two polarizations may be written as $\underline{i}$ and $\underline{j}$ giving the reference signal and subject signals at A as:

$$\underline{E}_r = E_r \hat{\underline{i}} \sin(\omega_r t + \phi_r) \qquad (A1.1)$$

$$\underline{E}_s = E_s \hat{\underline{j}} \sin(\omega_s t + \phi_s) \qquad (A1.2)$$

where E_r is the electric field of the reference signal of frequency ω_r and phase ϕ_r. Similar notation is used for the subject signal.

The electric fields are now polarized by the polarizing beamsplitter set at 45^{o}. The two directions of this polarization are:

$$\frac{1}{\sqrt{2}}\,(\hat{\underline{i}} + \hat{\underline{j}}) \text{ and } \frac{1}{\sqrt{2}}\,(\hat{\underline{i}} - \hat{\underline{j}})$$

The electric field, $\underline{E}_1$, at one photodetector is therefore given by

$$\underline{E}_1 = (\underline{E}_r - \underline{E}_s).\left[\frac{1}{\sqrt{2}}\,(\hat{\underline{i}} + \hat{\underline{j}})\right]\frac{1}{\sqrt{2}}\,(\hat{\underline{i}} + \hat{\underline{j}}) \qquad (A1.3)$$

which can be evaluated as

$$\underline{E}_1 = \frac{1}{2}(\hat{\underline{i}} + \hat{\underline{j}})\left[E_r\sin(\omega_r t + \phi_r) + E_s\sin(\omega_s t + \phi_s)\right] \qquad (A1.4)$$

The intensity, which is what the detector monitors, is given by

$$I_1 = \varepsilon.c\langle\underline{E}_1.\underline{E}_1\rangle \qquad (A1.5)$$

where c is the velocity of light in air and ε the permittivity of air and $\langle\underline{E}_1.\underline{E}_1\rangle$ is the time average value of $\underline{E}_1.\underline{E}_1$ over small time intervals.

This may be written as:

$$I_1 = \varepsilon c\left[\frac{E_r^2}{2}\,\langle\sin^2(\omega_r t+\phi_r)\rangle + \frac{E_s^2}{2}\,\langle\sin^2(\omega_s t+\phi_s)\rangle + \frac{E_s E_r}{2}\,\left[\langle\sin((\omega_r+\omega_s)t + \phi_r+\phi_s)\rangle + \langle\sin((\omega_r-\omega_s)t + \phi_r-\phi_s)\rangle\right]\right] \qquad (A1.6)$$

Evaluating the average leads to

$$I_1 = \frac{\varepsilon c}{4}\left[E_r^2+E_s^2 + 2E_sE_r\,\sin(\Delta\omega t+\Delta\phi)\right] \qquad (A1.7)$$

where $\Delta\omega = \omega_r-\omega_s$ and $\Delta\phi = \phi_r-\phi_s$.

The electric field at the other detector is given by

$$E_2 = (\underline{E}_r+\underline{E}_S) \cdot \left(\frac{1}{\sqrt{2}} (\hat{\underline{i}}-\hat{\underline{j}})\right) \frac{1}{\sqrt{2}} (\hat{\underline{i}}-\hat{\underline{j}}) \qquad (A1.7a)$$

leading to an intensity I_2 where

$$I_2 = \frac{\varepsilon c}{4} \left(E_r^2+E_S^2 - 2E_SE_r \sin(\Delta\omega t+\Delta\phi)\right) \qquad (A1.8)$$

The differential amplifier yields a voltage (V) which is proportional to the difference in equations (A1.7) and (A1.8). Therefore:

$$V = A \sin(\Delta\omega t + \Delta\phi) \qquad (A1.9)$$

where A is an arbitrary constant.

So far a fixed $\Delta\omega$ has been assumed. This is not true. A feedback loop in fact takes a signal from equation (A1.9) and uses this to provide a correction frequency ω_c where $\Delta\omega = \omega_c(t)$.

$\Delta\phi$ is governed by the difference in the lengths of the reference and subject arm (x(t)) and will be shown in chapter III to be given by $4\pi x(t)/\lambda$. Therefore using this and $\Delta\omega = \omega_c(t)$ then equation (A1.9) may be rewritten as:

$$V = A \sin\left(\int_o^t \omega_c(t')dt' + 4\pi x(t)/\lambda\right) \qquad (A1.10)$$

If the system is stable, then as $\sin(\alpha) \approx \alpha$ for small angles α equation (A1.10) becomes:

$$V(t) \approx A\int_o^t \omega_c(t').dt' + A.4\pi x(t)/\lambda \qquad (A1.11)$$

For equations (A1.10) and (A1.11) to be true then it is necessary to have the ability to provide a DC offset otherwise equation (A1.14) below cannot be satisfied. In the instrument described by Speake then this DC offset does

exist. At DC the frequency shifting cell acts as a variable wave retardation plate and as such can provide 0 to 2π of compensation. Now:

$$V(t) - V(0) = \int_0^t \frac{\partial V(t')}{\partial t'}.dt' \qquad (A1.12)$$

and $$x(t) - x(0) = \int_0^t \frac{\partial x(t')}{\partial t'}.dt' \qquad (A1.13)$$

From equation (A1.11)

$$V(0) = A4\pi x(0)/\lambda \qquad (A1.14)$$

equation (A1.11) may be rewritten as:

$$\int_0^t \frac{\partial V(t')}{\partial t'}.dt' = A\int_0^t \omega_c(t')dt' + \frac{4\pi A}{\lambda} \int_0^t \frac{\partial x(t')}{\partial t'}.dt' \qquad (A1.15)$$

therefore $$\int_0^t \left\{\frac{\partial V(t')}{\partial t'} - A\omega_c(t') - \frac{4\pi A}{\lambda} \frac{\partial x(t')}{\partial t'}\right\} dt' = 0 \qquad (A1.16)$$

hence $$\frac{\partial V(t')}{\partial t'} - A\omega_c(t') = \frac{4\pi A}{\lambda} \frac{\partial x(t')}{\partial t'} \qquad (A1.17)$$

If $\omega_c(t')$ is determined by a negative feedback technique then

$$\omega_c(t') = -BV(t') \qquad (A1.18)$$

therefore $$\frac{\partial V(t')}{\partial t'} + ABV(t') = \frac{4\pi A}{\lambda} \frac{\partial x(t')}{\partial t'} \qquad (A1.19)$$

The solution is obtained by using the integrating factor $e^{ABt'}$ on this differential equation and then (dropping the previous primes):

$$V(t) = \frac{4\pi A}{\lambda} \left[x(t) - e^{-ABt} \int_0^t x(t')ABe^{ABt'}dt'\right] \qquad (A1.20)$$

$x(t')$ may be Fourier analysed by a Fourier sine transform. If the frequency for one component is f then the following

two extremes exist (for a Fourier component written as $a(\delta f)\sin 2\pi ft$):

a) $AB >> 2\pi f$

$$V(t) \simeq \frac{4\pi A}{\lambda} \left(\frac{-fe^{-ABt}}{AB} \right) . a\delta f = 0 \qquad (A1.21)$$

b) $AB << 2\pi f$

$$V(t) \simeq \frac{4\pi A}{\lambda} \left(a\delta f \sin 2\pi ft + \frac{AB}{f} \left(a\delta f \cos 2\pi ft - e^{-ABt} \right) \right)$$

$$V(t) \simeq \frac{4\pi A x(t)}{\lambda} \qquad (A1.22)$$

Therefore the system has no response at low frequencies and provides an output, proportional to the subject mirror movement, at high frequencies. It is thus stabilized.

APPENDIX 2

The removal of laser intensity variation noise in interferometers

In a stabilized interferometer the output (V) is given as:

$$V = (I_1 + \delta I_1)(1 + \sin \frac{4\pi}{\lambda}(x_L + x_H) \qquad (A2.1)$$

where δI_1 is noise on the DC laser intensity reaching the photodetector (I_1) and x_L and x_H are low and high frequency components of the relative movement of the subject mirror to the reference mirror. In a stabilized device then $x_L = 0$ and so equation (A2.1) becomes (as $\sin(\alpha) \simeq \alpha$ for small α):

$$V \simeq (I_1 + \delta I_1)(1 + \frac{4\pi x_H}{\lambda}) \qquad (A2.2)$$

Therefore V can be rewritten as:

$$V = I_1 + \delta I_1 + I_1 \frac{4\pi x_H}{\lambda} + \delta I_1 \frac{4\pi x_H}{\lambda} \qquad (A2.3)$$

If the laser intensity if monitored directly then $(I_1 + \delta I_1)$ may be determined and subtracted from the output to give

$$V = I_1 \frac{4\pi x_H}{\lambda} \left(1 + \frac{\delta I_1}{I_1}\right) \qquad (A2.4)$$

Now $\delta I_1 / I_1 \simeq 10^{-2}$ and so the output is given approximately as

$$V = I_1 \frac{4\pi x_H}{\lambda} \qquad (A2.5)$$

In a quadrature interferometer the outputs are given

(see chapter III) as:

$$V_S = I_1\left(1 + \sin\left(\frac{4\pi}{\lambda}(x_L + x_H)\right)\right) \qquad (A2.6)$$

and $$V_C = I_1\left(1 + \cos\frac{4\pi}{\lambda}(x_L + x_H)\right) \qquad (A2.7)$$

When these outputs are frequency filtered, then the high frequency information may be obtained (see chapter III) which is:

$$V_S = I_1\left(\frac{4\pi y_H}{\lambda}\right)\cos\left(\frac{4\pi y_L}{\lambda}\right) + \delta I_1 + \delta I_1 \sin\left(\frac{4\pi x_L}{\lambda}\right) \qquad (A2.8)$$

$$V_C = -I_1\left(\frac{4\pi y_H}{\lambda}\right)\sin\left(\frac{4\pi y_L}{\lambda}\right) + \delta I_1 + \delta I_1 \cos\left(\frac{4\pi y_L}{\lambda}\right) \qquad (A2.9)$$

If the laser output intensity is monitored then δI_1 may be obtained (again by hi-pass filtering) and then subtracted from equation (A2.8) and (A2.9) leaving

$$V_S = I_1\left(\frac{4\pi y_H}{\lambda}\right)\cos\left(\frac{4\pi y_L}{\lambda}\right) + \delta I_1 \sin\left(\frac{4\pi x_L}{\lambda}\right) \qquad (A2.10)$$

and $$V_C = -I_1\left(\frac{4\pi y_H}{\lambda}\right)\sin\left(\frac{4\pi y_L}{\lambda}\right) + \delta I_1 \cos\left(\frac{4\pi y_L}{\lambda}\right) \qquad (A2.11)$$

Equations (A2.10) and (A2.11) may then be squared and added which leaves (as $\cos^2\alpha + \sin^2\alpha = 1$):

$$V = I_1^2\left\{\frac{4\pi y_H}{\lambda}\right\}^2 + \delta I_1^2 \qquad (A2.12)$$

δI_1^2 may be determined as above by monitoring the laser intensity output. Consequently, subtracting this from equation (A2.12) leads to

$$V = I_1^2\left(\frac{4\pi y_H}{\lambda}\right) \qquad (A2.13)$$

Laser noise in a quadrature interferometer may therefore be removed and is not then a fundamental problem.

APPENDIX 3

Numerical deconvolution of digitized data

As mentioned in section II.6.1, numerical deconvolution of data is possible with, for example, a theoretical waveform. Hsu and Hardy[8] have presented the method by which this is done. As this is a standard procedure their appendix is presented here.

"Method of Time Domain Deconvolution"

If the transfer function (the impulse response) of a linear system is known, the input function can be obtained by direct deconvolution of the measured output function with the transfer function. The concept has been discussed in many text books (for example, seen Bracewell[133]); and detailed procedures and examples have been given by Ko and Scott[134]. We outline the derivation as follows:

Let u(t) be the measured displacement at a particular location and g(t) be the transfer function for the structure which, of course, depends on both the source and sensor locations. g(t) has been determined theoretically for the infinite plate. Let f(t) be the input force function to be determined. Because the system is linear, the relation among u(t), g(t) and f(t) can be written as a convolution integral.

$$u(t) = \int_0^t f(\tau)g(t-\tau)d\tau \qquad (A3.1)$$

Here u(t), f(t) and g(t) are all assumed to be causal, i.e. they all are equal to zero for t < 0. We digitize these functions as a sampling interval of Δt, and denote

$$V(I) \equiv u(I\Delta t);$$

$$F(I) \equiv f(I\Delta t);$$

$$G(I) \equiv g(I\Delta t)\Delta t, \quad I - 1,2,3 \ldots$$

Equation (A3.1) can be written as:

$$U(I) = \sum_{K=1}^{I} F(K)G(I-K+1) \ldots \qquad \text{(A3.2)}$$

Rewrite equation (A3.2) in matrix form; we have:

$$\begin{bmatrix} U(1) \\ U(2) \\ U(3) \\ U(4) \\ . \\ . \\ . \end{bmatrix} = \begin{bmatrix} G(1) & 0 & 0 & 0 & 0\ldots \\ G(2) & G(1) & 0 & 0 & 0\ldots \\ G(3) & G(2) & G(1) & 0 & 0\ldots \\ G(4) & G(3) & G(2) & G(1) & 0\ldots \\ . & . & . & . & \ldots. \\ . & . & . & . & \ldots. \\ . & . & . & . & \ldots. \end{bmatrix} \begin{bmatrix} F(1) \\ F(2) \\ F(3) \\ F(4) \\ . \\ . \\ . \end{bmatrix} \qquad \text{(A3.3)}$$

In the AE experiments, u(t) is the measured displacement; g(t) has been solved theoretically; f(t) is the source function to be determined. Equation (A3.3) may be looked upon as a system of linear algebraic equations solving for unknown F(I). It is easy to see that F(I) can be solved successively by simple substitution and division, i.e.

$$F(1) = U(1)/G(1) \qquad (A3.4)$$

$$F(I) = \left[U(I) - \sum_{K-1}^{I-1} G(I-K+1)F(k)\right]/G(1) \quad I = 2,3,4...$$

Equation (A3.4) can be programmed and computed on a mini-computer. It takes approximately 2 minutes to compute 200 points on an 8/16 Interdata minicomputer.

The matrix [G] has its elements on each of the left to right diagonals the same one value, and all elements above the main diagonal equal to zero. This triangular matrix can be inversed since its inverse exists. Let $[H] = [G]^{-1}$, it can be shown that

$$[H] = \begin{bmatrix} H(1) & 0 & 0 & 0 & 0 & . \\ H(2) & H(1) & 0 & 0 & 0 & . \\ H(3) & H(2) & H(1) & 0 & 0 & . \\ H(4) & H(3) & H(2) & H(1) & 0 & . \\ . & . & . & . & . & . \\ . & . & . & . & . & . \\ . & . & . & . & . & . \end{bmatrix} \qquad (A3.5)$$

and

$$H(1) = \frac{1}{G(1)}$$

$$H(I) = \sum_{J=1}^{I-1} \frac{G(J+1)}{G(1)} H(I-J), \quad I>1 \ldots. \qquad (A3.6)$$

In other words, the inverse problem can be handled formally as a convolution integral:

$$f(t) = \int_o^t u(\tau)h(t-\tau)d\tau \qquad (A3.7)$$

where h is a continuous function such that

$$H(I) = h(I\Delta t)\Delta t$$

In terms of computational algorithms:

$$F(I) = \sum_{K=1}^{I} U(K)H(I-K+1) \qquad (A3.8)$$

APPENDIX 4

The attenuation of ultrasonic waves in steel and aluminium

There are three types of ultrasonic wave in a solid: longitudinal, transverse and Rayleigh. Each has a characteristic attenuation (α) associated with it. As the Rayleigh wave is a combination of longitudinal and shear waves then it would be expected that its attenuation factor could be linked to the attenuation factors for the other two waves. This is indeed possible. Viktorov[135] gives this combination as:

$$\alpha_R = A\alpha_L + (1 - A)\alpha_t \qquad (A4.1)$$

where α_R is an attenuation factor for Rayleigh waves, α_L for longitudinal waves and α_t for transverse waves. The values A and (1 - A) depend on Poisson's ratio and are given for steel as 0.11 and 0.89 respectively. For aluminium these figures are 0.07 and 0.93. This formula has been tested experimentally by Press and Healy[136] and found to be correct. Attenuation is usually given in terms of Nepers/unit distance which is termed here (δ) with δ being given by:

$$\delta = \left(\frac{1}{2d}\right) \log_e \left(\frac{I_o}{I_d}\right) \qquad (A4.2)$$

where the initial intensity I_o has decreased to I_d after a distance d. The attenuation factors α are linked to the various δ's by:

$$\alpha_i = \delta_i \cdot v_i \qquad (A4.3)$$

where v_i is the velocity of the ultrasound of type i. Equation (A4.1) may be written for mild steel therefore as:

$$\delta_R = 0.22\delta_l + 0.96\delta_t \qquad (A4.4)$$

and for aluminium as:

$$\delta_R = 0.15\delta_l + 1.00\delta_t \qquad (A4.5)$$

The figure in Nepers/unit length may be changed to dB/unit length termed (ε) via the formula

$$\varepsilon = 8.686\delta \qquad (A4.6)$$

For polycrystalline materials then Rayleigh scattering of the ultrasonic waves from grain boundaries is the dominating attenuation mechanism when the wavelength of the ultrasound, λ, is greater than the grain size (d) ($\lambda \gtrsim 2\pi d$)[137]. For grains of 0.2mm diameter this gives $\lambda \simeq 1.3$mm and, for shear waves, f ≃ 2.5MHz. For shorter wavelengths other effects come into play and simple relationships are then difficult to determine. Experimental measurements should therefore be used.

Papadakis[138] has measured attenuation in various metals. All the materials he tested indicated for frequencies of a few MHz that $\delta_l \simeq \frac{\delta_t}{4}$.

Vinogradov and Ul'yanov[139] give the attenuation of surface waves on steel 3 as 0.07 dB/cm at 2.5MHz. These workers also indicate by measurements made on other materials that the value at 10MHz would be approximately four times greater, that is 0.28dB/cm. This means at a distance of 36mm (often

used in the experimental measurements described) that the amplitudes of ultrasonic waves in steel 3 would have fallen approximately by the following fractions of the original amplitude:

Longitudinal wave: 0.89

Shear wave: 0.63

Rayleigh wave: 0.63

Therefore if steel were used for experimental measurements the frequency output would begin to fall off just below 10MHz at a distance of 36mm.

Moving on to aluminium now, Mason[137] gives δ_1 = 0.023 Neper/cm at 10MHz. The following amplitude ratios at 36mm might then be expected compared to the original:

Longitudinal wave: 0.92

Shear wave: 0.72

Rayleigh wave: 0.71

Therefore aluminium does not propagate 10MHz shear or Rayleigh waves to a distance of 36mm totally unchanged. Assuming a half power frequency point for the ultrasonic detection system of 10MHz then at this frequency the system amplitude response is down to 0.707. This therefore matches the amplitude ratios above and results in an overall system half power point of 6.5MHz. For the frequencies encountered in the experimental measurements this half power point then has no effect.

It should be noted that very large variations are found in the reported values of the attenuation coefficients. This is thought to be due to variations in grain size etc.

APPENDIX 5

The computer program used to predict the intensity patterns found in Michelson interferometers

The attached computer program for a Commodor PET computer calculates the intensity of the interference pattern at an array of points. The calculation assumes that the subject mirror moves a given distance (this is the maximum amplitude of the unwanted vibrations) and the reference mirror moves the same distance to compensate. The following is a list of variables used:

A - Difference in optical path length, between the centres of the images from each mirror as calculated at the image screen for the interference pattern.

B - The input value of B is the initial angle of tilt of the subject mirror. A further tilt is added when the piezoelectric bimorph bends to compensate for vibrations.

C - Focal length of the focussing lens (L_1) of the interferometer.

D - The input value of D is the distance the reference mirror is off the focus of lens (L_1) for no vibration. The vibration amplitude is added to give a total distance off focus for the reference mirror.

E - Distance between the image points from both mirrors, at the screen used to image the interference pattern, as measured perpendicular to the optic axis. (One mirror is assumed to produce an image on the optic axis).

F - Distance from lens (L_1) to the focus point of the

light from the laser power source.

G - Counter.

H - Counter

I - Intensity of the interference pattern at a given point on the screen.

J - Counter.

K - Integral value of the intensity. The range is 0 to 100, where 100 is written as AA.

L - The position of the image point from the subject mirror as measured from the lens used to focus the interfering light. This lens is taken as identical to L_1.

M - Optical path difference, in the interference pattern, between rays from the reference and subject mirrors as calculated relative to the path difference at the centre of the pattern.

N - Size of the array used for the interference pattern.

P - Length of the piezoelectric bimorph in metres.

Q - The length along the optic axis to the image point for the reference mirror.

R - Outer radius of the lens used to image the interference pattern. Inner radius is assumed to be zero.

S - Distance between the two image points, one from the reference mirror and one from the subject mirror, measured parallel to the optic axis.

T - Distance from the effective laser point source after the laser has been expanded through a microscope objective to the lens L_1 used to focus the laser light onto the mirrors.

U - Total intensity of the interference pattern summed over

the screen.

V - Maximum amplitude of unwanted vibration. This may be changed on the input.

W - Wavelength of the laser light.

X - Distance in one direction along the screen with the interference pattern on it.

Y - Distance in the other direction along the screen.

Z - Initial distance between the two mirrors. This is an input.

Outputs

Focal length - focal length of lens L_1.

Crystal length - length of PZT bimorph in metres.

Screen, rad - outer radius of lensL_1.

Dist. off centre - position of the centre of the image from the reference mirror relative to the centre of the printout.

The program then prints the values in the array and the total intensity.

A5.4

```
READY.

 100 N=4
 110 OPEN4,4
 120 PRINT#4," "
 130 CLOSE3
 140 PRINT"INPUT INITIAL ANGLE";
 150 INPUT E
 160 PRINT"INPUT TUBE LENGTH<LESS THAN 10>",
 170 INPUT T
 180 PRINT"INPUT MR. AMPLITUDE",
 190 INPUT V
 200 PRINT" INPUT DISTANCE OFF FOCUS",
 210 INPUT D
 220 LET D=D+V
 230 PRINT"INPUT INITIAL DISTANCE BETWEEN MIRRORS",
 240 INPUT Z
 250 PRINT"INPUT SIZE OF ARRAY",
 260 INPUT N
 270 LET W=6.328E-07
 280 LET F=40.007
 290 LET P=40.01
 300 LET P=0.003
 310 LET F=F*T.*T-C*
 315 PRINT F
 320 LET B=E*V.P+B
 330 LET L=(F+2*D+2*Z)*C/(F-C+2*D+2*Z)
 340 LET S=(F*(F+2*D)*C/(F-C+2*D)-L
 350 LET U=L+S
 360 LET Q=E*B*D*D/(F+2*D)
 370 OPEN4,4
 380 PRINT#4,"TUBE LENGTH  "T
 390 PRINT#3,"MIN : AMPL    "V
 400 PRINT#3,"D OFF FOCUS  "D-V
 410 PRINT#3,"WAVELENGTH   "W
 420 PRINT#3,"FOCALLENGTH  "C
 430 PRINT#3,"CRYSTALLENGTH"P
 440 PRINT#3,"SCREEN.RAD   "R
 450 PRINT#3,"DIST BET MIRR"Z
 460 PRINT#3,"DIST OFF CNT "E*N/(2*R)"ROWS"
 470 CLOSE3
 480 LETH=-SQR((2*B*D)12+(F+2*D)12)-SQR(E12+Q12)+L+F+2*D+2*Z+S
 500 LET G=0
 510 FOR H=0 TO N-1
 520 FOR I=G TO 19+G
 530 LET X=W-P+I*2*P/(N-1)
 540 LET Y=P-H*2*P/(N-1)
 550 LET M=(SQR(Q12+X12+(Y-E)12)-SQR(L12+X12+Y12))-S
 560 LET I= 50*(COS((2*π/W)*(M+R))+1)
 570 LET U=U+I
 580 LET K=INT(I)
 590 IF K=100 GOTO 650
 600 IF K<10 GOTO 790
 610 OPEN3,4
 620 PRINT#3,K;
 630 CLOSE3
 640 GOTO 680
 650 OPEN3,4
 660 PRINT#3," RR ";
 670 CLOSE3
 680 NEXT J
 690 OPEN3,4
 700 PRINT#3," "
 710 CLOSE3
 720 NEXT H
 730 LET G=G+20
 740 OPEN3,4
 750 PRINT#3," "
 760 CLOSE3
 770 IF G<N GOTO 510
 780 GOTO 830
 790 OPEN3,4
 800 PRINT#3," "K;
 810 CLOSE3
 820 GOTO 630
 830 OPEN3,4
 840 PRINT#3,"TOTAL INT."U
 850 CLOSE3
 860 END
READY.
```

375 PRINT#3, "INITIAL ANGLE" B-(2*V/P)

APPENDIX 6

The second order approximation to the signal processing problem in the quadrature interferometer

The substitutions made in equation (178) and (179) in section III.6.1 were correct to the first order of small quantities. That is

$$\left.\begin{aligned} \cos\,(4\pi a_h e^{i\omega_h t}/\lambda) &\simeq 1 \\ \text{and} \qquad \sin\,(4\pi a_h e^{i\omega_h t}/\lambda) &\simeq 4\pi a_h e^{i\omega_h t}/\lambda \end{aligned}\right\} \qquad (A6.1)$$

The second order approximations to equations (178) and (179) are now:

$$\cos\,(4\pi a_h e^{i\omega_h t}/\lambda) = 1 - \tfrac{1}{2}(4\pi a_h e^{i\omega_h t}/\lambda) \qquad (A6.2)$$

and

$$\sin\left(\frac{4\pi a_h e^{i\omega_h t}}{\lambda}\right) = \frac{4\pi a_h e^{i\omega_h t}}{\lambda} \qquad (A6.3)$$

The main error due to the approximation is now in the sine term and is 1½%. This effect is merely a calibration error while the error in the cosine approximation could introduce more serious errors. From equation (176) then

$$I_c = A\left[\cos(4\pi a_1 e^{i\omega_1 t}/\lambda)(1 - \tfrac{1}{2}(\frac{4\pi a_h e^{i\omega_h t_2}}{\lambda})\sin(\frac{4\pi a_1 e^{i\omega_1 t}}{\lambda})\right. \qquad (A6.4)$$

Filtering out the low frequency and putting $x_h = a_h e^{i\omega_h t}$ and $x_1 = a_1 e^{i\omega_1 t}$ then

$$I_c = -\frac{A}{2}\left[\cos(4\pi x_1/\lambda)(4\pi/\lambda)^2 x_h^2\right] - (4\pi A/\lambda)x_h \sin(4\pi x_1/\lambda) \qquad (A6.5)$$

Similarly

$$I_S = -\frac{A}{2}\sin(4\pi x_1/\lambda)(4\pi/\lambda)^2 x_h^2 + (4\pi A/\lambda)x_h.\cos(4\pi x_1/\lambda) \qquad (A6.6)$$

Consider the following cases:

1. $(4\pi x_1/\lambda)_{true} = n\pi$ (where this is the true low frequency phase) therefore

$$I_c = -(A/2)(4\pi/\lambda)^2 x_h^2 \qquad (A6.7)$$

$$I_s = (4\pi A x_h)/\lambda \qquad (A6.8)$$

One method of producing the calibrated signal is to divide the two outputs to obtain in the ideal case:

$$I_c/I_s = \tan(4\pi x_1/\lambda)_{true} \qquad (A6.9)$$

or
$$I_s/I_c = 1/\tan(4\pi x_1/\lambda)_{true} \qquad (A6.10)$$

In the case considered here then an effective value of the phase is found given by

$$I_c/I_s = 4\pi x_h/2\lambda \qquad (A6.11)$$

as opposed to the ideal case which gives:

$$I_c/I_s = 0 \qquad (A6.12)$$

Again in the ideal case the solution would be

$$\tan(4\pi x_1/\lambda)_{true} = 0 \qquad (A6.13)$$

and
$$\text{True signal} = I_s \qquad (A6.14)$$

However in the non-ideal case the effective value of the phase is found as is:

$$\tan(4\pi x_l/\lambda)_{eff} = 4\pi x_h/2\lambda \qquad (A6.15)$$

where $(4\pi x_l/\lambda)_{eff}$ is the effective or measured value of this parameter. As

$$\tan\theta \simeq \theta \qquad (A6.16)$$

$$\text{then} \quad x_l \simeq x_h/2 \qquad (A6.17)$$

$$\text{therefore} \quad \cos(4\pi x_l/\lambda)_{eff} \simeq 1 - \frac{x_h^2}{8}\left(\frac{4\pi}{\lambda}\right)^2 \qquad (A6.18)$$

In an attempt to calibrate the signal the above error in the cosine would constitute the calibration error because in the ideal case $\cos(4\pi x_l/\lambda)_{true} = 1$. The error is if $4\pi x_h/\lambda = \pi/10$ given by

$$\text{Error} = \frac{\pi^2}{100} \cdot \frac{1}{8} \simeq 1/80 \simeq 1\tfrac{1}{4}\% \qquad (A6.19)$$

2. $\underline{(4\pi x_l/\lambda)_{true} = \pi/4}$ Following the method outlined above:

$$I_c = \frac{-A}{2\sqrt{2}} \cdot \left(\frac{4\pi}{\lambda}\right)^2 x_h^2 - \frac{4\pi A x_h}{\lambda} \cdot \frac{1}{\sqrt{2}} \qquad (A6.20)$$

and

$$I_s = \frac{-A}{2\sqrt{2}} \cdot \left(\frac{4\pi}{\lambda}\right)^2 x_h^2 + \frac{4\pi A x_h}{\lambda} \cdot \frac{1}{\sqrt{2}} \qquad (A6.21)$$

therefore $I_s/I_c = (-2\pi x_h/\lambda + 1)/(-2\pi x_h/\lambda - 1)$

(A6.22)

$$\text{if} \quad \frac{4\pi x_h}{\lambda} = \frac{\pi}{10} \quad \text{then } I_s/I_c = (-1 + \pi/20)/(-1 - \pi/20)$$

$$= 0.728 \qquad (A6.23)$$

therefore $\tan(4\pi x_l/\lambda)_{eff} = 0.728$

therefore $(4\pi x_l/\lambda)_{eff} = 36^o \qquad (A6.24)$

Hence instead of

$$\cos(4\pi x_1/\lambda)_{true} = 1/\sqrt{2} = 0.71$$

then

$$\cos(4\pi x_1/\lambda)_{eff} = \cos\ 36^{o} = 0.81$$

This corresponds to a 14% calibration error. Working the calculation in reverse to obtain only a 5% error then

$$\cos(4\pi x_1/\lambda)_{eff} = 0.746 \qquad \text{(A6.25)}$$

$$(4\pi x_1/\lambda)_{eff} = 41.8^{o} \qquad \text{(A6.26)}$$

writing $(1 - x)/(1 + x) = \tan\ 41.8^{o}$ (A6.27)

therefore $(1 - x)/(1 + x) = 0.894$

therefore $x = 0.056$

$$x = \pi/56 \qquad \text{(A6.28)}$$

which means for an error of 5% or less then

$$(4\pi x_h/\lambda) \lesssim \pi/30$$

or $x_h \lesssim \lambda/120$

$$x_h \lesssim 55\mathring{A} \qquad \text{(A6.29)}$$

and not $x_h \lesssim 150\mathring{A}$ as given in the first order approximation outlined in section III.6.1.

APPENDIX 7

Bessel function expansion (Neumann series) of a sinusoidal function

In section III.6.1i) various processing techniques are considered in the quadrature interferometer. These involve filtering the signals. Therefore a frequency spectrum of the following function, which appears in equation (179), is required:

$$A \sin(x \sin \theta) \tag{A7.1}$$

This may be expanded thus:

$$A\sin(x \sin \theta) = 2A \sum_{n=0}^{\infty} J_{2n+1}(x)\sin\left[(2n+1)\right] \tag{A7.2}$$

Now if x is large the Bessel function J may be approximated by

$$J_{2n+1}(x) = \sqrt{\frac{2}{\pi x}} \cdot \cos\left\{x - \frac{(4n+3)\pi}{4}\right\} + O(x^{-3/2}) \tag{A7.3}$$

The actual expression required is for

$$\sin\left(\frac{4\pi a_1}{\lambda} \cdot \sin \omega_i t\right)$$

therefore $x \equiv 4\pi a_1/\lambda$

$$\theta \equiv \omega_1 t$$

If $a_1 = 2\lambda$ then $x \simeq 25$. Hence the error is $O(0.008)$. The approximation is valid for $2n + 1 \lesssim 25$. The following values may then be calculated (unfortunately tabulated values were not available).

n	$J_{2n+1}(25)$
0	-0.152
1	+0.127
2	-0.127
3	+0.127
4	-0.127
5	+0.127
6	-0.127
7	+0.127
8	-0.127
9	+0.127
10	-0.127
11	+0.127
12	-0.127

Above this value of n, $J_{2n+1}(25)$ falls rapidly to zero. The highest frequency is approximately 25X (frequency of the unwanted vibration). The amplitude of this frequency is approximately given by

$$2 \times 0.13 \times A$$

The expansion is therefore approximately given by

$$A\sin\left(\frac{4\pi a_1}{\lambda}\sin\omega_1 t\right) \simeq 0.26A(\sin\omega_1 t+\sin 3\omega_1 t+\ldots+\sin 23\omega_1 t + \sin 25\omega_1 t) \qquad (A7.4)$$

Consider applying a Butterworth first order with a cut-off frequency ω_c to this series where

$$\omega_c = 2\pi.10^4 \text{ Hz}$$

The gain of this filter is given by

$$|G| = (\omega/\omega_c)/(1 + (\omega/\omega_c)^2)^{\frac{1}{2}} \qquad (A7.5)$$

The following table may be used:

f/Hz	|G|
30	3.0×10^{-3}
90	9.0×10^{-3}
150	1.5×10^{-2}
210	2.1×10^{-2}
270	2.7×10^{-2}
330	3.3×10^{-2}
390	3.9×10^{-2}
450	4.5×10^{-2}
510	5.1×10^{-2}
570	5.7×10^{-2}
630	6.3×10^{-2}
690	6.9×10^{-2}
750	7.5×10^{-2}

The greatest rate of change, as stated before, occurs around t = 0. Consider a time interval of 20μs. At t = 0 then:

$$A \sin(25 \sin 2\pi.30.t) = 0 \qquad (A7.6)$$

At t = 20μs then, the following table can be compiled:

f/Hz	$\sin(2\pi f.20.10^{-6})$	$\|G\|.\sin(2\pi f.20.10^{-6})$
30	0.4×10^{-2}	0.0×10^{-3}
90	1.1 " "	0.1 " "
150	1.9 " "	0.3 " "
210	2.6 " "	0.5 " "
270	3.4 " "	0.9 " "
330	4.1 " "	1.4 " "
390	4.9 " "	1.9 " "
450	5.7 " "	2.6 " "
510	6.4 " "	3.3 " "
570	7.1 " "	4.0 " "
630	7.9 " "	5.0 " "

(cont.)

690	8.7×10^{-2}	6.0×10^{-3}
750	9.4×10^{-2}	7.1×10^{-3}
	$\Sigma = 63.6 \times 10^{-2}$	$\Sigma = 33.1 \times 10^{-3}$

The total displacement due to the sum in the brackets of equation (A7.4) is after filtering:

$$A\sin(8\pi\sin\omega_i t) \simeq 8.6 \times 10^{-3}A \qquad (A7.7)$$

If the approximation

$$A\sin(8\pi\sin\omega_i t) \simeq A\sin(8\pi\omega_i t) \qquad (A7.8)$$

is used, then the value at $t = 20\mu s$ is

$$\begin{aligned} A\sin(8\pi\sin\omega_i .20\mu s) &\simeq A|G(\omega=8\pi\omega_1)|.\sin(8\pi\omega_1 .20.10^{-6}) \\ &\simeq A.7.5.10^{-2}.9.4.10^{-2} \\ &\simeq A\ 7.1.10^{-3} \qquad (A7.9) \end{aligned}$$

The two results are approximately the same (equations A7.7 and A7.9), showing that in the worst case, i.e. where the rate of change of I_C or I_S is a maximum, i.e.

$$\partial^2 I_S/\partial t^2 = 0 \qquad (A7.10)$$

which has the solution

$$\sin(\omega_1 t) = 0 \qquad (A7.11)$$

then

$$\sin\left(\frac{4\pi a_1}{\lambda}.\sin\omega_1 t\right) \simeq \sin\left(\frac{4\pi a_1}{\lambda}.\omega_1 t\right) \qquad (A7.12)$$

APPENDIX 8

An estimate of the energy introduced into a material by an artificial source from measurements made on the travelling ultrasonic waves

The application of an artificial source to a material results in the generation of a dynamic stress distribution. The energy in this distribution is split evenly between potential and kinetic energy. The potential energy is given in an orthogonal co-ordinate system x,y,z as[118]:

$$V_o = \int\left(\tfrac{1}{2}\lambda e^2 + G(e_x^2+e_y^2+e_z^2) + \tfrac{1}{2}G(\gamma_{xy}^2+\gamma_{yz}^2+\gamma_{xz}^2)\right)dxdydz \qquad (A8.1)$$

where

$e = e_x + e_y + e_z$

$e_x = \frac{\partial u}{\partial x}$ (u is the wave displacement in the x-direction)

$e_y = \frac{\partial v}{\partial y}$ (v is the wave displacement in the y-direction)

$e_z = \frac{\partial w}{\partial z}$ (w is the wave displacement in the z-direction)

$\lambda = \frac{Ev}{(1+\nu)(1-2\nu)}$

(E is Young's Modulus, ν is Poisson's ratio)

$G = \frac{1}{2}\frac{E\nu}{(1+\nu)}$

(G is the bulk modulus)

$\gamma_{xy} = \frac{\partial u}{\partial y} + \frac{\partial v}{\partial x}$

$\gamma_{xz} = \frac{\partial u}{\partial z} + \frac{\partial w}{\partial x}$

$\gamma_{yz} = \frac{\partial v}{\partial z} + \frac{\partial w}{\partial y}$

Now an easy wave to measure experimentally is the Rayleigh wave. At a large distance from the source this wave dominates over other waves types as it spreads in

only two dimensions. Let the source be at (0,0,0) and the Rayleigh wave to propagate in x and y that is in the plane z = 0. Let also the z-direction be into the material. An estimate of the Rayleigh wave displacement is then:

$$w = 0 \qquad x \geq v_S$$

$$w = \frac{e^{-kz}u_o}{\tau(v_S - v_R)} \cdot (v_S\tau - x) \qquad v_S \geq x \geq v_R\tau$$

$$w = \frac{e^{-kz}u_o}{v_R(\delta\tau)} \quad (x - v_R\tau + v_R(\delta\tau)) \qquad v_R\tau \geq x \geq v_R\tau - v_R(\delta\tau)$$

$$w = 0 \qquad v_R - v_R(\delta\tau) \geq x$$

where v_S and v_R are the velocities of the shear and Rayleigh waves respectively, τ is the time elapsed since the source was applied, and $(\delta\tau)$ is a measure of the duration of the source. The factor e^{-kz} is taken from Kolsky[140] as an approximation of the attenuation of Rayleigh waves with depth. k is the wavevector. This waveform is shown schematically below:

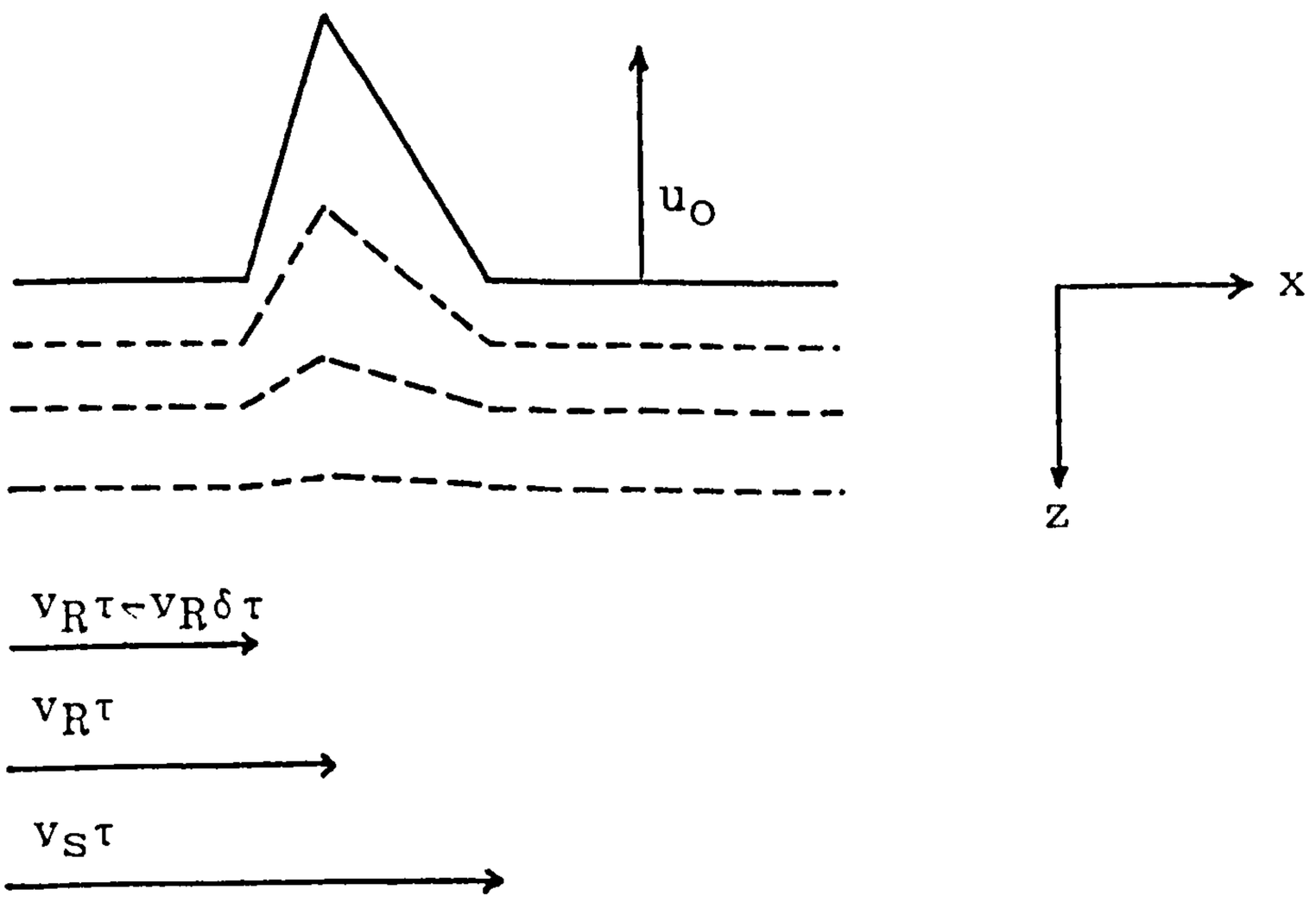

In reality the waveform changes shape with increasing z as the attenuation with depth depends on the wavevector k. Therefore a Fourier Series should be considered and the energy at each frequency determined. However, this is extremely complicated and k will be assumed to have a constant average value.

A second approximation has also been made in taking the Rayleigh wave displacement as that indicated above. This arises because the displacement of a particle in a Rayleigh wave follows an elliptical path. The displacement in the direction of motion being roughly one half of the out-of-plane motion. This effect will be approximated by including an extra factor of 3/2 in the final energy calculations and as such neglects the cross products in equation (A8.1).

For ease of calculation a short section of the wavefront is considered about the line y = 0 (see below). The wavefront can then be assumed plane at this point.

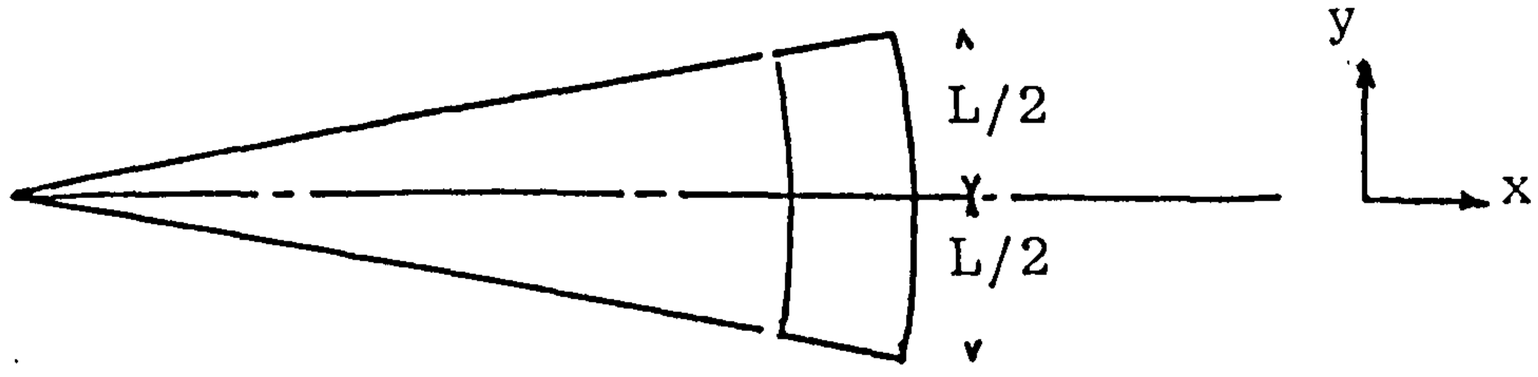

With the above approximations on the Rayleigh wave then

$$\frac{\partial w}{\partial y} = 0$$

$$u = v = 0$$

Therefore

$$V_o = \frac{3}{2} \int \left(\tfrac{1}{2}\lambda e_z^2 + G e_z^2 + \tfrac{1}{2} G \left(\frac{\partial w}{\partial x} \right)^2 \right) dx dy dz \qquad (A8.4)$$

Now for aluminium $E = 7.1 \times 10^9$ and $\nu = 0.34$ giving $\lambda = 0.79E$ and $G = 0.37E$. Substituting now into equation (A8.4) from equation (A8.2) and integrating yields:

$$V_o = \frac{3}{4} E L u_o^2 \left[0.26k \left(v_R(\delta\tau) + \tau(v_S - v_R) \right) + \frac{0.19}{k} \left(\frac{1}{v_R(\delta\tau)} + \frac{1}{\tau(v_S - v_R)} \right) \right] \qquad (A8.5)$$

So far this is an estimate of the potential energy in the Rayleigh wave over the short section of wavefront given by $|y| < L/2$. To include the entire wavefront a factor of $2\pi r/L$ is introduced where r is the distance travelled. The energy is then further assumed to be evenly distributed between the potential energy calculated above and kinetic energy. The total energy is therefore increased by a further factor of 2 in this case. Finally it is assumed one half of the energy from the source enters into the bulk of the material. Therefore to estimate the energy of the source equation (A8.5) should be multiplied by $8\pi r/L$.

All that is required now is an estimate of k. The source is considered to have a frequency spread which is

Gaussian with a full width half maximum (FWHM) value of $\Delta\omega$. The time duration of the Rayleigh pulse is $2(\delta\tau)$ (FWHM). From Hecht and Zajac[37] then $\Delta\omega 2(\delta\tau) \simeq 4\pi$, or $(\Delta\omega/2)(\delta\tau) \simeq \pi$. $(\Delta\omega/2)$ is now the frequency spread from zero to the half power frequency point of the source. The value of k is taken as that corresponding to $(\Delta\omega/2)$ and because $kv_R(\delta\tau) = (\Delta\omega/2)(\delta\tau)$ then $kv_R(\delta\tau) \simeq \pi$. Now $(\delta\tau)$ is measured to be $\sim 0.6\mu s$ and so $k \simeq 1.8mm^{-1}$. With $v_S = 3.11mm.\mu s^{-1}$ and $v_R = 2.91mm.\mu s^{-1}$ the total energy of the source can be calculated using equation (A8.5) together with the extra factor of $(8\pi r/L)$ when the values of u_o and r are measured. These are $7.2 \times 10^{-10}m$ and $80 \times 10^{-3}m$ respectively giving a total source energy of 200nJ. This figure agrees reasonably well with that of 350nJ estimated from the initial deformation (see section IV.1.1ii)b)i)).

APPENDIX 9

The flexing of the cantilever shown in Figure 95

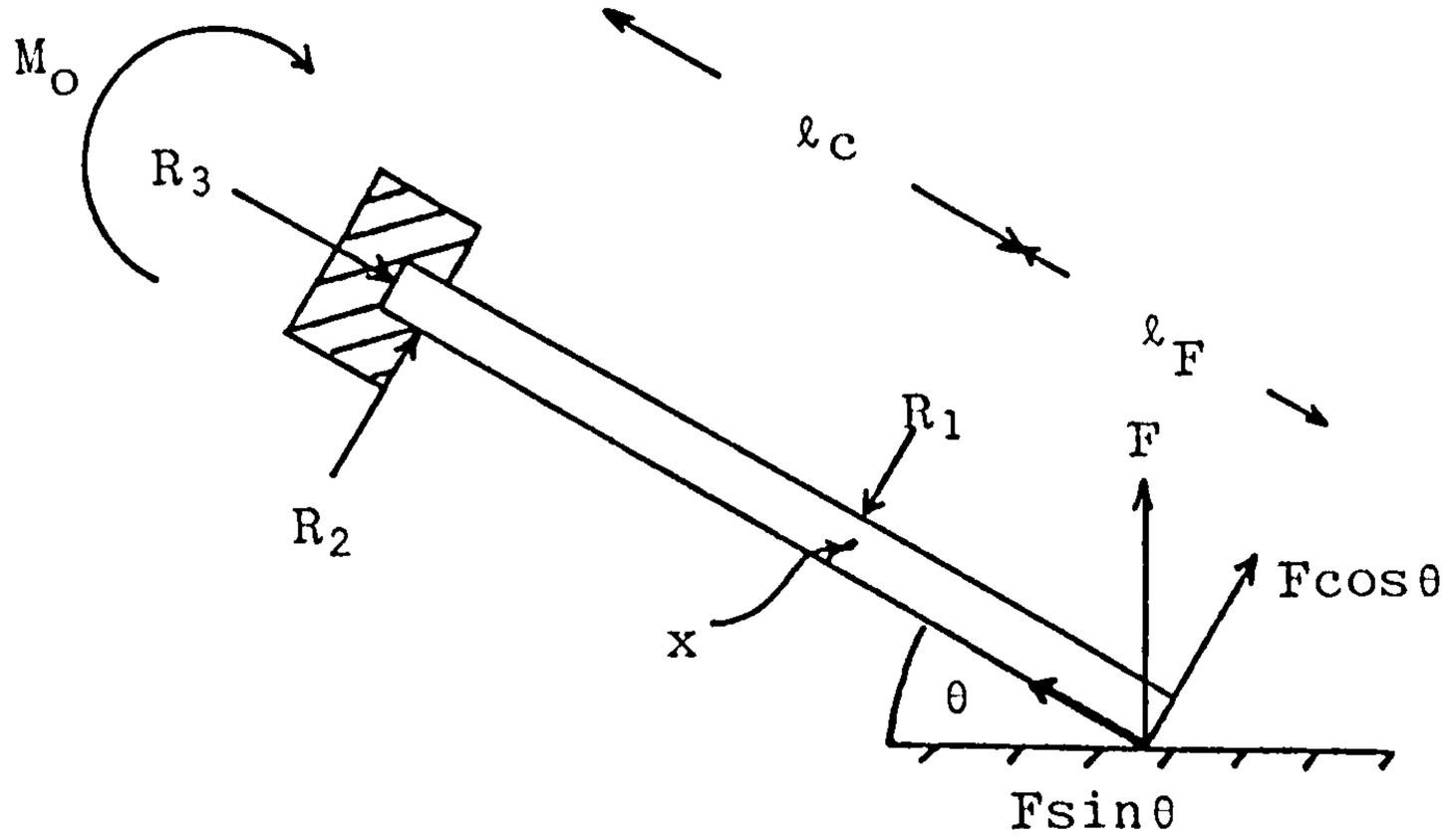

The forces on the rod may be derived as follows:

Resolving along the rod yields:

$$F\sin\theta = R_3 \qquad \text{(A9.1)}$$

Resolving perpendicularly to the rod's axis yields:

$$R_2 + F\cos\theta = R_1 \qquad \text{(A9.2)}$$

Taking moments about X yields:

$$R_2\ell_C + M_O = F\ell_F\cos\theta \qquad \text{(A9.3)}$$

Solving (A9.2) and (A9.3) for R_2 and M_O leads to:

$$R_2 = R_1 - F\cos\theta \qquad \text{(A9.4)}$$

$$M_O = F(\ell_F + \ell_C)\cos\theta - \ell_C R_1 \qquad \text{(A9.5)}$$

Consider the equilibrium of a section or rod now to determine the flexing.

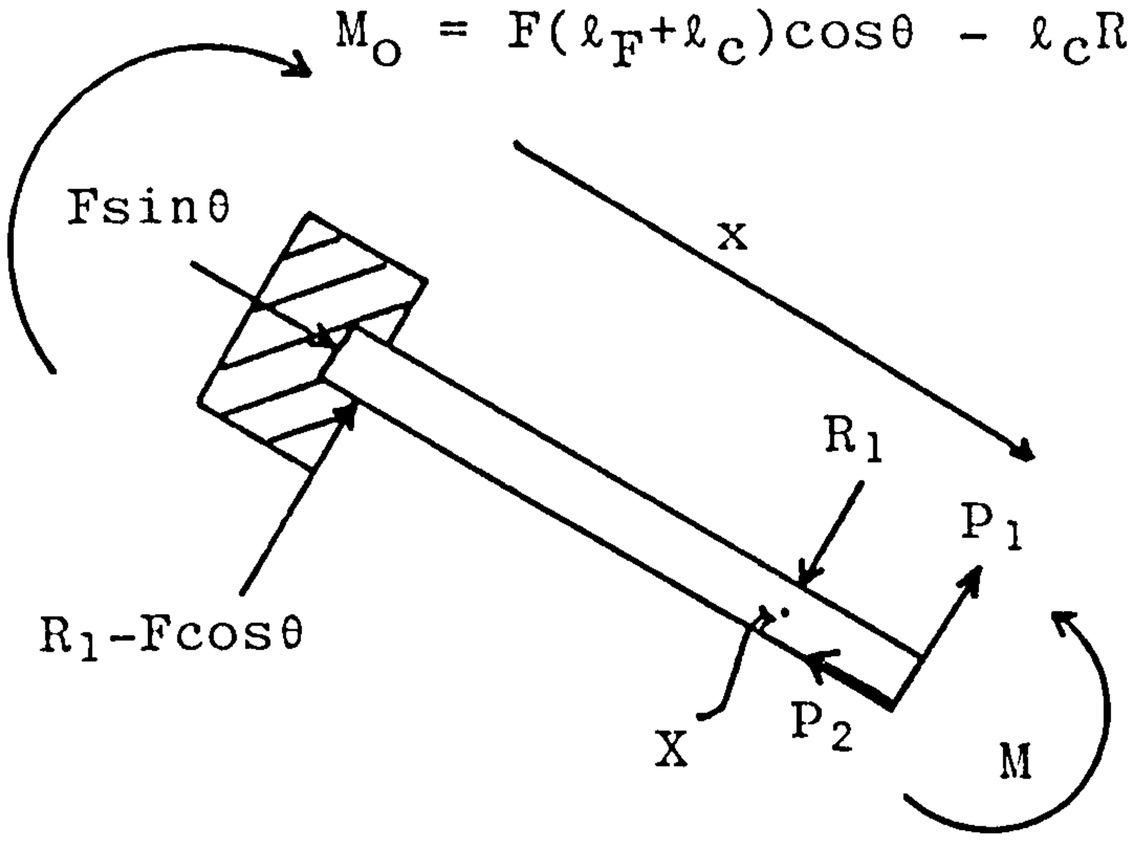

Resolving perpendicularly to the rod gives:

$$P_1 = F\cos\theta \qquad (A9.6)$$

and parallel gives:

$$P_2 = F\sin\theta \qquad (A9.7)$$

Taking moments above X again leaves:

$$M = F\cos\theta\ (\ell_F - x + \ell_C) \qquad (A9.8)$$

Taking now the equilibrium of another section:

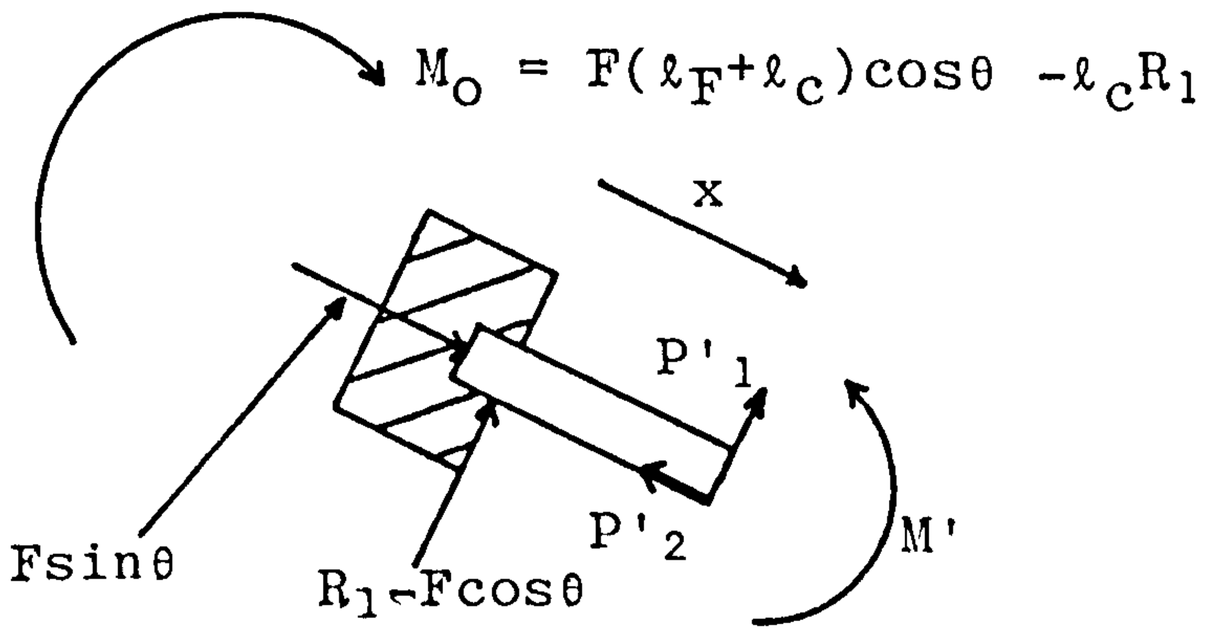

Solving in a similar manner to above

$$P_2' = F\sin\theta \qquad (A9.9)$$

$$P_1' = F\cos\theta - R_1 \qquad (A9.10)$$

$$M' = R_1(x - \ell_C) + F\cos\theta(\ell_F+\ell_C-x) \qquad (A9.11)$$

Returning now to equation (A9.8). It can be shown[119] that:

$$M = EI\frac{d^2y}{dx^2} \qquad (A9.12)$$

where E is Young's Modulus, I the second moment of area of the cross section and y the displacement of the axis along the beam.

Therefore from (A9.8):

$$EI\frac{d^2y}{dx^2} = F\cos\theta\ (\ell_R + \ell_C - x) \qquad (A9.13)$$

and in a similar manner equation (A9.11) leads to

$$EI\frac{d^2y}{dx^2} = R_1(x - \ell_C) + F\cos\theta\ (\ell_F + \ell_C - x) \qquad (A9.14)$$

Integrating (A9.14):

$$EI\frac{dy}{dx} = R_1\left(\frac{x^2}{2} - \ell_C x\right) + F\cos\theta\left(\ell_F x + \ell_C x - \frac{x^2}{2}\right) \qquad (A9.15)$$

where A is a constant of integration. The boundary conditions are at $x = 0$, $y = 0$ and $\frac{dy}{dx} = 0$ as this end is clamped. This means $A = 0$. Integrating (A9.15) again with $A = 0$ gives

$$EI_y = R_1\left(\frac{x^3}{6} - \frac{\ell_C x^2}{2}\right) + F\cos\theta\left(\frac{\ell_F x^2}{2} + \frac{\ell_C x^2}{2} - \frac{x^3}{6}\right) \qquad (A9.16)$$

where again the constant of integration is zero.

The second set of boundary conditions is at the point of application of R_1. In the practical situation R_1 occurs where the steel collar of the pencil touches the extending lead. It is assumed the collar is much more rigid than the lead and so at this point $x = \ell_C$ then $y = 0$. From equation (A9.16) this condition becomes:

$$0 = R_1\left(-2\ell_C{}^3\right) + F\cos\theta\left(2\ell_C{}^3 + 3\ell_F\ell_C{}^2\right) \qquad (A9.17)$$

Therefore

$$R_1 = F\left(\frac{2\ell_C + 3\ell_F}{2\ell_C}\right)\cos\theta \qquad (A9.18)$$

Returning the result of (A9.18) into (A9.16) gives:

$$y = \frac{F\ell_F}{4EI}\cos\theta\left(\frac{x^3}{\ell_C} - x^2\right) \qquad (A9.19)$$

Equation (A8.13) may now be integrated. This gives

$$EI\frac{dy}{dx} = F\cos\theta\left(\left(\ell_F x + \ell_C x - \frac{x^2}{2}\right) + C\right) \qquad (A9.20)$$

At $x = \ell_C$, $\frac{dy}{dx}$ from (A9.19) and (A9.20) should be the same. Therefore

$$\frac{F\ell_F\ell_C}{4}\cos\theta = F\cos\theta\left(\left(\ell_F\ell_C + \frac{\ell_C{}^2}{2}\right) + C\right) \qquad (A9.21)$$

giving

$$C = -\frac{3\ell_F\ell_C}{4} - \frac{\ell_C{}^2}{2} \qquad (A9.22)$$

Equation (A9.20) integrated again gives

$$EI_y = F\cos\theta\left(\frac{\ell_F x^2}{2} + \frac{\ell_C x^2}{2} - \frac{x^3}{6} - \frac{3\ell_F\ell_C x}{4} - \frac{\ell_C{}^2 x}{2} + D\right) \qquad (A9.23)$$

Solving for D using $y = 0$ at $x = \ell_C$ gives:

$$D = \frac{F\ell_C^2}{4} + \frac{\ell_C^3}{6} \qquad (A9.24)$$

Equation (A9.23) may now be rewritten as:

$$y = \frac{F\cos\theta}{EI}\left(\frac{-x^3}{6} + \left(\frac{\ell_F+\ell_C}{2}\right)x^2 - \left(3\ell_F\ell_C+2\ell_C^2\right)\frac{x}{4} + \frac{\ell_F\ell_C^2}{4} + \frac{\ell_C^3}{6}\right)$$

(A9.25)

One figure of interest that may be derived from this result is the displacement of the neutral axis at $x = \ell_F+\ell_C$. This is

$$y(x = \ell_F+\ell_C) = \frac{F\cos\theta}{12EI}\left(4\ell_F^3+3\ell_F^2\ell_C\right) \qquad (A9.26)$$

<u>or</u>

$$y(x = \ell_F+\ell_C) = \frac{F\ell_C^3}{12EI}\cos\theta\left(4\left(\frac{\ell_F}{\ell_C}\right)^3 + 3\left(\frac{\ell_F}{\ell_C}\right)^2\right)$$

(A9.27)

This value of y may be plotted as a function of (ℓ_F/ℓ_C). For a lead held in the pencil $\ell_C \approx 14.0 \pm 0.2$mm and for 12 clicks of the propelling mechanism $\ell_F = 7.0 \pm 0.1$mm giving $\ell_F/\ell_C = 0.50 \pm 0.01$.

The flexing of the beam is shown schematically below:

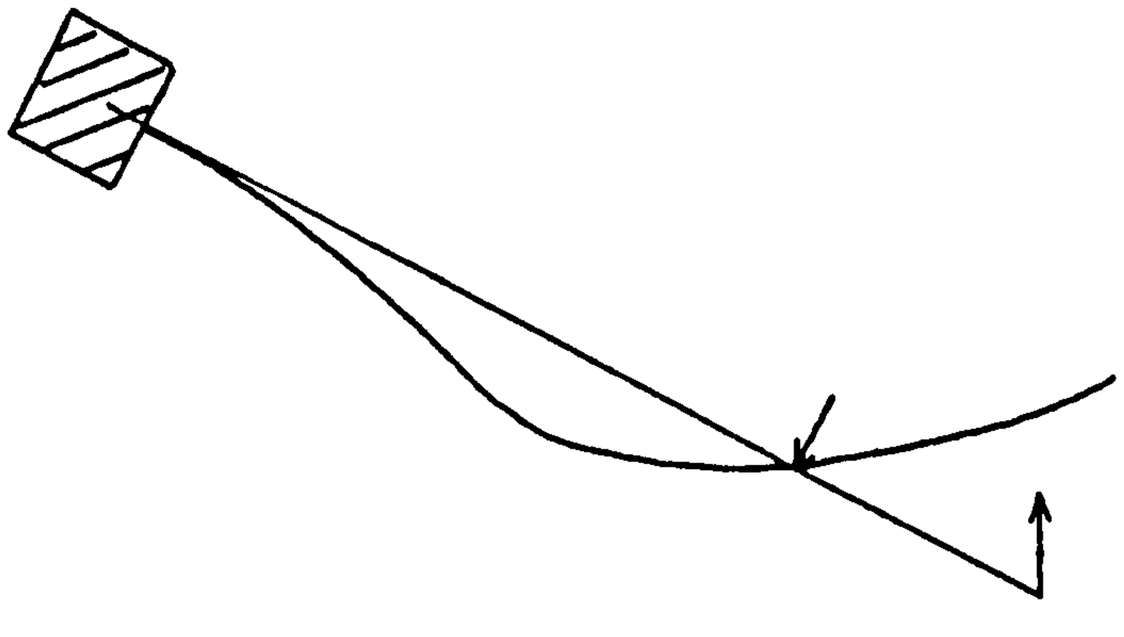

$y.\left(\frac{12EI}{F\ell_c^3\cos\theta}\right)$	ℓ_F/ℓ_c	Number of clicks
0	0.00	0
0.008	0.05	1.2
0.034	0.10	2.4
0.081	0.15	3.6
0.152	0.20	4.8
0.250	0.25	6
0.378	0.30	7.2
0.539	0.35	8.4
0.736	0.40	9.6
0.972	0.45	10.8
1.250	0.50	12

A second point of interest is the angle of bend of the free length of the lead. This may be approximated by determining $\frac{dy}{dx}$ at $x = \ell_c$ and $x = \ell_c + \ell_F$. Equation (A9.20) is

$$\frac{dy}{dx} = \frac{F\cos\theta}{EI}\left\{\left(\ell_F x + \ell_c - \frac{x^2}{2} - \frac{3\ell_F\ell_c}{4} - \frac{\ell_c^2}{2}\right)\right. \tag{A9.28}$$

At $x = \ell_c$ $\left.\frac{dy}{dx}\right)_{\ell_c} = \frac{F\cos\theta}{EI}\ \frac{\ell_F\ell_c}{4}$ (A9.29)

(A9.29)

At $x = \ell_c + \ell_F$ $\left.\frac{dy}{dx}\right)_{\ell_c+\ell_F} = \frac{F\cos\theta}{EI}\left(\frac{\ell_F^2}{2} + \frac{\ell_c\ell_F}{4}\right)$ (A9.30)

The difference in these gradients is approximately equal to the bending angle in radians, therefore

$$\theta\text{bend} = \frac{F\cos\theta}{EI}\left(\frac{\ell_F^2}{2}\right) \tag{A9.31}$$

Now that the form of the bending has been determined the fracture process will be considered.

The lead will fracture when the tensile stress at any one point exceeds a given critical value. It can be shown that the stress along the x-axis in the loaded beam is given by

$$\sigma_{xx} = zM/I \qquad (A9.32)$$

where z is the distance from the neutral axis. The neutral axis is the axis which for pure bending is unstressed. Taking the second differential of (A9.19) the position of maximum stress is found to occur, at $x = \ell_c$ which is the same position calculated from equation (A9.13). Using equation (A9.8) the stress at $x = \ell_c$ is given by

$$\sigma_{xx(x=\ell_c)} = \frac{z(F\cos\theta)\ell_F}{I} \qquad (A9.33)$$

Consider the fracture when $\theta = 0$. In this case $\sin\theta = 0$ and the only stress in the lead is that described by equation (A9.33).

The first result predicted by this theory is that the fracture force is inversely proportional to the free lead length.

A second result is that the part of the lead fracturing is under tension. A compressional release wave is therefore expected to reach the free end of the lead first and to be reflected from this end as a tensional wave. However, this wave arrives parallel to the surface being loaded and therefore will have little effect. As the lead is bent there will also be flexural waves set up. These

will have the largest amplitudes when the initial angle of bend is the largest. From equation (A9.31) this is found to occur when ℓ_F is long. Therefore when $\theta \simeq 0$ as the free lead length becomes longer then larger flexural waves travel towards the surface thus assuming the surface to experience a compressional force prior to the main releasing tensional force.

For the case when $\theta \neq 0$ the state of stress is given both by equation (A9.33) and also by a component due to the $F\sin\theta$ force which is

$$\sigma_{xx} = \frac{F\sin\theta}{\pi r^2} \qquad (A9.34)$$

where r is the cross sectional radius of the lead. The total stress is therefore

$$\sigma_{xx} = \frac{Z(F\cos\theta)\ell_F}{I} + \frac{F\sin\theta}{\pi r^2} \qquad (A9.35)$$

The lead fractures when $\sigma_{xx} = -T$ which occurs at $z = -r$ i.e. when

$$-T = -r\ (F\cos\theta)\ \frac{\ell_F}{I} + \frac{F\sin\theta}{\pi r^2} \qquad (A9.36)$$

If $\cos\theta = \sin\theta = 1/\sqrt{2}$, (A9.36) becomes

$$-T = \frac{+F}{\sqrt{2}} \left(\frac{-r\ell_F}{I} + \frac{1}{\pi r^2}\right) \qquad (A9.37)$$

I is of the order of $r^4/20$ and so (A9.37) is

$$-T = \frac{+F}{\sqrt{2}\pi r^2} \left(1 - \frac{20\ell_F\pi}{r}\right) \qquad (A9.38)$$

Therefore the solution is very nearly given by

$$-T = -r(F\cos\theta)\ \frac{\ell_F}{I} \qquad (A9.39)$$

No difference exists then in the state of stress for the two cases of $\theta = 0$ and $\theta \neq 0$ with the fracturing occurring due to flexure in each case. However for the case when $\theta \neq 0$ compressional and flexural waves travelling down the lead from the fracture may couple into the loaded surface more easily.

APPENDIX 10

Tests performed on the Fast Fourier Transform algorithm

The Fourier transform $g(\omega)$ of a function $f(t)$ and the function itself are related by[63]:

$$g(\omega) = \frac{1}{(2\pi)^{\frac{1}{2}}} \int_{-\infty}^{+\infty} f(t)e^{-i\omega t}\, dt \qquad (A10.1)$$

and

$$f(t) = \frac{1}{(2\pi)^{\frac{1}{2}}} \int_{-\infty}^{+\infty} g(\omega)e^{i\omega t}\, d\omega \qquad (A10.2)$$

where $g(\omega)$ is the Fourier coefficient at a frequency ω. Now only a finite length of trace can be captured in any real situation. The trace is assumed to exist over (0,T) and be zero at all other times. (There are certain exceptions to this,one example of which is shown in section VI.2.1). Equation (A10.1) may then be rewritten as

$$g(\omega) = \frac{1}{(2\pi)^{\frac{1}{2}}} \int_{0}^{T} f(t)e^{-i\omega t}\, dt \qquad (A10.3)$$

Now the trace actually consists of N discrete points over this period T. Therefore an upper frequency exists which is determined to have a time period of $\frac{2T}{N}$. The value, at all the N points, of a sinusoidal function of frequency greater than (2T/N) may always be determined by a function whose frequency is below (2T/N).

As the trace has been measured over a finite length T and is set to zero outside this period then its frequency spectrum may be described by a discrete set of values given by (p/T) where p is an integer. The complete set of frequencies (ω_p) is therefore:

$$0, \pm \frac{2\pi}{T}, \pm \frac{2.2\pi}{T} \pm \frac{3.2\pi}{T} \ldots\ldots \pm \left(\frac{2}{N} - 1\right)\frac{2\pi}{T}, \pm \frac{2}{N}\cdot\frac{2\pi}{T}$$

This gives N + 1 points and usually the $\frac{-4\pi}{NT}$ frequency is dropped. This set of frequencies may be considered as having cyclic periodicity. Usually only the first few frequencies are used.

Equation (A10.3) may be written then as

$$g(\omega_p) = \frac{1}{(2\pi)^{\frac{1}{2}}} \sum_{m=0}^{m=N} f\left(\frac{mT}{N}\right).e^{-i\omega p\frac{mT}{N}}.\ \frac{mT}{N} \qquad (A10.4)$$

where $\omega_p = 2\pi p/T$ with p an integer. This expression is then evaluated by computer and should yield the same result as equation (A10.1).

The inverse transform of equation (A10.2) may also be rewritten as

$$f(t_m) = \frac{1}{(2\pi)^{\frac{1}{2}}} \sum_{p=\left(\frac{2}{N} -1\right)\frac{2\pi}{T}}^{P=\frac{2}{N}\cdot\frac{2\pi}{T}} g(2\pi p/T)e^{\frac{i.2\pi p}{T}.t_m}.\ \frac{1}{T} \qquad (A10.5)$$

where $t_m = \frac{mT}{N}$ with m an integer.

This is also evaluated by computer and should yield the same result as equation (A10.2) at the discrete times shown and over the interval (0,T) as indicated.

To test the Fast Fourier transform used then a simple function is transformed both by the FFT and analytically. The function tested is as follows:

$$f(t) = 0 \qquad t < 0$$

$$f(t) = 3.81V \qquad 0 < t < 8.05\mu s$$

$$f(t) = 0 \qquad t > 8.05\mu s$$

with T = 10.24 s and N = 1024.

Equation (A10.1) is evaluated at first:

$$g(\omega) = \frac{1}{(2\pi)^{\frac{1}{2}}} \int_0^{0.786T} 3.81e^{-i\omega t}\, dt \qquad (A10.6)$$

It is found that the FFT produces a transform for this which is symmetric about zero for the real component and antisymmetric for the imaginary component as predicted by theory. Therefore only positive frequencies are tested. Equation (A10.6) provides the theoretical curves shown below in Figures (A10.1) and (A10.2) for the phase and modulus of the transform. The points are those generated by the FFT algorithm. The agreement is excellent indicating that the FFT (in the absence of significant noise) generates an accurate Fourier transform. The question of noise will now be looked at in more detail.

A similar waveform to that above is used to investigate the effects of noise. This is shown in Figure (A10.3). The waveform is made up of white noise superimposed on top on the following:

$$f(t) = \alpha \qquad t \leqslant 0$$

$$f(t) = \beta + \alpha \qquad 0 < t < 8.11\mu s$$

$$f(t) = \alpha \qquad t \geqslant 8.11\mu s$$

The small offset α results from the addition of noise and as it affects only the DC component it is ignored. Equation (A10.6) again provides theoretical curves for the phase and modulus of the transform shown in Figures (A10.4) and (A10.5). The results provided from the FFT

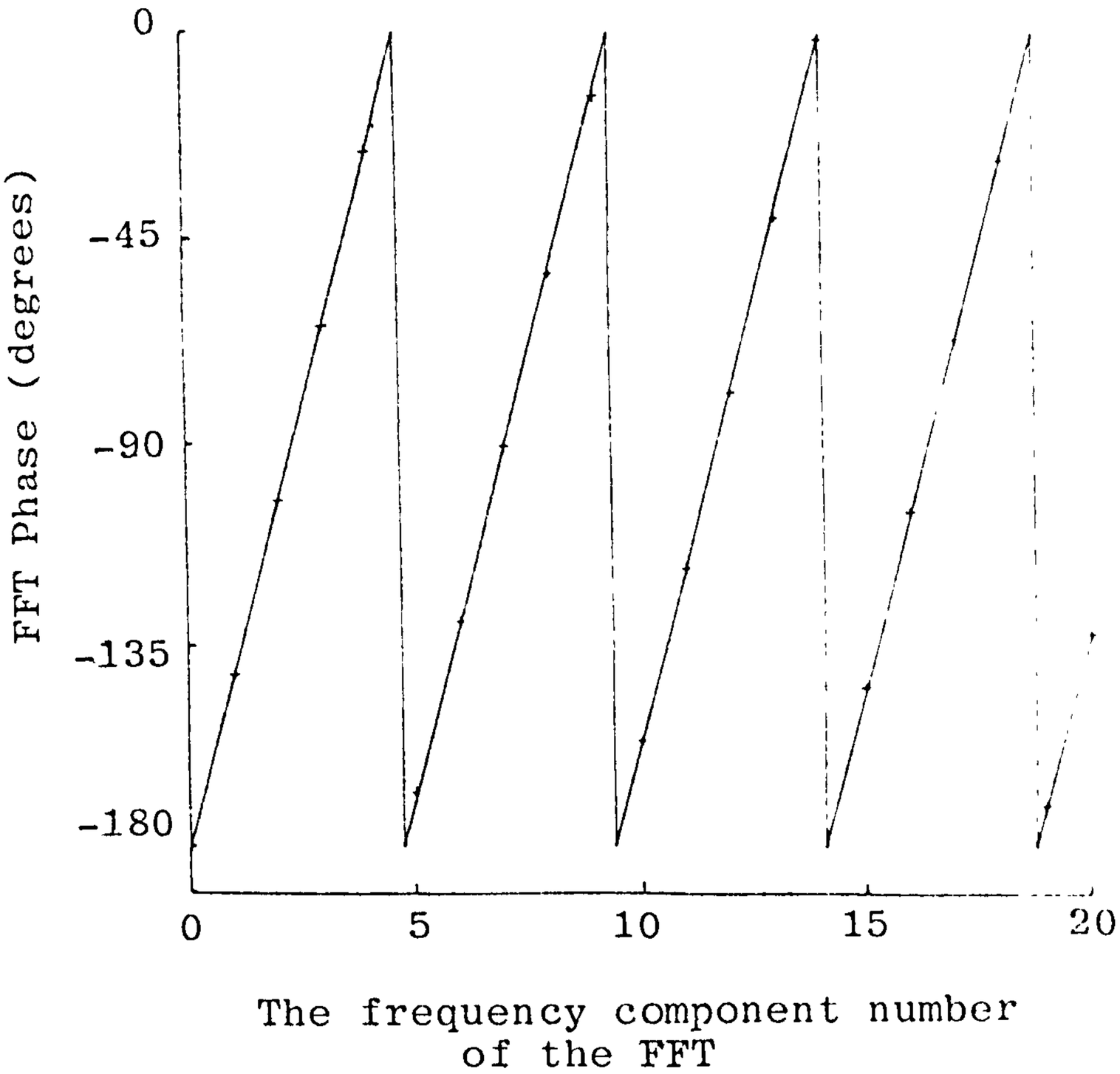

Figure A10.1

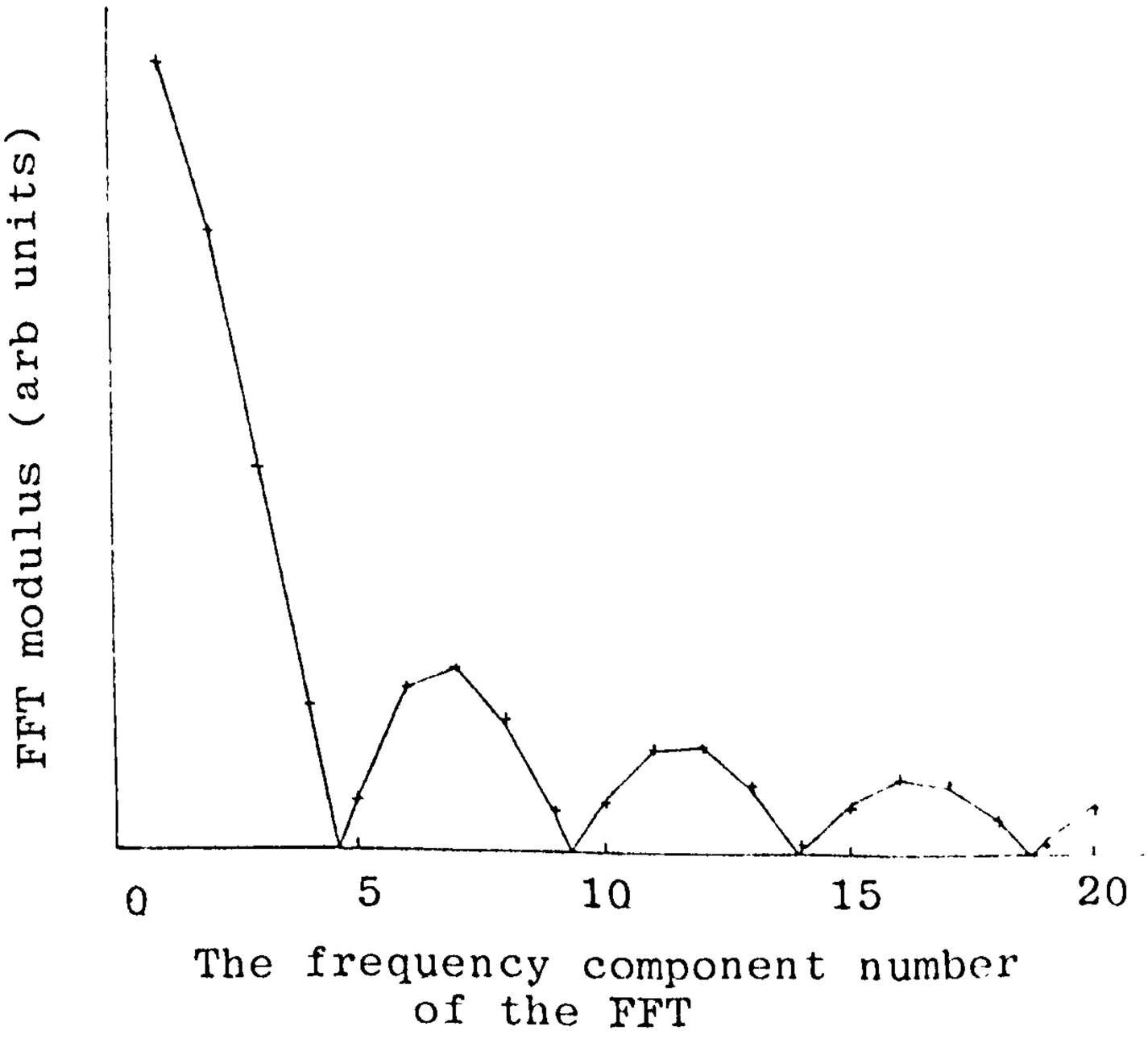

Figure A10.2

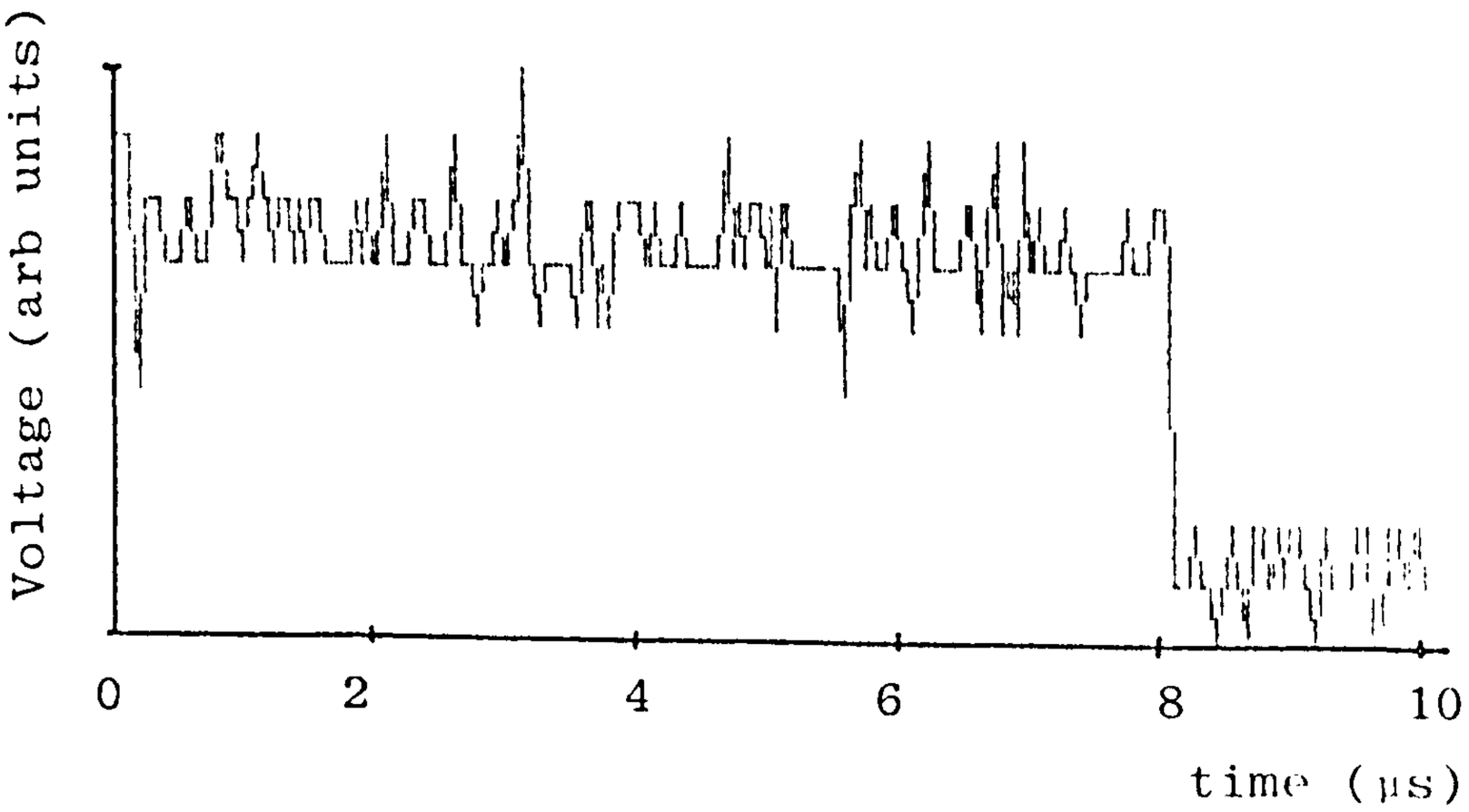

Figure A10.3

are then superimposed on top of these curves.

Clearly there is no longer perfect agreement between the FFT results and the true Fourier transform. In order to determine whether these errors are significant then the method in which the results will be used must be considered. The phase results are generally used in calibration calculations as part of a complex division. In other words, the difference between two phases is calculated, one phase arising from a calibrated, for example optical transducer, and the other from the transducer under test. The errors on the phase will in general make such subtractions subject to large uncertainties.

The modulus information, on the other hand, when used as part of a complex division is only utilised in the normal division part of the computation. The errors which would result from such a division are of the order of 20% or so for the higher frequency values. Therefore because

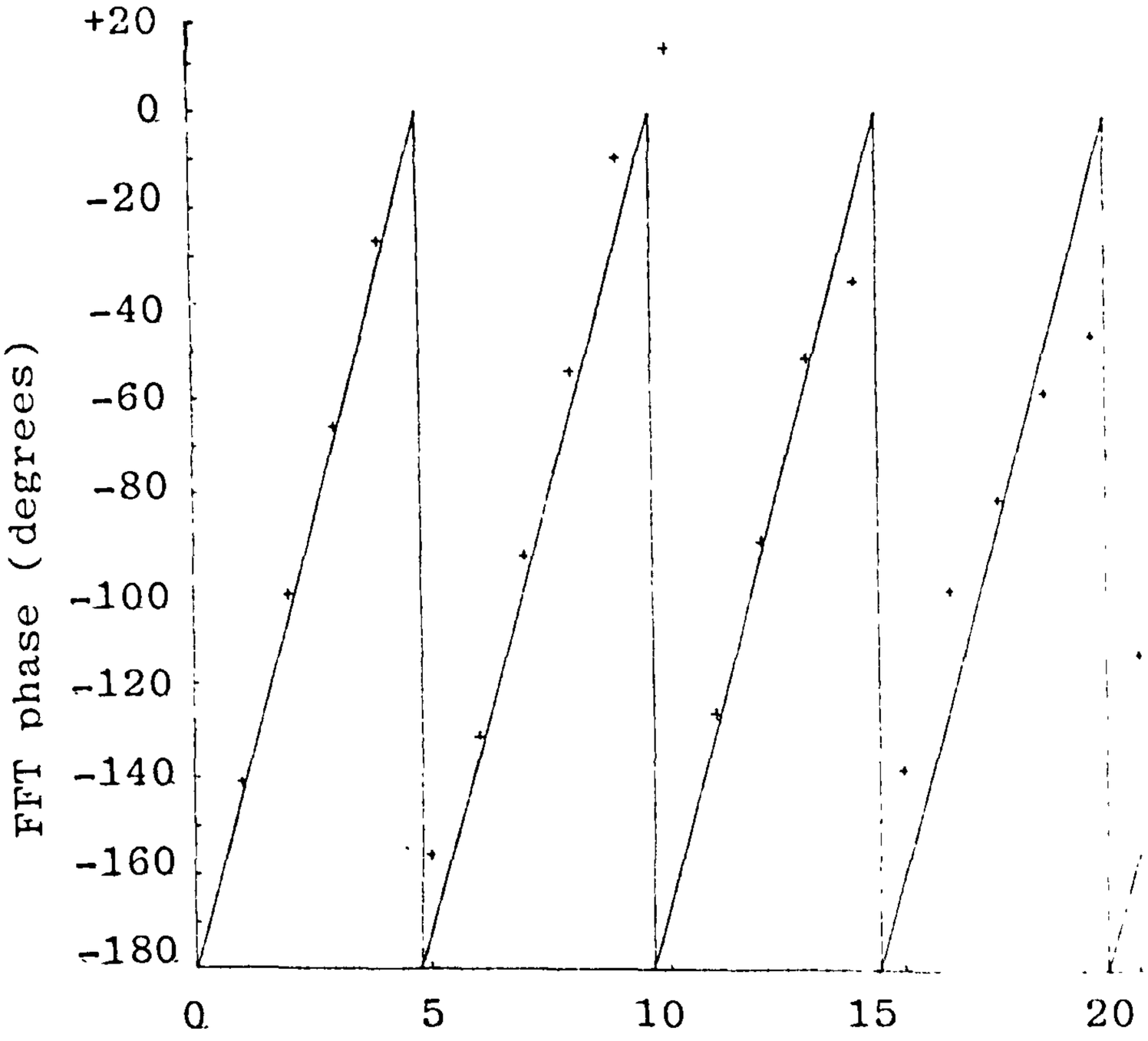

Figure A10.4

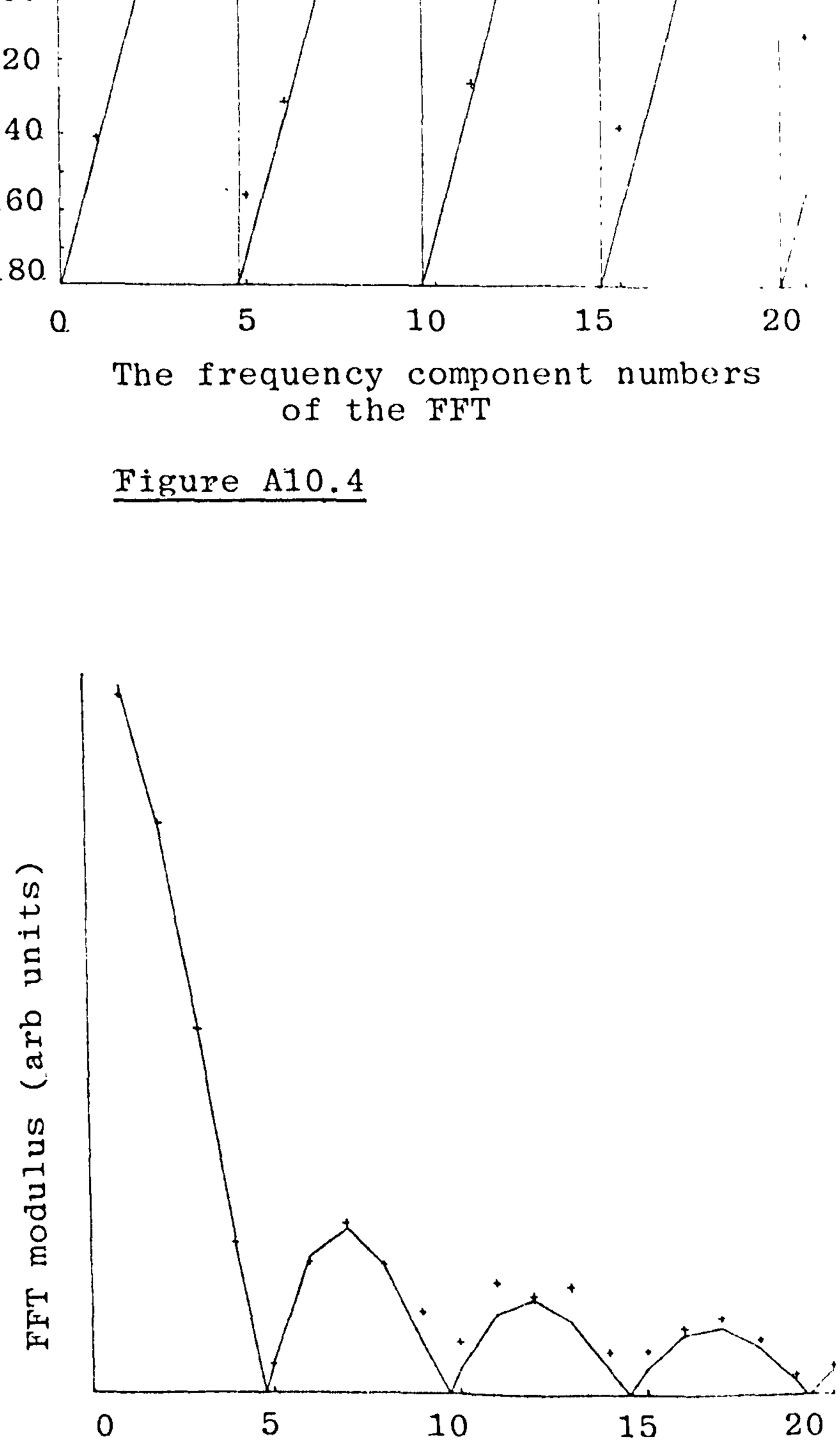

Figure A10.5

a division of large numbers has been performed here rather than a subtraction of small numbers the final value of the modulus part of the complex division is likely to be more accurate than the phase value.

Therefore calibration should be performed when the time division trace is noisy, in terms of the modulus only.

APPENDIX 11

The numerical convolution of an experimentally measured source function with a theoretical Green's function

In order to perform a convolution between a measured source function and a theoretical propagation function then equation (254) must be evaluated. To do this first of all the source is digitized.

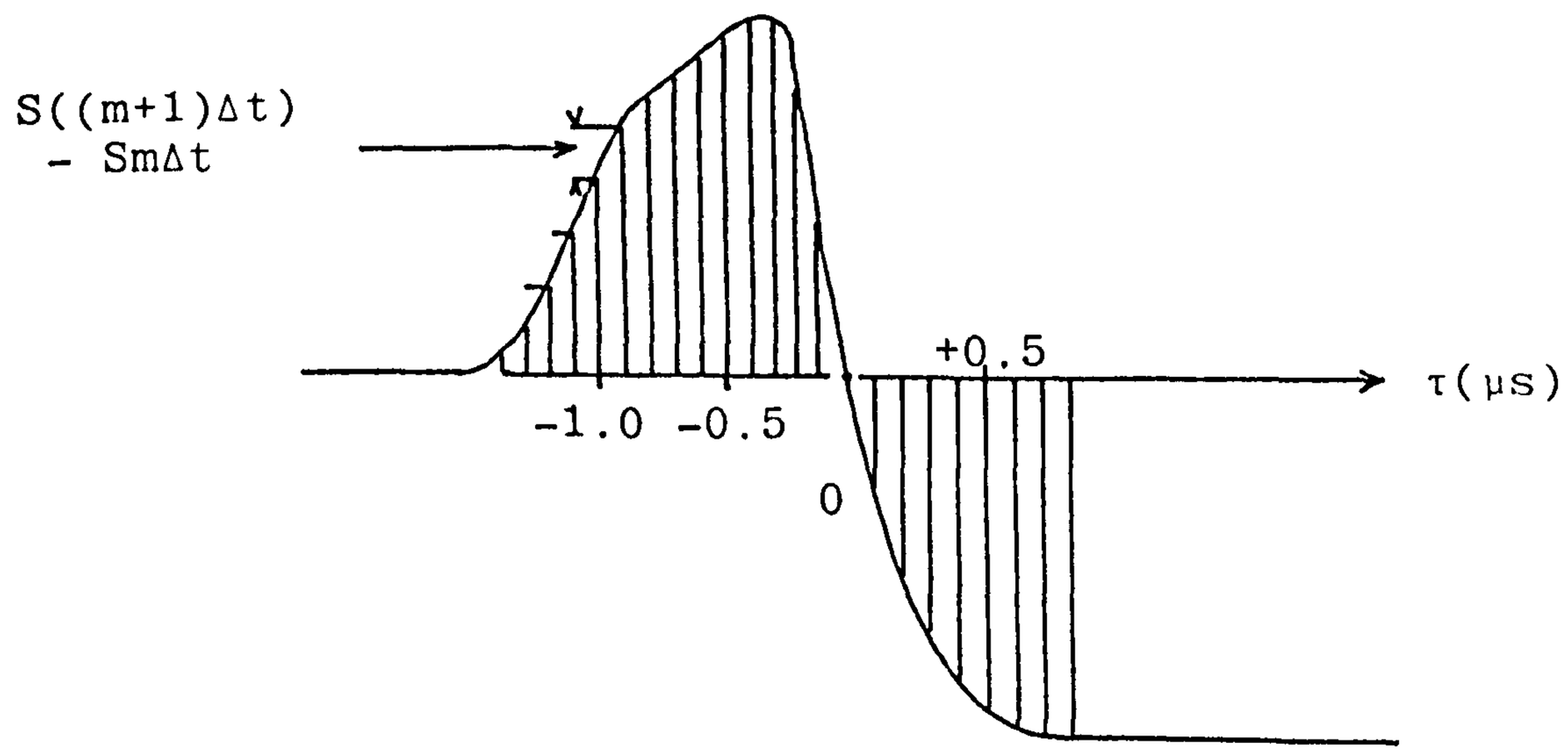

This is shown schematically above. The values are taken at time intervals (of 0.1μs) as shown. The figure of interest is then the difference between successive heights. This is the term (S((m+1)Δt) - S(mΔt)) in equation (254). These are as follows:

t/μs	Value of trace /arb. units	Height of step /arb. units
-1.4	0.0	0.0
-1.3	2.5	2.5
-1.2	7.0	4.5
-1.1	13.2	6.2
-1.0	17.0	3.8
-0.9	20.0	3.0
-0.8	23.9	3.9
-0.7	26.8	2.9
-0.6	30.0	3.2
-0.5	31.8	1.8
-0.4	34.3	2.5
-0.3	35.0	0.7
-0.2	29.0	-6.0
-0.1	22.9	-6.1
0	0.0	-22.9
+0.1	-18.8	-18.8
+0.2	-30.0	-11.2
+0.3	-36.5	-6.5
+0.4	-40.7	-4.2
+0.5	-42.0	-1.3
+0.6	-43.0	-1.0

The theoretical waveform for a zero rise time step is now digitized. The waveform is taken from Mooney[25] for ν(Poisson's ratio) = 1/3. The digitizing is performed as shown overleaf with values taken every 0.1μs again. This generates the series given in the table overleaf.

A11.3

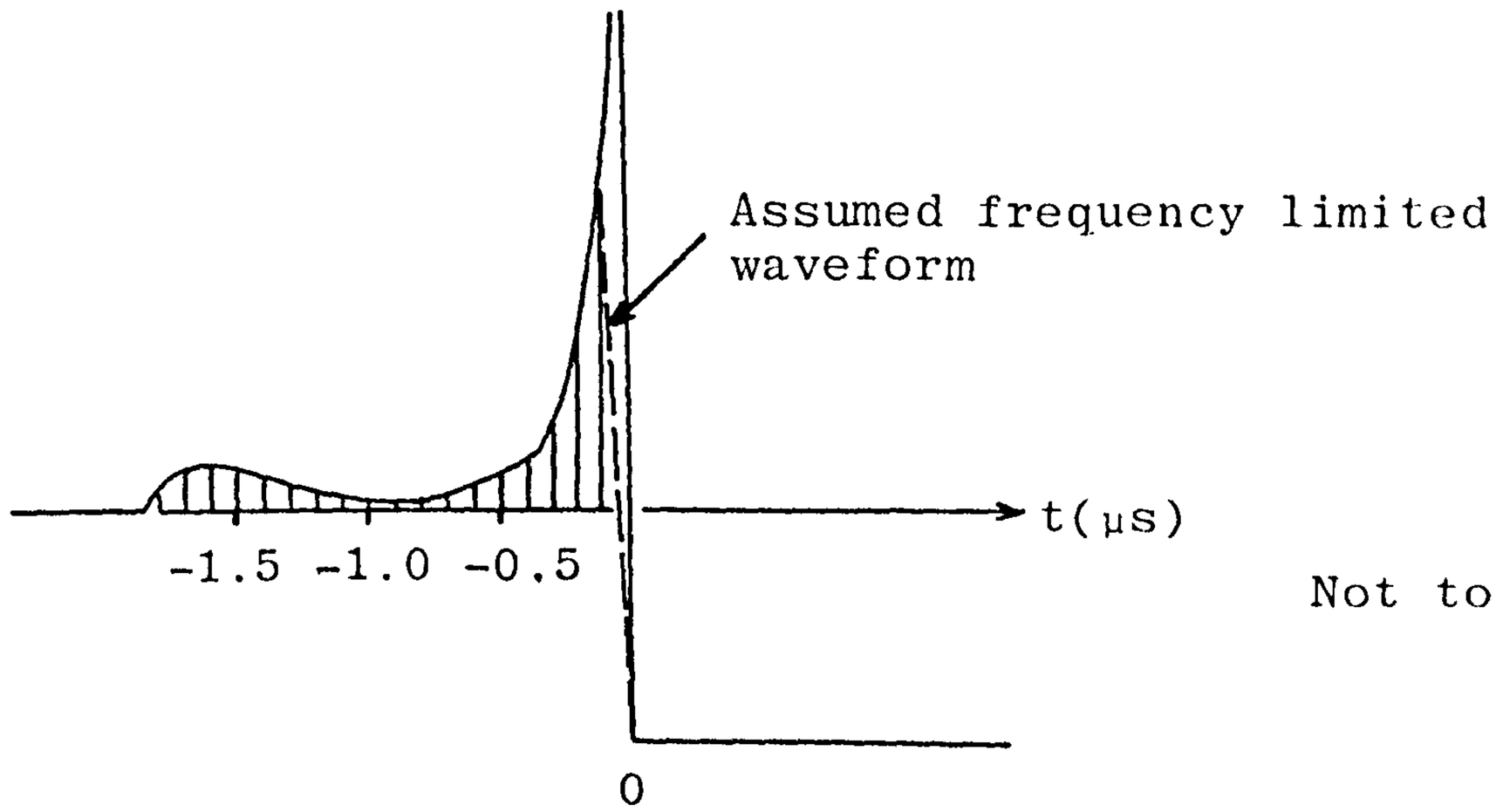

Not to scale

t/μs	Height of trace/arb. units	t/μs	Height of trace/arb. units
0.0	-8.7	-2.1	+0.71
-0.1	+26.8	-2.2	+0.65
-0.2	+14.9	-2.3	+0.62
-0.3	+11.0	-2.4	+0.59
-0.4	+7.3	-2.5	+0.55
-0.5	+5.8	-2.6	+0.50
-0.6	+4.3	-2.7	+0.48
-0.7	+3.0	-2.8	+0.48
-0.8	+2.6	-2.9	+0.45
-0.9	+2.15	-3.0	+0.44
-1.0	+1.92	-3.1	+0.42
-1.1	+1.75	-3.2	+0.40
-1.2	+1.60	-3.3	+0.39
-1.3	+1.44	-3.4	+0.40
-1.4	+1.30	-3.5	+0.40
-1.5	+1.20	-3.6	+0.40
-1.6	+1.12	-3.7	+0.41
-1.7	+1.05	-3.8	+0.42
-1.8	+0.95	-3.9	+0.44
-1.9	+0.86	-4.0	+0.46
-2.0	+0.80		

To calculate the final convoluted trace the following procedure is adopted. The height of the first step on the source (at -1.3μs) is multiplied by the height of the theoretical trace at every time interval. The theoretical trace is then moved on one interval and the height of the second step on the source is then multiplied by the now displaced theoretical trace. This gives another set of figures. These figures are added to the original set at the correctly corresponding times. The procedure is followed until the entire source is covered. As the theoretical trace does not start at zero then the calculation only yields figures up to a given time before the arrival of the Rayleigh wave.

The results of the sum is shown in Figure 128.

APPENDIX 12

The solution of equation (242)

The source function may be written as the sum of two functions:

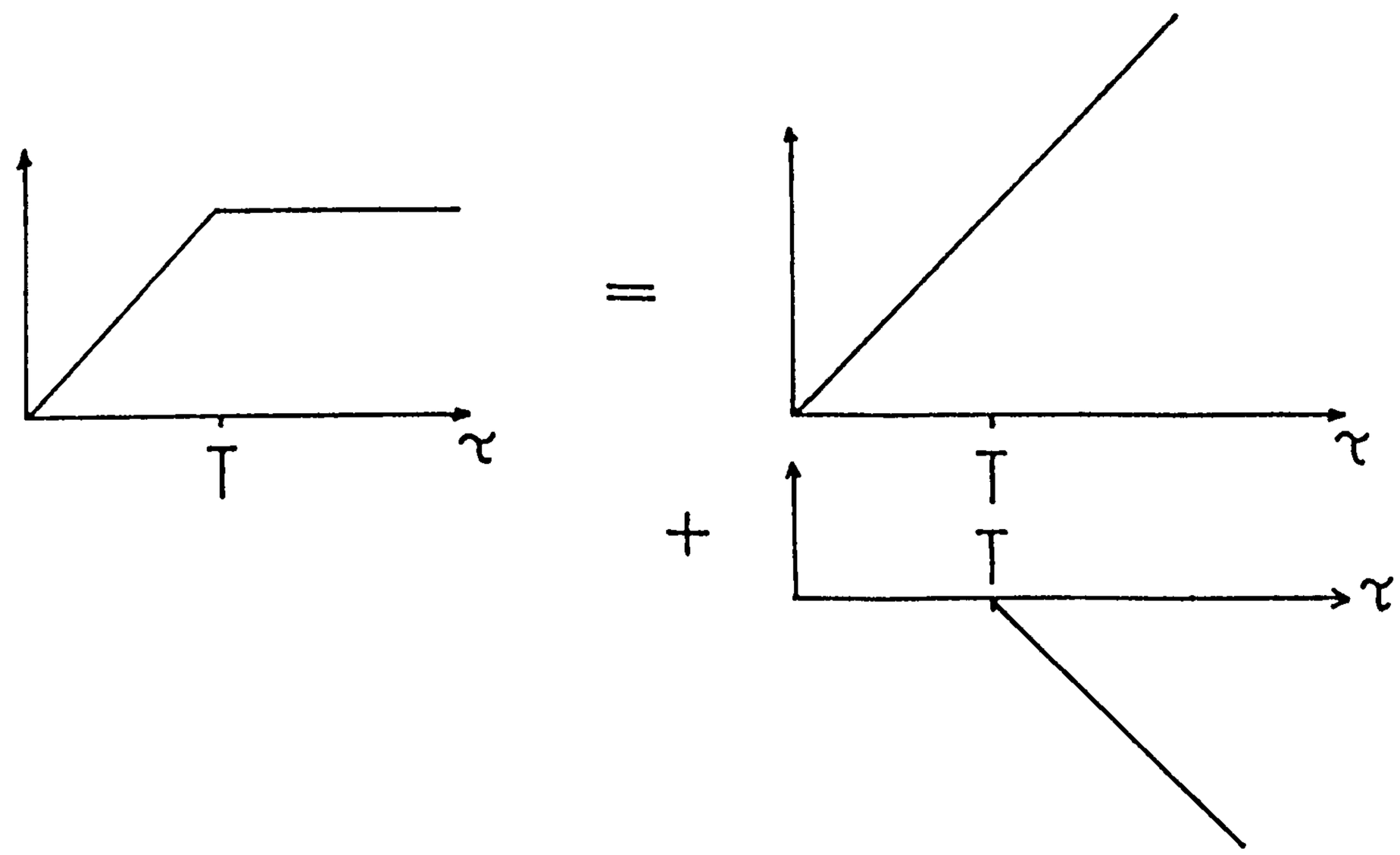

The solution of equation (242) is then simply the sum of the solutions of

$$\alpha \int_{o}^{t} G_{33}{}^{H}(\underline{x},\underline{x}_{o},t-v)dv$$

and

$$-\alpha \int_{T}^{T+t} G_{33}{}^{H}(\underline{x},\underline{x}_{o},(t-T) - v)dv$$

There is then no problem in terminating the convolution integrals.

REFERENCES

1. J. BLITZ, "Ultrasonics: methods and applications" sections 6.2 and 6.3, Publ. London Butterworths.

2. W. SACHSE and N.N. HSU, section IIE from chapter 4 "Ultrasonic transducers for materials testing and their characterization" taken from "Physical Acoustics, Principles and Methods vol XIV", Eds W.P. Mason, R.N. Thurston, Academic Press, New York.

3. J.A. OGILVY and J.A.G. TEMPLE, "Diffraction of elastic waves by cracks: application to time-of-flight inspection", Ultrasonics, pp.259-269, (Nov 1983)

4. D.A. HUTCHINS, "Non-contact ultrasonic transducer for non-destructive testing", Non-destr. Test. Commun. (GB), vol.1, no.2, pp.37-52.

5. A.M. AINDOW, R.J. DEWHURST, D.A. HUTCHINS and S.B. PALMER, "Laser-generated ultrasonic pulses at free metal surfaces", J. Acoust. Soc. Am. 69(2), pp.449-455, (Feb 1981).

6. N.N. HSU and F.R. BRECKENRIDGE, "Characterization and calibration of acoustic emission sensors", Mater. Eval. 39, pp.60-68, (Jan 1981).

7. J.E. MICHEALS, T.E. MICHEALS and W. SACHSE, "Applications of deconvolution to acoustic emission signal analysis", Mater. Eval. 39, pp.1032-1036, (Oct 1981).

8. N.N. HSU and S.C. HARDY, "Experiments in acoustic emission waveform analysis for characterization of AE sources, sensors and structures", from "Elastic Waves and Non-Destructive Testing of Materials AMD" vol.29,

pp.85-106, Ed Y.H. Pao, Publ. The American Society of Mechanical Engineering, 345 East 47th Street, New York, N.Y. 10017, (1978).

9. T.M. PROCTER JR., "An improved piezoelectric acoustic emission transducer", J. Acoust. Soc. Am. 71(5), pp.1163-1168, (May 1982).

10. H.N.G. WADLEY, C.B. SCRUBY and G. SHRIMPTON, "Quantitative acoustic emission source characteristics during low temperature cleavage and inter-granular fracture", Acta Metallurgia, vol.29, pp.399-414.

11. D. ROUBY, P. FLEISCHMANN and C. DUVERGIER, "Un modele de sources d'emission acoustique pour l'analyse de l'emission continue et de l'emission par salves: II verifications experimentales", Phil. Mag. A., vol.47, no.5, pp.689-705, (1983).

12. LORD RAYLEIGH, "On waves propagated along the plane surface of an elastic solid", Proc. Lond. Math. Soc., vol.17, pp.4-11 (1885).

13. Y.H. PAO, R.R. GAJEWSKI and A.N. CERANOGLU, "Acoustic emission and transient waves in an elastic plate", J. Acoust. Soc. Am. 65(1), pp.96-105, (Jan 1979).

14. J. BLITZ, "Ultrasonics: methods and applications", section 4.4, Publ. London Butterworths.

15. A.M. AINDOW, J.A. COOPER, R.J. DEWHURST and S.B. PALMER, "The physics of laser-generated surface acoustic waves in metals", from Quantum Electronics and Electro-Optics, pp.427-430, Ed. P.L. Knight, c 1983 John Wiley & Sons Ltd.

16. F.R. BRECKENRIDGE and M. GREENSPAN, "Surface-wave displacement: absolute measurements using a capacitative transducer", J. Acoust. Soc. Am. 69(4), (April 1981).

17. C.H. PALMER and R.E. GREEN JR., "Materials evaluation by optical detection of acoustic emission signals", Mater. Eval., pp.107-112, (Oct 1977).

18. T. KWAAITAAL, B.J. LUYMES and G.A. VON DER PIJLL, "Noise limitations of Michelson laser interferometers", J. Phys. D. Appl. Phys. 13, pp.1005-1015, (1980).

19. C.L. PEKERIS, "The seismic surface pulse", Proc. Nat. Acad. of Sci. of U.S.A., vol.41, pp.469-480, (1955).

20. C.L. PEKERIS and H. LIFSON, "Motion of the surface of a uniform elastic half space produced by a buried pulse", J. Acoust. Soc. Am., vol.29, no.11, pp.1233-1238.

21. R.J. DEWHURST, D.A. HUTCHINS, S.B. PALMER and C.B. SCRUBY, "The performance of thick piezoelectric transducers as wide-band ultrasonic detectors", Ultrasonics, pp.79-84, (March 1983).

22. A.E. LORD JR., "Acoustic emission" chapter 6 from "Physical Acoustics: Principles and Methods", vol.XI, Eds. W.P. Mason, R.N. Thurston, Publ. Academic Press, New York.

23. H. LAMB, "On the propagation of tremors over the surface of an elastic solid", Phil. Trans. vol.A203, pp.1-42 (1904).

24. L. KNOPOFF, "Surface motions of a thick plate", J. Appl. Phys. 29, pp.661-670, (1958).

25. H.M. MOONEY, "Some numerical solutions for Lamb's problem", Bull Seis. Soc. Am., vol.64, no.2, pp.473-491, (April 1974).

26. A.E. LORD JR,, "Acoustic emission - an update" chapter 4 from "Physical Acoustics: Principles and Methods" vol.XV, Eds. W.P. Mason, R.N. Thurston, Publ. Academic Press, New York.

27. T.W. PROCTER JR., "An improved piezoelectric acoustic emission transducer", J. Acoust. Soc. Am. 71(5), pp.1163-1168, (May 1982).

28. H. DUNEGAN and D. HARRIS, "Acoustic emission - a new non-destructive testing tool", Ultrasonics, vol.7, pp.160-166, (July 1969).

29. D.O. HARRIS and H.L. DUNEGAN, "Acoustic emission - 5.applications of acoustic emission to industrial problems", Non-Destructive Testing, pp.137-144 (1974).

30. R.G. WHITE, M.W. GODFREY and D.C. EMMONY, "Transducer calibration" presented at the XIIth EWGAE meeting in Cologne (1983).

31. P.G. BENTLEY, "Review of developments in acoustic emission for application to nuclear reactor systems", presented at the 2nd International Post-SMIRT Seminar on non-destructive examination in relation to structural integrity, Paris, (24 Aug 1981).

32. C.B. SCRUBY and H.N.G. WADLEY, "A calibrated capacitance transducer for the detection of acoustic emission", J. Phys. D.: Appl. Phys., vol.11, pp.1487-1494, (1978).

33. N.N. HSU and S.C. HARDY, "Experiments in acoustic emission waveform analysis for characterization of AE sources, sensors and structures", from "Elastic Waves and Non-Destructive Testing of Materials AMD - vol.29", pp.85-106, Ed. Y.H. Pao, Publ. The American Society of Mechanical Engineers, 345 East 47th Street, New York 10017, (1978).

34. A.M. AINDOW, J.A. COOPER, R.J. DEWHURST and S.B. PALMER, "The physics of laser-generated surface acoustic waves in metals", pp.427-430 of "Quantum Electronics and Electro-Optics", Ed. P.L. Knight, c 1983 John Wiley & Sons Ltd.

35. F.R. BRECKENRIDGE, C.E. TSCHIEGG and M. GREENSPAN, "Acoustic emission: some applications of Lamb's problem", J. Acoust. Soc. Am., vol.57, no.3, pp.626-631 (March 1975).

36. C.H. PALMER and R.E. GREEN JR., "Optical probing of acoustic emission waves" from "Non-Destructive Evaluation of Materials", Eds. J.J. Burke and V. Weiss, pp.347-378, (Plenum Publ. Corp. 1979).

37. E. HECHT and A. ZAJAC, "Optics", Publ. Addison-Wesley Publishing Co.

38. G.I. STEGEMAN, "Optical probing of surface waves and surface wave devices", IEEE Trans. Sonics. Ultrason. vol.SU-23, no.1, pp.33-63, (Jan 1976).

39. A. CORNEY, "Atomic and laser spectroscopy", Publ. Oxford Science Publications.

40. Product specification for Hughes Corp Helium Neon laser model no. 3222H-PC, c/o Barr & Stroud Ltd., Caxton St.,

Anniesland, Glasgow.

41. A.O. GARG and R.O. CLAUS, "Application of optical fibres to wide-band differential interferometry", Mater. Eval. 41, pp.106-109, (Jan 1983).

42. R. DÄNDLIKER,"Measuring displacement, velocity and vibration by laser interferometry", Laser 81 Opto-Electronik, Munich 1-4 (June 1981).

43. L.E. DRAIN, "The laser Doppler techniques", Publ. Wiley, 1980.

44. S. UEHA, S. SAKUMA and E. MORI, "Measurement of vibration and velocity distributions and mode analysis in thick discs of $Pb(Zr.Ti)O_3$", J. Acoust. Soc. Am., vol.73, no.5, pp.1842-1847, (May 1983).

45. L.E. DRAIN and B.C. MOSS, "The frequency shifting of laser light be electro-optic techniques", Opto-Electronics 4, pp.429-439, (1972).

46. R.P. DEPAULA, J.H. COLE and J.A. BUCARO, "Broadband ultrasonic sensor based on induced optical phase shifts in single-mode fibres", J. Lightwave Technol., vol.LT-1, pp.390-393, (1983).

47. K. FRITSCH and G. ADAMOVSKY, "Simple circuit for feedback stabilization of a single mode fibre interferometer", Rev. Sci. Instrum. 52(7), pp.996-1000, (July 1981).

48. R. KASHYAP and B.K. NAYAR, "A single-mode fibre Michelson interferometer sensor", 1st Int. Conf. on Optical Fibre Sensors, pp.38-42, (26-28 April 1983).

49. R.L. JUNGERMANN, J.E. BOWERS, J.B. GREEN and G.S. KINO, "Fibre optic laser probe for acoustic wave measurements", App. Phys. Lett., vol.40, no.4, pp.313-315, (15 Feb 1982).

50. E.R. PECK and S.W. OBETZ, "Wavelength or length measurement by reversible fringe counting", J. Opt. Soc. Am., vol.43, no.6, pp.505-509, (June 1953).

51. D. VILKOMERSON, "Measuring pulsed picometer displacements vibrations by optical interferometry", Appl. Phys. Lett. 29, pp.183-185, (1976).

52. R. REIBOLD, W. MOLKENSTRUCK, "Laser interferometric measurement and computerized evaluation of ultrasonic displacements", Acustica (Ger), vol.49, no.3, pp.205-211, (Nov 1981).

53. J.H. SPEAKE, "An absolute method of calibrating ultrasonic transducers using laser interferometry", from "Conference on the evaluation and calibration of ultrasonic transducers", London 11-12 May 1977, pp.106-114, Publ. IPC Science and Technology Press.

54. A. OLSSEN, C.L. TANG and E.L. GREEN, "Active stabilization of a Michelson interferometer by an electrooptically tuned laser", Appl. Optics, vol.19, no.12, pp.1897-1899, (15 June 1980).

55. A.N. BONDARENKO, YU.B. DROBOT and S.V. KRUGLOV, "Optical excitation and detection of nanosecond acoustic pulses in non-destructive testing", Sov. J. Nondest. Test., vol.12, pp.655-658, (1976).

56. "Piezoelectric ceramics" eds. J. van Randeraat, R.E. Setterington, Publ. Mullard Ltd., Mullard House,

Torrington Place, London, chapter 2.

57. As reference 56, chapter 4.

58. S. YAMASHITA, "Piezoelectric pile", Jpn. J. Appl. Phys. (Japan), vol.20, suppl.20-4 , pp.93-95, (1981), (Proc. 3rd meeting on Ferroelectric Materials and their Applications, Kyoto, Japan, 20-22 May 1981).

59. C.B. SCRUBY, J.C. COLLINGWOOD and H.N.G. WADLEY, "A new technique for the measurement of acoustic emission transients and their relationship to crack propagation", J. Phys. D. Appl. Phys., vol.11, pp.2359-2369, (1978).

60. N.N. HSU, J.A. SIMMONS and S.C. HARDY, "An approach to acoustic emission signal analysis - theory and experiment", Mater. Eval., vol.35, no.10, pp.100-106, (Oct 1977).

61. W. SACHSE and N.N. HSU, "Ultrasonic transducers for materials testing and their characterization", sections IIA and IIB of chapter 4 taken from "Physical Acoustics: Principles and Methods, vol.XIV", eds W.P. Mason, R.N. Thurston, Publ. Academic Press, New York.

62. R. REIBOLD and W. MOLKENSTRUCK, "Laser interferometric measurement and computerized evaluation of ultrasonic displacements", Acustica (Ger), vol.49, no.3, pp.205-211, (Nov 1981).

63. M.L. BOAS, "Mathematical methods in the physical sciences", Publ. Wiley.

64. N.N. HSU and D.G. EITZEN, "The inverse problem of acoustic emission - explicit determination of acoustic

emission source time-functions", pp.405-412 from "Review of Progress in Quantitative Non-destructive Evaluation", vol.1, Eds. D.O. Thompson, D.E. Chimenti, Proc. 8th Air Force/Defence Advanced Research Projects Agency, Symp. on Quant. NDE Aug 2-7, 1981, Boulder Co.

65. W. SACHSE and A. CERANOGLU, "Absolute ultrasonic measurements with piezoelectric transducers", pp.350-355 from conf: 1979 Ultrasonics Symp., Proc IEEE Cat. No. 79CH1482-959, IEEE NY (1979).

66. W. SACHSE and A. CERANOGLU, "Experiments with a well characterized acoustic emission system", pp.138-145 from conf: Ultrasonics International 1979, Publ. IPC Science and Technology Press, Guildford, England.

67. N. OHISA and T. KISHI, "Response characterization of piezoelectric transducers and wave media for acoustic emission source wave analysis" from Proc. of 1982 Joint Conference of Experimental Mechanics, Society for Experimental Stress Analysis.

68. T.M. PROCTER, F.R. BRECKENRIDGE and Y.H. PAO, "Transient waves in an elastic plate: theory and experiment compared", J. Acoust. Soc. Am. 74(6), pp.1905-1907, (Dec 1983).

69. R.M. WHITE, "Generation of elastic waves by transient surface heating", J. App. Phys., vol.34, no.12, pp.3559-3567, (Dec 1963).

70. M.P. FELIX, "Laser generated ultrasonic beams", Rev. Sci. Instrum, vol.45, no.9, pp.1106-1108, (Sept 1974).

71. W. SACHSE and N.N. HSU, section IIIB of chapter 4 "Ultrasonic transducer for materials testing and their characterization", from "Physical Acoustics: Principles and Methods, vol.XIV", eds. W.P. Mason, R.N. Thurston, Publ. Academic Press, New York.

72. C.B. SCRUBY, R.J. DEWHURST, D.A. HUTCHINS and S.N. PALMER, "Quantitative studies of thermally generated elastic waves in laser-irradiated metals", J. Appl. Phys. 51(12), pp.6210-6216, (Dec 1980).

73. D.A. HUTCHINS, R.J. DEWHURST, S.B. PALMER and C.B. SCRUBY, "Laser generation as a standard acoustic emission source in metals", Appl. Phys. Lett. 38(9), pp.677-679, (1 May 1981).

74. D.A. HUTCHINS, R.J. DEWHURST and S.B. PALMER, "Directivity patterns of laser generated ultrasound in aluminium", J. Acoust. Soc. Am. 70(5), pp.1362-1369, (Nov 1981).

75. C.B. SCRUBY, H.N.G. WADLEY, R.J. DEWHURST, D.A. HUTCHINS and S.B. PALMER, "A laser generated standard acoustic emission source", Mater. Eval. 39, pp.1250-1254, (Dec 1981).

76. R.J. DEWHURST, D.A. HUTCHINS and S.B. PALMER, "Quantitative measurements of laser generated acoustic waveforms", J. Appl. Phys. 53(6), pp.4064-4071, (June 1982).

77. H.N.G. WADLEY, C.K. STOCKTON, J.A. SIMMONS, M.ROSEN, S.D. RIDDER and R. MEHRABIAN, "Quantitative acoustic emission studies for materials processing", pp.421-431

from "Review of Progress in Quantitative Non-Destructive Evaluation", vol.1, Eds. D.O. Thompson, D.E. Chimenti.

78. W. SACHSE and N.N. HSU, section IVD of chapter 4 "Ultrasonic transducers for materials testing and their characterization" from "Physical Acoustics: Principles and Methods vol.XIV", Eds. W.P. Mason, R.N. Thurston, Publ. Academic Press, New York.

79. A.E. LORD JR., section IX from chapter 4 "Acoustic emission - an update" taken from "Physical Acoustics: Principles and Methods vol.XV", Eds. W.P. Mason, R.N. Thurston, Publ. Academic Press, New York.

80. N.N. DMITREVSKII, L.E. PAVLOV and S.V. SIL'VESTROV, "Application of the impedance method for determining the sensitivity of piezoelectric sound receivers", Sov. Phys. Acoust., vol.22, no.3, pp.201-203, (May-June 1976).

81. J.C. BABOUX, F. LAKESTANI, P. FLEISCHMANN and M. PERDIX, "Calibration of ultrasonic transmitters", NDT Int., vol.10, pp.135-138, (June 1977).

82. H. HALTANO, and E. MORI, "Acoustic emission transducer and its absolute calibration", J. Acoust. Soc. Am., vol.59, no.2, pp.344-349, (Feb 1976).

83. Y. HIGO, K. TAKASHIMA, S. NUNOMURA, H. NAKANURA and A. WADA, "On a new real-time calibration method for the acoustic emission measurement system with transducer, specimen and waveguide", pp.103-114 from 5th Intern. Acoustic Emission Symp., Tokyo, (1980).

84. A.E. LORD JR., section XI of chapter 4, "Acoustic emission - an update", taken from "Physical Acoustics: Principles and Methods vol.XV", Eds. W.P. Mason, R.N. Thurston, Publ. Academic Press, New York.

85. T. KISHI and T. OHIRA, "Dynamic crack growth during pop-in fracture in 7075 aluminium alloy", Trans. of the Japan Inst. of Metals, vol.24, no.4, pp.255-263, (April 1983), Publ. The Japan Institute of Metals.

86. K. TAKASHIMA, Y. HIGO and S. NUNOMURA, "Determination of the duration of transient phenomena by frequency-domain analysis of acoustic emission", Phil. Mag. A., vol.49, no.2, pp.221-229, (1984).

87. K. TAKASHIMA, Y. HIGO and S. NUNOMURA, "The propagation velocity of the martensitic transformation in 304 stainless steel", Phil. Mag. A., vol.49, no.2, pp.231-241, (1984).

88. Y. HIGO, K. TAKASHIMA and S. NUNOMURA, "The propagation velocity of Martensitic transformation in 304 stainless steel, measured by AE frequency analysis", to be published in "Proc. of Institute of Acoustics" 5th Intern. Conf. of Photoacoustic Spectroscopy, Dec 19-21, Chelsea College, London, (1983).

89. D. EITZEN, F. BRECKENRIDGE, R. CLOUGH, N.N. HSU, T. PROCTER and J. SIMMONS, "NBS developments in quantitative acoustic emission measurements", pp.433-442 from "Review of Progress in Quantitative Non-Destructive Evaluation", vol.1, Eds. D.O. Thompson and D.E. Chimenti.

90. M. SHIBATA, "A theoretical evaluation of acoustic emission signals - the rise time effect of dynamic forces", Mater. Eval. 42, pp.107-115 and pp.120, (Jan 1984).

91. A. NIELSON, "Acoustic emission source based on pencil lead breaking", Publ. The Danish Welding Institute, Copenhagen (1980), DK-2600 Glostrup, Copenhagen, Park Allé, 345 Denmark.

92. H.E. HJELMROTH, "Two types of artificial AE sources", Publ. The Danish Welding Institute, Copenhagen (1981), DK-2600 Glostrup, Copenhagen, Park Allé, 345 Denmark.

93. L.J. GRAHAM and G.A. ALERS, "Broadband ultrasonic attenuation measurements in unusual materials", Conf. Ultrason. Symp. Proc. IEEE Cat. No. 74CHO896-1 SU pp.703-706, (1974).

94. W.J. PARDEE and L.J. GRAHAM, "Analysis of acoustic emission frequency spectra", Conf. Ultrason. Symp. Proc. IEEE Cat. No. 75CHO994-4 SU, pp.597-600, (1975).

95. T.M. PROCTER JR., "Some details on the NBS conical transducer", J. of Acoust. Emission, vol.1, no.3, pp.173-178.

96. J. NIEWISCH and P. KRAMMER, "A piezoelectric displacement transducer for use in a pulse-shape based analysis of acoustic emission", Sensors and Actuators 3, pp.187-193, (1982/1983).

97. R.M. BOZARTH, chapter 13 "Stress and magnetostriction" taken from "Ferromagnetism", Publ. D. van Nostrand Co. Inc., Princeton, New Jersey.

98. A.B. WOOD, F.D. SMITH and J.A. McGEACHY, "A magnetostriction echo depth-recorder", J. Inst. Elec. Eng., vol.76, pp.550-566, (1935).

99. J.B. VETRANO, W.D. JOLLY, "In-service acoustic emission monitoring of reactor pressure vessels", Mater. Eval., vol.30, no.1, pp.9-12, (Jan 1972).

100. L.C. LYNNWORTH, E.P. PAPADAKIS and K.A. FOWLER, "Ultrasound propagation measurements and applications", International Advances in Non-Destructive Testing, vol.5, pp.71-115, (May 1977).

101. L.C. LYNNWORTH and J.E. BRADSHAW, "Magnetostriction transducers for acoustic emission, impulse, vibration and noise analysis", Materials Research and Standards, vol.11, pp.33-36, (Mar 1971).

102. J. GEARY, D. HOLMES and K. ZERINGUE, "Real-time interferogram simulation" from "Optical Interferograms - Reduction and Interpretations", Eds. A.H. Guenther, D.H. Liebenburg, ASTM Special Technical Publication 666.

103. J. MILLMAN and C.C. HALKAIS, "Integrated electronics: analog and digital circuits and systems", Publ. McGraw-Hill, Kogakusha Ltd.

104. Dunegan/Endevco Product information on the 1801 preamplifier, Dunegan/Endevco Ltd, Rancho Viezo Road, San Juan Capistraon, California 92675, U.S.A.

105. R.M. KINGSTON, "Detection of optical and infra-red radiation", Publ. Springer-Verlag, Berlin/Heidelburg/ New York.

106. "HA-2539 very high slew rate wideband operational amplifiers", Harris Systems Ltd., Semiconductor Group, P.O. Box 27, 153 Farnham Road, Slough SL1 4XD, England.

107. "Optics Guide 2", Publ. by Melles Griot Ltd., 15 South Street, Farnham, Surrey.

108. S.A. SELF, "Focussing of spherical Gaussian beams", Appl. Optics, vol.22, no.5, pp.658-661, (1 Mar 1983).

109. F. MANDL, "Statistical physics", Publ. John Wiley & Sons Ltd.

110. D.C. EMMONY, M.W. GODFREY and R.G. WHITE, "A miniature optical acoustic emission transducer", J. Acoust. Emission, vol.1, no.4, pp.263-265, (1982).

111. D.C. EMMONY, M.W. GODFREY and R.G. WHITE, "A miniature optical acoustic emission transducer", pp.533-538 from "Review of Progress in Quantitative Non-Destructive Evaluation", vol.2A, Eds. D.O. Thompson, D.E. Chimenti.

112. A.B. WILLIAMS, "Electronic filter design handbook", Publ. McGraw-Hill, New York.

113. M.J. BEESLEY, "Vibration induced during submerged arc welding", report from Risley Nuclear Labs., UKAEA, (2 Sept 1982).

114. H. HERTZ, taken from Problem no.1, pp.35 of "Theory of elasticity", vol.7 of "Course of Theoretical Physics" by L.D. Landau, E.M. Lifshitz, Publ. Pergamon Press, (1959).

115. N.N. HSU, Acoustic emissions simulator, US Patent 4018084 assigned to Lockheed Aircraft Corp., Burbank

California, (May 1976).

116. A. NIELSON, paper presented at the VIth EWGAE meeting in Rome, (21 Sept 1977).

117. R.G. WHITE, M.W. GODFREY and D.C. EMMONY, "Transducer calibration" presented at the XIIth EWGAE meeting in Cologne, (October 1983).

118. S.P. TIMOSCHENKO and J.N. GOODIER, "Theory of elasticity", 3rd ed., Publ. McGraw-Hill.

119. I.H. HALL, "Deformation of solids", Publ. T. Nelson & Sons Ltd.

120. L.D. CANDAN and E.M. LIFSHITZ, "Theory of elasticity", course of theoretical physics, vol.7, Publ. Pergamon Press, (1959).

121. R. BERKOVITZ, "The FFT: Big-time mathematics comes to audio", DB Sound Eng. Mag. (USA), vol.16, no.8, pp.44-46, (1982).

122. R.G. WHITE, M.W. GODFREY and D.C. EMMONY, "In situ transducer calibration" to be published in "Proc. of the Institute of Acoustics: 5th Intern. Conf. on Acoustic Emission and the 2nd Conf. on Photoacoustic Spectroscopy", (19-21 Dec 1983), Chelsea College, London, England.

123. M.W. GODFREY, R.G. WHITE and D.C. EMMONY, "High-fidelity transducers and their characterization" to be presented at the XIIIth EWGAE meeting, Harwell, Oxford, England, (Oct 1984).

124. D.C. EMMONY, "Diagnostics of the laser-liquid interaction", Journal de Physique, Colloque C9, supplément au n° 11, Tome 41, pp. C9-231→C9-236, (Nov 80).

125. Chapter 4, "Ultrasonic transducers for materials testing and their characterization" taken from "Physical Acoustic: Principles and Methods, vol.XIV", Eds. W.P. Mason, R.N. Thurston, Publ. Academic Press, New York.

126. TELCON METALS LTD., Manor Royal, Crawley, Sussex, "Typical properties of highly magnetostrictive materials".

127. R.G. WHITE and D.C. EMMONY, "Optical and inverse magnetostrictive transduction" presented at the XIth EWGAE meeting, Milan, Italy, (Oct 1982).

128. R.M. BOZORTH, chapter 17, "Change of magnetization with time" taken from "Ferromagnetism", Publ. D. van Nostrand Co, Princeton, New Jersey.

129. H. KOLSKY, Chapter III from "Stress waves in solids", Publ. Dover Publications Inc., New York.

130. P. LORRAIN and D. CORSON, "Electromagnetic fields and waves", W.H. Freeman & Co., San Francisco.

131. R.M. BOZORTH, Chapter 13 "Stress and magnetostriction" taken from "Ferromagnetism", Publ. D. van Nostrand Co. Inc., Princeton, New Jersey.

132. "Piezoelectric ceramics", Eds. J. van Randeraat and R.E. Setterington, chapter II, Publ. Mullard Ltd., Mullard House, Torrington Place, London.

133. R. BRACEWELL, Chapter 3, "Convolution", taken from "The Fourier Transform and its Applications", Publ. McGraw-Hill, New York, pp.24-50, (1965).

134. H. KO and R.F. SCOTT, "Deconvolution techniques for linear systems", Bull Seis. Soc. Am., vol.57, no.6,

pp.1393-1408.

135. I.A. VIKTOROV, "Rayleigh and Lamb waves: Physical theory and applications", Publ. Plenum Press, New York, (1967).

136. F. PRESS and J. HEALY, "Absorption of Rayleigh waves in low-loss media", J. Appl. Phys., vol.28, no.11, pp.1323-1325, (Nov 1957).

137. W.P. MASON, "Physical acoustics and the properties of solids", chapter VIII, Publ. D. van Nostrand Co. Inc., Princeton, New Jersey.

138. E.P. PAPADAKIS, "Ultrasonic attenuation caused by Rayleigh scattering in polycrystalline metals", J. Acoust. Soc. Am., vol.37, no.4, pp.711-717.

139. K.N. VINOGRADOV and G.K. UL'YANOV, "Measurement of the velocity and attenuation of ultrasonic surface waves in hard materials", Sov. Phys. Acoust., vol.5, pp.296-299.

140. H. KOLSKY, Chapter II from "Stress Waves in Solids", Publ. Dover Publications Inc., New York.

IV.1.1ii)b) The brittle fracture of ceramic pencil leads

As mentioned in chapter II, a common artificial source is the fracture of a ceramic pencil lead held in a normal propelling pencil. This source was first suggested independently by both Hsu[115] and Nielson[116]. The surface of the test specimen, in this case the aluminium block, is quasi-statically loaded as the tip of the lead is pushed onto the material. As the pencil is pivoted about the attached collar then the extended section of lead is subjected to higher and higher stresses (Figure 83) until it eventually fractures. Stresses built up in the material surface are then rapidly released producing an ultrasonic pulse. This source is usually termed a Hsu/Nielson source.

Previous studies of this source reviewed in chapter II have not been comprehensive leaving several questions unanswered. For example: where does the negative pulse preceeding the main release (Micheals et al[71]) originate from? What effect does the length and thickness of the lead have? What is the frequency domain reproducibility of the source? What happens if the angle of contact between the lead and the surface is changed?. Various experiments have been performed to attempt to answer these questions and the results will now be given.

IV.1.1ii)b)i) Propagation effects for the surface pulse generated by the fracture of a 0.5mm diameter 2H ceramic pencil lead on an aluminium block

The theoretical surface pulse shown in Figure 5 for